



HAL
open science

Scaling relations and stellar populations of galaxy clusters from their first epochs of assembly to the present

Stefania Amodeo

► **To cite this version:**

Stefania Amodeo. Scaling relations and stellar populations of galaxy clusters from their first epochs of assembly to the present. Astrophysics [astro-ph]. Université Paris sciences et lettres, 2018. English. NNT : 2018PSLEO012 . tel-02110958

HAL Id: tel-02110958

<https://theses.hal.science/tel-02110958>

Submitted on 25 Apr 2019

HAL is a multi-disciplinary open access archive for the deposit and dissemination of scientific research documents, whether they are published or not. The documents may come from teaching and research institutions in France or abroad, or from public or private research centers.

L'archive ouverte pluridisciplinaire **HAL**, est destinée au dépôt et à la diffusion de documents scientifiques de niveau recherche, publiés ou non, émanant des établissements d'enseignement et de recherche français ou étrangers, des laboratoires publics ou privés.

THÈSE DE DOCTORAT
DE L'UNIVERSITÉ PSL
Préparée à l'Observatoire de Paris

**Scaling relations and stellar populations of galaxy clusters
from their first epochs of assembly to the present**

Soutenue par

Stefania AMODEO

Le 20 septembre 2018

Ecole doctorale n° 127

**Astronomie et Astrophysique
d'Île-de-France**

Spécialité

Astronomie et Astrophysique

Composition du jury :

Gerard ROUSSET LESIA - Observatoire de Paris	<i>Président</i>
Adriano FONTANA INAF - Osservatorio Astronomico di Roma	<i>Rapporteur</i>
Jochen WELLER Universitaets - Sternwarte Muenchen	<i>Rapporteur</i>
Andrea BIVIANO INAF - Osservatorio Astronomico di Trieste	<i>Examineur</i>
Florence DURRET Institut d'Astrophysique de Paris	<i>Examineur</i>
David ELBAZ Département d'Astrophysique CEA Saclay	<i>Examineur</i>
Jean-Baptiste MELIN IRFU, CEA, Université Paris-Saclay	<i>Examineur</i>
Simona MEI LERMA – Observatoire de Paris	<i>Directeur de thèse</i>

ABSTRACT

According to the standard cosmological model, the Universe originated by the *Big Bang* singularity and then has undergone an expansion, which is accelerated at present. In the current scenario (Planck Collaboration et al., 2016a), the Universe has a flat geometry, it is composed of 69% of dark energy and 31% of matter; 5% of the matter component is baryonic and the rest is dark matter, which does not interact electromagnetically. Within this so-called *concordance* model structure formation takes place from the gravitational collapse of small perturbations in a quasi-homogeneous Universe, dominated by Cold Dark Matter (Peebles, 1993). These primordial fluctuations are believed to have arisen in an early inflationary era, and then have collapsed by self-gravity against the expansion pressure.

In this framework, the collapse proceeds from smaller to larger scales, in a *bottom up* sequence, giving rise to a hierarchical clustering of cosmic structures (Press and Schechter, 1974; Gott and Rees, 1975; White and Rees, 1978). In this context, galaxy clusters are important tools for understanding the formation and evolution of cosmic structures, being the largest and the last structures to form, through accretion and mergers of smaller structures. They typically contain hundreds to thousands galaxies in a region of virial radius ~ 1 Mpc but these constitute only the $\sim 5\%$ of their total composition. The $\sim 10\%$ consists of an intracluster gas at hot temperature ($T \sim 10^8$ K) and with low density ($n_{\text{gas}} \sim 10^{-3} \text{cm}^{-3}$); the remaining $\sim 85\%$ is dark matter (Peebles, 1993, and references therein).

Measurements of the number counts of galaxy clusters as a function of redshift can provide powerful constraints on cosmological parameters (Allen, Evrard, and Mantz, 2011; Kravtsov and Borgani, 2012; Weinberg et al., 2013). In fact, the cluster mass function (number of clusters of a given mass per unit comoving volume, at a given redshift) gives a direct measurement of the density perturbation amplitude at the present epoch, σ_8 , while its evolution with redshift is a function of the matter density of the Universe, Ω_m . The steps needed to measure the cluster mass function are: 1) detect clusters through large surveys and measure their redshift, 2) determine the surveyed volume and the survey selection function, 3) estimate the cluster masses through scaling relations with the survey observables, 4) count clusters as a function of mass and redshift, and 5) take into account statistic and systematic errors.

Surveys based on the Sunyaev-Zeldovich (SZ) effect (Sunyaev and Zeldovich, 1970; Birkinshaw, 1999; Carlstrom, Holder, and Reese, 2002), have revolutionized this field providing large mass-selected samples of clusters suitable for this cosmological analysis. In fact, since the integrated SZ flux is independent of distance, it does not suffer from cosmological dimming and it is also proportional to the cluster mass. The *Planck* satellite, launched on 2009 May 14, provided for the first time the possibility of detecting galaxy clusters through the SZ effect in a full sky survey. So far, it has provided a large sample of 1653 clusters detected via the SZ effect in the redshift range $[0.01, 0.97]$, and in the estimated mass range $[0.79, 16.12] \times 10^{14} M_{\odot}$, 439 of which have a high detection significance

(signal-to-noise larger than 4.5) and are used to constrain cosmological parameters from the cluster number counts (Planck Collaboration et al., 2014a, 2016b).

However, since the SZ effect does not provide redshift, dedicated follow-up programs are required to make the resulting catalogs scientifically useful. The *Planck* collaboration has undertaken a large follow-up effort to confirm cluster candidates and measure their redshifts. The first optical follow-up was based on observations with the Russian-Turkish 1.5 m telescope (Planck Collaboration et al., 2015c) and provided spectroscopic redshifts of 65 *Planck* clusters. The second optical follow-up, based on observations with telescopes at the Canary Islands Observatories, yielded 53 cluster spectroscopic redshifts (Planck Collaboration et al., 2016c). Recently, Barrena et al. (2018) and Streblyanska et al. (2018) reported on new optical follow-up observations of *Planck* cluster candidates at the Roque de los Muchachos Observatory. They confirm 53 and 37 clusters, respectively, by analysing the optical richness, the 2D galaxy distribution, and the velocity dispersions of clusters. The *Planck* collaboration has also carried out X-ray validation programs with XMM-Newton (Planck Collaboration et al., 2011a, 2012, 2013), where redshifts for 51 clusters were obtained from X-ray spectral fitting.

The first part of this thesis is dedicated to our own spectroscopic follow-up of 20 *Planck* cluster candidates with the Gemini and Keck telescopes (P.I. J.G. Bartlett and F.A. Harrison, respectively), for which we measured redshifts and velocity dispersions from member galaxies. Cluster members for spectroscopic follow-up were selected from our own Palomar, Gemini and Keck optical and (in some cases) infrared imaging, and SDSS (Sloan Digital Sky Survey; York et al., 2000) public imaging. Seven cluster redshifts were measured spectroscopically for the first time with this observing campaign, including one of the most distant *Planck* clusters confirmed to date, at $z = 0.782 \pm 0.010$, PSZ2 G085.95+25.23. For all these clusters we measured velocity dispersions.

This work is published in Amodeo et al. (2018), enclosed in Appendix B, and our catalogs were made public.

The second goal of this program was to have a sample of clusters covering a wide range of mass in order to obtain a statistical calibration of the *Planck* SZ mass estimator, which has become a hot topic since the *Planck* analysis uncovered a tension between the cosmological parameters determined from anisotropies in the cosmic microwave background (CMB) and those derived from cluster abundance measurements. To reconcile the *Planck* cluster constraints with those of the primary CMB requires a “mass bias” parameter of $(1 - b) = 0.58 \pm 0.04$, where $(1 - b)$ is the ratio between the mass determined by *Planck* and true cluster mass. This tension could indicate the need for new physics, such as non-minimal neutrino mass, or an important revision of the cluster mass scale. In fact, the estimate of cluster masses (step 3 above) is a crucial step that inevitably limits the precision of cluster cosmology because the cluster mass is not a directly observable quantity (Allen, Evrard, and Mantz, 2011). Mass can be estimated through several independent methods based on different physical properties that are each affected by their own set of specific systematic effects. Methods are based on the analysis of the thermal emission of the intracluster medium (ICM), observed either through the SZ effect or in the X-

rays, the dynamics of member galaxies, and gravitational lensing. Comparison of mass estimates using different techniques is a critical check on the reliability of each method under different conditions, and also a test of the cosmological scenario.

I have studied the scaling relation between the cluster velocity dispersion, calculated using redshifts from our optical spectroscopy, and the *Planck* SZ mass proxy, based on ICM properties, of a subsample of 17 clusters from our follow-up program. I have analyzed possible sources of systematics in the mass calibration, accounting for: *i*) effects due to finite aperture of the telescope, *ii*) Eddington bias, *iii*) correlated scatter between velocity dispersion and the *Planck* mass proxy, and *iv*) the ratio between the velocity dispersion of DM particles and that of galaxies in simulations, known as “velocity bias”, b_v , which quantifies how well the galaxy velocity dispersion traces the dark matter velocity dispersion.

Interestingly, the result for the mass bias parameter depends on the cube of the value of the galaxy velocity bias, which value is still under debate among different simulations. Therefore, the unknown velocity bias, of the member galaxy population, is the largest source of uncertainty in our result on the mass bias. Using a velocity bias of $b_v = 1.08$ from Munari et al. (2013), I obtain a mass bias of 0.64 ± 0.11 (i.e., I estimate that *Planck* masses are about 36% lower than the true masses), with an uncertainty of 17% with 17 clusters only, and it is within 1σ of the value needed to reconcile the *Planck* cluster counts with the primary CMB.

Turning my analysis around, I obtain observational constraints on the velocity bias by combining mass estimates from weak lensing measurements with velocity dispersion measurements. Assuming a prior on the mass bias from combined *Planck* and weak lensing observations from Penna-Lima et al. (2017), I derive $b_v \gtrsim 0.9$ at 3σ , excluding models that predict a negative velocity bias (e.g., Caldwell et al., 2016).

This analysis is published in Amodeo et al. (2017), enclosed in Appendix B.

The uncertainty of 17% on the mass bias is promising given the small sample, and shows that this technique is competitive with other methods, like gravitational lensing. Currently, the mass calibration is dominated by systematics that are of the order of 10%, but forthcoming cosmological surveys require an accuracy of few %, to be achieved with: 1) a larger sample of clusters especially extended to low masses ($< 5 \times 10^{14} M_\odot$), where still few objects have been detected, and 2) at higher redshift, to probe a possible evolution with time of the mass–observable scaling relation.

The *Euclid* mission will revolutionize this field of research with the discovery of thousands of clusters and proto-clusters at $z > 1.2$ and $M > 10^{14} M_\odot$ (Lau-reijs et al., 2011; Ascaso et al., 2017), which permit to double the figure of merit for cosmological constraints (Sartoris et al., 2016).

Characterizing galaxies and their stellar populations will be important to drive *Euclid* and other future surveys towards the search of this class of objects based on photometric redshifts. To obtain reliable photometric redshifts, it is important to know the observed spectral energy distributions/colors of galaxies at the redshift of interest.

In fact, selecting clusters based on galaxies of same color is one of the most promising method for optical and infrared surveys. Algorithms based on galaxy colors search for overdensities of galaxies of given colors. For example, at $z < 1$, they search for overdensities of red early type galaxies in the color-magnitude diagram, based on the observational evidence that large populations of this kind of objects can be found in the inner regions of galaxy clusters (Gladders and Yee, 2000; Thanjavur, Willis, and Crampton, 2009; Rykoff et al., 2014; Licitra et al., 2016b,a).

The second part of this thesis is devoted to the study of stellar populations in clusters and proto-clusters at high redshift, from the CARLA (Clusters Around Radio-Loud AGN) survey, with the goal to better characterize their galaxy colors and optimize their search with future surveys, such as the *Euclid* space mission surveys.

The CARLA survey targets powerful radio-loud AGNs since they are known to reside in dense environments (Wylezalek et al., 2013). It consists in a 400 hr Warm Spitzer program which has originally observed 420 radio-loud AGNs in the interval $1.3 < z < 3.2$, in two bands of the Infrared Array Camera (IRAC), $3.6\mu\text{m}$ and $4.5\mu\text{m}$. We identified galaxy cluster candidates as overdensities of galaxies with color $([3.6] - [4.5])_{\text{AB}} > -0.1$ (Wylezalek et al., 2013). The CARLA twenty densest cluster candidates, which span the redshift range $1.4 < z < 2.8$, have been observed with HST/WFC3 G141 slitless grism spectroscopy and F140W imaging (Noirot et al., 2016, 2018). Sixteen targets were confirmed according to the Eisenhardt et al. (2008) criteria to define a spectroscopically confirmed galaxy cluster. We also classified them according to the density of galaxy members with respect to the field. Eight of the sixteen confirmed candidates were also observed in the i-band with the auxiliary-port camera (ACAM; Benn, Dee, and Agócs, 2008) on the 4.2m William Herschel Telescope (WHT) in La Palma and the Gemini Multi-Object Spectrograph South instrument (GMOS-S; Hook et al., 2004) on Gemini-South in Chile (Cooke et al., 2015, 2016).

In this PhD thesis, I analyze the sixteen confirmed cluster candidates to characterize their galaxy population. I optimize a joint photometric analysis of Spitzer, HST, and ground-based optical images, taking advantage of the information given by the high-resolution ($0.06 \text{ arcsec pix}^{-1}$) F140W HST images, and use positions and surface brightness profiles of sources measured on F140W HST images as priors to derive PSF-matched fluxes in all the other bands. I derive photometry using the T-PHOT software (Merlin et al., 2015, 2016). This method allows to de-blend cluster members from fore- or background sources in the optical and Spitzer images and obtain robust photometric results. I discuss the cluster galaxy color-magnitude diagram and the existence of a red sequence, and the color-color diagrams to separate the passive and star-forming galaxies.

For the first time, this analysis has been performed on an homogeneous statistical sample of spectroscopically confirmed clusters at high redshift, ideal to investigate galaxy evolution in dense environments.

This work will be published in two papers in preparation, one of which I am the lead author (S. Amodeo et al., and S. Mei, S. Amodeo et al.).

This PhD thesis was performed within two collaborations. In the text and in the abstract, I use the pronoun “we” when referring to the effort of the entire collaboration, and the pronoun “I” when I describe my specific contribution. I use past verbs to indicate what was done before the thesis, and present verbs for what was done during the thesis.

RÉSUMÉ

Selon le modèle cosmologique standard, l'Univers est né de la singularité du Big Bang et puis il a subi une expansion, qui s'accélère actuellement. Dans le scénario actuel (Planck Collaboration et al., 2016a), l'Univers a une géométrie plate, il est composé de 69% d'énergie sombre et 31% de la matière; 5% de la matière est baryonique et le reste est de la matière noire qui n'interagit pas électromagnétiquement. Dans le cadre de ce modèle, dit de *concordance*, la formation des structures se produit à partir de l'effondrement gravitationnel de petites perturbations dans un Univers quasi-homogène, dominé par de la matière noire froide. On pense que ces fluctuations primordiales se sont produites au début de l'ère inflationniste, puis se sont effondrées par gravité contre la pression d'expansion. Dans ce cadre, l'effondrement passe d'une échelle plus petite à une échelle plus grande, dans un contexte dit *bottom up*, donnant lieu à un regroupement hiérarchique de structures cosmiques (Press and Schechter, 1974; Gott and Rees, 1975; White and Rees, 1978).

Dans ce contexte, les amas de galaxies sont des outils importants pour comprendre la formation et l'évolution des structures cosmiques, étant les plus grandes et les dernières structures à se former, par accréation et fusion de structures plus petites. Ils contiennent typiquement des centaines à des milliers de galaxies dans une région de rayon viriel ~ 1 Mpc, mais ceux-ci ne constituent que le $\sim 5\%$ de leur composition total. Le $\sim 10\%$ est constitué d'un gaz intra-amas à température chaude ($T \sim 10^8$ K) et à faible densité ($n_{\text{gas}} \sim 10^{-3} \text{ cm}^{-3}$); le $\sim 85\%$ restant est de la matière noire (Peebles, 1993, et les références qu'il contient).

Les mesures du nombre d'amas de galaxies en fonction du décalage vers le rouge ("*redshift*") peuvent fournir de puissantes contraintes sur les paramètres cosmologiques (Allen, Evrard, and Mantz, 2011; Kravtsov and Borgani, 2012; Weinberg et al., 2013). En fait, la fonction de masse des amas (nombre d'amas avec une masse donnée par unité de volume comobile, à un redshift donné) donne une mesure directe de l'amplitude de la perturbation de densité à l'époque actuelle, σ_8 , alors que son évolution avec le redshift est une fonction de la densité de matière de l'Univers, Ω_m . Les étapes nécessaires pour mesurer la fonction de masse des amas sont les suivantes: 1) détecter les amas au moyen de grandes enquêtes et mesurer leur redshift, 2) déterminer le volume de l'enquête et la fonction de sélection de l'enquête, 3) estimer les masses des amas au moyen de relations d'échelle avec les variables observables de l'enquête, 4) compter les amas en fonction de la masse et du redshift, et 5) tenir compte des erreurs statistiques et systématiques.

Les études basées sur l'effet Sunyaev-Zeldovich (SZ) (Sunyaev and Zeldovich, 1970; Birkinshaw, 1999; Carlstrom, Holder, and Reese, 2002), ont révolutionné ce domaine en fournissant de grands échantillons d'amas sélectionnés par leur masse, appropriés pour cette analyse cosmologique. En effet, le flux SZ intégré étant indépendant de la distance, il ne souffre pas de gradation cosmologique et il est également proportionnel à la masse de l'amas. Le satellite *Planck* lancé le 14 mai 2009, a fourni pour la première fois la possibilité de détecter des

amas de galaxies grâce à l'effet SZ dans une étude complète du ciel. Jusqu'à présent, il a fourni un large échantillon de 1653 clusters détectés par l'effet SZ dans l'intervalle de redshift $[0.01, 0.97]$ et dans l'intervalle de masse estimée $[0.79, 16.12] \times 10^{14} M_{\odot}$, dont 439 ont une signification de détection élevée (rapport signal/bruit supérieur à 4.5) et sont utilisés pour contraindre les paramètres cosmologiques à partir du nombre d'amas (Planck Collaboration et al., 2014a, 2016b).

Cependant, comme l'effet SZ ne fournit pas de redshift, des programmes de suivi dédiés sont nécessaires pour rendre les catalogues résultants scientifiquement utiles. La collaboration *Planck* a entrepris un vaste effort de suivi pour confirmer les amas candidats et mesurer leurs redshifts. Le premier suivi optique était basé sur des observations avec le télescope russo-turcissique de 1,5 m (Planck Collaboration et al., 2015c) et a fourni les redshift de 65 amas *Planck*. Le deuxième suivi optique, basé sur des observations avec des télescopes aux observatoires des îles Canaries, a donné 53 redshifts spectroscopiques (Planck Collaboration et al., 2016c). Récemment, Barrena et al. (2018) et Streblyanska et al. (2018) ont publié de nouvelles observations optiques de suivi des amas candidats à l'Observatoire Roque de los Muchachos. Ils confirment 53 et 37 amas, respectivement, en analysant la richesse optique, la distribution des galaxies 2D et la distribution des vitesses.

La collaboration de *Planck* a également réalisé des programmes de validation dans les rayons X avec *XMM-Newton* (Planck Collaboration et al., 2011a, 2012, 2013), où les redshifts de 51 amas ont été obtenus à partir des spectres en rayons X.

La première partie de cette thèse est consacrée à notre propre suivi spectroscopique de 20 candidats *Planck* à l'aide des télescopes Gemini et Keck (P.I. J.G. Bartlett et F.A. Harrison, respectivement), pour lesquels nous avons mesuré les redshifts et les dispersions de vitesse des galaxies membres. Les membres des amas pour le suivi spectroscopique ont été choisis parmi notre propre imagerie optique et (dans certains cas) infrarouge avec Palomar, Gemini et Keck, et l'imagerie publique de SDSS (Sloan Digital Sky Survey; York et al., 2000). Sept redshifts d'amas ont été mesurés par la spectroscopie pour la première fois avec cette campagne d'observation, y compris l'une des amas *Planck* les plus lointains confirmée à ce jour, à $z = 0.782 \pm 0.010$, PSZ2 G085.95+25.23. Pour tous ces amas, nous avons mesuré les dispersions de vitesse.

Ce travail est publié dans l'article Amodeo et al. (2018), en annexe B, et nos catalogues ont été rendus publics.

Le deuxième objectif de ce programme était d'avoir un échantillon d'amas couvrant un large intervalle de masse afin d'obtenir un étalonnage statistique de l'estimateur de masse *Planck* SZ, qui est devenu un sujet d'actualité depuis que l'analyse *Planck* a mis en évidence une tension entre les paramètres cosmologiques déterminés à partir des anisotropies dans le fond diffus cosmologique (CMB) et ceux dérivés des mesures de l'abondance des amas. Pour réconcilier les contraintes des amas *Planck* avec celles du CMB primaire, il faut un paramètre de "biais de masse" de $(1 - b) = 0,58 \pm 0,04$, où $(1 - b)$ est le rapport entre la masse déterminée par *Planck* et la masse réelle de l'amas. Cette tension pourrait indiquer la nécessité d'une nouvelle physique, comme

une masse non minimal des neutrinos, ou une révision importante de l'échelle de masse des amas. En fait, l'estimation des masses d'amas (étape 3 ci-dessus) est une étape cruciale qui limite inévitablement la précision de la cosmologie des amas parce que la masse des amas n'est pas une quantité directement observable (Allen, Evrard, and Mantz, 2011). La masse peut être estimée à l'aide de plusieurs méthodes indépendantes basées sur propriétés physiques différentes qui sont chacune affectées par leur propre ensemble d'effets systématiques spécifiques. Les méthodes sont basées sur l'analyse de l'émission thermique du milieu intra-amas (ICM), observée soit à travers l'effet SZ ou dans les rayons X, la dynamique des galaxies membres et l'effet de lentille gravitationnelle. La comparaison d'estimations de masse à l'aide de différentes techniques est une vérification critique de la fiabilité de chaque méthode dans des conditions différentes, ainsi qu'un test du scénario cosmologique.

J'ai étudié la relation d'échelle entre la dispersion de la vitesse des amas, calculée en utilisant les redshifts de notre spectroscopie optique, et la mesure de masse *Planck* SZ, basé sur les propriétés de l'ICM, d'un sous-échantillon de 17 amas de notre programme de suivi. J'ai analysé les sources possibles de systématique dans l'étalonnage de masse, en tenant compte de: *i*) effets dus à l'ouverture finie du télescope, *ii*) biais d'Eddington, *iii*) dispersion corrélée entre la dispersion de la vitesse et la mesure de masse *Planck* et *iv*) rapport entre la dispersion de la vitesse des particules de matière noire et celle des galaxies dans les simulations, connu sous le nom de "biais de vitesse", b_v , qui quantifie à quel point la dispersion de la vitesse de la galaxie retrace la dispersion de la vitesse de la matière noire.

Il est intéressant de noter que le résultat du paramètre du biais de masse dépend du cube de la valeur du biais de vitesse de la galaxie, valeur qui fait encore l'objet d'un débat entre les différentes simulations. Par conséquent, le biais de vitesse inconnu, de la population de la galaxie membre, est la plus grande source d'incertitude dans notre résultat sur le biais de masse. En utilisant un biais de vitesse de $b_v = 1.08$ de Munari et al. (2013), j'obtiens un biais de masse de 0.64 ± 0.11 (c.-à-d., j'estime que les masses *Planck* sont environ 36% inférieures aux masses vraies), avec une incertitude de 17% avec 17 clusters seulement, et il est à moins de 1σ de la valeur nécessaire pour réconcilier les comptes des amas *Planck* avec le CMB primaire.

En tournant mon analyse, j'obtiens des contraintes d'observation sur le biais de vitesse en combinant des estimations de masse à partir de mesures de lentilles faibles "*weak lensing*" avec des mesures de dispersion de la vitesse. En supposant un valeur du biais de masse obtenu à partir d'observations combinées de *Planck* et de *weak lensing* par Penna-Lima et al. (2017), je dérive $b_v \gtrsim 0.9$ à 3σ , à l'exclusion des modèles qui prédisent un biais de vitesse négatif (par exemple, Caldwell et al., 2016).

Cette analyse est publiée dans l'article Amodeo et al. (2017), en annexe B.

L'incertitude de 17% sur le biais de masse est prometteuse compte tenu du petit échantillon, et montre que cette technique est compétitive avec d'autres méthodes, comme la lentille gravitationnelle. Actuellement, l'étalonnage de masse est dominé par des systématiques de l'ordre de 10%, mais les prochaines études cosmologiques exigent une précision de quelques %, à réaliser avec : 1)

un plus grand échantillon d'amas particulièrement étendu aux faibles masses ($< 5 \times 10^{14} M_{\odot}$), où encore peu d'objets ont été détectés, et 2) un redshift plus élevé, pour sonder une évolution possible avec le temps de la relation d'échelle masse-observable.

Un progrès fondamental dans ce domaine sera d'avoir un échantillon statistique des amas les plus massifs (traçant les halos les plus massifs de matière noire) à haut redshift. La mission *Euclid* va révolutionner ce domaine de recherche avec la découverte de milliers de amas et de proto-amas à $z > 1.2$ et $M > 10^{14} M_{\odot}$ (Laureijs et al., 2011; Ascaso et al., 2016), ce qui permet de doubler le facteur de mérite pour les contraintes cosmologiques (Sartoris et al., 2016).

La caractérisation des galaxies et de leurs populations stellaires sera importante pour conduire *Euclid* et d'autres études futures vers la recherche de cette classe d'objets basée sur les décalages photométriques. Pour obtenir des décalages photométriques fiables, il est important de connaître les distributions d'énergie spectrale observées et les couleurs des galaxies au redshift d'intérêt.

En fait, la sélection d'amas de galaxies de même couleur est l'une des méthodes les plus prometteuses pour les relevés optiques et infrarouges. Les algorithmes basés sur les couleurs des galaxies recherchent les surdensités des galaxies de couleurs données. Par exemple, à $z < 1$, ils recherchent les surdensités des galaxies rouges de type précoce (*early-type*) dans le diagramme couleur-magnitude, basé sur la preuve d'observation que de grandes populations de ce type d'objets peuvent être trouvées dans les régions internes des amas de galaxies (Gladders and Yee, 2000; Thanjavur, Willis, and Crampton, 2009; Rykoff et al., 2014; Licitra et al., 2016b,a).

La deuxième partie de cette thèse est consacrée à l'étude des populations stellaires en amas et proto-amas à haut redshift, à partir de l'étude CARLA (Clusters Around Radio-Loud AGN), dans le but de mieux caractériser les couleurs de leurs galaxies et d'optimiser leur recherche avec *Euclid*.

L'étude CARLA cible les noyaux actifs radio-bruyants ("*Radio-Loud AGN*") puisqu'ils sont connus pour résider dans des environnements denses (Wylezalek et al., 2013). Il s'agit d'un programme de 400 heures de *Spitzer* qui a initialement observé 420 AGNs radio-bruyants dans l'intervalle $1.3 < z < 3.2$, dans deux bandes de la caméra infrarouge (IRAC), $3.6\mu\text{m}$ et $4.5\mu\text{m}$. Nous avons identifié les amas candidats comme étant des surdensités de galaxies de couleur $([3.6]-[4.5])_{\text{AB}} > 0.1$ (Wylezalek et al., 2013). Les vingt amas candidats les plus denses de CARLA, qui couvrent l'intervalle de redshift $1.4 < z < 2.8$, ont été observés avec la spectroscopie HST/WFC3 G141 et l'imagerie F140W (Noirot et al., 2016, 2018). Seize amas ont été confirmés selon les critères de Eisenhardt et al. (2008) pour définir un amas de galaxies confirmé par spectroscopie. Nous les avons également classés en fonction de la densité des galaxies membres par rapport au champ. Huit des seize candidats confirmés ont également été observés dans la bande *i* avec la caméra à port auxiliaire (ACAM; Benn, Dee, and Agócs, 2008) sur le télescope William Herschel (WHT) de 4,2 m à La Palma et l'instrument Gemini Multi-Object Spectrograph South (GMOS-S; Hook et al., 2004) sur Gemini-South au Chili (Cooke et al., 2015, 2016).

Dans cette thèse de doctorat, j'analyse les seize amas candidats confirmés pour caractériser leur population de galaxies. J'optimise une analyse photométrique conjointe des images *Spitzer*, HST et des images optiques au sol, en tirant parti de l'information fournie par les images HST F140W à haute résolution ($0,06 \text{ arcsec pix}^{-1}$), et j'utilise les positions et les profils de brillance de surface des sources mesurées sur les images HST F140W pour dériver les flux (appariés aux PSFs) dans toutes les autres bandes. Je dérive la photométrie à l'aide du logiciel T-PHOT (Merlin et al., 2015, 2016). Cette méthode permet de dé-mélanger les membres des amas de sources avant ou arrière dans les images optiques et *Spitzer* et d'obtenir des résultats photométriques robustes.

Je discute les diagrammes couleur-magnitude des galaxies d'amas et l'existence d'une séquence rouge, et les diagrammes couleur-couleur pour séparer les galaxies passives et les galaxies formant des étoiles.

Pour la première fois, cette analyse a été effectuée sur un échantillon statistique homogène d'amas confirmés par la spectroscopie, à haut redshift, idéal pour étudier l'évolution des galaxies dans des environnements denses.

Ce travail sera publié dans deux articles en préparation, (S. Amodeo et al. et S. Mei, S. Amodeo et al.).

Cette thèse de doctorat a été réalisée dans le cadre de deux collaborations. Dans le texte et dans le résumé, j'utiliserai le pronom "nous" pour faire référence à l'effort de toute la collaboration, et le pronom "je" lorsque je décris ma contribution spécifique. J'utilise des verbes passés pour indiquer ce qui a été fait avant la thèse, et des verbes présents pour ce qui a été fait pendant la thèse.

CONTENTS

1	THE Λ CDM COSMOLOGICAL MODEL	1
1.1	Basic principles	1
1.2	Formation and evolution of cosmic structures	3
1.2.1	The linear evolution of density perturbations	4
1.2.2	The power spectrum of density perturbations	6
1.2.3	The spherical top-hat collapse	7
1.2.4	The halo mass function	9
1.3	The concordance model	9
2	GALAXY CLUSTERS	11
2.1	Observable properties	11
2.1.1	Optical and near-infrared bands	11
2.1.2	X-ray band	16
2.1.3	The Sunyaev-Zeldovich effect	19
2.1.4	Gravitational lensing	21
2.1.5	CMB halo lensing	24
2.2	Comparison of mass proxies	25
3	CLUSTERS IN COSMOLOGICAL SURVEYS	27
3.1	Cosmology from cluster counts	27
3.2	The Planck tension	28
3.3	Cluster counts with future surveys	31
3.3.1	Euclid forecasts	33
3.4	Cluster cosmology and this PhD thesis	34
4	CALIBRATING THE GALAXY CLUSTER MASS SCALE WITH VELOCITY DISPERSIONS I: SAMPLE DESCRIPTION	37
4.1	Sample description	37
4.1.1	Gemini observations	38
4.1.2	Keck Observations	39
4.2	Cluster confirmation and measurements of spectroscopic redshifts	41
4.2.1	Discussion	53
5	CALIBRATING THE GALAXY CLUSTER MASS SCALE WITH VELOCITY DISPERSIONS II: RESULTS	55
5.1	The Planck mass proxy	55
5.1.1	The σ -M scaling relation – A cluster model	56
5.1.2	The mass bias and the velocity bias	59
5.1.3	Eddington Bias	63
5.1.4	Correlated Scatter	64
5.2	Discussion	64
5.2.1	Estimating the velocity bias b_v using a prior on the mass bias	66
5.3	Conclusions	66
6	PHOTOMETRIC ANALYSIS OF CLUSTERS AND PROTO-CLUSTERS FROM THE CARLA SURVEY	69
6.1	The sample	70
6.2	Observations	72
6.2.1	Spitzer/IRAC Imaging	72
6.2.2	HST WFC3 Imaging and Spectroscopy	76

6.2.3	Ground Based Optical Imaging	77
6.3	Photometric analysis	77
6.3.1	Source extraction and photometry	78
6.3.2	Estimate of uncertainties	79
6.4	Photometry and structural parameters measurements with GALAPAGOS	81
6.4.1	Photometry validation	82
7	STELLAR POPULATIONS OF HIGH-Z CLUSTERS FROM THE CARLA SURVEY	87
7.1	Ongoing analysis	98
8	COMPLEMENTARY WORKS	99
9	SUMMARY & OUTLOOK	103
A	BRIEF DESCRIPTION OF THE USED SOFTWARE	109
A.1	SExtractor	109
A.2	Swarp	110
A.2.1	Image resampling	111
A.3	PSFex	112
A.4	T-PHOT	112
B	PUBLISHED PAPERS	117
	Acknowledgements	191
	BIBLIOGRAPHY	193

THE Λ CDM COSMOLOGICAL MODEL

In this chapter, I present an overview of the cosmological background that is at the basis of the topics covered in this thesis. If not directly stated with a reference, the content of the following chapter is based on Peebles (1993), Coles and Lucchin (2002), and Borgani (2008).

1.1 BASIC PRINCIPLES

The standard cosmological model is based on the *Cosmological Principle*, which states that the Universe is homogeneous and isotropic on large scales. This means that physical properties are on average the same in different regions and the same laws of physics hold through the Universe.

The presence of cosmic structures on a variety of scales (stars, galaxy, galaxy groups and clusters) seems an obvious observational evidence against the *Cosmological Principle*, but there are in fact several independent observational tests that support it, when accounting for sufficiently large scales, of the order of hundreds of Mpc. The most often cited proof is the Cosmic Microwave Background (hereafter CMB), that has been found to be isotropic to one part in 10^5 , while homogeneity is inferred from isotropy if we exclude to occupy a privileged position in the Universe (*Copernican Principle*).

Gravity is the dominant force on large scales. The theory of gravity at the basis of modern cosmology is the Einstein's General Theory of Relativity, according to which the geometry of the space-time is determined by its content (in terms of energy distribution). The *Einstein field equations* set the relationship between the metric of the space-time, g_{ij} , and the matter-energy content of the Universe described by the relativistic energy-momentum tensor T_{ij} ($i, j = 0, 1, 2, 3$ with 0 indicating the time coordinate and 1, 2, 3 indicating the space coordinates):

$$R_{ij} - \frac{1}{2}g_{ij}R = \frac{8\pi G}{c^4}T_{ij}, \quad (1)$$

where R_{ij} is the Ricci tensor and R is the Ricci scalar. The quantity $8\pi G/c^4$ (G is Newton's gravitational constant, and c is the speed of light) ensures that the Poisson's equation:

$$\nabla^2\phi = 4\pi G\rho, \quad (2)$$

where ϕ is the gravitational potential, holds in the limit of Newtonian gravity. In order to obtain static solutions, Einstein later added the *Cosmological Constant* term Λ :

$$R_{ij} - \frac{1}{2}g_{ij}R - \Lambda_E g_{ij} = \frac{8\pi G}{c^4}T_{ij}. \quad (3)$$

In this context, the most general space-time metric describing a Universe in which the Cosmological Principle applies, is the *Friedmann-Robertson-Walker* metric (hereafter FRW):

$$ds^2 = c^2 dt^2 - a^2(t) \left[\frac{dr^2}{1 - kr^2} + r^2 d\Omega^2 \right], \quad (4)$$

where ds is the infinitesimal interval between two events in the space-time, dt is the time interval between two events, dr and $d\Omega$ are the spatial radial and angular interval, respectively, adopting spherical polar coordinates. The parameter k is the *curvature parameter*, which is a constant and can assume the values $k = -1, 0, 1$ for an open, flat or closed Universe, respectively. The time-dependent factor $a(t)$ is the *expansion parameter* or the *cosmic scale factor*; it multiplies the spatial component of the metric, giving the expansion factor of the Universe.

A more practical quantity, related to the expansion of the Universe, is the *redshift* of a source:

$$z \equiv \frac{\lambda_0 - \lambda_e}{\lambda_e}, \quad (5)$$

where λ_0 is the wavelength of the source radiation observed at the present time, t_0 , and λ_e is the wavelength of the radiation emitted by the source at the time t_e . The scale factor and the redshift measured for a source at time t are related by:

$$1 + z(t) = \frac{a(t_0)}{a(t)}, \quad (6)$$

where $a(t_0) \equiv 1$, and $z(t_0) = 0$.

Hubble (1929) provided the first observational evidence that the Universe is expanding, measuring a linear relation between the distance r and the redshift of galaxies, known as the *Hubble's law*:

$$z = \frac{H}{c} r. \quad (7)$$

The *Hubble parameter*, defined as $H(t) \equiv \dot{a}(t)/a(t)$, measures the rate of expansion, and at the present time is parametrized as $H_0 = 100h \text{ km s}^{-1} \text{ Mpc}^{-1}$.

For a perfect fluid with pressure p and energy density ρc^2 , the energy-momentum tensor is

$$T_{ij} = -pg_{ij} + (p + \rho c^2)U_i U_j, \quad (8)$$

where U_i is the fluid four-velocity. In the case of a Universe described by the Friedmann-Robertson-Walker metric, the Einstein equations for a perfect fluid have two important solutions, called the *Friedmann equations*, for the time evolution of the scale factor, $a(t)$:

$$\ddot{a} = -\frac{4}{3}\pi G \left(\rho + \frac{3p}{c^2} \right) a \quad (9)$$

for the time-time component, and

$$\dot{a}^2 + kc^2 = \frac{8}{3}\pi G \rho a^2 \quad (10)$$

for the space-space components. Solutions for the space-time components lead to obvious identities. Considering an adiabatic expansion of the Universe:

$$d(\rho c^2 a^3) = -p da^3, \quad (11)$$

the eq. 10 can be recovered from the eq. 9.

To determine the evolution of the scale factor, $a(t)$, the equation of state must be specified:

$$p(\rho) = w\rho c^2, \quad (12)$$

where w is the equation of state parameter and depends on the Universe components. The matter contribution is $w = 0$, while the radiation component contributes to pressure with $w = 1/3$.

Since the matter and radiation pressure and density are not negative, eq. 9 implies that in a Universe where matter and radiation are the dominant components, the acceleration of the scale factor is negative (i.e. the Universe expansion decelerates). When adding the cosmological constant, a static Universe is possible. For:

$$\Lambda_E = \frac{4\pi G\rho}{c^2}, \quad (13)$$

the Universe is static (it does not decelerate or accelerate).

Our present cosmological model, instead of the cosmological constant Λ_E , introduces another physical component, the *dark energy*, modelled as a fluid with a negative pressure ($w < 0$). The original Einstein model with a cosmological constant corresponds to the specific case in which $w = -1$.

The time evolution of density is then:

$$\rho_w(z) = \rho_{0w}(1+z)^{3(1+w)}. \quad (14)$$

From eq. 10, it is useful to define the *critical density* as:

$$\rho_c(t) \equiv \frac{3H^2(t)}{8\pi G}, \quad (15)$$

so that for $\rho = \rho_c$, $k = 0$ and the universe will be flat. Universes with $\rho > \rho_c$ will be closed and universes with $\rho < \rho_c$ will be open. The ratio between the density of a component w at a certain time and the critical density at the same time is called *density parameter* and can be written as:

$$\Omega_w(t) \equiv \frac{\rho_w(t)}{\rho_c(t)}, \quad \Omega_{\text{tot}} = \sum_w \Omega_w, \quad (16)$$

where Ω_{tot} is the total density of the Universe.

After these considerations, it is possible to rewrite eq. 9 for the matter (m), radiation (r) and cosmological constant (Λ) components as:

$$H^2(z) = H_0^2[(1 - \Omega_{0,\text{tot}})(1+z)^2 + \Omega_{0,m}(1+z)^3 + \Omega_{0,r}(1+z)^4 + \Omega_{0,\Lambda}]. \quad (17)$$

It is useful to define $E(z)$ as the quantity relating the Hubble parameter, $H(z)$, to its current value, H_0 :

$$E(z) \equiv \frac{H(z)}{H_0}. \quad (18)$$

1.2 FORMATION AND EVOLUTION OF COSMIC STRUCTURES

In this section, I briefly summarize the theory of cosmic structure formation through the process of gravitational instability of small initial density perturbations.

In the standard model of the *Hot Big Bang*, the primordial Universe was very dense and hot, made of a fully ionized plasma of photons and matter. Thomson scattering of photons by free electrons was the main interaction mechanism

between radiation and matter, making the Universe completely opaque. The different evolution of components as a function of time implies that in the very first phases of the Universe, its density was dominated by the radiation density. Then, as the Universe expanded, the matter density dominated, and finally the dark energy density, which is the dominant component today.

While expanding, the average Universe temperature cooled down ($T \propto 1/a(t)$). When the temperature reached $T \sim 3000\text{K}$ and ions and electrons combined to form neutral atoms (*recombination epoch*), the photons decoupled from the electrons, and the Universe became transparent. This time marks the farthest photons that we can receive, defining the so-called *last scattering surface*. These photons are observed as a Cosmic Microwave Background radiation (CMB, Penzias and Wilson, 1965) with a black body distribution at a radiation temperature of $T \sim 2.7\text{K}$ (Mather et al., 1994). The CMB shows temperature fluctuations of the order of $\frac{\delta T_r}{T_r} \sim 10^{-5}$ that correspond to matter density perturbations, $\frac{\delta T_m}{T_m} \propto \frac{\delta T_r}{T_r}$, with $\rho_m(t) \propto T_m^3$, since photons and matter just decoupled.

1.2.1 The linear evolution of density perturbations

The evolution of small perturbations in a uniform and static Universe was modelled by Jeans (1902). In the linear regime, it is possible to apply his theory to an expanding Universe. Let us consider an initial density perturbation field characterized by its *density contrast* :

$$\delta(\vec{x}) \equiv \frac{\rho(\vec{x}) - \rho_b}{\rho_b}, \quad (19)$$

where $\rho(\vec{x})$ is the matter density field at the position \vec{x} and ρ_b is the mean matter density of the background Universe.

The characteristic length scale for the self-gravity of the gas is the *Jeans length*, λ_J , defined as

$$\lambda_J = \sqrt{\frac{15k_B T}{4\pi G \mu \rho_{gas}}}, \quad (20)$$

with k_B the Boltzmann constant, T the gas temperature, μ the mean molecular weight and ρ_{gas} the gas mass density. For perturbations on scales smaller than λ_J , the velocity dispersion of the gas particles is large enough that their self-gravity can not hold them, and the fluid fluctuations are then dissipated by this process called “*free-streaming*”. On the other hand, perturbations on scales larger than λ_J will grow with time and can finally collapse.

In the following, I will restrict to the interesting case for structure formation. I will consider a Universe dominated by a pressureless and self-gravitating fluid, as the dark matter component, where the scale of the density fluctuations is larger than the Jeans length.

On large enough scales, the Newtonian treatment can be applied and the evolution of density perturbations is regulated by the continuity, the Euler and the Poisson equations:

$$\frac{\partial \delta}{\partial t} + \vec{\nabla} \cdot [(1 + \delta)\vec{u}] = 0, \quad (21)$$

$$\frac{\partial \vec{u}}{\partial t} + 2H(t)\vec{u} + (\vec{u} \cdot \vec{\nabla})\vec{u} = -\frac{\vec{\nabla}\phi}{a^2}, \quad (22)$$

$$\nabla^2 \phi = 4\pi G \rho_b a^2 \delta, \quad (23)$$

where the spatial derivatives are with respect to the comoving coordinate \vec{x} , such that $\vec{r} = a(t)\vec{x}$ is the proper coordinate, $\vec{v} = \dot{\vec{r}} = \dot{a}\vec{x} + \vec{u}$ is the total velocity of a fluid element (with $\dot{a}\vec{x}$ and $\vec{u} = a(t)\dot{\vec{x}}$ giving the Hubble flow and the peculiar velocity, respectively), $\phi(\vec{x})$ is the gravitational potential.

In the case of small density fluctuations, all the non linear terms in the fields δ and \vec{u} can be neglected and the above equations can be written as

$$\frac{\partial^2 \delta}{\partial t^2} + 2H(t) \frac{\partial \delta}{\partial t} = 4\pi G \rho_b \delta, \quad (24)$$

having as a solution:

$$\delta(\vec{x}, t) = \delta_+(\vec{x}, t_i) D_+(t) + \delta_-(\vec{x}, t_i) D_-(t), \quad (25)$$

where $D_+(t)$ and $D_-(t)$ are the growing and the decaying factors of $\delta(\vec{x}, t)$, respectively, and $\delta_+(\vec{x}, t_i)$ and $\delta_-(\vec{x}, t_i)$ the corresponding spatial distributions of the primordial density field. The density growing factor depends on the underlying cosmology. For example, in a flat matter-dominated Einstein-de-Sitter Universe ($\Omega_m = 1, \Omega_\Lambda = 0$), $H(t) = 2/(3t)$, so that $D_+(t) = (t/t_i)^{2/3} \propto a(t)$ and $D_-(t) = (t/t_i)^{-1}$. Therefore, cosmic expansion with time scale $t_{\text{exp}} \propto (G\rho_b)^{-1/2}$ and gravitational instability with time scale $t_{\text{dyn}} \propto (G\rho)^{-1/2}$ proceed at the same rate, being $\rho \simeq \rho_b$ for small perturbations. On the contrary, for cosmological models with $\Omega_m < 1$, such as a flat one with $\Omega_m = 0.3$, there is an epoch, when the cosmological constant begins to be significant, at which the expansion time scale turns out to be shorter than in the Einstein-de-Sitter case. After that epoch, cosmic expansion proceeds faster than the gravitational collapse, causing a freezing of the perturbation growth. Therefore, any observational evidence of the degree of evolution of density perturbations is a sensitive probe of cosmological parameters. Clusters of galaxies provide such a probe, since the evolution of their number density is directly related to the growth rate of perturbations.

In the context of the linear Jeans theory it is possible to obtain a lower limit to the mass of perturbations that grow and evolve in cosmic structures instead of being dissipated, called *Jeans mass* M_J , according to the assumed model for the dark matter component.

Historically, two alternative models have been proposed: the *Cold Dark Matter* (CDM) model, according to which dark matter is composed of massive, non-baryonic, collisionless sub-relativistic particles and the *Hot Dark Matter* (HDM) model, for which dark matter is constituted by non-baryonic, collisionless, relativistic massless or with very small mass particles. The threshold value of M_J depends on the velocity of the dark matter particles, so it will be greater in the HDM model than in the CDM one. In particular, inside the particle horizon and at the *equivalence* redshift z_{eq} (when $\rho_m = \rho_r$ and the perturbations start growing):

$$M_{J,\text{HDM}}(z_{\text{eq}}) \approx 10^{12} - 10^{15} M_\odot, \quad (26)$$

$$M_{J,\text{CDM}}(z_{\text{eq}}) \approx 10^5 - 10^6 M_\odot. \quad (27)$$

Therefore, according to the HDM model the first structures to form should be the most massive ones, such as galaxy clusters, while the smaller structures should

form by fragmentation of the first ones in a *top-down* scenario. The CDM model predicts instead that the first structures to form are low-mass objects, such as globular clusters, which subsequently aggregate to form larger structures in the so-called *hierarchical* or *bottom-up* scenario. A comparison between the formation age of galaxies and galaxy groups or clusters provide a support for the CDM scenario and a confutation for the HDM (Seigar, 2015). For example, the Milky Way appears older than the Local Group and its formation redshift z_f is much higher ($z_f > 4$) than the one predicted by HDM models ($z_f \lesssim 1$).

The CDM model is also validated by observations and is at the basis of the current standard cosmological model. In particular, this means that galaxy clusters are the latest structures that form in the Universe, their number decreases with increasing redshift and strongly depends on the cosmological model.

1.2.2 The power spectrum of density perturbations

A convenient representation for $\delta(\vec{x})$ is given by its Fourier transform

$$\hat{\delta}(\vec{k}) \equiv (2\pi)^{-3/2} \int d\vec{x} \delta(\vec{x}) e^{i\vec{k}\cdot\vec{x}}. \quad (28)$$

In addition, we can define the two-point correlation function of $\delta(\vec{x})$ as

$$\xi(r) \equiv \langle \delta(\vec{x}_1) \delta(\vec{x}_2) \rangle, \quad (29)$$

which depends only on the distance between the considered points, $r = |\vec{x}_1 - \vec{x}_2|$, and describes whether the density field is more ($\xi > 0$) or less ($\xi < 0$) correlated than a random distribution. It can be demonstrated that the Fourier transform of $\xi(r)$ corresponds to the power spectrum of the density fluctuations:

$$P(k) \equiv \langle |\hat{\delta}(\vec{k})|^2 \rangle = \frac{1}{2\pi} \int dr r^2 \xi(r) \frac{\sin(kr)}{kr}, \quad (30)$$

which, assuming isotropy, depends only on the modulus of the wave-vector \vec{k} . This quantity provides a full statistical description of an isotropic Gaussian field. Inflationary models predict a nearly Gaussian density perturbation field characterized by a scale-invariant spectrum $P(k) = Ak^n$, where A is the normalization and $n \simeq 1$ is the spectral index.

To analyze the collapse of primordial fluctuations on scales $R \propto (M/\rho_b)^{1/3}$, forming objects of mass M , it is useful to define a window function $W_R(r)$ which filters out the modes on smaller scales. The corresponding density field is:

$$\delta_R(\vec{x}) = \delta_M(\vec{x}) = \int \delta(\vec{y}) W_R(|\vec{x} - \vec{y}|) d\vec{y}, \quad (31)$$

and the variance of the perturbation field at the scale R is given by

$$\sigma_R^2 = \sigma_M^2 = \langle \delta_R^2 \rangle = \frac{1}{2\pi^2} \int dk k^2 P(k) \hat{W}_R^2(k), \quad (32)$$

where $\hat{W}_R(k)$ is the Fourier transform of the window function. The shape of the power spectrum is uniquely determined by the parameters Ω_m , Ω_b and H_0 , whereas the normalization has to be inferred from observations of the cosmic large scale structure or of CMB anisotropies. A common way to parametrize this normalization is through the quantity σ_8 , which is the variance estimated

within a comoving sphere of radius $R = 8h^{-1} \text{Mpc}$. This choice has been made after Davis and Peebles (1983) found that at this radius the variance of the galaxy counts is close to unity. The number density of galaxy clusters at a given epoch is very sensitive to the value of σ_8 , providing a direct constraint on the normalization of the power spectrum.

1.2.3 The spherical top-hat collapse

When fluctuations reach amplitudes of the order of unity, the Jeans theory is no longer valid. The structures observed at present have overdensities with $\delta \gg 1$; for example, a cluster of galaxies corresponds to $\delta \gtrsim 100$. In this case, non-linear models or numerical simulations are required to describe the evolution of density perturbations.

The only case in which the non-linear evolution can be analytically calculated is that of a spherically symmetric collapse (see Gunn and Gott, 1972). Even though this is a very simplified model, it is useful to characterize the formation and evolution of virialized dark matter halos.

In this model, the perturbation is considered as an overdense sphere with initial amplitude δ_i in an expanding background Universe. The perturbation can be treated as a separate universe in which the FRW metric is valid, with null velocity at its boundaries. In an Einstein-de-Sitter background Universe ($\Omega_m = 1$), the evolution of a density perturbation can be written as:

$$\delta = \delta_+(t_i) \left(\frac{t}{t_i} \right)^{2/3} + \delta_-(t_i) \left(\frac{t}{t_i} \right)^{-1}. \quad (33)$$

Thus, after a short period of time the growing mode will dominate over the decaying mode. At the initial time t_i , the condition of null velocity at the boundary of the spherical region requires $\delta_+(t_i) = \frac{3}{5} \delta_i$, and the perturbation density parameter is then: $\Omega_p(t_i) = \Omega(t_i)(1 + \delta_i)$. The condition for which the perturbation can collapse and form a structure is $\Omega_p(t_i) > 1$. Under this condition, the perturbation will reach a maximum expansion at the time t_m , called *turn-around* point, after which it will detach from the expansion of the background and will collapse under the dominant gravitational force until it reaches an equilibrium state at the time t_{vir} , when the virial condition between the kinetic K and the potential U energy is satisfied: $U = -2K$. The formed structure will be called “virialized”. At the turn around, the perturbation (a sphere of mass M and radius R_m) has a totally potential energy:

$$E_m = U = -\frac{3}{5} \frac{GM^2}{R_m}. \quad (34)$$

At the virialization, recalling the condition $E_{\text{vir}} = K + U = -K$, results:

$$E_{\text{vir}} = \frac{U}{2} = -\frac{1}{2} \left(\frac{3}{5} \frac{GM^2}{R_{\text{vir}}} \right), \quad (35)$$

where R_{vir} is the radius of the virialized structure. Assuming energy conservation during the evolution into this equilibrium state gives $R_m = 2R_{\text{vir}}$ and the non-linear overdensity at t_{vir} turns out to be $\Delta_{\text{vir}} \simeq 178$. On the contrary, the linear theory predicts:

$$\delta_+(t_{\text{vir}}) = \left(\frac{t_{\text{vir}}}{t_m} \right)^{2/3} \delta_+(t_m) \simeq 1.69. \quad (36)$$

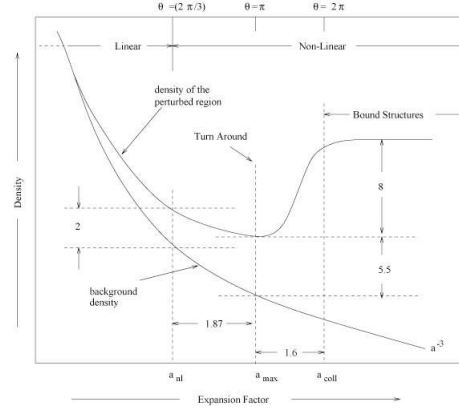


Figure 1 – Evolution of an over-dense region in a spherical top-hat model. Adapted from Padmanabhan (1993).

This value gives the overdensity threshold that a perturbation in the initial density field must exceed to evolve and collapse into a virialized structure. A scheme of the evolution of an over-dense region in a spherical top-hat model, adapted from Padmanabhan (1993), is shown on Fig. 1.

The above considerations are valid for an Einstein-de-Sitter cosmology but they can be extended to any other cosmological model. For $\Omega_m < 1$ the expansion rate of the Universe is larger than for $\Omega_m = 1$; this cause a faster decreasing of the background density from t_m to t_{vir} and, as a consequence, a larger value of the overdensity at virialization.

Despite the approximations made, this model provides a value for the overdensity which is consistent with that found by N-body simulations of dark matter halos.

A halo at redshift z is characterized by a virial radius r_{vir} , defined as the radius of a sphere within which the mean density is Δ_{vir} times the critical density of the Universe at that redshift $\rho_{cr}(z)$, a virial mass

$$M_{vir} = \frac{4}{3}\pi\Delta_{vir}\rho_{cr}(z)r_{vir}^3, \quad (37)$$

and a circular velocity

$$V_c = \left(\frac{GM_{vir}}{r_{vir}}\right)^{1/2}. \quad (38)$$

In this thesis I will use the overdensity threshold $\Delta = 200$, which is commonly considered as typical for a dark matter halo which has reached the virial equilibrium. Corresponding values for mass and radius are M_{200} , and R_{200} . I will also use $\Delta = 500$, M_{500} , R_{500} , which are commonly used in X-rays and SZ surveys.

This definition has the advantage of being independent of cosmology. On the contrary, the virial overdensity Δ_{vir} is a function of the matter density and thus depends on cosmology.

Numerical N-body simulations of structure formation in a CDM Universe predict that the density profiles of dark matter halos on all mass scales can be described by a universal profile, the so-called *Navarro-Frenk-White* profile (hereafter NFW; Navarro, Frenk, and White, 1997):

$$\rho(r) = \frac{\rho_s}{(r/r_s)(1+r/r_s)^2}, \quad (39)$$

where the only two parameters are the scale radius r_s , and the scale density ρ_s .

A common parametrization of the NFW profile uses the total mass enclosed within a certain radius R_Δ (chosen to describe the halo on the scale of interest), and the concentration parameter $c_\Delta \equiv R_\Delta/r_s$:

$$M_\Delta = 4\pi\rho_s r_s^3 \left(\ln(1 + c_\Delta) - \frac{c_\Delta}{1 + c_\Delta} \right). \quad (40)$$

1.2.4 The halo mass function

A powerful tool to follow the evolution of dark matter halos and determine the history which gave origin to the structures we observe today is the halo mass function (hereafter HMF).

The HMF is the number density of collapsed objects at redshift z , with mass between M and $M + dM$ in a given comoving volume:

$$\frac{dn(M, z)}{d \ln M} = \frac{\rho_m}{M} \left| \frac{d \ln \sigma_M}{d \ln M} \right| f(\sigma_M, z), \quad (41)$$

where $f(\sigma_M, z)$ is a model-dependent function of the filtered power spectrum (eq. (32)), which needs to be calibrated using numerical simulations (see e. g. Murray, Power, and Robotham, 2013, for a comparison of different HMFs available in literature).

Press and Schechter (1974) performed the first analytical attempt to derive the HMF, based on the spherical top-hat collapse model combined with the growth function for the linear perturbation theory. The main idea of this formalism is that any collapsed object with mass $\geq M$ at redshift z arises from regions where $\delta_M \geq \delta_c$, being δ_M the linearly extrapolated density field, filtered on a mass scale M , and δ_c the critical overdensity for collapse. According to the spherical collapse model, $\delta_c \simeq 1.69$, independently of redshift, for an Einstein-de-Sitter cosmology. The function $f(\sigma_M, z)$ gives the probability of a given point to be within a region satisfying the above condition and can be written as

$$f(\sigma_M, z) = \sqrt{\frac{2}{\pi}} \frac{\delta_c}{\sigma_M(z)} \exp \left[-\frac{\delta_c^2}{2\sigma_M^2(z)} \right], \quad (42)$$

which only depends on the ratio $\nu \equiv \delta_c(z)/\sigma_M(z)$, called *peak height*.

Even if this derivation is rigorous only for spherical collapse, eq. (41) already demonstrates that the mass function of galaxy clusters is a powerful probe of cosmological models. Cosmological parameters enter in eq. (41) through the mass variance σ_M which depends on the power spectrum and on the density parameters. In the limit of massive objects, the HMF is dominated by the exponential tail. This implies that it becomes exponentially sensitive to the choice of the cosmological parameters and therefore a reliable determination of the mass function of very massive clusters is important to put constraints on cosmological parameters.

1.3 THE CONCORDANCE MODEL

A cosmological model is defined by a set of parameters specifying the geometry of the Universe, the mean density of its components, its evolution with time and the initial density perturbation spectrum. The current established cosmological model is the so-called “*Lambda Cold Dark Matter*” (hereafter Λ CDM)

model, according to which the Universe is flat, the total energy density is dominated by the cosmological constant component Λ ($w = -1$) and the remaining fraction is mainly cold dark matter, while the standard baryonic matter is only a few percent.

This model is supported by many observations which allow a precise estimate of the cosmological parameters. The most recent mission devoted to this purpose is the ESA *Planck* mission. Planck Collaboration et al. (2016a) released the last cosmological parameter results, based on observations of temperature and polarization anisotropies of the CMB, which reflect the density perturbation power spectrum at the time of recombination. I list in Table 1 the values of the cosmological parameters that are of interest for this thesis, derived from the CMB power spectrum, in combination with *Planck* lensing data.

Parameter	68% limits	Definition
H_0	67.8 ± 0.9	current expansion rate in $\text{km s}^{-1} \text{Mpc}^{-1}$
Ω_m	0.308 ± 0.012	total matter density divided by the critical density today
Ω_Λ	0.692 ± 0.012	dark energy density divided by the critical density today
n	0.968 ± 0.006	scalar spectrum power-law index
σ_8	0.8149 ± 0.0093	rms matter fluctuations today in linear theory

Table 1 – Cosmological parameters for the Λ CDM model derived by Planck Collaboration et al. (2016a).

Galaxy clusters are the largest gravitationally bound structures in the present Universe. They form from the highest density peaks of the dark matter primordial perturbation field (see Chapter 1), which collapse over a region of few Mpc. Dark matter is $\sim 85\%$ of their total mass composition and constitutes a deep potential well where intergalactic baryons fall being heated by adiabatic compression and shocks until they reach the virial equilibrium with the underlying dark matter potential at a temperature of the order of 10^7 K. At this temperature, this so-called intra-cluster medium (hereafter, ICM) is fully ionised and emits in the X-ray band via thermal bremsstrahlung. It constitutes the $\sim 10\%$ of the cluster total mass, while galaxies are $\sim 5\%$ (e.g. Mulchaey, Dressler, and Oemler, 2004, and references therein). The cluster total mass is typically larger than $10^{14} M_{\odot}$ (Evrard et al., 2008a).

Thanks to their multicomponent nature, clusters can be detected and studied through a variety of observables across the electromagnetic spectrum (e.g., Sarazin, 1988).

In this chapter, I describe how clusters are observed at different wavelengths, and how their mass can be estimated using different, independent techniques.

2.1 OBSERVABLE PROPERTIES

2.1.1 *Optical and near-infrared bands*

2.1.1.1 *Detection*

Clusters of galaxies were identified for the first time in the 1930's in the optical band and they important role in the comprehension of the Universe was soon clear as they provided the first observational evidence of the existence of dark matter: measuring the velocity dispersion of the galaxies within the Coma cluster, Zwicky (1937) concluded that this velocity dispersion could not be explained by the visible mass only.

The first extensive catalog was provided by Abell (1958), who observed 2712 objects with the Palomar Observatory Sky Survey (Minkowski and Abell, 1963) in the Northern hemisphere. Clusters were identified as large overdensities in the projected galaxy distribution, and were selected by their “richness”, i.e. the number of galaxies within the detection aperture. The adopted criteria concerned:

- a minimum number of 50 galaxies in the magnitude range $[m_3, m_3 + 2]$, where m_3 is the magnitude of the third brightest galaxy;
- a minimum circle of radius $1.7/z$ arcmin within which the galaxies could be grouped;
- a fixed redshift range $0.02 < z < 0.20$, in order to obtain a statistically complete sample.

Finally, the selected sample consisted of 1682 clusters, expanded by Abell, Corwin, and Olowin (1989) with objects in the Southern hemisphere. This catalog

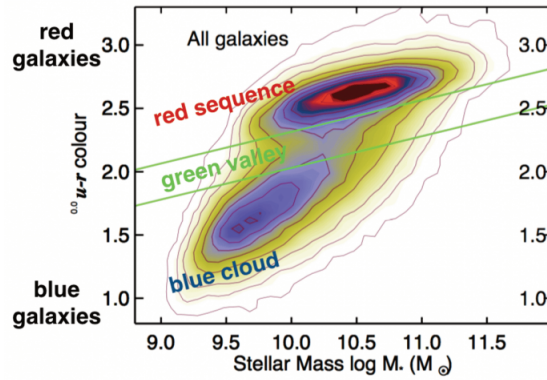


Figure 2 – The color-stellar mass diagram of galaxies from the Galaxy Zoo project (Lintott et al., 2008). It reveals a bimodal distribution of galaxies with a tight “red sequence”, mostly populated by quiescent galaxies, and a diffuse “blue cloud”, mostly populated by star-forming galaxies (Bower, Lucey, and Ellis, 1992), plus a “green valley”, interpreted as a transition population. Figure adapted from Schawinski et al. (2014).

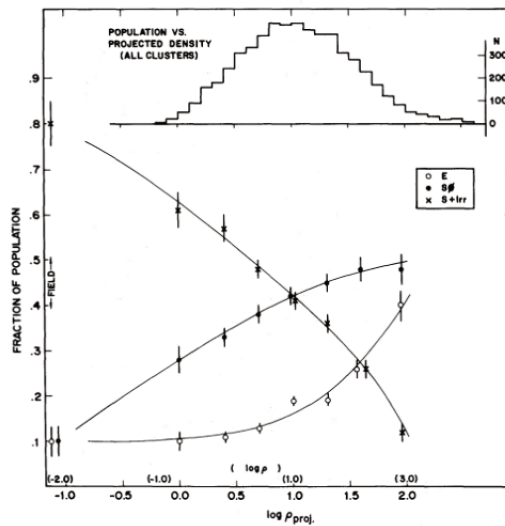


Figure 3 – Morphology-density relation from Dressler (1980). Dense environments are mostly populated by early-type (elliptical E and spheroidal S0) galaxies, ETGs, while field is mostly populated by late-type (spiral) galaxies.

has been the most important resource in the study of galaxy clusters for many decades.

Modern optical identification techniques extend this basic approach with information about galaxy colors. This approach is based on two main observational evidence:

- diagrams of galaxy colors vs magnitudes (or stellar masses), as Fig.2 adapted from Schawinski et al. (2014), reveal a bimodal distribution of galaxies with a tight “red sequence”, mostly populated by quiescent galaxies, and a diffuse “blue cloud”, mostly populated by star-forming galaxies (Bower, Lucey, and Ellis, 1992), plus a “green valley”, interpreted as a transition population (Schawinski et al., 2014);
- the morphology of a galaxy correlates with its environment: dense environments are mostly populated by early-type (elliptical and spheroidal) galaxies, ETGs, while in the field mostly late-type (spiral) galaxies are found, as shown in Fig.3 by Dressler (1980).

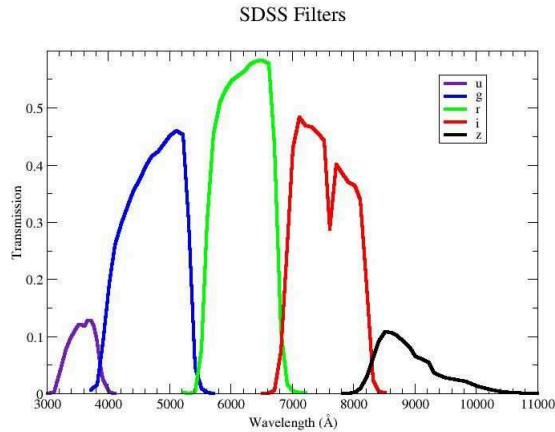


Figure 4 – Filter responses for the SDSS camera set u, g, r, i, z . Credit: www.sdss.org.

Galaxy colors are particularly needed to identify distant clusters. At $z \gtrsim 0.2$, the number of field galaxies dominates over galaxy overdensities associated with clusters, and the two populations are difficult to distinguish looking only at the two-dimensional galaxy distribution, especially if using a single filter in the optical band. An efficient detection method is to observe galaxy colors, and use filters in the near-infrared band (hereafter near-IR), which collect the light of evolved stars (Stanford et al., 1997). In fact, galaxies in the cluster cores are found to be significantly redder than field galaxies at similar redshift, and lie on the *red sequence*, up to at least $z \sim 1.4$ (Mei et al., 2009; Brodwin et al., 2013).

To trace the old stellar populations in a wide interval of redshifts, observations with multiple filters are needed. The Sloan Digital Sky Survey (SDSS; York et al., 2000) has provided the largest catalog of sources obtained from a five-band photometry (see Fig. 4), which is currently the best resource of cluster candidates in the optical and near-infrared band.

Rykoff et al. (2014) have built a cluster detection algorithm based on the existence of the red sequence, named “redMaPPer”, and applying it to SDSS data, they have provided a catalog of ~ 25000 clusters over the redshift range $[0.08, 0.55]$.

Licitra et al. (2016b,a) introduced a new cluster detection algorithm based on the red-sequence technique, named “RedGOLD” (Red-sequence Galaxy Over-density cLUster Detector), optimized to detect massive galaxy clusters ($M_{200} > 10^{14} M_{\odot}$), and to produce optical cluster catalogs with high completeness and purity out to $z \sim 1$. They applied this algorithm to the Canada-France-Hawaii Telescope Legacy Survey (CFHT-LS; Gwyn, 2012) Wide 1 field, detecting 652 clusters up to $z = 1.1$, and to the Next Generation Virgo Cluster Survey (NGVS; Ferrarese et al., 2012), detecting 279 on the $\sim 20 \text{ deg}^2$ of the NGVS covered by 5 bands, and 1704 clusters on the entire NGVS without the r -band coverage, at $0.1 < z < 1.1$.

The galaxy selection used for our spectroscopic observations, described in Chapter 4, is based on the approach implemented in RedGOLD, adapted for our available bandpasses. In brief, it consists in:

- using rest-frame colors (U - B) and (B - V) to select ETGs on the red sequence and exclude star-forming galaxies;
- using the empirical red-sequence model from Mei et al. (2009) (rest-frame zero point, slope, and scatter);

- selecting only ETGs with a NFW (Navarro, Frenk, and White, 1997) radial density profile;
- centering the cluster detection on the ETG with the highest number of red companions, weighted on luminosity.

Once a cluster is identified as an overdensity of galaxies, spectroscopic follow-up observations measuring the redshift, z , and the radial velocities, v_r , of galaxies allow to confirm their membership (against projection effects) and measure the cluster's mass.

For a relaxed cluster, the distribution of the radial velocities of member galaxies in the velocity space is expected to be Gaussian, and galaxies with velocities well outside (generally $> 3\sigma$) the Gaussian best fit, $\langle v_r \rangle$, are considered outliers (Yahil and Vidal, 1977).

Once the cluster membership is defined, the fit of the velocity distribution function:

$$f(v_r) = v_0 e^{-\frac{(v_r - \langle v_r \rangle)^2}{2\sigma_{1D}^2}}, \quad (43)$$

to the velocities of the cluster galaxies gives the line-of-sight (one-dimensional) velocity dispersion of the cluster, σ_{1D} .

Actually, not all clusters are dynamically relaxed. Many of them show strong asymmetries and clumpiness in their velocity distribution (e.g., Geller and Beers, 1982; Dressler and Shectman, 1988; Mohr et al., 1995), that reflect the merging processes in which they are involved.

The accuracy in the velocity dispersion measurement depends on the method used to eliminate non-member galaxies, and on the number of the confirmed galaxies with measured velocities (Girardi et al., 1993).

This issue is examined in more detail in Chapter 4, which is focused on the confirmation of a sample of galaxy clusters from optical spectroscopic observations, and on the measurement of their galaxy velocity dispersions.

2.1.1.2 *Mass proxy*

Historically, the velocity distribution of the cluster member galaxies has provided the first method to estimate cluster masses. This method is based on the assumptions that the cluster is spherical, isolated and at the virial equilibrium (see e.g. Binney and Tremaine, 2008): $2K + U = 0$. The kinetic energy can be approximated as $K \simeq 3/2 M \sigma_v^2$, where σ_v is the velocity dispersion along the line of sight; the gravitational potential energy can be approximated as $U \simeq GM^2/R_{\text{vir}}$, where R_{vir} is the radius at which the cluster reaches the virial equilibrium:

$$R_{\text{vir}} \equiv \frac{GM}{3\sigma^2}. \quad (44)$$

In simulations, it is calculated from the position of the cluster members:

$$R_{\text{vir}} = N^2 \left(\sum_{i>j} r_{ij}^{-1} \right)^{-1}, \quad (45)$$

where N is the total number of galaxies and r_{ij} is the projected separation between the i -th and the j -th galaxies.

The cluster mass can be then recovered from the *virial theorem* as:

$$M \simeq \frac{3\sigma_v^2 R_{\text{vir}}}{G}. \quad (46)$$

Zwicky (1937) applied this method to the Coma cluster. He measured a value of $\sigma \approx 1000$ km/s which is typical for cluster velocity dispersions. Zwicky concluded that the luminous matter accounted for only a small fraction of the total mass inferred from the virial theorem. This was the first observational evidence of the existence of dark matter.

However, the virial theorem only provides an approximation of the exact cluster mass because clusters might have not necessarily reached complete virial equilibrium. In order to measure the true mass, one should have detailed information on the spatial distribution of the galaxy velocities. The best of such measurements are currently available for a few of the distant clusters which are interesting for cosmology, from the CLASH-VLT program (Rosati et al., 2014), a spectroscopic follow-up with the Very Large Telescope of 13 massive clusters ($0.187 < z < 0.570$) in the CLASH sample (Cluster Lensing And Supernova survey with Hubble, Postman et al., 2012), with ~ 500 spectroscopic confirmed members per cluster, out to $\sim 2 R_{\text{vir}}^1$.

The alternative to detailed observations is to use numerical simulations to calibrate the relation between velocity dispersion and mass.

Evrard et al. (2008a) analyzed a set of N-body (dark matter, DM) simulations with different cosmologies, physics, and resolutions and found that the velocity dispersion of DM particles within the virial radius can be expressed as a tight function of the halo virial mass, regardless of the simulation details, with only 4% scatter at fixed mass:

$$\sigma_{\text{DM}}(M, z) = \sigma_{\text{DM},15} \left[\frac{h(z)M_{200}}{10^{15}M_{\odot}} \right]^{\alpha}, \quad (47)$$

where $\sigma_{\text{DM},15} = 1082.9 \pm 4.0$ km s⁻¹ is the normalization, the mass M_{200} is given in units of $10^{15}h^{-1}M_{\odot}$, and $\alpha = 0.3361 \pm 0.0026$ is the logarithmic slope

Munari et al. (2013) analyzed the velocity dispersion-mass relation in both N-body and hydrodynamical simulations, using DM particles, subhaloes and galaxies as different tracers of the cluster velocity dispersion. They confirmed the trend $\sigma_{\text{DM}} \propto M^{1/3}$ for DM particles, while they found slightly steeper relations ($\alpha > 1/3$) and larger values of the normalization for subhaloes and galaxies, which depend on the halo mass, redshift and physics implemented in the simulation.

Quantifying the differences between the dynamical properties of DM particles and galaxies in simulations is still an open issue, but is crucial to accurately determine cluster masses from velocity dispersions. This is known as the “*velocity bias*” problem, where the velocity bias is defined as the ratio between the galaxy and the DM velocity dispersions.

This is one of the key arguments of this thesis and will be discussed in depth in Chapter 5.

Sifón et al. (2016) reported a $\sim 30\%$ of systematic uncertainties in the dynamical masses of a large sample of 44 clusters with an average of 55 spectroscopic members per cluster, and estimated an additional $\sim 15\%$ uncertainty due to the velocity bias.

1. Results for five clusters are currently released.

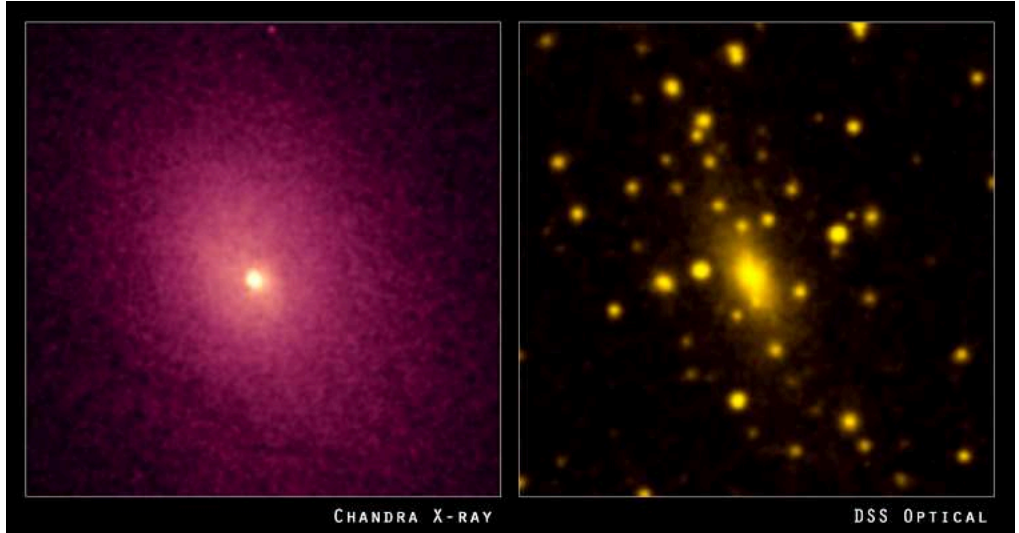


Figure 5 – *Left*: X-ray image of Abell 2029 observed with *Chandra*; figure from NASA. *Right*: optical image of the same cluster from the Palomar Observatory Digitized Sky Survey (from the webpage chandra.harvard.edu).

2.1.2 X-ray band

2.1.2.1 Detection

The largest cluster catalog after the Abel catalog was obtained from the X-ray *ROSAT* All-Sky survey (RASS, Truemper, 1993) in the 1990s.

In the X-ray band, clusters appear as a well-defined, extended emission of the intracluster gas, with typical luminosities of $10^{43} - 10^{46} \text{ erg s}^{-1}$. The X-ray emission is mainly due to thermal bremsstrahlung from the hot and fully ionised ICM, at a temperature $T \sim 10^7 - 10^8 \text{ K}$ and a density $n \sim 10^{-1} - 10^{-4} \text{ cm}^{-3}$ (see e.g. Sarazin, 1988, for a review).

The first X-ray observations of clusters were made in the 1970s with the *Uhuru* satellite (Giacconi et al., 1972) and then with the *Einstein* satellite (Gioia et al., 1990), showing that the ICM is filled by hot gas emitting in the X-rays mainly via thermal bremsstrahlung, with a total luminosity that is proportional to the square of the gas density. Since then, many X-ray surveys have efficiently selected clusters which clearly stand out against less dense background, minimizing the projection effects (Rosati, Borgani, and Norman, 2002).

For the first time, the RASS has covered large areas of the sky and provided hundreds of cluster candidates up to a maximum redshift of $z \sim 0.5$, with a few objects beyond (e.g. Bright Cluster Sample / BCS in Ebeling et al., 1998, the Northern *ROSAT* All-Sky Survey / NORAS in Böhringer et al., 2000, the *ROSAT*-ESO flux limited X-ray / REFLEX 1 in Böhringer et al., 2001, the Massive Cluster Survey / MACS in Ebeling, Edge, and Henry, 2001, the North Ecliptic Pole / NEP survey in Henry et al., 2001, the Highest X-ray flux Galaxy Cluster Sample / HIFLUGCS in Reiprich and Böhringer, 2002). The current generation of X-ray satellites, *Chandra* and *XMM-Newton* with improved angular resolution and sensitivity, has allowed deeper studies of the cluster emission to trace their mass distribution.

A comparison between an optical and an X-ray observation of the same cluster is shown in Fig. 5, for Abell 2029. The optical image shows the galactic component of the cluster while the X-ray image reveals the presence of hot gas.

Both optical galaxy and X-ray surveys provide flux-limited cluster samples, depending on the sensitivity of the telescope.

An additional detection limit for distant sources is the strong decline of the surface brightness (SB, flux per unit solid angle) with redshift, $(1+z)^{-4}$, due to the expansion of the Universe. X-ray surveys are affected by this limit, known as “*cosmological dimming*”, and currently provide sample of clusters up to $z \sim 1.4$ (e.g. Stanford et al., 2006).

2.1.2.2 Mass proxy

The mass of galaxy clusters can be estimated from the X-ray observations of the ICM under the assumption that the gas is in hydrostatic equilibrium with the underlying gravitational potential ϕ :

$$\nabla P_{gas} = -\rho_{gas} \nabla \phi, \quad (48)$$

where P_{gas} and ρ_{gas} are the gas pressure and the gas density, respectively. This assumption is justified by the fact that the time t_s needed for a sound wave in the ICM to cross the cluster diameter D :

$$t_s = 6.6 \times 10^8 \left(\frac{T}{10^8 \text{K}} \right)^{-1/2} \left(\frac{D}{1 \text{Mpc}} \right) \text{yr}, \quad (49)$$

is shorter than the cluster age $t_{age} \sim H_0^{-1} \sim 13.6 \text{Gyr}$. Assuming also that the ICM has a spherically-symmetric distribution, we can rewrite eq. (48) as :

$$\frac{1}{\rho_{gas}} \frac{dP_{gas}}{dr} = -\frac{d\phi}{dr} = -\frac{GM_{tot}(< r)}{r^2}, \quad (50)$$

where r is the distance from the cluster centre and $M_{tot}(< r)$ is the total (gas + stars + dark matter) cluster mass within r . This is known as the “hydrostatic equilibrium equation”. To solve it, the equation of state of an ideal gas is generally assumed for the gas pressure:

$$P_{gas}(r) = \frac{\rho_{gas}(r)kT_{gas}(r)}{\mu m_p}, \quad (51)$$

where μ is the mean molecular weight of the gas ($\mu \simeq 0.6$ for a solar composition) and $m_p = 1.66 \times 10^{-24} \text{g}$ is the proton mass. We can then solve eq. (50) for the total mass:

$$M_{tot}(< r) = -\frac{kT_{gas}(r)r}{\mu m_p G} \left(\frac{d \ln n_{gas}}{d \ln r} + \frac{d \ln T_{gas}}{d \ln r} \right), \quad (52)$$

where $n_{gas} = \rho_{gas}/\mu m_p$ is the sum of the electron and the proton densities.

Ideally, one should have enough data (photon count statistics) to measure both the density and temperature radial profiles, $n_{gas}(r)$ and T_{gas} , in order to directly solve eq. 52 for $M_{tot}(< r)$ (see e.g. the review by Ettori et al., 2013).

In practice, it is not always possible to derive temperature profiles, since they require a large number of X-ray photons to be divided into multiple energy bins (to get the spectrum in every radial bin).

In this case, one needs scaling laws to relate the X-ray observables, luminosity and temperature, with mass, based on the self-similar model proposed by Kaiser (1986): assuming that gravity, which does not have a preferred scale, is the only force that determines the thermodynamical properties of the ICM, then clusters

of different sizes are scaled version of each other. If M is the mass enclosed within the radius R at a given overdensity Δ , we can obtain a mass-radius relation ($M - R$): $M \propto \rho_{c,z} \Delta R^3$. The critical density of the Universe evolves with redshift as $\rho_{c,z} = \rho_{c,0} E^2(z)$, thus the cluster radius scales as

$$R \propto M^{1/3} E^{-2/3}(z). \quad (53)$$

The virial temperature of the diffuse gas into the potential well of the dark matter is $T_{\text{vir}} \sim GM\mu m_p/kR_{\text{vir}} \sim 10^8 \text{K}$ where M is the total mass, μ is the mean molecular weight, k is the Boltzmann constant and R_{vir} is the virial radius. Assuming that the cluster is an isothermal sphere at the hydrostatic equilibrium the virial temperature is given by: $kT \propto M/R \propto M^{2/3} E^{2/3}(z)$. Then, mass and temperature ($M - T$) are related by

$$M \propto T^{3/2} E^{-1}(z). \quad (54)$$

From the relations (53) and (54) it is possible to derive the relation between temperature and luminosity ($L - T$) emitted by the ICM through thermal bremsstrahlung emission: $L_X \propto \rho_{\text{gas}}^2 \Lambda V$, where ρ_{gas} is the average gas density, Λ is the cooling function that in the bremsstrahlung regime is proportional to $T^{1/2}$. Assuming also that, for a bolometric emission, the gas density traces the dark matter density ($\rho_{\text{gas}} \propto \rho_{\text{DM}} \propto \rho_{c,z}$), we can rewrite $L_X \propto \rho_0 E^2(z) T^{1/2} M \propto E^2(z) T^{1/2} T^{3/2} E^{-1}(z)$ and the resulting relation is

$$L_X \propto T^2 E(z). \quad (55)$$

By combining the $M - T$ relation with the $L - T$ relation we obtain the $M - L$ relation that links the mass to the X-ray luminosity:

$$M \propto L_X^{3/4} E^{-7/4}(z). \quad (56)$$

This scaling relations must be calibrated with numerical simulations (e.g. Borgani et al., 2004) or high-quality observations (e.g. Reiprich and Böhringer, 2002; Arnaud, Pointecouteau, and Pratt, 2005).

Besides the observational limits, it is important to note that the assumption of hydrostatic equilibrium is not always accurate since clusters might be dynamically young systems and may undergo mergers through which they accrete gas. Moreover, mergers cause the presence of bulk motions in the ICM which introduce a non-thermal pressure component. This causes an underestimate of the cluster total mass of the 10-25%, which is larger in the cluster outskirts where the ICM is less relaxed, as emerged from some numerical works that have applied the X-ray approach to mock observations (e.g. Nagai, Vikhlinin, and Kravtsov, 2007; Piffaretti and Valdarnini, 2008; Meneghetti et al., 2010). Other effects, such as instrument calibration or temperature inhomogeneities in the gas (Rasia et al., 2006, 2014) can additionally bias hydrostatic mass measurements. Simulations and comparison of different X-ray analyses indicate that X-ray estimates underestimate the mass of a factor in the range 0 - 40%, with a baseline value of 20% (Mazzotta et al., 2004; Nagai, Vikhlinin, and Kravtsov, 2007; Piffaretti and Valdarnini, 2008; Lau, Kravtsov, and Nagai, 2009; Kay et al., 2012; Rasia et al., 2012; Rozo et al., 2014a,b,c).

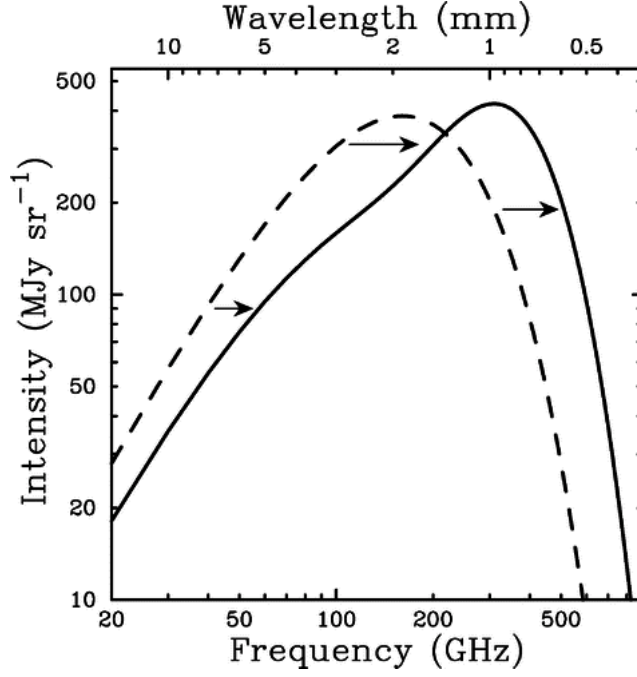


Figure 6 – Spectrum of the Cosmic Microwave Background, undistorted (dashed line) and distorted (solid line) by the Sunyaev-Zeldovich effect. Credit: Carlstrom, Holder, and Reese (2002).

2.1.3 The Sunyaev-Zeldovich effect

2.1.3.1 Detection

After the ROSAT survey, the latest all-sky cluster survey has been the *Planck* Sunyaev-Zeldovich cluster survey (Planck Collaboration et al., 2014b, 2015b).

Hot gas in clusters can also be observed through the so-called *Sunyaev-Zeldovich effect* (hereafter SZ; Sunyaev and Zeldovich, 1970, 1972). The high-energy electrons in the ICM interact with the low-energy CMB photons via Inverse Compton scattering. This interaction produces an increase of the energy of the CMB photons of a factor $\approx k_B T_e / m_e c^2$, where T_e and m_e are the electron temperature and mass, respectively, causing a distortion of the blackbody spectrum of the CMB. In particular, this appears as a decrease in the CMB intensity at the frequencies $\lesssim 218$ GHz and an increase at higher frequencies. This effect is illustrated in Fig. 6 for a fictional cluster with a mass 1000 times larger than the typical cluster mass, with the aim to show the small distortion.

The amplitude of this effect can be parametrised by the *Compton parameter* $y(D_A)$:

$$y(D_A) \equiv \frac{\sigma_T}{m_e c^2} \int P_e(\vec{r}) dl, \quad (57)$$

where D_A is the angular distance from the cluster centre, σ_T is the Thomson cross-section, $P_e \equiv n_e(\vec{r}) k_B T_e(\vec{r})$ is the pressure of the electrons of the ICM at the volume element of coordinate \vec{r} and l is the line of sight.

The total SZ signal (integrated over the whole cluster) is proportional to the integrated Compton parameter Y_{SZ} , so that

$$Y_{SZ} D_A^2 = \frac{\sigma_T}{m_e c^2} \int P_e dV. \quad (58)$$

This measurement has the big advantage of being independent of distance, unlike the optical and the X-ray surface brightness.

Therefore, in principle, a dedicated SZ cluster survey would identify clusters efficiently out to arbitrarily high redshifts. In practice, SZ surveys are limited by the instrument sensitivity and beam (Carlstrom, Holder, and Reese, 2002).

Surveys dedicated to such observations are providing very large samples of high redshift clusters, like the South Pole Telescope (SPT; Carlstrom et al., 2011), the Atacama Cosmology Telescope (ACT; Marriage et al., 2011) and the *Planck* satellite (Planck Collaboration et al., 2015a).

The *Planck* satellite, launched on 2009 May 14, has produced two catalogs of SZ sources with two all-sky cluster surveys, observing in six bands covering the frequency range [100-857 GHz], and with respective beam widths in the range [9.659-4.216 arcmin] (Planck Collaboration et al., 2014b, 2015b): the PSZ1 based on 15.5 months of data which has selected 1227 cluster candidates, and the PSZ2 which has selected 1653 cluster candidates from the full mission dataset of 29 months.

Three algorithms have been used to detect clusters, using the generalized NFW (Navarro, Frenk, and White, 1997) profile of Arnaud et al. (2010) as baseline pressure profile model (the so-called “*universal pressure profile*”). Two algorithms are based on the “Matched Multi-filter” technique, (MMF1, Herranz et al., 2002, and MMF3, Melin, Bartlett, and Delabrouille, 2006a), while the third algorithm is based on Bayesian inference (Carvalho et al., 2012, PwS for PowellSnakes.). For each detection, the algorithms derive a probability distribution in the flux-size ($Y_{500} - \theta_{500}$) plane, where the SZ flux inside a sphere of radius R_{500} , (Y_{500} , and the angular size θ_{500} are found to be highly degenerate (Planck Collaboration et al., 2014b).

The detections of these three methods, having a signal-to-noise ratio $S/N > 4.5$, have been combined to obtain the final catalog. Of the 1653 PSZ2 candidates, 1203 have been confirmed by ancillary data and 1094 have redshift estimates, in the range $0 < z < 1$, with a mean redshift of $z \sim 0.25$.

2.1.3.2 *Mass proxy*

Observations of the SZ effect give another probe of the cluster mass.

Since the gas pressure P_e is related to the depth of the gravitational potential, the product $Y_{SZ} D_A^2$ is a probe of the cluster mass:

$$Y_{SZ} D_A^2 \propto T_e \int n_e dV = M_{gas} T_e = f_{gas} M_{tot} T_e, \quad (59)$$

where f_{gas} is the gas fraction.

Recalling the $T - M$ relation: $T_e \propto M_{tot}^{2/3} E^{2/3}(z)$, we can obtain the following scaling relations:

$$Y_{SZ} D_A^2 \propto f_{gas} T_e^{5/2} E^{-1}(z), \quad (60)$$

$$Y_{SZ} D_A^2 \propto f_{gas} M_{tot}^{5/3} E^{2/3}(z). \quad (61)$$

In order to use the integrated Compton parameter to measure the cluster mass with *Planck* one needs to break the size-flux degeneracy by assuming a prior on the cluster size e.g., to the X-ray size.

Planck Collaboration et al. (2014a, 2016b) used a subsample of 71 *Planck* clusters detected at $S/N > 7$, from the XMM-*Newton* validation programme (Planck Collaboration et al., 2011a, 2012, 2013), to derive the scaling relation between the X-ray analogue of the SZ signal introduced by Kravtsov, Vikhlinin, and Nagai (2006), Y_X (defined as the product of the gas mass within R_{500} , $M_{g,500}$, and the spectroscopic temperature measured in the $[0.15-0.75] R_{500}$ aperture, T_X), and the mass determined by assuming hydrostatic equilibrium of the ICM, $M_{500}^{Y_X}$. The SZ Y_{500} is then measured within the radius corresponding to $M_{500}^{Y_X}$, and the scaling relations between the SZ observables, Y_{500} and θ_{500} , and the cluster mass and redshift are finally derived:

$$E^{-\beta}(z) \left[\frac{D_A^2(z) Y_{500}}{10^{-4} \text{Mpc}^2} \right] = Y_* \left[\frac{h}{0.7} \right]^{-2+\alpha} \left[\frac{(1-b) M_{500}}{6 \times 10^{14} M_\odot} \right]^\alpha, \quad (62)$$

and

$$\theta_{500} = \theta_* \left[\frac{h}{0.7} \right]^{-2/3} \left[\frac{(1-b) M_{500}}{3 \times 10^{14} M_\odot} \right]^{1/3} E^{-2/3}(z) \left[\frac{D_A(z)}{500 \text{ Mpc}} \right]^{-1}, \quad (63)$$

where $\theta_* = 6.997 \text{ arcmin}$, $\log Y_* = -0.19 \pm 0.02$, $\alpha = 1.79 \pm 0.08$, $\beta = 0.66 \pm 0.50$, $D_A(z)$ is the angular diameter distance, and $E(z) \equiv H(z)/H_0$. The intrinsic scatter of eq. 62, assumed to be log-normal and constant with mass and redshift, is $\sigma_{\ln Y} = 0.173 \pm 0.023$.

The ‘‘mass bias’’ parameter, $(1-b)$, accounts for the difference between the X-ray determined masses, $M_{500}^{Y_X}$, and true cluster halo mass, M_{500} , like the departure from hydrostatic equilibrium, absolute instrument calibration, temperature inhomogeneities, residual selection bias, etc.:

$$M_{500}^{Y_X} = (1-b) M_{500}, \quad (64)$$

This mass bias can be quantified by comparing the observed relation with predictions from numerical simulations (Planck Collaboration et al., 2014a) or incorporating new mass estimates from different observables (e.g. from lensing, Planck Collaboration et al., 2016b), but it turns out to be the largest source of uncertainty in the SZ analysis, with differences of up to 30% among the different estimates, in the range $1-b = [0.7, 1.0]$ (Planck Collaboration et al., 2016b).

The cosmological implications of this calibration are discussed in Chapter 3.

Constraining the value of the mass bias parameter is one of the main goal of this thesis. I present the state of the art of the contributions on this subject, including my own results, in Chapter 5.

Assuming a baseline value of $1-b = 0.8$, constant with mass and redshift, the confirmed clusters in the PSZ2 catalog have mass estimated in the range $0.79 < M_{500}^{\text{Pl}}/10^{14} M_\odot < 16.12$, with the mean mass over the whole redshift range being $M_{500}^{\text{Pl}} = 4.82 \times 10^{14} M_\odot$ (Planck Collaboration et al., 2015b). Fig. 7 shows the PSZ2 mass distribution as a function of redshift, compared to other SZ cluster surveys. *Planck* detects the rarest clusters in the high (M-z) region, while SPT and ACT detect lower mass clusters at higher redshift (up to $z \sim 1.5$).

2.1.4 Gravitational lensing

Zwicky (1937) suggested that galaxy clusters behave as lenses of background galaxies.

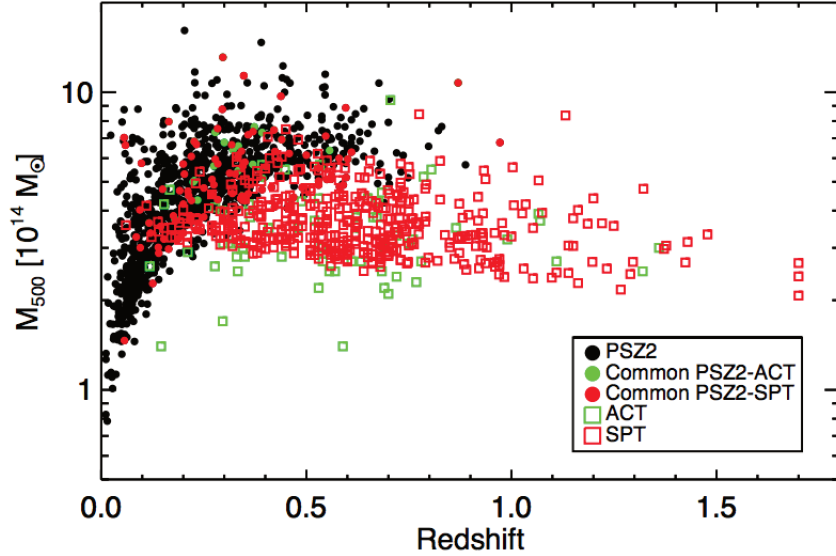


Figure 7 – Distribution of the PSZ2 clusters with associated redshift in the $M_{500} - z$ plane compared to the SPT (Bleem et al., 2015) and ACT (Hasselfield et al., 2013) catalogues. Credit: Planck Collaboration et al. (2015b).

In General Relativity, since the light is affected gravity, the light coming from galaxies that are in the background of a cluster is distorted by the cluster gravitational potential, and analyses of such distortions allow to reconstruct the potential and then the mass of the cluster which caused them (Bartelmann, King, and Schneider, 2001).

Fig. 8 schematically shows the gravitational lensing effect of a cluster on a background galaxy. According to the lens surface density and to the angular separation between the lens and the lensed source, *strong lensing* or *weak lensing* events can be observed.

Strong lensing occurs when the projected surface mass density in the inner regions of a cluster is sufficiently high to produce multiple and distorted, arc-shaped images of a background galaxy. This effect is rarely observed because it requires a perfect alignment of the background galaxy, the massive cluster, and the observer.

Weak lensing is instead a more frequent phenomenon, since it is observed at large radii from the cluster centre, and it does not require a perfect alignment of the background galaxy, the massive cluster, and the observer. The gravitational field caused by the cluster mass distribution produces elongated, tangential distortions of background galaxies. These distortions are very small (of the order of 2 - 3%) and cannot be measured for a single galaxy. The weak lensing observable is the “*shear*” distortion of an entire field of background galaxies, resulting from a statistical analysis, which provide a direct estimate of the density profile of the cluster lens (Bartelmann, King, and Schneider, 2001).

In principle, gravitational lensing could be used to detect massive galaxy clusters, using aperture mass statistics that associates high S/N peaks in lensing maps with massive structures along the line of sight (e.g. Wittman et al., 2001, 2003; Dahle et al., 2003; Schirmer et al., 2003). In practice, this method is strongly affected by projection effects and is very sensitive to uncertainties in galaxy shape measurements, due to the intrinsic galaxy ellipticity. The contamination level in

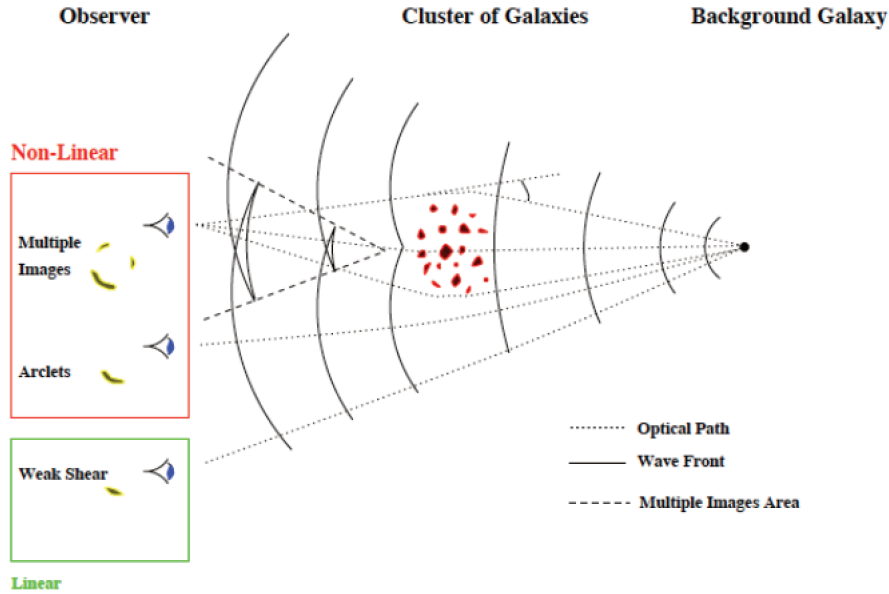


Figure 8 – Schematic representation of the gravitational lensing effect by a cluster on a background galaxy. At small angular distances from the cluster centre, the lensing effect produces large distortions and multiple images of the background galaxy (*strong lensing*). At large angular distances, it produces small tangential distortions of the background galaxy (*weak lensing*). Credit: Kneib and Natarajan (2011).

current lensing surveys is too high (Kratovich, Haiman, and May, 2010; Yang et al., 2011), and they are not yet used to detect galaxy clusters.

On the other hand, weak lensing analyses are particularly efficient in estimating cluster masses because the shear is sensitive to the total cluster mass, independently of its baryon content or its dynamical state.

Cluster samples with high quality gravitational shear mass measurements have been recently obtained by three big surveys: Weighing the Giants (WtG, von der Linden et al., 2014a), Cluster Lensing And Supernova survey with Hubble (CLASH Postman et al., 2012; Merten et al., 2015; Umetsu et al., 2016), and Canadian Cluster Comparison Project (CCCP Hoekstra et al., 2015a).

The most common technique used to infer cluster masses from weak lensing analyses is fitting the observed, averaged gravitational shear profile with a simple parameterized mass model (Hoekstra et al., 2013, and references therein). Discussing the details of this and other techniques available in the literature is beyond the aim of this thesis. I refer the reader to Bartelmann (2010) and Hoekstra et al. (2013) for comprehensive reviews on cluster mass estimation from weak lensing analyses.

For this thesis purposes, what is important is to understand the uncertainties in the lensing mass measurements.

Meneghetti et al. (2010) performed simulations of lensing observations of galaxy clusters, with the aim of investigating the biases that affect such analysis in the estimate of their mass profiles. They found that the best performance was obtained combining strong and weak lensing analyses. In this case, the projected masses within R_{200} could be constrained with a $\sim 10\%$ accuracy, while the scatter around the true 3D mass was larger (by more than a factor of two), mainly due to the deprojection of the lensing masses. The accuracy of the 3D

mass estimates depended on the orientation of the lens with respect to the line of sight, since clusters have a triaxial shape. An over-estimation of the 3D mass was obtained if the major axis points toward the observer, while an under-estimation was obtained for clusters oriented perpendicularly to the line of sight. They also found that important mass under-estimations might be due to the presence of substructures which dilute the tangential shear signal.

Using dark matter cosmological simulations, Becker and Kravtsov (2011) fitted the cluster shear profiles with NFW models and concluded that weak-lensing masses were generally biased towards lower values by a factor depending on the outer radius of the fit. They found a bias of $\sim 10\%$ for masses estimated at R_{500} , for clusters at $z = 0.25, 0.5$. This bias was mostly due to the fact that the NFW model was a poor description of the actual shear profile of the clusters, while the scatter in the mass measurements was due to the halo triaxiality and, with a minor contribution, to correlated large-scale structures. For ground-based observations, the scatter was dominated by the shape noise due to the intrinsic ellipticity of the background galaxies used to measure the shear. They estimated that a large number of background galaxies could reduce the scatter. For example, for clusters at $z = 0.25$, the total scatter on M_{500} decreased from $\sim 37\%$ for 10 galaxies/arcmin² to $\sim 25\%$ for galaxies/arcmin², and the bias decreased by $\sim 5\%$.

Rasia et al. (2012) confirmed these results using mock observations. They found a scatter in mass of the order of $\sim 10\text{-}25\%$, with lower values for clusters with a regular morphology, and a bias $\leq 10\%$ within R_{500} caused, this time, by the presence of substructures and by the triaxiality of the systems. They estimated weak-lensing masses $\sim 30\%$ larger at R_{500} than X-ray masses also obtained from mock observations.

In summary, numerical simulations showed that weak lensing derived masses are biased towards lower values by a factor of $\sim 5\text{-}10\%$, with a scatter of $\sim 10\text{-}25\%$ per cent (Meneghetti et al., 2010; Becker and Kravtsov, 2011; Rasia et al., 2012).

2.1.5 CMB halo lensing

Lensing of the CMB anisotropies by galaxy clusters was discussed for the first time by Zaldarriaga and Seljak (1999). This effect was a new opportunity to measure cluster masses at all redshifts Lewis and Challinor (2006), still not yet fully developed today.

With simulations of *Planck* observations, Melin and Bartlett (2015), analyzed the distortions of the CMB anisotropies caused by the gravitational potential of a front cluster. After removing the distortion due to the thermal SZ signal, they constructed a map of the cluster gravitational potential by applying a quadratic estimator on the background CMB temperature map. Then, they used a matched filter to extract the lens mass, assuming an NFW profile. They showed that this method could provide cluster masses even in low S/N conditions. Simulating 62 observations of A2163, one of the most massive clusters known, with X-ray mass $M_{500}^X = 1.9 \times 10^{15} M_{\odot}$, at $z = 0.203$, they found $M_{500}^{\text{lens}}/M_{500}^X = 1.01 \pm 0.13$, which corresponded to an unbiased recovery of the sample mass scale with 13% of uncertainties. Then they simulated 62 clusters from a mock subsample of the *Planck* Early SZ sample with good X-ray observations (ESZ-XMM), with masses in the range $[2 \times 10^{14} - 2 \times 10^{15} M_{\odot}]$, finding $M_{500}^{\text{lens}}/M_{500}^X = 0.99 \pm$

0.28. The larger uncertainty in this case was due to the larger range of masses used.

Even if this method is new and its systematics are not yet fully analyzed, it is very promising in probing the cluster mass up to higher redshifts with respect to shear measurements, since it uses the CMB as a source plane, instead of galaxies.

2.2 COMPARISON OF MASS PROXIES

As seen in the previous section, cluster masses can be estimated through several, independent techniques which are based on different physical properties and require different assumptions.

In Table 2, I summarize the observables related to mass in different wavelengths, and the uncertainties in their use as proxies of the cluster mass.

Band	Mass proxy	Scatter	Systematics	Reference
Optical, NIR	richness	40%		Rozo+10
	optical luminosity	40%		Mantz+10, Vikhlinin+09
	velocity dispersion	10-15%	30%	White+10, Sifon+16
WL	shear	10-25 %	5-10%	Meneghetti+10, Becker & Kravtsov 2011, Rasia+12
X-rays	gas mass	<10%	25-30%	Allen+11
	gas temperature	<15%		Arnaud+07, Vikhlinin+09a, Mantz+10a
	X-ray luminosity	<10%		Mantz+10a
SZ	integrated Compton parameter	20-30%	up to 30%	Hallman+07, Shaw+08, Planck+14a, Planck+16a

Table 2 – Summary of the mass proxies used at different wavelengths.

From the comparison between the results obtained with different methods one can verify the reliability of each method under different conditions and understand the systematics.

So far, the systematics on the weak lensing mass estimates are found to be smaller with respect to the other methods (5-10%), and they are used as the reference for the total mass in cosmological surveys.

CLUSTERS IN COSMOLOGICAL SURVEYS

As seen Chapter 1, galaxy clusters trace the high density tail of the primordial perturbation field of the dark matter, and they are, for this reason, powerful cosmological probes.

The study of galaxy clusters offer several approaches to constrain cosmological parameters:

- the cluster counts as a function of mass and redshift are related to the present amplitude of density fluctuations, σ_8 , and its redshift evolution is related to the linear growth of linear density perturbations, thus providing constraints on the matter density parameter, Ω_m , and the dark energy equation of state parameter, w (Allen, Evrard, and Mantz, 2011; Vikhlinin et al., 2009);
- assuming that the baryon fraction in clusters ($f_{\text{gas}} = \Omega_b/\Omega_m$) reflects the baryon content of the Universe, it can be used to constrain the matter density parameter Ω_m , if the baryon density parameter Ω_b is known from independent estimates, like Primordial Nucleosynthesis calculations (Steigman, 2006) or analysis of the CMB power spectrum (Hinshaw et al., 2013);
- the observed relation between the mass and the dark matter concentration in galaxy clusters constrains Ω_m and σ_8 . For example, in models with lower values of Ω_m and σ_8 , clusters assemble later, so less concentrated halos are expected at a given mass (Dolag et al., 2004; Neto et al., 2007; Macciò, Dutton, and van den Bosch, 2008).

In this chapter, I focus on the “cluster counts” method, which is the most used in cluster cosmological surveys.

3.1 COSMOLOGY FROM CLUSTER COUNTS

From the theoretical perspective, the cluster number density, or *abundance*, is a function of halo mass and redshift. Observationally, we can measure the dependence on redshift of the observables that trace the mass function.

For a given cluster sample we can measure the number of clusters, dN , within a given solid angle, $d\Omega$, and redshift interval $[z, z + dz]$, that fall into the range $[X, X+dX]$ of the observable X (e.g. Carlstrom, Holder, and Reese, 2002; Voit, 2005, and references therein). We can relate the observed distribution of clusters as a function of redshift, dN/dz , to their theoretical expectation, with the following likelihood:

$$\frac{dN}{dz} = \int d\Omega \int dM F(X|z, M, \theta_{\text{fwhm}}, \sigma_N^2) \frac{dN}{dzdMd\Omega}, \quad (65)$$

where:

- Ω is the solid angle of the sky covered by the survey,
- the mass M is derived from a scaling relation with the survey observable X ,
- $F(X|z, M, \theta_{\text{fwhm}}, \sigma_N^2)$ is the selection function, which characterizes the population of clusters detected among the targets present in the survey

area. It is defined as the joint distribution of the cluster observables (X), given the intrinsic cluster properties (M, z), the survey conditions (e.g. the FWHM of an assumed Gaussian beam, θ_{fwhm} , and the map noise variance, σ_N^2), and on the algorithm used to find clusters. It incorporates the intrinsic and the observational scatter in the mass-observable relation.

$dN/(dzdMd\Omega)$ is the theoretical mass function obtained with numerical simulations. Currently, the standard reference is Tinker et al. (2008), used also in Planck Collaboration et al. (2014a, 2016b). This is based on the Press-Schechter formalism introduced in Section 1.2.4, which is indeed a good description of the observed halo abundances. Combining eq. 41 and 42, we have a useful formula that reveals the dependence on the cosmological parameters:

$$\frac{dn(M, z)}{d \ln M} = \sqrt{\frac{2}{\pi}} \frac{\rho_m}{M} \left| \frac{d \ln \sigma_M}{d \ln M} \right| \frac{\delta_c}{\sigma_M(z)} \exp \left[-\frac{\delta_c^2}{2\sigma_M^2(z)} \right]. \quad (66)$$

Cosmology enters this expression through the mass function and the volume element, $d\Omega$.

The matter density parameter, Ω_m , enters through ρ_m . The amplitude of the matter power spectrum, σ_8 , enters through $\sigma(M)$.

Massive objects are less likely, since the halo mass function decreases exponentially at high masses. On the other hand, this also implies that the halo mass function becomes exponentially sensitive to the choice of the cosmological parameters, and therefore, a reliable determination of the mass function of very massive clusters is important to constrain cosmological parameters.

Carlstrom, Holder, and Reese (2002) reviewed the first cosmological studies from the cluster counts. More recently, Mantz et al. (2015) used weak lensing mass measurements of clusters in the RASS catalog, from the Weighing the Giants project (WtG von der Linden et al., 2014b), and showed that clusters provide tight constraints on Ω_m and σ_8 , which are approximately orthogonal to CMB anisotropy constraints from WMAP and *Planck* (see Fig. 9a).

Moreover, both the geometry of the Universe ($\rho_m, d\Omega$) and growth of structure (the power spectrum) are affected by a change in the dark energy equation of state parameter w . In fact, clusters provide some of the tightest constraints on dark energy in the $w - \Omega_m$ plane, and the combination with other probes, like the CMB anisotropies, the type Ia supernova distances (SNIa), and the baryonic acoustic oscillation (BAO), leads to very tight constraints on w at the few percent level (Mantz et al., 2015), as shown in Fig. 9b.

It is clear that a full knowledge of the mass-observable relation $M(X, z)$ and its scatter, as a function of redshift, is crucial to reliably constrain the cosmological parameters.

At present, the cluster mass scale is the largest source of uncertainty in interpretation of the cluster counts. This thesis contributes to this effort with the study of the scaling relation between the cluster velocity dispersion and mass, compared to other mass proxies. This study is presented in Chapter 5, with the main result showed in Figure 23, and it has been published in Amodeo et al. (2017).

3.2 THE PLANCK TENSION

The *Planck* survey, introduced in Section 2.1.3, has produced a *cosmological* sample of clusters with signal-to-noise ratio $S/N > 6$ used to constrain cosmo-

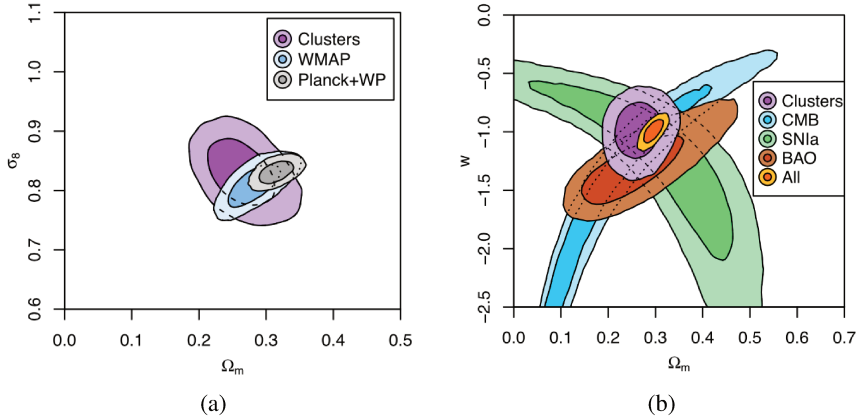


Figure 9 – (a): constraint on Ω_m and σ_8 from galaxy cluster counts by Mantz et al. (2015) compared to two different measurements of the CMB anisotropies, WMAP and *Planck*, assuming a flat Λ CDM cosmology. (b): constraints on w and Ω_m from galaxy cluster counts by Mantz et al. (2015) compared to CMB, supernovae (SNIa), and baryonic acoustic oscillation (BAO), for flat, constant- w models. In both figures, the dark and light colors indicate the 68.3 and 95.4% confidence regions, respectively. Credit: Mantz et al. (2015).

logical parameters from the cluster number counts, with the method described in Section 3.1. They found fewer clusters with respect to the number (as a function of mass and redshift) predicted by the *Planck*'s base Λ CDM model. This difference corresponds to a discrepancy between the cosmological parameters Ω_m and σ_8 obtained from the cluster counts and the CMB anisotropies, respectively.

Planck Collaboration et al. (2014a) accounted for a mass bias $(1 - b) = 0.8$, reflecting the average $\sim 20\%$ of hydrostatic bias estimated in the literature (see Section 2.1.3), while a value of $(1 - b) \sim 0.6$ would be needed to reconcile the tension with the CMB anisotropies.

Planck Collaboration et al. (2016b) relied, in addition, on gravitational lensing studies of the SZ signal-mass relation, which provided an estimate of the mass bias independent of the dynamical state of the cluster (see Section 2.1.4). In particular, they used two results from weak-lensing mass measurements, and one result from CMB lensing mass measurements of *Planck* clusters:

- the Weighing the Giants (WtG, von der Linden et al., 2014b) program analyzed the gravitational shear of 22 *Planck* clusters. Applying a weak lensing analysis, they derived considerably larger masses than *Planck* measuring an average mass ratio of $\langle M_{\text{Planck}}/M_{\text{WtG}} \rangle = 0.688 \pm 0.072$, with decreasing values for larger *Planck* masses. They claim a mass-dependent calibration problem, possibly due to the fact that the X-ray hydrostatic measurements used to calibrate the *Planck* cluster masses rely on a temperature-dependent calibration.
- the Canadian Cluster Comparison Project (CCCP, Hoekstra et al., 2015a) found a smaller bias of 0.76 ± 0.092 , from the comparison of 20 clusters with both weak lensing and SZ mass measurements. They indicated the uncertainty in the determination of photometric redshifts as the largest source of systematic error.
- the CMB lensing technique, implemented as in Melin and Bartlett (2015) (see Section 2.1.5) on the full cluster cosmology sample of more than 400 clusters, gave $1/(1 - b) = 0.99 \pm 0.19$.

These estimates of the mass bias were used as prior information in the analysis of the cluster counts.

The constraints on the cosmological parameters Ω_m and σ_8 from the different priors are shown in Fig. 10a, compared to the constraints from the CMB anisotropies (from Planck Collaboration et al., 2016a). The results obtained with the WtG mass bias lie at the very extreme of the range allowed by the primary CMB analysis and would substantially reduce the tension, while the result from CCCP and CMB lensing, are in much greater tension. This is even more evident from Fig. 10b, which compares the three prior distributions for the mass bias, to the mass bias required to solve the tension by the primary CMB. The latter value was obtained from a joint analysis of the cluster counts (using the MMF3 algorithm) and the CMB, leaving the mass bias as a free parameter. The best-fit value is $(1 - b) = 0.58 \pm 0.04$, more than 1σ below the central WtG value.

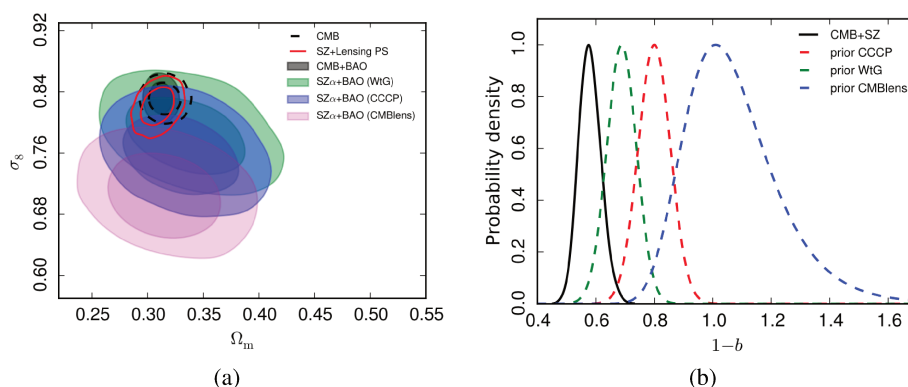


Figure 10 – (a): Comparison of constraints from the CMB to those from the cluster counts in the $(\Omega_m - \sigma_8)$ plane. The green, blue and violet contours give the cluster constraints at 68 and 95% for the WtG, CCCP, and CMB lensing mass calibrations, respectively. (b): Comparison of cluster and primary CMB constraints, expressed in terms of the mass bias, $(1-b)$. The solid black curve shows the distribution of values required to reconcile the counts and primary CMB in the standard Λ CDM model. Credit: Planck Collaboration et al. (2016b).

The tension with the primary CMB results is not unique to the *Planck* cluster counts. Results from other SZ cluster surveys, both SPT and ACT, agree with *Planck* findings. For example, Bocquet et al. (2015), using SPT data, showed a significant shift between the cluster mass scale determined from the cluster velocity dispersion or Y_X and the mass scale needed to match with *Planck* or WMAP9 CMB constraints. Moving to X-ray surveys, Böhringer, Chon, and Collins (2014) and Böhringer and Chon (2016) reported constraints on $(\Omega_m - \sigma_8)$ in agreement with Planck Collaboration et al. (2016b), studying the REFLEX X-ray luminosity function, i.e. using a sample with a very different selection.

On the other hand, Mantz et al. (2015) found a good match between the X-ray cluster counts and the primary CMB constraints, when using the WtG mass calibration, as seen in Fig. 9b.

The comparison between the results from the cluster counts and the CMB anisotropies is very interesting because the two methods probe the amplitude of the density perturbations at two different epochs: the redshift range of the observed clusters, and the recombination epoch, respectively. Therefore, there are two alternative explanations can justify this discrepancy: either *i*) clusters are more massive than determined by the SZ signal-mass scaling relation (i.e.

the cluster observable-mass relation is not well calibrated), or *ii*) the standard Λ CDM model must be extended with, e.g., non-minimal neutrino masses or non-zero curvature, in order to describe the evolution of the density perturbations from recombination until today.

The first part of this PhD thesis is dedicated to understand this tension, by obtaining an independent statistical calibration of the *Planck* SZ mass estimator, from the velocity dispersion of cluster member galaxies, and giving constraints on the mass bias (see Chapter 5).

3.3 CLUSTER COUNTS WITH FUTURE SURVEYS

Many ongoing and forthcoming surveys are or will be used for cluster cosmology, including (in alphabetic order): CCAT (Cerro Chajnantor Atacama Telescope; Woody et al., 2012), DES (Dark Energy Survey; DES Collaboration et al., 2017), eBOSS (Extended Baryon Oscillation Spectroscopic Survey; Zhao et al., 2016), eROSITA (extended ROentgen Survey with an Imaging Telescope Array; Merloni et al., 2012), *Euclid* (Laureijs et al., 2011), KiDS (Kilo-Degree Survey; de Jong et al., 2013), LSST (Large Synoptic Survey Telescope; LSST Science Collaboration et al., 2009), Pan-STARRS (Panoramic Survey Telescope and Rapid Response System; Chambers et al., 2016), *Planck*-SZ (Planck Collaboration et al., 2014a, 2016b), SPT-SZ (South Pole Telescope; de Haan et al., 2016).

While SZ surveys, and in particular *Planck*, have provided the largest samples of cluster catalogs for cosmological studies so far, large optical and near-infrared surveys in the near future will be able to detect a high number of well characterized clusters, such as *Euclid* (up to $z \sim 2$), and LSST (up to $z \sim 1.5$).

Ascaso et al. (2017) consistently compared the selection functions of different next-generation surveys, in terms of the limiting cluster mass threshold as a function of redshift, as shown in Fig. 11. They used an empirical detection of clusters and groups in cosmological simulations. Assuming completeness and purity rates of the cluster selection $>80\%$, they predicted that the limiting cluster mass for *Euclid* would be $< 2 \times 10^{14} M_{\odot}$ up to $z \sim 1.5$, and $\leq 10^{14} M_{\odot}$ up to $z \sim 1$, in the ‘‘pessimistic’’ scenario in which the *Euclid* photometry would be only complemented by the five-band optical photometry from DES. With the additional six-band photometry from LSST (‘‘optimistic’’ scenario), the predicted limiting mass would be shifted by $\sim 10\%$ towards lower values. For LSST, the predicted limiting mass would be $8 - 9 \times 10^{13} M_{\odot}$ up to $z \sim 0.7$. The other optical/near-IR survey analyzed, J-PAS (Benitez et al., 2014), would reach ~ 1.5 lower masses at $z < 0.7$ thanks to its very accurate photometric redshifts obtained with 54 narrow bands. It is interesting to note that comparable values could be obtained only up to $z \sim 0.2$ with the e-Rosita X-ray survey (Merloni et al., 2012). For the SZ surveys SPTpol (Carlstrom et al., 2011) and ACTpol (Marriage et al., 2011) the limiting mass would be $4 \times 10^{14} M_{\odot}$ ($7 \times 10^{14} M_{\odot}$) at $z = 2$, decreasing to $\times 10^{14} M_{\odot}$ ($4 \times 10^{14} M_{\odot}$) at $z = 1.5$ (Weinberg et al., 2013).

This means that optical and near-infrared surveys will be of fundamental importance to detect low mass galaxy clusters at low to medium redshift.

I focus here on the *Euclid* mission and the developments that are being planned to use clusters as cosmological probes, since I joined the *Euclid* consortium in the Science Working Group ‘‘Cluster of Galaxies’’.

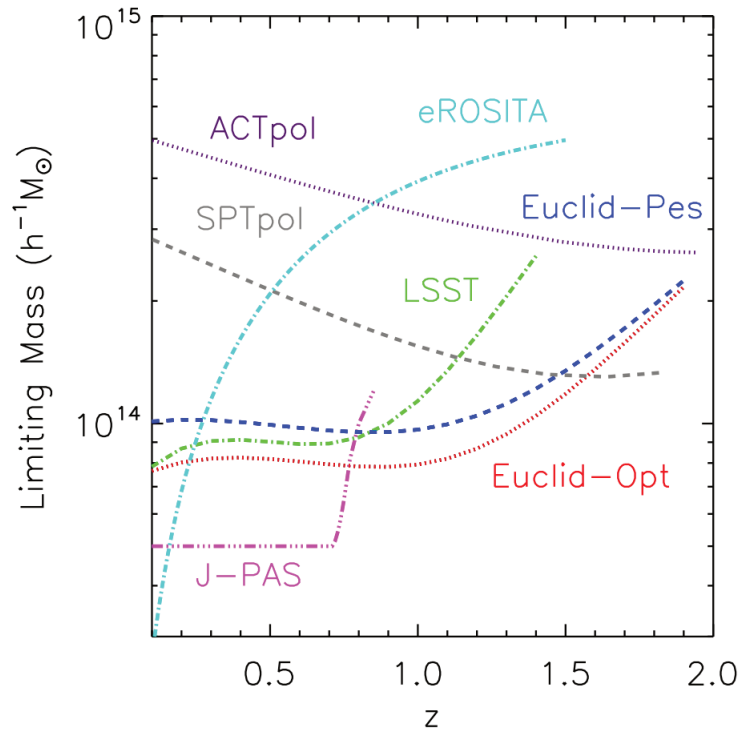


Figure 11 – Selection function for different next-generation surveys. In the optical and near-IR band: *Euclid*-Optimistic (red dotted line), *Euclid*-Pessimistic (blue dashed line), LSST (green dot-dashed line), obtained by Ascaso et al. (2017) by imposing completeness and purity rates $>80\%$, J-PAS (pink three dot-dashed line), obtained by Ascaso et al. (2016). In the X-rays: eROSITA (cyan dot-dashed line), obtained by Pillepich, Porciani, and Reiprich (2012). SZ: ACTpol and SPTpol SZ survey (purple dotted and dashed grey lines, respectively), obtained by Weinberg et al. (2013). Credit: Ascaso et al. (2017).

3.3.1 *Euclid* forecasts

Euclid is a European Space Agency (ESA) mission, aimed at studying the evolution of the cosmic web up to $z \sim 2$ (i.e. over the past 10 billion years), in order to understand the nature of dark energy and dark matter (Laureijs et al., 2011). It is optimized to exploit two primary cosmological probes:

1. weak gravitational lensing, through imaging on sub-arcsec scales for the galaxy shape measurements, and photometry at visible and infrared wavelengths to measure the photometric redshifts of each lensed galaxy out to $z \sim 2$;
2. galaxy clustering, through accurate near-infrared spectroscopy to measure redshifts of galaxies out to $z \sim 0.7$, to better than 0.1%.

Planned for launching in the year 2022, *Euclid* will orbit around the 2nd Lagrange Point of the Sun-Earth System. In six years, it will complete one wide survey and one deep survey.

The *Euclid Wide Survey* will observe 15000 deg² of the extragalactic sky (not contaminated by the light from our Galaxy). The visual instrument (VIS) will produce imaging photometry in one broad visible band (550-900 nm), with a pixel size of 0.1 arcsec, allowing to measure the shape of 30 galaxies per arcmin² down to a limiting AB magnitude of 24.5. The near-infrared instrument (NISP) will be equipped to perform photometry in three bands in the range 920-2000 nm, with a pixel size of 0.3 arcsec, allowing to observe galaxies down to an AB magnitude of 24, and measure their redshift (in combination to auxiliary ground-based data) with a precision of $\sigma_z(1+z) < 0.05$.

The *Euclid Deep Survey* will observe 40 deg² in at least two deep fields, reaching two magnitudes deeper than the wide survey. It will use the NISP instrument to perform slitless spectroscopy (one blue grism covering 920-1250 nm + three red grisms covering 1250-1850 nm with different orientations) with a spectral resolution of $\lambda/\delta\lambda \sim 380$ for a 0.5 arcsec source, and measure galaxy redshifts with an accuracy of $\sigma_z(1+z) < 0.001$.¹

In addition to the primary science, the *Euclid* surveys will provide data for complementary cosmological probes, including galaxy cluster counts.

Sartoris et al. (2016) provided forecasts on the constraints that can be obtained with *Euclid* cluster counts. Based on an analytical estimate of the cluster selection function in the photometric *Euclid* survey, they predicted that $\sim 2 \times 10^6$ clusters will be detected² at 3σ with a minimum mass of $M_{200} \sim 8 \times 10^{13} M_\odot$ almost constant with redshift up to $z = 2$, and about one-fifth of them will be at $z \geq 1$.

These results globally agree with the empirical selection function found by Ascaso et al. (2017) for the *Euclid*-Optimistic case (red-dotted line in Fig. 11), which instead steepens at $z > 1$.

Following a Fisher matrix formalism, Sartoris et al. (2016) derived constraints on σ_8 , Ω_m , dark energy equation of state, primordial non-Gaussianity, modified gravity, and neutrino masses. They applied the analysis to number counts (NC) and progressively added information of the matter power spectrum (PS), assumed to have a perfect knowledge of the observable-mass scaling relation

1. These numbers refer to the “mission characteristics” published on <https://www.euclid-ec.org>, last updated the 27th Dec, 2017.

2. The number of galaxies within R_{500} is required to be at least three times the rms of the field counts within the same radius.

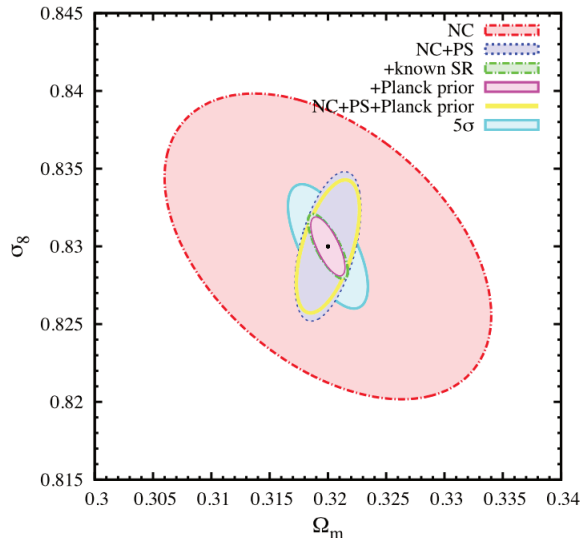


Figure 12 – 68% confidence levels on σ_8 and Ω_m . Forecasts are obtained with the 3σ cluster selection in the analysis including: (i) number counts (NC, red dash-dotted contour); (ii) the combination of number counts and power spectrum information (NC+PS, blue dotted contour); (iii) a perfect knowledge of the of the scaling relation between the true and the observed cluster mass (NC+PS+known SR, green dash-dotted contour); (iv) priors from *Planck* CMB data (NC+PS+known SR+*Planck* prior, magenta solid contour); (v) NC+PS+*Planck* prior, without accurate mass estimates (yellow solid contour); (vi) forecasts obtained with a 5σ detection in the case NC+PS+known SR+*Planck* prior (cyan solid contour). Credit: Sartoris et al. (2016).

(knownSR), and added priors from *Planck* CMB data. Fig. 12 shows the 68% confidence levels obtained with the different probes for the $\Omega_m - \sigma_8$ plane. It is remarkable how the “known scaling relation” tighten the constraints on the cosmological parameters, even without the *Planck* priors (green dash-dotted contours). For this reason, the goal of *Euclid* will be to have an accuracy of 1% on the cluster mass.

The accuracy of the constraints obtained for a pair of joint parameters, (p_i, p_j) , can be quantified by the figure of merit (FoM; Albrecht et al., 2006) defined as:

$$\text{FoM} = \frac{1}{\sqrt{\det[\text{Cov}(p_i, p_j)]}}, \quad (67)$$

where $\text{Cov}(p_i, p_j)$ is the covariance matrix between the two parameters. In short, a larger value of the figure of merit indicates higher accuracy.

Fig. 13 clearly shows that the cosmological constraints with cluster number counts will be heavily improved thanks to the broad redshift range covered by *Euclid*. In fact, the FoM of a survey reaching out to $z \leq 2$ is a factor of two larger than the FoM of an equivalent survey limited to $z \leq 1.2$. This prediction calls for a great effort to optimize the detection and build catalogs of clusters out to $z = 2$ with a high level of completeness and purity.

3.4 CLUSTER COSMOLOGY AND THIS PHD THESIS

In this PhD thesis we will address two main aspect of cluster cosmology discussed in this chapter.

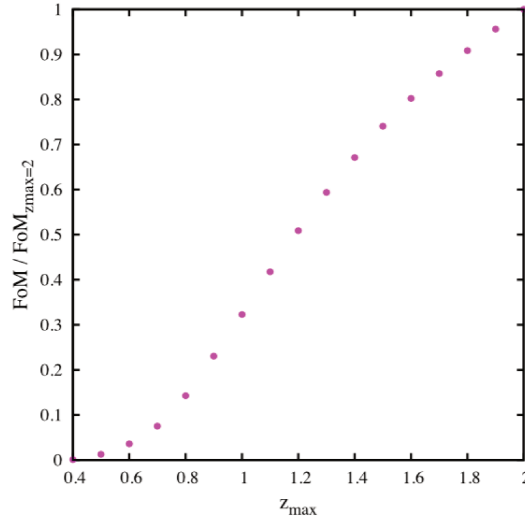


Figure 13 – Figure of merit, FoM, for the number count analysis of the 3σ cluster selection of the *Euclid* photometric survey, as a function of the limiting redshift z_{\max} . The FoM is evaluated within $0.2 \leq z \leq z_{\max}$ with respect to the FoM evaluated within $0.2 \leq z \leq 2.0$. Credit: Sartoris et al. (2016).

One: understand the systematics in the cluster mass estimation with different observables to help improving its calibration (Chapters 4, 5).

We have conducted a spectroscopic follow-up of 20 *Planck* cluster candidates with the Gemini and Keck telescopes (P.I. J.G. Bartlett and F.A. Harrison, respectively), for which we measured redshifts and velocity dispersions from member galaxies. For a subsample of 17 clusters, I study the scaling relation between the cluster velocity dispersion, calculated using redshifts from our optical spectroscopy, and the *Planck* SZ mass proxy, based on ICM properties. I analyze possible sources of systematics in the mass calibration, and I compare my results with mass determinations for the *Planck* clusters in other works.

Two: characterize the cluster galaxy population at high redshift to help planning cluster detection for future surveys (Chapters 6, 7).

I analyze sixteen clusters from the Cluster Around Radio-Loud AGN (CARLA) survey at $1.4 < z < 2.8$, which are an homogeneous statistical sample of spectroscopically confirmed clusters at high redshift, ideal to investigate galaxy evolution in dense environments. Most of the thesis work is devoted to optimize a joint photometric analysis of *Spitzer*, HST, and ground-based *i*-band images, based on the T-PHOT software (Merlin et al., 2015, 2016), which allows to take advantage of the information given by our high-resolution ($0.06 \text{ arcsec pix}^{-1}$) F140W HST images, and use positions and surface brightness profiles of sources measured on this band as priors to derive PSF-matched fluxes in the lower resolution bands. I discuss my preliminary results on color-color diagrams; their comparison to rest-frame UVJ colors gives an indication of the fraction of star-forming and quiescent galaxies, while color-magnitude diagrams show their location with respect to the galaxy red sequence.

CALIBRATING THE GALAXY CLUSTER MASS SCALE WITH VELOCITY DISPERSIONS I: SAMPLE DESCRIPTION

In this chapter, I describe the observation campaigns from which we have selected the sample used to study the cluster mass scale.

I present the spectroscopic follow-up of 20 *Planck* cluster candidates with the Gemini and Keck telescopes (P.I.s: J.G. Bartlett and F.A. Harrison, respectively), from which we have derived the cluster redshifts and velocity dispersions. Seven cluster redshifts are measured for the first time, including one of the most distant *Planck* cluster confirmed to date, at $z = 0.782 \pm 0.010$. The results of this study are published in Amodeo et al. (2017, 2018), enclosed to this thesis in Appendix B. In addition, catalogs of the spectroscopic redshifts of member galaxies of each confirmed cluster are published as online tables.

4.1 SAMPLE DESCRIPTION

The goal of our Gemini program was to obtain a statistical calibration of the *Planck* SZ mass estimator. For this purpose, we mostly chose clusters that were detected with a *Planck* SZ S/N of about 4.5σ or larger, distributed in the northern and southern hemispheres, spanning a wide range in *Planck* SZ masses, $2 \times 10^{14} M_{\odot} < M_{500}^{\text{Pl}} < 10^{15} M_{\odot}$, in the redshift range $0.16 < z < 0.44$.

Our sample was built from optical imaging observations with the Gemini, Keck, and Palomar (also infrared imaging) telescopes, used to select cluster members for spectroscopic follow-up with Gemini and Keck. The details of each observing run (pre-imaging and optical spectroscopy) are listed in Table 3.

Table 3 – Observation details.

Run	Semester	PI	Tel./Inst.	Program ID	N_{cl}
1	2010B	Lawrence	Palomar/LFC,WIRC		11
2	2011A	Lawrence	Palomar/LFC		25
3	2011B	Lawrence	Palomar/LFC		15
2	2011A	Bartlett	Gemini-N/GMOS	GN-2011A-Q-119	11
3	2011B	Bartlett	Gemini-N/GMOS	GN-2011B-Q-41	11
4	2012B	Lawrence	Palomar/LFC		9
5	2012A	Bartlett	Gemini-S/GMOS	GS-2012A-Q-77	9
6	2013B	Harrison	Keck/LRIS	UT 2013 October 4-5	1

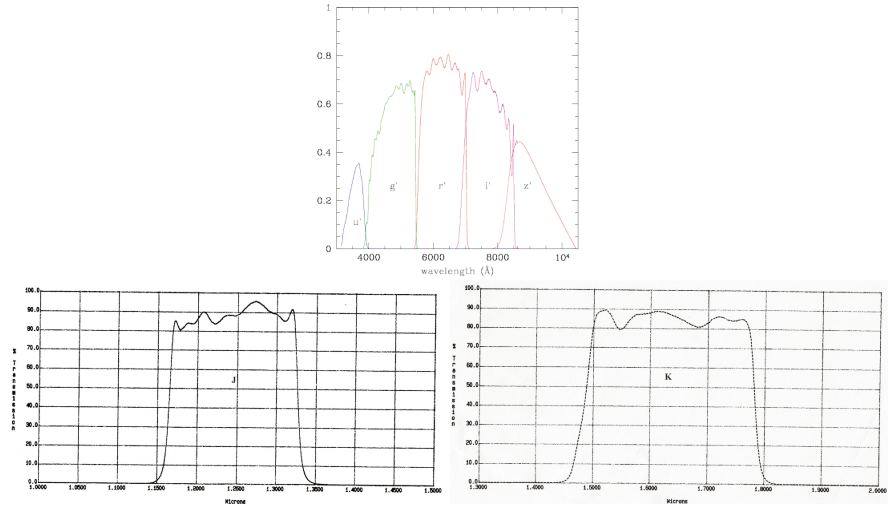


Figure 14 – Filter responses for (*top*): the LFC camera (u', g', r', i', z') and (*bottom*): the WIRC camera (J, K) of the Palomar telescope. Credit: <http://www.astro.caltech.edu>.

As discussed in Section 2.1.1, early-type galaxies (ETGs) in clusters define a tight red-sequence up to redshift $z \sim 1.5$ (Mei et al., 2009), and can be easily identified with respect to field background galaxies. Therefore, we selected cluster members to follow-up with spectroscopy from optical and infrared imaging using a red sequence search method (Gladders and Yee, 2000; Licitra et al., 2016b,a). For most clusters, we used g' and i' filters for imaging, since the ETG ($g - i$) color is monotonic over the redshift range in which most of *Planck* clusters are detected, $z < 1$. We also observed the r' band, when possible within our exposure time constraints, to obtain better photometric redshifts. For the candidates that appeared to be at $z > 0.6$ from their *WISE* imaging in the mid-infrared (see the *WISE* analysis in Planck Collaboration et al., 2015b), we obtained near-infrared observations in the J and K bandpasses. For some of our targets, we could not obtain images at two different wavelengths and used SDSS photometry when available. Cluster members were selected as red sequence galaxies by their colors, using Bruzual and Charlot (2003) stellar population models and Mei et al. (2009) empirical red sequence measurements, following the cluster member selection technique described in Licitra et al. (2016b,a), and summarized in Section 2.1.1, adapted for the bandpasses available for these observations.

The filter responses as a function of the wavelength of the instruments used in this thesis are shown in Figures 14, 15.

4.1.1 *Gemini observations*

The Gemini imaging and spectroscopic follow-up was performed with GMOS-N and GMOS-S at the Gemini-North and Gemini-South Telescopes, respectively, in the programs GN-2011A-Q-119, GN-2011B-Q-41, and GS-2012A-Q-77 (P.I. J.G. Bartlett). This sample consists of 19 *Planck*-detected galaxy clusters, 17 of which are part of the *Planck* PSZ2 catalog (Planck Collaboration et al., 2015b), and one is published in the *XMM-Newton* validation follow-up of *Planck* cluster candidates (Planck Collaboration et al., 2013). Two clusters are not part of the already published *Planck* papers: (1) PLCK G183.33-36.69 has a detection

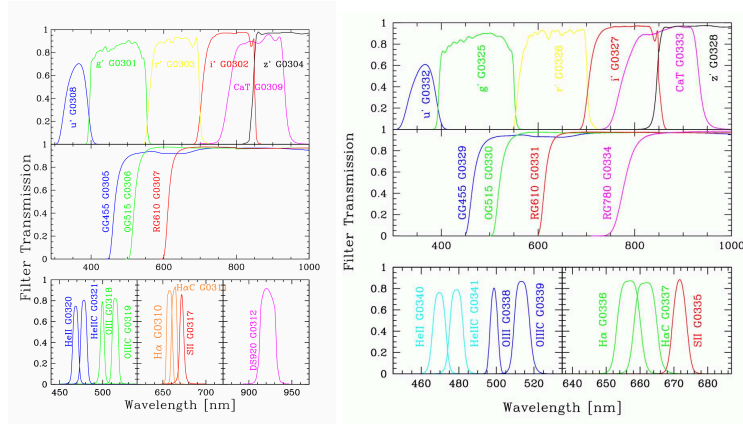


Figure 15 – Transmission curves for the Gemini GMOS-N (*left*) and GMOS-S (*right*) cameras. Credit: <http://www.gemini.edu>.

signal-to-noise ratio (S/N) just below the *Planck* catalog selection threshold and (2) PLCK G147.32-16.59 is in the *Planck* cluster mask.

In Figure 16, I compare our sample to the full PSZ2 catalog. These histograms show that our selection has an average redshift larger than the PSZ2 catalog, and a mass range covering most of the mass range of the PSZ2 catalog. In fact, our sample has an average redshift of $z = 0.37$ and an average mass of $M = 6.2 \times 10^{14} M_{\odot}$, compared to the average PSZ2 redshift and mass of $z = 0.25$ and $4.8 \times 10^{14} M_{\odot}$, respectively. The larger average redshift was chosen to cover most of the cluster members within $\sim R_{200}$ in the field of view of the Gemini and Keck telescopes.

The Northern sample was selected in the area covered by the SDSS, and we used the SDSS public releases and our GMOS-N pre-imaging in the *r*-band (150 s) to detect red galaxy over-densities around the *Planck* detection center. When unknown, we estimated the approximate cluster redshift using its red sequence to calculate the appropriate exposure times for the spectroscopic follow-up. For PSZ2 G139.62+24.18, PSZ2 G157.43+30.34 and PLCK G183.33-36.69, we used imaging obtained with the Palomar telescope. For the Southern sample, we obtained GMOS-S pre-imaging in the *g* and *i*-bands (200 s and 90 s integrations, respectively).

Our GMOS spectroscopic observations were reduced by our collaborator Adam Stanford using the IRAF Gemini GMOS package and standard techniques. After co-adding the reduced exposures, one-dimensional spectra were extracted in each slitlet and were initially inspected visually to identify optical features such as the 4000 Å break, G-band, Ca H+K absorption lines, and, rarely, [O II] λ 3727 emission. More precise galaxy redshifts were determined by running the IRAF task *xcsao*. In Figure 17, I show two Gemini/GMOS spectra of galaxies in the cluster PSZ2 G250.04+24.14. Table 4 lists spectroscopically confirmed clusters.

4.1.2 Keck Observations

We obtained spectroscopy of PSZ2 G085.95+25.23 on the nights of UT 2013 October 4-5 using the dual-beam Low Resolution Imaging Spectrometer (LRIS; Oke et al., 1995) on the Keck I telescope atop Mauna Kea. These slitmask observations were obtained with the $400 \ell \text{ mm}^{-1}$ grism on the blue arm of

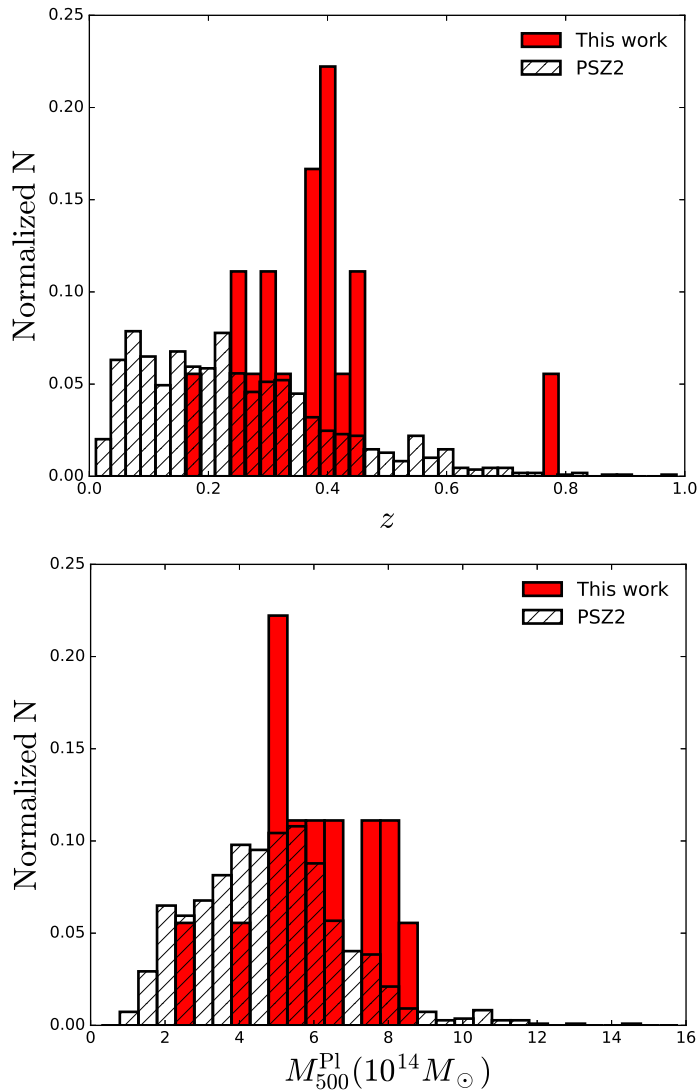


Figure 16 – Histograms of the redshifts (left) and the masses (right) of our spectroscopic sample compared to the full PSZ2 catalog. These histograms are normalized to the total number of objects in each sample. We have selected cluster candidates with redshift $z > 0.2$ (with average redshift larger than the PSZ2 catalog), and larger average mass than the PSZ2 catalog, with cluster masses in the range $2.3 \times 10^{14} M_{\odot} < M_{500}^{\text{Pl}} < 9.4 \times 10^{14} M_{\odot}$. The cluster mass shown here is the *Planck* mass proxy (Planck Collaboration et al., 2015b).

LRIS ($\lambda_{\text{blaze}} = 3400 \text{ \AA}$), the $400 \ell \text{ mm}^{-1}$ grating on the red arm of LRIS ($\lambda_{\text{blaze}} = 8500 \text{ \AA}$), and the 5600 \AA dichroic was used to split the light. We obtained three 1200 s integrations on the first night through variable cloud cover, and two 1200 s integrations on the second night in photometric conditions. After some experimentation, we based our analysis on the single best exposure from the first night combined with the two exposures from the second night. The data were processed by our collaborator Daniel Stern using standard techniques within IRAF, and flux calibrated using standard stars from Massey and Gronwall (1990) observed on the second night. In Figure 18, I show two Keck/LRIS spectra of galaxies in the cluster PSZ2 G085.95+25.23.

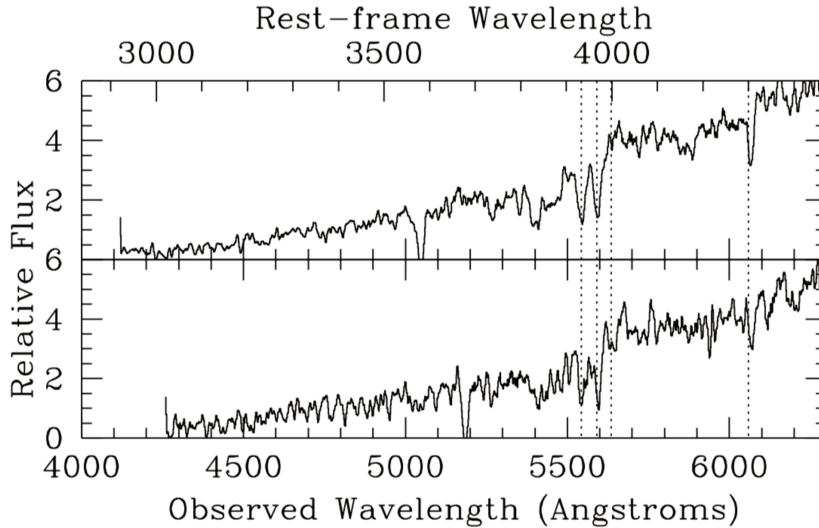


Figure 17 – Spectra obtained with Gemini/GMOS for two galaxies in the cluster PSZ2 G250.04+24.14 ($z = 0.411$). The vertical dotted lines represent Ca H+K, D4000, and the G-band, respectively.

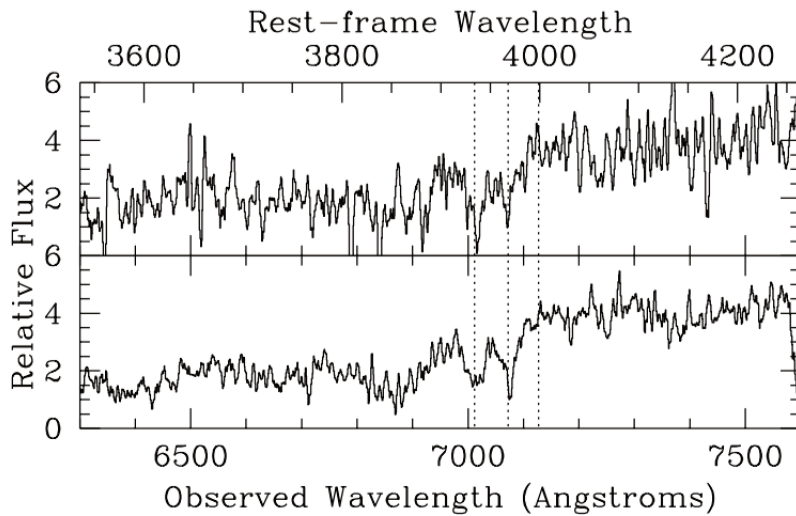


Figure 18 – Spectra obtained with Keck/LRIS for two galaxies in the cluster PSZ2 G085.95+25.23 ($z = 0.782$). The vertical dotted lines represent Ca H+K and D4000, respectively.

4.2 CLUSTER CONFIRMATION AND MEASUREMENTS OF SPECTROSCOPIC REDSHIFTS

Our collaborator Adam Stanford calculated the cluster redshifts and velocity dispersions using the ROSTAT software (Beers, Flynn, and Gebhardt, 1990) with the biweight method (see Table 5). This is appropriate to our clusters where there are typically 20 confirmed members. I also report the dispersion σ_G determined from the gapper estimator (as implemented in ROSTAT), which is to be preferred for clusters with fewer than 10-15 members (see Girardi et al., 1993, 2005). I find

Table 4 – Spectroscopically confirmed cluster sample. Clusters are named after their PSZ2 ID, when available. When it is not available, we use the prefix ‘PLCK’ followed by a notation in Galactic coordinates similar to that used in the PSZ2 paper. Right ascension and declination indicate the optical cluster centre. Filter names used for imaging, spectroscopic observing times and the number of masks are also stated. The last column lists the observing run(s) for each target, including pre-imaging.

Name	R.A. (deg)	Decl. (deg)	Filter	t_{exp} (s)	N_{mask}	Run
PSZ2 G033.83-46.57	326.3015	-18.7159	<i>g,i</i>	1800	2	GS-2012A-Q-77
PSZ2 G053.44-36.25	323.8006	-1.0493	<i>r</i>	1800	1	GN-2011A-Q-119,GN-2011B-Q-41
PSZ2 G056.93-55.08	340.8359	-9.5890	<i>r</i>	1800	2	GN-2011A-Q-119,GN-2011B-Q-41
PSZ2 G081.00-50.93	347.9013	3.6439	<i>r</i>	1800	1	GN-2011A-Q-119,GN-2011B-Q-41
PSZ2 G083.29-31.03	337.1406	20.6211	<i>r</i>	1800	1	GN-2011A-Q-119,GN-2011B-Q-41
PSZ2 G085.95+25.33	277.6164	56.8823	–	3600	2	Keck Telescope
PSZ2 G108.71-47.75	3.0715	14.0191	<i>r</i>	1800	2	GN-2011A-Q-119,GN-2011B-Q-41
PSZ2 G139.62+24.18 ^a	95.4529	74.7014	<i>r</i>	900	2	GN-2011A-Q-119,GN-2011B-Q-41
PLCK G147.32-16.59 ^b	44.1101	40.2853	<i>r</i>	1800	2	GN-2011A-Q-119,GN-2011B-Q-41
PSZ2 G157.43+30.34 ^a	117.2243	59.6974	<i>r</i>	3600	2	GN-2011A-Q-119,GN-2011B-Q-41
PLCK G183.33-36.69 ^a	57.2461	4.5872	<i>r</i>	1800	2	GN-2011A-Q-119,GN-2011B-Q-41
PSZ2 G186.99+38.65	132.5314	36.0717	<i>r</i>	1800	2	GN-2011A-Q-119,GN-2011B-Q-41
PSZ2 G216.62+47.00	147.4658	17.1196	<i>r</i>	1800	2	GN-2011A-Q-119,GN-2011B-Q-41
PSZ2 G235.56+23.29	134.0251	-7.7207	<i>g,i</i>	900	2	GS-2012A-Q-77
PSZ2 G250.04+24.14	143.0626	-17.6481	<i>g,i</i>	1800	2	GS-2012A-Q-77
PSZ2 G251.13-78.15	24.0779	-34.0014	<i>g,i</i>	900	2	GS-2012A-Q-77
PSZ2 G272.85+48.79	173.2938	-9.4812	<i>g,i</i>	900	2	GS-2012A-Q-77
PSZ2 G329.48-22.67	278.2527	-65.5555	<i>g,i</i>	900	2	GS-2012A-Q-77
PSZ2 G348.43-25.50	291.2293	-49.4483	<i>g,i</i>	900	2	GS-2012A-Q-77
PSZ2 G352.05-24.01	290.2320	-45.8430	<i>g,i</i>	1200	2	GS-2012A-Q-77

that biweight and gapper estimates are perfectly consistent, with the absolute difference between the velocity dispersions calculated from the two methods being on average of (0.04 ± 0.14) sigma, and never higher than 0.5 sigma. Since the line-of-sight cluster velocity dispersion can be highly anisotropic, small galaxy samples lead to large systematic uncertainties, with estimated uncertainties of $\lesssim 10\%$ (White, Cohn, and Smit, 2010) for samples with more than ~ 10 -15 galaxies like ours.

I retain as possible cluster members the galaxies within 3σ of the average cluster velocity/redshift. Standard deviations are in the range 0.001-0.008 in redshift, for the clusters that we confirm, apart PLCK G147.32-16.59 that shows evidence for an undergoing merger event (see discussion below). In Fig. 19 and 20, I present the redshift distributions of the cluster member galaxies (left), the optical image of the cluster with the selected members (middle), and the SZ maps in units of S/N (right), for the Northern and the Southern samples, respectively. I also present Gaussian fits to the redshift distributions in the left-hand panels.

In the middle panels of Fig. 19 and 20 I show the optical pre-imaging, within the Gemini field of view of 5.5×5.5 arcmin², indicating spectroscopically confirmed members by green circles.

For PSZ2 G056.93-55.08, we visually observed three spatially separated galaxy groups, but all at the same redshift and within one virial radius. We derived the virial radius $R_{200} = (2.00 \pm 0.05)$ Mpc from the SZ mass estimate of $M_{500}^{\text{Pl}} = (9.4 \pm 0.5) \times 10^{14} M_{\odot}$ ¹. At the cluster redshift, $z = 0.443$, 2 Mpc correspond to 5.7 arcmin in a Planck cosmological model (Planck Collaboration et al., 2016a). We could not obtain a separate mass estimate for each group because the *Planck* beam includes all the three groups and we did not have enough spectroscopic members of each group for deriving the group mass from velocity dispersions. Therefore, in this analysis, I consider the three groups as being part of a single cluster detection.

For all targets but PSZ2 G352.05-24.01, the red circled area is centered on the optical center of the cluster and has a 1 arcmin radius. The optical center was obtained as the brightest cluster member in the densest cluster region, following a modified version of the centering algorithm from Licitra et al. (2016b). For PSZ2 G352.05-24.01, we used the coordinates of the X-ray center, marked with a red cross.

In the right-hand panels, I show the SZ maps with the same area enclosed by the black circles and centered on the optical position. The SZ maps have an angular resolution of 5 arcmin and are given in units of S/N. All the detections lie above $S/N = 4.5$, except for PLCK G183.33-36.69 with $S/N = 2$.

1. See Chapter 5 for details of the conversion from M_{500}^{Pl} to M_{200}^{Pl} .

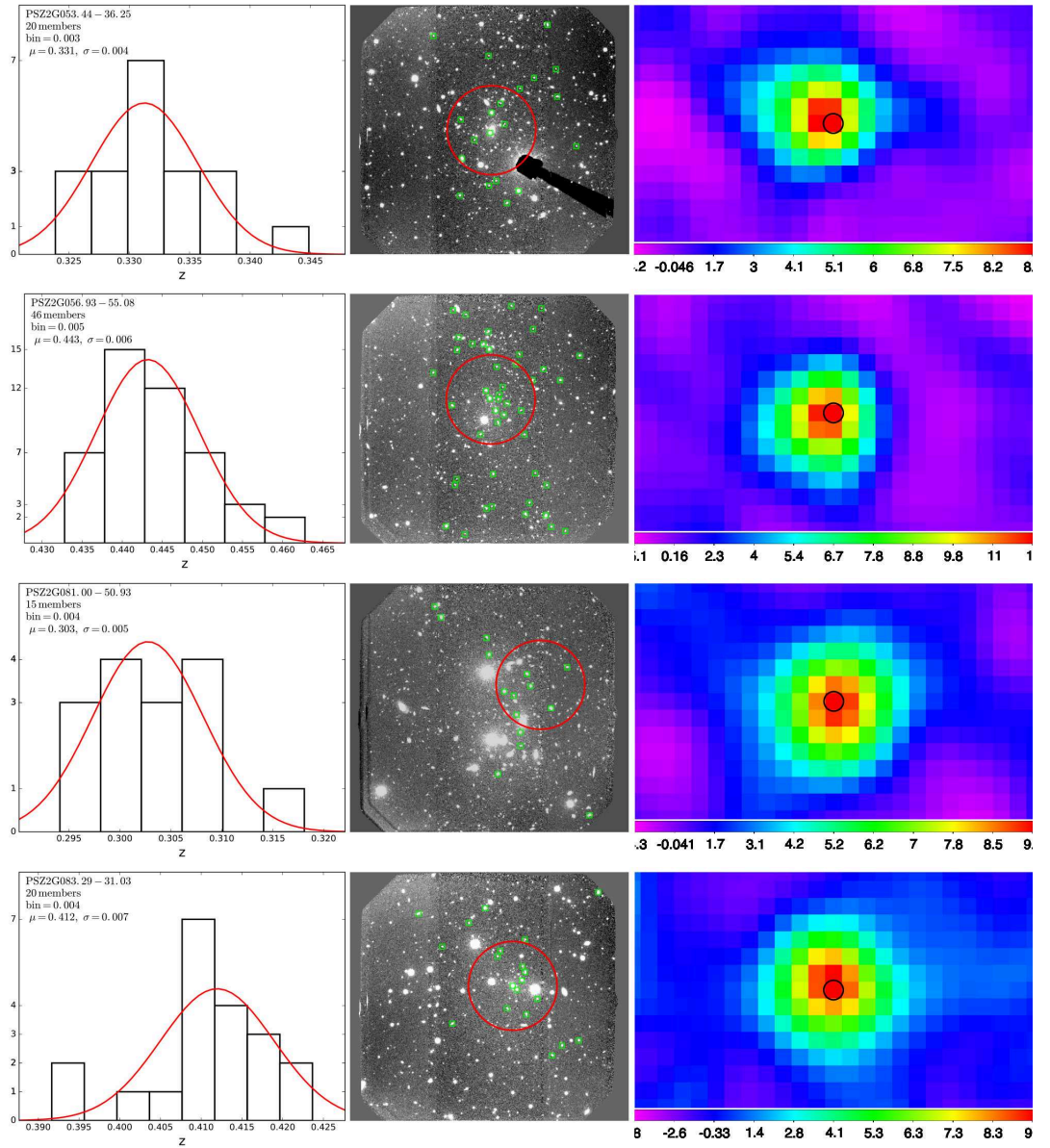


Figure continued

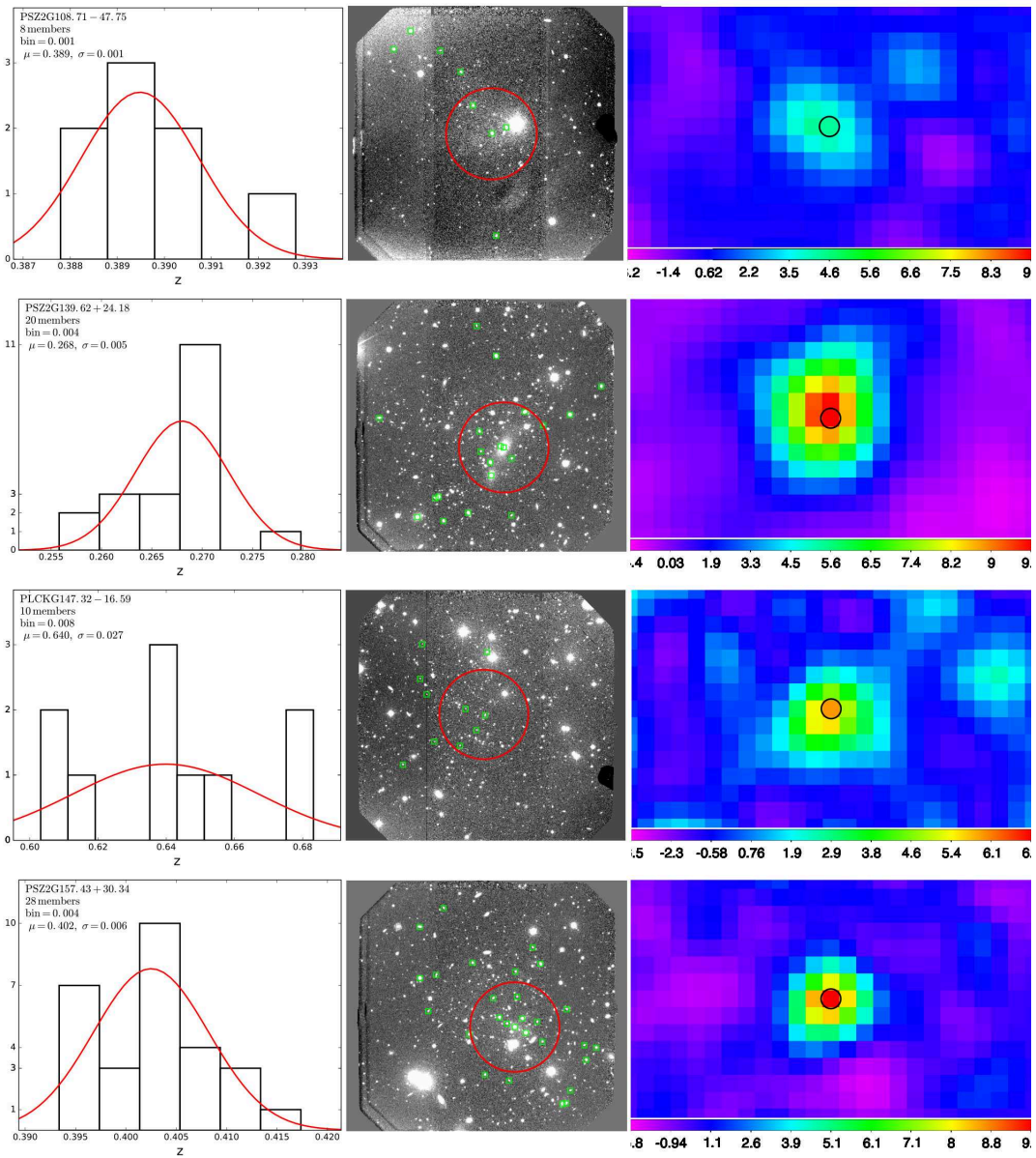


Figure continued

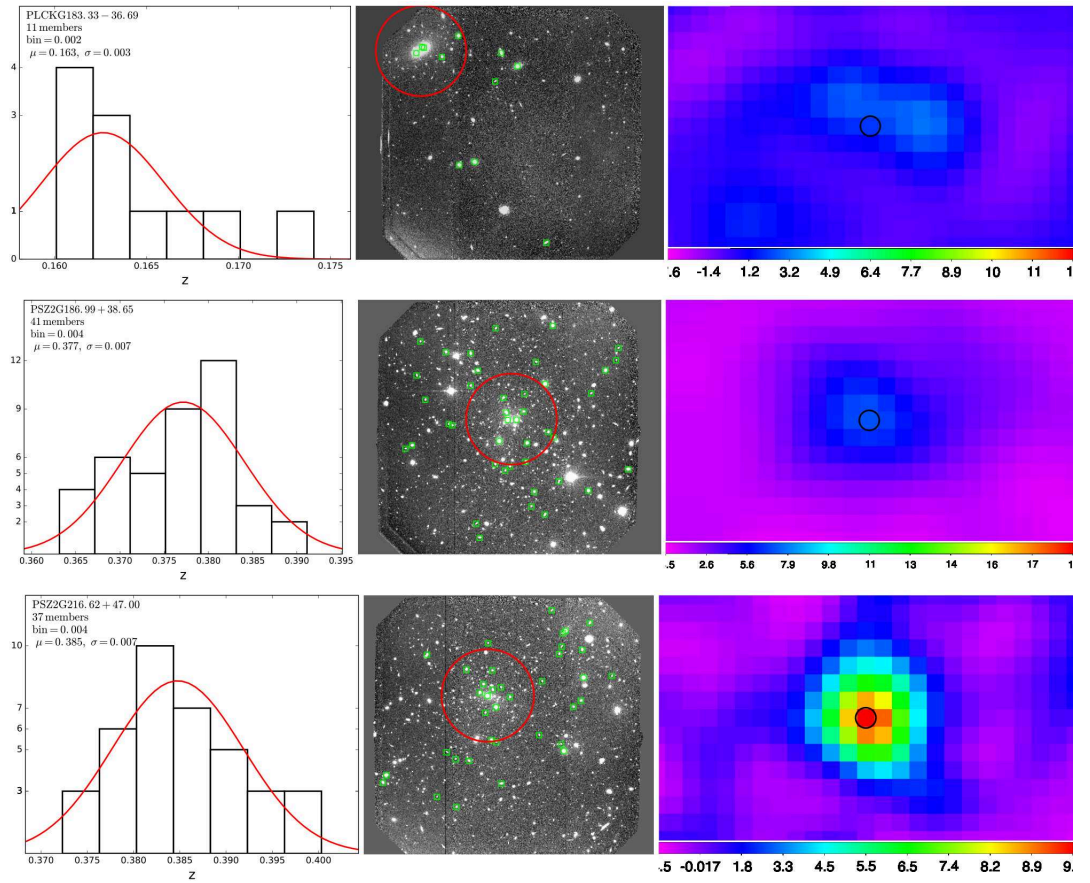


Figure 19 – Redshift histograms (left), optical images (middle) and SZ maps in signal-to-noise units (right) of clusters in the Northern sample. The red curve in the histograms is a Gaussian fit with mean (μ) and standard deviation (σ) indicated in the legends, calculated for the redshift distribution using the bi-weight method. We also indicate the number of members in each cluster and the size of the redshift bins. The red (black) circles in the images encloses a circle of radius 1 arcmin around the optical (SZ) center of the clusters, while the confirmed member galaxies are shown by green squares.

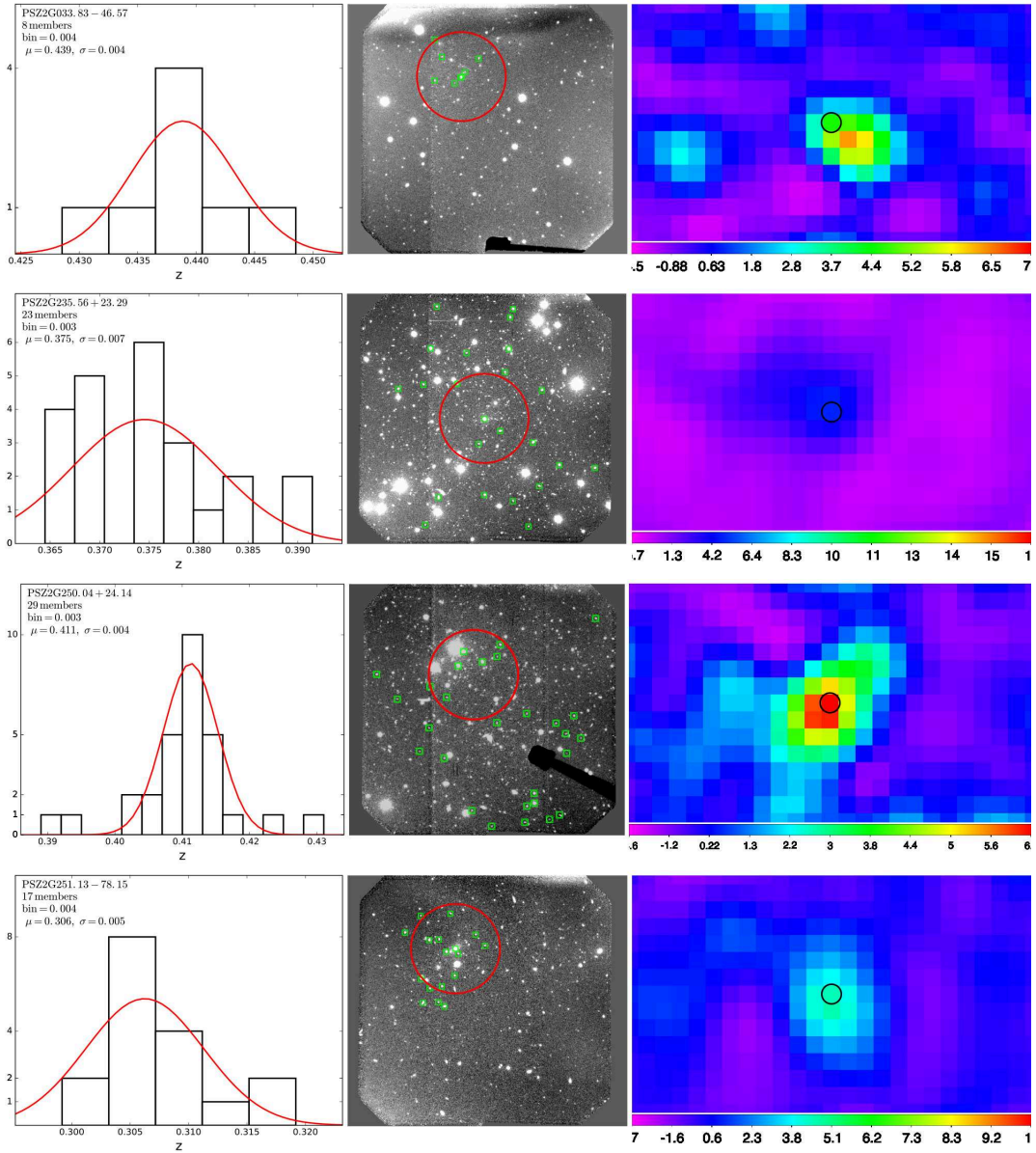


Figure continued

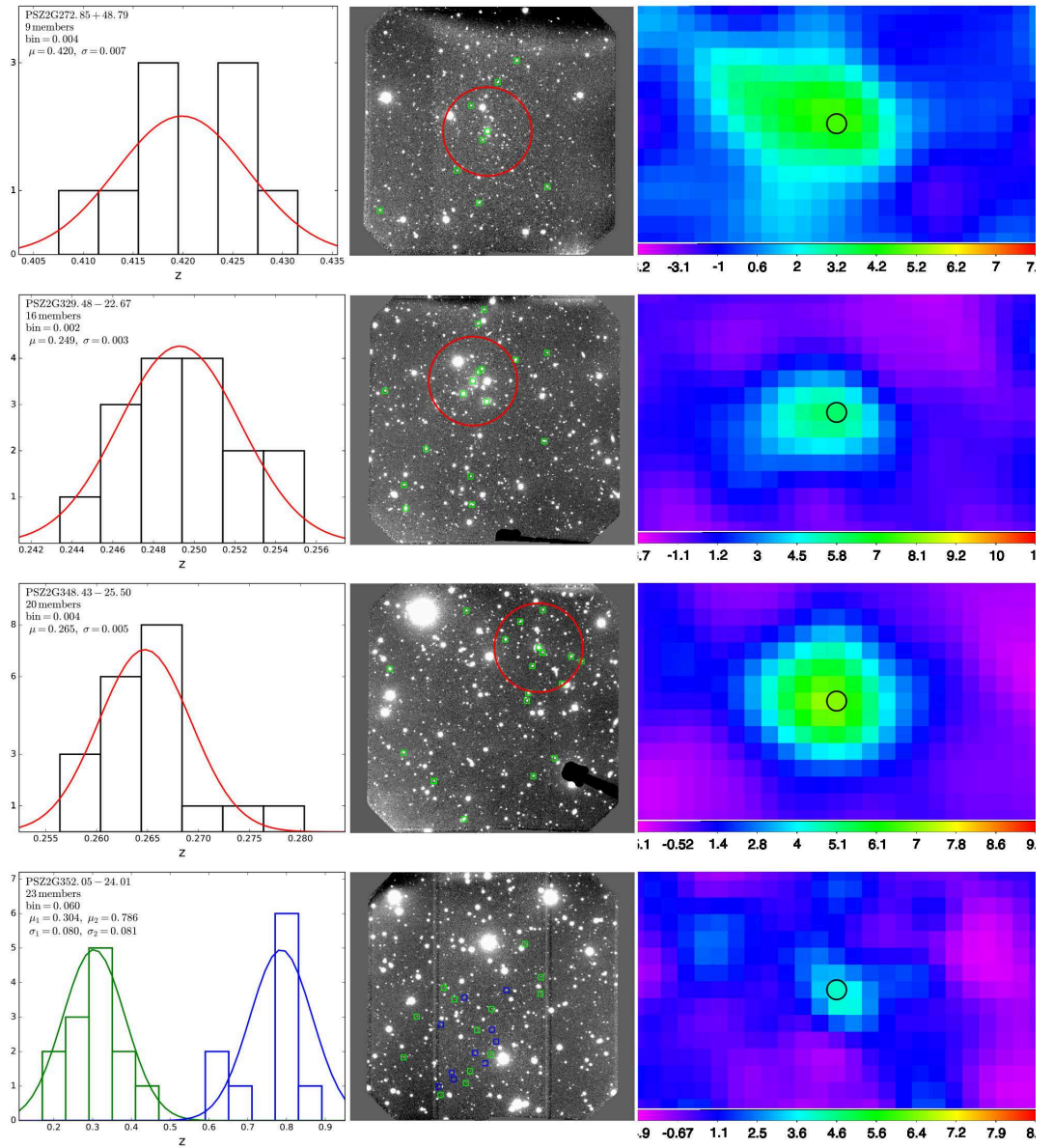


Figure 20 – Redshift histograms, optical images and SZ maps of clusters in the Southern sample. Symbols are the same as for Figure 19. For PSZ2 G352.05-24.01, we know only the coordinates of the X-ray center, marked with a red cross.

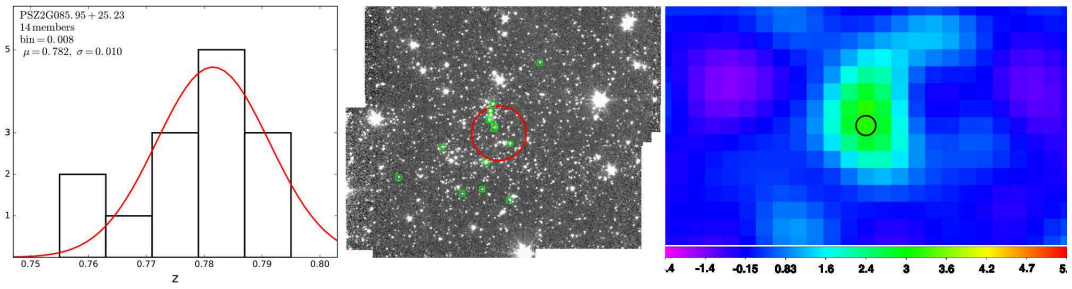


Figure 21 – Redshift histogram, IRAC image and SZ map of PSZ2 G085.95+25.23 observed at the Keck telescope. Symbols are the same as for Figure 19.

Table 5 – Results of the spectroscopical analysis. Columns from left to right list the cluster ID, our measured spectroscopic redshift, the new spectroscopic redshift estimates, redshift estimates obtained including the available redshifts in the SDSS DR14, the total number of galaxies with measured redshifts in the cluster field, the number of confirmed member galaxies, and our measured velocity dispersions using the biweight and the gapper methods (Beers, Flynn, and Gebhardt, 1990). The next three columns give, respectively, the signal-to-noise ratio, the number of detection methods and the *Planck* mass proxy, as reported in the PSZ2 catalog (we calculated these numbers for the two objects not listed in the PSZ2 catalog). The last three columns list, respectively, the Kolmogorov-Smirnov (K-S) and the Shapiro-Wilk (S-W) statistics for the probability that the redshift distributions are Gaussian, and the K-S test for a uniform distribution.

Name	z_{spec}	New z_{spec}	$z_{\text{spec}+\text{DR14}}$	N_{tot}	$N_{\text{gal}}^{\text{conf}}$	σ_{BI} (km s^{-1})	$\sigma_{\text{BI}+\text{DR14}}$ (km s^{-1})	σ_{G} (km s^{-1})	S/N	Det. Meth.	M_{500}^{Pl} ($10^{14} M_{\odot}$)	K-S gaussian prob.	S-W gaussian prob.	K-S uniform prob.
PSZ2 G033.83-46.57	0.439 ± 0.001	+		10	8	985^{+451}_{-277}		1051^{+309}_{-214}	4.6	2	$5.4^{+0.7}_{-0.8}$	0.96	0.71	0.50
PSZ2 G053.44-36.25	0.331 ± 0.001	+	0.3295 ± 0.0003	21	20	1011^{+242}_{-131}	1215^{+167}_{-100}	1025^{+224}_{-117}	8.9	3	$7.5^{+0.5}_{-0.6}$	0.99	0.80	0.07
PSZ2 G056.93-55.08	0.443 ± 0.001		0.4430 ± 0.0001	49	46	1356^{+192}_{-127}	1331^{+194}_{-128}	1345^{+170}_{-113}	11.5	3	9.4 ± 0.5	0.76	0.12	0.01
PSZ2 G081.00-50.93	0.303 ± 0.001	+	0.3051 ± 0.0001	15	15	1292^{+360}_{-185}	1552^{+175}_{-154}	1300^{+326}_{-140}	9.2	3	6.7 ± 0.5	0.97	0.96	0.14
PSZ2 G083.29-31.03	0.412 ± 0.002		0.4123 ± 0.0001	21	20	1434^{+574}_{-320}	1153^{+111}_{-94}	1591^{+376}_{-262}	9.1	3	$7.8^{+0.5}_{-0.6}$	0.83	0.90	0.004
PSZ2 G085.95+25.23	0.782 ± 0.003	+		16	14	1049^{+210}_{-180}		1041^{+195}_{-119}	5.0	2	$5.2^{+0.6}_{-0.7}$	0.91	0.05	0.06
PSZ2 G108.71-47.75	0.389 ± 0.001		0.3897 ± 0.0002	11	8	900^{+458}_{-190}	861^{+327}_{-216}	900^{+460}_{-183}	4.3	1	$5.1^{+0.7}_{-0.8}$	0.99	0.87	0.65
PSZ2 G139.62+24.18	0.268 ± 0.001			20	20	1120^{+366}_{-238}		1127^{+305}_{-171}	9.6	3	7.3 ± 0.5	0.51	0.25	0.20
PLCK G147.32-16.59	0.640 ± 0.009			10	10	–		–	5.9	1	$8.1^{+0.8}_{-0.9}$	0.91	0.91	0.86
PSZ2 G157.43+30.34	0.402 ± 0.001	+		28	28	1244^{+192}_{-109}		1242^{+195}_{-103}	8.8	2	8.2 ± 0.6	0.99	0.73	0.23
PLCK G183.33-36.69	0.163 ± 0.001			11	11	897^{+437}_{-275}		979^{+263}_{-187}	2.1	1	$2.3^{+0.7}_{-0.9}$	0.59	0.05	0.04
PSZ2 G186.99+38.65	0.377 ± 0.001		0.3774 ± 0.0003	41	41	1506^{+164}_{-120}	1426^{+133}_{-87}	1462^{+165}_{-102}	7.1	3	$6.6^{+0.6}_{-0.7}$	0.83	0.32	0.40
PSZ2 G216.62+47.00	0.385 ± 0.001		0.3864 ± 0.0003	37	37	1546^{+174}_{-132}	1779^{+207}_{-153}	1524^{+178}_{-110}	9.7	3	$8.4^{+0.5}_{-0.6}$	0.97	0.45	0.86
PSZ2 G235.56+23.29	0.375 ± 0.002			27	23	1644^{+285}_{-192}		1636^{+294}_{-141}	4.9	3	$5.7^{+0.7}_{-0.8}$	0.95	0.16	0.13
PSZ2 G250.04+24.14	0.411 ± 0.001			29	29	1065^{+447}_{-285}		1466^{+380}_{-241}	6.2	3	6.2 ± 0.6	0.94	0.97	0.10
PSZ2 G251.13-78.15	0.306 ± 0.001	+		17	17	801^{+852}_{-493}		1188^{+205}_{-155}	4.8	1	4.1 ± 0.6	0.56	0.19	0.26
PSZ2 G272.85+48.79	0.420 ± 0.002			10	9	1462^{+389}_{-216}		1498^{+345}_{-175}	4.8	2	$5.3^{+0.7}_{-0.8}$	0.98	0.61	0.62
PSZ2 G329.48-22.67	0.249 ± 0.001	+		19	16	835^{+179}_{-119}		746^{+152}_{-64}	6.0	3	$5.0^{+0.7}_{-0.8}$	0.99	0.90	0.46
PSZ2 G348.43-25.50	0.265 ± 0.001			21	20	1065^{+411}_{-198}		1160^{+277}_{-167}	7.1	3	6.0 ± 0.6	0.85	0.18	0.02
PSZ2 G352.05-24.01 ^a	0.786 ± 0.026			23	10	–	–	–	4.1	1	$6.2^{+0.9}_{-1.0}$	0.35	0.02	0.03
	0.304 ± 0.022			23	13	–	–	–				0.99	0.94	0.98

^a Two structures observed, not confirmed as clusters (see text and Figure 20).

Our collaborator Jean-Baptiste Melin recalculated masses and S/N from a re-extraction of the SZ signal using the Matched Multi-Filter MMF3 (Melin, Bartlett, and Delabrouille, 2006b; Planck Collaboration et al., 2011b, 2014b, 2015b), described in Section 2.1.3, fixing the position to the optical position and varying the filter size. They are reported in Table 5. In particular, the quoted S/N is the maximum across the various filter sizes at the optical position. The masses are obtained from the re-extracted SZ signal following the method described in Sec. 7.2.2 of Planck Collaboration et al., 2014b.

In Table 5, I also show the number of detection methods from Planck Collaboration et al. (2015b), described in Section 2.1.3. The Planck selection function is very reliable ($> 90\%$) for detections obtained with $S/N > 4.5$ by at least one detection method. For objects detected with all three detection methods, the probability of being a cluster is $> 98\%$ with $S/N > 4.5$ (Planck Collaboration et al., 2015b). In order to confirm each target as galaxy cluster, I combine this information with the probability that the galaxy redshift distribution is Gaussian, the characteristic distribution of a virialized cluster, from the Kolmogorov-Smirnov (K-S, e.g. Fasano and Franceschini, 1987) and the Shapiro-Wilk (S-W, Shapiro and Wilk, 1965) statistics, as well as the probability of a uniform distribution from a K-S test. The results of these tests are shown in the last three columns of Table 5.

Eleven of our cluster candidates have $> 98\%$ probability of being a galaxy cluster, since they were detected with three detection methods and have $S/N > 4.5$. For these targets, the probabilities that the redshift distributions are Gaussian are almost always $> 80\%$ and the probabilities to be uniform always $< 50\%$ and mostly $< 10\%$. Only one object, PSZ2 G139.62+24.18 at $z=0.268$, has a $S/N = 9.5$, which corresponds to a *Planck* reliability of being a cluster of $\sim 100\%$, but a K-S (S-W) probability of having a Gaussian redshift distribution of $\sim 50\%$ ($\sim 20\%$), and the probability of having a uniform redshift distribution of $\sim 20\%$. It shows a very luminous BCG at the center, and has 20 spectroscopically confirmed galaxies at the same redshift. All these elements seem to indicate that this is a galaxy cluster, and it was also confirmed as a cluster in the PSZ2 catalog. All the other ten targets are mostly likely galaxy clusters, and I assume that they are. Of those, I confirm three clusters that were not originally confirmed in the PSZ2.

The other cluster candidates that were detected with at least one detection method and $S/N > 4.5$ have a $> 90\%$ probability of being galaxy clusters. For these candidates, I confirm a cluster when the probability that their redshift distribution is a Gaussian is $> 95\%$ ($\sim 2\sigma$). On the other hand, I do not confirm a cluster when the probability of a uniform distribution is $> 50\%$. In fact, since the *Planck* detection and the galaxy redshift distribution are two independent events, I can multiply the *Planck* probability of not being a cluster ($\sim 10\%$) by the probability of having a uniform distribution of galaxy redshifts. If this last is $< 50\%$, the total probability that the candidate is not a cluster is $< 5\%$. Among these last targets, three have a probability that their redshift distribution is Gaussian is $> 95\%$ ($\sim 2\sigma$), and I consider them as confirmed clusters. All three are new confirmation with respect to PSZ2.

Three of the targets that were only detected by one method, though, and one candidate detected with two methods show less definitive results. I discuss these last cluster candidates in more detail below.

PLCK G147.32-16.59 was detected by one method with a high S/N ($S/N \sim 6$), and its redshift distribution has a probability of $\sim 90\%$ of being Gaussian; however, it also has a $\sim 10\%$ probability of not being a cluster. With only 10 confirmed members, its confirmation is not very reliable, but it is more probable that it is a cluster or a group of galaxies than a uniform redshift distribution, and I consider it a confirmed cluster. *XMM-Newton* observations (Planck Collaboration et al., 2013) reveal two substructures in the X-ray surface brightness, indicating that it is undergoing a merger event (see also van Weeren et al., 2014; Mroczkowski et al., 2015). Because of the undergoing merger, I exclude this cluster from the analysis of the velocity dispersion–mass relation in Chapter 5.

PLCK G183.33-36.69 was detected by one method with a $S/N \sim 2$ (*Planck* reliability of $< 70\%$), its redshift distribution has a K-S (S-W) probability of $\sim 60\%$ ($\sim 5\%$) to be Gaussian, and a $\sim 1\%$ total probability of not being a cluster. However, the two bright central galaxies in the Gemini image are clearly visible, and the cluster center is close to the border of the Gemini field. It seems that this cluster was not enough well centered in the Gemini imaging and spectroscopy to obtain a significant sample to confirm it, even if it has a larger probability to be a cluster or group of galaxies instead of an uniform galaxy distribution. The SZ flux gives a mass of $M_{500}^{\text{Pl}} = 2.3_{-0.9}^{+0.7} \times 10^{14} M_{\odot}$, and its galaxy velocity dispersion is $\sigma_{200} = 842_{-451}^{+297} \text{ km s}^{-1}$. I consider it as a confirmed cluster, and warn the reader about the larger uncertainty (with respect to most of the remaining sample) in the velocity dispersion measurement and its redshift distribution skewness, which both might indicate an unrelaxed dynamical state. I keep this cluster in my sample for the mass scale study because, due to the large uncertainty on the velocity dispersion measurement, it does not significantly weight on my final results.

PSZ2 G251.13-78.15 was detected by one method with a $S/N \sim 4.8$ (*Planck* reliability of $\sim 90\%$), its redshift distribution has a K-S and a S-W probability of $\sim 60\%$ and $\sim 20\%$, respectively, to be Gaussian, and a $\sim 3\%$ probability of not being a cluster. I consider it as a confirmed cluster, and again notice the larger uncertainty in its confirmation, mass and velocity dispersion estimates. This is a newly spectroscopically confirmed cluster.

PSZ2 G272.85+48.79 was detected by two methods with a $S/N \sim 5$ (*Planck* reliability of $\sim 92\%$). From the combined *Planck* and K-S Gaussian probabilities, it has a 90% probability of being a cluster. On the other hand, from the combined *Planck* and K-S uniform probabilities, it has a 5% of probability of not being a cluster. According to my criteria this is at the limit of being confirmed as a cluster of galaxies. However, I assume it is confirmed, also considering that it is more massive than $10^{14} M_{\odot}$ (e.g. Evrard et al., 2008b).

For PSZ2 G352.05-24.01, the redshift obtained from the X-ray analysis is $z = 0.79$ (Planck Collaboration et al., 2013), but I observe galaxies in a wider redshift range. In fact, I can distinguish two structures at $z \sim 0.8$ and $z \sim 0.3$, shown in blue and green, respectively, in Figure 20. Both redshift distributions have a standard deviation of ~ 0.08 , much wider of what expected for a cluster of galaxies. This target is not a cluster of galaxies, and I exclude it from the analysis of the velocity dispersion–mass relation in Chapter 5.

PSZ2 G085.95+25.23, confirmed at $z = 0.782 \pm 0.010$, is one of the highest redshift confirmed *Planck* clusters.

Newly confirmed clusters are labeled with the sign "+" in Table 5.

I provide the cluster catalogs as electronic documents in Amodeo et al. (2018), including the following parameters for each cluster galaxy:

1. the galaxy identification number ID
2. the J2000 right ascension R.A., in hours
3. the J2000 declination decl., in deg
4. the measured spectroscopic redshift SPECZ
5. the error in spectroscopic redshift eSPECZ

An example is shown in Table 6 for PSZ2G053.44-36.25.

Table 6 – Catalog of galaxies detected for cluster PSZ2G053.44-36.25. The full spectroscopic catalog is available in the online version of Amodeo et al. (2018).

ID	R.A.	decl.	SPECZ	eSPECZ
1	21.58816	-1.08456	0.330601	0.0002
2	21.58506	-1.06186	0.332352	0.0001
3	21.58748	-1.05329	0.336274	0.0001
4	21.58530	-1.08879	0.330425	0.0003
5	21.58638	-1.05156	0.336117	0.0003
6	21.58564	-1.06893	0.325783	0.0002
7	21.58671	-1.05585	0.335890	0.0001
8	21.58600	-1.06488	0.330109	0.0002
9	21.58632	-1.02193	0.334395	0.0003
10	21.58714	-1.04561	0.327720	0.0002
11	21.58603	-1.02659	0.334505	0.0002
12	21.58648	-1.05931	0.323872	0.0002
13	21.58509	-1.07221	0.331592	0.0002
14	21.58678	-1.07722	0.332152	0.0003
15	21.58659	-1.03027	0.325034	0.0003
16	21.58745	-1.03873	0.333472	0.0001
17	21.58458	-1.04332	0.330652	0.0002
18	21.58804	-1.03449	0.389051	0.0006
19	21.58677	-1.02851	0.342437	0.0004
20	21.58674	-1.04831	0.327634	0.0002

4.2.1 Discussion

In the context of the optical identification of *Planck* cluster candidates, our sample, although small, is chosen to have a wide range of mass with the aim of obtaining a statistical calibration of the *Planck* SZ mass estimator. In this section, I compare it with previous *Planck* cluster redshift measurements.

Eight of our targets are in the SDSS and DR8 redMaPPer cluster catalogs (Wen, Han, and Liu, 2012; Rykoff et al., 2014). Five of them (PSZ2G108.71-47.75, PSZ2 G186.99+38.65, PSZ2 G216.62+47.00, PSZ2 G056.93-55.08, and PSZ2 G083.29-31.03) have previous redshift spectroscopic measurements in agreement with our values.

The *Planck* collaboration has undertaken two important optical follow-up programs to confirm *Planck* cluster candidates and to measure their redshifts.

The first was based on observations with the Russian-Turkish 1.5 m telescope (Planck Collaboration et al., 2015c) and provided spectroscopic redshifts of 65 *Planck* clusters. It included our targets PSZ2 G139.62+24.18, for which they got a spectroscopic redshift of 0.268 consistent with our measurement, and PSZ2 G157.43+30.34, for which they got a photometric redshift of 0.45, while we measure $z = 0.402 \pm 0.006$, where the error is the standard deviation of the redshift distribution of member galaxies. The second program, based on observations with telescopes at the Canary Islands Observatories, gave 53 spectroscopic redshift determinations (Planck Collaboration et al., 2016c). It included again our target PSZ2 G139.62+24.18, for which they measured $z = 0.266$ from 22 spectroscopic confirmed members, consistent with our value of $z = 0.268 \pm 0.005$ obtained with from 20 galaxies. Recently, Barrena et al. (2018) and Streblyanska et al. (2018) reported on new optical follow-up observations of *Planck* cluster candidates at the Roque de los Muchachos Observatory. They confirmed 53 and 37 clusters, respectively, by analysing the optical richness, the 2D galaxy distribution, and the velocity dispersions of clusters.

In the frame of the optical identification of *Planck* cluster candidates, I emphasise that this sample, although small, is chosen to have a wide range of mass with the aim to obtain a statistical calibration of the *Planck* SZ mass estimator.

Aside from the optical follow-up programs, the *Planck* collaboration has also carried out X-ray validation programs with XMM-*Newton* (Planck Collaboration et al., 2011a, 2012, 2013), where redshifts z_{Fe} have been obtained from X-ray spectral fitting. Targets PSZ2 G250.04+24.14 and PSZ2 G272.85+48.79 were analyzed in Planck Collaboration et al. (2011a), PSZ2 G235.56+23.29 in Planck Collaboration et al. (2012), PSZ2 G348.43-25.50 and PLCK G147.32-16.59 in Planck Collaboration et al. (2013), finding consistent redshifts with our values. Planck Collaboration et al. (2013) also included the X-ray analysis of PSZ2 G329.48-22.67. They observed a double projected system at redshifts 0.24 and 0.46. In our GMOS analysis, we measure $z = 0.249 \pm 0.003$ observing 16 spectroscopic members, with no detections at higher redshift. Finally, Planck Collaboration et al. (2013) quoted a redshift $z_{\text{Fe}} = 0.77$ for PSZ2 G352.05-24.01. The authors gave $z_{\text{Fe}} = 0.12, 0.40$ as other possible solutions of the spectral fitting, but these were excluded from the comparison between the X-ray and SZ properties of the source (Y_{X}/Y_{500}). We observe at the same coordinates two groups of galaxies: 13 at $z = 0.786 \pm 0.081$ and 10 at $z \sim 0.304 \pm 0.080$. Thus, we can not confirm the redshift measurement for this cluster.

In conclusion, six of our clusters have spectroscopic redshifts from previous optical studies, seven more have redshift measurements from X-ray spectral fitting. For the remaining seven clusters, spectroscopic redshift are published in Amodeo et al. (2018) for the first time.

I use the *Planck* clusters confirmed with our GMOS spectroscopy for my cluster mass calibration discussed in Chapter 5 and published in Amodeo et al. (2017).

Since I obtained the confirmation of the $z=0.78$ cluster with Keck spectroscopy after the analysis with the GMOS data was completed and published, I will not use it for the mass calibration analysis in order to be consistent with the published results. I have verified, though, that including this cluster does not change the interpretation of my main results.

CALIBRATING THE GALAXY CLUSTER MASS SCALE WITH VELOCITY DISPERSIONS II: RESULTS

In this Chapter, I present my calibration of the *Planck* cluster mass scale using dynamical mass measurements based on velocity dispersions of the sample introduced in Chapter 4.

The results of this Chapter are published in Amodeo et al. (2017), enclosed to this thesis in Appendix B.

5.1 THE PLANCK MASS PROXY

The *Planck* SZ mass proxy, used in the last two *Planck* cluster catalog papers (Planck Collaboration et al., 2014b, 2015b), is based on a combination of *Planck* data and an X-ray scaling relation established with *XMM-Newton*, as discussed in Section 2.1.3.2.

With respect to the PSZ2, our collaborator J.B. Melin has derived new cluster mass estimates, taking into account the cluster centers from our optical follow-up. For each cluster, we measure the SZ flux, Y_{500} , inside a sphere of radius R_{500} using the Multifrequency Matched Filter (MMF3, Melin, Bartlett, and Delabrouille, 2006c). The filter combines the six highest frequency bands (100-857 GHz) weighted to optimally extract a signal with the known SZ spectral shape and with an assumed spatial profile. For the latter, we adopt the so-called *universal pressure profile* from Arnaud et al. (2010). We center the filter on the optical position and vary its angular extent θ_{500} over the range [0.9 - 35] arcmin to map out the signal-to-noise surface over the flux-size ($Y_{500} - \theta_{500}$) plane. In the *Planck* data there is a degeneracy between the measured flux and cluster size defined by this procedure, which we break using an X-ray determined scaling relation as a prior constraint (i.e., an independent $Y - \theta$ relation obtained from the combination of Eq. 62 and 63). The intersection of this prior with the *Planck* degeneracy contours yields a tighter constraint on the flux Y_{500} , which we then convert to halo mass, M_{500}^{Pl} , using Eq. 62. It is important to note that the mass proxy is therefore calibrated on the *XMM-Newton* scaling relation. These masses are reported in Table 7.

To compare our mass measurements to other independent estimates, I rescale the *Planck* masses to M_{200}^{Pl} using the mass-concentration relation of Dutton and Macciò (2014). This relation is derived from N-body simulations of relaxed dark matter halos in a *Planck* cosmology, as adopted here. It is in good agreement with the recently proposed universal model of Diemer and Kravtsov (2015a), which includes both relaxed and unrelaxed halos, for the mass and redshift range of interest. I assume a Navarro-Frenk-White (NFW, Navarro, Frenk, and White, 1997) density profile, and I choose an input value for the concentration $c_{200} = 5$, which is consistent with the model of Dutton and Macciò (2014) for a $10^{15} h^{-1} M_{\odot}$ cluster in the redshift range $0 < z < 0.5$. I then convert to M_{200}^{Pl} :

$$M_{200}^{\text{Pl}} = M_{500}^{\text{Pl}} \frac{f(c_{200})}{f(c_{500})}, \quad (68)$$

where $f(c_\Delta) = \log(1 + c_\Delta) - \frac{c_\Delta}{1+c_\Delta}$ indicates a general density contrast. I calculate c_{500} from

$$M_{500}^{\text{Pl}} = 4\pi\rho_s r_s^3 f(c_{500}), \quad (69)$$

where c_{500} is the only unknown quantity, because the scale density parameter, ρ_s , is fixed by the NFW profile,

$$\rho_s = \rho_{c,z} \frac{200}{3} \frac{c_{200}^3}{\ln(1 + c_{200}) - \frac{c_{200}}{1+c_{200}}}, \quad (70)$$

and the scale radius is

$$r_s = \frac{R_{500}}{c_{500}}, \quad (71)$$

with

$$R_{500} = \left[M_{500}^{\text{Pl}} \frac{3}{4\pi} \frac{1}{500 \rho_{c,z}} \right]^{1/3}. \quad (72)$$

I solve Eq. (69) for c_{500} using the ZBRENT.PRO routine in IDL and obtain a first estimate of M_{200}^{Pl} from Eq. (68). I then use the mass-concentration relation in Eq. (8) of Dutton and Macciò (2014) to get a new value for c_{200} . I iterate this algorithm until reaching 5% accuracy on M_{200}^{Pl} (i.e., the difference between the mass estimated at the iteration i and the mass estimated at the iteration $i-1$ is less than 0.05). I find smaller concentrations than the starting value of 5, with a mean $c_{200} = 4.2$. I have verified that the algorithm converges to the same values of M_{200}^{Pl} when changing the initial input value of c_{200} .

I implement this procedure in a Monte Carlo simulation with 1000 inputs for each cluster, sampling the *Planck* mass, M_{500}^{Pl} , according to a normal distribution with a standard deviation taken as the geometric mean of the uncertainties listed in Table 7. Similarly, I consider a log-normal distribution for c_{200} with a mean given by Eq. (8) in Dutton and Macciò (2014) and standard deviation equal to the intrinsic scatter of 0.11 dex in the mass-concentration relation. This yields a log-normal distribution of calculated M_{200}^{Pl} values from Eq. (68), whose mean and standard deviation are also listed in Table 7.

5.1.1 The σ - M scaling relation – A cluster model

The GMOS spectrographs provide imaging and spectroscopy over a 5.5×5.5 arcmin² field of view, allowing measurements for only the central part of clusters. The radial coverage provided for each cluster at a given redshift, calculated for the *Planck* 2015 cosmology, is quoted in Table 7 as R_{max} , in units of R_{200} , along with R_{200} . We typically sample out to about half R_{200} , with R_{max} ranging over $[0.35 - 0.58]R_{200}$. However, I need to estimate the velocity dispersion within R_{200} to compare to the σ - M relation from simulations (see next section). Sifón et al. (2016) determined the radial profile of the velocity dispersion using mock observations of subhalos in the Multidark simulation (Prada et al., 2012), as described in Section 3.2 of their paper. I interpolate the correction factors presented in their Table 3 to our values of R_{max}/R_{200} to translate our velocity dispersion measurements obtained with the biweight method, $\sigma_{\text{BI}}(< R_{\text{max}})$, to R_{200} . The velocity dispersions thusly estimated, σ_{200} , are listed in Table 7, where the uncertainties account for our measurement errors and the scatter in the velocity

Table 7 – Columns from left to right list the cluster ID, our measured average redshift, the number of confirmed member galaxies, the maximum radius probed by GMOS, R_{\max} , R_{200} , our measured velocity dispersion, $\sigma_{\text{BI}}(< R_{\max})$, the velocity dispersion estimated within R_{200} , σ_{200} , the reference PSZ2 M_{500}^{Pl} and the M_{200}^{Pl} derived in this work based on SZ.

Name	z	N_{gal}	R_{\max} (R_{200})	R_{200} (Mpc)	$\sigma_{\text{BI}}(< R_{\max})$ (km s^{-1})	σ_{200} (km s^{-1})	M_{200}^{Pl} ($10^{14} M_{\odot}$)	M_{500}^{Pl} ($10^{14} M_{\odot}$)
PSZ2 G033.83-46.57	0.439	10	0.58	1.66 ± 0.08	985^{+451}_{-277}	953^{+454}_{-282}	7.8 ± 1.1	$5.4^{+0.7}_{-0.8}$
PSZ2 G053.44-36.25	0.331	20	0.42	1.93 ± 0.06	1011^{+242}_{-131}	956^{+260}_{-161}	10.9 ± 1.0	$7.5^{+0.5}_{-0.6}$
PSZ2 G056.93-55.08	0.443	46	0.49	2.00 ± 0.05	1356^{+192}_{-127}	1290^{+218}_{-164}	13.8 ± 1.1	9.4 ± 0.5
PSZ2 G081.00-50.93	0.303	15	0.41	1.88 ± 0.06	1292^{+360}_{-185}	1220^{+381}_{-223}	9.8 ± 0.9	6.7 ± 0.5
PSZ2 G083.29-31.03	0.412	20	0.49	1.89 ± 0.06	1434^{+574}_{-320}	1365^{+584}_{-338}	11.3 ± 1.0	$7.8^{+0.5}_{-0.6}$
PSZ2 G108.71-47.75	0.390	10	0.55	1.65 ± 0.08	900^{+458}_{-190}	865^{+461}_{-198}	7.3 ± 1.1	$5.1^{+0.7}_{-0.8}$
PSZ2 G139.62+24.18	0.268	20	0.36	1.96 ± 0.06	1120^{+366}_{-238}	1052^{+390}_{-273}	10.6 ± 0.9	7.3 ± 0.5
PSZ2 G157.43+30.34	0.402	28	0.47	1.94 ± 0.05	1244^{+192}_{-109}	1182^{+216}_{-148}	12.1 ± 1.0	8.2 ± 0.6
CL G183.33-36.69	0.163	11	0.35	1.38 ± 0.17	897^{+437}_{-275}	842^{+451}_{-297}	3.3 ± 1.2	$2.3^{+0.7}_{-0.9}$
PSZ2 G186.99+38.65	0.377	41	0.49	1.81 ± 0.06	1506^{+164}_{-120}	1432^{+200}_{-166}	9.5 ± 1.0	$6.6^{+0.6}_{-0.7}$
PSZ2 G216.62+47.00	0.385	37	0.45	1.97 ± 0.05	1546^{+174}_{-132}	1466^{+218}_{-186}	12.3 ± 1.0	$8.4^{+0.5}_{-0.6}$
PSZ2 G235.56+23.29	0.374	23	0.51	1.73 ± 0.08	1644^{+285}_{-192}	1568^{+308}_{-224}	8.2 ± 1.2	$5.7^{+0.7}_{-0.8}$
PSZ2 G250.04+24.14	0.411	29	0.53	1.75 ± 0.07	1065^{+447}_{-285}	1020^{+452}_{-293}	8.9 ± 1.0	6.2 ± 0.6
PSZ2 G251.13-78.15	0.304	9	0.48	1.59 ± 0.08	801^{+852}_{-493}	762^{+854}_{-497}	5.9 ± 0.9	4.1 ± 0.6
PSZ2 G272.85+48.79	0.420	10	0.57	1.65 ± 0.08	1462^{+389}_{-216}	1411^{+397}_{-231}	7.6 ± 1.1	$5.3^{+0.7}_{-0.8}$
PSZ2 G329.48-22.67	0.249	11	0.38	1.73 ± 0.07	835^{+179}_{-119}	786^{+200}_{-149}	7.2 ± 0.9	$5.0^{+0.5}_{-0.6}$
PSZ2 G348.43-25.50	0.265	20	0.37	1.84 ± 0.06	1065^{+411}_{-198}	1003^{+427}_{-230}	8.7 ± 0.9	6.0 ± 0.6

dispersion profile found by Sifón et al. (2016). The mean corrections are of order 5%, while the uncertainty increases up to 32%. Figure 23 plots the velocity dispersions within R_{200} versus M_{200}^{Pl} .

My goal is to find the *Planck* cluster mass scale using velocity dispersion as an independent mass proxy calibrated on numerical simulations. I define the mass bias factor, $(1 - b)$, in terms of the ratio between the *Planck*-determined mass, M_{200}^{Pl} , and true cluster mass, M_{200} (Planck Collaboration et al., 2015b; von der Linden et al., 2014a; Hoekstra et al., 2015b). I assume that it is a constant and independent of over-density, choosing to work at M_{200} :

$$M_{200}^{\text{Pl}} = (1 - b)M_{200}. \quad (73)$$

While the mass bias may depend on mass and other cluster properties, my small sample only permits to constrain a characteristic value averaged over the sample.

To construct an estimator for the mass bias, I adopt a multivariate log-normal model for the cluster observables σ_{BI} and M_{200}^{Pl} at fixed true mass, M_{200} , following White, Cohn, and Smit (2010) and Stanek et al. (2010) (see also, Allen, Evrard, and Mantz, 2011; Rozo et al., 2014b; Evrard et al., 2014). It is then convenient to work with the logarithm of these quantities: $s_v = \ln(\sigma_{\text{BI}}/\text{km s}^{-1})$, $s_{\text{Pl}} = \ln(E(z)M_{200}^{\text{Pl}}/10^{15} M_{\odot})$ and $\mu = \ln(E(z)M_{200}/10^{15} M_{\odot})$, where I in-

corporate self-similar evolution with redshift, $E(z)$, with the masses. Power-law scaling relations give the observable mean values at true mass as:

$$\bar{s}_{Pl} \equiv \langle s_{Pl} | \mu \rangle = \ln(1 - b) + \mu, \quad (74)$$

$$\bar{s}_v \equiv \langle s_v | \mu \rangle = \alpha_v + \alpha_v \mu, \quad (75)$$

where the averages are taken over both intrinsic cluster properties and measurement errors. The first relation is simply the definition of the mass bias, Eq. (73), and in practice I take $\alpha_v = 1/3$, its self-similar value, in the second relation.

Each observable is also associated to a log-normal dispersion about its mean that includes both intrinsic and measurement scatter:

$$\Sigma_{\ln \sigma_{BI}}^2 = \tilde{\sigma}_{\ln \sigma_{BI}}^2 + \sigma_{\ln \sigma_{BI}}^2, \quad (76)$$

$$\Sigma_{\ln M_{200}^{Pl}}^2 = \tilde{\sigma}_{\ln M_{200}^{Pl}}^2 + \sigma_{\ln M_{200}^{Pl}}^2, \quad (77)$$

where the first terms are the intrinsic log-normal scatter and the second ones are the measurement error. Although measurement error is Gaussian in the observed quantity, rather than log-normal, I treat its fractional value as a log-normal dispersion; this is an approximation good to first order in the fractional measurement error. The second terms in the above expressions will therefore be understood as fractional measurement errors. The intrinsic dispersions may be correlated with correlation coefficient $\tilde{r} = \langle (s_v - \bar{s}_v)(s_{Pl} - \bar{s}_{Pl}) \rangle / (\tilde{\sigma}_{\ln \sigma_{BI}} \tilde{\sigma}_{\ln M_{200}^{Pl}})$.

It is then possible to show that the predicted scaling between velocity dispersion and *Planck* mass is:

$$\langle s_v | s_{Pl} \rangle = \alpha_v + \alpha_v \left[s_{Pl} - \ln(1 - b) - \beta \Sigma_{\ln M_{200}^{Pl}}^2 + \tilde{r} \beta \alpha_v^{-1} \Sigma_{\ln \sigma_{BI}} \Sigma_{\ln M_{200}^{Pl}} \right], \quad (78)$$

where β is the slope of the mass function on cluster scales, $\beta \approx 3$. The second to last term is the Eddington bias, proportional to the full dispersion, intrinsic and measurement, in the sample selection observable, s_{Pl} . In the last term, $r = \tilde{r} (\tilde{\sigma}_{\ln \sigma_{BI}} / \Sigma_{\ln \sigma_{BI}}) (\tilde{\sigma}_{\ln M_{200}^{Pl}} / \Sigma_{\ln M_{200}^{Pl}})$, i.e., the intrinsic correlation coefficient diluted by the measurement errors. The last term is therefore equivalent to $\tilde{r} \beta \alpha_v^{-1} \tilde{\sigma}_{\ln \sigma_{BI}} \tilde{\sigma}_{\ln M_{200}^{Pl}}$. This is the prediction for my measured scaling relation. A comparison to my fit identifies:

$$\ln A = \alpha_v - \alpha_v \left[\ln(1 - b) + \beta \Sigma_{\ln M_{200}^{Pl}}^2 - \tilde{r} \beta \alpha_v^{-1} \tilde{\sigma}_{\ln \sigma_{BI}} \tilde{\sigma}_{\ln M_{200}^{Pl}} \right], \quad (79)$$

which leads to my estimator:

$$(1 - b) = \left(\frac{A_g}{A} \right)^3 f_{EB} f_{corr}, \quad (80)$$

with

$$f_{EB} = e^{-\beta \Sigma_{\ln M_{200}^{Pl}}^2}, \quad (81)$$

$$f_{corr} = e^{3 \tilde{r} \beta \tilde{\sigma}_{\ln \sigma_{BI}} \tilde{\sigma}_{\ln M_{200}^{Pl}}}, \quad (82)$$

after setting $\alpha_v = 1/3$. As expected, the Eddington bias correction increases true cluster mass at given M_{200}^{Pl} , increasing the mass bias, b (decreasing $1 - b$). A positive correlation between velocity dispersion and *Planck* mass has the opposite effect.

5.1.2 The mass bias and the velocity bias

Complete virialization predicts a power-law relation between velocity dispersion, σ_{200} , and mass, M_{200} . Following the approach used in simulations, I work with the logarithm of these quantities, $s_v = \ln(\sigma_{200}/\text{km s}^{-1})$, $\mu = \ln(E(z)M_{200}/10^{15} M_\odot)$, where $h(z) \equiv H(z)/(100 \text{ km s}^{-1} \text{ Mpc}^{-1}) = hE(z)$ is the dimensionless Hubble parameter at redshift z , and we consider the log-linear relation

$$\langle s_v | \mu \rangle = \alpha_d + \alpha_d \mu. \quad (83)$$

The so-called self-similar slope expected from purely gravitational effects is $\alpha_d = 1/3$. The angle brackets indicate that this is the mean value of s_v given μ . From a suite of simulations, Evrard et al. (2008a) determined a precise relation between the dark matter velocity dispersion and halo mass consistent with this expectation. They found a normalization $\alpha_d = \ln(1082.9 \pm 4.0) + \alpha_d \ln h$; in the following, I will also refer to $A_d \equiv e^{\alpha_d}$. This result is insensitive to cosmology and to non-radiative baryonic effects, and the relation is very tight with only 4% scatter at fixed mass.

Galaxies, however, may have a different velocity dispersion than their dark matter host because they inhabit special locations within the cluster, e.g., subhalos. This leads to the concept of velocity bias, in which the scaling of galaxy velocity dispersion with host halo mass will in general be fit by a relation of the form of Eq. (83), but with different parameters, $A_g \equiv e^{\alpha_g}$ and α_g . Simulations typically found the exponent α_g to be consistent with the self-similar value of $1/3$, so I quantify any velocity bias in terms of the normalization, A_g . I do so by introducing the velocity bias parameter, $b_v \equiv A_g/A_d$.

Different simulation-based or empirical analyses found discordant behaviour for the velocity bias, leaving even the sense of the effect (i.e., $b_v > 1$ or $b_v < 1$) in debate.

Using hydrodynamical simulations with star formation, gas cooling and heating by supernova explosions and AGN feedback, Munari et al. (2013) found that subhalos and galaxies had a slightly *higher* velocity dispersion than the dark matter, i.e., a *positive* velocity bias with $b_v > 1$, as shown in the top panel of Fig. 22, where the right quadrant refers to structures of the typical masses of galaxy clusters. For galaxies in their AGN-feedback model, for example, they found $\tilde{A}_g = 1177 \text{ km s}^{-1}$, corresponding to $b_v = 1.08$.

From combined N-body and hydrodynamical simulations, Wu et al. (2013) found that velocity bias depended on the tracer population, as shown in the bottom left panel of Fig. 22. In particular, subhalos in pure N-body simulations tended to have large positive bias compared to galaxies identified in the hydrodynamical simulations, perhaps because over-merging in the former case removes slower, low mass dark matter halos from the tracer population. Consistent with this picture where smaller objects are more efficiently destroyed, all tracers in their simulations showed increasingly positive velocity bias with decreasing subhalo mass or galaxy luminosity, independent of redshift. The brightest cluster galaxies tended to underestimate, and faint galaxies slightly overestimate, the dark matter halo velocity dispersion, with the velocity bias ranging from ~ 0.9 for the five brightest cluster galaxies to an asymptotic value of $b_v = 1.07$ when including the 100 brightest galaxies. For samples of more than ~ 50 galaxies, their result converged to the value of Munari et al. (2013) ($b_v = 1.08$). The 10-

20 brightest galaxies, similar to our observational sample, represented a nearly unbiased measurement of the halo velocity dispersion, i.e., $b_v = 1$.

On the other hand, Guo et al. (2015) observed the opposite trend with luminosity when measuring the velocity bias of galaxies in the Sloan Digital Sky Survey (SDSS) Data Release 7, as shown in the bottom right panel of Fig. 22. They found $b_v \simeq 1.1$ for the brightest galaxies, falling to 0.85 for faint galaxies. It is worth noting that this analysis was based on modeling of the projected and redshift-space two-point correlation functions, and it is probably not very sensitive to velocity bias in the most massive halos, such as we have in the *Planck* sample. Farahi et al. (2016) used the velocity bias from the bright subsample of Guo et al. (2015) ($b_v = 1.05 \pm 0.08$) to estimate the mass of redMaPPer clusters with stacked galaxy velocity dispersions. Their derived mass scale was consistent with estimates based on weak lensing observations reported by Simet et al. (2016). The Guo et al. (2015) observational result was also consistent with the value $b_v = 1.08$ from the N-body hydrodynamical simulations of Munari et al. (2013).

In another study, Caldwell et al. (2016) found a negative velocity bias, $b_v = 0.896$, for galaxies in their simulations when they adjusted feedback efficiencies to reproduce the present-day stellar mass function and the hot gas fraction of clusters and groups.

These different studies do not yet present a clear picture of the magnitude of cluster member velocity bias, and this quantity remains the primary factor limiting interpretation of dynamical cluster mass measurements at present. We use the Munari et al. value of the velocity bias, $b_v = 1.08$, as our baseline in the following. The uncertainty on Munari et al.'s velocity bias is $\sim 0.6\%$.

My model of constant mass bias, $(1 - b)$, predicts a log-linear scaling relation of the form Eq. (83) between the observed velocity dispersion and the *Planck* mass proxy. I therefore construct an estimator for $(1 - b)$ by fitting for the normalization, A , and exponent, α , of this relation to the data in Fig. 23. I perform the fit using the MPFIT routine in IDL (Williams, Bureau, and Cappellari, 2010; Markwardt, 2009) and taking into account only the uncertainties in the velocity dispersion (i.e., at fixed *Planck* SZ mass¹). Since our sample is selected on SZ signal, there is no Malmquist bias correction to the relation fitted in this way.

For a robust estimation of the best-fit parameters, I perform 1000 bootstrap resamplings of the pairs $(M_{200}^{\text{Pl}}, \sigma_{200})$, re-computing the best-fit parameters each time. This yields $A \equiv e^\alpha = (1172 \pm 93) \text{ km s}^{-1}$ and a slope $\alpha = 0.28 \pm 0.20$ (at 68.3% confidence). The slope is consistent with the self-similar expectation of $\alpha = 1/3$, although with large uncertainty. I henceforth set $\alpha = 1/3$ and refit to find $A = (1158 \pm 61) \text{ km s}^{-1}$. The dispersion of the velocity measurements about the best-fit line (i.e., at given M_{200}^{Pl}) is $\langle \delta_{\ln \sigma}^2 \rangle^{1/2} = 0.189 \pm 0.009$. The best fit together with the data is plotted in Fig. 23. A model with a zero slope is excluded at $\sim 2\sigma$ confidence, using the χ^2 difference (the χ^2 for the best-fit model is 12.2, the χ^2 for the zero-slope model is 14.3). I also perform the fit using only clusters with greater than 20 member galaxies. Once again fixing $\alpha = 1/3$, I find $A = (1156 \pm 58) \text{ km s}^{-1}$ in this case, consistent with the previous value.

1. Taking into account errors on both velocity and mass measurements, as is often done, does not noticeably change the result; this however is not strictly what should be done as we are fitting for σ_{200} given M_{200}^{Pl} .

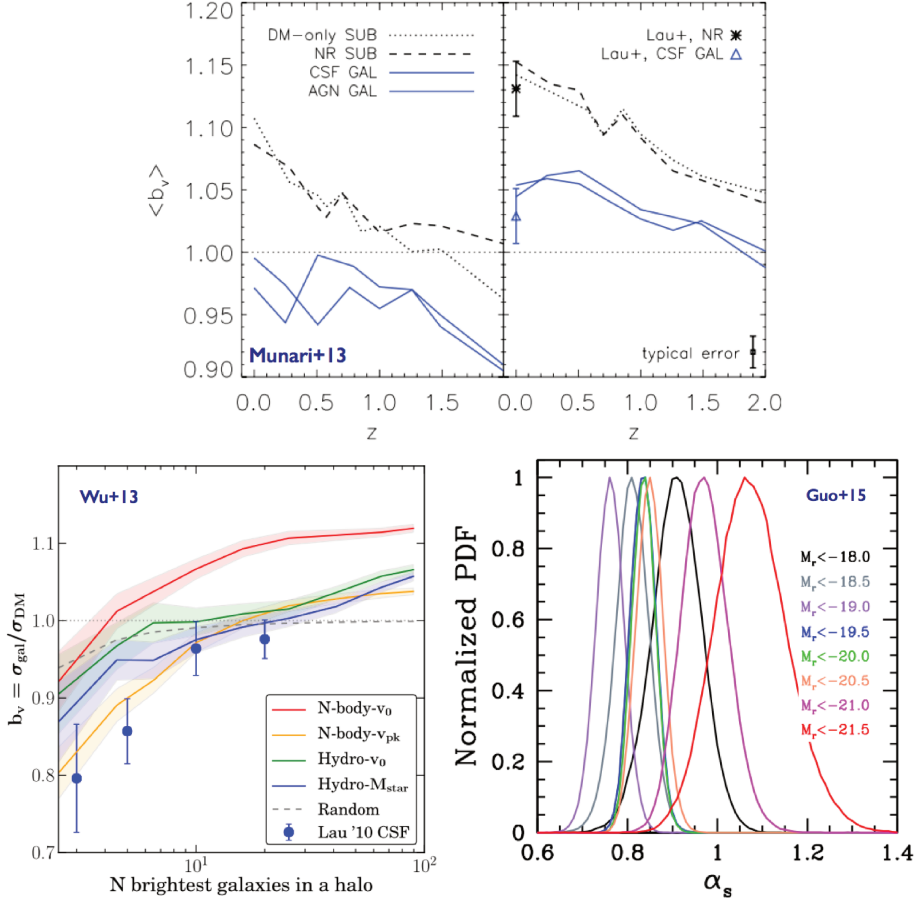


Figure 22 – Different results on the velocity bias from the literature. *Top*: from Munari et al. (2013), the average values of the velocity bias for subhaloes (black lines) and galaxies (blue lines), as a function of redshift, for haloes in the low-mass sample ($h(z)M_{200} < 10^{14}M_\odot$, left quadrant) and in the high-mass sample ($h(z)M_{200} > 3 \times 10^{14}M_\odot$, right quadrant). Results are presented for different sets of simulations: dark matter only (dotted line), hydrodynamic non-radiative (dashed line) refers to substructures in the NR set, radiative (blue lines) including star formation and the effect of feedback triggered by supernova explosions (CSF), and the effect of AGN feedback (AGN). Points are the $z = 0$ values from Lau, Nagai, and Kravtsov (2010). *Bottom left*: from Wu et al. (2013), velocity bias as a function of the number of brightest galaxies used to estimate the velocity dispersion. The curves refer to different simulations: N-body with galaxies ranked by their maximum circular velocity at $z=0$, v_0 (red), or at the peak value, v_{pk} (orange), hydrodynamic using v_0 (green), or the galaxy stellar mass, M_{star} (blue). Blue points are from the simulations of Lau, Nagai, and Kravtsov (2010) including cooling and star formation. *Bottom right*: from Guo et al. (2015), 1D probability distribution of the satellite galaxy velocity bias parameter (α_s) for samples with different luminosity thresholds (r -band absolute magnitude, M_r).

My estimator for the mass bias then follows from the formalism of Section 5.1.1 (Eq. 80):

$$(1 - b) = \left(\frac{A_g}{A}\right)^3 f_{\text{EB}} f_{\text{corr}} = \left(\frac{A_d}{A}\right)^3 b_v^3 f_{\text{EB}} f_{\text{corr}}, \quad (84)$$

where f_{EB} (Eq. 81) is the Eddington bias correction and f_{corr} (Eq. 82) is a correction for correlated scatter between velocity dispersion and the *Planck* mass

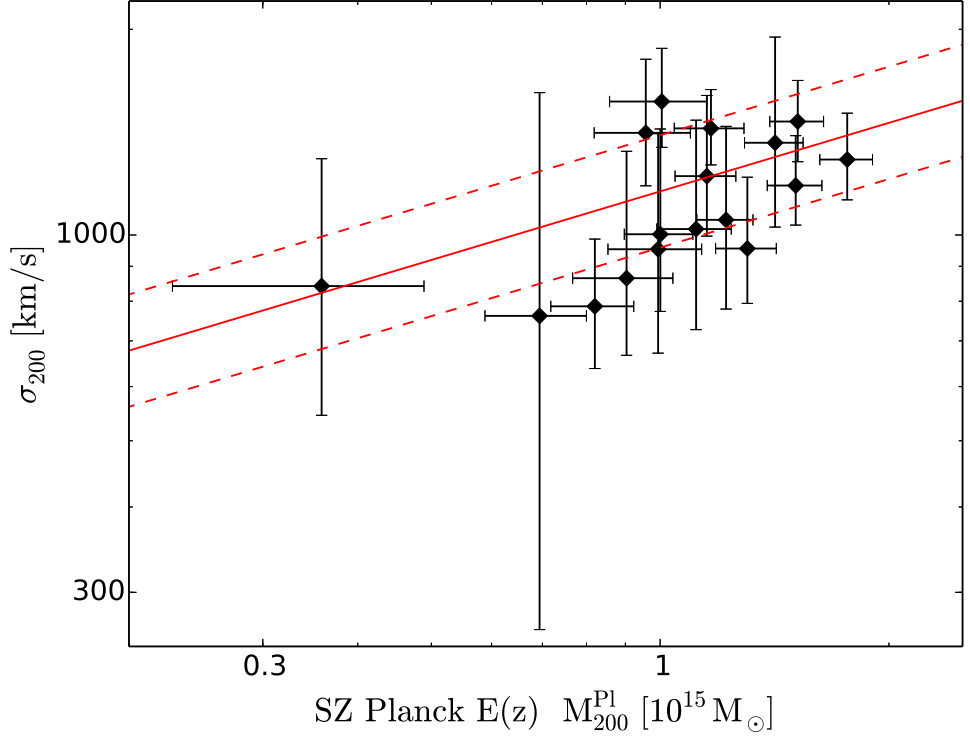


Figure 23 – Relation between the *Planck* SZ mass proxy and velocity dispersion for our sample of 17 galaxy clusters observed with Gemini (diamonds). The velocity dispersions and the *Planck* masses have been converted to σ_{200} and M_{200}^{Pl} , respectively, with corresponding uncertainties, following the procedure described in the text. The solid red line shows the best fit to the functional form of Eq. (83) in log-space, where the slope is set to 1/3, with the dashed lines delineating the dispersion of the data about the best-fit line.

proxy. With my value for the normalization from the fit to the data and the value for dark matter from Evrard et al. (2008a), I have numerically,

$$(1 - b) = (0.55 \pm 0.09) b_v^3 f_{\text{EB}} f_{\text{corr}}. \quad (85)$$

In the next two subsections, I propose $f_{\text{EB}} = 0.93 \pm 0.01$ and $f_{\text{corr}} \approx 1.01$ as reference values. My final value for the mass bias also depends on the cube of the velocity bias. Adopting as baseline value $b_v = 1.08$ from Munari et al. (2013), I have

$$(1 - b) = (0.64 \pm 0.11) \left(\frac{f_{\text{corr}}}{1.01} \right). \quad (86)$$

The quoted uncertainty accounts for measurement error, uncertainty on the Eddington bias correction and uncertainty on the velocity bias given by the different simulators; it is dominated by the measurement error. It is more difficult to assign an uncertainty to the correction for correlated scatter, as this depends on the details of cluster physics. I argue below that feedback makes this a minor correction, as reflected in my fiducial value of $f_{\text{corr}} = 1.01$. In any case, these uncertainties are dwarfed by the difference between the two possible values for the velocity bias, which severely hampers the interpretation of my results.

A summary of best-fit parameters is presented in Table 8 for several velocity dispersion–mass relations. Where the slope is set to 1/3, I quote my estimates of the *Planck* mass bias for the velocity bias derived by Munari et al. (2013),

$b_v = 1.08$. I distinguish results obtained for the full sample from results obtained for the subsample of clusters with at least 20 member galaxies.

Table 8 – Best-fit values and vertical scatter (i.e., at given mass) of the velocity dispersion–mass relation, $\sigma = A[E(z)M/10^{15}M_\odot]^B$, together with mass bias estimates. Results are given for our velocity dispersion estimates, $\sigma_{\text{BI}}(< R_{\text{max}})$, and for the derived velocity dispersions within R_{200} , σ_{200} . We distinguish the case where all clusters in the sample are included in the fit from the case where only those with at least 20 member galaxies are considered.

Relation	A (km s ⁻¹)	B	scatter $\langle \delta_{\ln \sigma}^2 \rangle^{1/2}$	$(1 - b)/b_v^3 f_{\text{EB}} f_{\text{corr}}$	$(1 - b)_{\text{Munari}}^a$
<i>All clusters</i>					
$\sigma_{\text{BI}}(< R_{\text{max}}) - M_{200}^{\text{Pl}}$	1239 ± 99	0.29 ± 0.21	0.189 ± 0.018	–	–
$\sigma_{\text{BI}}(< R_{\text{max}}) - M_{200}^{\text{Pl}}$	1226 ± 68	1/3	0.182 ± 0.012	0.47 ± 0.08	0.55 ± 0.09
$\sigma_{200} - M_{200}^{\text{Pl}}$	1172 ± 93	0.28 ± 0.20	0.198 ± 0.018	–	–
$\sigma_{200} - M_{200}^{\text{Pl}}$	1158 ± 61	1/3	0.189 ± 0.009	0.55 ± 0.09	0.64 ± 0.11
<i>Only clusters with $N_{\text{gal}} \geq 20$</i>					
$\sigma_{\text{BI}}(< R_{\text{max}}) - M_{200}^{\text{Pl}}$	1250 ± 71	1/3	0.168 ± 0.014	0.44 ± 0.08	0.51 ± 0.09
$\sigma_{200} - M_{200}^{\text{Pl}}$	1156 ± 58	1/3	0.136 ± 0.012	0.56 ± 0.08	0.66 ± 0.09

^a The values of the mass bias quoted in the last column are obtained using the velocity bias, b_v , derived by Munari et al., 2013, following the notation of Eq. (86), where the Eddington bias correction is also included.

5.1.3 Eddington Bias

The Eddington bias correction:

$$f_{\text{EB}} = e^{-\beta \Sigma_{\ln M_{200}^{\text{Pl}}}^2}, \quad (87)$$

depends on the local slope of the mass function on cluster scales, $\beta \approx 3$, and the total dispersion, $\Sigma_{\ln M_{200}^{\text{Pl}}}$, of the *Planck* mass proxy at fixed true mass. This is because I assume that my sample is a random draw from the parent sample selected on M_{200}^{Pl} . As described in Sec. 5.1, the mass proxy is calculated as an intersection of *Planck* SZ measurements and the X-ray based scaling relation in Planck Collaboration et al. (2014a). I characterize the measurement uncertainty on M_{200}^{Pl} by averaging the calculated uncertainty over my cluster sample: $\sigma_{\ln M_{200}^{\text{Pl}}} = 0.13 \pm 0.02$. To estimate the intrinsic scatter, I convert the 0.17 ± 0.02 dispersion of the $Y - M^{5/3}$ relation (Planck Collaboration et al., 2014a) to $\tilde{\sigma}_{\ln M_{200}^{\text{Pl}}} = (3/5)(0.17 \pm 0.02) = 0.10 \pm 0.01$. Combining the two, I obtain a total scatter of:

$$\Sigma_{\ln M_{200}^{\text{Pl}}} = 0.16 \pm 0.02. \quad (88)$$

This is an approximate estimate. In particular, my estimate for the intrinsic scatter in the *Planck* mass may be optimistic. I show below the effect of considering a larger correction. Setting $\beta = 3$, I calculate an Eddington bias correction of:

$$\ln f_{\text{EB}} = -0.08(1 \pm 0.19), \quad (89)$$

or a reference value of $f_{\text{EB}} = 0.93(1 \pm 0.01) = 0.93 \pm 0.01$.

5.1.4 Correlated Scatter

The second correction to my mass bias estimator arises from correlated scatter between velocity dispersion and the *Planck* mass proxy. It is given by:

$$f_{\text{corr}} = e^{3\tilde{r}\beta\tilde{\sigma}_{\ln\sigma_{\text{BI}}}\tilde{\sigma}_{\ln M_{200}^{\text{Pl}}}}, \quad (90)$$

because only the intrinsic scatter is correlated. Stanek et al. (2010) examined the covariance between different cluster observables using the Millennium Gas Simulations (Hartley et al., 2008). They found significant intrinsic correlation between velocity dispersion and SZ signal, $\tilde{r} = 0.54$, in the simulation with only gravitational heating. In the simulation additionally including cooling and pre-heating, however, the correlation dropped to $\tilde{r} = 0.079$. This would seem to make sense as we might expect non-gravitational physics, such as feedback and cooling, to decouple the SZ signal, which measures the total thermal energy of the gas, from the collisionless component.

While the scatter of the dark matter velocity dispersion is only 4%, Munari et al. (2013) found a scatter in the range 0.1 – 0.15 for their subhalos and galaxies, not too different from the scatter of 0.19 found by Caldwell et al. (2016). Fixing $\beta = 3$ and taking $\tilde{r} = 0.08$, $\tilde{\sigma}_{\ln\sigma_{\text{BI}}} = 0.15$ and $\tilde{\sigma}_{\ln M_{200}^{\text{Pl}}} = (3/5)0.17 = 0.10$ as reference values, I have:

$$\ln f_{\text{corr}} = 0.010 \left(\frac{\tilde{r}}{0.08} \right) \left(\frac{\tilde{\sigma}_{\ln\sigma_{\text{BI}}}}{0.15} \right) \left(\frac{\tilde{\sigma}_{\ln M_{200}^{\text{Pl}}}}{0.10} \right), \quad (91)$$

or a reference value of $f_{\text{corr}} = 1.01$. I consider this reference value reasonable since simulations require strong feedback to reproduce observed cluster properties (e.g., Caldwell et al., 2016). I emphasize, though, that important modeling uncertainty remains.

5.2 DISCUSSION

The possible tension between cluster and primary CMB cosmology has motivated a number of recent studies of the cluster mass bias in both X-ray and SZ catalogues (e.g., Sifón et al., 2013, 2016; Ruel et al., 2014; Bocquet et al., 2015; Battaglia et al., 2015; Simet et al., 2015; Smith et al., 2016). For a like-to-like comparison, I focus here on determinations for the *Planck* clusters.

Rines et al. (2016) compared SZ and dynamical mass estimates of 123 clusters from the *Planck* SZ catalog in the redshift range $0.05 < z < 0.3$. They used optical spectroscopy from the Hectospec Cluster Survey (Rines et al., 2013) and the Cluster Infall Regions in SDSS project (Rines and Diaferio, 2006), observing a velocity dispersion–SZ mass relation in good agreement with the virial scaling relation of dark matter particles. They found neither significant bias of the SZ masses compared to the dynamical masses, nor evidence of large galaxy

velocity bias. They concluded that the mass calibration of *Planck* clusters cannot solve the CMB–SZ tension and another explanation, such as massive neutrinos, is required.

von der Linden et al. (2014b) examined 22 clusters from the Weighing the Giants (WtG) project that were also used in the *Planck* cluster count cosmology analysis. Applying a weak lensing analysis, they derived considerably larger masses than *Planck*, measuring an average mass ratio of $\langle M_{\text{Planck}}/M_{\text{WtG}} \rangle = 0.688 \pm 0.072$ with decreasing values for larger *Planck* masses. They claimed a mass-dependent calibration problem, possibly due to the fact that the X-ray hydrostatic measurements used to calibrate the *Planck* cluster masses rely on a temperature-dependent calibration. A similar result was obtained by Hoekstra et al. (2015a) based on a weak lensing analysis of 50 clusters from the Canadian Cluster Comparison Project (CCCP). For the clusters detected by *Planck*, they found a bias of $0.76 \pm 0.05(\text{stat}) \pm 0.06(\text{syst})$, with the uncertainty in the determination of photometric redshifts being the largest source of systematic error. Planck Collaboration et al. (2016b) used these latter two measurements as priors in their analysis of the SZ cluster counts. They also employed a novel technique based on CMB lensing (Melin and Bartlett, 2015) to find $1/(1 - b) = 0.99 \pm 0.19$ when averaged over the full cluster cosmology sample of more than 400 clusters. As pointed out by Battaglia et al. (2015), these constraints should be corrected for Eddington bias².

Smith et al. (2016) used three sets of independent mass measurements to study the departures from hydrostatic equilibrium in the Local Cluster Substructure Survey (LoCuSS) sample of 50 clusters at $0.15 < z < 0.3$. The mass measurements comprised weak-lensing masses (Okabe and Smith, 2016; Ziparo et al., 2015), direct measurements of hydrostatic masses using X-ray observations (Martino et al., 2014), and estimated hydrostatic masses from Planck Collaboration et al. (2015b). They found agreement between the X-ray-based and *Planck*-based tests of hydrostatic equilibrium, with an X-ray bias of 0.95 ± 0.05 and an SZ bias of 0.95 ± 0.04 .

Finally, Penna-Lima et al. (2017) used lensing mass measurements from the Cluster Lensing And Supernova (CLASH, Postman et al., 2012) survey with Hubble to find a *Planck* mass bias of $(1 - b) = 0.73 \pm 0.10$. Employing a Bayesian analysis of CLASH and *Planck* SZ measurements, they modelled the CLASH selection function and astrophysical effects, such as scatter in lensing and SZ masses and their potential correlated scatter, as well as possible bias in the lensing measurements. Their quoted uncertainty accounted for these effects by marginalizing over the associated nuisance parameters.

Comparing to the values above, my results is $\sim 30\%$ lower (at $\sim 2.5\sigma$) than both the Smith et al. (2016) lensing determination and the Rines et al. (2016) determination, also based on velocity dispersions, both of which favor little or no mass bias. However, my result agree within 1σ with the results from WtG (von der Linden et al., 2014b), the CCCP (Hoekstra et al., 2015a) and the CLASH (Postman et al., 2012) analysis by Penna-Lima et al. (2017).

My value of $(1 - b) = (0.58 \pm 0.097)(f_{\text{corr}}/1.01)$, obtained with 50% larger intrinsic scatter on *Planck* masses (see Sect. 5.1.3), would still agree within 2σ with the results from weak lensing cited above. In both cases, my estimate of the

2. There is some confusion in the nature of these corrections. Battaglia et al. (2015) propose a correction for WtG and CCCP that is more akin to a Malmquist bias, i.e., due to selection effects arising from the fact that some clusters in the WtG and CCCP samples do not have *Planck* mass proxy measurements.

mass bias is within 1σ of the value $(1 - b) = (0.58 \pm 0.04)$ needed to reconcile the cluster counts with the primary CMB.

5.2.1 Estimating the velocity bias b_v using a prior on the mass bias

Given the large differences in the velocity bias as predicted by simulations, it is worth turning the vice – the strong dependence of our mass calibration on velocity bias – into a virtue: relying on accurate mass estimates provided by weak lensing analyses, I derive a constraint on b_v from our measured velocity dispersions. I adopt the *Planck* mass calibration obtained by Penna-Lima et al. (2017), based on lensing mass measurements from CLASH: $(1 - b) = 0.73 \pm 0.10$. This is a reasonable prior, since the Penna-Lima et al. (2017) sample is characteristic in mass (and I also assume in mass bias) of *Planck* detected clusters. Using this as a prior on the mass bias in Eq. (85), with my reference value for the Eddington bias given in Section 5.1.3, I then deduce the constraint:

$$b_v = 1.12 \pm 0.07 \left(\frac{1.01}{f_{\text{corr}}} \right)^{1/3}. \quad (92)$$

This positive velocity bias agrees with the value from the Munari et al. (2013) simulations and the Guo et al. (2015) result for samples more luminous than $M_r = 20.5 (L_*)$. It is reasonably consistent (within 2σ) with the results of Wu et al. (2013) that predict nearly unbiased velocities for the brightest 10-30 galaxies, appropriate for our sample. This result is discrepant, at 3σ , with the negative velocity bias $b_v \lesssim 0.9$, as for example found by Caldwell et al., 2016 simulations.

5.3 CONCLUSIONS

I have examined the *Planck* cluster mass bias using a sample of 17 *Planck* clusters for which we measured velocity dispersions with GMOS at the Gemini observatory. The unknown velocity bias, b_v , of the member galaxy population is the largest source of uncertainty in our final result: $(1 - b) = (0.51 \pm 0.09)b_v^3$. Using a baseline value for b_v from Munari et al. (2013), I find $(1 - b) = (0.64 \pm 0.11)$, consistent within just over 1σ with WtG, CCCP and CLASH, and within 1σ of the value $(1 - b) = (0.58 \pm 0.04)$ needed to reconcile the *Planck* cluster counts with the primary CMB.

I conclude that the velocity bias is the primary factor limiting interpretation of dynamical cluster mass measurements at this time. It is essential to eliminate this modeling uncertainty if velocity dispersion is to be a robust mass determination method.

Turning the analysis around, observational constraints on the velocity bias can be obtained by combining accurate mass estimates from weak lensing measurements with velocity dispersion measurements. Assuming a prior on the mass bias from Penna-Lima et al. (2017), I derive $b_v = 1.12 \pm 0.07$, consistent with the value from Munari et al. (2013) ($b_v = 1.08$) and with results from Wu et al. (2013) and Guo et al. (2015), but discrepant at 3σ with negative velocity bias $b_v \lesssim 0.9$, as for example found by Caldwell et al., 2016.

Apart from modeling uncertainty on the velocity bias, I have achieved a precision of 17% on the mass bias measurement with 17 clusters. Assuming that the simulations will eventually settle on a value for the velocity bias, this mo-

tivates continued effort to increase our sample size to produce a 10% or better determination, comparable to recent weak lensing measurements.

Forthcoming cosmological surveys will require an accuracy of few % for which a sample of clusters spanning a large redshift range is needed to probe a possible evolution with time of the mass-observable relation. In particular, as discussed in Chapter 3, including a sample of clusters at $z > 1.2$ will allow to double the figure of merit for cosmological constraints (Sartoris et al., 2016).

The second part of this thesis is dedicated to the study of stellar populations of galaxies in clusters at $1.4 < z < 2.8$ from the CARLA (Clusters Around Radio-Loud AGN), with the aim to optimize their search with future surveys, like *Euclid*.

PHOTOMETRIC ANALYSIS OF CLUSTERS AND PROTO-CLUSTERS FROM THE CARLA SURVEY

The second part of this PhD thesis is devoted to the study of the cluster galaxy population at the highest redshifts that will be accessible by future surveys, i.e. $z > 1.3$, to help planning their detection and building statistically significant samples of galaxy clusters at these redshifts, of crucial importance in cosmology, as discussed in Section 3.3.

At these redshifts, the number of currently known clusters is very small, as emerge from the review by Overzier (2016), and the definition of “cluster” itself is questioned since, at this epoch, we can mostly observe the progenitors of the massive ($M \gtrsim 10^{14} M_{\odot}$) virialized structures observed at lower redshifts, usually referred to as “proto-clusters”. While the cluster assembly can be followed in simulations, it is more difficult to make this distinction in observational data.

Therefore, in this thesis I will not distinguish between these two class of objects and I will use the term *cluster* for simplicity, even if, more rigorously, I should speak about overdensities of galaxies detected observationally, which have a given probability of being a cluster (see Section 6.1).

In Fig. 24, I present the status of the search for high-redshift clusters which have been confirmed until 2016. The complete references can be found in Chiang, Overzier, and Gebhardt (2013) and Overzier (2016).

As dicussed in Chapter 2, at $z < 1.5$ clusters are mostly detected in large X-ray and SZ surveys, while at higher redshifts clusters are identified as overdensities of some galaxies populations, like e.g. star-forming galaxies, Lyman break galaxies, H α emitters, Ly α emitters, providing highly heterogeneous samples.

The CARLA survey (Clusters Around Radio-Loud AGN), which will be analyzed in this part of the thesis, targeted the environments of radio galaxies and quasars, which are a promising location for overdense structures. For example, Galametz et al. (2012) found that the 73% of the fields around 48 radio galaxies observed with *Spitzer* at $1.2 < z < 3$ were denser than the median field density of the survey, and the 23% was a $\gtrsim 2\sigma$ overdensity. With a HST grism spectroscop-

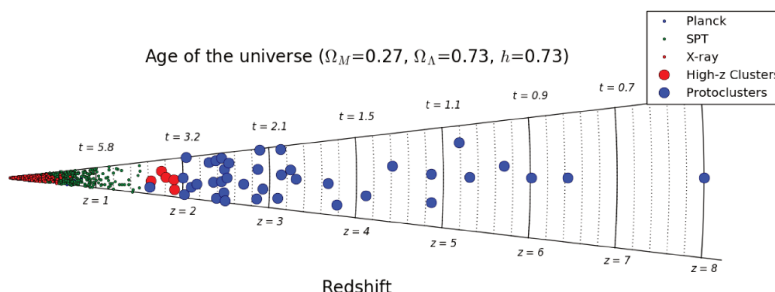


Figure 24 – Redshift distribution of clusters and proto-clusters confirmed from the literature, as of 2016. Small points are the detections at $z < 1.5$ from X-ray (red) and SZ (*Planck* blue, and SPT, green) surveys, collected from Bleem et al. (2015). Large circles are clusters (red) and proto-clusters (blue) at $z > 1.5$. Complete references for these detections can be found in Chiang, Overzier, and Gebhardt (2013) and Overzier (2016). Figure from Overzier (2016).

ical follow-up of the CARLA 20 densest fields, sixteen CARLA clusters have been confirmed spectroscopically by Noirot et al. (2016, 2018) in the redshift interval $1.37 < z < 2.8$, thus doubling the number of confirmed clusters in this range (see Fig. 24, which shows the known clusters and proto-clusters in 2016, before the CARLA confirmations) and, most importantly, giving an homogeneously selected sample more suited to derive information on cluster evolution.

In the following sections, I present the CARLA survey and my photometric analysis aimed at studying the galaxy populations of the CARLA clusters.

All magnitudes are given in the AB photometric system (Oke and Gunn, 1983).

6.1 THE SAMPLE

The sample analyzed in this thesis consists of sixteen fields around radio-loud active galactic nuclei (hereafter, RLAGN) observed with the *Spitzer* Infrared Array Camera (IRAC Fazio et al., 2004) at $3.6\mu\text{m}$ and $4.5\mu\text{m}$. The full CARLA-*Spitzer* program is presented in Wylezalek et al. (2013), including the description of the infrared observations and data reduction. Briefly, CARLA was a 400 hr *Warm Spitzer* program which aimed at identifying massive galaxies at high redshift. It has targeted 420 RLAGN, uniformly selected in radio luminosity over the redshift range $1.3 < z < 3.2$, and equally representative of unobscured radio-loud quasars (RLQs or type-1) and obscured high-redshift radio galaxies (HzRGs or type-2), with 209 and 211 elements respectively, according to the classification of the standard AGN unification model (Urry and Padovani, 1995).

This survey has allowed, for the first time, a systematic study of the environments of a large sample of powerful RLAGN (Galametz et al., 2012; Wylezalek et al., 2013), and of the luminosity function of candidate cluster galaxies (Wylezalek et al., 2014).

Galaxy cluster candidates were identified as IRAC color-selected galaxy overdensities in the fields of the targeted RLAGN. Following Papovich (2008) and Sorba and Sawicki (2010), Wylezalek et al. (2013) applied the color cut $([3.6] - [4.5])_{\text{AB}} > -0.1$ mag to select galaxies at $z > 1.3$. This criterion is based on the fact that the spectral energy distributions (SEDs) of galaxies, regardless their evolutionary phase, have a prominent bump at $1.6\mu\text{m}$, due to a minimum in the opacity of the H-ion which is present in the atmospheres of cool stars (John, 1988). As the rest-frame $1.6\mu\text{m}$ bump changes wavelength with redshift and passes through two adjacent bands, the color between those bands changes from blue to red. At $z \sim 1.3$, the bump is shifted to $\sim 3.7\mu\text{m}$ and enters the range between the 3.6 and $4.5 \mu\text{m}$ IRAC bands, as illustrated in Fig. 25. Therefore, selecting colors $([3.6] - [4.5])_{\text{AB}} > -0.1$ mag allows to efficiently select galaxies at $z > 1.3$. The contamination from foreground sources, which may include strongly star-forming galaxies at $0.2 < z < 0.5$ and powerful AGN at all redshifts, is estimated around 20% (e.g. Muzzin et al., 2013, from the comparison to spectroscopic redshifts).

In order to select over-dense environments, the densities of the CARLA fields were compared to the blank field surface density of sources in the *Spitzer* UKIDSS Ultra Deep Survey (SpUDS, P.I. J. Dunlop, Rieke et al., 2004), selected with the same IRAC-color cut, in a 1 arcmin radius aperture centered on the RLAGN, which corresponds to ~ 500 kpc at $1 < z < 3$ (see Fig. 26). The 46% of the CARLA fields which showed at least a 2σ overdensity were identi-

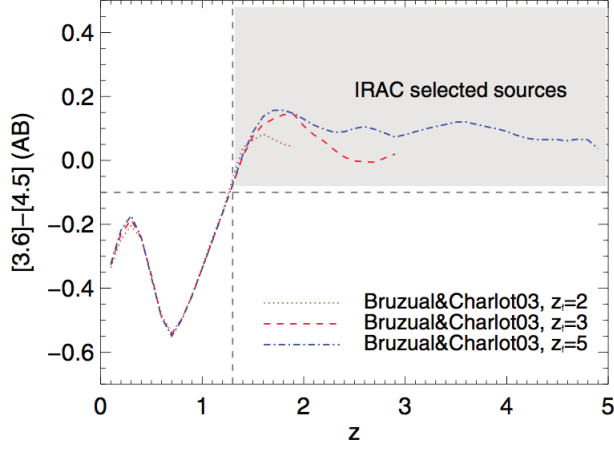


Figure 25 – Change in color between the 3.6 μm and 4.5 μm IRAC bands as a function of redshift, from Bruzual and Charlot (2003) models for different formation redshifts z_f , assuming a Salpeter initial mass function and a single exponentially decaying burst of star formation with a timescale of 0.1 Gyr. The change in color from blue to red happens at $z \sim 1.3$. Figure from Wylezalek et al. (2013).

fied as galaxy cluster candidates ($\Sigma_{\text{CARLA}} > \Sigma_{\text{SpUDS}} + 2\sigma_{\text{SpUDS}}$). Interestingly, their surface density increases toward the position of the targeted RLAGN, and slightly decreases with redshift, supporting the hypothesis that these galaxies belong to a cluster with a RLAGN in the core (Wylezalek et al., 2013).

On the other hand, no correlation between the radio luminosity and the environment was found, nor a significant difference between the RLQ and HzRG fields.

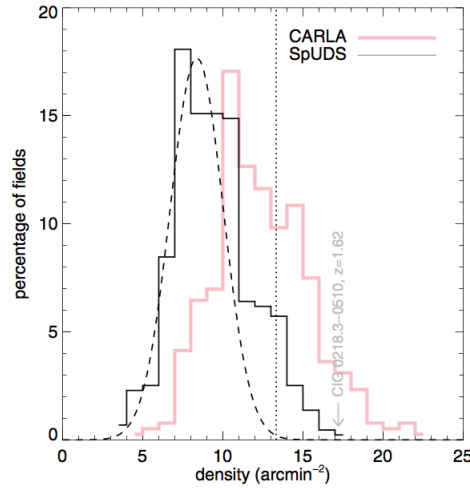


Figure 26 – Histograms of the densities of IRAC-selected sources in the CARLA fields and the SpUDS survey. The dashed black curve is the gaussian fit to the low-density half of the SpUDS density. The vertical dotted line corresponds to $\Sigma_{\text{SpUDS}} + 3\sigma$ density. Figure from Wylezalek et al. (2013).

The CARLA twenty densest cluster candidates (with 5.8-9.0 σ overdensities), which span the redshift range $1.4 < z < 2.8$, were chosen for follow-up observations (P.I. Stern) with the Wide Field Camera 3/Infrared channel (WFC3/IR) aboard the Hubble Space Telescope (HST), using G141 slitless grism spectroscopy and F140W imaging (Noirot et al., 2016, 2018). Noirot et al. (2018)

selected sixteen targets as confirmed candidates, adopting the Eisenhardt et al. (2008) criteria to define a spectroscopically confirmed galaxy cluster, i.e., having at least five spectroscopically confirmed galaxies within a projected physical distance of 2 Mpc and within $\pm 2000 (1 + \langle z_{\text{spec}} \rangle)$ km s⁻¹. In addition, they also discovered and confirmed seven serendipitous structures at $0.87 < z < 2.12$ not associated with the targeted RLAGNs. Following Mei et al. (2015), they assigned to each cluster candidate a probability to be a cluster (i.e. a virialized region) rather than a filament of the cosmic web, based on the comparison between the density of the spectroscopically confirmed members in the CARLA fields and predictions for cluster, sheet and filament overdensities from numerical simulations from Cautun et al. (2014) (see Appendix B in Noirot et al., 2018). They classified three confirmed CARLA structures (J1017+6116, J1753+6310, and J2039-2514) as highly probable confirmed clusters (HPC), and the remaining 13 as probable confirmed clusters (PC). As discussed in Noirot et al. (2018), this additional classification confirms that our confirmed cluster candidate sample is robust and does not suffer from strong contamination from groups, sheets and filaments.

In this thesis, I concentrate on the sixteen confirmed clusters, listed in Table 9 with their classification. In Fig. 27 I present the F140W images of the sixteen RLAGN fields, showing the spatial distribution of the confirmed members. The red stars indicate the RLAGN, and the green circles indicate confirmed member galaxies.

Eight of the sixteen confirmed candidates were also observed in the *i*-band with the auxiliary-port camera (ACAM) on the 4.2m William Herschel Telescope (WHT) in La Palma and the Gemini Multi-Object Spectrograph South instrument (GMOS-S Hook et al., 2004) on Gemini-South in Chile. These observations were part of a large survey which targeted 37 of the densest CARLA fields in the *i*-band, with the aim of tracing the early formation history of massive cluster galaxies (Cooke et al., 2015).

6.2 OBSERVATIONS

I present in Table 10 a summary of the characteristics of the *Spitzer*, HST, and ground-based observations which I discuss in the following subsections.

6.2.1 *Spitzer*/IRAC Imaging

The CARLA-*Spitzer* program (Galametz et al., 2012; Wylezalek et al., 2013, 2014) targeted 420 RLAGNs, with an equal fraction of high-redshift galaxies (HzRGs) and radio-loud quasars (RLQs), in the IRAC channels 1 and 2 (3.6 and 4.5 μm bands, respectively), with rest-frame radio luminosities $L_{500\text{MHz}} \geq 10^{27.5} \text{WHz}^{-1}$, and spanning a redshift range $1.3 < z < 3.2$. The observations were obtained during a 400 hr *Warm Spitzer* program, for areas of 5.2×5.2 arcmin² with an original resolution of 1.22 arcsec pix⁻¹.

RLAGNs at $1.3 < z < 2$ were observed during the *Spitzer* Cycle 7 for total exposure times of 800 s in the 3.4 μm channel and 2000 s in the 4.5 μm channel, while sources at higher redshift ($z > 2$) were observed during the *Spitzer* Cycle 8 for total exposure times of 1000 s in the 3.4 μ channel and 2100 s in the 4.5 μ channel. These exposure times were chosen to have similar depths in both channels. Comparing the CARLA galaxy number counts to number counts from

Table 9 – CARLA sample of spectroscopically confirmed structures (adapted from Noirot et al., 2018). Columns from left to right list: the J2000 right ascension and declination, in degrees, of the RLAGN; the median redshift of structures members; the number of confirmed structures members, detected in our HST/F140W imaging; the confirmed structure classification (HPC: highly probable confirmed cluster, PC: probable confirmed cluster, CGC: confirmed galaxy concentration); the redshift, number of galaxies, and classification of serendipitously discovered structures in some of our targets’ fields. Note that one of the serendipitous discoveries is associated to an unconfirmed CARLA structure and is not displayed in this table.

Name	RA _{RLAGN} (deg)	Dec _{RLAGN} (deg)	\bar{z}_{cl}	Confirmed members	Class.	Ser. overden.
CARLA J0116-2052	19.21423	-20.86858	1.430	12	PC	
CARLA J0800+4029	120.06714	40.49877	1.986	10	PC	
CARLA J0958-2904	149.52016	-29.06885	1.396	8	PC	
CARLA J1017+6116	154.35778	61.27424	2.801	7	HPC	1.234(5)CGC
CARLA J1018+0530	154.61609	5.50834	1.953	8	PC	
CARLA J1052+0806	163.13254	8.10260	1.648	6	PC	
CARLA J1103+3449	165.85947	34.82977	1.443	8	PC	
CARLA J1129+0951	172.30880	9.86639	1.531	12	PC	
CARLA J1131-2705	172.76566	-27.08814	1.445	9	PC	
CARLA J1300+4009	195.13874	40.15214	1.676	8	PC	
CARLA J1358+5752	209.57334	57.86789	1.373	14	PC	
CARLA J1510+5958	227.52465	59.98143	1.719	6	PC	0.875(6)PC 0.976(7)CGC
CARLA J1753+6310	268.39736	63.18044	1.581	5	HPC	2.117(6)PC
CARLA J2039-2514	309.85203	-25.34187	2.000	9	HPC	
CARLA J2227-2705	336.93027	-27.08379	1.686	7	PC	1.357(10)PC 1.478(6)PC
CARLA J2355-0002	358.89833	-0.04631	1.489	12	PC	

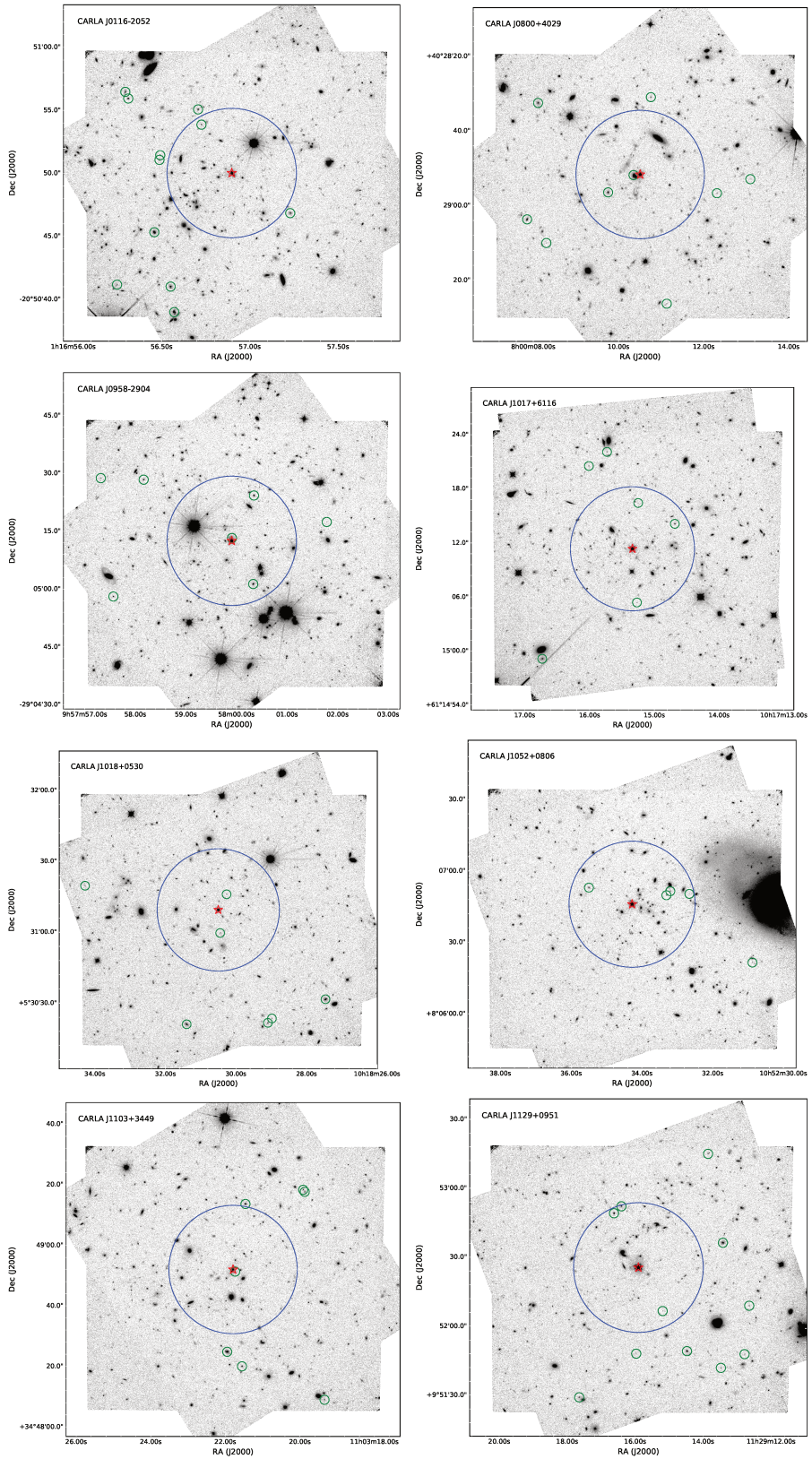


Figure continued

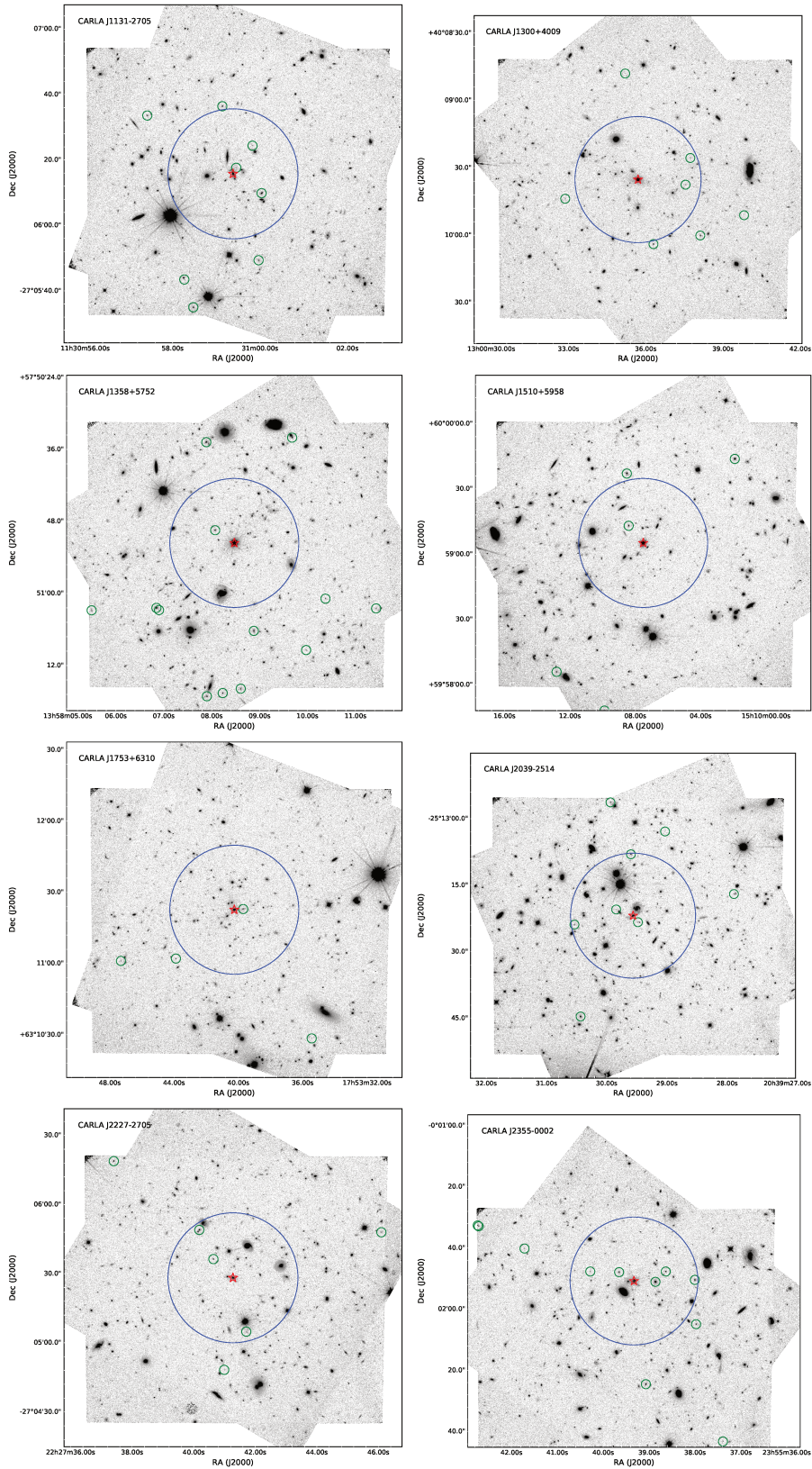


Figure 27 – F140W images of the sixteen RLAGN fields, showing the spatial distribution of the confirmed members. The red stars indicate the RLAGN, and the green circles indicate confirmed member galaxies. The blue circle encloses an area of radius 0.5 arcmin around the position of the RLAGN.

Table 10 – Summary of the characteristics of the observations obtained for the CARLA survey, used in this PhD thesis.

Instrument	Filter	Area (arcmin ²)	λ_{central} (μm)	Bandwidth (μm)	Angular resolution (arcsec pix ⁻¹)	Depth (mag _{AB})
HST/WFC3	F140W	2×2.3	1.40	0.40	0.06	26.6 (5 σ)
<i>Spitzer</i> /IRAC	[3.6]	5.2×5.2	3.550	0.750	0.61	22.6 (95% compl.)
<i>Spitzer</i> /IRAC	[4.5]	5.2×5.2	4.493	1.015	0.61	22.9 (95% compl.)
WHT/ACAM	SInI	$\pi \times 8.3^2/4$	0.7565	0.2111	0.25	25.0 ^a (5 σ)
Gemini/GMOS-S	<i>i</i>	5.5×5.5	0.780	0.144	0.146	24.9 ^a (5 σ)

Depths for the HST, *Spitzer*, and ground *i*-band observations are derived by Noirot et al. (2016), Wylezalek et al. (2013), and Cooke et al. (2015), respectively.

^a Average values. The 5 σ depths for each ground-based observed field are listed in Table 11.

SpUDS, the survey reached a 95% completeness at 22.6 and 22.9 mag for the 3.4 μm and 4.5 μm observations, respectively. The images were reduced using the MOPEX package (Makovoz and Khan, 2005) and resampled to a pixel scale of 0.61 arcsec. Full details of the program and data reduction are presented in Wylezalek et al. (2013, 2014).

6.2.2 HST WFC3 Imaging and Spectroscopy

The twenty richest CARLA fields are 5.8 σ -9.0 σ denser than the mean SpUDS density, and their RLAGN redshift is $1.4 < z < 2.8$. Interestingly, ten fields out of twenty are associated with HzRGs and the other ten are associated with RLQs, meaning that there is no dependence of the galaxy density on the AGN type (Wylezalek et al., 2013, 2014).

Imaging and spectroscopy of these twenty fields were observed with HST/WFC3 between October 2014 and April 2016 (Program ID: 13740; P.I. D. Stern). The program consisted of 40 HST orbits, with two visit with different orientation per field to mitigate contamination from overlapping spectra. Each visit consisted in 500 s of WFC3/F140W direct imaging and 2000 s of slitless spectroscopy with the WFC3/G141 grism. The WFC3 camera has a field of view of 2×2.3 arcmin², and combining the two exposures we re-sampled the final image to a pixel scale of 0.06 arcsec pix⁻¹ using the aXe software (v2.2.4, Kümmel et al., 2009). The WFC3 G141 grism covers the wavelength interval 1.08 - 1.70 μm with a throughput $> 10\%$ at low spectral resolution, $R \equiv \lambda/\Delta\lambda = 130$. This wavelength range enabled to identify strong spectroscopic features at the redshifts of the cluster candidates: H α at $0.65 < z < 1.59$, [OIII] at $1.16 < z < 2.40$, H β at $1.22 < z < 2.50$, and [OII] at $1.90 < z < 3.56$. The observation strategy allowed to spectroscopically confirm star-forming galaxies with strong, narrow emission lines, but did not allow to confirm any possible population of passive galaxies, for which deeper spectroscopy is required (Noirot et al., 2018). Noirot et al. (2016, 2018) present the details of the HST program and the results of the spectroscopic analysis.

6.2.3 Ground Based Optical Imaging

Cooke et al. (2015) obtained optical *i*-band imaging for eight of the sixteen confirmed CARLA cluster candidates with the auxiliary-port camera (ACAM) on the 4.2m William Herschel Telescope (WHT) in La Palma and the Gemini Multi-Object Spectrograph South instrument (GMOS-S; Hook et al. 2004) on Gemini-South in Chile, as summarized in Table 11.

The field of view of ACAM is circular, with a diameter of 8.3 arcmin and pixel scale $0.25 \text{ arcsec pix}^{-1}$, while GMOS-S covers an area of $5.5 \times 5.5 \text{ arcmin}^2$ with a pixel scale of $0.146 \text{ arcsec pix}^{-1}$. Exposure times were adapted to take into account seeing variations, in order to obtain a consistent depth across all fields, and are also listed in Table 11 (see also Table 1 in Cooke et al., 2015).

The *i*-band images were reduced using the THELI software (Erben et al., 2005; Schirmer, 2013), as described in Cooke et al. (2015). The zero-points were calculated comparing the fluxes of unsaturated stars to the fluxes of SDSS stars or standard stars, for targets in the northern or in the southern hemisphere, respectively. The median 5σ depth is of 25.0 mag for the WHT images, and of 24.9 mag for the Gemini images, calculated by measuring the flux in 100000 random apertures of 2.5 arcsec diameter.

Table 11 – Subsample of ground-based optical observations.

Name	<i>z</i>	Inst.	optical band	Exp.time (s)	5σ depth (mag)	Seeing (arcsec)
CARLA J0800+4029	1.986	ACAM	<i>i</i>	6600	25.16	0.93
CARLA J1018+0530	1.953	ACAM	<i>i</i>	7200	25.19	0.81
CARLA J1052+0806	1.648	GMOS-S	<i>i</i>	2645	25.04	0.66
CARLA J1103+3449	1.443	ACAM	<i>i</i>	7800	24.76	1.12
CARLA J1129+0951	1.531	GMOS-S	<i>i</i>	2645	24.78	0.44
CARLA J1358+5752	1.373	ACAM	<i>i</i>	8400	24.95	0.89
CARLA J1753+6310	1.581	ACAM	<i>i</i>	6000	25.08	0.74
CARLA J2355-0002	1.487	ACAM	<i>i</i>	6000	24.99	0.81

6.3 PHOTOMETRIC ANALYSIS

In order to characterize the stellar populations of the clusters confirmed in the CARLA survey, I perform a photometric analysis of the observations summarized in Table 10. In this section, I describe the procedure to get my reference photometry (6.3.1), and I present the tests I have made to validate this photometry (6.4.1). In Appendix A, I give a brief description of the softwares that I have used in my analysis.

6.3.1 Source extraction and photometry

In this Section, I describe my analysis of the CARLA observations, focusing on the steps to get my reference photometry with the T-PHOT program (Merlin et al., 2015, 2016). This program has been successfully tested on large datasets, on a broad range of wavelengths, from UV to sub-mm, and is currently used for the photometry of big surveys like CANDELS, Frontier Fields, and AEGIS. Compared to similar codes like TFIT (Laidler et al., 2007) and CONVPHOT (De Santis et al., 2007), T-PHOT has proven to be more robust and large computational time saving (Merlin et al., 2015).

T-PHOT is designed to perform precision photometry of a low resolution image using the information given by a higher resolution image of the same field (see Section A.4). In this case, I can take advantage of the information given by the high-resolution ($0.06 \text{ arcsec pix}^{-1}$) images obtained with HST, and use positions and surface brightness profiles of sources measured on HST/F140W images as priors to derive the fluxes in all the bands analysed here: F140W (HST), $3.6\mu\text{m}$ and $4.5\mu\text{m}$ (*Spitzer*), i (ground-based telescopes), accounting for the different point spread functions (PSFs). This method allows to de-blend cluster members from fore- or background sources even in the low-resolution optical and *Spitzer* images and obtain robust photometric results. I proceed with the following main steps:

Step 1: From the F140W/HST image, I extract a catalogue of sources and a segmentation map using the SExtractor program (Bertin and Arnouts, 1996, see the description in Appendix A). I adopt the same configuration of parameters used for the catalogs released by the Cosmic Assembly Near-IR Deep Extragalactic Legacy Survey (CANDELS, Grogin et al., 2011; Koekemoer et al., 2011), and published by Galametz et al. (2013) and Guo et al. (2013). I use two detection modes, the *cold* and the *hot* modes, optimized to detect bright and faint objects, respectively, and then combined to get the final catalog following the implementation described in (Barden et al., 2012): a first catalog is build including all the *cold* sources; then, for every source detected in the *hot* mode, if its central position lies inside the Kron ellipse of any *cold* source, it is discarded, otherwise it is included in the final catalog. I give in Table 12 the key SExtractor parameters used in my source detection.

Step 2: I register the “low-resolution” images ($3.6\mu\text{m}$, $4.5\mu\text{m}$, i , hereafter called with the generic name LRI, on the HST frame, using the Swarp package (Bertin et al., 2002, see Section A.2), so that they have the same orientation and pixel scale as the F140W images, with pixel boundaries consistently overlapping. After many tests to check the consistency of photometry of the image before and after resampling, presented in Section A.2.1, I adopt the AIT (Aitoff) projection type, which is an equal-area projection (it conserves relative areas), and the NEAREST resampling method, which performs a “nearest-neighbour” interpolation. With this choice, the differences in magnitudes before and after resampling are on average of 0.02 mag, and < 0.05 mag in the entire magnitude range, for all bands.

Step 3: I estimate the PSFs of each imaging observation, using the PSFex software (Bertin, 2011), and checking that the shape of each PSF is consistent

Table 12 – SExtractor parameters.

SExtractor	Cold Mode	Hot Mode
DETECT_MINAREA	5.0	10.0
DETECT_THRESH	0.75	0.7
ANALYSIS_THRESH	5.0	0.8
FILTER_NAME	tophat_9.0_9x9.conv	gauss_4.0_7x7.conv
DEBLEND_NTHRESH	16	64
DEBLEND_MINCONT	0.0001	0.001
BACK_SIZE	256	128
BACK_FILTERSIZE	9	5
BACKPHOTO_THICK	100	48

with the shape and the FWHM of unsaturated stars (see Section A.3). Then, I obtain a convolution kernel, K , matching the PSFs of the LRI and the F140W images so that: $\text{PSF}_{\text{LRI}} = K \otimes \text{PSF}_{\text{F140W}}$, where \otimes is the symbol for convolution. Finally, I resample the kernel to the F140W pixel scale ($0.06 \text{ arcsec pix}^{-1}$).

Step 4: To get the final photometry, I use the standard pipeline implemented in T-PHOT (Merlin et al., 2015, 2016) and described in Section A.4, which consists in two runs. In the first run, the program creates stamps of sources using the catalog and the segmentation map from the high-resolution F140W/HST image. Then, it convolves each high-resolution stamp with the convolution kernel K to obtain models of the sources at the LRI resolution. Then, the fitting stage solves a linear system to match each template flux with the measured one. I use the *cells-on-object* fitting method. This method orders objects by decreasing flux, building a cell around each source including all its potential contaminants, solving the linear system in that cell and assigning to the source the obtained flux. In the last stage, the program obtains a local convolution kernel, that is used in a second run of the convolution and fitting stages, to obtain more astrometrically precise results. I give in Table 13 the key parameters used in T-PHOT.

From this procedure, I obtain PSF-matched catalogs of sources with photometry in the bands: HST-F140W (J-H boundary, with peak at $1.4 \mu\text{m}$), *Spitzer*-IRAC $3.6 \mu\text{m}$ and $4.5 \mu\text{m}$, and, when available, *i*. Using the HST selection I measure fainter magnitudes, down to 25.2 mag at $3.6 \mu\text{m}$, and 26.7 mag in the *i*-band, at 5σ .

6.3.2 Estimate of uncertainties

T-PHOT provides estimates of the statistical uncertainty on photometry, σ_{TPHOT} , as the square root of the diagonal element of the covariance matrix constructed during the fitting stage for each source. The covariance matrix is built from the scientific and the weight maps of the images, which include the error due the background, the dark current, the gain, and the read-out noise. As a consistency check, I also run 1000 Monte Carlo realizations of background areas (not overlapping to selected sources) with apertures in the range of the sizes

Table 13 – T-PHOT parameters.

Pipeline	1st pass	priors, convolve, fit, diags, dance
	2nd pass	convolve, fit, diags, archive
Priors stage	usereal	true
	usemodels	false
	useunresolved	false
Convolution stage	FFTconv	true
Fitting stage	fitting	coo
	cellmask	true
	maskfloor	1e-9
	fitbackground	false
	threshold	0.0
	linsysolver	lu
	clip	true

of our sources, centered in random positions. The standard deviation of their magnitude distribution is given by the background noise, the dark current, the gain, and the read-out noise. This test confirms that the errors estimated with the Monte Carlo are consistent with those estimated by T-PHOT.

To get the total error budget, I add in quadrature the shot noise, σ_{shot} , of the source and the error on the zero-point, σ_{ZP} :

$$\sigma_{\text{tot}} = \sqrt{\sigma_{\text{TPHOT}}^2 + \sigma_{\text{shot}}^2 + \sigma_{\text{ZP}}^2}. \quad (93)$$

I calculate the flux uncertainties due to the shot noise of the source as the square root of the number of electrons received by each source in the area used for the photometry. I use as uncertainty on the zero-point 0.02 mag for the HST/WFC3 F140W images¹, and 0.05 mag for the *Spitzer*/IRAC1 images². For the ground-based observations, I use uncertainties on the zero-points of 0.022 mag for GMOS-S (obtained by comparing the fluxes of unsaturated stars to the fluxes of standard stars), and 0.05 mag for ACAM (Chris Benn, private communication).

In addition, T-PHOT assigns a flag to each source indicating possible causes of systematic uncertainties, such as a saturated or negative flux of the prior, a blended prior, or a source at the border of the image. I report the flag values in my final catalog.

Since we base our detections on the F140W images, we exclude from the following analysis the sources with photometric error in the F140W band larger than the maximum error at the F140W 5σ depth 26.6 mag, as illustrated in Fig.

1. http://www.stsci.edu/hst/wfc3/phot_zp_lbn

2. <http://irsa.ipac.caltech.edu/data/SPITZER/docs/irac/iracinstrumenthandbook/>

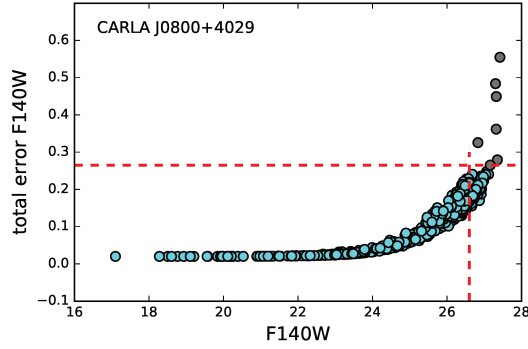


Figure 28 – HST/WFC3 F140W photometric error estimated by T-PHOT as a function of magnitude. Sources with photometric error in the F140W band larger than the maximum error at the F140W 5σ depth 26.6 mag (grey points) are excluded from the analysis. Our selection is shown by the dashed red line.

28. As a consequence, for magnitudes fainter F140W than 26.6 our completeness dramatically drops.

6.4 PHOTOMETRY AND STRUCTURAL PARAMETERS MEASUREMENTS WITH GALAPAGOS

In order to test my reference photometry described above, I have obtained independent estimates of magnitude from GALAPAGOS (Galaxy Analysis over Large Areas: Parameter Assessment by GALFITting Objects from SExtractor), an IDL code designed to process images of large surveys which can operate either in single or multi-band mode. The main steps of the program are:

- detection of sources;
- estimate of the local background;
- cutting of a *stamp* image for each detected source;
- creation of object masks;
- fit of the light profile to a Sérsic profile (one or two components);
- compilation of all objects in a final output catalog.

GALAPAGOS uses SExtractor (Bertin and Arnouts, 1996) to detect sources and the GALFIT program by Peng et al. (2002) to derive photometry and structural parameters of the sources by fitting their light profiles to a Sérsic profile (Sersic, 1968).

For source detection, I use the same catalogs obtained for the T-PHOT photometry. Namely, I run SExtractor on the HST/F140W images in the *cold* and *hot* modes, which are optimized to detect bright and faint objects, respectively. Then, I follow the implementation described in (Barden et al., 2012) in order to get my final catalog of sources: the first catalog includes all the *cold* sources; then, for every source detected in the *hot* mode, if its central position lies inside the Kron ellipse of any *cold* source, it is discarded, otherwise it is included in the final catalog.

For the photometric analysis, the surface brightness profile of each detected source, $\Sigma(R)$, is fitted to a Sérsic model:

$$\Sigma(R) = \Sigma_e \exp\{-k_n[(R/R_e)^{1/n} - 1]\}, \quad (94)$$

where R_e is the half-light (effective) radius, Σ_e is the surface brightness within R_e , n is the Sérsic index, which I allow to vary between 0.2 and 8, and k_n is a

normalization constant. An exponential profile, with $n = 1$, reproduces the observed light profiles of the stellar disks of spiral galaxies (Freeman, 1970), while a “de Vaucouleurs” profile with $n = 4$ reproduces the observed light profiles of elliptical galaxies (de Vaucouleurs, 1948).

For this thesis purposes, I only use to the magnitudes obtained with GALAPAGOS, the GALFIT magnitudes, as alternative estimates to test my photometric results.

On the other hand, the best fit parameters of the Sérsic model give information on the morphology of the sources, which will be presented in a forthcoming work (S. Mei, S. Amodeo and the CARLA collaboration, in preparation).

6.4.1 *Photometry validation*

In this Section, I compare the results obtained with my reference photometry based on T-PHOT to results obtained with different approaches (see Appendix A for a description of the methods):

- AUTO: magnitudes obtained from flexible elliptical apertures around the detected objects, as described in Kron (1980) and implemented in SExtractor (Bertin and Arnouts, 1996);
- GALFIT: magnitudes obtained from the fit of the surface brightness profile of the detected objects to a Sérsic profile, as implemented in GALAPAGOS (Barden et al., 2012);
- for the *i*-band photometry I also use APER estimates, following the approach of Cooke et al. (2015): these are magnitudes obtained from fixed circular apertures around the detected objects, with aperture size of 2.5 arcsec diameter, chosen to be $\sim 2.5\times$ the seeing and a compromise between including as much flux as possible, and avoiding blending. Fluxes within the aperture are then corrected to total fluxes using correction factors measured from the growth curves of unsaturated stars, which are typically 1.15 for ACAM images and 1.04 for GMOS-S images.

In Figures 29, 30, 31, 32, I present the median difference between couples of magnitude estimates, in intervals of 0.5 mag (results are the same if using mean differences instead of the median). For example, the top panel of Fig. 29 shows the median difference between F140W AUTO and TPHOT for TPHOT magnitudes in the ranges [20, 20.5], [20.5, 21], ..., [26.5, 27].

For the F140W photometry, the AUTO estimates are systematically fainter than T-PHOT, up to 0.5 mag for the faintest objects, while there are smaller differences between T-PHOT and GALFIT estimates, (<0.3 at all magnitudes), which is encouraging considering that they are independent methods. We observe comparable differences between AUTO and T-PHOT for the IRAC photometry, but this time with a slight dependence on magnitude, with AUTO giving increasingly brighter magnitudes for decreasing T-PHOT magnitudes.

In the *i*-band, there is a difference of about 0.5 mag between the T-PHOT and SExtractor estimates (AUTO, APER). For the clusters who show the largest differences between the SExtractor and TPHOT magnitudes (J0800+4029, J1018+0530, J1129+0951, J1358+5752), I also show the comparison with GALFIT (Fig. 32). We observe that for magnitudes brighter than ~ 24 , TPHOT and GALFIT are consistent (within 0.4 mag), while TPHOT is less consistent with SExtractor (AUTO, APER). A random check on the GALFIT fitting model and

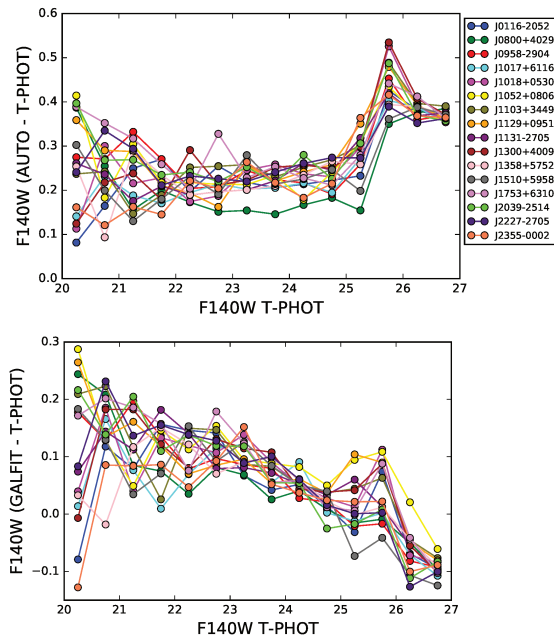


Figure 29 – Comparison between estimates of F140W magnitudes obtained with T-PHOT and AUTO (top), GALFIT (bottom). Color codes of different clusters are indicated in the legend.

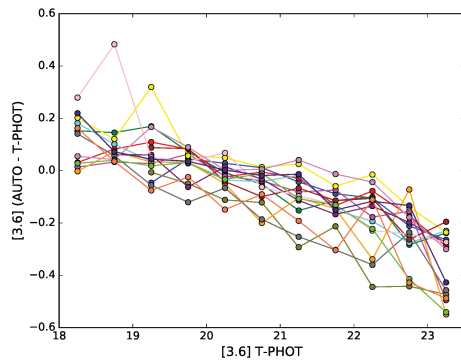


Figure 30 – Comparison between estimates of 3.6 μ m magnitudes obtained with T-PHOT and AUTO. Color codes are the same as Fig. 29.

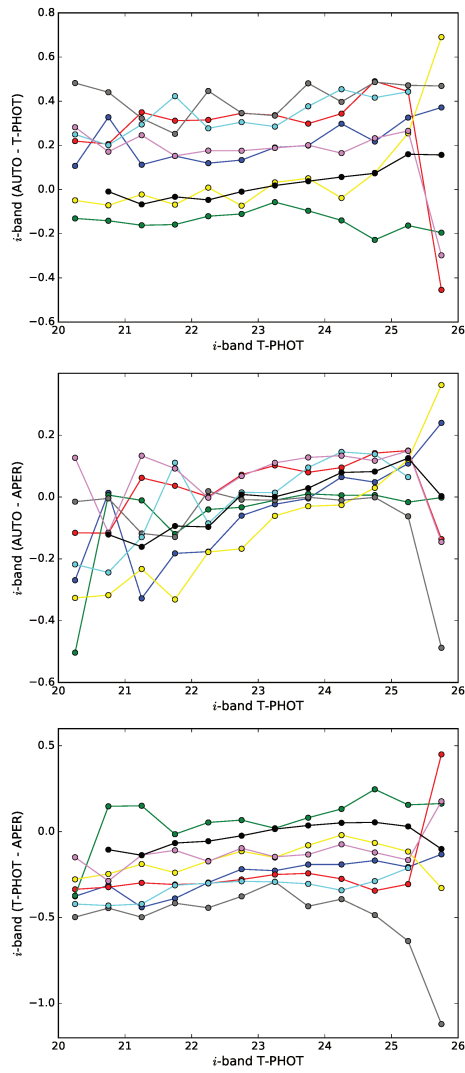


Figure 31 – Comparison of *i*-band magnitude estimates: AUTO - T-PHOT (top), AUTO - APER (middle), T-PHOT - APER (bottom). Color codes of clusters with available *i*-band images are the same as Fig. 29.

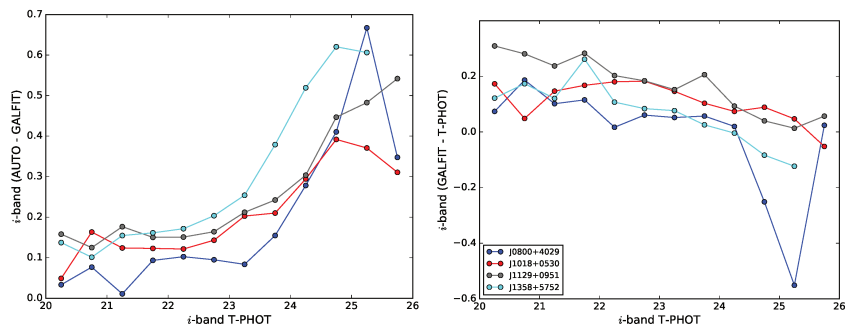


Figure 32 – Comparison between GALFIT and AUTO (left), T-PHOT (right) estimates, for the clusters with the largest differences between the SExtractor and TPHOT magnitudes, indicated in the legend.

residuals reveals that this method performs poorly at fainter magnitudes ($i > 24$ mag).

It is important to note that T-PHOT and GALFIT give PSF-matched photometries, unlike AUTO and APER. The correction factors computed from the stars' growth curves and applied to the aperture magnitudes (APER) only approximately account for PSF effects.

The differences among different methods are not new from the literature. The AUTO magnitude by SExtractor has found to be an imperfect estimator, as pointed out by Mei et al. (2009). For example, Blakeslee et al. (2006) found an offset of 0.2 mag between AUTO and GALFIT magnitudes in the HST/F775W band, in the range $20.5 < F775W < 23.5$ mag. Giavalisco et al. (2004) also found a similar offset between AUTO magnitudes in the HST/F606W band and the magnitudes of simulated galaxies convolved with the PSF.

Overall, our comparison shows a ~ 0.4 mag systematic uncertainty on our photometry due to the use of different methods. We assume that T-PHOT photometry is the most robust given that it is based on high-resolution priors, and prevent blending of nearby sources which can instead contaminate simple aperture flux measurements (see also the conclusions in the analysis by Merlin et al., 2016). This is especially important for IRAC images with large PSFs.

STELLAR POPULATIONS OF HIGH-Z CLUSTERS FROM THE CARLA SURVEY

In this chapter, I present the results of my photometric analysis on the CARLA clusters.

At the redshifts of our CARLA targets, the *i*-band approximately corresponds to the U-band rest-frame, the HST/F140W to the V-band rest-frame and the *Spitzer*/IRAC [3.6] to the J-band rest-frame.

Williams et al. (2009) investigated the stellar populations of 30108 galaxies in the range of photometric redshifts $0 < z_{\text{phot}} < 2.5$, derived from multi-band photometry from the UKIDSS Ultra-Deep Survey in the near-IR (Lawrence et al., 2007), the Subaru-*XMM* Deep Survey in the optical (Sekiguchi and SXDS Team, 2004) and the *Spitzer* Wide-Area Infrared Extragalactic Survey in the mid-IR (Lonsdale et al., 2003). They observed that galaxies up to $z=2$ occupied two distinct regions in the rest-frame (U-V) versus (V-J) (hereafter UVJ) color space: one population lied on a diagonal from blue to red (V-J), clearly following the Bruzual and Charlot (2003) evolutionary tracks of star-forming stellar populations, and above was the other population on a localized clump, red in (U-V) and blue in (V-J), consistent with the Bruzual and Charlot (2003) passive stellar population models, and also overlying the “old passively-evolving galaxies” which were spectroscopically confirmed at $0.8 < z < 1$ from Yamada et al. (2005) with little or no detected line emission. This bimodality was additionally supported by the distribution of the specific star formation rates.

The work by Williams et al. (2009), relying on a large statistics, confirmed the interpretation previously suggested by Labbé et al. (2005) and Wuyts et al. (2007), that quiescent and star-forming galaxies are well separated in a rest-frame UVJ plane, at least up to $z=2$.

Basically, using two colors allows to break the degeneracy between galaxies which have *red* (U-V) color from their evolved stellar populations, and starburst which appear *red* because of dust obscuration. In fact, dust-free quiescent galaxies have *bluer* (V-J) color and occupy a distinct region of the UVJ plane.

In our sample, we can separate passive from star-forming galaxies only in the case of the CARLA targets that have been observed in the *i*-band. At the redshifts of our CARLA targets, the (i-F140W) colors corresponds to the (U-V) rest-frame color and allow us to separate passive from dusty galaxies which are both *red* in the (F140W-[3.6]) color (which corresponds to the (V-J) rest-frame color).

For the CARLA fields without *i*-band data I present the color-magnitude diagrams (F140W-[3.6]) versus [3.6] in Fig. 33. CARLA candidates (red squares) are selected with a *Spitzer*/IRAC color cut $([3.6] - [4.5]) > -0.1$. Candidates confirmed spectroscopically by Noirot et al. (2018) are shown as black diamonds. The data are compared to stellar population models with a formation redshift in the range $3 < z_f < 7$, adapted from Mei et al. (2009, see below). Since for these targets we do not have V-band rest-frame observations, these diagrams show both the red-passive and the red-dusty star-forming galaxies on the same red sequence and we cannot separate them.

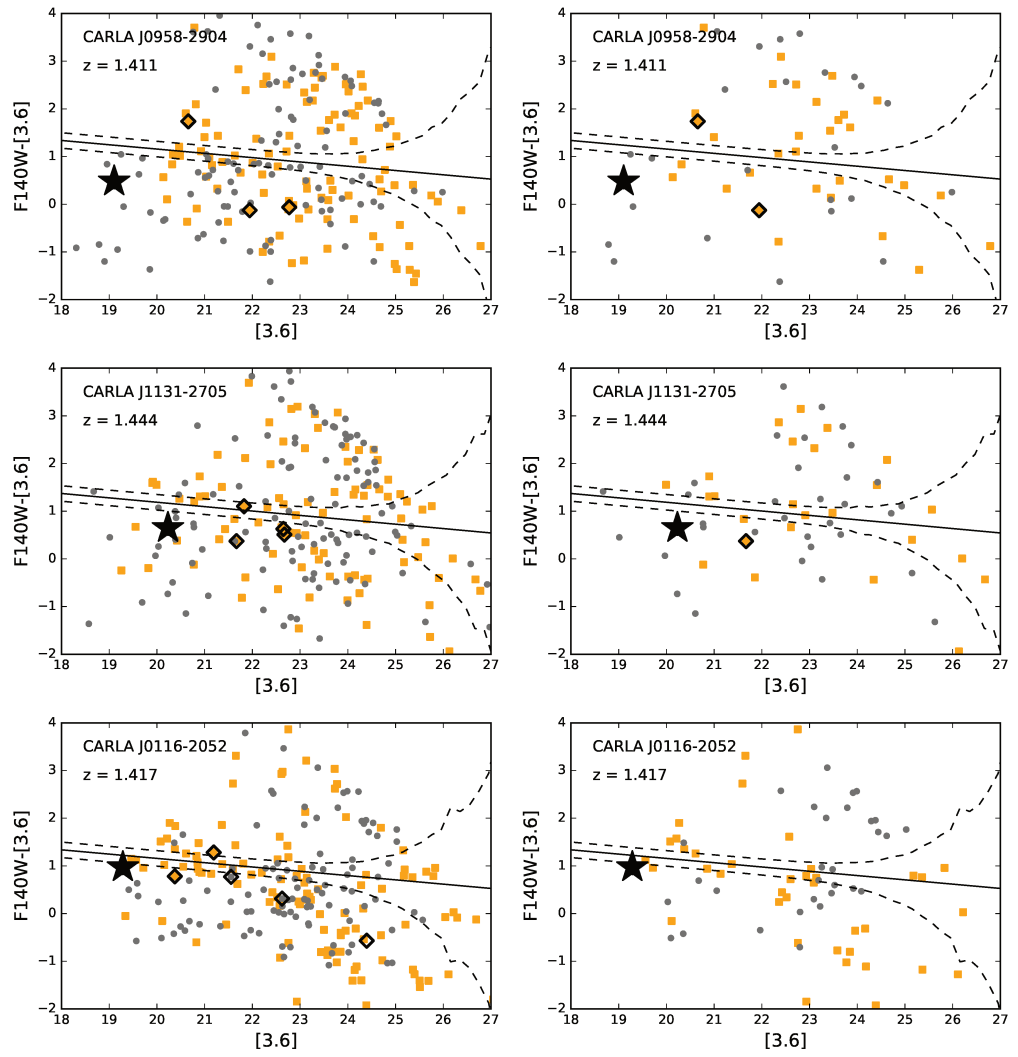


Figure 33 continued

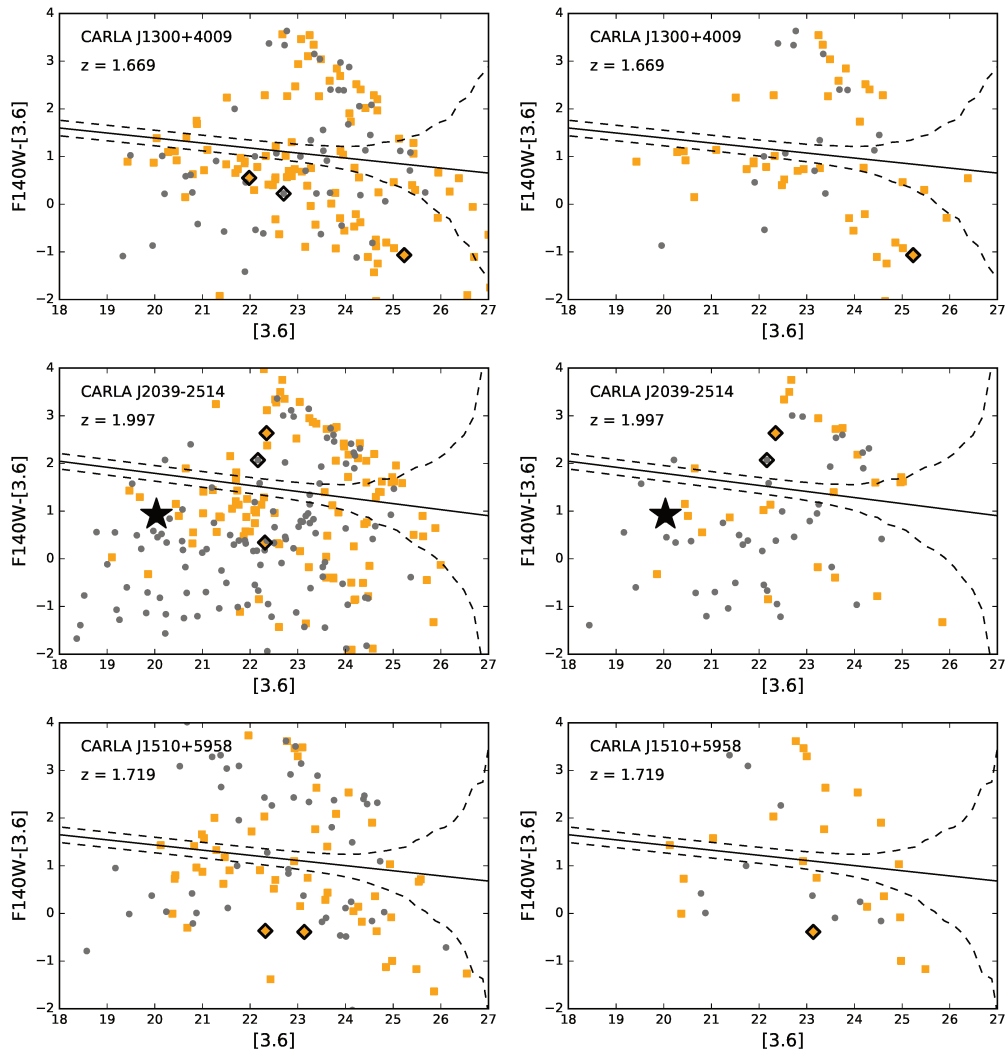


Figure 33 continued

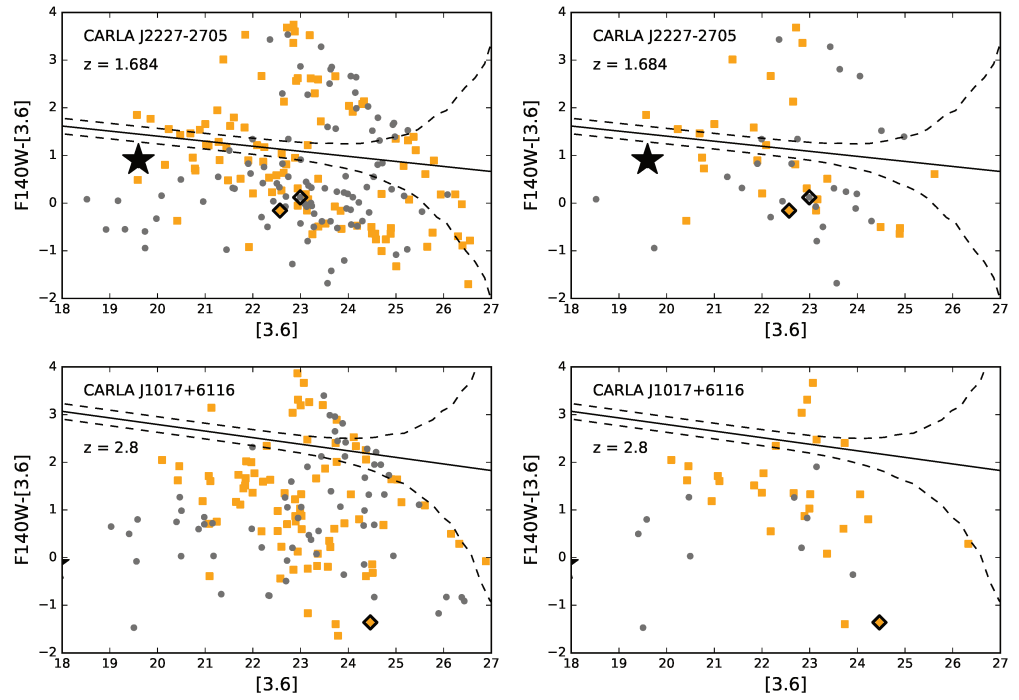


Figure 33 – Color-magnitude diagrams ($F140W-[3.6]$) vs $[3.6]$ for targets without i -band observations, from (*left*) sources selected in a circle of 1 arcmin radius, and (*right*) sources selected in a circle of 0.5 arcmin radius around the RLAGN. IRAC-selected sources, with $([3.6] - [4.5])_{AB} > -0.1$, are indicated by orange squares, while sources with IRAC colors < -0.1 mag (AB) are shown as grey circles. Black diamonds highlight confirmed cluster members from Noirod et al. (2018). The black line gives estimates from a stellar population model with formation redshift in the range $3 < z_f < 7$. The 3σ scatter (black-dashed lines) include the intrinsic scatter of the prediction and the observational errors.

For the CARLA fields with three bands available, I build instead color-color diagrams $i\text{-F140W}$ versus $\text{F140W}-[3.6]$, to separate passive from dusty star-forming galaxies.

I adopt the empirical separation between quiescent (passive) and star-forming galaxies from Williams et al. (2009), which in the redshift range of our interest, $1 < z < 2$, consists in the following diagonal cut in the rest-frame bandpasses:

$$(U - V) > 0.88 \times (V - J) + 0.49, \quad (95)$$

and in additional horizontal and vertical cuts to exclude unobscured and dusty star-forming galaxies, respectively, from the quiescent galaxies, which are the same at all redshifts:

$$(U - V) > 1.3, \quad (V - J) < 1.6. \quad (96)$$

I present our color-color diagrams in the top panels of figures 34-37, ordered by increasing redshift. The boundaries separating passive from star-forming populations have been converted into our observed colors by S. Mei, following the approach described in Appendix B of Mei et al. (2009), adapted for our bands. In brief, we use Bruzual and Charlot (2003) stellar population models with galaxy formation redshifts averaged between 3 and 7, and metallicities equal to 40% solar, solar and 2.5 times solar, letting them passively evolve until the redshifts of our clusters.

In summary, following Williams et al. (2009), the passive members are located in the upper left reddish quadrant of figures 34-37, the star-forming members are located below the horizontal line, whereas the dusty star-forming galaxies lie on the right of the vertical boundary.

The middle and bottom panels of Fig. 34-37 show the color-magnitude diagrams ($i\text{-F140W}$) versus F140W , and $(\text{F140W}-[3.6])$ versus $[3.6]$, respectively, for the clusters that I have analyzed so far. We compare our observations with the color-magnitude relation observed in Mei et al. (2009) for confirmed X-ray and infrared detected clusters at redshift $z \sim 1$. This relation was derived using HST/ACS filters that correspond to rest-frame $(U - B)$ and M_B in the observed range $0.8 < z < 1.3$. For our comparison, this relation has been passively evolved at the redshifts of our clusters, and converted to our bandpasses by S. Mei, using Bruzual and Charlot (2003) stellar population models with galaxy formation redshifts between three and seven, and metallicities equal to 40% solar, solar, and 2.5 times solar. The converted relation is indicated in the plots by the black solid line, while the dashed lines show the 3σ dispersion around the mean evolved passively to the redshift of our clusters, plus the observational photometric errors (added in quadrature).

Noirot et al. (2016) already analyzed the stellar populations of CARLA J0800+4029, based on the SExtractor MAG_AUTO photometry, obtaining the color-color and color-magnitude diagrams shown in Fig. 38. From a one-to-one comparison between my PSF-matched and Noirot's SExtractor photometry, I find differences of 0.1-0.3 mag on the ($i\text{-F140W}$) color, up to $\text{F140W} < 25$ mag, and a difference of 0.5 mag in the range $25 < \text{F140W} < 26.6$, which is expected due to the different methodologies adopted (see discussion in Section 6.4.1). Interestingly, we both find that this cluster at $z=2$ does not host passive candidates consistent with a cluster red sequence, and we observe the same behaviour for the other cluster at $z \sim 2$, CARLA J1018+0530. Noirot et al. (2016) also compared the data to the predictions at $z=2$ of an exponentially decaying model of

star formation (orange area in the bottom panel of Fig. 38), finding that most of the confirmed members did not seem to agree with this model either. A possible interpretation is that this galaxy population has undergone multiple episodes of star formation, consistently with the analysis of Cooke et al. (2015), who showed that the star-formation histories of CARLA cluster galaxies are best described by multiple bursts of star formation over a timescale of few Gyr.

The comparison of our data with the predictions from models of exponentially decaying stellar populations is an important step to complete the interpretation of our results, that we plan to address in the future.

On the other hand, for CARLA clusters at $z < 2$ that I have analyzed so far, the majority of the passive galaxies identified following Williams et al. (2009) follow the red sequence obtained with a passive evolution, although with a larger scatter than calculated at $z \sim 1$.

For example, for CARLA J1753+6310 at $z=1.576$, we observe a well defined red-sequence of passive galaxies. This structure was already studied by Cooke et al. (2016) and recognized as a mature cluster at high-redshift. Using the same *Spitzer*/3.6 μm and *i*-band/ACAM images as this work, and a *J*-band image obtained with the long-slit intermediate resolution infrared spectrograph (LIRIS) at WHT, they found that a remarkably high fraction (80%) of galaxies with broadband colors indicative of a passive population lied on the red sequence. They also showed that half of the cluster galaxies in the core were quiescent, as compared to only 16% of field galaxies of similar mass and redshift from the UKIDSS Ultra Deep Survey (UDS; Hartley et al., 2013). This picture is also consistent with the small number of spectroscopically confirmed star-forming members (only 5) compared to the other CARLA structures at similar redshift, indicating that this is likely an evolved cluster mostly composed of passive members.

In the future, we will estimate the contamination from field galaxies from CANDELS observations in order to reliably obtain the fraction of passive galaxies in each cluster.

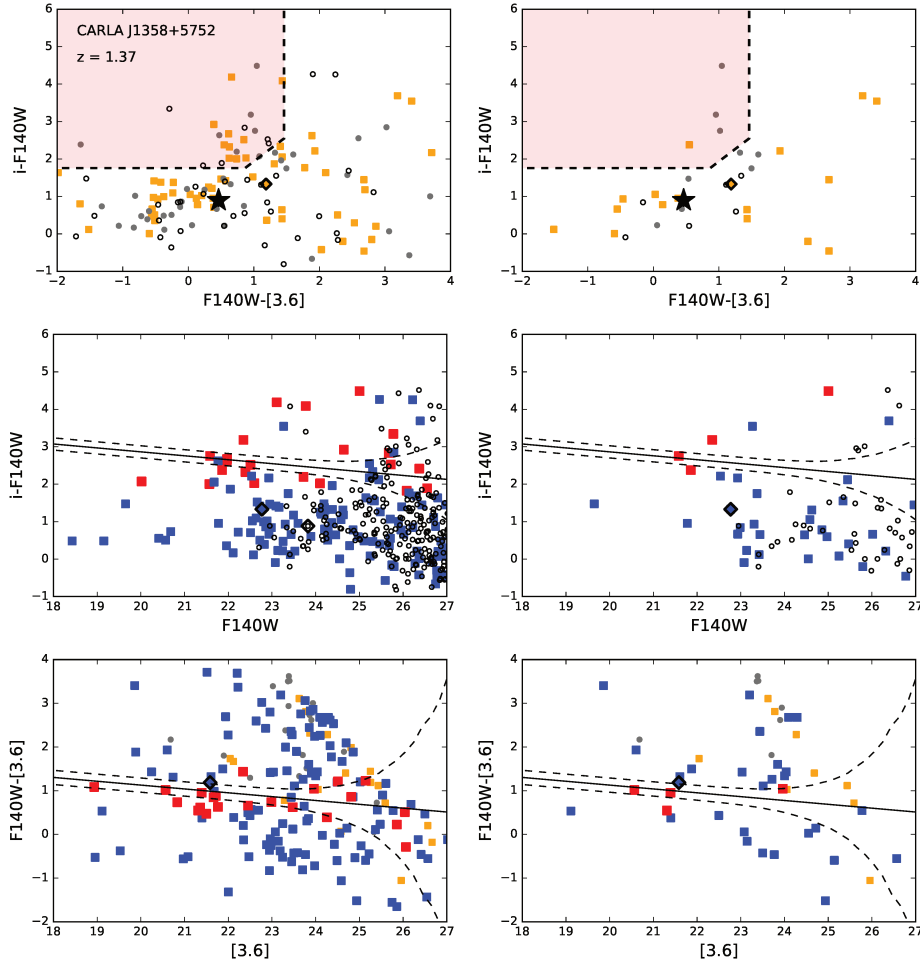


Figure 34 – Color-magnitude and color-color diagrams for CARLA J1358+5752. Left panels show sources selected in a circle of 1 arcmin radius, while right panels show sources selected in a circle of 0.5 arcmin radius around the RLAGN. *Top*: Color-color diagram ($i\text{-F140W}$) vs ($\text{F140W}-[3.6]$). The dashed lines, adapted from Williams et al. (2009), separate passive from star-forming galaxies. Passive galaxies are located inside the upper left reddish quadrant, while dusty SF galaxies are on the right side of the quadrant vertical boundary. IRAC-selected sources, with $([3.6] - [4.5])_{\text{AB}} > -0.1$, are indicated by orange squares, while sources with IRAC colors < -0.1 mag (AB) are shown as grey circles. Black open circles show the sources without [4.5] photometry. Black diamonds indicate the confirmed cluster members from Noirod et al. (2018), and the black star highlight the RLAGN. *Middle*: ($i\text{-F140W}$) vs F140W . Red squares indicate the passive galaxies in the reddish quadrant in the top panels, while blue squares are the star-forming galaxies outside the quadrant. Black open circles are the sources without *Spitzer*/IRAC photometry. The black line gives estimates from a stellar population model with formation redshift in the range $3 < z_f < 7$. The 3σ scatter (black-dashed lines) include the intrinsic scatter of the prediction and the observational errors. *Bottom*: ($\text{F140W}-[3.6]$) vs $[3.6]$. Symbols and colors are the same as the top and middle panels.

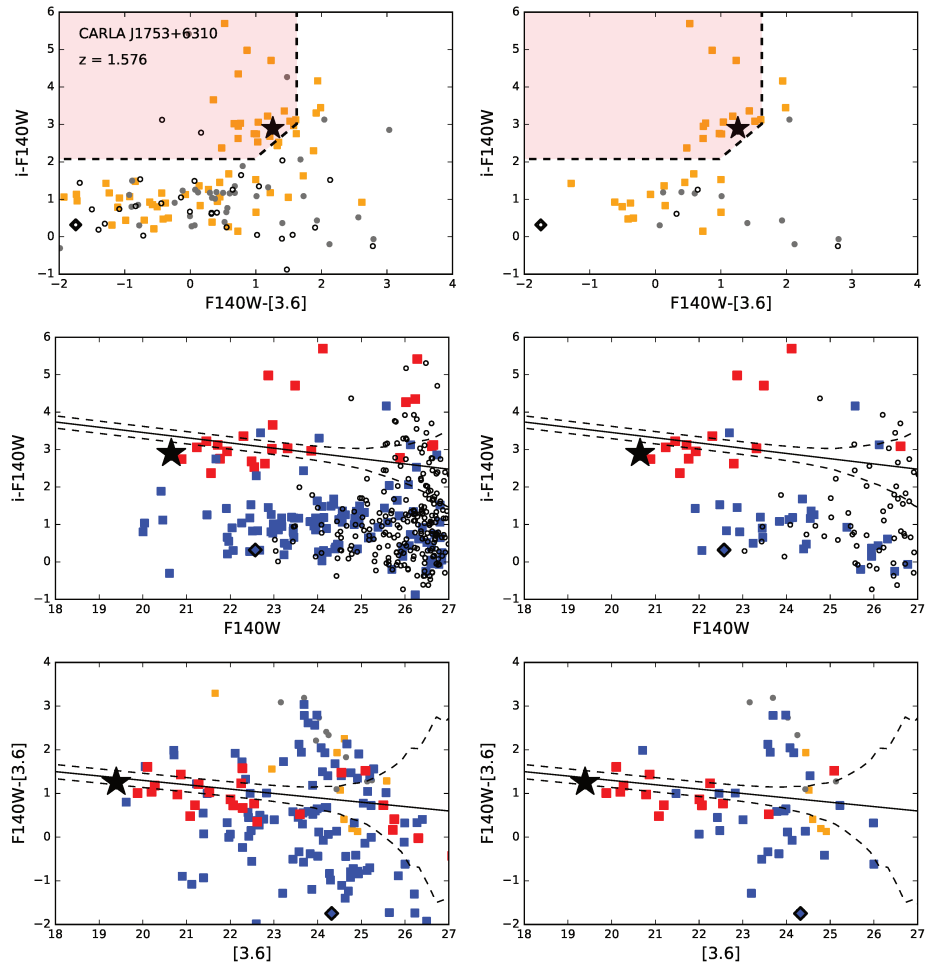


Figure 35 – Color-magnitude and color-color diagrams for CARLA J1753+6310. Symbols and colors are the same as Fig. 34.

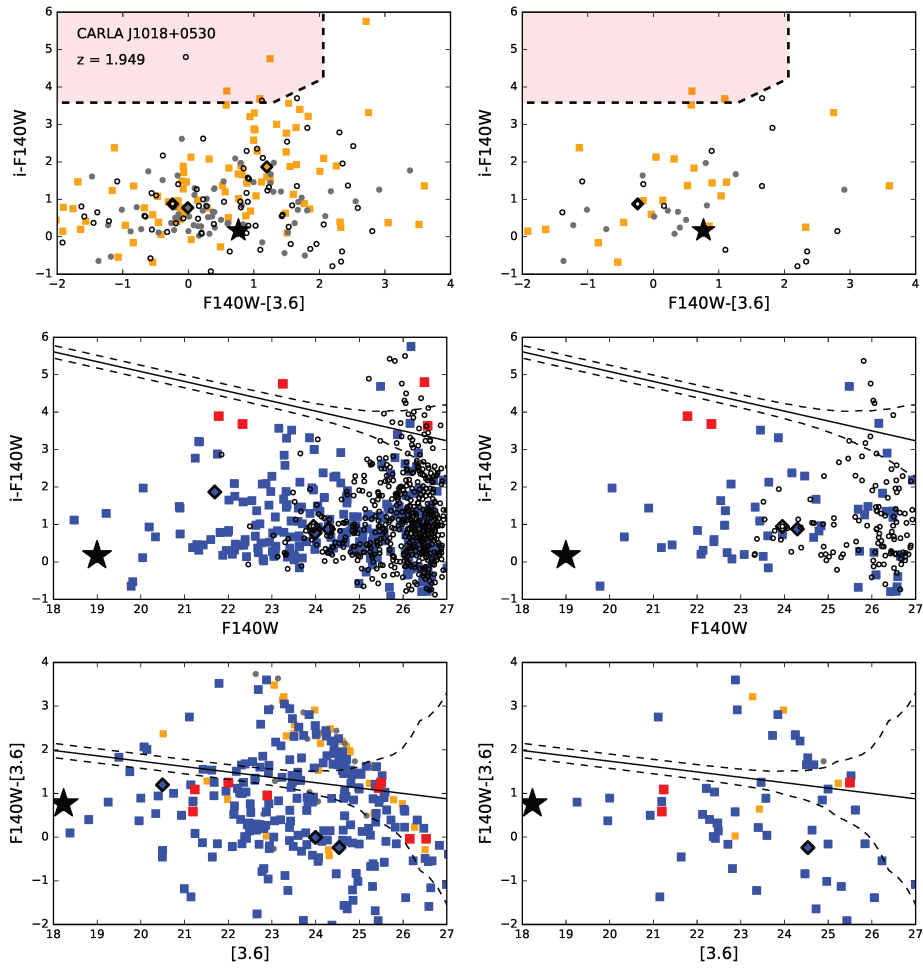


Figure 36 – Color-magnitude and color-color diagrams for CARLA J1018+0530. Symbols and colors are the same as Fig. 34.

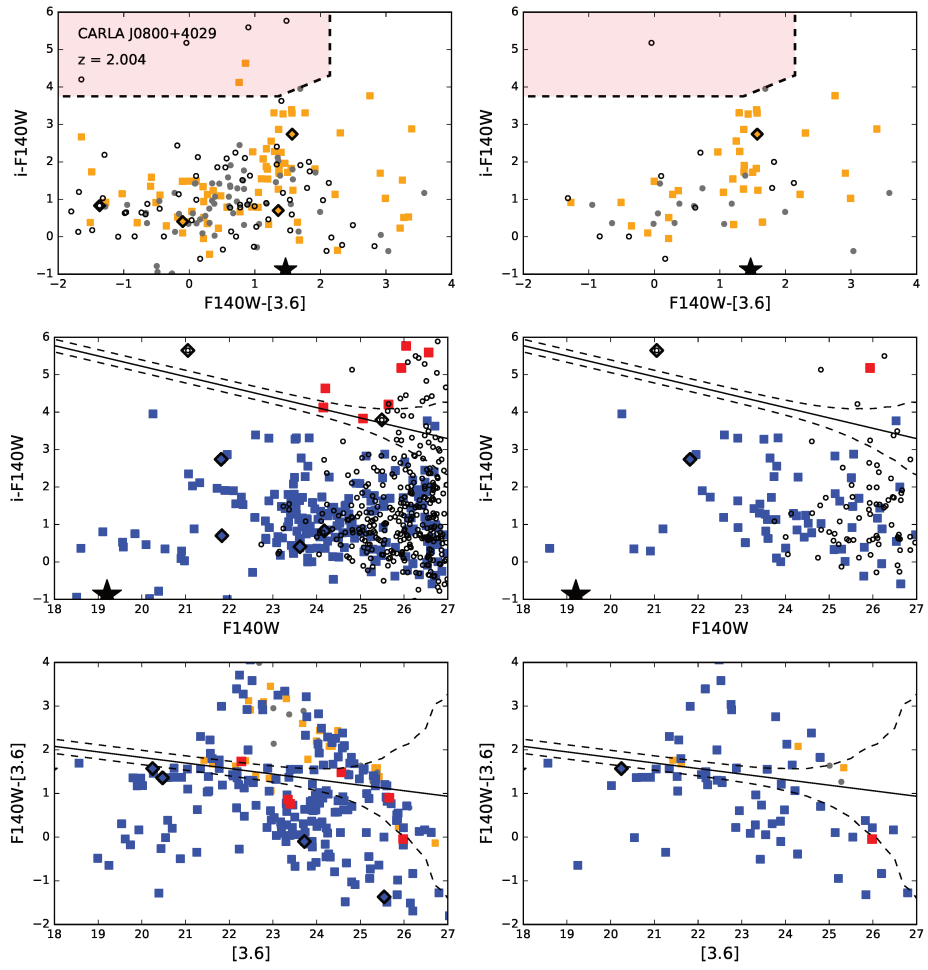


Figure 37 – Color-color and color-magnitude diagrams for CARLA J0800+4029. Symbols and colors are the same as Fig. 34.

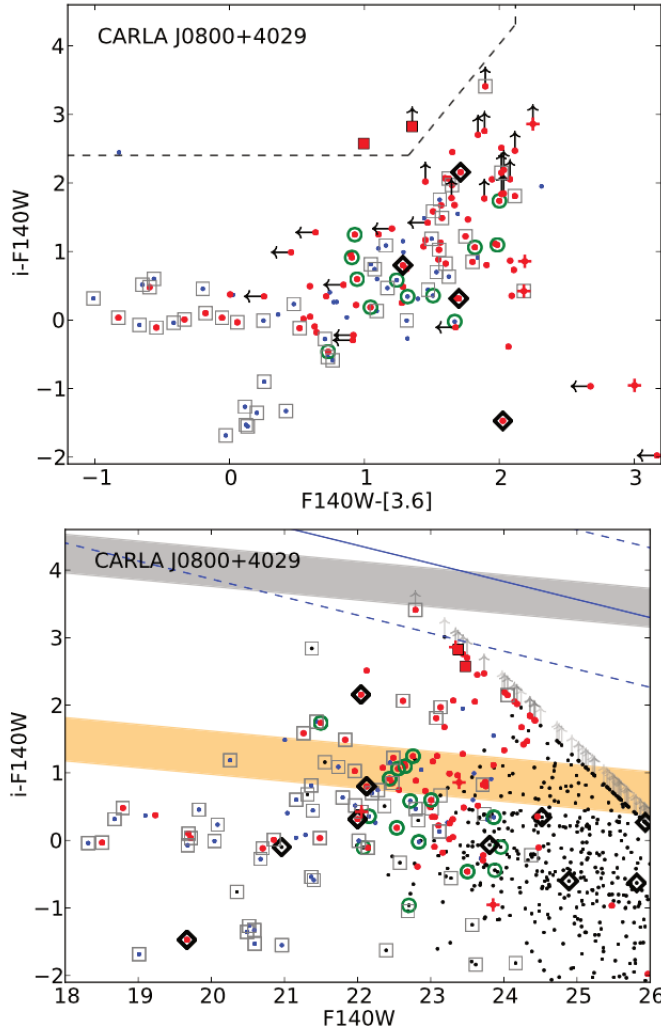


Figure 38 – Color-color (*top*) and color-magnitude (*bottom*) diagrams of CARLA J0800+4029 from Noiroot et al. (2016). The dashed lines, adapted from Williams et al. (2009), separate passive from star-forming galaxies. The IRAC-selected candidates are shown by red markers, with the passive candidates highlighted by red squares and the dusty star-forming candidates by red “+” signs; sources with IRAC colors < -0.1 mag (AB) are shown by solid blue circles. Black diamonds are the confirmed cluster members, and green rings are spectroscopically confirmed non-members. Open grey squares indicate continuum-only sources identified in the grism data. Sources below the detection limit at $3.6\mu\text{m}$ and in the i -band are set to these limits and are indicated by leftward and upward arrows, respectively. In the color-magnitude diagram, the addition of sources detected in the i -band and F140W but not detected at $3.6\mu\text{m}$ are shown by small black dots. The grey and orange shaded areas represent estimates of a $z=2$ red sequence for delta-burst and exponentially decaying stellar populations, respectively. The solid blue lines represent the $z=1$ color-magnitude relation by Mei et al. (2009) passively evolved to $z=2$.

7.1 ONGOING ANALYSIS

I am currently completing the color-color diagram analysis for all clusters with *i*-band observations and I am measuring the fraction of quiescent galaxies as a function redshift.

The first basic point is to assess the level of contamination of our cluster selected galaxies from foreground and background field galaxies. The HST/WFC3 grism spectroscopic campaign allowed to confirm only star-forming galaxies with strong emission lines, while a more extensive multi-slit ground-based spectroscopy and deep multi-band observations would be needed to obtain more spectroscopic redshifts, and robust photometric redshifts for all galaxies. The spectroscopic measurements by Noirot et al. (2018) assigned galaxy membership based on redshift determination from emission lines and could also identify line-emitter outliers. This analysis allows to remove part of the interlopers but we do not have spectroscopic redshifts for all the detected sources.

Following Cooke et al. (2015), I am currently statistically estimating the level of contamination by interlopers using cuts in the color-magnitude diagrams.

With our available photometry on F140W (HST), $3.6\mu\text{m}$ (*Spitzer*-IRAC), and *i*-band from ground telescopes, I can identify foreground bright interlopers at lower redshifts, by performing the same photometric analysis on field galaxies of known photometric redshift. For this purpose, I am using the 3D-HST/GOODS-South field (Skelton et al., 2014; Giavalisco et al., 2004), for which the same bands are available, and perform a photometric analysis with the same procedure used for the CARLA fields. For these sources, photometric redshifts have been released in the CANDELS multi-wavelength catalog by Guo et al. (2013). In addition, I will be able to statistically subtract the number of field contaminants and obtain the fraction of passive galaxies in each cluster and study its evolution as a function of redshift. I am currently validating my preliminary results.

In conclusion, this work will open an important view on the cluster galaxy population at high redshift, and will be particularly useful in preparation of large optical and near-infrared surveys which, in the near future, will be able to detect a high number of clusters, such as *Euclid* (up to $z\sim 2$), and LSST (up to $z\sim 1.5$). A well characterized galaxy population will help planning the detection of clusters at high redshift and building robust samples, which are of great interest for cosmology.

I submitted a draft of a refereed paper that present my results presented in Chapter 6 and 7 to the CARLA collaboration, and I plan to submit it in the Fall 2018.

In parallel with the main research goals of my thesis, I have obtained other scientific results in the context of a collaboration with researchers from the University of Bologna, Italy, where I got my Master's degree. I focused on the relation between the cluster mass and the dark matter concentration as a powerful cosmological probe, and published my results in Amodeo et al. (2016).

As discussed in Chapter 2, the emission of the hot gas in the X-ray band is an important source of information to investigate the global properties of galaxy clusters from the observational point of view. Thanks to the high sensitivity and angular resolution of the last generation of X-ray satellites, such as *Chandra* and *XMM-Newton* X-ray cluster studies have been performed with unprecedented accuracy in recent years.

On the theoretical side, numerical N-body simulations predict that dark matter halos have a universal density profile (Navarro, Frenk, and White, 1997) characterized by two parameters: the scale radius R_s , and the concentration $c_{200} = R_{200}/R_s$. In a Universe where structures form hierarchically (low-mass objects form earlier than high-mass ones) and collapsed objects retain information on the background density at the time of their formation (the background average matter density was higher in the past), concentration and mass must be related so that systems with higher masses are less concentrated and, at a given mass, lower concentrations are expected at higher redshifts.

Numerical simulations by e.g. Duffy et al. (2008), Bhattacharya et al. (2013), De Boni et al. (2013), Dutton and Macciò (2014) indicate that concentration and mass are indeed anti-correlated for all the mass ranges and redshifts investigated, with a mass dependence that is slightly reduced at $z > 0$. Observations of galaxy clusters at low redshift ($z < 0.7$) confirm the expected anti-correlation even if they generally find a steeper slope and a higher normalization compared to the theoretical relation (e.g. Buote et al., 2007; Schmidt and Allen, 2007; Ettori et al., 2010; Merten et al., 2015). Whether this discrepancy is due to observational selection biases or to the lack of some fundamental physics in numerical models is still an open question. Both simulations (e.g. De Boni et al., 2013) and observations (Ettori et al., 2010) agree on the influence of the dynamical state of a cluster on its concentration: more relaxed systems are more concentrated, at a fixed mass.

On the other hand, Prada et al. (2012) predict that at $z > 1$ the $c - M$ relation has a plateau and an upturn, at masses $M_{200} > 10^{14} M_{\odot}$, typical of galaxy clusters.

The aim of the study presented in Amodeo et al. (2016) is to investigate the relation between concentration and mass for X-ray galaxy clusters at high redshift, where there are still no observational constraints on this issue, and probe a possible evolution with redshift.

We select a sample of 47 clusters observed in the X-rays with *Chandra* at $0.4 < z < 1.2$, from archival exposures of targets with no major mergers and with sufficient X-ray signal to allow us to recover the hydrostatic mass properly. Using X-ray morphological estimators, about 1/3 of the sample is not completely relaxed and that this fraction rises to 0.5 in the objects at $z > 0.8$. As conse-

quence of this selection, our sample is not statistically complete and includes targets that were selected differently for their original observations. However, we verify that (*i:*) the sample presents a gas mass - temperature relation that behaves very similarly to the relation estimated locally, and (*ii:*) since the selected objects are very luminous in the X-ray band, the selection applied is, in practice, on the total mass and properly represents the very massive high end of the cluster halo function, in particular at high redshift.

I have performed spatial and spectral analyses of the ICM to extract the radial profiles of the gas temperature and density. Assuming that the distribution of the X-ray emitting gas is spherically symmetric and in the hydrostatic equilibrium with the underlying gravitational potential, I have combined the deprojected gas density and spectral temperature profiles through the hydrostatic equilibrium equation to recover the total mass distribution consistent with a NFW profile, following the method described in Ettori et al. (2010).

Here is a summary of our main results:

- we consider the largest sample investigated so far at $z > 0.4$ and we provide the first constraint on the c - M relation at $z > 0.7$ from X-ray data only.
- we estimate a total mass M_{200} in the range (1st and 3rd quartile) $8.1 - 18.6 \times 10^{14} M_{\odot}$ and a concentration c_{200} between 2.7 and 5. The distribution of concentrations is well approximated by a log-normal function in all the mass and redshift ranges investigated.
- our hydrostatic mass estimates are in very good agreement with the result from weak-lensing analysis available in literature. In particular, the c - M relation calculated for the clusters shared with the CLASH sample (Umetsu et al., 2016) is fully consistent within the errors. In the redshift range $0.8 < z < 1.5$, constraints on the $c - M$ relation were also derived in Sereno and Covone (2013) for a heterogeneous sample of 31 massive galaxy clusters with weak- and strong-lensing signals, obtaining similar results.
- our data confirm the expected trend of lower concentrations for higher mass systems and, at a fixed mass range, lower concentrations for higher redshift systems, as shown in Fig. 39. The fit to the linear function $\log c_{200} = A + B \times \log M_{200}/(10^{14} M_{\odot}) + C \times \log(1 + z) \pm \sigma_{\log c_{200}}$ gives a normalisation $A = 1.15 \pm 0.29$; a slope $B = -0.50 \pm 0.20$, which is slightly steeper than the value predicted by numerical simulations ($B \sim -0.1$); a redshift evolution $C = 0.12 \pm 0.61$, which is consistent with zero; and an intrinsic scatter on the concentration $\sigma_{\log c_{200}} = 0.06 \pm 0.04$.
- the predictions from numerical simulations of the estimates of the normalisation A and slope B are in a reasonable agreement with our observational constraints at $z > 0.4$, once the correlation between them is fully considered. Values from Dutton and Macciò (2014) are consistent at the 1σ level. Larger deviations, but still close to the $\sim 2\sigma$ level of confidence, are associated with the predictions from Diemer and Kravtsov (2015b) and Prada et al. (2012), where the latter is more in tension with our measurements. It is worth noticing, however, that we are characterising the high-mass end of the distribution of galaxy clusters even at $z \sim 1$, which is a regime that is hardly accessible to the present numerical simulations.

This work has been expanded in Ghirardini et al. (2017) with an analysis of the pressure and entropy profiles of the same sample of clusters, and it has contributed

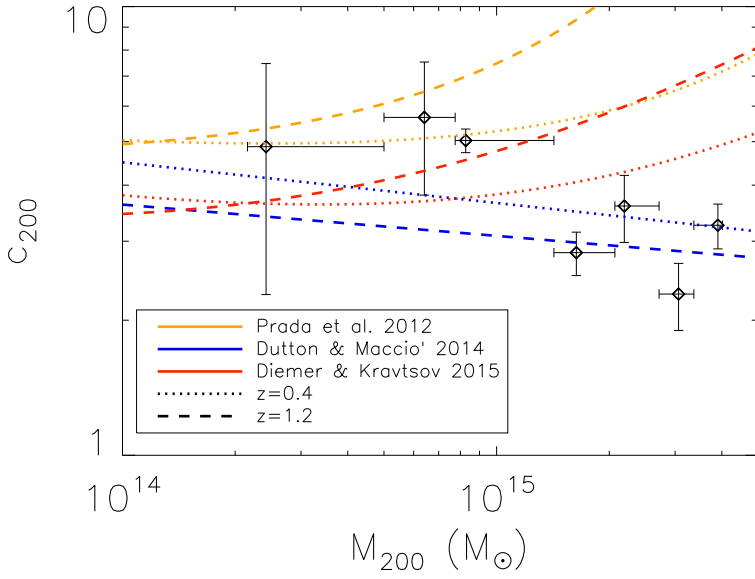


Figure 39 – Concentration-mass relation obtained from the X-ray analysis of 47 *Chandra* clusters in Amodeo et al. (2016), divided into 7 mass bins. For each bin, error-weighted means for concentration and mass are calculated (black diamonds) and the error bars represent the errors on the weighted means. Colored lines are predictions based on different numerical simulations calculated for $z = 0.4$ (dotted lines) and $z = 1.2$ (dashed lines), which are the lowest and highest redshifts in the observed sample.

to test an alternative cosmological probe, the halo *sparsity*, in Corasaniti et al. (2017).

In Ghirardini et al. (2017), we present the entropy and pressure profiles of these clusters. Compared to the self-similar behaviour predicted from gravitational structure formation (Voit, 2005), we find that these profiles deviate from the baseline prediction as function of redshift, in particular at $z > 0.75$, where, in the central regions, we observe higher values of the entropy (by a factor of ~ 2.2) and systematically lower estimates (by a factor of ~ 2.5) of the pressure with respect to the outskirts. Such behaviour is consistent with a scenario in which galaxy clusters are the last gravitationally bound structures to form, and mostly unrelaxed objects are expected at $z \sim 1$ from ongoing merging processes.

In Corasaniti et al. (2017), we use the hydrostatic masses derived for this sample of clusters at $0.4 < z < 1.2$, combined with a lower redshift sample of 57 clusters ($0.05 < z < 0.3$) from Ettori et al. (2010, 2018), to test the cosmological utility of the dark matter halo “sparsity”. This quantity, defined as the ratio of two halo masses at two different overdensities, does not require any explicit assumption about the form of the halo density profile, and therefore, it is useful to characterise the mass profiles of halos even when their density profile deviates from a NFW.

From this first analysis we find large uncertainties, of 20% level, on the cluster sparsity, which allow to get weak constraints on Ω_m and σ_8 . Assuming the mass function from Despali et al. (2016), we find $\Omega_m = 0.42 \pm 0.17$, and $\sigma_8 =$

0.80 ± 0.31 , which are compatible with those inferred from Planck Collaboration et al. (2016a) within 1σ .

Future cluster surveys will provide larger datasets and opportunities for precise measurements of the sparsity. From a Fisher matrix analysis, we forecast find that a sample of ~ 300 clusters with mass estimate errors at $\sim 1\%$ level can improve the *Planck* constraints on Ω_m and σ_8 of a factor of ~ 2 .

This three papers are enclosed in Appendix B.

SUMMARY & OUTLOOK

This PhD thesis is dedicated to the study of galaxy clusters in order to improve the use of cluster counts in cosmology.

For this purpose, two main topics have been addressed: (i) the calibration of the scaling relation between cluster observables, specifically the velocity dispersion and mass, (ii) the study of the galaxy populations in clusters at high redshift ($1.4 < z < 2.8$).

In this final chapter, I summarize the content and the main results of this thesis, and I discuss future perspectives.

The first part of this thesis aims to understand the systematics in different proxies of the cluster mass to help improving its calibration for cosmology.

I analyze the case of a sample of *Planck*-detected clusters, which is interesting for two main reasons: (i) the *Planck* mission has provided the largest sample of galaxy cluster candidates to date, detected via the SZ effect, which can be used to constrain cosmological parameters from the cluster number counts (Planck Collaboration et al., 2014a, 2016b) once the cluster candidates are confirmed; (ii) results from *Planck* have uncovered a remarkable discrepancy between the cosmological parameters determined from the cosmic microwave background and those derived from cluster counts. This has questioned either the reliability of the *Planck* mass estimator, and called for an accurate estimate of the cluster mass bias ($(1 - b) = M_{\text{Planck}}/M_{\text{true}}$), or, in the absence of a large mass bias, called for a modification of the standard Λ CDM cosmological model. A mass bias of $(1 - b) = 0.58 \pm 0.04$ is required to bring the cluster counts and the cosmic microwave background into full agreement.

With our *Planck* spectroscopic follow-up, I confirm a sub-sample of the *Planck*-detected clusters by measuring redshifts and velocity dispersions of cluster member galaxies (Chapter 4), and I use our velocity dispersions to calibrate the *Planck* mass (Chapter 5).

In particular, I confirm 19 clusters with the Gemini and Keck telescopes, including seven new confirmations, among which one of the most distant *Planck* cluster confirmed to date, PSZ2 G085.95+25.23 at $z = 0.782 \pm 0.010$.

For a subsample of clusters confirmed with Gemini¹, I study the scaling relation between the cluster velocity dispersion and the *Planck* SZ mass proxy, which are two independent probes of the cluster mass (the former is based on the dynamics of the member galaxies, while the latter is based on the properties of the intracluster medium), in order to estimate the mass bias.

Among the possible sources of systematics analyzed (the telescope finite aperture, the Eddington bias, the correlated scatter between the velocity dispersion and the *Planck* mass proxy, and the velocity bias, i.e. the ratio between the galaxy and the dark matter velocity dispersion), I identify the velocity bias of the

1. Since we obtained the confirmation of the $z = 0.78$ cluster with Keck spectroscopy after the analysis with the Gemini data was completed and published, I have not considered this cluster for the scaling relation analysis discussed in this thesis, in order to be consistent with the published results. I have verified, though, that including this cluster does not change the interpretation of our main results, as it lies on the same relation found for the Gemini-confirmed clusters.

member galaxy population, b_v , as the one having the largest impact, since the mass bias depends on the cube of the velocity bias: $(1 - b) = (0.51 \pm 0.09)b_v^3$. A precise measurement of b_v is therefore essential to calibrate the mass, while a full comprehension of this bias has not been reached yet (Sec. 5.1.2).

Using the positive velocity bias obtained from the simulations of Munari et al. (2013), $b_v = 1.08$, I find a mass bias of $(1 - b) = (0.64 \pm 0.11)$, which means that *Planck* masses are about 36% lower than the dynamical masses. This result is within 1σ of the value $(1 - b) = (0.58 \pm 0.04)$ needed to reconcile the *Planck* cluster counts with the primary CMB, indicating that the mass calibration can solve the tension.

Comparing to other works, my result is $\sim 30\%$ lower (at $\sim 2.5\sigma$) than the lensing determination by Smith et al. (2016) and the Rines et al. (2016) determination, also based on velocity dispersions, both of which favor little or no mass bias. However, my result agrees within 1σ with the results from the lensing analysis with WtG (von der Linden et al., 2014b), CCCP (Hoekstra et al., 2015a) and CLASH (Penna-Lima et al., 2017).

Focusing on the velocity bias problem, I obtain observational constraints on the velocity bias by combining our velocity dispersion measurements with mass estimates from weak lensing from Penna-Lima et al. (2017), which give a prior on the cluster mass bias. I derive $b_v \gtrsim 0.9$ at 3σ , consistent with Munari et al. (2013), but discrepant with models that predict a negative velocity bias, as for example found by Caldwell et al. (2016).

In conclusion, the uncertainty on the velocity bias has to be precisely estimated in order to reliably determine cluster masses through velocity dispersions. Apart from this, I have achieved a precision of $\sim 17\%$ on the mass bias measurement with 17 clusters only (covering a large *Planck* mass range, $2.3 \times 10^{14} M_\odot < M_{500}^{\text{Pl}} < 9.4 \times 10^{14} M_\odot$), which is promising given the small sample. For comparison, Sifón et al. (2016) obtain a $\sim 12\%$ precision on the mass bias from 44 clusters observed with ACT.

This motivates continued effort to improve the dynamical mass estimates as proxies of the cluster mass complementary to e.g. lensing estimates.

The second part of this PhD thesis is devoted to the study of the cluster galaxy population at the highest redshifts that will be accessible by future surveys, i.e. $z > 1.3$, to help planning their detection and building statistical samples of galaxy clusters at these redshifts, which will significantly improve the constraints on the cosmological parameters derived from cluster count measurements.

I analyze sixteen spectroscopically confirmed clusters from the Cluster Around Radio-Loud AGN (CARLA) survey at $1.4 < z < 2.8$, which are an homogeneous statistical sample of spectroscopically confirmed clusters at high redshift, ideal to investigate galaxy evolution in dense environments. Most of the thesis work has been devoted to optimize a joint photometric analysis of *Spitzer*, HST, and ground-based *i*-band images, based on the T-PHOT software (Merlin et al., 2015, 2016), which allows to take advantage of the information given by our high-resolution ($0.06 \text{ arcsec pix}^{-1}$) F140W HST images, and use positions and surface brightness profiles of sources measured on this band as priors to derive PSF-matched fluxes in the bands with a lower resolution (Chapter 6.)

My preliminary results on the color-color and color-magnitude diagrams indicate that clusters at $z < 2$ have a red sequence of passive galaxies already in place, while clusters at $z \sim 2$ do not (Chapter 7). However, a complete view of

our sample and other works (Strazzullo et al., 2013; Cooke et al., 2015; Wang et al., 2016; Noirot et al., 2016, 2018) also reveal that clusters with similar galaxy overdensities as the targets I already analyzed do show a red sequence at $z \sim 2$. This means that the cluster population at $z \sim 2$ includes both clusters that present a red sequence and clusters that do not.

The study of clusters and proto-clusters at $z > 1.5$ is a relatively young, but rapidly growing, field of research. In the last few years, the search of these objects has been conducted through a variety of techniques. Most of the cluster candidates at $z > 1.5$ have been identified as overdensities of passive galaxies, galaxies red in the *Spitzer*/IRAC colors, bright in the far-infrared, or as line-emitter overdensities (e.g., Castellano et al., 2007; Kurk et al., 2009; Papovich et al., 2010; Tanaka, Finoguenov, and Ueda, 2010; Stanford et al., 2012; Zeimann et al., 2012; Muzzin et al., 2013; Newman et al., 2014; Mei et al., 2015), sometimes coinciding with an extended X-ray emission (e.g., Andreon et al., 2009; Gobat et al., 2011; Santos et al., 2011).

Our CARLA sample is unique because of the large number of targets selected homogeneously, spectroscopically confirmed and statistically classified as highly probable and probable clusters (Noirot et al., 2018).

The picture that can be drawn so far is somewhat variegated and confirms the variety of galaxies hosted by our CARLA sample. In fact, also in other works some clusters show evidence, already at $z \sim 2$, of a collapsed halo of the size of a mature cluster, and host an high concentration of quiescent galaxies, with a well-defined red sequence, in the core (Papovich et al., 2010; Gobat et al., 2011; Stanford et al., 2012; Andreon et al., 2014; Newman et al., 2014).

Mei et al. (2015) confirmed one proto-cluster at $z = 1.84$ and one galaxy group at $z = 1.9$, both populated by star-forming early-type galaxies which have not formed a red-sequence yet.

Other studies find large fractions ($\sim 50\%$) of star-forming galaxies in high- z clusters, indicating that most of the quenching of star formation observed at lower redshift had not yet occurred (Tran et al., 2010; Fassbender et al., 2011; Hayashi et al., 2011; Tadaki et al., 2012; Zeimann et al., 2012; Brodwin et al., 2013; Gobat et al., 2013; Strazzullo et al., 2013; Clements et al., 2014; Webb et al., 2015; Valentino et al., 2015).

Some studies find an enhanced specific star formation in cluster galaxies with respect to field galaxies, suggesting a reversal of the star formation-density relation (Elbaz et al., 2007; Tran et al., 2010; Brodwin et al., 2013; Santos et al., 2015). For our CARLA sample, Noirot et al. (2018) find the contrary: our line-emitters show lower SFR when compared to star formation rates obtained in the same mass range from the CANDELS survey (Whitaker et al., 2014). At these redshifts, it has also been observed a higher number of star-forming members in the cluster cores with respect to the outer regions (Brodwin et al., 2013; Noirot et al., 2018).

Wang et al. (2016) discovered a very peculiar cluster at $z = 2.5$ detected in the X-rays, with a large number of member galaxies (17), confirmed from CO and H α emission lines from multiple spectroscopic observations (IRAM-NOEMA, VLT/KMOS, JVLA). The core of this structure (central 80 kpc) is dominated by star-forming galaxies and has a high star formation rate of $\sim 3400 M_{\odot} \text{yr}^{-1}$, with a depletion time of 200 Myr, suggests that this structure is in the transition phase between proto-cluster and mature cluster.

My photometric analysis of the CARLA clusters, which reveals so far mixed galaxy populations in clusters at high redshift, is still in progress and I plan to include it in the final version of the thesis. In conclusion, this work will open an important view on the cluster galaxy population at high redshift, since it is based on a homogeneously selected sample of clusters, and will be particularly useful in preparation of forthcoming cosmological survey based on optical and near-IR observations.

In particular, the ESA mission *Euclid* is planned for launching in 2022, and will operate for six years, completing one wide survey and one deep survey.

Euclid will discover thousands of clusters and proto-clusters at high redshift (Laureijs et al., 2011; Sartoris et al., 2016; Ascaso et al., 2017) and is expected to provide tight cosmological constraints from cluster counts.

Sartoris et al. (2016) provided forecasts on such constraints. Based on an analytical estimate of the cluster selection function in the photometric *Euclid* survey, they predicted that $\sim 2 \times 10^6$ clusters will be detected at 3σ with a minimum mass of $M_{200} \sim 8 \times 10^{13} M_{\odot}$, almost constant with redshift up to $z = 2$, and about one-fifth of them will be at $z \geq 1$. Thanks to the broad redshift range covered, the cosmological constraints with cluster number counts will be heavily improved, with a figure of merit of a factor of two larger than an equivalent survey limited to $z \leq 1.2$.

In this context, the analysis of the CARLA clusters using optical, near-IR and mid-IR data will contribute to characterize the stellar populations of high-redshift clusters and understand what future optical and near-IR surveys, such as *Euclid*, will observe.

Tight constraints on the cosmological parameters from cluster counts can only be obtained with a perfect knowledge of the observable-mass scaling relation. For this reason, the goal of *Euclid* will be to have an accuracy of 1% on the cluster mass, obtained from weak-lensing estimates. In this context, my analysis of the velocity dispersion - mass relation of *Planck* clusters is useful to understand the systematics that affect the dynamical and the SZ mass estimates and improve their use as proxies of the cluster mass complementary to lensing estimates.

The future of this research field, in terms of cluster cosmological surveys, can be summarized by Fig. 11, from the work of Ascaso et al. (2017), which contains a consistent comparison of the selection functions of next-generation surveys, assuming completeness and purity rates of the cluster selection $>80\%$. Of course surveys at different wavelengths will map different populations of clusters, and a synergy among them is required to have a complete picture of the cluster population. At $z < 0.7$, among the optical and near-IR surveys, the best performance in terms of the limiting cluster mass threshold, will be reached by J-PAS ($5 \times 10^{13} M_{\odot}$), thanks to its very accurate photometric redshifts obtained with 54 narrow bands, while LSST will reach ~ 1.5 higher masses. It is interesting to note that comparable depths can be obtained only up to $z \sim 0.2$ with the e-Rosita X-ray survey. *Euclid* will reach $\leq 10^{14} M_{\odot}$ up to $z \sim 1$ in the ‘‘pessimistic’’ case in which the *Euclid* photometry would be only complemented by the five-band optical photometry from DES, it will reach $\sim 10\%$ lower values in the ‘‘optimistic’’ case in which it will be complemented by six additional bands from LSST. At $z > 1.3$, *Euclid* will be more competitive with respect to the other surveys, together with the SZ survey SPTpol. The SZ and X-ray surveys will have the advantage of building mass-selected samples of clusters, based on the

properties of the intra-cluster gas. While the X-ray selection function of e-Rosita steeply increases with redshift, the limiting mass of the SZ surveys SPTpol and ACTpol is almost flat/slightly decreases with redshift, and these surveys will be able to build lower mass samples of clusters at the highest redshifts. In particular, they will reach a limiting mass of $4 \times 10^{14} M_{\odot}$ (SPTpol), $7 \times 10^{14} M_{\odot}$ (ACTpol) at $z = 2$ decreasing to $\times 10^{14} M_{\odot}$ (SPTpol), $4 \times 10^{14} M_{\odot}$ (ACTpol) at $z = 1.5$.

For the near future, I plan to expand my expertise in cluster surveys in order to strengthen my understanding of cluster physics.

I will join the group of N. Battaglia at the Cornell University, who have strong expertise in SZ surveys. I will be highly involved in the preparation of new submillimeter/millimeter instruments, such as CCAT-prime and the Simons Observatory.

In particular, I will use observations from the current SZ ACTpol surveys which have detected clusters at lower mass than *Planck* ($M_{500} < 10^{14} M_{\odot}$), up to $z \sim 1.4$ (see Fig. 7), to build an interesting sample to constrain the scatter and redshift evolution of the cluster mass-observable scaling relation.

In addition, I will analyze the kinetic SZ effect on clusters observed with ACT with high signal-to-noise measurements, which are very promising to probe the total pressure support in combination with the analysis of thermal SZ effect, test the validity of the hydrostatic equilibrium approximation, and infer properties of the feedback processes in clusters.

BRIEF DESCRIPTION OF THE USED SOFTWARE

In this Appendix, I give a brief description of the softwares that I have used in my photometric analysis of the CARLA clusters.

A.1 SExtractor

SExtractor (Source-Extractor) is a free software implemented by Bertin and Arnouts (1996) that builds a catalog of sources from an astronomical image, optimized for large scale galaxy-survey data. It handles images with variable noise by using the weight maps computed in the image reduction process, which describe the noise intensity at each pixel.

The program starts by constructing a background map to be subtracted to the image. It divides the image in a grid and estimates the local background in each mesh of the grid. The local background histogram is clipped iteratively until convergence at $\pm 3\sigma$ around its median; if σ changes less than 20% during this process, the field is considered not crowded and the mean of the clipped histogram is taken as a value for the background; otherwise the considered value is the mode defined as: $2.5 \times (\text{median}) - 1.5 \times (\text{mean})$. In order to suppress possible overestimations of the background due to bright stars, a median filter can be applied to the grid. The resulting background map is a bicubic-spline interpolation between the meshes of the grid. For this step, one has to choose the mesh size (BACK_SIZE), considering that if it is too small, the background estimation is affected by the presence of objects and random noise, and part of the flux of the most extended objects can be absorbed in the background map, while if the mesh size is too large, it cannot reproduce the small scale variations of the background. Another parameter is the size of the median filter (BACK_FILTERSIZE), and the thickness of the background local annulus (BACKPHOTO_THICK).

The following step is the detection of sources, as part of a process called "segmentation", which consists in separating objects from the background. First, a detection is identified as a group of connected pixels that exceed some threshold above the background. In particular, there are three requirements for a candidate objects:

- all the pixels must be above the value of DETECT_THRESH (expressed in terms of σ above the local background)
- all these pixels must be adjacent to each other (they must have either corners or sides in common).
- there are more than the minimum number of pixels specified in DETECT_MINAREA.

In addition, the parameter ANALYSIS_THRESH defines the threshold value to compute the FWHM of the sources and the star/galaxy separation.

In order to help detecting faint, extended sources, the program can apply a filter that smooths the image (FILTER_NAME), which must be chosen according to the FWHM of the seeing and the detection threshold.

Once sources have are selected from thresholding criteria, the "deblending" process establishes whether a group of adjacent pixels is a single object or not.

The program performs a multi-thresholding on a number of levels defined by the parameter `DEBLEND_NTHRESH` between the primary extraction threshold and the maximum count in the object. At each level, it separates the pixels above the threshold from the pixels below it, designing a *branch of a tree*. Each branch is then considered as a separate component if *i*): the integrated pixel intensity of the branch is larger than a certain fraction of the total intensity of the composite object, defined by the parameter `DEBLEND_MINCONT`, and *ii*): condition (*i*) is verified for at least one more branch at the same level.

After deblending the objects, the source selection is completed and `SExtractor` can perform astrometry, photometry and compute some geometric parameters. For each detected source, we are interested in:

- the coordinate of the barycenter in the world coordinates system (`ALPHA_J2000`, `DELTA_J2000`)
- the minimum and maximum x and y-coordinates among the detected pixels (`XMIN`, `YMIN`, `XMAX`, `YMAX`)
- the value of the background at centroid position (`BACKGROUND`)
- the isophotal flux, derived from the counts above the threshold minus the background (`FLUX_ISO`)
- the Kron radius, which is the typical size of the flexible aperture, computed as the first moment of the intensity profiles $I(R)$ and defined as:

$$R_{\text{Kron}} = \frac{\sum R I(R)}{\sum I(R)}. \quad (97)$$

Even though I use another method to get my final photometry, I am interested in the photometry performed by `SExtractor` for comparison purposes (see Section 6.4.1). In particular, I will refer to the automatic aperture photometry, obtained from flexible elliptical apertures (the kron radius) around the detected objects (`MAG_AUTO`), and to the photometry from circular apertures specified by the user (`MAG_APER`).

A.2 SWARP

`SWarp` is a program by Bertin et al. (2002) that resamples astronomical images to a common frame, and to a specified pixel scale, applying a geometrical transformation using any arbitrary astrometric projection defined in the WCS standard (it can also combine images but I do not use this feature in my analysis).

The program is based on an “inverse mapping” technique, where the output frame is scanned pixel-per-pixel and line-by-line. The center of each output pixel is associated to a position in the input frame (inverse projection), where the image is interpolated.

There are several options for the projection. The traditional gnomonic projection, where great circles are displayed as straight lines, is the tangential projection (`TAN`). For large sky surveys, equal-area projections (that conserve relative areas) are preferred because they conserve the surface-brightness and allow summing pixel values to measure fluxes. I use the zenithal equal-area (`ZEA`), and the Aitoff (`AIT`), which is a pseudo-cylindrical projection.

The resampling involves interpolation between pixels. In detail, at each position x , the interpolated value is the dot-product between a local kernel, $k(x)$, and the values of the neighbouring pixels, f . The kernel is derived locally from

an interpolation function that can be chosen among several options. I test the following interpolation functions:

- NEAREST: a square box response function, with width 1 pixel (the so-called “nearest-neighbour” interpolation). It produces a kernel over a single input pixel;
- LANCZOS3: a response function of the form: $\text{sinc}(\pi x)\text{sinc}(\pi x)$, with $(-3 < x \leq 3)$. It produces a kernel over 6×6 pixels;
- LANCZOS4: a response function of the form: $\text{sinc}(\pi x)\text{sinc}(\pi x)$, with $(-4 < x \leq 4)$. It produces a kernel over 8×8 pixels.

In theory, the larger the kernel, the better is the resampling. However, in practice, large kernels can create artifacts around image discontinuities. The choice should be the best compromise.

A.2.1 Image resampling

Step 2 of my photometric analysis (Section 6.3.1) requires that the low-resolution image is registered on the same astrometry and the same pixel scale of the high-resolution image used to select sources. In order to make this operation, which consists in registering the images in the *Spitzer* and the *i* bands on the HST/F140W-image frames, I use the program Swarp (Bertin et al., 2002). As described in Section A.2, several astrometric projections and interpolation functions are possible.

In order to make the best choice for my photometry, I consider a random CARLA field, and calculate the magnitudes (MAG_AUTO by SExtractor) of sources selected in the same way on the original and the resampled image, for different choices of projections and interpolation functions.

To begin with, I check the effect of the resampling process on the HST images, by simply applying a projection, without changing the pixel scale. The smallest differences in magnitudes result from an equal-area projection (AIT), and a Lanczos3/Nearest interpolation function (see Table 14).

The same test, on the *Spitzer* images gives slightly smaller difference when using the NEAREST interpolation function, which I finally adopt (see Table 15).

To conclude, I present in Table 16 the magnitude differences obtained when resampling the *Spitzer* images to the HST pixel scale, with an AIT projection and a NEAREST interpolation.

Table 14 – Median and mean differences between magnitudes obtained from a random original HST image and magnitudes of sources selected in the same way from the resampled image, for different choices of projections and interpolation functions.

Projection	Interp.	mag _{AB} < 26	mag _{AB} < 25	mag _{AB} < 24.5
		Median (Mean) diff.	Median (Mean) diff.	Median (Mean) diff.
NEAREST	AIT	0.0057 ± 0.1058 (0.0138 ± 0.4523)	−0.0001 ± 0.0842 (0.010 ± 0.409)	−0.0005 ± 0.0777 (0.0097 ± 0.3975)
NEAREST	ZEA	0.0056 ± 0.1059 (0.0126 ± 0.4641)	−0.0001 ± 0.084 (0.0096 ± 0.419)	−0.0003 ± 0.0777 (0.0089 ± 0.4077)
LANCZOS3	AIT	0.0024 ± 0.0937 (−0.005 ± 0.3895)	0.0004 ± 0.0762 (−0.003 ± 0.359)	0.0002 ± 0.0716 (−0.003 ± 0.352)
LANCZOS4	AIT	0.0011 ± 0.0942 (−0.006 ± 0.407)	0.0009 ± 0.0787 (−0.007 ± 0.374)	0.0009 ± 0.0737 (−0.007 ± 0.366)

Table 15 – Median and mean differences between magnitudes obtained from a random original *Spitzer*/IRAC image and magnitudes of sources selected in the same way from the resampled image, at the original IRAC pixel scale, for different choices of projections and interpolation functions.

Projection	Interp.	mag _{AB} < 23	mag _{AB} < 22	mag _{AB} < 21
		Median (Mean) diff.	Median (Mean) diff.	Median (Mean) diff.
NEAREST	AIT	-0.0011 ± 0.2459 (-0.066 ± 0.586)	-0.0151 ± 0.2319 (-0.099 ± 0.576)	-0.021 ± 0.229 (-0.118 ± 0.587)
LACZOS3	AIT	-0.0443 ± 0.2404 (-0.0812 ± 0.5705)	-0.0593 ± 0.2321 (-0.1118 ± 0.5471)	-0.0639 ± 0.2248 (-0.1313 ± 0.5635)
LANCZOS4	AIT	-0.0290 ± 0.2424 (-0.0589 ± 0.5989)	-0.0474 ± 0.2262 (-0.1058 ± 0.5855)	-0.0561 ± 0.2336 (-0.1372 ± 0.6116)

Table 16 – Median and mean differences between magnitudes obtained from a random original *Spitzer*/IRAC image and magnitudes of sources selected in the same way from the resampled image, at the HST pixel scale, for the AIT projection and the NEAREST interpolation function.

Projection	Interp.	mag _{AB} < 23	mag _{AB} < 22	mag _{AB} < 21
		Median (Mean) diff.	Median (Mean) diff.	Median (Mean) diff.
NEAREST	AIT	0.0126 ± 0.0882 (-0.00047 ± 0.2308)	0.0129 ± 0.0790 ($-3.0518e-05 \pm 0.2344$)	0.0187 ± 0.0524 (0.0123 ± 0.2024)
LANCZOS3	AIT	0.0092 ± 0.1005 (-0.0142 ± 0.3233)	0.0096 ± 0.0809 (-0.0225 ± 0.3291)	0.0165 ± 0.0520 (-0.0147 ± 0.3517)

A.3 PSFEX

PSFEx (PSF Extractor) is a program by Bertin (2011) that extracts models of the Point Spread Functions (PSFs) from astronomical images processed by SExtractor. PSFEx pre-selects detections which are likely to be point sources (stars), finding the position of the stellar locus in a magnitude vs half-light-radius diagram (Kaiser, Squires, and Broadhurst, 1995), based on source characteristics such as half-light radius and ellipticity, while rejecting saturated objects. The selected sources are those whose shape does not depend on the flux and, among the image profiles of all real sources, those with the smallest FWHM. This selection is iterated several times to minimize contamination of the sample by image artifacts, multiple stars and compact galaxies.

In Fig. 40, I present the radial profiles of the PSFs I obtain for my F140W, 3.6 μ m, 4.5 μ m images (for the space images I derive one PSF per band from the best image providing unsaturated stars and I use it for all the images in same band), one example of a PSF obtained for ACAM and one for GMOS-S images (for the ground images I derive one PSF for each observed field). The FWHM of the PSFs, in pixel units, is the last number on the bottom right of each figure.

A.4 T-PHOT

T-PHOT is a program designed by Merlin et al. (2015, 2016) to perform precision photometry of a low resolution image (LRI) using the spatial and mor-

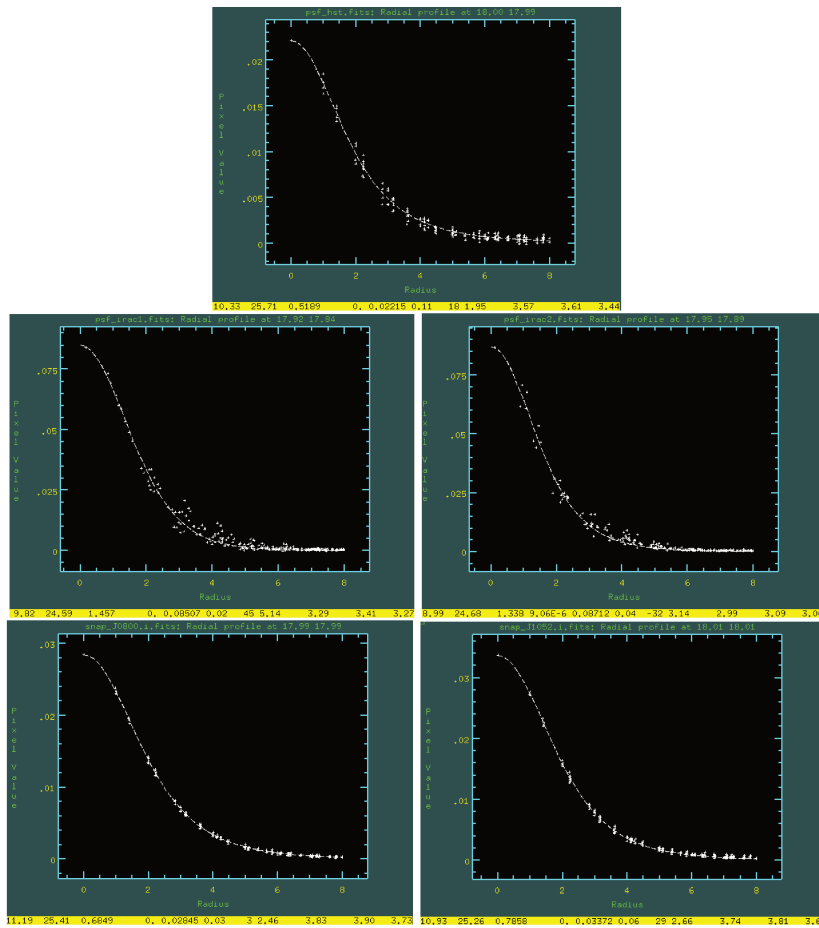


Figure 40 – Radial profiles of the PSFs obtained, from top left to bottom right, for our F140W, 3.6 μ m, 4.5 μ m images (for the space images I derive one PSF per band from the best image providing unsaturated stars and I use it for all the images in same band), the ACAM image of CARLA J0800+4029, and the GMOS-S image of CARLA J1052+0806. The last number on the bottom right indicates the FWHM in pixel units.

phological information given by a higher resolution image (HRI) of the same field. More specifically, with true high-resolution priors (from HST/F140W in my case), T-PHOT uses:

- a detection, high-resolution image (HRI);
- a catalog of the sources in the HRI, obtained with SExtractor, including: (ID, X, Y, XMIN, YMIN, XMAX, YMAX, BACKGROUND, FLUX_ISO);
- a segmentation map of the HRI;
- a convolution kernel K, matching the PSFs of the HRI and the LRI so that $\text{PSF(LRI)} = \text{K} \otimes \text{PSF(HRI)}$ (\otimes is the symbol for convolution), and having the HRI pixel scale.

The T-PHOT analysis consists in different steps:

Step 1: Priors.

It creates stamps of the sources using the coordinates and the boundaries indicated in the input catalog and the segmentation map.

Step 2: Convolve.

It convolves each high-resolution stamp with the kernel K to obtain models of the sources at the LRI resolution, normalized to the total flux. The convolution is performed in Fourier space, using fast FFTW3 libraries.

Step 3: Fit.

It performs the fitting procedure, solving a linear system and obtaining the multiplicative factors to match each template flux with the measured one. The linear system is defined as:

$$\sum_{m,n} I(m, n) = \sum_{m,n} \sum_i^N F_i P_i(m, n), \quad (98)$$

where m and n are the pixel indexes, I contains the pixel values of the fluxes in the LRI, P_i is the normalized flux of the template for the i th objects in the LRI, and F_i is the multiplicative scaling factor for each object, i.e., the flux of each object in the LRI. The best fit of the fluxes is derived by minimizing the following χ^2 statistic:

$$\frac{\delta \chi^2}{\delta F_i} = 0, \quad \chi^2 = \left[\frac{\sum_{m,n} I(m, n) - M(m, n)}{\sigma(m, n)} \right]^2, \quad (99)$$

where

$$M(m, n) = \sum_i F_i P_i(m, n), \quad (100)$$

and σ is the value of the rms map at the (m, n) pixel position.

In order to refine the procedure, a threshold can be imposed so that only pixels with a flux higher than this level will be used in the fit.

I use the *cells-on-object* fitting method, which is computationally time-saving and is sufficiently accurate for images where the blending of sources is not dramatic. This method first orders objects by decreasing flux; it builds a cell around each source of the dimensions of the object template, and then it enlarges the cell to include all the overlapping objects which are appended to the cell list. The linear system is solved in that cell for the central object and the obtained

flux is assigned to the source. Then, the central object is subtracted from the image and the fit is performed on the rest of the cell (to avoid that bright objects contaminate the fit of fainter sources).

Step 4: Diags.

The program selects the best fits and produces the final output catalogs with fluxes and errors. Statistical errors are calculated as the square root of the diagonal element of the covariance matrix constructed during the fitting stage for each source. In particular, the covariance matrix is build from the scientific and the weight maps of the images, which in our case include the error due the background, the dark current, the gain, and the read-out noise. In addition, T-PHOT assigns a flag to each source indicating possible causes of systematic uncertainties, as follows:

- +1: the prior has saturated or negative flux;
- +2: the prior is blended (from the segmentation map);
- +4: the source is at the border of the image.

Step 5: Dance.

The program obtains local convolution kernels for the second pass, in order to obtain more astrometrically precise results. In details:

- the LRI is divided into cells of a given size; in each cell, the LRI is cross-correlated with the model image and a linear shift is computed;
- for the regions where the previous registration process gives large shifts, above a given threshold parameter, interpolated shifts are computed;
- the computed shifts are used to create a new set of kernels by linearly interpolating their positions.

Step 6: Archive.

At the end of the second pass, the program archives all results in a subdirectory.

PUBLISHED PAPERS

In this Appendix, I enclose my publications.

The first part of my PhD thesis, discussed in Chapters 4 and 5, is published in two articles, of which I am the leading author:

1. **Amodeo, S.**, Mei, S., Stanford, S. A., Bartlett, J. G., Melin, J. B., Lawrence, C. R., Chary, R. R., Shim, H., Marleau, F. R., Stern, D. (2017), “*Calibrating the Planck Cluster Mass Scale with Cluster Velocity Dispersions*”, ApJ, 844, 101
2. **Amodeo, S.**, Mei, S., Stanford, S. A., Lawrence, C. R., Bartlett, J. G., Stern, D., Chary, R. R., Shim, H., Marleau, F. R., Melin, J. B., Rodríguez-González, C. (2018), “*Spectroscopic confirmation and velocity dispersions for twenty Planck galaxy clusters at $0.16 < z < 0.78$* ”, ApJ, 853, 36

My complementary work, described in Chapter 8, is published in the following three articles - in one I am the leading author:

3. **Amodeo, S.**, Ettori, S., Capasso, R., Sereno, M. (2016), “*The relation between mass and concentration in X-ray galaxy clusters at high redshift*”, A&A, 590, A126
4. Ghirardini, V., Ettori, S., **Amodeo, S.**, Capasso, R., Sereno, M. (2017), “*On the evolution of the entropy and pressure profiles in X-ray luminous galaxy clusters at $z > 0.4$* ”, A&A, 604, A100
5. Corasaniti, P. S., Ettori, S., Rasera, Y., Sereno, M., **Amodeo, S.**, Breton, M.-A., Ghirardini, V., Eckert, D. (2017), “*Probing cosmology with dark matter halo sparsity using X-ray cluster mass measurements*”, ApJ, 862, 40

My results on the analysis of the CARLA cluster galaxy population are planned to be published in other two papers in preparation. I will be the first author of the paper describing the photometric catalog, the analysis of the galaxy stellar populations using their colors, and the evolution of the passive galaxy fraction. I will be the second author of a paper on the morphology and structural properties of the galaxies hosted by the confirmed CARLA clusters.



Calibrating the *Planck* Cluster Mass Scale with Cluster Velocity Dispersions

Stefania Amodeo¹, Simona Mei^{1,2,3,4,5}, Spencer A. Stanford^{6,7}, James G. Bartlett^{3,8}, Jean-Baptiste Melin⁹, Charles R. Lawrence³, Ranga-Ram Chary⁵, Hyunjin Shim^{10,5}, Francine Marleau^{11,5}, and Daniel Stern³

¹ LERMA, Observatoire de Paris, PSL Research University, CNRS, Sorbonne Universités, UPMC Univ. Paris 06, F-75014 Paris, France

² Université Paris Denis Diderot, Université Paris Sorbonne Cité, F-75205 Paris Cedex 13, France

³ Jet Propulsion Laboratory, California Institute of Technology, 4800 Oak Grove Drive, Pasadena, CA, USA

⁴ Cahill Center for Astronomy & Astrophysics, California Institute of Technology, Pasadena, CA 91125, USA

⁵ Infrared Processing and Analysis Center, California Institute of Technology, Pasadena, CA 91125, USA

⁶ Department of Physics, University of California Davis, One Shields Avenue, Davis, CA 95616, USA

⁷ Institute of Geophysics and Planetary Physics, Lawrence Livermore National Laboratory, Livermore, CA 94550, USA

⁸ APC, AstroParticule et Cosmologie, Université Paris Diderot, CNRS/IN2P3, CEA/Irfu, Observatoire de Paris, Sorbonne Paris Cité, 10 rue Alice Domon et Léonie Duquet, F-75205, Paris Cedex 13, France

⁹ DRF/Irfu/SPP, CEA-Saclay, F-91191, Gif-sur-Yvette Cedex, France

¹⁰ Department of Earth Science Education, Kyungpook National University, Korea

¹¹ Institute of Astro and Particle Physics, University of Innsbruck, A-6020, Innsbruck, Austria

Received 2016 October 18; revised 2017 April 20; accepted 2017 April 27; published 2017 July 27

Abstract

We measure the *Planck* cluster mass bias using dynamical mass measurements based on velocity dispersions of a subsample of 17 *Planck*-detected clusters. The velocity dispersions were calculated using redshifts determined from spectra that were obtained at the Gemini observatory with the GMOS multi-object spectrograph. We correct our estimates for effects due to finite aperture, Eddington bias, and correlated scatter between velocity dispersion and the *Planck* mass proxy. The result for the mass bias parameter, $(1 - b)$, depends on the value of the galaxy velocity bias, b_v , adopted from simulations: $(1 - b) = (0.51 \pm 0.09)b_v^3$. Using a velocity bias of $b_v = 1.08$ from Munari et al., we obtain $(1 - b) = 0.64 \pm 0.11$, i.e., an error of 17% on the mass bias measurement with 17 clusters. This mass bias value is consistent with most previous weak-lensing determinations. It lies within 1σ of the value that is needed to reconcile the *Planck* cluster counts with the *Planck* primary cosmic microwave background constraints. We emphasize that uncertainty in the velocity bias severely hampers the precision of the measurements of the mass bias using velocity dispersions. On the other hand, when we fix the *Planck* mass bias using the constraints from Penna-Lima et al., based on weak-lensing measurements, we obtain a positive velocity bias of $b_v \gtrsim 0.9$ at 3σ .

Key words: cosmic background radiation – cosmology: observations – galaxies: clusters: general – galaxies: distances and redshifts

1. Introduction

Galaxy clusters are fundamental tools for tracing the evolution of cosmic structures and constraining cosmological parameters. Their number density at a given epoch is strongly dependent on the amplitude of density fluctuations, σ_8 (the standard deviation within a comoving sphere of radius $8 h^{-1}$ Mpc), and the matter density of the Universe, Ω_m (see, e.g., the review by Allen et al. 2011). The mass of galaxy clusters is a key quantity in their use as cosmological probes. Unfortunately, mass is not directly observable, but it can be estimated through several independent methods based on different physical properties that are each affected by their own set of specific systematic effects. Methods are based on the analysis of the thermal emission of the intracluster medium (ICM), observed either in the X-rays or through the Sunyaev–Zeldovich (SZ) effect (Sunyaev & Zeldovich 1970), the dynamics of member galaxies, and gravitational lensing. Comparison of mass estimates using different techniques is a critical check on the reliability of each method under different conditions, and also a test of the cosmological scenario.

The SZ effect originates from the transfer of energy from the heated electrons in the ICM to the photons of the cosmic microwave background (CMB) via inverse Compton scattering (see the review by Carlstrom et al. 2002). This scattering generates a distortion of the blackbody spectrum of the CMB, which appears as a decrease in intensity at frequencies below

218 GHz and as an increase in intensity at higher frequencies. The amplitude of this effect is quantified by the Compton parameter integrated along the line of sight, $y \propto T_e n_e$, where T_e and n_e are the electron temperature and density, respectively; or equivalently, is quantified by its solid-angle integral, $Y = \int y d\Omega$. Unlike optical or X-ray emission, the surface brightness of the SZ effect (relative to the mean CMB brightness) is independent of distance. Dedicated SZ cluster surveys can therefore efficiently find clusters out to high redshifts. Moreover, since the SZ signal is proportional to the thermal energy of the ICM, it can be used to estimate total cluster mass, and numerical simulations (e.g., Kravtsov et al. 2006) show that the integrated Compton signal, Y , tightly correlates with the mass.

Recent millimeter-wave surveys are providing large samples of SZ-detected clusters and applying them in cosmological analysis: the South Pole Telescope (SPT; Bleem et al. 2015; de Haan et al. 2016), the Atacama Cosmology Telescope (ACT; Marriage et al. 2011; Hasselfield et al. 2013), and the *Planck* satellite (Planck Collaboration et al. 2015). *Planck* produced two all-sky SZ cluster catalogs, the PSZ1 with 1227 detections based on 15.5 months of data, and the PSZ2 with 1653 detections from the full mission data set of 29 months (Planck Collaboration et al. 2014b, 2016b). Using subsamples of confirmed clusters at higher detection significance, *Planck* constrained cosmological parameters from the cluster counts (Planck Collaboration et al. 2014a, 2016a), noting tension with

the values of σ_8 and Ω_m favored by the primary CMB anisotropies.

The largest source of uncertainty in cosmological inference from the cluster counts is the SZ-signal-halo mass relation. Higher angular resolution SZ observations show that the *Planck* determination of the SZ signal is robust (Rodríguez-González et al. 2017; Sayers et al. 2016). *Planck* calibrates the relation with mass proxies from *XMM-Newton* X-ray observations (Arnaud et al. 2010); the proxies are in turn calibrated, assuming the hydrostatic equilibrium of the ICM (see the Appendix of Planck Collaboration et al. 2014a). This assumption, however, neglects possible contributions from bulk motions and non-thermal sources to the pressure support of the ICM. Analyses of mock data from simulations indicate that these can cause a 10%–25% underestimate of cluster total mass (e.g., Nagai et al. 2007; Piffaretti & Valdarnini 2008; Meneghetti et al. 2010). Other effects, such as instrument calibration or temperature inhomogeneities in the gas (Rasia et al. 2006, 2014), can additionally bias hydrostatic mass measurements. It is common to lump all possible astrophysical and observational biases into the mass bias parameter, $(1 - b)$, defined in Section 3. Simulations and comparison of different X-ray analyses indicate the range, $b = 0\% - 40\%$, with a baseline value of 20% (Mazzotta et al. 2004; Nagai et al. 2007; Piffaretti & Valdarnini 2008; Lau et al. 2009; Kay et al. 2012; Rasia et al. 2012; Rozo et al. 2014a, 2014b, 2014c). To reconcile the *Planck* cluster constraints with those of the primary CMB, a mass bias of $(1 - b) = 0.58 \pm 0.04$ is required (Planck Collaboration et al. 2016a). The comparison of *Planck* and CARMA-8 measurements by Rodríguez-González et al. (2017) shows that this tension is not due to any bias in the *Planck* flux measurements. Moreover, a recent analysis of the local X-ray cluster temperature function finds that the same mass bias value is needed to reconcile the X-ray cluster abundance with the CMB cosmology (Ilic et al. 2015).

Weak gravitational lensing (WL) provides an alternate method of measuring cluster mass (e.g., Hoekstra & Jain 2008). The bending of light by the cluster gravitational field distorts the images of background galaxies, elongating them tangentially around the cluster. Statistical analysis of such distortions gives a direct estimate of the density profile of the cluster and its total mass. Gravitational lensing is particularly efficient in estimating cluster mass because it is sensitive to the total mass, independently of cluster composition or dynamical state. However, since WL measures the projected mass, cluster triaxiality and the presence of substructures along the line of sight introduce significant noise; nevertheless, the noise can be reduced by stacking the WL signal from a large number of clusters to yield an unbiased estimate of the sample mass (Sheldon et al. 2004; Johnston et al. 2007; Corless & King 2009; Meneghetti et al. 2010; Becker & Kravtsov 2011).

Several recent WL calibrations of the *Planck* cluster scale have found results in the range of $0 < b < 30\%$, at the 10% precision level (von der Linden et al. 2014; Hoekstra et al. 2015; Simet et al. 2017a; Smith et al. 2016). Melin & Bartlett (2015) propose a new technique to measure cluster masses through lensing of CMB temperature anisotropies. First detections of this effect have been reported by Planck Collaboration et al. (2016b), Baxter et al. (2015) for SPT, and Madhavacheril et al. (2015) for ACT, which holds great promise for the future. Battaglia et al. (2016) have pointed out the potential impact of the Eddington bias—the steep mass function scattering the meaning is: the scatter is larger for low-mass objects more low-mass than high-mass objects into an SZ-signal bin—on these mass calibrations. Using a complete

Bayesian analysis to account for this and other effects, Penna-Lima et al. (2016) obtained a value of $b \sim 25\%$, which is consistent with previous measurements. This illustrates the importance of the cluster mass measurements and the need for independent determinations, as well as the need for increasing precision.

An additional, widely used method to constrain cluster mass takes the velocity dispersion of member galaxies as a measure of the gravitational potential of the dark-matter halo, which is assumed to be in virial equilibrium. The scaling relation between velocity dispersion and mass has been well established by cosmological N -body and hydrodynamical simulations (e.g., Evrard et al. 2008; Munari et al. 2013), which confirm the trend of $\sigma \propto M^{1/3}$ expected from the virial relation for a broad range of masses, redshift, and cosmological models. Cluster member galaxies may not, however, share the same velocity dispersion as the bulk of the dark matter, as they are hosted by subhalos whose dynamical states may differ. This introduces the concept of the velocity bias (e.g., Carlberg 1994; Colín et al. 2000) that mass estimates must be able to account for. Recently, Sifón et al. (2016) presented dynamical mass estimates based on galaxy velocity dispersions for a sample of 44 clusters observed with ACT. Their sample spans a redshift range of $0.24 < z < 1.06$, with an average of 55 spectroscopic members per cluster. Comparing dynamical and SZ mass estimates, they find a mass bias of $(1 - b) = 1.10 \pm 0.13$ (i.e., $b = -10\%$).

In the present work, we study the relation between velocity dispersion and the SZ *Planck* mass for a sample of 17 *Planck* clusters observed at the Gemini Observatory to estimate the mass bias parameter. All but one cluster are in the PSZ2. In Section 2 we describe the observations and the sample, and then present our results in Section 3. We discuss the resulting mass bias measurement and compare our results to previous measurements in Section 4; we also turn the analysis around to constrain the velocity bias by adopting a constraint on the mass bias from WL observations. Section 5 concludes. Throughout, we adopt the *Planck* base Λ CDM model (Planck Collaboration et al. 2016b): a flat universe with $\Omega_m = 0.307$ and $H_0 = 67.74 \text{ km s}^{-1} \text{ Mpc}^{-1}$ ($h \equiv H_0 / (100 \text{ km s}^{-1} \text{ Mpc}^{-1})$). Mass measurements are quoted at a radius of R_Δ , within which the cluster density is Δ times the critical density of the universe at the cluster’s redshift, where $\Delta = \{200, 500\}$. All quoted uncertainties are at a 68.3% (1σ) confidence level, unless otherwise stated.

2. The Data Set

2.1. Gemini/GMOS Spectroscopy

The goal of our program was to obtain an independent statistical calibration of the *Planck* SZ mass estimator. We chose *Planck* SZ-selected clusters that were detected with a signal-to-noise of 4.5σ or larger, distributed in the north and in the south, with a broad range in mass. We obtained pre-imaging and optical spectroscopy with GMOS-N and GMOS-S at the Gemini-North and Gemini-South Telescopes (Programs GN-2011A-Q-119, GN-2011B-Q-41, and GS-2012A-Q-77; P.I. J.G. Bartlett), respectively, of 19 galaxy clusters, spanning a range of $2 \times 10^{14} M_\odot \lesssim M_{500,\text{SZ}} \lesssim 10^{15} M_\odot$ in *Planck* SZ masses (a more detailed discussion of these observations will follow in a companion paper). We were able to obtain velocity dispersion measurements for 17 clusters, which constitute our sample in this paper. All but one (PLCK G183.33-36.69) are in the PSZ2 catalog.

The northern sample was selected in the SDSS (Sloan Digital Sky Survey (SDSS); York et al. 2000) area. We used the SDSS

Table 1
The Cluster Sample Used in This Paper

Name	R.A. (deg)	Decl. (deg)	Im. Filter	t_{exp} (s)	N_{mask}	Run
PSZ2 G033.83–46.57	326.3015	–18.7159	<i>g, i</i>	1800	2	GS-2012A-Q-77
PSZ2 G053.44–36.25	323.8006	–1.0493	<i>r</i>	1800	1	GN-2011A-Q-119,GN-2011B-Q-41
PSZ2 G056.93–55.08	340.8359	–9.5890	<i>r</i>	1800	2	GN-2011A-Q-119,GN-2011B-Q-41
PSZ2 G081.00–50.93	347.9013	3.6439	<i>r</i>	1800		GN-2011A-Q-119,GN-2011B-Q-41
PSZ2 G083.29–31.03	337.1406	20.6211	<i>r</i>	1800		GN-2011A-Q-119,GN-2011B-Q-41
PSZ2 G108.71–47.75	3.0715	14.0191	<i>r</i>	1800	2	GN-2011A-Q-119,GN-2011B-Q-41
PSZ2 G139.62+24.18	95.4529	74.7014	<i>r</i>	900	2	GN-2011A-Q-119,GN-2011B-Q-41
			<i>g, i, r, J, K</i>			Palomar Hale Telescope
PSZ2 G157.43+30.34	117.2243	59.6974	<i>r</i>	3600	2	GN-2011A-Q-119,GN-2011B-Q-41
			<i>g, i, r, J, K</i>			Palomar Hale Telescope
PLCK G183.33–36.69	57.2461	4.5872	<i>r</i>	1800	2	GN-2011A-Q-119,GN-2011B-Q-41
			<i>g, J, K</i>			Palomar Hale Telescope
PSZ2 G186.99+38.65	132.5314	36.0717	<i>r</i>	1800	2	GN-2011A-Q-119,GN-2011B-Q-41
PSZ2 G216.62+47.00	147.4658	17.1196	<i>r</i>	1800	2	GN-2011A-Q-119,GN-2011B-Q-41
PSZ2 G235.56+23.29	134.0251	–7.7207	<i>g, i</i>	900	2	GS-2012A-Q-77
PSZ2 G250.04+24.14	143.0626	–17.6481	<i>g, i</i>	1800		GS-2012A-Q-77
PSZ2 G251.13–78.15	24.0779	–34.0014	<i>g, i</i>	900	2	GS-2012A-Q-77
PSZ2 G272.85+48.79	173.2938	–9.4812	<i>g, i</i>	900	2	GS-2012A-Q-77
PSZ2 G329.48–22.67	278.2527	–65.5555	<i>g, i</i>	900	2	GS-2012A-Q-77
PSZ2 G348.43–25.50	291.2293	–49.4483	<i>g, i</i>	900	2	GS-2012A-Q-77

Note. We list the PSZ2 cluster ID, when available. When it is not available, we use the prefix “PLCK” followed by a notation in galactic coordinates similar to that used in the PSZ2 paper.

public releases and GMOS-N pre-imaging in the *r*-band for 150 s to detect red galaxy overdensities at the *Planck* detection, and, when unknown, estimate the approximate redshift using their red sequence. For PSZ2 G139.62+24.18 and PSZ2 G157.43+30.34, we used imaging obtained with the Palomar telescope (PI: C. Lawrence). For the Southern sample, we obtained GMOS-S imaging in the *g*- and *i*-bands for 200 s and 90 s, respectively. Red galaxy overdensities and cluster members were selected by their colors using Bruzual & Charlot (2003) stellar population models and Mei et al. (2009) empirical red sequence measurements. In Table 1, we list our sample properties and the spectroscopy observing times.

The GMOS spectra were reduced using the tasks in the IRAF Gemini GMOS package and standard longslit techniques. After co-adding the reduced exposures, one-dimensional spectra for the objects in each slitlet were extracted and inspected visually to identify optical features such as the 4000 Å break, G-band, Ca H+K absorption lines, and, rarely, [O II]λ3727. More precise redshifts were determined by running the IRAF xcsao task on these spectra. We calculate the cluster velocity dispersions using the ROSTAT software (Beers et al. 1990) with both the Gaussian and biweight methods, which are appropriate for our clusters where there are typically 10–20 confirmed members. We retain cluster members galaxies within 3σ of the average cluster redshift. From the original sample of 19 clusters, we have excluded 2, which have complex non-Gaussian velocity distribution profiles. In a companion paper (S. Amodeo et al. 2017, in preparation), we show the velocity histograms of all observed clusters and publish catalogs of spectroscopic redshift measurements.

An important assumption that we make for this analysis is that our cluster sample is a representative, random subsample of the *Planck* SZ-selected catalog. In this case there are no corrections for selection effects, such as Malmquist bias, because we determine the mean scaling for the velocity dispersion given the SZ mass proxy.

2.2. Planck Mass Proxy

The *Planck* SZ mass proxy is based on a combination of *Planck* data and an X-ray scaling relation established with *XMM-Newton*. It has been used in the last two *Planck* cluster catalog papers (Planck Collaboration et al. 2014b, 2016b). Here we give a brief summary and refer the reader to section 7.2.2 of Planck Collaboration et al. (2014b) for more details.

With respect to the PSZ2, in this paper we derive new cluster mass estimates, taking into account the cluster centers from our Gemini/Palomar optical follow-up. For each cluster, we measure the SZ flux, Y_{500} , inside a sphere of radius of R_{500} using the Multifrequency Matched Filter (MMF3, Melin et al. 2006). The filter combines the six highest frequency bands (100–857 GHz) weighted to optimally extract a signal with the known SZ spectral shape and with an assumed spatial profile. For the latter, we adopt the so-called universal pressure profile from Arnaud et al. (2010). We center the filter on the optical position and vary its angular extent, θ_{500} , over the range of [0.9–35] arcmin to map out the signal-to-noise surface over the flux-size (Y_{500} – θ_{500}) plane. In the *Planck* data there is a degeneracy between the measured flux and cluster size defined by this procedure, which we break using an X-ray determined scaling relation as a prior constraint (i.e., an independent Y – θ relation obtained from the combination of Equations (7) and (9) of Planck Collaboration et al. 2014a). The intersection of the former with that of the *Planck* degeneracy contours yields a tighter constraint on the flux Y_{500} , which we then convert to halo mass, M_{500}^{Pl} , using Equation (7) of Planck Collaboration et al. (2014a). It is important to note that the mass proxy is therefore calibrated on the *XMM-Newton* scaling relation. These masses are reported in Table 2. In order to compare our mass measurements to those of the other independent estimates, we rescale the *Planck* masses to M_{200}^{Pl} using the mass–concentration relation of Dutton & Macciò (2014). The

Table 2
Redshifts, Velocity Dispersions, and SZ Masses

Name	z	N_{gal}	R_{max} (R_{200})	R_{200} (Mpc)	$\sigma_{1D}(<R_{\text{max}})$ (km s^{-1})	σ_{200} (km s^{-1})	M_{200}^{Pl} ($10^{14} M_{\odot}$)	M_{500}^{Pl} ($10^{14} M_{\odot}$)
PSZ2 G033.83–46.57	0.439	10	0.58	1.66 ± 0.08	985^{+451}_{-277}	953^{+454}_{-282}	7.8 ± 1.1	$5.4^{+0.7}_{-0.8}$
PSZ2 G053.44–36.25	0.331	20	0.42	1.93 ± 0.06	1011^{+242}_{-131}	956^{+260}_{-161}	10.9 ± 1.0	$7.5^{+0.5}_{-0.6}$
PSZ2 G056.93–55.08	0.443	46	0.49	2.00 ± 0.05	1356^{+192}_{-127}	1290^{+218}_{-164}	13.8 ± 1.1	9.4 ± 0.5
PSZ2 G081.00–50.93	0.303	15	0.41	1.88 ± 0.06	1292^{+360}_{-185}	1220^{+381}_{-223}	9.8 ± 0.9	6.7 ± 0.5
PSZ2 G083.29–31.03	0.412	20	0.49	1.89 ± 0.06	1434^{+574}_{-320}	1365^{+584}_{-338}	11.3 ± 1.0	$7.8^{+0.5}_{-0.6}$
PSZ2 G108.71–47.75	0.390	10	0.55	1.65 ± 0.08	900^{+458}_{-190}	865^{+461}_{-198}	7.3 ± 1.1	$5.1^{+0.7}_{-0.8}$
PSZ2 G139.62+24.18	0.268	20	0.36	1.96 ± 0.06	1120^{+366}_{-238}	1052^{+390}_{-273}	10.6 ± 0.9	7.3 ± 0.5
PSZ2 G157.43+30.34	0.402	28	0.47	1.94 ± 0.05	1244^{+192}_{-109}	1182^{+216}_{-148}	12.1 ± 1.0	8.2 ± 0.6
CL G183.33–36.69	0.163	11	0.35	1.38 ± 0.17	897^{+437}_{-275}	842^{+451}_{-297}	3.3 ± 1.2	$2.3^{+0.7}_{-0.9}$
PSZ2 G186.99+38.65	0.377	41	0.49	1.81 ± 0.06	1506^{+164}_{-120}	1432^{+200}_{-166}	9.5 ± 1.0	$6.6^{+0.6}_{-0.7}$
PSZ2 G216.62+47.00	0.385	37	0.45	1.97 ± 0.05	1546^{+174}_{-132}	1466^{+218}_{-186}	12.3 ± 1.0	$8.4^{+0.5}_{-0.6}$
PSZ2 G235.56+23.29	0.374	23	0.51	1.73 ± 0.08	1644^{+285}_{-192}	1568^{+308}_{-224}	8.2 ± 1.2	$5.7^{+0.7}_{-0.8}$
PSZ2 G250.04+24.14	0.411	29	0.53	1.75 ± 0.07	1065^{+447}_{-285}	1020^{+452}_{-293}	8.9 ± 1.0	6.2 ± 0.6
PSZ2 G251.13–78.15	0.304	9	0.48	1.59 ± 0.08	801^{+852}_{-493}	762^{+854}_{-497}	5.9 ± 0.9	4.1 ± 0.6
PSZ2 G272.85+48.79	0.420	10	0.57	1.65 ± 0.08	1462^{+389}_{-216}	1411^{+397}_{-231}	7.6 ± 1.1	$5.3^{+0.7}_{-0.8}$
PSZ2 G329.48–22.67	0.249	11	0.38	1.73 ± 0.07	835^{+179}_{-119}	786^{+200}_{-149}	7.2 ± 0.9	$5.0^{+0.5}_{-0.6}$
PSZ2 G348.43–25.50	0.265	20	0.37	1.84 ± 0.06	1065^{+411}_{-198}	1003^{+427}_{-230}	8.7 ± 0.9	6.0 ± 0.6

Note. From left to right the columns list the Cluster ID, our measured average redshift, the number of confirmed member galaxies, the maximum radius probed by GMOS, R_{max} , R_{200} , our measured velocity dispersion, $\sigma(<R_{\text{max}})$, the velocity dispersion estimated within R_{200} , σ_{200} , the reference PSZ2 M_{500}^{Pl} , and the M_{200}^{Pl} derived in this work based on SZ.

Table 3

Best-fit Values and Vertical Scatter (i.e., at Given Mass) of the Velocity Dispersion–Mass Relation, $\sigma = A[E(z)M/10^{15} M_{\odot}]^B$, Together with Mass Bias Estimates

Relation	A (km s^{-1})	B	Scatter ($\delta_{\ln \sigma}^2$) ^{1/2}	$(1-b)/b_{\nu}^3 f_{\text{EB}} f_{\text{corr}}$	$(1-b)_{\text{Munari}}^a$
<i>All clusters</i>					
$\sigma_{1D}(<R_{\text{max}})-M_{200}^{\text{Pl}}$	1239 ± 99	0.29 ± 0.21	0.189 ± 0.018
$\sigma_{1D}(<R_{\text{max}})-M_{200}^{\text{Pl}}$	1226 ± 68	1/3	0.182 ± 0.012	0.47 ± 0.08	0.55 ± 0.09
$\sigma_{200}-M_{200}^{\text{Pl}}$	1172 ± 93	0.28 ± 0.20	0.198 ± 0.018
$\sigma_{200}-M_{200}^{\text{Pl}}$	1158 ± 61	1/3	0.189 ± 0.009	0.55 ± 0.09	0.64 ± 0.11
<i>Only clusters with $N_{\text{gal}} \geq 20$</i>					
$\sigma_{1D}(<R_{\text{max}})-M_{200}^{\text{Pl}}$	1250 ± 71	1/3	0.168 ± 0.014	0.44 ± 0.08	0.51 ± 0.09
$\sigma_{200}-M_{200}^{\text{Pl}}$	1156 ± 58	1/3	0.136 ± 0.012	0.56 ± 0.08	0.66 ± 0.09

Notes. Results are given for our velocity dispersion estimates, $\sigma_{1D}(<R_{\text{max}})$, and for the derived velocity dispersions within R_{200} , σ_{200} . We distinguish the case where all clusters in the sample are included in the fit from the case where only those with at least 20 member galaxies are considered.

^a The values of the mass bias quoted in the last column are obtained using the velocity bias, b_{ν} , derived by Munari et al. (2013), following the notation of Equation (5), where the Eddington bias correction is also included.

rescaling procedure is described in Appendix A and the resulting values of M_{200}^{Pl} are listed in Table 2.

2.3. Correcting Velocity Dispersions for GMOS Finite Aperture

The GMOS spectrographs provide imaging and spectroscopy over a 5.5×5.5 arcmin² field of view, allowing measurements for only the central part of clusters. The radial coverage provided for each cluster at a given redshift, calculated for the *Planck* 2015 cosmology, is quoted in Table 2 as R_{max} in units of R_{200} , along with R_{200} . We typically sample out to about half R_{200} , with R_{max} ranging over $[0.35-0.58]R_{200}$. However, we need to estimate the velocity dispersion within

R_{200} , $\sigma_{200} \equiv \sigma(<R_{200})$ to compare to the σ – M relation from the simulations (see the next section). Sifón et al. (2016) determine the radial profile of the velocity dispersion using mock observations of subhalos in the Multidark simulation (Prada et al. 2012), as described in Section 3.2 of their paper. We interpolate the correction factors presented in their Table 3 to our values of R_{max}/R_{200} to translate our velocity dispersion measurements, $\sigma_{1D}(<R_{\text{max}})$, to σ_{200} . Thus, the estimated velocity dispersions are listed in Table 2, where the uncertainties account for our measurement errors and the scatter in the velocity dispersion profile found by Sifón et al. (2016). The mean corrections are of the order of 5%, while the uncertainty increases up to 32%. Figure 1 plots the velocity dispersions σ_{200} versus M_{200}^{Pl} .

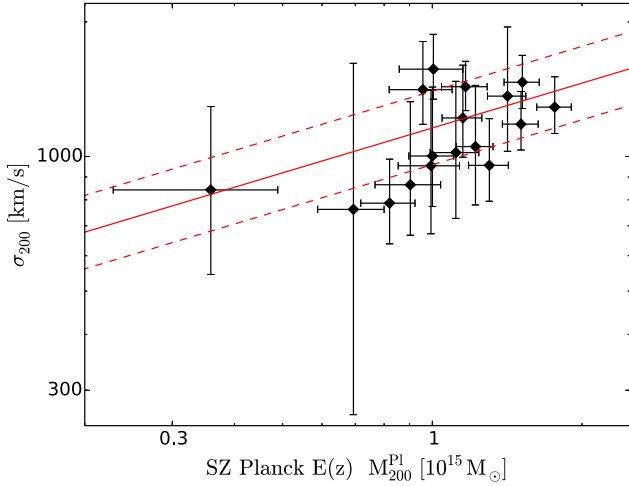


Figure 1. Relation between the *Planck* SZ mass proxy and velocity dispersion for our sample of 17 galaxy clusters observed with Gemini (diamonds). The velocity dispersions and the *Planck* masses have been converted to σ_{200} and M_{200}^{Pl} , respectively, with corresponding uncertainties following the procedure described in the text. The solid red line shows the best fit to the functional form of Equation (2) in log-space, where the slope is set to $1/3$, with the dashed lines delineating the dispersion of the data about the best-fit line.

3. Analysis: The Mass Bias

3.1. The Mass Bias and the Velocity Bias

Our goal is to find the *Planck* cluster mass scale using velocity dispersion as an independent mass proxy calibrated on numerical simulations. We define the mass bias factor, $(1 - b)$, in terms of the ratio between the *Planck*-determined mass, M_{200}^{Pl} , and true cluster mass, M_{200} (von der Linden et al. 2014; Hoekstra et al. 2015; Planck Collaboration et al. 2016b). We assume that mass bias factor is a constant and independent of overdensity. In fact, while the mass bias may depend on the mass and other cluster properties, our small sample only permits us to constrain a characteristic value averaged over the sample. For M_{200} , the mass bias is defined as

$$M_{200}^{\text{Pl}} = (1 - b)M_{200}. \quad (1)$$

Complete virialization predicts a power-law relation between velocity dispersion, σ_{200} , and mass, M_{200} . Following the approach used in the simulations, we work with the logarithm of these quantities, $s_v = \ln(\sigma_{200}/\text{km s}^{-1})$, $\mu = \ln(E(z)M_{200}/10^{15} M_{\odot})$, where $h(z) \equiv H(z)/(100 \text{ km s}^{-1} \text{ Mpc}^{-1}) = hE(z)$ is the dimensionless Hubble parameter at redshift z , and we consider the log-linear relation of

$$\langle s_v | \mu \rangle = a_d + \alpha_d \mu. \quad (2)$$

The so-called self-similar slope that is expected from purely gravitational effects is $\alpha_d = 1/3$. The angle brackets indicate that this is the mean value of s_v , given μ . From a suite of simulations, Evrard et al. (2008) determined a precise relation between the dark-matter velocity dispersion and the halo mass that was consistent with this expectation. They find a normalization of $a_d = \ln(1082.9 \pm 4.0) + \alpha_d \ln h$; in the following, we will also refer to $A_d \equiv e^{a_d}$. The result is insensitive to cosmology and to nonradiative baryonic effects, and the relation is very tight, with only 4% scatter at fixed mass.

Galaxies, however, may have a different velocity dispersion than their dark-matter hosts because they inhabit special locations

within the cluster, e.g., subhalos. This leads to the concept of velocity bias, in which the scaling of galaxy velocity dispersion with host halo mass will, in general, be fit by a relation of the form of Equation (2), but with different parameters, $A_g \equiv e^{a_g}$ and α_g . Simulations typically find the exponent α_g to be consistent with the self-similar value of $1/3$, so we can quantify any velocity bias in terms of the normalization, A_g . We do so by introducing the velocity bias parameter of $b_v \equiv A_g/A_d$.

Different simulation-based or empirical analyses find discordant behavior for the velocity bias, leaving the sense of the effect (i.e., $b_v > 1$ or $b_v < 1$) up for debate.

Using hydrodynamical simulations with star formation, gas cooling and heating by supernova explosions, and AGN feedback, Munari et al. (2013) found that subhalos and galaxies have a slightly higher velocity dispersion than that of the dark matter, i.e., a positive velocity bias with $b_v > 1$. For galaxies in their AGN-feedback model, for example, they find $A_g = 1177$, corresponding to $b_v = 1.08$.

From combined N -body and hydrodynamical simulations, Wu et al. (2013) found that velocity bias depends on the tracer population, in particular, that subhalos in pure N -body simulations tend to have large positive bias compared to galaxies identified in the hydrodynamical simulations, perhaps because over-merging in the former case removes slower, low-mass dark-matter halos from the tracer population. Consistent with this notion where smaller objects are more efficiently destroyed, all tracers in their simulations show increasingly positive velocity bias with decreasing subhalo mass or galaxy luminosity, independent of redshift. The brightest cluster galaxies tend to underestimate the dark-matter halo velocity dispersion, while faint galaxies slightly overestimate the dark-matter halo velocity dispersion, with the velocity bias ranging from ~ 0.9 for the five brightest cluster galaxies to an asymptotic value of $b_v = 1.07$ when including the 100 brightest galaxies (see Figure 1 in their paper). For samples of more than ~ 50 galaxies, their result converges to the value of Munari et al. (2013; $b_v = 1.08$). The 10–20 brightest galaxies, similar to our observational sample, represent a nearly unbiased measurement of the halo velocity dispersion, i.e., $b_v = 1$.

On the other hand, Guo et al. (2015) observe the opposite trend with luminosity when measuring the velocity bias of galaxies in the SDSS Data Release 7 (see their Figure 9). They find $b_v \simeq 1.1$ for the brightest galaxies, falling to 0.85 for faint galaxies. It is worth noting that this analysis is based on modeling of the projected and redshift-space two-point correlation functions, and it is probably not very sensitive to velocity bias in the most massive halos, such as those in the *Planck* sample. Farahi et al. (2016) use the velocity bias from the bright subsample of Guo et al. (2015) ($b_v = 1.05 \pm 0.08$) to estimate the mass of redMaPPer clusters with stacked galaxy velocity dispersions. Their derived mass scale is consistent with the estimates based on weak-lensing observations reported by Simet et al. (2017b). The Guo et al. (2015) observational result is also consistent with the value $b_v = 1.08$ from the N -body hydrodynamical simulations of Munari et al. (2013). In another study, Caldwell et al. (2016) find a negative velocity bias, $b_v = 0.896$, for galaxies in their simulations when they adjust feedback efficiencies to reproduce the present-day stellar mass function and the hot-gas fraction of clusters and groups.

These different studies do not yet present a clear picture of the magnitude of cluster member velocity bias, and this quantity remains the primary factor limiting interpretation of dynamical cluster mass measurements at present. We use the

Munari et al. value of the velocity bias, $b_v = 1.08$, as our baseline in the following. The uncertainty on Munari et al.'s velocity bias is $\sim 0.6\%$.

3.2. Measurement of the Mass Bias

As detailed in Appendix B, our model of constant mass bias, $(1 - b)$, predicts a log-linear scaling relation of the form of Equation (2) between the observed velocity dispersion and the *Planck* mass proxy. We therefore construct an estimator for $(1 - b)$ by fitting for the normalization, a , and exponent, α , of this relation to the data in Figure 1. We perform the fit using the MPFIT routine in IDL (Markwardt 2009; Williams et al. 2010) and taking into account only the uncertainties in the velocity dispersion (i.e., at fixed *Planck* SZ mass¹²).

For a robust estimation of the best-fit parameters, we perform 1000 bootstrap resamplings of the pairs $(M_{200}^{\text{Pl}}, \sigma_{200})$, re-computing the best-fit parameters each time. This yields $A \equiv e^a = (1172 \pm 93)$, and a slope of $\alpha = 0.28 \pm 0.20$ (at 68.3% confidence). The slope is consistent with the self-similar expectation of $\alpha = 1/3$, although with large uncertainty. We henceforth set $\alpha = 1/3$ and refit to find $A = (1158 \pm 61)$. The dispersion of the velocity measurements about the best-fit line (i.e., at given M_{200}^{Pl}) is $(\delta_{\ln \sigma}^2)^{1/2} = 0.189 \pm 0.009$. The best fit together with the data is plotted in Figure 1. A model with a zero slope is excluded at $\sim 2\sigma$ confidence, using the χ^2 difference (the χ^2 for the best-fit model is 12.2, the χ^2 for the zero-slope model is 14.3). We also performed the fit using only clusters with more than 20 member galaxies. Once again fixing $\alpha = 1/3$, we find that $A = (1156 \pm 58)$, in this case, consistent with the previous value.

Our estimator for the mass bias then follows from the formalism of Appendix B (Equation (23)),

$$(1 - b) = \left(\frac{A_g}{A}\right)^3 f_{\text{EB}} f_{\text{corr}} = \left(\frac{A_d}{A}\right)^3 b_v^3 f_{\text{EB}} f_{\text{corr}}, \quad (3)$$

where f_{EB} (Equation (24)) is the Eddington bias correction and f_{corr} (Equation (25)) is a correction for correlated scatter between velocity dispersion and the *Planck* mass proxy. With our value for the normalization fit to the data and the value for dark matter from Evrard et al. (2008), we have numerically,

$$(1 - b) = (0.55 \pm 0.09) b_v^3 f_{\text{EB}} f_{\text{corr}}. \quad (4)$$

In the next two subsections, we propose $f_{\text{EB}} = 0.93 \pm 0.01$ and $f_{\text{corr}} \approx 1.01$ as reference values. Our final value for the mass bias also depends on the cube of the velocity bias. Adopting our baseline of $b_v = 1.08$ from Munari et al. (2013), we have

$$(1 - b) = (0.64 \pm 0.11) \left(\frac{f_{\text{corr}}}{1.01}\right). \quad (5)$$

The quoted uncertainty accounts for measurement error, uncertainty on the Eddington bias correction, and uncertainty on the velocity bias given by Munari et al. (2013); it is dominated by the measurement error. The uncertainty on Munari et al.'s velocity bias ($\sim 0.6\%$) is a negligible contribution to our total error budget. It is more difficult to assign an uncertainty to the correction for correlated scatter, as this depends on the details of cluster physics; we argue below

¹² Taking into account errors on both velocity and mass measurements does not noticeably change the result.

that feedback makes this a minor correction, as reflected in our fiducial value of $f_{\text{corr}} = 1.01$.

A summary of best-fit parameters for several velocity dispersion–mass relations is provided in Table 3. Where the slope is set to 1/3, we quote our estimates of the *Planck* mass bias for the velocity bias derived by Munari et al. (2013), $b_v = 1.08$. We distinguish results for the full sample from results for the subsample of clusters with at least 20 member galaxies.

Our value of $(1 - b) = 0.64 \pm 0.11$ lies within 1σ of the value $(1 - b) = 0.58 \pm 0.04$ needed to reconcile the cluster counts with the primary CMB constraints.

3.3. Eddington Bias

In this section, we detail our Eddington bias correction. The Eddington bias correction (Equation (24)),

$$f_{\text{EB}} = e^{-\beta \Sigma_{\text{spi}}^2}, \quad (6)$$

depends on the local slope of the mass function on cluster scales, $\beta \approx 3$, and the total dispersion, Σ_{spi} , of the *Planck* mass proxy at a fixed true mass. This is because we assume that our sample is a random draw from the parent sample selected on M_{200}^{Pl} . As described in Section 2.2, the mass proxy is calculated as an intersection of *Planck* SZ measurements and the X-ray based scaling relation in Planck Collaboration et al. (2014a). We characterize the measurement uncertainty on M_{200}^{Pl} by averaging the calculated uncertainty over our cluster sample, $\sigma_{\text{spi}} = 0.13 \pm 0.02$. To estimate the intrinsic scatter, we convert the 0.17 ± 0.02 dispersion of the $Y - M^{5/3}$ relation (Planck Collaboration et al. 2014a) to $\tilde{\sigma}_{\text{spi}} = (3/5)(0.17 \pm 0.02) = 0.10 \pm 0.01$. Combining the two, we arrive at a total scatter of

$$\Sigma_{\text{spi}} = 0.16 \pm 0.02. \quad (7)$$

Setting $\beta = 3$, we calculate an Eddington bias correction of

$$\ln f_{\text{EB}} = -0.08(1 \pm 0.19), \quad (8)$$

or a reference value of $f_{\text{EB}} = 0.93(1 \pm 0.01) = 0.93 \pm 0.01$.

Our estimate for the intrinsic scatter in the *Planck* mass from Planck Collaboration et al. (2014a) may be optimistic. If we allow a value 50% larger, we get a correction of $f_{\text{EB}} = 0.84 \pm 0.027$. The resulting mass bias would be $(1 - b) = (0.58 \pm 0.097)(f_{\text{corr}}/1.01)$.

3.4. Correlated Scatter

The second correction to our mass bias estimator arises from correlated scatter between velocity dispersion and the *Planck* mass proxy. It is given by (Equation (25)),

$$f_{\text{corr}} = e^{3\tilde{r}\beta\tilde{\sigma}_{\text{sv}}\tilde{\sigma}_{\text{spi}}}, \quad (9)$$

because only the intrinsic scatter is correlated. Stanek et al. (2010) examined the covariance between different cluster observables using the Millennium Gas Simulations (Hartley et al. 2008). They found significant intrinsic correlation between velocity dispersion and SZ signal, $\tilde{r} = 0.54$, in the simulation with only gravitational heating. In the simulation that additionally included cooling and pre-heating, however, the correlation dropped to $\tilde{r} = 0.079$. This would seem to make sense, as we might expect nongravitational physics, such as feedback and cooling, to decouple the SZ signal, which

measures the total thermal energy of the gas from the collisionless component.

While the scatter of the dark-matter velocity dispersion is only 4%, Munari et al. (2013) find a scatter in the range 0.1–0.15 for their subhalos and galaxies. Fixing $\beta = 3$ and taking $\tilde{r} = 0.08$, $\tilde{\sigma}_{sv} = 0.15$, and $\tilde{\sigma}_{spi} = (3/5)0.17 = 0.10$ as reference values, we have

$$\ln f_{\text{corr}} = 0.010 \left(\frac{\tilde{r}}{0.08} \right) \left(\frac{\tilde{\sigma}_{sv}}{0.15} \right) \left(\frac{\tilde{\sigma}_{spi}}{0.10} \right), \quad (10)$$

or a reference value of $f_{\text{corr}} = 1.01$.

4. Discussion

We have estimated the *Planck* cluster mass bias parameter by measuring the velocity dispersion of 17 SZ-selected clusters observed with Gemini. It is corrected for both Eddington bias and possible correlated scatter between velocity dispersion and the SZ mass proxy. These corrections are based on a multivariate log-normal model for the cluster observables that is detailed in Appendix B. We do not correct individual cluster masses for Eddington bias (e.g., Sifón et al. 2016), but rather apply a global correction to the mean scaling relation between velocity dispersion and *Planck* mass proxy.

Our primary objective in calibrating the mass bias of *Planck* clusters is to inform the cosmological interpretation of the *Planck* cluster counts. Planck Collaboration et al. (2014a) and Planck Collaboration et al. (2016a) found tension between the observed cluster counts and the counts predicted by the base Λ CDM model fit to the primary CMB anisotropies, with the counts preferring lower values of the power spectrum normalization, σ_8 . The importance of the tension, however, depends on the normalization of the SZ signal–mass scaling relation. The *Planck* team uses a relation calibrated on *XMM-Newton* observations of clusters (see the Appendix of Planck Collaboration et al. 2014a), and proposed that the mass bias parameter, b , accounts for possible systematic offsets in this calibration due to astrophysics and (X-ray) instrument calibration. No offset corresponds to $b = 0$, while the value needed to reconcile the observed cluster counts with the base Λ CDM model is $(1 - b) = 0.58 \pm 0.04$ (Planck Collaboration et al. 2016a).

The possible tension between clusters and primary CMB has motivated a number of recent studies of the cluster mass bias in both X-ray and SZ catalogs (e.g., Sifón et al. 2013, 2016; Ruel et al. 2014; Battaglia et al. 2016; Bocquet et al. 2015; Simet et al. 2017a; Smith et al. 2016). For a like-to-like comparison, we focus here on determinations for the *Planck* clusters.

Rines et al. (2016) compare SZ and dynamical mass estimates of 123 clusters from the *Planck* SZ catalog in the redshift range of $0.05 < z < 0.3$. They use optical spectroscopy from the Hectospec Cluster Survey (Rines et al. 2013) and the Cluster Infall Regions in the SDSS project (Rines & Diaferio 2006), observing a velocity dispersion–SZ mass relation that is in good agreement with the virial scaling relation of dark-matter particles. They find neither significant bias of the SZ masses compared to the dynamical masses nor any evidence of large galaxy velocity bias. They conclude that the mass calibration of *Planck* clusters cannot solve the CMB–SZ tension and another explanation, such as massive neutrinos, is required.

von der Linden et al. (2014) examine 22 clusters from the Weighing the Giants (WtG) project that are also used in the

Planck cluster count cosmology analysis. Applying a weak-lensing analysis, they derive considerably larger masses than *Planck*, measuring an average mass ratio of $\langle M_{\text{Planck}}/M_{\text{WtG}} \rangle = 0.688 \pm 0.072$ with decreasing values for larger *Planck* masses. They claim a mass-dependent calibration problem, possibly due to the fact that the X-ray hydrostatic measurements used to calibrate the *Planck* cluster masses rely on a temperature-dependent calibration. A similar result is obtained by Hoekstra et al. (2015) based on a weak-lensing analysis of 50 clusters from the Canadian Cluster Comparison Project (CCCP). For the clusters detected by *Planck*, they find a bias of $0.76 \pm 0.05(\text{stat}) \pm 0.06(\text{syst})$, with the uncertainty in the determination of photometric redshifts being the largest source of systematic error. Planck Collaboration et al. (2016a) used these latter two measurements as priors in their analysis of the SZ cluster counts. They also employed a novel technique based on CMB lensing (Melin & Bartlett 2015) to find $1/(1 - b) = 0.99 \pm 0.19$ when averaged over the full cluster cosmology sample of more than 400 clusters. As later pointed out by Battaglia et al. (2016), these constraints should be corrected for Eddington bias.¹³

Smith et al. (2016) use three sets of independent mass measurements to study the departures from hydrostatic equilibrium in the Local Cluster Substructure Survey (LoCuSS) sample of 50 clusters at $0.15 < z < 0.3$. The mass measurements comprise weak-lensing masses (Ziparo et al. 2016; Okabe & Smith 2016), direct measurements of hydrostatic masses using X-ray observations (Martino et al. 2014), and estimated hydrostatic masses from Planck Collaboration et al. (2016b). They found agreement between the X-ray-based and *Planck*-based tests of hydrostatic equilibrium, with an X-ray bias of 0.95 ± 0.05 and an SZ bias of 0.95 ± 0.04 .

Finally, Penna-Lima et al. (2016) used lensing mass measurements from the Cluster Lensing And Supernova (CLASH, Postman et al. 2012) survey with Hubble to find a *Planck* mass bias of $(1 - b) = 0.73 \pm 0.10$. Employing a Bayesian analysis, they modeled the CLASH selection function and astrophysical effects, such as scatter in lensing and SZ masses and their potential correlated scatter, as well as possible bias in the lensing measurements. Their quoted uncertainty accounts for these effects by marginalizing over the associated nuisance parameters. They also provide a summary of recent mass calibration measurements, including the Eddington bias correction proposed by Battaglia et al. (2016) for the WtG and CCCP determinations. Sereno et al. (2017) found a result similar to Penna-Lima for the *Planck* mass bias, $(1 - b) = 0.76 \pm 0.08$, using weak-lensing masses from the Canada–France–Hawaii Telescope Lensing Survey (CFHTLenS; Heymans et al. 2012) and the Red Cluster Sequence Lensing Survey (RCSLenS; Hildebrandt et al. 2016).

Comparing to the values above, our result is $\sim 30\%$ lower (at $\sim 2.5\sigma$) than both the Smith et al. (2016) lensing determination and the Rines et al. (2016) determination, also based on velocity dispersions; both determinations favor little or no mass bias. However, we agree within 1σ with the results from WtG (von der Linden et al. 2014), the CCCP (Hoekstra et al. 2015),

¹³ There is some confusion in the nature of these corrections. Battaglia et al. (2016) propose a correction for WtG and CCCP that is really more akin to a Malmquist bias, i.e., due to selection effects arising from the fact that some clusters in the WtG and CCCP samples do not have *Planck* mass proxy measurements.

and the CLASH (Postman et al. 2012) analysis by Penna-Lima et al. (2016).

If we use our value of $(1 - b) = (0.58 \pm 0.097)(f_{\text{corr}}/1.01)$, obtained with 50% larger intrinsic scatter on *Planck* masses (see Section 3.3), it would still agree within 2σ with the results from weak lensing cited above. In both cases, our value of the mass bias is within 1σ of the value $(1 - b) = (0.58 \pm 0.04)$ needed to reconcile the cluster counts with the primary CMB.

4.1. Estimating the Velocity Bias b_v Using a Prior on the Mass Bias

Given the large differences in the velocity bias as predicted by simulations, it is worth turning the vice—the strong dependence of our mass calibration on velocity bias—into a virtue. Relying on accurate mass estimates provided by weak-lensing analyses, we derive a constraint on b_v from our measured velocity dispersions. We adopt the *Planck* mass calibration obtained by Penna-Lima et al. (2016), based on the lensing mass measurements from the Cluster Lensing And Supernova survey with Hubble (CLASH). Using a Bayesian analysis of CLASH mass measurements and *Planck* SZ measurements, they marginalize over nuisance parameters describing the cluster scaling relations and the sample selection function to obtain $(1 - b) = 0.73 \pm 0.10$. This is a reasonable prior, since the Penna-Lima et al. (2016) sample is characteristic in mass (and we also assume in mass bias) of *Planck*-detected clusters. Using this as a prior on the mass bias in Equation (4), with our reference value for the Eddington bias given in Section 3.3, we then deduce the constraint to be

$$b_v = 1.12 \pm 0.07 \left(\frac{1.01}{f_{\text{corr}}} \right)^{1/3}. \quad (11)$$

This positive velocity bias agrees with the value from the Munari et al. (2013) simulations and the Guo et al. (2015) result for samples more luminous than $M_r = 20.5$ (L_*). It is reasonably consistent (within 2σ) with the results of Wu et al. (2013) that predict nearly unbiased velocities for the brightest 10–30 galaxies that are appropriate for our sample. Our result is discrepant, at 3σ , with a negative velocity bias of $b_v \lesssim 0.9$, as found, for example, by the Caldwell et al. (2016) simulations.

5. Conclusions

We have examined the *Planck* cluster mass bias using a sample of 17 *Planck* clusters for which we measured velocity dispersions with GMOS at the Gemini observatory. The unknown velocity bias, b_v , of the member galaxy population, is the largest source of uncertainty in our final result, $(1 - b) = (0.51 \pm 0.09)b_v^3$. Using our baseline value for b_v from Munari et al. (2013), we find $(1 - b) = (0.64 \pm 0.11)$, consistent within just over 1σ with WtG, CCCP, and CLASH, and within 1σ of the value $(1 - b) = (0.58 \pm 0.04)$ needed to reconcile the *Planck* cluster counts with the primary CMB.

We conclude that velocity bias is the primary factor limiting interpretation of dynamical cluster mass measurements at this time. It is essential to eliminate this modeling uncertainty if velocity dispersion is to be a robust mass determination method.

Turning the analysis around, observational constraints on the velocity bias can be obtained by combining accurate mass estimates from weak-lensing measurements with velocity

dispersion measurements. Assuming a prior on the mass bias from Penna-Lima et al. (2016), we derive $b_v = 1.12 \pm 0.07$, consistent with our baseline value from Munari et al. (2013; $b_v = 1.08$) and with results from Wu et al. (2013) and Guo et al. (2015), but discrepant at 3σ , with a negative velocity bias of $b_v \lesssim 0.9$, as found by Caldwell et al. (2016).

Apart from modeling uncertainty on the velocity bias, we have achieved a precision of 17% on the mass bias measurement with 17 clusters. Assuming that the simulations will eventually settle on a value for the velocity bias, this motivates continued effort to increase our sample size to produce a 10% or better determination, comparable to recent weak-lensing measurements.

We thank our referee, Gus Evrard, for constructive discussion that helped improve the presentation of this work. We thank Andrea Biviano and Ian McCarthy for useful discussions. Based on observations obtained at the Gemini Observatory (Programs GN-2011A-Q-119, GN-2011B-Q-41, and GS-2012A-Q-77; P.I. J.G. Bartlett), which is operated by the Association of Universities for Research in Astronomy, Inc., under a cooperative agreement with the NSF on behalf of the Gemini partnership: the National Science Foundation (United States), the National Research Council (Canada), CONICYT (Chile), Ministerio de Ciencia, Tecnología e Innovación Productiva (Argentina), and Ministério da Ciência, Tecnologia e Inovação (Brazil). Supported by the Gemini Observatory, which is operated by the Association of Universities for Research in Astronomy, Inc., on behalf of the international Gemini partnership of Argentina, Brazil, Canada, Chile, and the United States of America. This material is based upon work supported by AURA through the National Science Foundation under AURA Cooperative Agreement AST 0132798 as amended. J.G.B. and S.M. acknowledge financial support from the Institut Universitaire de France (IUF) as senior members. The work of J.G.B., C.L., and D.S. was carried out at the Jet Propulsion Laboratory, California Institute of Technology, under a contract with NASA. The research of S.M. was supported by an appointment to the NASA Postdoctoral Program at the Jet Propulsion Laboratory, administered by Universities Space Research Association under contract with NASA.

Facilities: Gemini:South, Gemini:Gillet, Hale, *Planck*.

Appendix A Conversion from M_{500}^{Pl} to M_{200}^{Pl}

To compare our mass measurements to other independent estimates, we rescale the *Planck* masses to M_{200}^{Pl} using the mass–concentration relation of Dutton & Macciò (2014). This relation is derived from N -body simulations of relaxed dark-matter halos in a *Planck* cosmology, as adopted here. It is in good agreement with the recently proposed universal model of Diemer & Kravtsov (2015), which includes both relaxed and unrelaxed halos, for the mass and redshift range of interest.

We assume a Navarro–Frenk–White (NFW, Navarro et al. 1997) density profile, and we choose an input value for the concentration $c_{200} = 5$, which is consistent with the model of Dutton & Macciò (2014) for a $10^{15} h^{-1} M_{\odot}$ cluster in the redshift range of $0 < z < 0.5$. We then convert M_{500}^{Pl} to

$$M_{200}^{\text{Pl}} = M_{500}^{\text{Pl}} \frac{f(c_{200})}{f(c_{500})}, \quad (12)$$

where $f(c_\Delta) = \log(1 + c_\Delta) - \frac{c_\Delta}{1 + c_\Delta}$ indicates a general density contrast. We calculate c_{500} from

$$M_{500}^{\text{Pl}} = 4\pi\rho_s r_s^3 f(c_{500}), \quad (13)$$

where c_{500} is the only unknown quantity, because the scale density parameter, ρ_s , is fixed by the NFW profile,

$$\rho_s = \rho_{c,z} \frac{200}{3} \frac{c_{200}^3}{\ln(1 + c_{200}) - \frac{c_{200}}{1 + c_{200}}}, \quad (14)$$

and the scale radius is

$$r_s = \frac{R_{500}}{c_{500}}, \quad (15)$$

with

$$R_{500} = \left[M_{500}^{\text{Pl}} \frac{3}{4\pi} \frac{1}{500 \rho_{c,z}} \right]^{1/3}. \quad (16)$$

We solve Equation (13) for c_{500} using the ZBRENT.PRO routine in IDL and obtain a first estimate of M_{200}^{Pl} from Equation (12). We then use the mass–concentration relation in Equation (8) of Dutton & Macciò (2014) to get a new value for c_{200} . We iterate this algorithm until we reach 5% accuracy on M_{200}^{Pl} (i.e., the difference between the mass estimated at the iteration i and the mass estimated at the iteration $i-1$ is less than 0.05). We find smaller concentrations than the starting value of 5, with a mean $c_{200} = 4.2$. We have verified that the algorithm converges to the same values of M_{200}^{Pl} when changing the initial input value of c_{200} .

We implemented this procedure in a Monte Carlo simulation with 1000 inputs for each cluster, sampling the *Planck* mass, M_{500}^{Pl} , according to a normal distribution with a standard deviation taken as the geometric mean of the uncertainties listed in Table 2. Similarly, we consider a log-normal distribution for c_{200} with a mean given by Equation (8) in Dutton & Macciò (2014) and standard deviation equal to the intrinsic scatter of 0.11 dex in the mass–concentration relation. This yields a log-normal distribution of calculated M_{200}^{Pl} values from Equation (12), whose mean and standard deviation are also listed in Table 2.

Appendix B Cluster Model

To construct an estimator for the mass bias, we adopt a multivariate log-normal model for the cluster observables σ_{1D} and M_{200}^{Pl} at fixed true mass, M_{200} , following White et al. (2010) and Stanek et al. (2010; see also, Allen et al. 2011; Evrard et al. 2014; Rozo et al. 2014b). It is then convenient to work with the logarithm of these quantities: $s_v = \ln(\sigma_{\text{1D}}/\text{km s}^{-1})$, $s_{\text{Pl}} = \ln(E(z)M_{200}^{\text{Pl}}/10^{15} M_\odot)$, and $\mu = \ln(E(z)M_{200}/10^{15} M_\odot)$, where we incorporate self-similar evolution with redshift, $E(z)$, with the masses. Power-law scaling relations give the observable mean values at true mass as,

$$\bar{s}_{\text{Pl}} \equiv \langle s_{\text{Pl}} | \mu \rangle = \ln(1 - b) + \mu, \quad (17)$$

and

$$\bar{s}_v \equiv \langle s_v | \mu \rangle = a_v + \alpha_v \mu, \quad (18)$$

where the averages are taken over both intrinsic cluster properties and measurement errors. The first relation is simply

our definition of the mass bias, Equation (1), and in practice we take $\alpha_v = 1/3$, its self-similar value, in the second relation.

Each observable is also associated with a log-normal dispersion about its mean that includes both intrinsic and measurement scatter,

$$\Sigma_{s_v}^2 = \tilde{\sigma}_{s_v}^2 + \sigma_{s_v}^2, \quad (19)$$

and

$$\Sigma_{s_{\text{Pl}}}^2 = \tilde{\sigma}_{s_{\text{Pl}}}^2 + \sigma_{s_{\text{Pl}}}^2, \quad (20)$$

where the first terms are the intrinsic log-normal scatter and the second ones are the measurement error. Although measurement error is Gaussian in the observed quantity rather than in the log-normal, we treat its fractional value as a log-normal dispersion; this is an approximation that is good to first order in the fractional measurement error. The second terms in the above expressions will therefore be understood as fractional measurement errors. The intrinsic dispersions may be correlated with the correlation coefficient $\tilde{r} = \langle (s_v - \bar{s}_v)(s_{\text{Pl}} - \bar{s}_{\text{Pl}}) \rangle / (\tilde{\sigma}_{s_v} \tilde{\sigma}_{s_{\text{Pl}}})$.

It is then possible to show that the predicted scaling between velocity dispersion and *Planck* mass is

$$\langle s_v | s_{\text{Pl}} \rangle = a_v + \alpha_v [s_{\text{Pl}} - \ln(1 - b) - \beta \Sigma_{s_{\text{Pl}}}^2 + r \beta \alpha_v^{-1} \Sigma_{s_v} \Sigma_{s_{\text{Pl}}}], \quad (21)$$

where β is the slope of the mass function on cluster scales, $\beta \approx 3$. The second to last term is the Eddington bias, proportional to the full dispersion, intrinsic, and measurement, in the sample selection observable, s_{Pl} . In the last term, $r = \tilde{r}(\tilde{\sigma}_{s_v}/\Sigma_{s_v})(\tilde{\sigma}_{s_{\text{Pl}}}/\Sigma_{s_{\text{Pl}}})$, the intrinsic correlation coefficient is diluted by the measurement errors. The last term is therefore equivalent to $\tilde{r} \beta \alpha_v^{-1} \tilde{\sigma}_{s_v} \tilde{\sigma}_{s_{\text{Pl}}}$.

This is the prediction for our measured scaling relation. Comparison to our fit identifies

$$\ln A = a_v - \alpha_v [\ln(1 - b) + \beta \Sigma_{s_{\text{Pl}}}^2 - \tilde{r} \beta \alpha_v^{-1} \tilde{\sigma}_{s_v} \tilde{\sigma}_{s_{\text{Pl}}}], \quad (22)$$

which leads to our estimator

$$(1 - b) = \left(\frac{A_g}{A} \right)^3 f_{\text{EB}} f_{\text{corr}}, \quad (23)$$

with

$$f_{\text{EB}} = e^{-\beta \Sigma_{s_{\text{Pl}}}^2}, \quad (24)$$

and

$$f_{\text{corr}} = e^{3\tilde{r}\beta\tilde{\sigma}_{s_v}\tilde{\sigma}_{s_{\text{Pl}}}}, \quad (25)$$

after setting $\alpha_v = 1/3$. As expected, the Eddington bias correction increases true cluster mass at given M_{200}^{Pl} , increasing the mass bias, b (decreasing $1 - b$). A positive correlation between velocity dispersion and *Planck* mass has the opposite effect.




References

- Allen, S. W., Evrard, A. E., & Mantz, A. B. 2011, *ARA&A*, 49, 409
 Arnaud, M., Pratt, G. W., Piffaretti, R., et al. 2010, *A&A*, 517, A92
 Battaglia, N., Leauthaud, A., Miyatake, H., et al. 2016, *JCAP*, 08, 013
 Baxter, E. J., Keisler, R., Dodelson, S., et al. 2015, *ApJ*, 806, 247
 Becker, M. R., & Kravtsov, A. V. 2011, *ApJ*, 740, 25
 Beers, T. C., Flynn, K., & Gebhardt, K. 1990, *AJ*, 100, 32
 Bleem, L. E., Stalder, B., de Haan, T., et al. 2015, *ApJS*, 216, 27

- Bocquet, S., Saro, A., Mohr, J. J., et al. 2015, *ApJ*, **799**, 214
- Bruzual, G., & Charlot, S. 2003, *MNRAS*, **344**, 1000
- Caldwell, C. E., McCarthy, I. G., Baldry, I. K., et al. 2016, *MNRAS*, **462**, 4117
- Carlberg, R. G. 1994, *ApJ*, **433**, 468
- Carlstrom, J. E., Holder, G. P., & Reese, E. D. 2002, *ARA&A*, **40**, 643
- Colín, P., Klypin, A. A., & Kravtsov, A. V. 2000, *ApJ*, **539**, 561
- Corless, V. L., & King, L. J. 2009, *MNRAS*, **396**, 315
- de Haan, T., Benson, B. A., Bleem, L. E., et al. 2016, *ApJ*, **832**, 95
- Diemer, B., & Kravtsov, A. V. 2015, *ApJ*, **799**, 108
- Dutton, A. A., & Maccio, A. V. 2014, *MNRAS*, **441**, 3359
- Evrard, A. E., Arnault, P., Huterer, D., & Farahi, A. 2014, *MNRAS*, **441**, 3562
- Evrard, A. E., Bialek, J., Busha, M., et al. 2008, *ApJ*, **672**, 122
- Farahi, A., Evrard, A. E., Rozo, E., Rykoff, E. S., & Wechsler, R. H. 2016, *MNRAS*, **460**, 3900
- Guo, H., Zheng, Z., Zehavi, I., et al. 2015, *MNRAS*, **453**, 4368
- Hartley, W. G., Gazzola, L., Pearce, F. R., Kay, S. T., & Thomas, P. A. 2008, *MNRAS*, **386**, 2015
- Hasselfield, M., Hilton, M., Marriage, T. A., et al. 2013, *JCAP*, **7**, 008
- Heymans, C., Van Waerbeke, L., Miller, L., et al. 2012, *MNRAS*, **427**, 146
- Hildebrandt, H., Choi, A., Heymans, C., et al. 2016, *MNRAS*, **463**, 635
- Hoekstra, H., Herbonnet, R., Muzzin, A., et al. 2015, *MNRAS*, **449**, 685
- Hoekstra, H., & Jain, B. 2008, *ARNPS*, **58**, 99
- Ilic, S., Blanchard, A., & Douspis, M. 2015, *A&A*, **582**, A79
- Johnston, D. E., Sheldon, E. S., Tasitsiomi, A., et al. 2007, *ApJ*, **656**, 27
- Kay, S. T., Peel, M. W., Short, C. J., et al. 2012, *MNRAS*, **422**, 1999
- Kravtsov, A. V., Vikhlinin, A., & Nagai, D. 2006, *ApJ*, **650**, 128
- Lau, E. T., Kravtsov, A. V., & Nagai, D. 2009, *ApJ*, **705**, 1129
- Madhavacheril, M., Sehgal, N., Allison, R., et al. 2015, *PhRvL*, **114**, 151302
- Markwardt, C. B. 2009, in ASP Conf. Ser. 411, *Astronomical Data Analysis Software and Systems XVIII*, ed. D. A. Bohlender, D. Durand, & P. Dowler (San Francisco, CA: ASP), 251
- Marriage, T. A., Acquaviva, V., Ade, P. A. R., et al. 2011, *ApJ*, **737**, 61
- Martino, R., Mazzotta, P., Bourdin, H., et al. 2014, *MNRAS*, **443**, 2342
- Mazzotta, P., Rasia, E., Moscardini, L., & Tormen, G. 2004, *MNRAS*, **354**, 10
- Mei, S., Holden, B. P., Blakeslee, J. P., et al. 2009, *ApJ*, **690**, 42
- Melin, J.-B., & Bartlett, J. G. 2015, *A&A*, **578**, A21
- Melin, J.-B., Bartlett, J. G., & Delabrouille, J. 2006, *A&A*, **459**, 341
- Meneghetti, M., Rasia, E., Merten, J., et al. 2010, *A&A*, **514**, A93
- Munari, E., Biviano, A., Borgani, S., Murante, G., & Fabjan, D. 2013, *MNRAS*, **430**, 2638
- Nagai, D., Kravtsov, A. V., & Vikhlinin, A. 2007, *ApJ*, **668**, 1
- Navarro, J. F., Frenk, C. S., & White, S. D. M. 1997, *ApJ*, **490**, 493
- Okabe, N., & Smith, G. P. 2016, *MNRAS*, **461**, 3794
- Penna-Lima, M., Bartlett, J. G., Rozo, E., et al. 2016, arXiv:1608.05356
- Piffaretti, R., & Valdarnini, R. 2008, *A&A*, **491**, 71
- Planck Collaboration, Ade, P. A. R., Aghanim, N., et al. 2014a, *A&A*, **571**, A20
- Planck Collaboration, Ade, P. A. R., Aghanim, N., et al. 2014b, *A&A*, **571**, A29
- Planck Collaboration, Ade, P. A. R., Aghanim, N., et al. 2015, *A&A*, **581**, A14
- Planck Collaboration, Ade, P. A. R., Aghanim, N., et al. 2016a, *A&A*, **594**, A24
- Planck Collaboration, Ade, P. A. R., Aghanim, N., et al. 2016b, *A&A*, **594**, A27
- Postman, M., Coe, D., Benítez, N., et al. 2012, *ApJS*, **199**, 25
- Prada, F., Klypin, A. A., Cuesta, A. J., Betancort-Rijo, J. E., & Primack, J. 2012, *MNRAS*, **423**, 3018
- Rasia, E., Ettori, S., Moscardini, L., et al. 2006, *MNRAS*, **369**, 2013
- Rasia, E., Lau, E. T., Borgani, S., et al. 2014, *ApJ*, **791**, 96
- Rasia, E., Meneghetti, M., Martino, R., et al. 2012, *NJPh*, **14**, 055018
- Rines, K., & Diaferio, A. 2006, *AJ*, **132**, 1275
- Rines, K., Geller, M. J., Diaferio, A., & Kurtz, M. J. 2013, *ApJ*, **767**, 15
- Rines, K. J., Geller, M. J., Diaferio, A., & Hwang, H. S. 2016, *ApJ*, **819**, 63
- Rodriguez-Gonzalez, C., Chary, R., Muchovej, S., et al. 2017, *MNRAS*, **464**, 2378
- Roza, E., Bartlett, J. G., Evrard, A. E., & Rykoff, E. S. 2014a, *MNRAS*, **438**, 78
- Roza, E., Evrard, A. E., Rykoff, E. S., & Bartlett, J. G. 2014b, *MNRAS*, **438**, 62
- Roza, E., Rykoff, E. S., Bartlett, J. G., & Evrard, A. 2014c, *MNRAS*, **438**, 49
- Ruel, J., Bazin, G., Bayliss, M., et al. 2014, *ApJ*, **792**, 45
- Sayers, J., Golwala, S. R., Mantz, A. B., et al. 2016, *ApJ*, **832**, 26
- Sereno, M., Covone, G., Izzo, L., et al. 2017, arXiv:1703.06886
- Sheldon, E. S., Johnston, D. E., Frieman, J. A., et al. 2004, *AJ*, **127**, 2544
- Sifón, C., Battaglia, N., Hasselfield, M., et al. 2016, *MNRAS*, **461**, 248
- Sifón, C., Menanteau, F., Hasselfield, M., et al. 2013, *ApJ*, **772**, 25
- Simet, M., Battaglia, N., Mandelbaum, R., & Seljak, U. 2017a, *MNRAS*, **466**, 3663
- Simet, M., McClintock, T., Mandelbaum, R., et al. 2017b, *MNRAS*, **466**, 3103
- Smith, G. P., Mazzotta, P., Okabe, N., et al. 2016, *MNRAS*, **456**, L74
- Stanek, R., Rasia, E., Evrard, A. E., Pearce, F., & Gazzola, L. 2010, *ApJ*, **715**, 1508
- Sunyaev, R. A., & Zeldovich, Y. B. 1970, *Ap&SS*, **7**, 3
- von der Linden, A., Mantz, A., Allen, S. W., et al. 2014, *MNRAS*, **443**, 1973
- White, M., Cohn, J. D., & Smit, R. 2010, *MNRAS*, **408**, 1818
- Williams, M. J., Bureau, M., & Cappellari, M. 2010, *MNRAS*, **409**, 1330
- Wu, H.-Y., Hahn, O., Evrard, A. E., Wechsler, R. H., & Dolag, K. 2013, *MNRAS*, **436**, 460
- York, D. G., Adelman, J., Anderson, J. E., Jr., et al. 2000, *AJ*, **120**, 1579
- Ziparo, F., Smith, G. P., Okabe, N., et al. 2016, *MNRAS*, **463**, 4004



Spectroscopic Confirmation and Velocity Dispersions for 20 *Planck* Galaxy Clusters at $0.16 < z < 0.78$

Stefania Amodeo¹, Simona Mei^{1,2,3,4} , Spencer A. Stanford^{5,6}, Charles R. Lawrence³, James G. Bartlett^{3,7}, Daniel Stern³ , Ranga-Ram Chary⁸ , Hyunjin Shim⁹, Francine R. Marleau^{11,10}, Jean-Baptiste Melin¹², and Carmen Rodríguez-González⁸

¹ LERMA, Observatoire de Paris, PSL Research University, CNRS, Sorbonne Universités, UPMC Univ. Paris 06, F-75014 Paris, France

² Université Paris Denis Diderot, Université Paris Sorbonne Cité, F-75205 Paris Cedex 13, France

³ Jet Propulsion Laboratory, California Institute of Technology, 4800 Oak Grove Drive, Pasadena, California 91011, USA

⁴ Cahill Center for Astronomy & Astrophysics, California Institute of Technology, Pasadena, CA 91125, USA

⁵ Department of Physics, University of California Davis, One Shields Avenue, Davis, CA 95616, USA

⁶ Institute of Geophysics and Planetary Physics, Lawrence Livermore National Laboratory, Livermore, CA 94550, USA

⁷ APC, AstroParticule et Cosmologie, Université Paris Diderot, CNRS/IN2P3, CEA/Irfu, Observatoire de Paris, Sorbonne Paris Cité, 10 rue Alice Domon et Léonie Duquet, F-75205, Paris Cedex 13, France

⁸ Infrared Processing and Analysis Center, California Institute of Technology, Pasadena, CA 91125, USA

⁹ Department of Earth Science Education, Kyungpook National University, Korea

¹⁰ National Optical Astronomy Observatory, Tucson, AZ 85719, USA

¹¹ Institute of Astro and Particle Physics, University of Innsbruck, A-6020, Innsbruck, Austria

¹² IRFU, CEA, Université Paris-Saclay, F-91191 Gif-sur-Yvette, France

Received 2017 August 21; revised 2017 October 20; accepted 2017 October 25; published 2018 January 19

Abstract

We present Gemini and Keck spectroscopic redshifts and velocity dispersions for 20 clusters detected via the Sunyaev–Zel’dovich (SZ) effect by the *Planck* space mission, with estimated masses in the range $2.3 \times 10^{14} M_{\odot} < M_{500}^{\text{Pl}} < 9.4 \times 10^{14} M_{\odot}$. Cluster members were selected for spectroscopic follow-up with Palomar, Gemini, and Keck optical and (in some cases) infrared imaging. Seven cluster redshifts were measured for the first time with this observing campaign, including one of the most distant *Planck* clusters confirmed to date, at $z = 0.782 \pm 0.010$, PSZ2 G085.95+25.23. The spectroscopic redshift catalogs of members of each confirmed cluster are included as online tables. We show the galaxy redshift distributions and measure the cluster velocity dispersions. The cluster velocity dispersions obtained in this paper were used in a companion paper to measure the *Planck* mass bias and to constrain the cluster velocity bias.

Key words: cosmology: observations – galaxies: clusters: general – galaxies: distances and redshifts

Supporting material: machine-readable table

1. Introduction

Massive galaxy clusters are sensitive cosmological probes (e.g., Allen et al. 2011), yet these are rare objects best found in all-sky surveys covering large volumes. The *ROSAT* All-Sky Survey (RASS; Truemper 1993) dates back to the early 1990s and has served the community as a workhorse since, providing hundreds of cluster candidates. A subsequent important step has been taken by the *Planck* satellite, launched on 2009 May 14. *Planck* detects clusters based on the Sunyaev–Zel’dovich (SZ) effect (Sunyaev & Zeldovich 1970; Birkinshaw 1999; Carlstrom et al. 2002), i.e., the distortion of the energy spectrum of cosmic microwave background (CMB) photons passing through the cluster due to inverse Compton scattering with hot electrons. Being independent of distance, the SZ signal does not suffer from cosmological dimming and it is proportional to the cluster mass. Benefiting from this, *Planck* extends the (X-ray) RASS catalog to higher redshift and contains a large fraction of massive objects of the type most prized for cosmological studies.

Planck has produced two all-sky cluster surveys through the SZ effect (Planck Collaboration et al. 2014, 2016a): the PSZ1 with 1227 candidates based on 15.5 months of data, and the PSZ2 with 1653 candidates from the full mission data set of 29 months. Of the PSZ2 candidates, 1203 have been confirmed by ancillary data and 1094 have redshift estimates, in the range $0 < z < 1$, with a mean redshift of $z \sim 0.25$. The mean mass

of the confirmed clusters over the whole redshift range is $M_{500}^{\text{Pl}} = 4.82 \times 10^{14} M_{\odot}$ (see the definition of M_{500}^{Pl} below).

The *Planck* collaboration has undertaken a large follow-up effort to confirm cluster candidates and measure their redshifts. The first optical follow-up was based on observations with the Russian–Turkish 1.5 m telescope (Planck Collaboration et al. 2015) and provided spectroscopic redshifts of 65 *Planck* clusters. The second optical follow-up, based on observations with telescopes at the Canary Islands Observatories, yielded 53 cluster spectroscopic redshifts (Planck Collaboration et al. 2016b). The *Planck* collaboration has also carried out X-ray validation programs with *XMM-Newton* (Planck Collaboration et al. 2011b, 2012, 2013), where redshifts for 51 clusters were obtained from X-ray spectral fitting.

Our follow-up program presented in this paper includes the spectroscopic follow-up of 20 *Planck* cluster candidates with the Gemini and Keck telescopes (P.I.’s: J.G. Bartlett and F.A. Harrison, respectively). The goals of our programs were: (1) to confirm *Planck* SZ detections as clusters and measure their redshifts; (2) to estimate their masses using cluster galaxy velocity dispersions; and (3) to measure the *Planck* mass and velocity bias. We use Sloan Digital Sky Survey (SDSS; York et al. 2000), and Palomar and Gemini imaging to select the cluster galaxies to target with spectroscopy.

In this paper, we describe our observations and publish the optical spectroscopy of cluster members, from which we derive the cluster redshifts and velocity dispersions. In a companion

Table 1
Observation Details

Run	Semester	PI	Tel./Inst.	Program ID	N_{cl}
1	2010B	Lawrence	Palomar/ LFC,WIRC		11
2	2011A	Lawrence	Palomar/LFC		25
3	2011B	Lawrence	Palomar/LFC		15
2	2011A	Bartlett	Gemini- N/GMOS	GN-2011A- Q-119	11
3	2011B	Bartlett	Gemini- N/GMOS	GN-2011B- Q-41	11
4	2012B	Lawrence	Palomar/LFC		9
5	2012A	Bartlett	Gemini- S/GMOS	GS-2012A- Q-77	9
6	2013B	Harrison	Keck/LRIS	UT 2013 Oct 4–5	1

paper (Amodeo et al. 2017), we use these observations to estimate the clusters’ dynamical masses and calibrate the all-important relation between the SZ Compton parameter, Y , and mass.

The paper is organized as follows. In Section 2, we present our sample of *Planck*—selected clusters and describe the observing programs carried out at the Palomar, Gemini, and Keck telescopes. A table describing all the targets observed with the Palomar telescope is given in Appendix A. In Section 3, we describe the spectroscopic redshift and galaxy velocity dispersion measurements. For clusters with a spectroscopic follow-up, we include figures of redshift histograms, optical images and SZ maps in Appendix B. Catalogs of cluster member galaxies with spectroscopic measurements are included as online tables. We illustrate the parameters published in the catalogs in Section 4 and give an example in Appendix C. In Section 5, we discuss our results in the context of optical identifications of *Planck* clusters.

Throughout this paper, masses are quoted at a radius R_{Δ} , within which the cluster density is Δ times the critical density of the universe at the cluster’s redshift, where $\Delta = \{200, 500\}$. We refer to the $\Delta = 200$ radius as the “virial radius”, R_{200} . Mass and radius are directly connected via $M_{\Delta} \equiv \Delta H_z^2 R_{\Delta}^3 / (2G)$, where H_z is the Hubble constant at the cluster’s redshift.

2. Data and Observations

In this section, we describe our spectroscopic observations with the Gemini and Keck telescopes, and the Palomar telescope imaging that was used to select cluster members. The details of each observing run (pre-imaging and optical spectroscopy) are listed in Table 1.

Since it is well-known that early-type galaxies (ETGs) in clusters define a tight red sequence up to redshift $z \sim 1.5$ (Mei et al. 2009), and can be easily identified with respect to field background galaxies, we selected cluster members to follow-up with spectroscopy from optical and infrared imaging using a red sequence search method (Gladders & Yee 2000; Licitra et al. 2016a, 2016b). For most clusters, we used g' and i' filters for imaging, since the ETG ($g - i$) color is monotonic over the redshift range in which most *Planck* clusters are detected, $z < 1$. We also observed the r' band, when possible within our

exposure time constraints, to obtain better photometric redshifts. For the candidates that appeared to be at $z > 0.6$ from their *WISE* imaging in the mid-infrared (see the *WISE* analysis in Planck Collaboration et al. 2016a), we obtained near-infrared observations in the J and K bandpasses. For some of our targets, we could not obtain images at two different wavelengths and used SDSS photometry when available.

Cluster members were selected as red sequence galaxies by their colors, using Bruzual & Charlot (2003) stellar population models and Mei et al. (2009) empirical red sequence measurements, following the cluster member selection technique described in Licitra et al. (2016a, 2016b), adapted for the bandpasses available for these observations.

2.1. Gemini Observations

The Gemini imaging and spectroscopic follow-up was performed with GMOS-N and GMOS-S at the Gemini-North and Gemini-South Telescopes, respectively, in the programs GN-2011A-Q-119, GN-2011B-Q-41, and GS-2012A-Q-77 (P. I. J.G. Bartlett). This sample consists of 19 *Planck*-detected galaxy clusters, 17 of which are part of the *Planck* PSZ2 catalog (Planck Collaboration et al. 2016a), and one is published in the *XMM-Newton* validation follow-up of *Planck* cluster candidates (Planck Collaboration et al. 2013). Two clusters are not part of the already published *Planck* papers: (1) PLCK G183.33-36.69 has a detection signal-to-noise ratio (S/N) just below the *Planck* catalog selection threshold and (2) PLCK G147.32-16.59 is in the *Planck* cluster mask.

The goal of our Gemini program was to obtain a statistical calibration of the *Planck* SZ mass estimator. For this purpose, we mostly chose clusters that were detected with a *Planck* SZ S/N of about 4.5σ or larger, distributed in the northern and southern Hemispheres, spanning a wide range in *Planck* SZ masses, $2 \times 10^{14} M_{\odot} \lesssim M_{500}^{\text{Pl}} \lesssim 10^{15} M_{\odot}$, in the redshift range $0.16 < z < 0.44$. In Figure 1, we compare our sample to the full PSZ2 catalog. These histograms show that our selection has an average redshift larger than the PSZ2 catalog, and a mass range covering most of the mass range of the PSZ2 catalog. In fact, our sample has an average redshift of $z = 0.37$ and an average mass of $M = 6.2 \times 10^{14} M_{\odot}$, compared to the average PSZ2 redshift and mass of $z = 0.25$ and $4.8 \times 10^{14} M_{\odot}$, respectively. The larger average redshift was chosen to cover most of the cluster members within $\sim R_{200}$ in the field of view of the Gemini and Keck telescopes.

The northern sample was selected in the area covered by the SDSS, and we used the SDSS public releases and our GMOS-N pre-imaging in the r -band (150 s) to detect red galaxy overdensities around the *Planck* detection center. When unknown, we estimated the approximate cluster redshift using its red sequence to calculate the appropriate exposure times for the spectroscopic follow-up. For PSZ2 G139.62+24.18, PSZ2 G157.43+30.34, and PLCK G183.33-36.69, we used imaging obtained with the Palomar telescope. For the southern sample, we obtained GMOS-S pre-imaging in the g and i bands (200 s and 90 s integrations, respectively).

Our GMOS spectroscopic observations were reduced using the IRAF Gemini GMOS package and standard techniques. After coadding the reduced exposures, we extracted one-dimensional spectra for the objects in each slitlet and initially

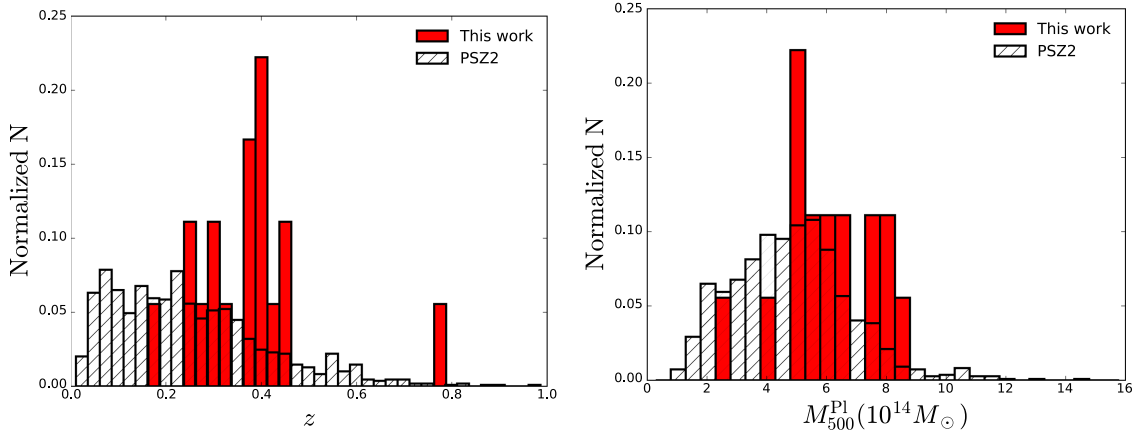


Figure 1. Histograms of the redshifts (left) and the masses (right) of our spectroscopic sample compared to the full PSZ2 catalog. These histograms are normalized to the total number of objects in each sample. We have selected cluster candidates with redshift $z > 0.2$ (with average redshift larger than the PSZ2 catalog), and larger average mass than the PSZ2 catalog, with cluster masses in the range $2.3 \times 10^{14} M_{\odot} < M_{500}^{\text{Pl}} < 9.4 \times 10^{14} M_{\odot}$. The cluster mass shown here is the *Planck* mass proxy (Planck Collaboration et al. 2016a).

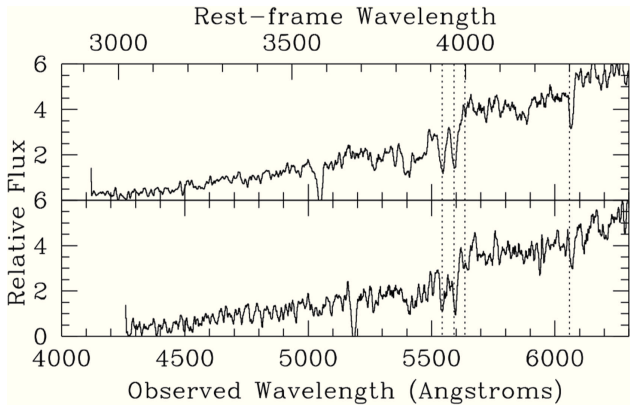


Figure 2. Spectra obtained with Gemini/GMOS for two galaxies in the cluster PSZ2 G250.04+24.14 ($z = 0.411$). The vertical dotted lines represent Ca H+K, D4000, and the G band, respectively.

inspected them visually to identify optical features such as the 4000 Å break, G-band, Ca H+K absorption lines, and, rarely, [O II] $\lambda 3727$ emission. We determined more precise galaxy redshifts by running the IRAF task *xcsao*. In Figure 2, we show two Gemini/GMOS spectra of galaxies in the cluster PSZ2 G250.04+24.14.

The clusters that we followed-up with the Gemini telescopes are listed in Table 2 (see also Table 1 from Amodeo et al. 2017). The mass calibration derived from the velocity dispersions of the clusters in this sample is discussed in Amodeo et al. (2017), in which we measured the *Planck* mass bias and constrained the cluster velocity bias.

2.2. Keck Observations

We obtained spectroscopy of PSZ2 G085.95+25.23 on the nights of UT 2013 October 4–5 using the dual-beam Low Resolution Imaging Spectrometer (LRIS; Oke et al. 1995) on the Keck I telescope atop Maunakea. These slitmask observations were obtained with the $400 \ell \text{ mm}^{-1}$ grism on the blue arm of LRIS ($\lambda_{\text{blaze}} = 3400 \text{ \AA}$), the $400 \ell \text{ mm}^{-1}$ grating on the red arm of LRIS ($\lambda_{\text{blaze}} = 8500 \text{ \AA}$), and the 5600 \AA dichroic was used to split the light. We obtained three 1200 s integrations on

the first night through variable cloud cover, and two 1200 s integrations on the second night in photometric conditions. After some experimentation, we base our analysis on the single best exposure from the first night combined with the two exposures from the second night. The data were processed using standard techniques within IRAF, and flux calibrated using standard stars from Massey & Gronwall (1990) observed on the second night.

In Figure 3, we show two Keck/LRIS spectra of galaxies in the cluster PSZ2 G085.95+25.23.

2.3. Palomar Optical and Infrared Imaging

The Palomar optical and infrared imaging, used to select cluster members, was obtained with a dedicated *Planck* follow-up program (PI: C. Lawrence) that included several runs. Our Palomar sample is presented in the Appendix A, in Table 4.

For the Palomar/WIRC data reduction, we pre-processed the images using a dedicated IRAF package `noao.imred.ccdred`. Master dark frames of different exposure times were constructed for each night of observation, and these were subtracted from science images of the corresponding exposure time. Dark-subtracted individual science images were then divided by the master flat image in the same filter. We tested two ways of constructing the master flat image: first, by combining dome flats after the dark correction (master domeflat) and, second, by median combining all science images (master skyflat). Since there was little difference between the two master flat images, we chose to use the master domeflat in the flat correction. Sky subtraction, bad pixel and cosmic-ray masking, image aligning and combining were done using the IRAF package `xdimsum`.¹³ Bad pixel masks were created from the master skyflat image by identifying bad, hot, or warm pixels significantly ($>20\sigma$) lower or higher than the average background. After calculating the shifting of the images that were to be sky subtracted, we performed the sky subtraction correcting for bad pixels and cosmic rays. The six adjacent images were used to calculate the sky. Once the mosaic image was created, we created an object mask from the mosaic image, and repeated the sky subtraction

¹³ Experimental Deep Infrared Mosaicing Software.

Table 2
Spectroscopically Confirmed Cluster Sample

Name	R.A. (degree)	Decl. (degree)	Filter	t_{exp} (s)	N_{mask}	Run
PSZ2 G033.83-46.57	326.3015	-18.7159	<i>g,i</i>	1800	2	GS-2012A-Q-77
PSZ2 G053.44-36.25	323.8006	-1.0493	<i>r</i>	1800	1	GN-2011A-Q-119,GN-2011B-Q-41
PSZ2 G056.93-55.08	340.8359	-9.5890	<i>r</i>	1800	2	GN-2011A-Q-119,GN-2011B-Q-41
PSZ2 G081.00-50.93	347.9013	3.6439	<i>r</i>	1800	1	GN-2011A-Q-119,GN-2011B-Q-41
PSZ2 G083.29-31.03	337.1406	20.6211	<i>r</i>	1800	1	GN-2011A-Q-119,GN-2011B-Q-41
PSZ2 G085.95+25.33	277.6164	56.8823	...	3600	2	Keck Telescope
PSZ2 G108.71-47.75	3.0715	14.0191	<i>r</i>	1800	2	GN-2011A-Q-119,GN-2011B-Q-41
PSZ2 G139.62+24.18 ^a	95.4529	74.7014	<i>r</i>	900	2	GN-2011A-Q-119,GN-2011B-Q-41
PLCK G147.32-16.59 ^b	44.1101	40.2853	<i>r</i>	1800	2	GN-2011A-Q-119,GN-2011B-Q-41
PSZ2 G157.43+30.34 ^a	117.2243	59.6974	<i>r</i>	3600	2	GN-2011A-Q-119,GN-2011B-Q-41
PLCK G183.33-36.69 ^a	57.2461	4.5872	<i>r</i>	1800	2	GN-2011A-Q-119,GN-2011B-Q-41
PSZ2 G186.99+38.65	132.5314	36.0717	<i>r</i>	1800	2	GN-2011A-Q-119,GN-2011B-Q-41
PSZ2 G216.62+47.00	147.4658	17.1196	<i>r</i>	1800	2	GN-2011A-Q-119,GN-2011B-Q-41
PSZ2 G235.56+23.29	134.0251	-7.7207	<i>g,i</i>	900	2	GS-2012A-Q-77
PSZ2 G250.04+24.14	143.0626	-17.6481	<i>g,i</i>	1800	2	GS-2012A-Q-77
PSZ2 G251.13-78.15	24.0779	-34.0014	<i>g,i</i>	900	2	GS-2012A-Q-77
PSZ2 G272.85+48.79	173.2938	-9.4812	<i>g,i</i>	900	2	GS-2012A-Q-77
PSZ2 G329.48-22.67	278.2527	-65.5555	<i>g,i</i>	900	2	GS-2012A-Q-77
PSZ2 G348.43-25.50	291.2293	-49.4483	<i>g,i</i>	900	2	GS-2012A-Q-77
PSZ2 G352.05-24.01	290.2320	-45.8430	<i>g,i</i>	1200	2	GS-2012A-Q-77

Notes. Clusters are named after their PSZ2 ID, when available. When it is not available, we use the prefix “PLCK” followed by a notation in galactic coordinates similar to that used in the PSZ2 paper. R.A. and decl. indicate the optical cluster center. Filter names used for imaging, spectroscopic observing times and the number of masks are also stated. The last column lists the observing run(s) for each target, including pre-imaging.

^a Also observed at Palomar, see Table 4.

^b Target PLCK G147.32-16.59 is confirmed in the *XMM-Newton* cluster validation (Planck Collaboration et al. 2013), but it is not included in the two *Planck* catalogs of SZ sources released so far.

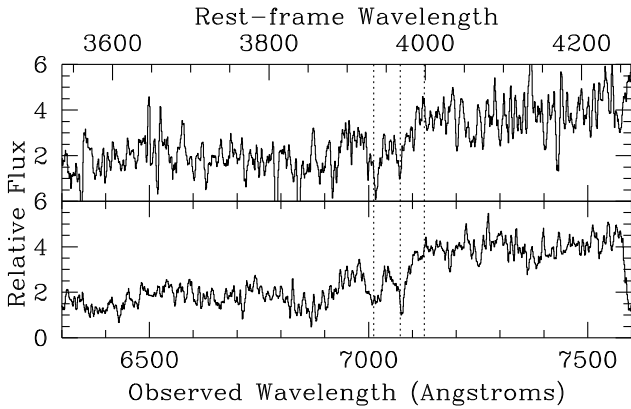


Figure 3. Spectra obtained with Keck/LRIS for two galaxies in the cluster PSZ2 G085.95+25.23 ($z = 0.782$). The vertical dotted lines represent Ca H +K and D4000, respectively.

and combining process to obtain the final mosaic image as well as the exposure time map. Astrometric calibration was done using the 2MASS point source catalog as a reference through the IRAF package `cmap`.

The optical Palomar/LFC data reduction comprised basic pre-processing (i.e., bias, dark, flat, cross-talk, and overscan/trim correction), satellite trail removal, bad pixel and cosmic-ray correction, and aligning and coadding individual images to produce the final mosaic images. Since the LFC data were

stored in a multi-extension fits (MEF) format, we mostly used the IRAF package `mscred` (Valdes et al. 1995) as well as `ccdred` for the analysis. The initial bad pixel masks were generated from the ratio between two flat-field images with different exposure times. After the bias, dark, flat, cross-talk, and overscan correction using `ccdproc`, satellite trails in each image were identified using the IRAF task `satzap` and corrected. In addition, initial bad pixels and cosmic rays were identified using average sigma clipping. The updated bad pixel masks were converted to weight images used later in the coadding step.

Fringe correction was necessary for images taken with the *i'*-band filter. The fringe effect is less noticeable in images with short exposure times (<300 s), but the interference pattern significantly affects the background for longer exposures. For fringe correction, we first made an object mask and the resulting sky map for each image using the IRAF `nproto.objmasks`. Then the output sky maps were combined using `mscred.sflatcombine` to produce the response sky image, from which the median-filtered response was subtracted to derive the fringe pattern. Using the fringe pattern as the input in `mscred.rmfringe`, the fringes in *i'*-band images were successfully divided out. After these corrections, astrometric calibration was done with `cmap` using the USNO-B1.0 catalog as a reference. Then the images for each target were registered and mosaicked using the Terapix/*Swarp* software. The images were background subtracted, resampled, and combined to produce weighted means of the individual images

Table 3
Results of the Spectroscopical Analysis

Name	z_{spec}	New z_{spec}	$z_{\text{spec+DR14}}$	N_{tot}	$N_{\text{gal}}^{\text{conf}}$	σ_{BI} (km s^{-1})	$\sigma_{\text{BI+DR14}}$ (km s^{-1})	σ_{G} (km s^{-1})	S/N	Det. Meth.	M_{500}^{pl} ($10^{14} M_{\odot}$)	K-S gaussian prob.	S-W gaussian prob.	K-S uniform prob.
PSZ2 G033.83-46.57	0.439 ± 0.001	+		10	8	985_{-277}^{+451}		1051_{-214}^{+309}	4.6	2	$5.4_{-0.8}^{+0.7}$	0.96	0.71	0.50
PSZ2 G053.44-36.25	0.331 ± 0.001	+	0.3295 ± 0.0003	21	20	1011_{-131}^{+242}	1215_{-100}^{+167}	1025_{-117}^{+224}	8.9	3	$7.5_{-0.6}^{+0.5}$	0.99	0.80	0.07
PSZ2 G056.93-55.08	0.443 ± 0.001		0.4430 ± 0.0001	49	46	1356_{-127}^{+192}	1331_{-128}^{+194}	1345_{-113}^{+170}	11.5	3	9.4 ± 0.5	0.76	0.12	0.01
PSZ2 G081.00-50.93	0.303 ± 0.001	+	0.4430 ± 0.0001	15	15	1292_{-185}^{+360}	1552_{-154}^{+175}	1300_{-140}^{+326}	9.2	3	6.7 ± 0.5	0.97	0.96	0.14
PSZ2 G083.29-31.03	0.412 ± 0.002		0.3051 ± 0.0001	21	20	1434_{-320}^{+574}	1153_{-94}^{+111}	1591_{-262}^{+376}	9.1	3	$7.8_{-0.6}^{+0.5}$	0.83	0.90	0.004
PSZ2 G085.95+25.23	0.782 ± 0.003	+		16	14	1049_{-180}^{+210}		1041_{-119}^{+195}	5.0	2	$5.2_{-0.7}^{+0.6}$	0.91	0.05	0.06
PSZ2 G108.71-47.75	0.389 ± 0.001		0.3897 ± 0.0002	11	8	900_{-190}^{+458}	861_{-216}^{+327}	900_{-183}^{+460}	4.3	1	$5.1_{-0.8}^{+0.7}$	0.99	0.87	0.65
PSZ2 G139.62+24.18	0.268 ± 0.001			20	20	1120_{-238}^{+366}		1127_{-171}^{+305}	9.6	3	7.3 ± 0.5	0.51	0.25	0.20
PLCK G147.32-16.59	0.640 ± 0.009			10	10	—		—	5.9	1	$8.1_{-0.9}^{+0.8}$	0.91	0.91	0.86
PSZ2 G157.43+30.34	0.402 ± 0.001	+		28	28	1244_{-109}^{+192}		1242_{-103}^{+195}	8.8	2	8.2 ± 0.6	0.99	0.73	0.23
PLCK G183.33-36.69	0.163 ± 0.001			11	11	897_{-275}^{+437}		979_{-187}^{+263}	2.1	1	$2.3_{-0.9}^{+0.7}$	0.59	0.05	0.04
PSZ2 G186.99+38.65	0.377 ± 0.001		0.3774 ± 0.0003	41	41	1506_{-120}^{+164}	1426_{-87}^{+133}	1462_{-102}^{+165}	7.1	3	$6.6_{-0.7}^{+0.6}$	0.83	0.32	0.40
PSZ2 G216.62+47.00	0.385 ± 0.001		0.3864 ± 0.0003	37	37	1546_{-132}^{+174}	1779_{-153}^{+207}	1524_{-110}^{+178}	9.7	3	$8.4_{-0.6}^{+0.5}$	0.97	0.45	0.86
PSZ2 G235.56+23.29	0.375 ± 0.002			27	23	1644_{-192}^{+285}		1636_{-141}^{+294}	4.9	3	$5.7_{-0.8}^{+0.7}$	0.95	0.16	0.13
PSZ2 G250.04+24.14	0.411 ± 0.001			29	29	1065_{-285}^{+447}		1466_{-241}^{+380}	6.2	3	6.2 ± 0.6	0.94	0.97	0.10
PSZ2 G251.13-78.15	0.306 ± 0.001	+		17	17	801_{-493}^{+852}		1188_{-155}^{+205}	4.8	1	4.1 ± 0.6	0.56	0.19	0.26
PSZ2 G272.85+48.79	0.420 ± 0.002			10	9	1462_{-216}^{+389}		1498_{-175}^{+345}	4.8	2	$5.3_{-0.8}^{+0.7}$	0.98	0.61	0.62
PSZ2 G329.48-22.67	0.249 ± 0.001	+		19	16	835_{-119}^{+179}		746_{-64}^{+152}	6.0	3	$5.0_{-0.8}^{+0.7}$	0.99	0.90	0.46
PSZ2 G348.43-25.50	0.265 ± 0.001			21	20	1065_{-198}^{+411}		1160_{-167}^{+277}	7.1	3	6.0 ± 0.6	0.85	0.18	0.02
PSZ2 G352.05-24.01 ^a	0.786 ± 0.026			23	10	—	—	—	4.1	1	$6.2_{-1.0}^{+0.9}$	0.35	0.02	0.03
	0.304 ± 0.022			23	13	—	—	—				0.99	0.94	0.98

Note. From left to right the columns list: measured spectroscopic redshift, the new spectroscopic redshift estimates, redshift estimates obtained including the available redshifts in the SDSS DR14, the total number of galaxies with measured redshifts in the cluster field, the number of confirmed member galaxies, and our measured velocity dispersions using the Biweight and the Gapper methods (Beers et al. 1990). The next three columns give, respectively, the signal-to-noise ratio, the number of detection methods and the *Planck* mass proxy, as reported in the PSZ2 catalog (we calculated these numbers for the two objects not listed in the PSZ2 catalog). The last three columns list, respectively, the Kolmogorov–Smirnov (K–S) and the Shapiro–Wilk (S–W) statistics for the probability that the redshift distributions are Gaussian, and the K–S test for a uniform distribution.

^a Two structures observed, not confirmed as clusters (see the text and Figure 5).

for flux conservation. The weight images previously created from the final bad pixel masks were used.

Many of our Palomar nights were not photometric, and we could not obtain accurate photometric redshifts with only a few bandpasses. However, we could use SDSS and our Palomar images to select cluster member candidates for our Gemini spectroscopic observations.

3. Cluster Confirmation and Spectroscopic Redshift Measurements

We calculated the cluster redshifts and velocity dispersions using the ROSTAT software (Beers et al. 1990) with the biweight method (see Table 3). This is appropriate to our clusters where there are typically 20 confirmed members. We also report the dispersion σ_G determined from the gapper estimator (as implemented in ROSTAT), which is to be preferred for clusters with fewer than 10–15 members (see Girardi et al. 1993, 2005). We find that biweight and gapper estimates are perfectly consistent, with the absolute difference between the velocity dispersions calculated from the two methods being on average of $(0.04 \pm 0.14)\sigma$, and never higher than 0.5σ . Since the line-of-sight cluster velocity dispersion can be highly anisotropic, small galaxy samples lead to large systematic uncertainties, with estimated uncertainties of $\lesssim 10\%$ (White et al. 2010) for samples with more than ~ 10 –15 galaxies like ours.

We retain as possible cluster members the galaxies within 3σ of the average cluster velocity/redshift. Standard deviations are in the range 0.001–0.008 in redshift, for the clusters that we confirm, apart PLCK G147.32-16.59 that shows evidence for an ongoing merger event (see the discussion below). Figures 4 and 5 show the redshift distributions of the cluster member galaxies (left), the optical image of the cluster with the selected members (middle), and the SZ maps in units of S/N (right), for the northern and the southern samples, respectively. We also present Gaussian fits to the redshift distributions in the left-hand panels.

The middle panels of Figures 4 and 5 show the optical pre-imaging, within the Gemini field of view of 5.5×5.5 arcmin². Spectroscopically confirmed members are indicated by green circles.

For PSZ2 G056.93-55.08, we visually observe three spatially separated galaxy groups, but all at the same redshift and within one virial radius. We derived the virial radius $R_{200} = (2.00 \pm 0.05)$ Mpc from the SZ mass estimate of $M_{500}^{\text{Pl}} = (9.4 \pm 0.5) \times 10^{14} M_{\odot}$.¹⁴ At the cluster redshift, $z = 0.443$, 2 Mpc correspond to 5.7 arcmin in a Planck cosmological model (Planck Collaboration et al. 2016c). We cannot obtain a separate mass estimate for each group because the Planck beam includes all the three groups and we do not have enough spectroscopic members of each group for deriving the group mass from velocity dispersions. Therefore, we consider the three groups as being part of a single cluster detection.

For all targets but PSZ2 G352.05-24.01, the red circled area is centered on the optical center of the cluster and has a 1 arcmin radius. The optical center was obtained as the brightest cluster member in the densest cluster region, following a modified version of the centering algorithm from

Licitra et al. (2016b). For PSZ2 G352.05-24.01, we used the coordinates of the X-ray center, marked with a red cross.

In the right-hand panels, we show the SZ maps with the same area enclosed by the black circles and centered on the optical position. The SZ maps have an angular resolution of 5 arcmin and are given in units of S/N. All the detections lie above $S/N = 4.5$, except for PLCK G183.33-36.69 with $S/N = 2$.

Masses and S/N were recalculated from a re-extraction of the SZ signal using the Matched Multi-Filter MMF3 (Melin et al. 2006; Planck Collaboration et al. 2011a, 2014, 2016a), fixing the position to the optical position and varying the filter size. They are reported in Table 3. The quoted S/N is the maximum across the various filter sizes at the optical position. The masses are obtained from the re-extracted SZ signal following the method described in Section 7.2.2 of Planck Collaboration et al. (2014).

In Table 3, we also show the number of detection methods from Planck Collaboration et al. (2016a). The Planck selection function is very reliable ($>90\%$) for detections obtained with $S/N > 4.5$ by at least one detection method. For objects detected with all three detection methods, the probability of being a cluster is $>98\%$ with $S/N > 4.5$ (Planck Collaboration et al. 2016a). In order to confirm each target as galaxy cluster, we combine this information with the probability that the galaxy redshift distribution is Gaussian, the characteristic distribution of a virialized cluster, from the Kolmogorov–Smirnov (K–S, e.g., Fasano & Franceschini 1987) and the Shapiro–Wilk (S–W, Shapiro & Wilk 1965) statistics, as well as the probability of a uniform distribution from a K–S test. The results of these tests are shown in the last three columns of Table 3.

Eleven of our cluster candidates have a $>98\%$ probability of being a galaxy cluster, since they were detected with three detection methods and have $S/N > 4.5$. For these targets, the probabilities that the redshift distributions are Gaussian are almost always $>80\%$ and the probabilities to be uniform are $<50\%$ and mostly $<10\%$. Only one object, PSZ2 G139.62+24.18 at $z = 0.268$, has an $S/N = 9.5$, which corresponds to a *Planck* reliability of being a cluster of $\sim 100\%$, but a K–S (S–W) probability of having a Gaussian redshift distribution of $\sim 50\%$ ($\sim 20\%$), and the probability of having a uniform redshift distribution of $\sim 20\%$. It shows a very luminous BCG at the center, and has 20 spectroscopically confirmed galaxies at the same redshift. All of these elements lead us to believe that this is a galaxy cluster, and it was also confirmed as a cluster in the PSZ2 catalog. All the other 10 targets are most likely galaxy clusters, and we assume that they are. Of those, we confirm three clusters that were not originally confirmed in the PSZ2.

The other cluster candidates that were detected with at least one detection method and $S/N > 4.5$ have a $>90\%$ probability of being galaxy clusters. For these candidates, we assume that we confirm a cluster when the probability that their redshift distribution is Gaussian is $>95\%$ ($\sim 2\sigma$). On the other hand, we do not confirm a cluster when the probability of a uniform distribution is $>50\%$. In fact, since the *Planck* detection and the galaxy redshift distribution are two independent events, we can multiply the *Planck* probability of not being a cluster ($\sim 10\%$) by the probability of having a uniform distribution of galaxy redshifts. If this last is $<50\%$, the total probability that the candidate is not a cluster is $<5\%$. Among these last targets,

¹⁴ See Appendix A in Amodeo et al. (2017) for the conversion from M_{500}^{Pl} to M_{200}^{Pl} .

three have a probability that their redshift distribution is Gaussian of $>95\%$ ($\sim 2\sigma$), and we consider them as confirmed clusters. All three are new confirmations with respect to PSZ2.

Three of the targets that were only detected by one method, though, and one candidate detected with two methods show less definitive results. We discuss these last cluster candidates in more detail below.

PLCK G147.32-16.59 was detected by one method with a high S/N ($S/N \sim 6$), and its redshift distribution has a probability of $\sim 90\%$ of being Gaussian; however, it also has an $\sim 10\%$ probability of not being a cluster. With only 10 confirmed members, its confirmation is not very reliable, but it is more probable that it is a cluster or a group of galaxies than a uniform redshift distribution, and we consider it a confirmed cluster. *XMM-Newton* observations (Planck Collaboration et al. 2013) reveal two substructures in the X-ray surface brightness, indicating that it is undergoing a merger event (see also van Weeren et al. 2014; Mroczkowski et al. 2015). Because of the undergoing merger, we have excluded this cluster from the analysis of the velocity dispersion–mass relation in Amodeo et al. (2017).

PLCK G183.33-36.69 was detected by one method with an $S/N \sim 2$ (*Planck* reliability of $<70\%$), its redshift distribution has a K–S (S–W) probability of $\sim 60\%$ ($\sim 5\%$) to be Gaussian, and a $\sim 1\%$ total probability of not being a cluster. However, we can clearly see the two bright central galaxies in the Gemini image, and the cluster center is close to the border of the Gemini field. It seems to us that this cluster was not well centered enough in the Gemini imaging and spectroscopy to obtain a significant sample to confirm it, even if it has a larger probability to be a cluster or group of galaxies instead of a uniform galaxy distribution. The SZ flux gives a mass of $M_{500}^{\text{Pl}} = 2.3_{-0.9}^{+0.7} \times 10^{14} M_{\odot}$, and its galaxy velocity dispersion is $\sigma_{200} = 842_{-451}^{+297} \text{ km s}^{-1}$. We consider it to be a confirmed cluster, and warn the reader about the larger uncertainty (with respect to most of the remaining sample) in the velocity dispersion measurement and its redshift distribution skewness, which both might indicate an unrelaxed dynamical state. We kept this cluster in our sample in Amodeo et al. (2017) because, due to the large uncertainty on the velocity dispersion measurement, it does not significantly weight on our final results.

PSZ2 G251.13-78.15 was detected by one method with a $S/N \sim 4.8$ (*Planck* reliability of $\sim 90\%$), its redshift distribution has a K–S and an S–W probability of $\sim 60\%$ and $\sim 20\%$, respectively, to be Gaussian, and an $\sim 3\%$ probability of not being a cluster. We consider it as a confirmed cluster, and again notice the larger uncertainty in its confirmation, mass, and velocity dispersion estimates. This is a newly spectroscopically confirmed cluster.

PSZ2 G272.85+48.79 was detected by two methods with an $S/N \sim 5$ (*Planck* reliability of $\sim 92\%$). From the combined Planck and K–S Gaussian probabilities, it has a 90% probability of being a cluster. On the other hand, from the combined Planck and K–S uniform probabilities, it has a 5% probability of not being a cluster. According to our criteria, this is at the limit of being confirmed as a cluster of galaxies. However, we assume it is confirmed, also considering that it is more massive than $10^{14} M_{\odot}$ (e.g., Evrard et al. 2008).

For PSZ2 G352.05-24.01, the redshift obtained from the X-ray analysis is $z = 0.79$ (Planck Collaboration et al. 2013), but we observe galaxies in a wider redshift range. In fact, we can distinguish two structures at $z \sim 0.8$ and $z \sim 0.3$, shown in blue and green, respectively, in Figure 5. Both redshift distributions have a standard deviation of ~ 0.08 , much wider of what is expected for a cluster of galaxies. This target is not a cluster of galaxies, and we have excluded it from the analysis of the velocity dispersion–mass relation in Amodeo et al. (2017).

PSZ2 G085.95+25.23, confirmed at $z = 0.782 \pm 0.010$, is one of the highest redshift confirmed *Planck* clusters.

Newly confirmed clusters are labeled with the sign “+” in Table 3.

4. Spectroscopic Redshift Catalogs

We provide the cluster catalogs as electronic documents, including the following parameters for each cluster galaxy.

1. The galaxy identification number ID.
2. The J2000 right ascension, R.A., in hours.
3. The J2000 declination, decl., in degree.
4. The measured spectroscopic redshift SPECZ.
5. The error in spectroscopic redshift eSPECZ.

An example is shown in Table 5 for PSZ2 G053.44-36.25.

5. Discussion

In the context of the optical identification of *Planck* cluster candidates, our sample, though small, is chosen to have a wide range of mass with the aim of obtaining a statistical calibration of the *Planck* SZ mass estimator. In this section, we compare it with previous *Planck* cluster redshift measurements.

Eight of our targets are in the SDSS DR8 redMaPPer cluster catalogs (Wen et al. 2012; Rykoff et al. 2014). Five of them (PSZ2 G108.71-47.75, PSZ2 G186.99+38.65, PSZ2 G216.62+47.00, PSZ2 G056.93-55.08, and PSZ2 G083.29-31.03) have previous spectroscopic redshift measurements in agreement with our values.

Measurements of galaxy redshifts are available in the SDSS DR14 in seven of our fields. A search within two virial radii from the center of each of our clusters finds spectroscopic catalogs for galaxies in the following clusters ($N_{\text{gal, DR14}}$): PSZ2 G053.44-36.25 (15), PSZ2 G056.93-55.08 (3), PSZ2 G081.00-50.93 (8), PSZ2 G083.29-31.03 (32), PSZ2 G108.71-47.75 (3), PSZ2 G186.99+38.65 (24), PSZ2 G216.62+47.00 (19). We included these redshifts and we recalculated the cluster redshifts and velocity dispersions with the same procedure (see Table 3). The redshift estimates do not change, while the uncertainties are smaller. Velocity dispersions are on average within $(0.28 \pm 0.17)\sigma$ the values obtained with our measurements only, and never above 0.5σ . For the other targets, there are not public spectroscopic redshifts for single galaxies to our knowledge.

The *Planck* collaboration has undertaken two important optical follow-up programs to confirm *Planck* cluster candidates and to measure their redshifts. The first is based on observations with the Russian–Turkish 1.5 m telescope (Planck Collaboration et al. 2015) and provides spectroscopic redshifts for 65 *Planck* clusters. It includes our targets PSZ2 G139.62+24.18, for which they obtain a spectroscopic redshift of 0.268 consistent with our measurement, and PSZ2 G157.43+30.34,

for which they find a photometric redshift of 0.45. Vorobyev et al. (2016) report on additional spectroscopic observations of the latter cluster from the 2.2 m Calar Alto Observatory telescope, obtaining $z = 0.403$ with an error of 1%, consistent with our value of $z = 0.402 \pm 0.006$.

The second program, based on observations with telescopes at the Canary Islands Observatories (Gran Telescopio Canarias, Isaac Newton Telescope, William Herschel Telescope, Telescopio Nazionale Galileo, Nordic Optical Telescope, IAC80 telescope), provided 53 cluster spectroscopic redshifts, and is published in Planck Collaboration et al. (2016b). Again it includes our target PSZ2 G139.62+24.18, for which they measure $z = 0.266$ from 22 spectroscopically confirmed members, consistent with our value of $z = 0.268 \pm 0.005$ obtained from 20 galaxies.

The *Planck* collaboration has also carried out X-ray validation programs with *XMM-Newton* (Planck Collaboration et al. 2011b, 2012, 2013), where redshifts z_{Fe} have been obtained from X-ray spectral fitting of the iron emission line. Targets PSZ2 G250.04+24.14 and PSZ2 G272.85+48.79 are analyzed in Planck Collaboration et al. (2011b), PSZ2 G235.56+23.29 in Planck Collaboration et al. (2012), and PSZ2 G348.43-25.50 and PLCK G147.32-16.59 in Planck Collaboration et al. (2013). In all cases, *XMM-Newton* finds redshifts consistent with our values. Planck Collaboration et al. (2013) also includes the X-ray analysis of PSZ2 G329.48-22.67. They observe a double projected system at redshifts 0.24 and 0.46. In our GMOS analysis, we measure $z = 0.249 \pm 0.003$ based on 16 spectroscopic members, with no detections at higher redshift.

Finally, Planck Collaboration et al. (2013) quote a redshift $z_{\text{Fe}} = 0.77$ for PSZ2 G352.05-24.01. The authors give $z_{\text{Fe}} = 0.12, 0.40$ as other possible solutions to the spectral fitting, but these are excluded from the comparison between the X-ray and SZ properties of the source (Y_X/Y_{500}). We observe a sparse galaxy distribution, with two (small) peaks with more than five galaxies, one with six galaxies at $z = 0.798 \pm 0.021$ and the other with 11 at $z = 0.334 \pm 0.025$. However, these large dispersions ($\sim 3500 \text{ km s}^{-1}$ at $z = 0.798$ and $\sim 5600 \text{ km s}^{-1}$ at $z = 0.334$) do not confirm clusters of galaxies, and we do not consider this target as a confirmed cluster.

In conclusion, six of our clusters have spectroscopic redshifts from previous optical studies, seven have redshift measurements from X-ray spectral fitting. Their velocity dispersions are published in this paper for the first time. For the remaining seven clusters, spectroscopic redshifts and velocity dispersions are published in this paper for the first time.

6. Conclusions

This article presents spectroscopic redshifts and velocity dispersions for 20 *Planck* SZ clusters. We spectroscopically confirm 19 clusters with Gemini-North and Gemini-South/GMOS, 6 of which were spectroscopically confirmed in this paper for the first time. We also confirm and measure the redshift and velocity dispersion of the *Planck* cluster PSZ2 G085.95+25.23 with Keck/LRIS spectroscopy, measuring a mean redshift of $z = 0.782 \pm 0.010$, one of the *Planck*'s highest redshift confirmed clusters. Eighteen of our clusters are

included in the last released *Planck* SZ source catalog, PSZ2 (Planck Collaboration et al. 2016a).

We provide online catalogs for each cluster spectroscopic member redshift (an example is shown in Table 5).

In a companion paper (Amodeo et al. 2017), we use the cluster galaxy velocity dispersions to measure the *Planck* mass bias, and to constrain the cluster velocity bias.

Based on observations obtained at the Gemini Observatory (Programs GN-2011A-Q-119, GN-2011B-Q-41, and GS-2012A-Q-77; P.I. J.G. Bartlett), which is operated by the Association of Universities for Research in Astronomy, Inc., under a cooperative agreement with the NSF on behalf of the Gemini partnership: the National Science Foundation (United States), the National Research Council (Canada), CONICYT (Chile), Ministerio de Ciencia, Tecnología e Innovación Productiva (Argentina), and Ministério da Ciência, Tecnologia e Inovação (Brazil). Supported by the Gemini Observatory, which is operated by the Association of Universities for Research in Astronomy, Inc., on behalf of the international Gemini partnership of Argentina, Brazil, Canada, Chile, and the United States of America. This material is based upon work supported by AURA through the National Science Foundation under AURA Cooperative Agreement AST 0132798 as amended. We are pleased to acknowledge the Palomar Observatory staff for their enthusiastic and excellent support. Part of the data presented herein were obtained at the W. M. Keck Observatory, which is operated as a scientific partnership among the California Institute of Technology, the University of California and the National Aeronautics and Space Administration. The Observatory was made possible by the generous financial support of the W. M. Keck Foundation. The authors wish to recognize and acknowledge the very significant cultural role and reverence that the summit of Maunakea has always had within the indigenous Hawaiian community. We are most fortunate to have the opportunity to conduct observations from this mountain. We thank the P.I. of the Keck observations, Fiona Harrison, and Mislav Baloković and George Lansbury for participating in the Keck observations. J.G.B. and S.M. acknowledge financial support from the *Institut Universitaire de France (IUF)* as senior members. Part of the work of J.G.B., C.L., and D.S. was carried out at the Jet Propulsion Laboratory, California Institute of Technology, under a contract with NASA. S.M.'s research was supported by an appointment to the NASA Postdoctoral Program at the Jet Propulsion Laboratory, administered by Universities Space Research Association under contract with NASA. We thank the referee for useful comments that helped improve the presentation of this work, and Joanne Cohn for useful discussion.

Facilities: Gemini:South, Gemini:North, Palomar:Hale, Keck:I (LRIS), Planck.

Appendix A

Planck Clusters Observed with the Palomar Telescope

In Table 4, we present the sample of clusters observed at the Palomar telescope, and discussed in Section 2.3.

Table 4
Planck Clusters Observed with the Palomar Telescope

Name	R.A. (degree)	Decl. (degree)	Filter	Instrument	Run
PSZ2 G019.12+31.23	249.1420	3.1528	g', i'	LFC	2011A
PLCK G024.20+58.78	225.5920	18.6586	g', i'	LFC	2011A
PLCK G030.89+42.25	243.3310	16.4481	g', i', r'	LFC	2011A
PSZ2 G066.41+27.03	269.2120	40.1156	g', i', r'	LFC	2011A
PLCK G071.59-63.16	351.9458	-8.9647	i'	LFC	2012B
PSZ2 G074.08-54.68	347.0917	-1.9106	i'	LFC	2012B
PSZ2 G078.67+20.06	282.9920	49.0257	g', i'	LFC	2011A
PSZ2 G082.31-67.00	357.9500	-8.9647	i'	LFC	2012B
PSZ2 G086.93+53.18	228.4790	52.7775	g', i'	LFC	2011A
PLCK G087.67+23.00	282.3250	57.8956	g', i'	LFC	2011A
PSZ2 G091.83+26.11	277.8080	62.2317	i', r'	LFC	2011A
PSZ2 G094.56+51.03	227.0960	57.8706	g', i', r'	LFC	2011A
PLCK G096.88+24.22	284.0750	66.3819	g', i'	LFC	2011A
PSZ2 G107.83-45.45	1.8753	16.1423	g', r', J, K	LFC, WIRC	2010B
PSZ1 G108.52+32.30	256.9920	76.4697	g', r', i'	LFC	2011A
PLCK G109.35+64.36	202.3080	51.7589	g', i'	LFC	2011A
PLCK G113.07-74.37	10.1610	-11.7062	r', J, K	LFC, WIRC	2010B
PLCK G113.66+70.59	197.2970	46.2171	g', i'	LFC	2011A
PLCK G114.92-20.06	2.6792	42.1783	i'	LFC	2012B
PLCK G116.80-25.18	5.8708	37.3600	i'	LFC	2012B
PLCK G117.14-26.47	6.4417	36.1117	i'	LFC	2012B
PSZ1 G121.09+57.02	194.8400	60.0897	g', i', r'	LFC	2011A
PSZ1 G129.07-24.12	20.0000	38.4531	g', i'	LFC	2011B
PSZ2 G134.26-44.28	21.3542	17.8808	g', i'	LFC	2011B
PSZ2 G138.11+42.06	157.0542	70.6081	g', i', r', J, K	LFC, WIRC	2010B, 2011A, 2011B
PSZ2 G139.62+24.18	95.4912	74.7042	g', i', r', J, K	LFC, WIRC	2010B, 2011A
PLCK G142.35+17.59	78.8752	69.7009	g', J	LFC, WIRC	2010B, 2011A
PLCK G147.32-16.59 ^a	44.1000	40.2911	g', i', r'	LFC	2011B
PSZ2 G157.43+30.34	117.2208	59.6944	g', i', r', J, K	LFC, WIRC	2010B, 2011A, 2011B
PLCK G159.41-62.64	28.7625	-4.3600	g'	LFC	2011B
PSZ2 G171.98-40.66	48.2307	8.3805	g', r', K	LFC, WIRC	2010B
PSZ2 G172.93+21.34	106.8920	44.3050	r'	LFC	2011A
PLCK G183.33-36.69	57.2936	4.5974	g', J, K	LFC, WIRC	2010B
PSZ2 G183.30+34.98	127.4042	38.4325	g', i'	LFC	2011B
PLCK G184.34+29.07	120.3380	36.4269	g', i'	LFC	2011A
PSZ2 G193.31-46.13	53.9592	-6.9853	g', r', J, K	LFC, WIRC	2010B
PSZ2 G193.63+54.85	152.5750	32.8472	i'	LFC	2011B
PSZ2 G194.68-49.76	51.3625	-9.6181	i'	LFC	2012B
PSZ2 G196.65-45.51	55.7583	-8.7039	i'	LFC	2012B
PLCK G196.72+23.27	118.2330	24.2689	g', i'	LFC	2011A
PLCK G198.13-24.68	74.3315	0.9310	r', J, K	LFC, WIRC	2010B
PSZ2 G198.90+18.16	113.4333	20.3083	g', i'	LFC	2011B
PLCK G201.89+32.14	128.5292	22.7656	g', i'	LFC	2011B
PSZ1 G203.88+62.50	161.7580	27.9606	i'	LFC	2011A
PSZ2 G204.24+14.51	112.1375	14.1283	g', i'	LFC	2012B
PSZ2 G205.90+73.76	174.5833	27.9186	g', i'	LFC	2011B
PLCK G211.37+49.36	148.5583	21.2128	g', i'	LFC	2011B
PSZ2 G212.44+63.19	163.2292	24.2128	g', i'	LFC	2011B
PLCK G214.57+36.96	137.1950	14.7084	r'	LFC	2011A
PLCK G219.13+52.94	153.8580	17.8178	g', i', r', J, K	LFC, WIRC	2010B, 2011A
PSZ1 G223.80+58.50	160.3292	17.5111	g', i'	LFC	2011B
PLCK G247.33+63.53	170.8870	10.6117	g', i'	LFC	2011A
PSZ1 G263.75+53.85	170.9875	-2.2161	g', i'	LFC	2011B

Note. Clusters are named after their PSZ2 or PSZ1 ID, when available. When it is not available, we use the prefix “PLCK” followed by a notation in galactic coordinates similar to that used in the PSZ2 paper.

^a Target PLCK G147.32-16.59 is confirmed in the *XMM-Newton* cluster validation (Planck Collaboration et al. 2013), but it is not included in the two *Planck* catalogs of SZ sources released so far.

Appendix B

Redshift Histograms, Optical Images, and SZ Maps

We present redshift histograms, optical images, and SZ maps of clusters observed at Gemini-N (Figure 4), Gemini-S (Figure 5), and Keck (Figure 6).

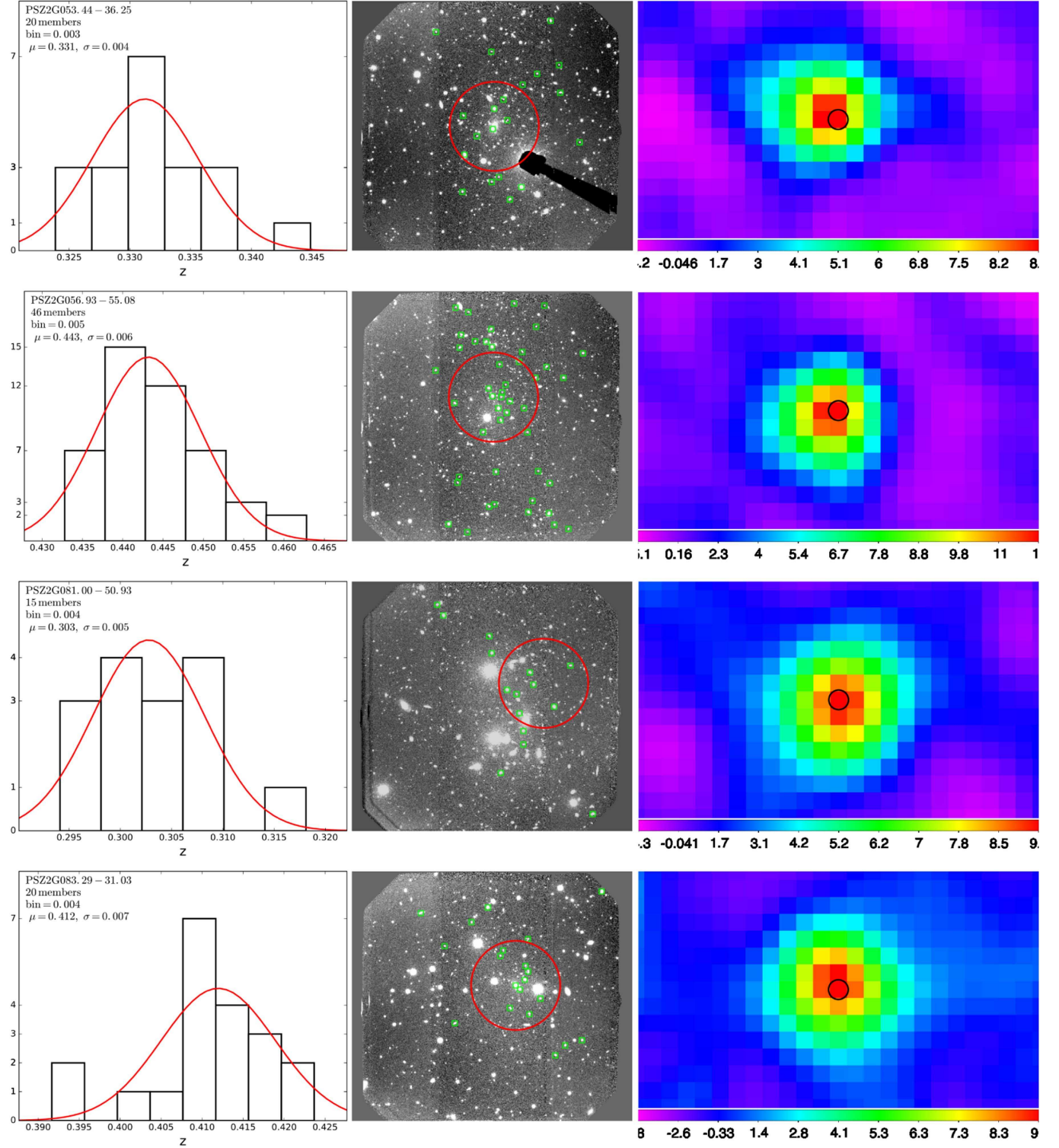


Figure 4. Redshift histograms (left), optical images (middle), and SZ maps in signal-to-noise units (right) of clusters in the northern sample. The red curve in the histograms is a Gaussian fit with mean (μ) and standard deviation (σ) indicated in the legends, calculated for the redshift distribution using the biweight method. We also indicate the number of members in each cluster and the size of the redshift bins. The red (black) circles in the images enclose a circle of radius 1 arcmin around the optical (SZ) center of the clusters, while the confirmed member galaxies are shown by green squares.

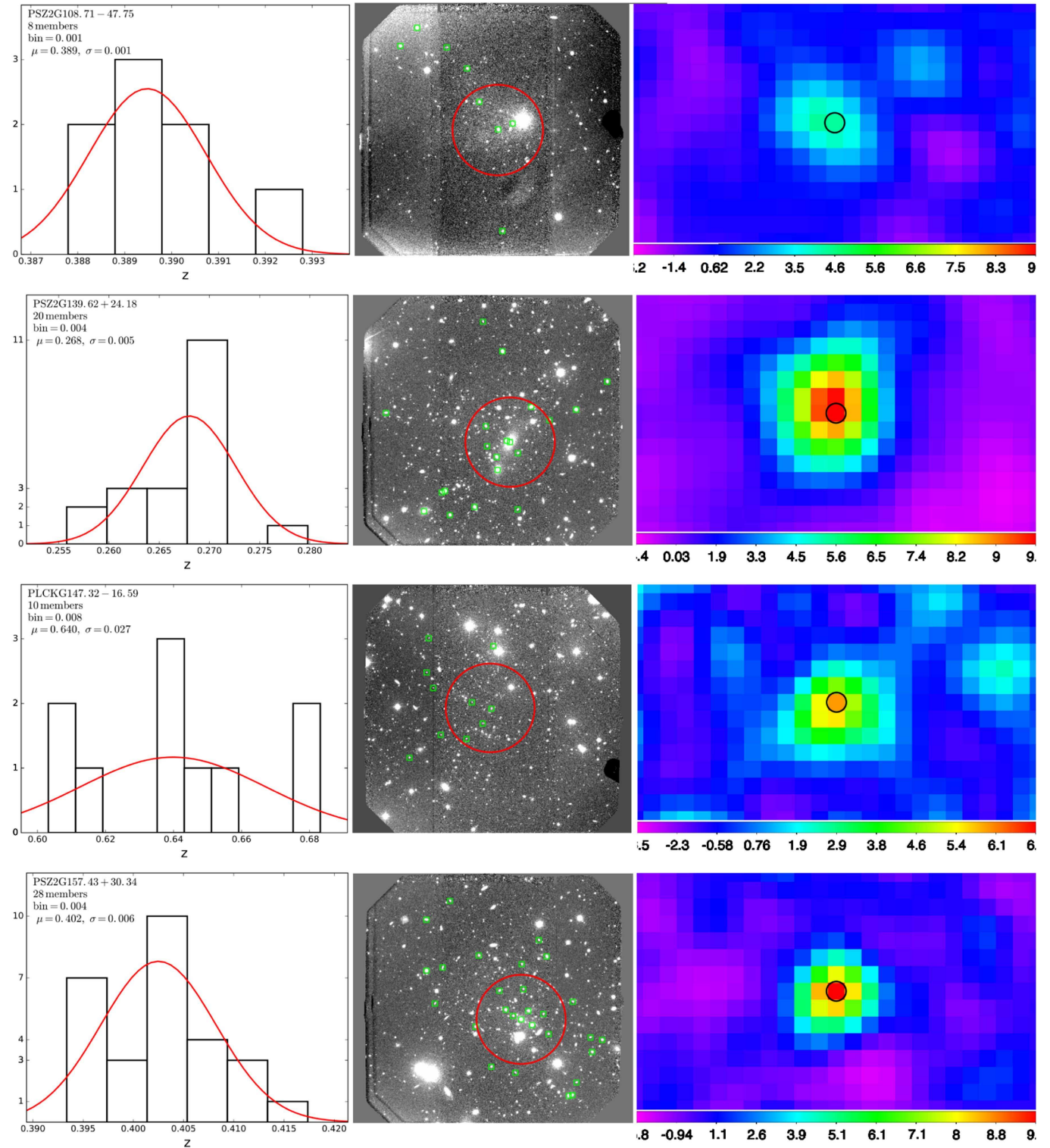


Figure 4. (Continued.)

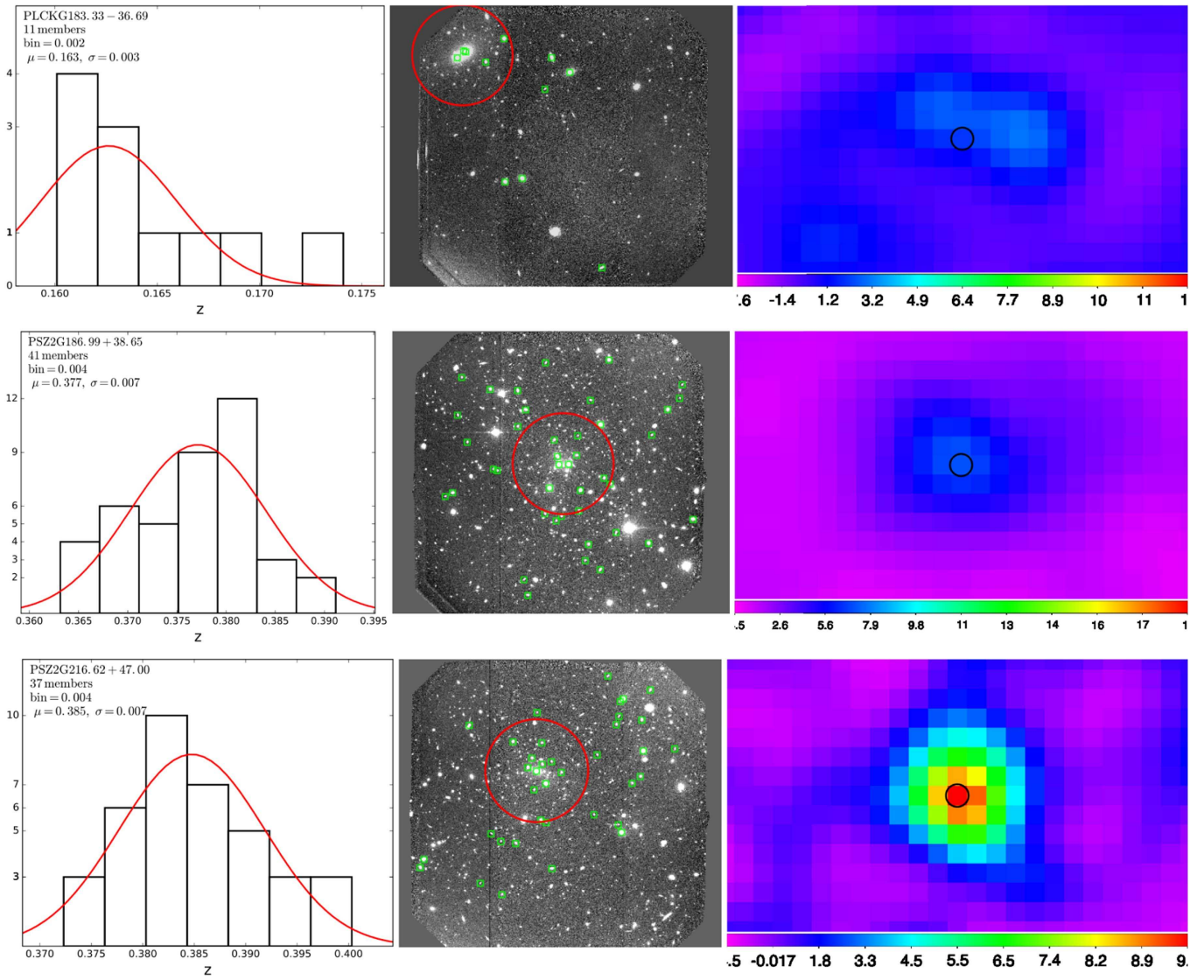


Figure 4. (Continued.)

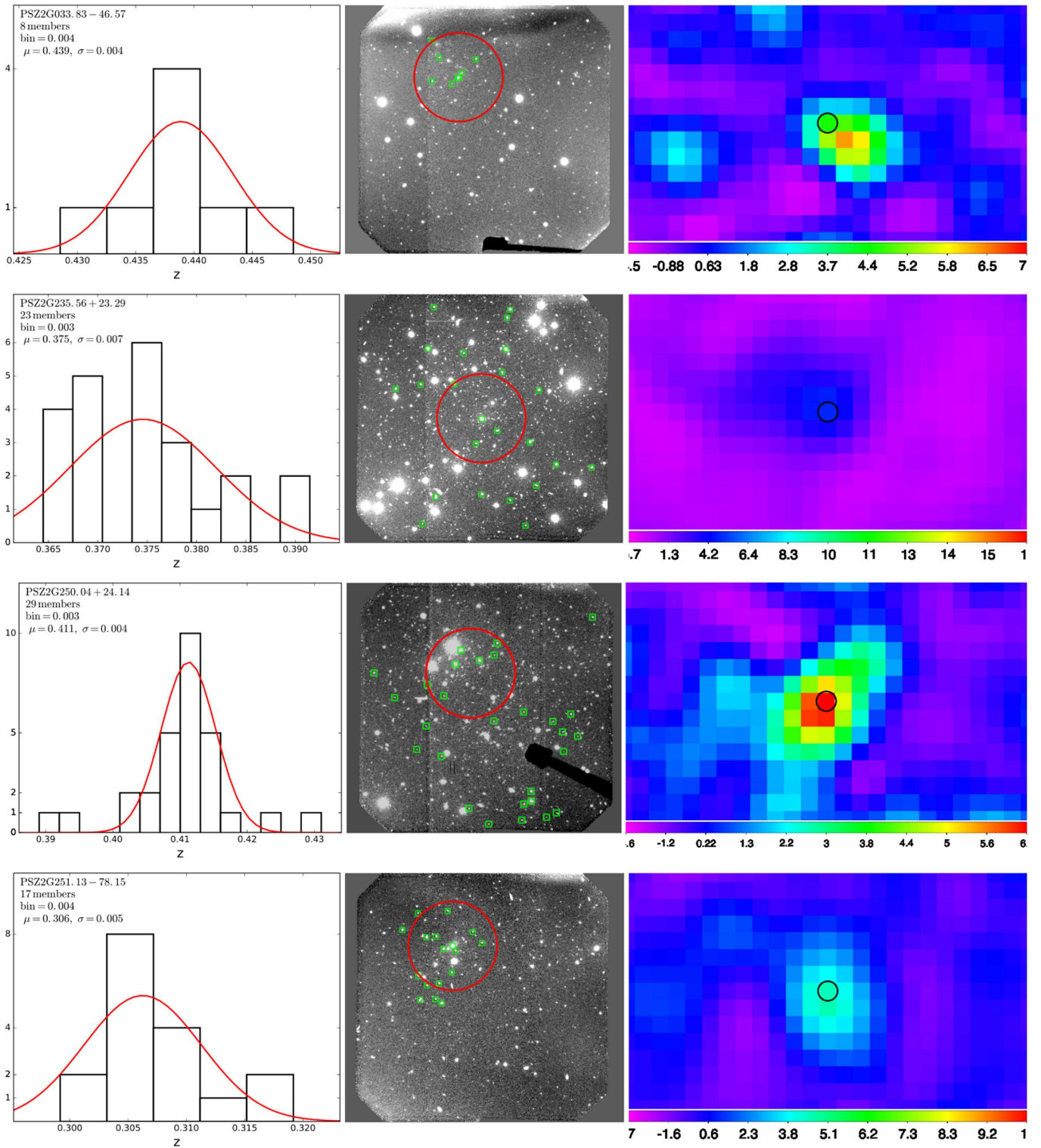


Figure 5. Redshift histograms, optical images, and SZ maps of clusters in the southern sample. Symbols are the same as those in Figure 4. For PSZ2 G352.05-24.01, we know only the coordinates of the X-ray center, marked with a red cross.

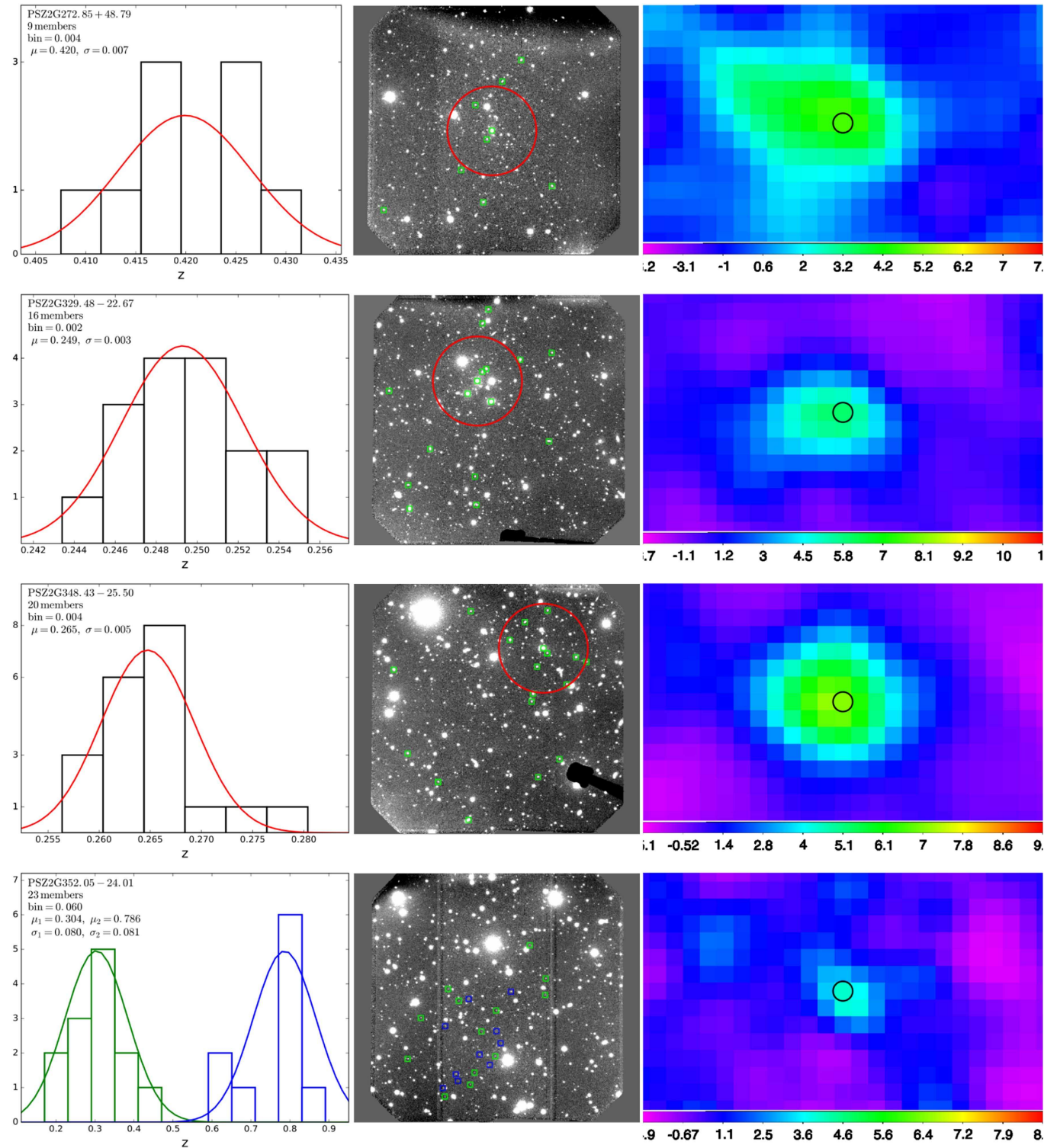


Figure 5. (Continued.)

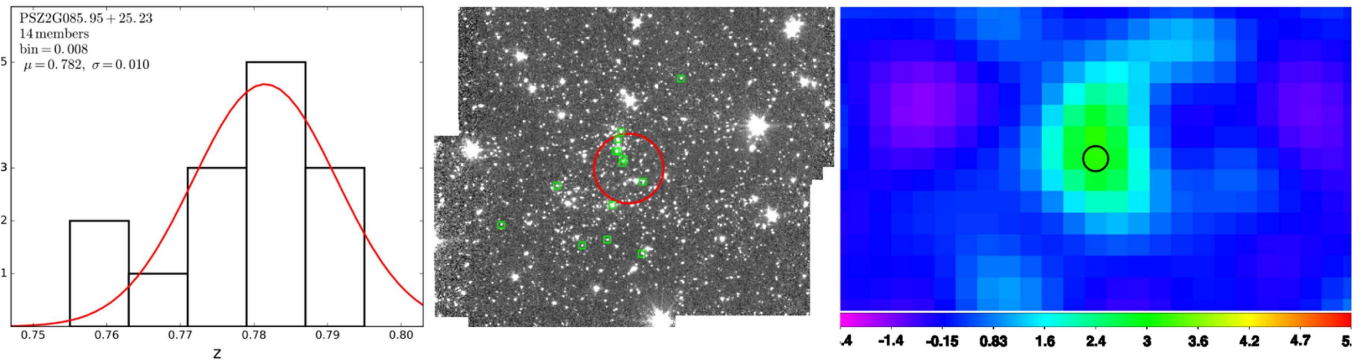


Figure 6. Redshift histogram, IRAC image, and SZ map of PSZ2 G085.95+25.23 observed at the Keck telescope. Symbols are the same as those in Figure 4.

Appendix C Spectroscopic Redshift Catalogs

In the online version of the journal, we provide catalogs of galaxies detected for our spectroscopic sample of 20 clusters, in machine-readable form. We show an example in Table 5 for PSZ2 G053.44-36.25.

Table 5
The Catalog of Galaxies Detected for Cluster PSZ2 G053.44-36.25

ID	R.A. (hr)	Decl. (degree)	SPECZ	eSPECZ
1	21.58816	-1.08456	0.3306	0.0002
2	21.58506	-1.06186	0.3324	0.0001
3	21.58748	-1.05329	0.3363	0.0001
4	21.58530	-1.08879	0.3304	0.0003
5	21.58638	-1.05156	0.3361	0.0003
6	21.58564	-1.06893	0.3258	0.0002
7	21.58671	-1.05585	0.3359	0.0001
8	21.58600	-1.06488	0.3301	0.0002
9	21.58632	-1.02193	0.3344	0.0003
10	21.58714	-1.04561	0.3277	0.0002
11	21.58603	-1.02659	0.3345	0.0002
12	21.58648	-1.05931	0.3239	0.0002
13	21.58509	-1.07221	0.3316	0.0002
14	21.58678	-1.07722	0.3322	0.0003
15	21.58659	-1.03027	0.3250	0.0003
16	21.58745	-1.03873	0.3335	0.0001
17	21.58458	-1.04332	0.3307	0.0002
18	21.58804	-1.03449	0.3891	0.0006
19	21.58677	-1.02851	0.3424	0.0004
20	21.58674	-1.04831	0.3276	0.0002

Note. The full spectroscopic catalogs for all 20 clusters are available in the online version of the journal.

(This table is available in its entirety in machine-readable form.)

ORCID iDs

Simona Mei <https://orcid.org/0000-0002-2849-559X>

Daniel Stern <https://orcid.org/0000-0003-2686-9241>
Ranga-Ram Chary <https://orcid.org/0000-0001-7583-0621>

References

- Allen, S. W., Evrard, A. E., & Mantz, A. B. 2011, *ARA&A*, 49, 409
Amodeo, S., Mei, S., Stanford, S. A., et al. 2017, *ApJ*, 844, 101
Beers, T. C., Flynn, K., & Gebhardt, K. 1990, *AJ*, 100, 32
Birkinshaw, M. 1999, *PhR*, 310, 97
Bruzual, G., & Charlot, S. 2003, *MNRAS*, 344, 1000
Carlstrom, J. E., Holder, G. P., & Reese, E. D. 2002, *ARA&A*, 40, 643
Evrard, A. E., Bialek, J., Busha, M., et al. 2008, *ApJ*, 672, 122
Fasano, G., & Franceschini, A. 1987, *MNRAS*, 225, 155
Girardi, M., Biviano, A., Giuricin, G., Mardirossian, F., & Mezzetti, M. 1993, *ApJ*, 404, 38
Girardi, M., Demarco, R., Rosati, P., & Borgani, S. 2005, *A&A*, 442, 29
Gladders, M. D., & Yee, H. K. C. 2000, *AJ*, 120, 2148
Licitra, R., Mei, S., Raichoor, A., et al. 2016a, *ApJ*, 829, 44
Licitra, R., Mei, S., Raichoor, A., Erben, T., & Hildebrandt, H. 2016b, *MNRAS*, 455, 3020
Massey, P., & Gronwall, C. 1990, *ApJ*, 358, 344
Mei, S., Holden, B. P., Blakeslee, J. P., et al. 2009, *ApJ*, 690, 42
Melin, J.-B., Bartlett, J. G., & Delabrouille, J. 2006, *A&A*, 459, 341
Mroczkowski, T., Kovács, A., Bulbul, E., et al. 2015, *ApJL*, 808, L6
Oke, J. B., Cohen, J. G., Carr, M., et al. 1995, *PASP*, 107, 375
Planck Collaboration, Ade, P. A. R., Aghanim, N., et al. 2011a, *A&A*, 536, A8
Planck Collaboration, Ade, P. A. R., Aghanim, N., et al. 2013, *A&A*, 550, A130
Planck Collaboration, Ade, P. A. R., Aghanim, N., et al. 2014, *A&A*, 571, A29
Planck Collaboration, Ade, P. A. R., Aghanim, N., et al. 2015, *A&A*, 582, A29
Planck Collaboration, Ade, P. A. R., Aghanim, N., et al. 2016a, *A&A*, 594, A27
Planck Collaboration, Ade, P. A. R., Aghanim, N., et al. 2016b, *A&A*, 586, A139
Planck Collaboration, Ade, P. A. R., Aghanim, N., et al. 2016c, *A&A*, 594, A13
Planck Collaboration, Aghanim, N., Arnaud, M., et al. 2011b, *A&A*, 536, A9
Planck Collaboration, Aghanim, N., Arnaud, M., et al. 2012, *A&A*, 543, A102
Rykoff, E. S., Rozo, E., Busha, M. T., et al. 2014, *ApJ*, 785, 104
Shapiro, S. S., & Wilk, M. B. 1965, *Biometrika*, 52, 591
Sunyaev, R. A., & Zeldovich, Y. B. 1970, *Ap&SS*, 7, 3
Truemper, J. 1993, *Sci*, 260, 1769
Valdes, F. G., Campusano, L. E., Velasquez, J. D., & Stetson, P. B. 1995, *PASP*, 107, 1119
van Weeren, R. J., Intema, H. T., Lal, D. V., et al. 2014, *ApJL*, 781, L32
Vorobyev, V. S., Burenin, R. A., Bikmaev, I. F., et al. 2016, *AstL*, 42, 63
Wen, Z. L., Han, J. L., & Liu, F. S. 2012, *ApJS*, 199, 34
White, M., Cohn, J. D., & Smit, R. 2010, *MNRAS*, 408, 1818
York, D. G., Adelman, J., Anderson, J. E., Jr., et al. 2000, *AJ*, 120, 1579

The relation between mass and concentration in X-ray galaxy clusters at high redshift

S. Amodeo^{1,*}, S. Ettori^{2,3}, R. Capasso^{1,4,5}, and M. Sereno^{2,1}

¹ Dipartimento di Fisica e Astronomia, Università di Bologna, viale Berti Pichat 6/2, 40127 Bologna, Italy
e-mail: stefania.amodeo@obspm.fr

² INAF, Osservatorio Astronomico di Bologna, via Ranzani 1, 40127 Bologna, Italy

³ INFN, Sezione di Bologna, viale Berti Pichat 6/2, 40127 Bologna, Italy

⁴ Faculty of Physics, Ludwig-Maximilians-Universität, Scheinerstr. 1, 81679 München, Germany

⁵ Excellence Cluster Universe, Boltzmannstr. 2, 85748 Garching, Germany

Received 23 October 2015 / Accepted 5 April 2016

ABSTRACT

Context. Galaxy clusters are the most recent, gravitationally bound products of the hierarchical mass accretion over cosmological scales. How the mass is concentrated is predicted to correlate with the total mass in the halo of the cluster, wherein systems at higher mass are less concentrated at given redshift and, for any given mass, systems with lower concentration are found at higher redshifts.

Aims. Through a spatial and spectral X-ray analysis, we reconstruct the total mass profile of 47 galaxy clusters observed with *Chandra* in the redshift range $0.4 < z < 1.2$, which we selected to exclude major mergers, to investigate the relation between the mass and dark matter concentration and the evolution of this relation with redshift. This sample is the largest investigated so far at $z > 0.4$, and is well suited to providing the first constraint on the concentration–mass relation at $z > 0.7$ from X-ray analysis.

Methods. Under the assumption that the distribution of the X-ray emitting gas is spherically symmetric and in the hydrostatic equilibrium with the underlined gravitational potential, we combine the deprojected gas density and spectral temperature profiles through the hydrostatic equilibrium equation to recover the parameters that describe a Navarro-Frenk-White total mass distribution. The comparison with results from weak-lensing analysis reveals a very good agreement both for masses and concentrations. The uncertainties are however too large to make any robust conclusion about the hydrostatic bias of these systems.

Results. The distribution of concentrations is well approximated by a log-normal function in all the mass and redshift ranges investigated. The relation is well described by the form $c \propto M^B(1+z)^C$ with $B = -0.50 \pm 0.20$, $C = 0.12 \pm 0.61$ (at 68.3% confidence). This relation is slightly steeper than that predicted by numerical simulations ($B \sim -0.1$) and does not show any evident redshift evolution. We obtain the first constraints on the properties of the concentration–mass relation at $z > 0.7$ from X-ray data, showing a reasonable good agreement with recent numerical predictions.

Key words. galaxies: clusters: general – intergalactic medium – X-rays: galaxies – cosmology: observations – dark matter

1. Introduction

Within the standard cosmological model, structure formation takes place from the gravitational collapse of small perturbations in a quasi-homogeneous Universe dominated by cold dark matter (CDM). The collapse proceeds from smaller to larger scales giving rise to a hierarchical clustering of cosmic structures. In this framework, galaxy clusters, as they are the largest nearly virialised collapsed objects in the observable Universe, are also the last to form. Therefore, they are fundamental tools for understanding the formation and evolution of cosmic structures.

Numerical N -body simulations predict that dark matter halos have a universal density profile characterised by two parameters: the scale radius r_s , defined as the radius at which the logarithmic density slope is -2 , and the concentration c , defined as the ratio between R_{200}^1 and r_s (Navarro et al. 1997, hereafter NFW). Because of the hierarchical nature of structure formation (low-mass objects form earlier than high-mass objects) and the

fact that collapsed objects retain information on the background density at the time of their formation (the background average matter density was higher in the past), concentration and mass are related so that systems with higher masses are less concentrated and, at a given mass, lower concentrations are expected at higher redshifts (e.g. Muñoz-Cuartas et al. 2011). Moreover, the properties of the background Universe depend on the set of cosmological parameters adopted. Models with lower matter density and lower normalisation of the linear power spectrum result in a later assembly redshift, so less concentrated halos are expected at a given mass. Therefore, the $c(M, z)$ relation contains a wealth of cosmological information. Several works have been performed to characterise this relation, both numerically and observationally, but there are tensions between them. Numerical simulations by Dolag et al. (2004), Duffy et al. (2008), Bhattacharya et al. (2013), De Boni et al. (2013), Ludlow et al. (2014), and Dutton & Macciò (2014) indicate that concentration and mass are anti-correlated for all the mass ranges and redshifts investigated with a mass dependence that is slightly reduced at larger redshift. Observations of galaxy clusters at low redshift confirm the expected anti-correlation between c and M , but they generally find a steeper slope and a higher

* Present address: GEPI, Paris Observatory, 77 Av. Denfert-Rochereau, 75014 Paris, France.

¹ R_{200} is the radius within which the cluster density is 200 times the critical density of the Universe at the cluster's redshift.

normalisation compared to the theoretical relation (Buote et al. 2007; Schmidt & Allen 2007; Ettori et al. 2010; Merten et al. 2015). Whether this discrepancy is due to observational selection biases (e.g. Meneghetti et al. 2014; Sereno et al. 2015) or to the lack of some fundamental physics in numerical models is still an open question. Both simulations (e.g. De Boni et al. 2013) and observations (Ettori et al. 2010) agree about the influence of the dynamical state of a cluster on its concentration; that is, more relaxed systems are more concentrated at a fixed mass. A different trend emerges from simulations by Prada et al. (2012) and Klypin et al. (2014). They predict that at high redshifts the $c(M)$ relation has a plateau and an upturn at the typical masses of galaxy clusters. However, as shown in Ludlow et al. (2012; see also Correa et al. 2015), the plateau and the upturn disappear when the relaxed halos are the only ones considered. Properties of observed mass-concentration relations are strongly sample dependent (Sereno et al. 2015). The predicted slope in signal-selected samples can be much steeper than that of the underlying population characterising dark matter-only clusters. Over-concentrated clusters can be preferentially included and this effect is more prominent at the low-mass end. Sereno et al. (2015) found this trend both in the X-ray selected samples Cluster Lensing And Supernova survey with *Hubble* (CLASH; Postman et al. 2012) and Local Cluster Substructure Survey (LOCUSS; Okabe et al. 2010) and in the lensing selected sample Sloan Giant Arcs Survey (SGAS; Hennawi et al. 2008). Statistical and selection biases in observed relations are then to be carefully considered when compared with predictions of the Λ CDM model (Meneghetti et al. 2014). Among the methods used to characterise the $c(M)$ relation, X-ray observations are found to be rather successful since galaxy clusters have a well-resolved, extended emission with a total luminosity that is proportional to the square of the gas density.

In this work, we perform spatial and spectral analysis for a sample of 47 galaxy clusters observed with *Chandra* in the redshift range $0.4 < z < 1.2$, which we selected to exclude major mergers with the aim to (1) reconstruct their total mass profile by assuming a spherical symmetry for the intracluster medium (ICM) distribution and hydrostatic equilibrium between the ICM and the gravitational potential of each cluster; and (2) investigate the relation between their mass and concentration and its evolution with redshift. We consider the largest sample investigated so far at $z > 0.4$ with the additional purpose of probing the $c(M)$ relation at $z > 0.7$ for the first time using X-ray data.

The paper is organised as follows: in Sect. 2, we present the sample of *Chandra* observations selected for the analysis; in Sects. 3 and 4, we describe the data analysis and the method used to reconstruct the clusters mass profiles, respectively; in Sect. 5, we investigate our $c(M, z)$ relation and its redshift evolution. We discuss the properties of the sample and its representativeness in Sect. 6 and we draw our conclusions in Sect. 7. We assume a flat Λ CDM cosmology with $\Omega_m = 0.3$, $\Omega_\Lambda = 0.7$, $H_0 = 70 \text{ km s}^{-1} \text{ Mpc}^{-1}$ and $h(z) = \sqrt{\Omega_m(1+z)^3 + \Omega_\Lambda}$. All quoted errors are 68.3% (1σ) confidence level, unless otherwise stated.

2. The dataset

We retrieved all observations of galaxy clusters with redshift $z \geq 0.4$ available at 2 March 2014 from the *Chandra* public archive. We excluded those galaxy clusters with exposure time shorter than 20 ks in order to have sufficient X-ray count statistics, in particular, for spectral analysis. We also excluded galaxy

clusters that to a visual inspection showed evidence of dynamic activity (e.g. presence of major substructures). This restriction minimises the systematic scatter in the mass estimate, since the higher the degree of regular morphology in the X-ray image, the more the cluster is expected to be dynamical relaxed and the more robust is the assumption of the hydrostatic equilibrium of the ICM in the cluster potential well (e.g. Rasia et al. 2006; Poole et al. 2006; Mahdavi et al. 2013; Nelson et al. 2014). Another selection criterion is related to the choice of adopting a NFW as functional form of the cluster gravitational profile, which has two free parameters (scale radius r_s and concentration c). Considering that our procedure to reconstruct the mass profile requires independent spectral measurements of the gas temperatures (see Sect. 4), we need a number of independent radial bins that is larger than the number of mass modelling parameters ($=2$). Therefore, we used only the targets for which we could measure the temperature in at least three independent bins. The final sample is then composed of 47 galaxy clusters spanning a redshift range $0.4 < z < 1.2$, as listed in Table 1.

The acquired data are reduced using the CIAO 4.7 software (*Chandra* Interactive Analysis of Observations, Fruscione et al. 2006) and the calibration database CALDB 4.6.5 (December 2014 release²). This procedure includes a filter for the good time intervals associated with each observation and a correction for the charge transfer inefficiency. It removes photons detected in bad CCD columns and pixels, it computes calibrated photon energies by applying ACIS gain maps and it corrects for their time dependence. Moreover, it examines the background light curves during each observation to detect and remove flaring episodes. We identify bright point sources using the wavdetect algorithm by Vikhlinin et al. (1998), check the results by visual inspection, mask all the detected point sources and exclude them from the following analysis.

3. Spatial and spectral analysis

Obtaining good brightness and temperature profiles is crucial for the quality of the mass estimates. This strongly depends on the quantity and quality of data obtained for each observation, namely the number of counts measured for the observed target and the fraction of counts on the background.

We extract surface brightness radial profiles from the images in the [0.7–2] keV band by constructing a set of circular annuli around the X-ray emission peak, each one containing at least 100 net source counts. The background counts are estimated from local regions of the same exposure that are free from source emissions (on the same chip as the source region or on another chip of the same type used in the observation). Following this criterion, we manually select from two to four background regions for each cluster. The surface brightness profile is then extracted over an area where the signal-to-noise ratio is always larger than 2, up to the radius $R_{\text{out}}^{\text{spat}}$. In Table 1, we quote the number of counts measured for each target in the [0.7–2] keV band, the number of radial bins obtained to sample the surface brightness profile, and $R_{\text{out}}^{\text{spat}}$.

For the spectral analysis, we use the CIAO *specextract* tool to extract the source and background spectra and to construct the redistribution matrix files (RMF) and the ancillary response files (ARF) for each annulus. The RMF associates the appropriate photon energy with each instrument channel, while the ARF includes information on the effective area, the

² <http://cxc.harvard.edu/caldb/>

Table 1. Sample of the galaxy clusters analysed in this work.

Cluster	z	Detector	Exposure [ks]	RA [J2000]	Dec [J2000]	tot cts	$R_{\text{out}}^{\text{spat}}$ [kpc]	$n_{\text{bin}}S_b$	$R_{\text{out}}^{\text{spec}}$ [kpc]	$n_{\text{bin}}T$
MACS J0159.8-0849	0.405	ACIS-I	29.1	01 59 49.50	-08 49 59.3	20 250	1130	56	786	13
MACS J2228.5+2037	0.412	ACIS-I	16.5	22 28 32.41	+20 37 30.5	9234	1511	27	680	5
MS1621.5+2640	0.426	ACIS-I	27.5	16 23 35.40	+26 34 11.2	9277	1109	20	856	5
MACS J1206.2-0848	0.440	ACIS-I	21.1	12 06 12.38	-08 48 07.4	10 559	1131	29	516	5
MACS J2243.3-0935	0.447	ACIS-I	18.5	22 43 21.57	-09 35 42.4	9432	1305	31	537	5
MACS J0329.7-0211	0.450	ACIS-I	28.4	03 29 41.40	-02 11 44.4	12 870	950	34	660	8
RXJ 1347.5-1145	0.451	ACIS-I	29.2	13 47 30.87	-11 45 09.9	29 013	1266	66	829	10
V1701+6414	0.453	ACIS-I	31.1	17 01 23.41	+64 14 11.5	9841	892	15	633	6
MACS J1621.6+3810	0.465	ACIS-I	29.9	16 21 24.69	+38 10 08.6	11 048	794	22	471	6
CL0522-3624	0.472	ACIS-I	26.4	05 22 15.29	-36 25 02.7	6871	587	16	440	3
MACS J1311.0-0310	0.494	ACIS-I	44.5	13 11 01.87	-03 10 39.8	11 297	634	25	381	6
MACS J2214.9-1400	0.503	ACIS-I	15.4	22 14 57.48	-14 00 09.6	7837	1318	19	872	5
MACS J0911.2+1746	0.505	ACIS-I	23.0	09 11 10.61	+17 46 30.9	4220	1283	16	904	8
MACS J0257.1-2326	0.505	ACIS-I	17.0	02 57 09.13	-23 26 04.3	3832	1389	17	478	8
V1525+0958	0.516	ACIS-I	28.2	15 24 40.04	+09 57 48.9	3613	575	8	435	4
MS0015.9+1609	0.541	ACIS-I	31.0	00 18 33.36	+16 26 12.6	9652	1375	41	913	9
CL0848.6+4453	0.543	ACIS-I	125.2	08 48 47.73	+44 56 13.9	13 613	300	5	282	3
MACS J1423.8+2404	0.543	ACIS-S	105.4	14 23 47.90	+24 04 42.2	35 182	899	33	603	10
MACS J1149.5+2223	0.544	ACIS-I	51.4	11 49 35.52	+22 23 52.7	23 253	1470	26	875	8
MACS J0717.5+3745	0.546	ACIS-I	74.6	07 17 31.22	+37 45 22.6	34 326	1389	62	1090	21
CL1117+1744	0.548	ACIS-I	37.5	11 17 29.89	+17 44 52.1	7098	520	8	500	3
MS0451.6-0305	0.550	ACIS-S	37.0	04 54 11.04	-03 00 57.8	18 100	955	33	486	6
MS2053.7-0449	0.583	ACIS-I	35.0	20 56 21.12	-04 37 48.4	5428	463	11	293	3
MACS J2129.4-0741	0.589	ACIS-I	18.0	21 29 25.64	-07 41 32.0	6226	1055	13	611	5
MACS J0647.7+7014	0.591	ACIS-I	17.9	06 47 49.95	+70 14 56.2	5362	1028	20	274	4
CL1120+4318	0.600	ACIS-I	18.6	11 20 07.23	+43 18 03.6	3452	722	13	599	4
CLJ0542.8-4100	0.640	ACIS-I	49.9	05 42 49.63	-40 59 56.3	5026	744	12	771	4
LCDCS954	0.670	ACIS-S	26.9	14 20 29.25	-11 34 19.4	1005	586	8	384	3
MACS J0744.9+3927	0.698	ACIS-I	48.7	07 44 52.82	+39 27 26.1	9257	1106	23	508	5
V1221+4918	0.700	ACIS-I	74.3	12 21 25.71	+49 18 30.4	2411	592	14	595	5
SPT-CL0001-5748	0.700	ACIS-I	29.4	00 00 59.91	-57 48 34.7	7544	525	14	244	3
RCS2327.4-0204	0.704	ACIS-I	73.4	23 27 27.68	-02 04 38.5	13 778	944	28	705	8
SPT-CLJ2043-5035	0.720	ACIS-I	76.6	20 43 17.48	-50 35 32.0	5006	594	11	380	3
CIJ1113.1-2615	0.730	ACIS-I	92.5	11 13 05.42	-26 15 39.2	660	330	10	288	3
CLJ2302.8+0844	0.734	ACIS-I	100.6	23 02 48.05	+08 43 49.3	3649	627	10	350	3
SPT-CL2337-5942	0.775	ACIS-I	19.7	23 37 24.65	-59 42 22.7	2013	557	10	254	3
RCS2318+0034	0.780	ACIS-I	112.5	23 18 30.88	+00 34 01.6	22 445	446	13	380	4
MS1137.5+6625	0.782	ACIS-I	101.3	11 40 22.53	+66 08 14.3	3454	440	14	402	7
RXJ 1350.0+6007	0.810	ACIS-I	55.2	13 50 48.18	+60 07 13.4	4564	698	8	450	3
RXJ 1716.9+6708	0.813	ACIS-I	50.7	17 16 48.94	+67 08 25.2	1180	418	9	481	3
EMSS1054.5-0321	0.831	ACIS-S	63.5	10 57 00.07	-03 37 33.1	3872	566	11	574	5
CLJ1226.9+3332	0.888	ACIS-I	29.9	12 26 58.07	+33 32 46.0	3450	779	15	277	4
XMMUJ1230+1339	0.975	ACIS-S	38.4	12 30 17.06	+13 39 08.5	6538	344	9	287	4
J1415.1+3612	1.030	ACIS-S	97.5	14 15 11.01	+36 12 04.1	8727	419	20	260	4
SPT-CL0547-5345	1.067	ACIS-I	28.0	05 46 37.25	-53 45 30.6	3492	657	8	597	3
SPT-CLJ2106-5844	1.132	ACIS-I	47.1	21 06 03.38	-58 44 29.6	7552	680	11	432	3
RDCS1252-2927	1.235	ACIS-I	148.7	12 52 54.58	-29 27 16.9	13 103	378	7	286	3

Notes. Columns from left to right list the target name, adopted redshift, detector used in the observation, net exposure time (in kilo-seconds) after all cleaning processes, position of the adopted X-ray centre in equatorial J2000 coordinates, and number of counts measured for each target in the [0.7–2] keV band, up to the radial limit $R_{\text{out}}^{\text{spat}}$. The last four columns list the upper limit of the radial range investigated in the spatial analysis ($R_{\text{out}}^{\text{spat}}$) and in the spectral analysis ($R_{\text{out}}^{\text{spec}}$) with the number of bins with which we can sample the surface brightness and temperature profiles (the temperature bins are obtained by integrating the spectra between 0.6 and 7 keV).

efficiency of the instrument in revealing photons, and any additional energy-dependent efficiencies. The background spectra are extracted from the same background regions used for the spatial analysis. The source spectra are extracted from at least three concentric annuli centred on the X-ray surface brightness centroid up to the radius $R_{\text{out}}^{\text{spec}}$ where the signal-to-noise is larger than 0.3 in the [0.6–7] keV band. Each spectrum contains at least 500 net source counts in the [0.6–7] keV band. For five objects (CL0848.6+4453, LCDCS954, CLJ1113.1-2615, CLJ2302.8+0844, and RDCS1252-2927), we consider a minimum of 200 net counts to resolve the temperature profile in three independent radial bins. In Table 1, we also report the radial limit probed in the spectral analysis ($R_{\text{out}}^{\text{spec}}$) and the number of bins with which we can sample the temperature profiles by integrating the spectra between 0.6 and 7 keV.

For each annulus, the spectrum is analysed with the X-ray spectral fitting software XSPEC (Arnaud 1996). We adopt a collisionally ionised diffuse gas emission model (apec) multiplied by an absorption component (tbabs). In this model, we fix the redshift to the value obtained from the optical spectroscopy and the absorbing equivalent hydrogen column density N_{H} to the value of the Galactic absorption inferred from radio HI maps in Dickey & Lockman (1990). Then, the free parameters in the spectral fitting model are the emission-weighted temperature, metallicity, and normalisation of the thermal spectrum. The fit is performed in the energy range [0.6–7] keV applying Cash statistics (Cash 1979) as implemented in XSPEC. Cash statistics is a maximum-likelihood estimator based on the Poisson distribution of the detected source plus background counts and is preferable for low signal-to-noise spectra (e.g. Nousek & Shue 1989).

The gas density profile is then obtained through the geometrical deprojection (e.g. Fabian et al. 1981; Ettori et al. 2002) of both the surface brightness profile S_b and the normalisation K of the thermal model fitted in the spectral analysis.

4. The hydrostatic mass profile

The total mass of X-ray luminous galaxy clusters can be estimated from the observed gas density n_{gas} and temperature T_{gas} profiles. The Euler equation for a spherically symmetric distribution of gas with pressure P_{gas} and density ρ_{gas} , in hydrostatic equilibrium with the underlying gravitational potential ϕ , requires (Binney & Tremaine 1987)

$$\frac{1}{\rho_{\text{gas}}} \frac{dP_{\text{gas}}}{dr} = -\frac{d\phi}{dr} = -\frac{GM_{\text{tot}}(<r)}{r^2}, \quad (1)$$

which is better known as the hydrostatic equilibrium equation (HEE). Solving Eq. (1) for the total mass M_{tot} and considering the perfect gas law, $P_{\text{gas}} = \rho_{\text{gas}} kT_{\text{gas}}/(\mu m_p) = n_{\text{gas}} kT_{\text{gas}}$, we can obtain the total mass of the clusters as a function of our observables, gas density and temperature profiles (see e.g. Ettori et al. 2013, for a recent review),

$$M_{\text{tot}}(<r) = -\frac{kT_{\text{gas}}(r)r}{\mu m_p G} \left(\frac{d \ln n_{\text{gas}}}{d \ln r} + \frac{d \ln T_{\text{gas}}}{d \ln r} \right). \quad (2)$$

Here, G is the gravitational constant, k is the Boltzmann's constant, m_p is the proton mass, $\mu = 0.6$ is the mean molecular weight of the gas, and $n_{\text{gas}} = \rho_{\text{gas}}/\mu m_p$ is the sum of the electron and ion densities.

We consider a galaxy cluster to be a spherical region with a radius R_Δ , where Δ is the mean over-density with respect to the critical density of the Universe at the redshift of the cluster. We define all the quantities describing the mass profile of the cluster in relation to the over-density $\Delta = 200$. We define the masses with respect to the critical density of the Universe. Diemer & Kravtsov (2015) pointed out that the time evolution of the concentration with the peak height ν exhibits the smallest deviations from universality if this definition is adopted.

As described in Ettori et al. (2013), Eq. (2) can be solved at least with two different approaches, adopting either a backwards method or a forwards method.

The backwards method follows the approach described in Ettori et al. (2010). Briefly, it consists in adopting a functional form to describe the total mass profile, while there is no parametrisation of the gas temperature and density profiles. We adopt the NFW profile, so that

$$\begin{aligned} M_{\text{tot}}(<r) &= 4\pi r_s^3 \rho_s f(x), \\ \rho_s &= \rho_{c,z} \frac{200}{3} \frac{c^3}{\ln(1+c) - c/(1+c)}, \\ f(x) &= \ln(1+x) - \frac{x}{1+x}, \end{aligned} \quad (3)$$

where $x = r/r_s$. This model is a function of two parameters: the scale radius r_s and concentration c , which are related by the relation $R_{200} = c_{200} \times r_s$. The best-fit parameters are searched over a grid of values in the (r_s, c) plane and they are constrained by minimising the following χ^2 statistics:

$$\chi_T^2 = \sum_i \frac{(T_{\text{data},i} - T_{\text{model},i})^2}{\epsilon_{T,i}^2}, \quad (4)$$

where the sum is performed over the annuli of the spectral analysis; T_{data} are the temperature measurements obtained in the spectral analysis; T_{model} are the values obtained by projecting the estimates of T_{gas} (recovered from the inversion of the HEE Eq. (2) for a given gas density and total mass profiles) over the annuli used in the spectral analysis, according to Mazzotta et al. (2004); and ϵ_T is the error on the spectral measurements. The search for the minimum in the χ_T^2 distribution proceeds, first, in identifying a minimum over a grid of 50×50 points in which the range of the two free parameters ($50 \text{ kpc} < r_s < \max(R_{\text{out}}^{\text{spat}}, R_{\text{out}}^{\text{spec}})$; $0.2 < c < 20$) is divided regularly. Then, we obtain the refined best-fit values for the (r_s, c) parameters, looking for a minimum over a 100×100 grid in a 5σ range around the first identified minimum. Considering the strong correlation present between the free parameters and to fully represent their probability distribution, we estimate and quote the probability weighted means of the concentration c_{200} and of the mass M_{200} in Table 2. The mass is obtained as $200 \rho_{c,z} 4/3\pi R_{200}^3$, where $R_{200} = r_s \times c_{200}$ and propagates the joint probability distribution evaluated for the grid of values of the (r_s, c) parameters. In Table 2, we quote the best-fit results for c_{200} and M_{200} derived from the backwards method.

In the forwards method some parametric functions are used to model the three-dimensional gas density and temperature radial profiles. This is similar to what is described in, for example Vikhlinin et al. (2006), where the adopted functional forms are projected along the line of sight to fit the observed projected quantities. In the present analysis, we model the deprojected three-dimensional profiles directly. The gas density distribution is parametrised by a double β -model,

$$n_{\text{gas}}(r) = \frac{n_0}{[1 + (r/r_0)^2]^{1.5\alpha}} + \frac{n_1}{[1 + (r/r_1)^2]^{1.5\beta}} \quad (5)$$

where $n_0, n_1, r_0, r_1, \alpha, \beta$ are the free parameters of the model. The three-dimensional temperature profile is modelled as

$$T(r) = T_0 \frac{a + (r/r_{\text{in}})^b}{[1 + (r/r_{\text{in}})^b][1 + (r/r_{\text{out}})^2]^d}, \quad (6)$$

where $T_0, r_{\text{in}}, r_{\text{out}}, a, b, d$ are the free parameters of the model. These profiles, with their best-fit values and intervals, are then used to recover the mass profile through Eq. (2).

The two methods show a good agreement between the two estimates of the mass contained within the outermost radius measured in the spectral analysis, as shown in Fig. 1. In fact, the ratio between the two mass estimates has a median (1st, 3rd quartile) value of 0.92 (0.75, 1.11). The distributions of the relative errors are also very similar with a median value of 22% for the forwards method and 16% for the backwards method. For the following analysis, we have chosen to follow the backwards method since it requires only two parameters and provides more reliable estimates of the uncertainties (see e.g. Mantz & Allen 2011).

Eleven clusters in our sample are among the targets of the CLASH programme (Postman et al. 2012). The CLASH was a Hubble Multi-Cycle Treasury programme with the main science goal to obtain well-constrained, gravitational-lensing mass profiles for a sample of 25 massive galaxy clusters in the redshift range 0.2–0.9. Twenty of these clusters were selected to have relatively round X-ray isophotes centred on a prominent brightest central galaxy. The remaining five were chosen for their capability of providing extraordinary signal for gravitational lensing. Donahue et al. (2014) derive the mass profiles of the CLASH clusters from X-ray observations (either Chandra or XMM-Newton) to compare them with lensing results. We

Table 2. Results of the mass reconstruction.

name	z	kT [keV]	$M_{\text{gas},500}[10^{14} M_{\odot}]$	c_{200}	$M_{200}[10^{14} M_{\odot}]$	$\chi^2/\text{d.o.f.} (P)$
MACS J0159.8-0849	0.405	9.2 ± 0.6	1.29 ± 0.07	4.3 ± 0.8	17.8 ± 5.4	1.42 (0.84)
MACS J2228.5+2037	0.412	9.4 ± 0.7	1.57 ± 0.12	2.7 ± 1.1	15.6 ± 5.1	0.09 (0.04)
MS1621.5+2640	0.426	6.7 ± 0.6	0.95 ± 0.06	2.4 ± 0.9	13.0 ± 4.1	0.82 (0.52)
MACS J1206.2-0848	0.440	12.5 ± 1.0	2.25 ± 0.10	2.5 ± 0.5	38.1 ± 10.3	1.62 (0.82)
MACS J2243.3-0935	0.447	8.4 ± 0.6	1.73 ± 0.11	2.7 ± 1.2	14.5 ± 4.4	1.29 (0.73)
MACS J0329.7-0211	0.450	7.7 ± 0.6	1.00 ± 0.06	3.5 ± 0.7	15.9 ± 5.6	0.62 (0.29)
RXJ 1347.5-1145	0.451	15.1 ± 0.8	2.43 ± 0.11	4.5 ± 0.6	40.1 ± 11.2	0.73 (0.33)
V1701+6414	0.453	6.3 ± 0.7	0.78 ± 0.07	2.2 ± 1.0	7.8 ± 3.4	0.86 (0.52)
MACS J1621.6+3810	0.465	9.1 ± 1.0	0.81 ± 0.05	3.4 ± 1.0	21.7 ± 10.9	0.62 (0.35)
CL0522-3624	0.472	4.2 ± 1.2	0.23 ± 0.03	6.3 ± 4.9	6.1 ± 4.6	0.02 (0.11)
MACS J1311.0-0310	0.494	5.7 ± 0.4	0.77 ± 0.03	2.6 ± 0.8	18.6 ± 7.8	0.52 (0.28)
MACS J2214.9-1400	0.503	11.9 ± 1.6	1.41 ± 0.13	4.4 ± 2.9	17.9 ± 9.0	0.59 (0.38)
MACS J0911.2+1746	0.505	7.9 ± 1.0	1.12 ± 0.74	2.5 ± 1.0	15.5 ± 5.1	1.16 (0.68)
MACS J0257.1-2326	0.505	8.6 ± 0.9	1.31 ± 0.13	3.9 ± 2.3	17.3 ± 8.7	0.63 (0.29)
V1525+0958	0.516	4.7 ± 0.7	0.52 ± 0.03	2.5 ± 1.3	11.1 ± 5.5	1.05 (0.65)
MS0015.9+1609	0.541	9.9 ± 0.8	1.78 ± 0.12	2.3 ± 0.6	19.9 ± 5.1	0.92 (0.51)
CL0848.6+4453	0.543	4.9 ± 0.8	0.16 ± 0.01	5.2 ± 4.3	9.4 ± 8.6	0.11 (0.26)
MACS J1423.8+2404	0.543	7.5 ± 0.3	0.70 ± 0.03	6.2 ± 0.4	7.8 ± 0.8	1.44 (0.83)
MACS J1149.5+2223	0.544	10.8 ± 0.7	1.73 ± 0.10	3.3 ± 2.0	13.3 ± 4.5	0.85 (0.47)
MACS J0717.5+3745	0.546	7.9 ± 0.5	2.52 ± 0.12	3.6 ± 0.9	21.7 ± 4.0	1.52 (0.93)
CL1117+1744	0.548	2.5 ± 1.2	0.19 ± 0.02	4.8 ± 4.5	2.2 ± 1.6	0.45 (0.50)
MS0451.6-0305	0.550	11.2 ± 0.7	1.78 ± 0.06	3.2 ± 1.4	28.5 ± 11.3	1.30 (0.73)
MS2053.7-0449	0.583	5.6 ± 1.6	0.36 ± 0.03	4.3 ± 3.7	8.1 ± 6.0	0.40 (0.47)
MACS J2129.4-0741	0.589	11.6 ± 2.1	1.23 ± 0.08	6.5 ± 4.4	16.0 ± 9.6	0.91 (0.57)
MACS J0647.7+7014	0.591	13.2 ± 2.5	1.74 ± 0.12	3.7 ± 2.4	25.6 ± 15.2	0.62 (0.46)
CL1120+4318	0.600	4.9 ± 1.4	0.65 ± 0.09	4.7 ± 4.0	7.0 ± 4.2	1.03 (0.65)
CLJ0542.8-4100	0.640	6.0 ± 0.8	0.43 ± 0.03	7.0 ± 5.2	6.5 ± 3.6	1.13 (0.68)
LCDCS954	0.670	3.9 ± 0.8	0.17 ± 0.02	4.8 ± 4.5	2.2 ± 1.7	1.75 (0.81)
MACS J0744.9+3927	0.698	9.0 ± 0.7	1.05 ± 0.07	6.2 ± 2.8	9.7 ± 4.9	1.08 (0.65)
V1221+4918	0.700	6.3 ± 0.8	0.40 ± 0.03	6.1 ± 4.8	6.6 ± 4.3	1.46 (0.78)
SPT-CL0001-5748	0.700	6.5 ± 1.0	0.52 ± 0.03	5.1 ± 3.3	13.3 ± 11.4	0.25 (0.38)
RCS2327.4-0204	0.704	9.8 ± 0.5	1.66 ± 0.07	2.2 ± 0.4	31.3 ± 7.7	0.72 (0.37)
SPT-CLJ2043-5035	0.720	6.5 ± 1.1	0.98 ± 0.06	2.6 ± 1.3	15.1 ± 8.1	0.18 (0.33)
CIJ1113.1-2615	0.730	3.9 ± 0.7	0.17 ± 0.02	6.0 ± 4.4	8.1 ± 6.8	0.68 (0.59)
CLJ2302.8+0844	0.734	11.4 ± 2.9	0.38 ± 0.04	3.2 ± 2.9	7.9 ± 5.0	3.29 (0.93)
SPT-CL2337-5942	0.775	9.3 ± 1.7	1.14 ± 0.06	4.8 ± 3.8	21.2 ± 14.1	0.05 (0.18)
RCS2318+0034	0.780	10.4 ± 2.2	0.80 ± 0.03	4.8 ± 3.7	22.9 ± 17.3	0.27 (0.24)
MS1137.5+6625	0.782	5.2 ± 0.4	0.48 ± 0.03	3.6 ± 1.9	15.2 ± 8.8	2.07 (0.93)
RXJ 1350.0+6007	0.810	4.0 ± 0.6	0.22 ± 0.03	5.0 ± 4.5	2.8 ± 1.5	0.02 (0.12)
RXJ 1716.9+6708	0.813	4.7 ± 0.8	0.28 ± 0.02	6.6 ± 5.3	6.5 ± 4.9	1.75 (0.81)
EMSS1054.5-0321	0.831	11.1 ± 1.2	1.15 ± 0.03	3.8 ± 3.2	16.3 ± 8.8	0.71 (0.45)
CLJ1226.9+3332	0.888	14.3 ± 2.4	1.66 ± 0.10	4.2 ± 2.9	33.7 ± 21.2	0.11 (0.11)
XMMUJ1230+1339	0.975	4.3 ± 1.1	0.37 ± 0.03	4.2 ± 3.7	8.7 ± 7.1	0.35 (0.30)
J1415.1+3612	1.030	6.2 ± 0.7	0.34 ± 0.02	3.3 ± 2.5	10.0 ± 6.9	0.71 (0.51)
SPT-CL0547-5345	1.067	6.9 ± 1.8	0.58 ± 0.07	6.0 ± 4.7	11.9 ± 8.8	0.20 (0.34)
SPT-CLJ2106-5844	1.132	8.9 ± 1.2	1.23 ± 0.06	4.9 ± 4.5	9.0 ± 5.4	1.57 (0.79)
RDCS1252-2927	1.235	3.7 ± 1.0	0.22 ± 0.03	4.6 ± 3.9	5.6 ± 4.5	0.25 (0.38)

Notes. Columns from left to right list the target name, adopted redshift, mean spectral gas temperature, gas mass within R_{500} , probability weighted mean of the mass concentration and of the mass within $\Delta = 200$ obtained as described in Sect. 4 and χ^2 divided by the degrees of freedom (i.e. the number of temperature bins listed in the last column of Table 1 minus two), and the corresponding probability that a random variable from a χ^2 distribution with a given degrees of freedom is less or equal to the observed χ^2 value.

compare the masses at the radius R_{500} listed in their Table 4 for the *Chandra* data with the masses derived from our *backwards* analysis, calculated at the same physical radius. Donahue et al. (2014) invoke the HEE as we do, but they reconstruct the mass profiles in a different way. They use the Joint Analysis of Clusters Observations fitting tool (JACO; Mahdavi et al. 2007), which employs parametric models for both dark matter and gas

density profiles (a NFW model and a combination of β -models, respectively, in this case) under the assumption of a spherically-symmetric ICM in hydrostatic equilibrium with the dark matter potential to reconstruct the projected spectra in each annular bin that are then jointly fitted to the observed events to constrain the model parameters. We find an encouraging agreement between the two outcomes. The median (1st, 3rd quartile) of the

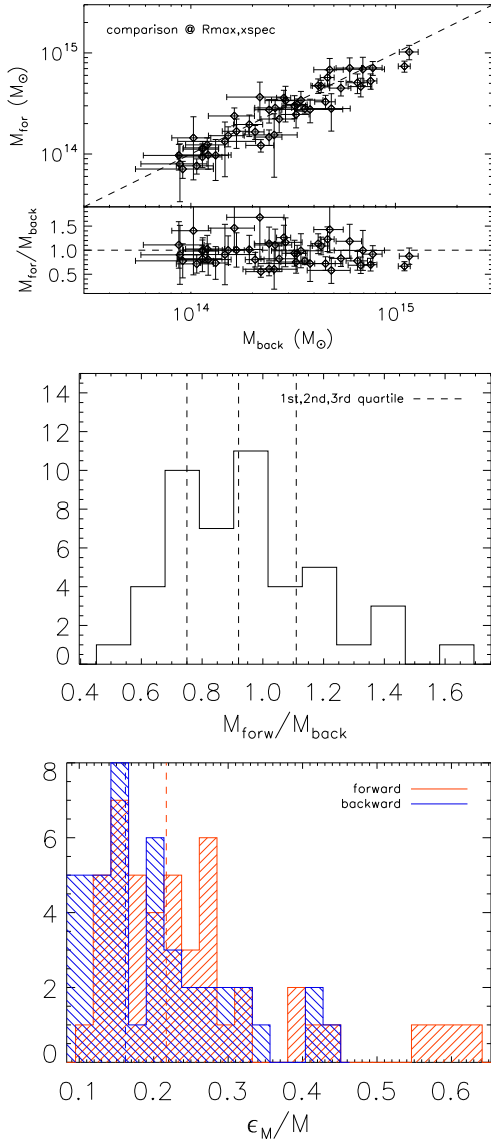


Fig. 1. *Top:* comparison between mass estimates obtained following the forwards method (M_{for}) and backwards method (M_{back}) for the 47 clusters of our sample. The *lower panel* shows the $M_{\text{for}}/M_{\text{back}}$ ratio of individual clusters against M_{back} . The dashed line shows the one-to-one relation. The comparison is made at the outermost radius measured in the spectral analysis for each cluster. *Middle:* distribution of the mass ratios. *Bottom:* distribution of the relative errors.

$M_{\text{back}}/M_{\text{CLASH}}$ distribution for the 11 shared clusters is 1.09 (0.86, 1.44). The distributions of the relative errors provided by the two analyses are also comparable with a median value of 21% for our backwards method and 26% for the method employed by Donahue et al. (2014).

4.1. Comments on the best-fit parameters

The radial extension probed with our X-ray measurements span a typical range $35 \text{ kpc} \lesssim R_{\text{spat}} \lesssim 700 \text{ kpc}$ and $65 \text{ kpc} \lesssim R_{\text{spec}} \lesssim 480 \text{ kpc}$ for the spatial and spectral analyses, respectively. We use the results on the $c - M$ relation estimated at R_{200} to enable a direct comparison with the predictions from simulations. We compare our estimates of R_{200} with the upper limit of the radial range investigated in the spatial and spectral analyses for each cluster to check the significance of our estimates. The results are

shown in Fig. 2, where we also show the distributions of each of the ratios investigated.

As usual in the X-ray analysis, the estimate of R_{200} exceeds the radial extension of the spatial and spectral analyses in almost all cases. For the $R_{\text{out}}^{\text{spat}}/R_{200}$ ratio, we measure a median value (1st, 3rd quartiles) of 0.49 (0.30, 0.59) and a median relative dispersion of 21%, while we obtain 0.29 (0.20, 0.40) and a median relative dispersion of 20% for the $R_{\text{out}}^{\text{spec}}/R_{200}$ ratio.

This means that we are not able to sample our objects directly up to R_{200} in both the surface brightness and temperature profiles, as expected given that both the observational strategy and background characterisation were not optimised to this purpose (see e.g. Ettori & Molendi 2011).

However, R_{200} is treated as a quantity derived from the best-fit parameters of our procedure for the assumed mass model ($R_{200} = r_s \times c_{200}$) and does not imply a direct extrapolation of the mass profile to recover it.

More interesting is to consider the goodness of the fitting procedure. As we quote in the last column of Table 2, the NFW model provides a reasonable description of the cluster gravitational potential for all our clusters. The probability that a random variable from a χ^2 distribution with a given degree of freedom is less or equal to the observed χ^2 value is 50% (median of the observed distribution)³. We have only one object with a very low probability (<5%; MACSJ2228.5+2037) that suggests an over-estimate of the error bars, and no object with a probability larger than 95%. Nonetheless, deviations are expected in a sample of about 50 clusters and this object has also been considered in the following analysis.

4.2. Comparison with lensing estimates

A useful test for the reliability of our hydrostatic mass estimates is the comparison with results from lensing. The LC^2 -single catalogue is a collection of 506 galaxy clusters from the literature with mass measurements based on weak lensing (Serenio 2015). Cluster masses in LC^2 -single are uniformed to our reference cosmology. By cross-matching with the LC^2 catalogue⁴ we find that 32 out of 47 clusters of our sample have weak-lensing reconstructed mass.

To assess the agreement between the two measurements, we adopt two methods. First, we consider the (natural) logarithm of the mass ratios (Rozo et al. 2014; Serenio & Ettori 2015a). We consider the backwards method masses. This estimator is not affected by the exchange of numerator and denominator. Since quoted errors in compiled catalogs may account for different sources of statistical and systematic uncertainties and published uncertainties are unable to account for the actual variance seen in sample pairs, we conservatively perform an unweighted analysis.

The agreement between mass estimates is good; see Fig. 3. For the masses at R_{200} , we measure a ratio $\ln(M_X/M_{\text{lens}}) = 0.16 \pm 0.65$, where the first estimate is the median and the second is the dispersion of the distribution of mass ratios. Mass differences are inflated when computed at R_{200} owing to the different volumes. We then also consider the masses enclosed within a fixed physical radius, 1 Mpc. We find $\ln(M_X/M_{\text{lens}}) = 0.01 \pm 0.45$.

Seven clusters of our sample are also covered with ground weak-lensing studies by the CLASH programme. Umetsu et al. (2016) perform a joint shear-and-magnification,

³ A reduced χ^2 of 1 would have an associated probability of 68.3% for a degree-of-freedom of 1 and of 51.9% for d.o.f. = 100.

⁴ We use the LC^2 -single_v2.0.dat version publicly available at <http://pico.bo.astro.it/~serenio/CoMaLit/LC2/>

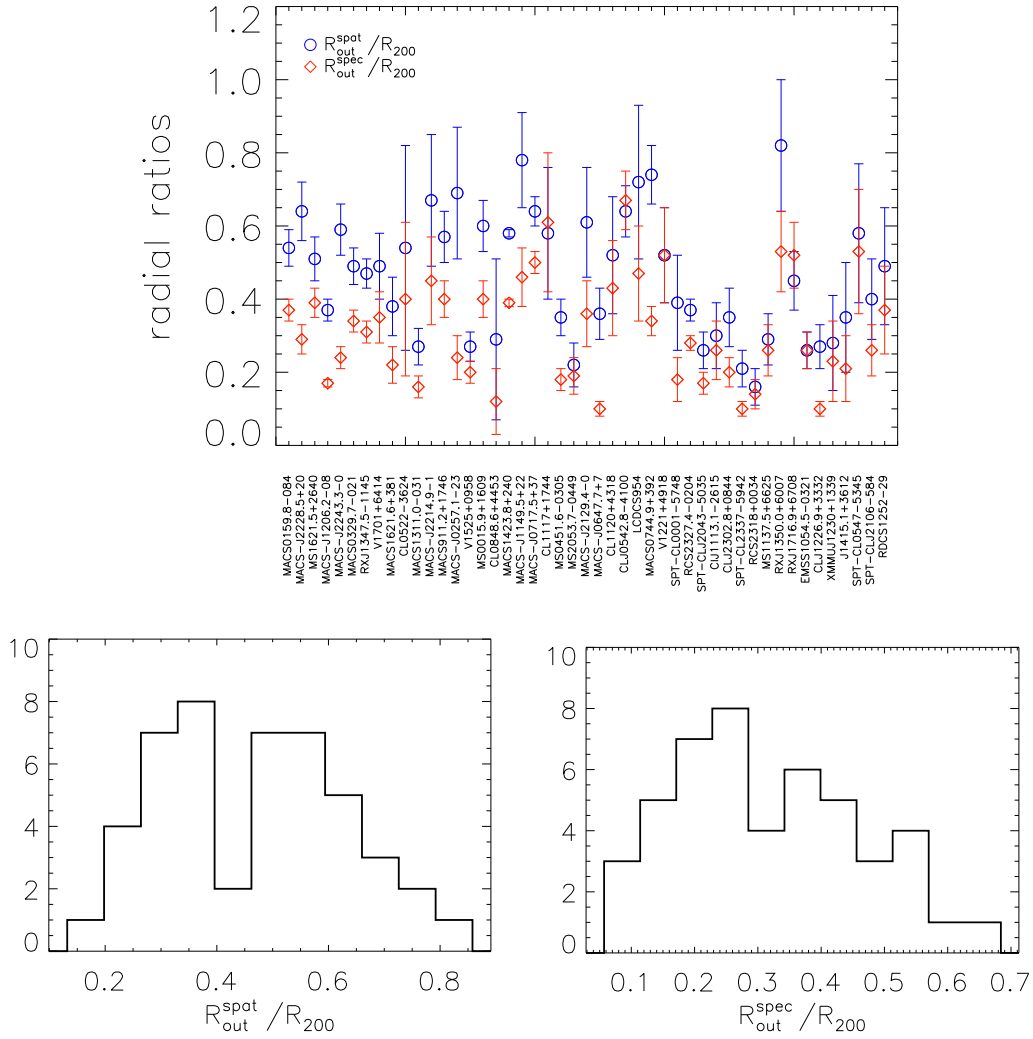


Fig. 2. *Top:* for each cluster in the final sample, we show: the ratio between the upper limit of the radial range investigated in the spatial analysis and our estimate of R_{200} (blue circles); the ratio between the maximum radial extension of the spectral analysis and R_{200} (red diamonds). *Bottom:* distributions of the radial ratios.

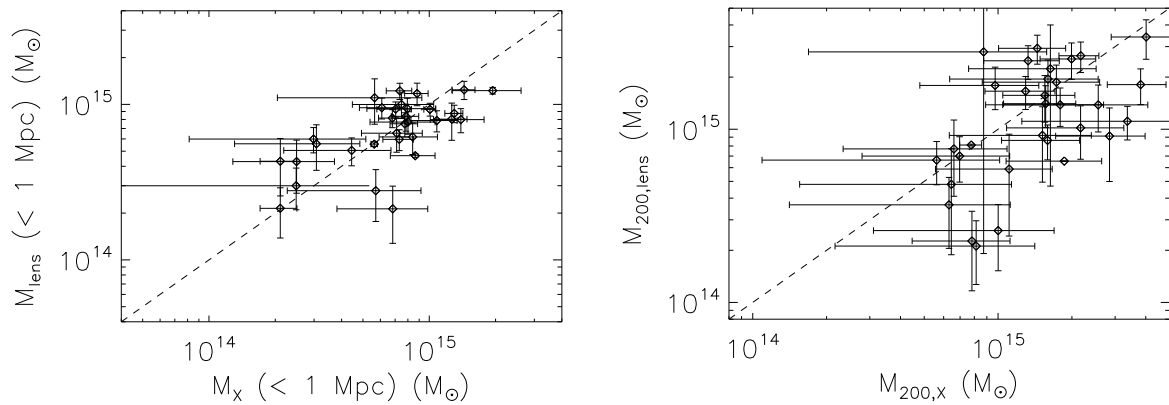


Fig. 3. Comparison on the mass estimates within 1 Mpc (*left*) and R_{200} (*right*) for the objects in common between our sample of X-ray measurements and those available in the lensing LC^2 -single catalogue.

weak-lensing analysis with additional strong lensing constraints of a subsample of 16 X-ray regular and 4 high-magnification galaxy clusters in the redshift range $0.19 \lesssim z \lesssim 0.69$. For these clusters, we find $\ln(M_X/M_{\text{lens}}) = 0.12 \pm 0.58$ at R_{200} and $\ln(M_X/M_{\text{lens}}) = -0.32 \pm 0.74$ within 1 Mpc, which is consistent with the full lensing sample.

Concentrations are consistent as well; see Fig. 4. For the seven CLASH clusters, we find $\ln(c_{200,X}/c_{200,\text{lens}}) = 0.19 \pm 0.53$.

As a second method, we estimate the mass bias by regressing the hydrostatic against the lensing masses. We follow the approach detailed in Sereno & Ettori (2015a,b), which accounts for heteroscedastic errors, time dependence, and intrinsic scatter

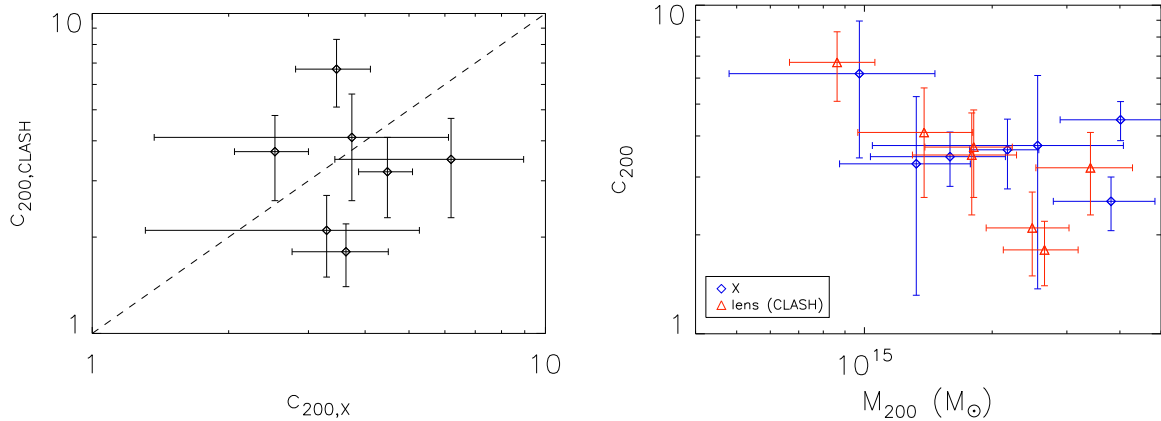


Fig. 4. Comparison between our constraints from X-ray data and CLASH lensing estimates for the 7 objects in common on the mass concentrations (*left*) and $c - M$ distribution (*right*).

in both the independent and response variable. This accounts for both M_{lens} and M_X being scattered proxy of the true mass. We fit the data with the model $M_{X,200} = \alpha + \beta M_{\text{lens},200} + \gamma \log(1+z)$. First, we assume that the mass ratio $M_{X,200}/M_{\text{lens},200}$ is constant at given redshift ($\beta = 1$) and we find $\alpha = 0.08 \pm 0.15$. This bias is consistent with what found with the mass-ratio approach described before. The value γ is consistent with zero, $\gamma = -0.15 \pm 0.75$, i.e. we cannot detect any redshift dependence in the bias. For the scatters, we find $\sigma_{\log(M_{\text{lens},200})} = 0.11 \pm 0.07$ and $\sigma_{\log(M_{X,200})} = 0.04 \pm 0.04$. Then, we check the above assumption by letting the slope free. We find $\alpha = 0.40 \pm 0.28$, $\beta = 0.74 \pm 0.20$, $\gamma = -0.32 \pm 0.73$, $\sigma_{\log(M_{\text{lens},200})} = 0.08 \pm 0.07$, and $\sigma_{\log(M_{X,200})} = 0.07 \pm 0.05$. The slope β is fully consistent with one and the other parameters are in full agreement with the determination assuming $\beta = 1$.

We conclude that the X-ray masses are in very good agreement with the lensing masses, $M_{X,200}/M_{\text{lens},200} \sim 1$. Uncertainties are too large to make statements about deviations from equilibrium or non-thermal contributions that can bias the results towards low X-ray masses (Sereni & Ettori 2015a).

5. The concentration-mass relation

We present our results on the $c_{200} - M_{200}$ relation. We stress that our sample, because of the adopted selection criteria (discussed in Sect. 2), is not statistically complete, but represents well the high-mass end of the cluster population even at high redshift (see also discussion in Sect. 6.1).

The concentration-mass relation for the 47 clusters of our sample is shown in Fig. 5. The large error bars are due to the uncertainties in determining the observable surface brightness and spectrum of each cluster, which are consistently propagated up to the concentration and mass derivation.

The right panel of Fig. 5 is obtained by dividing the sample into seven mass bins and estimating, for each bin, the error-weighted mean of the values of the concentration and error on the mean. This operation is made to enhance the observed signal, giving more weight to more precise measurements and to find the mean properties of the sample.

Overall, our data confirm the expected trend of lower concentrations corresponding to higher masses. We investigate the distribution of the concentrations for clusters in two mass ranges below and above the median value of $M_{200} = 1.3 \times 10^{15} M_{\odot}$, respectively. The overall distribution is well approximated by a

log-normal function with a mean value $\langle \log c_{200} \rangle$ and a scatter σ ,

$$P(\log c_{200}) = \frac{1}{\sigma \sqrt{2\pi}} \exp \left[-\frac{1}{2} \left(\frac{\log c_{200} - \langle \log c_{200} \rangle}{\sigma} \right)^2 \right]. \quad (7)$$

We obtain a mean value for the total concentration distribution of $\langle \log c_{200} \rangle = 0.60$ and a scatter of $\sigma(\log c_{200}) = 0.15$. By considering the two mass ranges, we find a mean of $\langle \log c_{200} \rangle = 0.66$ (0.54) and a scatter of 0.14 (0.12) for the low- (high-) mass case. The central peak is shifted towards the low concentrations in the high-mass case, as expected, while we have a slightly larger scatter in the low-mass case. We also investigate the distribution of the concentrations in two redshift ranges, considering the median redshift of the sample, $z = 0.6$ as threshold. We find a mean of $\langle \log c_{200} \rangle = 0.55$ (0.66) and a scatter of $\sigma(\log c_{200}) = 0.14$ (0.13) for the low (high) redshift case, consistent with the above estimates.

In Fig. 5, we also compare our data with three recent results from numerical simulations: Diemer & Kravtsov (2015, hereafter DK15), Dutton & Macciò (2014, hereafter DM14), Prada et al. (2012, hereafter P12). The range of the predicted results is delimited by a dotted line, corresponding to the lowest redshift in the sample ($z = 0.4$), and a dashed line, corresponding to the highest redshift in the sample ($z = 1.2$). The comparison with these theoretical works is carried out using the public code *Colossus* provided by DK15⁵. It is a versatile code that implements a collection of models for the $c - M$ relation, including those of interest here, allowing the choice of a set of cosmological parameters and the conversion among different mass definitions. It turns out to be very useful for our purpose to homogenise the results presented in the original papers to our cosmological model of reference and to masses defined at $\Delta = 200$ with respect to the critical density of the Universe, as in our analysis.

However, it must be noted that we investigate a mass range that might exceed those probed by numerical simulations slightly, in particular, at $z \sim 1$. In fact, there are no numerical predictions for the behaviour of the $c - M$ relation for masses larger than $10^{15} M_{\odot}$ in the range of redshifts considered in our work. We proceed using the numerical predictions as extrapolated from the available datasets⁶ to compare with our results.

⁵ www.benediktdiemer.com/code

⁶ In the case of the adopted code *Colossus*, see the description of the models implemented at bdiemer.bitbucket.org/halo_concentration.html

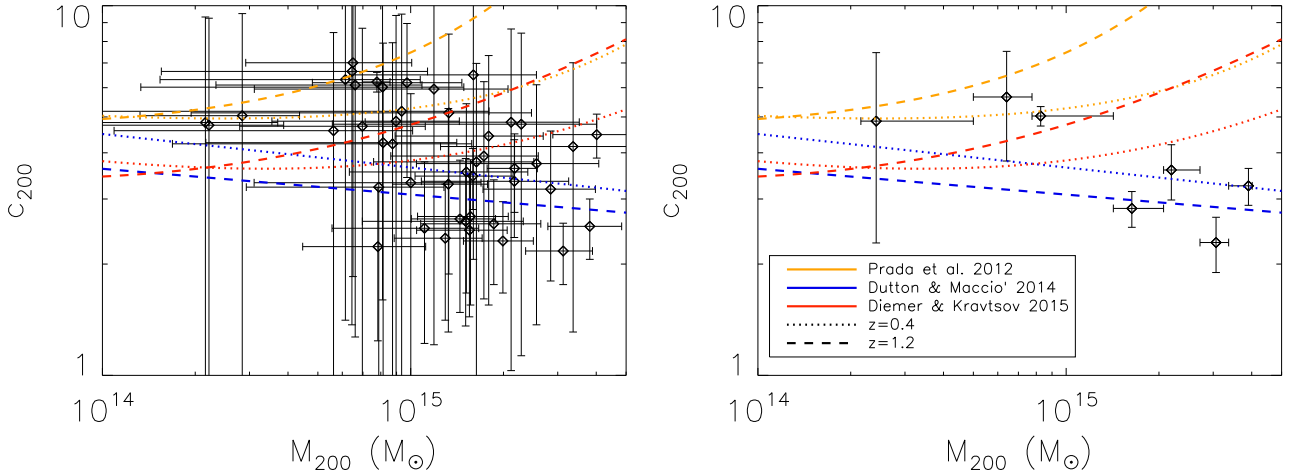


Fig. 5. *Left:* concentration–mass relation obtained for the final cluster sample in the case $\Delta = 200$ (black diamonds). The cluster total masses are obtained following the backwards method described in Ettori et al. (2002). A NFW profile is adopted to describe the gravitational potential. We overplot the $c_{200} - M_{200}$ relations predicted by P12 (yellow lines), DM14 (blue lines), and DK15 (red lines). They are calculated for $z = 0.4$ (dotted lines) and $z = 1.2$ (dashed lines), which are the lowest and highest redshifts in the sample. *Right:* the same as the left panel, but here the sample is divided into 7 mass bins. For each bin, error-weighted means for concentration and mass are calculated (black diamonds) and the error bars represent the errors on the weighted means.

In order to quantify the deviations from numerical predictions, we use the following χ^2 estimator:

$$\chi^2 = \sum_i \frac{(\log c_{\text{obs},i}(M, z) - \log c_{\text{sim},i}(M, z))^2}{\epsilon_{\log c_{\text{obs},i}}^2 + \sigma_{\log c_{\text{sim}}}^2}, \quad (8)$$

where the sum is carried out over the 47 clusters of our sample; c_{obs} and $\epsilon_{c_{\text{obs}}}$ are the estimates of concentrations and corresponding errors, respectively, listed in Table 2 (we omit the label “200” to simplify the notation); c_{sim} are the values derived from the models for fixed mass and redshift; and $\sigma_{\log c_{\text{sim}}}$ is the intrinsic scatter on the simulated concentrations, assumed to be equal to 0.11 (e.g. DM14). We obtain a χ^2 of 272.4, 26.3, and 69.4 when the models by P12, DM14, and DK15, respectively, are considered. A random variable from the χ^2 distribution in Eq. (8) with 47 degrees of freedom has a probability of 100, 0.6, and 98 per cent to be lower than the measured values, respectively, indicating a tension with the P12 and DK15 models in the mass ($10^{14} - 4 \times 10^{15} M_{\odot}$) and redshift (0.4–1.2) ranges investigated in the present analysis.

It is clear from the right panel of Fig. 5 that our results show the lowest concentrations for the highest masses and are not compatible with an upturn at high masses. This is indeed expected for a sample of relaxed clusters only (see e.g. Ludlow et al. 2012; Correa et al. 2015). The models considered here characterise different halo samples: P12 and DK15 include all the halos, regardless their degree of virialisation, whereas DM14 exclude the unrelaxed halos. Even though the selection is different, we consider objects that show no major mergers and are closer to the selection for relaxed halos applied in numerical simulations. Moreover, the concentrations calculated in P12 are derived from the circular ratio V_{max}/V_{200} , rather than from a direct fit to the mass profile and the halos are binned according to their maximum circular velocity, rather than in mass. As pointed out in Meneghetti & Rasia (2013), such methodological differences lead to large discrepancies both in the amplitude and in the shape of the $c - M$ relation, especially on the scales of galaxy clusters, making the comparison with the predictions in P12 not straightforward.

5.1. Evolution with redshift

With the aim of investigating the dependence of the cluster concentrations on mass and redshift, we consider the three-parameter functional form, $c = c_0 M^B (1+z)^C$, and we linearly fit our data to the logarithmic form of this function,

$$\log c_{200} = A + B \log \left(\frac{M_{200}}{10^{14} M_{\odot}} \right) + C \log(1+z) \pm \sigma_{\log c_{200}}. \quad (9)$$

We use the Bayesian linear regression method implemented in the R package LIRA by Sereno (2016). We assume a uniform prior for the intercept A and a Student’s t -prior for both the mass slope B and the slope of the time evolution C . For the intrinsic scatter, we assume that $1/\sigma_{\log c_{200}}^2$ follows a gamma distribution. We obtain the following best-fit parameters: $A = 1.15 \pm 0.29$ and $B = -0.50 \pm 0.20$, $C = 0.12 \pm 0.61$ and an intrinsic scatter $\sigma_{\log c_{200}} = 0.06 \pm 0.04$. This value is lower than the estimates presented in Sect. 5 since here we are correcting for the intrinsic scatter in the hydrostatic masses. The additional correction for this intrinsic scatter of the mass distribution steepens the relation. On the other hand, by taking the covariance between mass and concentration into account, we find a flatter relation, as already pointed out from previous work (e.g. Sereno & Covone 2013).

These values are fully consistent, within the estimated errors, with the IDL routine MLINMIX_ERR by Kelly (2007), which also employs a Bayesian method and with the MPFIT routine in IDL (Williams et al. 2010; Markwardt 2009) that looks for the minimum of the χ^2 distribution by taking the errors on both the variables into account. We quote the best-fit values in Table 3. The probability distributions of the best-fit values obtained with LIRA are shown Fig. 6, while the two-dimensional 1-(2-) σ confidence regions are shown in Fig. 7.

We measure a normalisation $A \approx 1$ and a mass slope $B \approx -0.5$ that is lower than the value predicted by numerical simulations (-0.1). By fixing the parameter B to -0.1 , we find $A = 0.61 \pm 0.12$, $C = 0.38 \pm 0.64$, and $\sigma_{\log c_{200}} = 0.10 \pm 0.02$.

With the Bayesian methods we measure a typical error that is larger by a factor of 2 in normalisation and by a factor of 2.5 in the mass slope with respect to the corresponding values obtained through the covariance matrix of the MPFIT method.

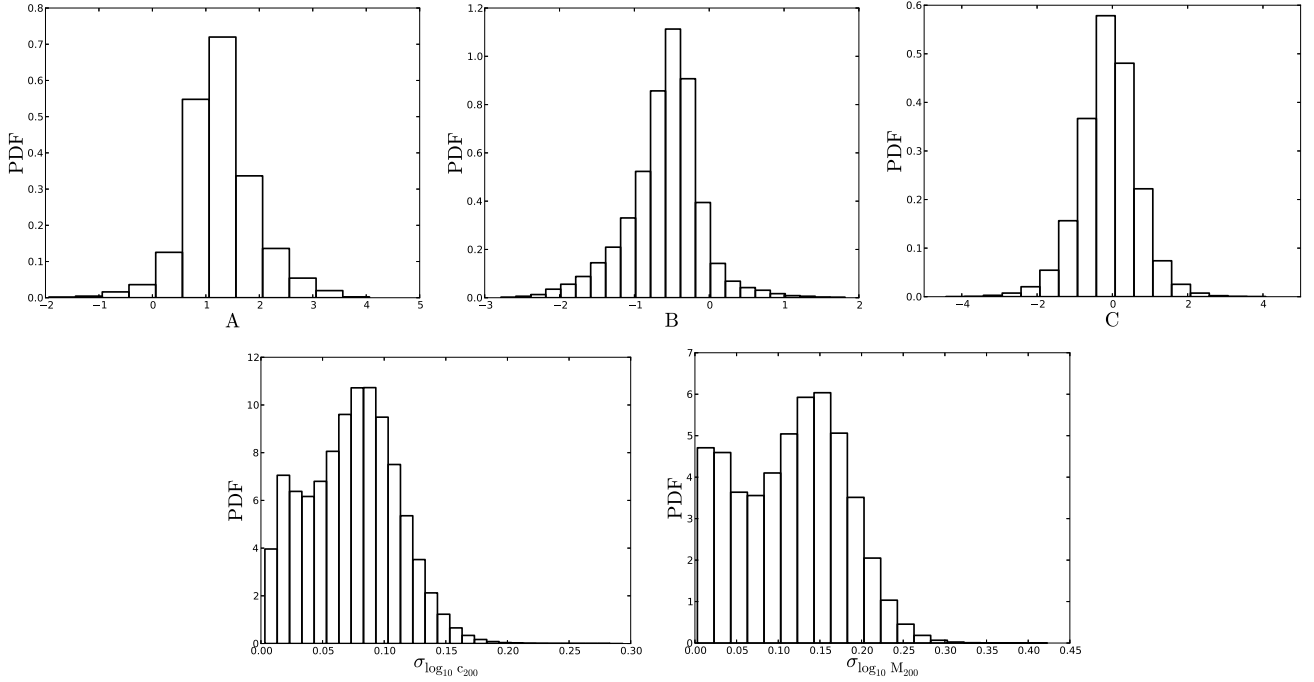


Fig. 6. Probability distributions of the best-fit parameters of the $c - M - z$ relation Eq. (9) obtained with LIRA, where the covariance between mass and concentration is taken into account.

Table 3. Best-fit values of the $c - M - z$ relation.

Method	A	B	C	$\sigma_{\log_{10} c_{200}}$	$\sigma_{\log_{10} M_{200}/10^{14}}$
LIRA	1.15 ± 0.29	-0.50 ± 0.20	0.12 ± 0.61	0.06 ± 0.04	...
LIRA (covxy)	1.23 ± 0.55	-0.54 ± 0.41	-0.08 ± 0.69	0.07 ± 0.04	0.12 ± 0.07
LIRA ($C = 0$)	1.19 ± 0.24	-0.51 ± 0.20	0	0.06 ± 0.04	...
LIRA ($B = -0.1$)	0.61 ± 0.12	-0.10	0.38 ± 0.64	0.10 ± 0.02	...
MLINMIX_ERR	1.07 ± 0.37	-0.42 ± 0.21	-0.02 ± 0.97	0.09 ± 0.03	...
MPFIT	1.34 ± 0.15	-0.53 ± 0.07	-0.57 ± 0.65

Notes. Best-fit parameters refer to Eq. (9) and are obtained using two Bayesian multiple linear regression methods, LIRA and MLINMIX_ERR and the linear least-squares fitting MPFITFUN. All the methods account for heteroscedastic errors in both the independent and dependent variables.

All the methods estimate large errors in the redshift dependence and the best-fit values of the redshift slope are consistent with zero (at 1σ level).

The concentration-redshift relation is shown in Fig. 8 for clusters in two mass ranges, considering the median mass $1.33 \times 10^{15} M_{\odot}$ as threshold. The sample is divided into three redshift bins for each mass range, which are chosen to have approximately an equal number of clusters in each bin as follows: [0.426–0.583], [0.600–0.734], [0.810–1.235] for the low-mass case, and [0.412–0.494], [0.503–0.591], [0.700–0.888] for the high-mass case. We calculate the error-weighted means of the concentrations and errors on the means for each bin, obtaining 5.06 ± 0.31 , 5.18 ± 1.36 , 4.39 ± 1.52 for the low-mass case, 3.16 ± 0.27 , 2.90 ± 0.42 , 2.41 ± 0.37 for the high-mass case. At a fixed mass range, the concentration slightly decreases with redshift, as expected by the fact that the concentration of the cluster is determined by the density of the Universe at the assembly redshift.

Finally, we test the $c-M$ relation in the high redshift regime against the different theoretical models. We use models by P12, DM14, and DK15 to obtain predictions of the measurements of the normalisation and slope of the $c - M$ relation at the median redshift of our sample in the mass range ($10^{14} - 4 \times 10^{15} M_{\odot}$)

investigated in the present analysis (we consider 50 log-mass constant points for the fit). As we show in Fig. 9, the predictions from numerical simulations agree well with our constraints, where values from DM14 model are consistent at 1σ level and with larger deviations (but still close to the $\sim 2\sigma$ confidence level) associated with the P12 and DK15 expectations.

In particular, once we consider only the 18 clusters of our sample with $z \geq 0.7$ and we re-calculate the χ^2 estimator in Eq. (8), we obtain 62.3, 6.1, and 17.7 when the models by P12, DM14, and DK15, respectively, are considered. This means that a random variable from the χ^2 distribution with 18 degrees of freedom has a probability of 99.9, 0.4, and 52.5 per cent to be lower than the measured values, respectively, indicating that only the P12 model deviates more significantly from our estimates in the (0.7–1.2) redshift range.

6. Sample properties

As discussed in Sect. 2 and 3, a cluster at $z > 0.4$, and with exposures available in the *Chandra* archive, is included in our sample if 1) it is observed with sufficient X-ray count statistics to obtain a temperature profile with at least three radial bins; and 2) to a visual inspection of the X-ray maps, it appears to

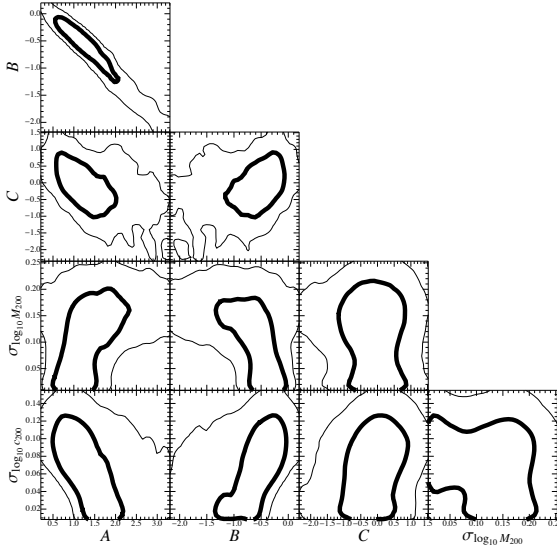


Fig. 7. Probability distributions of the best-fit parameters of the $c-M-z$ relation Eq. (9) obtained with LIRA, where the covariance between mass and concentration is taken into account. The thick (thin) lines include the 1-(2)- σ confidence region in two dimensions, here defined as the region within which the value of the probability is larger than $\exp[-2.3/2]$ ($\exp[-6.17/2]$) of the maximum.

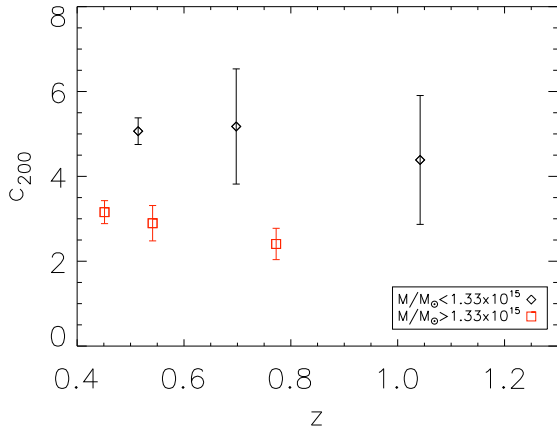


Fig. 8. Concentration-redshift relation calculated in two mass ranges: $M \leq 1.33 \times 10^{15} M_{\odot}$ (black) and $M > 1.33 \times 10^{15} M_{\odot}$ (red). For each mass range, the points are the error-weighted means of the concentrations and the error bars are the errors on the means for three redshift bins. The sample is approximately evenly divided in each bin and we show the median redshift for simplicity.

have a regular morphology, so that we can consider it to be close to the hydrostatic equilibrium. Thus, we exclude the objects with a strongly elongated shape or those containing major substructures. Although we do not use any quantitative criterion for this selection, we provide a morphological analysis to present the statistical properties of the sample and to enable comparison with other X-ray samples. We analyse the morphology of each cluster according to the following two indicators: first, the X-ray brightness concentration parameter, c_{SB} , defined as the ratio between the surface brightness, S_{b} , within a circular aperture of radius 100 kpc and the surface brightness enclosed within a circular aperture of 500 kpc,

$$c_{\text{SB}} = \frac{S_{\text{b}}(r < 100 \text{ kpc})}{S_{\text{b}}(r < 500 \text{ kpc})}. \quad (10)$$

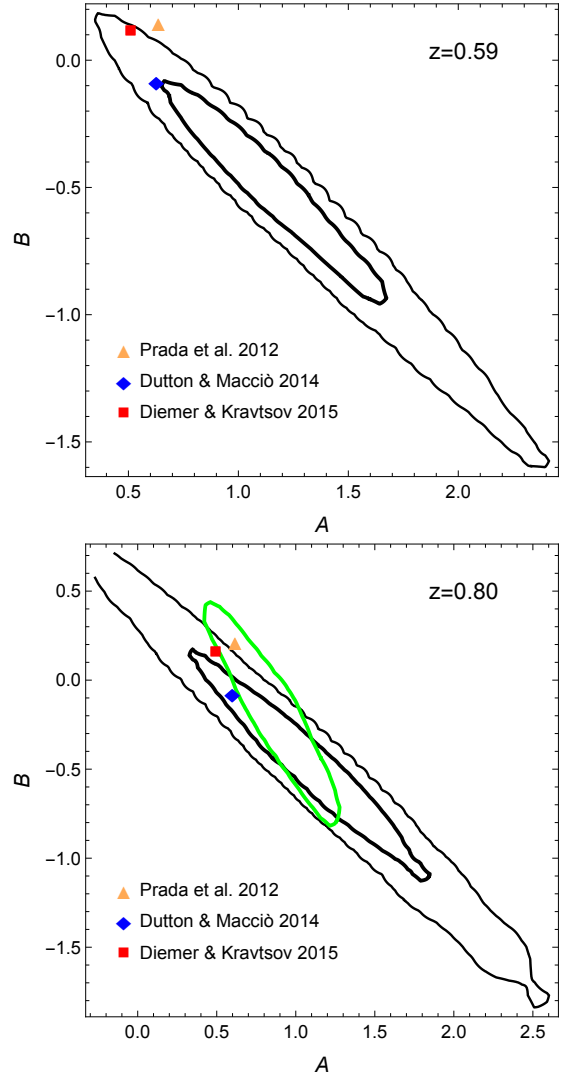


Fig. 9. Probability distributions of the A and B parameters of the $c-M$ relation Eq. (9) calculated with LIRA, for the full sample (*top*) and for the subsample of clusters at $z \geq 0.7$ (*bottom*). The relations are normalised at the median redshift of the sample considered (0.59 and 0.80, respectively). The confidence regions are defined as in Fig. 7. The coloured symbols show the estimates of the parameters from simulations by P12, DM14, and DK15 evaluated at the quoted redshift. The green contour shows the constraints from Sereno & Covone (2013) at 1σ .

and, second, the centroid shift, w , calculated as the standard deviation of the projected separation between the X-ray peak and centroids estimated within circular apertures of increasing radius from 25 kpc to $R_{\text{ap}} = 500$ kpc, with steps of 5%,

$$w = \left[\frac{1}{N-1} \sum_i (\Delta_i - \langle \Delta \rangle)^2 \right]^{1/2} \frac{1}{R_{\text{ap}}}, \quad (11)$$

where Δ_i is the distance between the X-ray peak and centroid of the i th aperture.

Figure 10 shows that the X-ray concentration is anti-correlated with the centroid shift, qualitatively following the relation found by Cassano et al. (2010). According to their results, clusters with $c_{\text{SB}} > 0.2$ and $w < 0.012$ are classified as “relaxed” (upper left quadrant in Fig. 10), while those with $c_{\text{SB}} < 0.2$ and $w > 0.012$, about 1/3 in our sample, are classified as “disturbed” (lower right quadrant). The relative composition

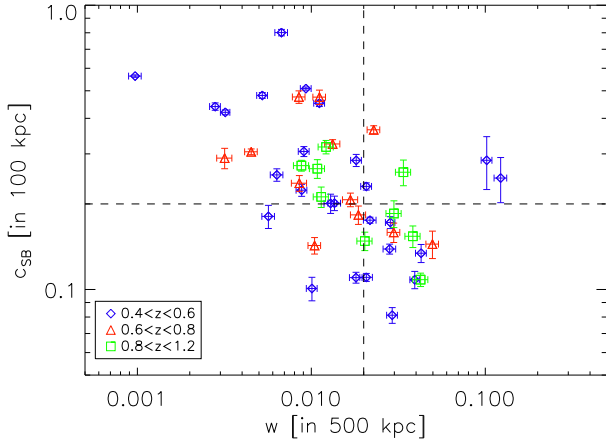


Fig. 10. Relation between the X-ray brightness concentration and centroid shift. Dashed lines trace the thresholds indicated by Cassano et al. (2010) to define relaxed and disturbed clusters (see text). Different symbols and colours are used for clusters in different redshift intervals.

of relaxed/disturbed clusters changes with the redshift, as 50% of the clusters observed at $z > 0.8$ are disturbed.

We characterise the general physical properties of the sample by investigating the relation between the mass and temperature of the gas. We consider the error-weighted mean of the temperatures measured in the spectral analysis at radii above 70 kpc. The gas mass is calculated by integrating the gas density profile over a spherical volume of radius R_{500} evaluated from the mass profile that we constrain as discussed in Sect. 4. We fit the relation

$$\log\left(\frac{h(z)M_{\text{gas},500}}{M_{\odot}}\right) = \log N + \tau \log\left(\frac{T}{5 \text{ keV}}\right), \quad (12)$$

using the Bayesian regression code LIRA of Sereno (2016). We obtain $\log N = 13.70 \pm 0.04$ and $\tau = 1.98 \pm 0.18$ with an intrinsic scatter $\sigma_{\text{int}} = 0.134 \pm 0.023$. Figure 11 shows the $M_{\text{gas},500} - T$ relation for the clusters in the sample together with the best-fitting relation, compared to the relation found by Arnaud et al. (2007) for a sample ten morphologically relaxed nearby clusters observed with *XMM-Newton* in the temperature range 2–9 keV. We find that the two relations are in agreement within the scatter, that in our sample is a factor ~ 4 higher than that measured for the sample of relaxed local systems in Arnaud et al. (2007). Once we consider only the most “relaxed” systems, that is those identified in the upper left quadrant of Fig. 10, the agreement does not improve. This suggests that more relevant selection biases affect any comparison between our sample and that in Arnaud et al. (2007).

We also compare the same relation with the gas mass estimated within a radius R_{2500} to the results obtained for the CLASH sample (Postman et al. 2012; Donahue et al. 2014). As shown in Fig. 11, our best-fit relation agrees well with the relation derived for the CLASH clusters with a remarkable agreement on the intrinsic scatter ($\sigma_{\text{int}} = 0.113 \pm 0.008$ for our sample, 0.093 ± 0.002 for CLASH).

Overall, we conclude that our sample, spanning a wide range both in redshift (0.41–1.24) and in the dynamical properties as inferred from proxies based on the X-ray morphology, is certainly less homogeneous than the samples of local massive objects. Our sample, however, compares in its physical properties to, for example the CLASH systems, which were only selected

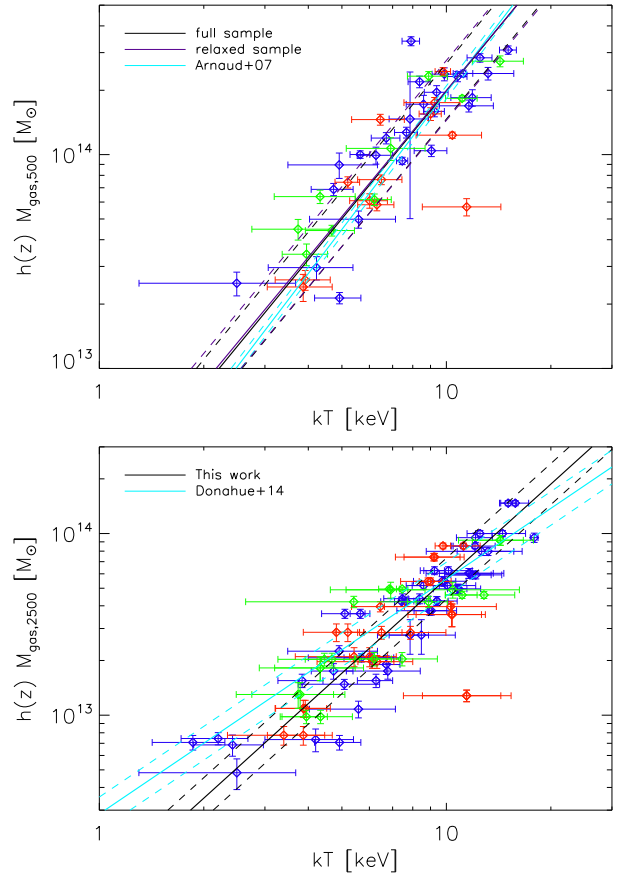


Fig. 11. Top panel: relation between the gas mass within R_{500} and temperature. The black and purple curves show the best-fit relation and its intrinsic scatter obtained for our full and relaxed sample, respectively. The cyan curves represent the relation of Arnaud et al. (2007). Bottom panel: relation between the gas mass within R_{2500} and temperature. The black curves show the best-fit relation and its intrinsic scatter. The cyan curves represent the relation obtained for the CLASH sample. Coloured symbols as in Fig. 10.

to be X-ray morphologically not disturbed and massive (i.e. very X-ray luminous) at intermediate to high redshifts similar to the manner in which we select our targets.

6.1. On the completeness of the sample

Some completeness properties of the selected objects can be studied through the analysis of the mass distribution of the clusters in the sample (see Appendix A in Sereno & Ettori 2015b). In so far as the mass distribution is well approximated by a regular and peaked distribution, the completeness of the observed sample can be usually approximated as a complementary error function

$$\chi(\mu) \simeq \frac{1}{2} \text{erfc}\left(\frac{\mu_{\chi} - \mu}{\sqrt{2}\sigma_{\chi}}\right), \quad (13)$$

where μ is logarithm of the mass. At first order, μ_{χ} and σ_{χ} can be approximated by the mean and standard deviation of the observed mass distribution.

We perform the analysis of the completeness together with the $c - M$ relation, as LIRA fits the scaling parameters and

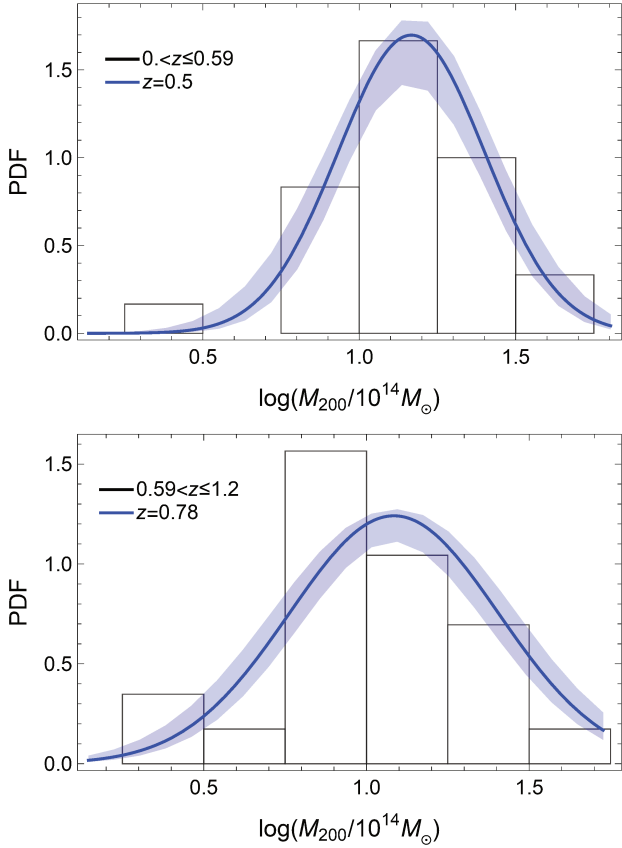


Fig. 12. Mass distribution of the selected clusters in two redshift bins. The black histogram bins the observed masses. The blue line is the normal approximation estimated from the regression at the median redshift (see text for details). The shaded blue region encloses the 68.3 per cent probability region around the median relation due to parameter uncertainties. Redshift increases *from top to bottom panel*. The median and boundaries of the redshift bins are indicated in the legends of the respective panels.

distribution of the covariate at the same time. The mass distribution for the observed masses is estimated from the regression output, i.e. the function of the true masses, by smoothing the prediction with a Gaussian whose variance is given by the quadratic sum of the intrinsic scatter of the (logarithmic) mass with respect to the true temperature and median observational uncertainty. In Fig. 12, we plot the mass distributions in two redshifts bins and we show that the log-normal distribution provides an acceptable approximation to these mass distributions.

In Fig. 13, we plot the redshift dependence of the selected clusters. The mass completeness limits are fairly constant, differently to survey selected clusters, where the mass limits usually increase with the distance. The selection criteria we imposed on the temperature profile and morphological properties effectively selected the very massive high end of the cluster halo function in the investigated redshift range.

Notwithstanding some heterogeneity in the selection criteria, the sample is well behaved, suggesting that the targeted observations of X-ray clusters cover the very luminous end at each redshift. The effective flux threshold decreases with redshift so that the number of high redshift objects is comparable to the number of intermediate redshift objects.

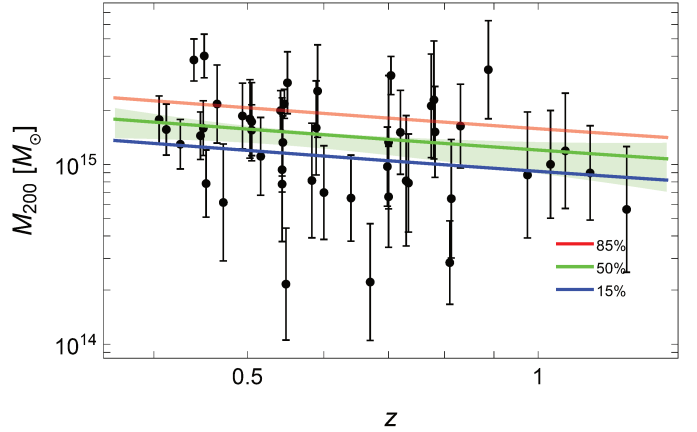


Fig. 13. Completeness functions compared to the distribution of the selected clusters in the $M_{200}-z$ plane (black points). The full lines plot the true value of mass (see text and Appendix A in Sereno & Ettori 2015b for details) below which a given fraction (from top to bottom: 85, 50, and 15 per cent levels, respectively) of the selected sample is contained. The shaded green region encloses the 68.3 per cent confidence region around the 50 per cent level due to uncertainties on the parameters.

7. Summary and conclusions

We investigate the concentration-mass relation for a sample of 47 galaxy clusters observed with *Chandra* in the redshift range $0.4 < z < 1.2$. We consider the largest sample investigated so far at $z > 0.4$ and we provide the first constraint on the $c(M)$ relation at $z > 0.7$ from X-ray data only.

We select archival exposures of targets with no major mergers and with sufficient X-ray signal to allow us to recover the hydrostatic mass properly. Using X-ray morphological estimators, we verify that about 1/3 of the sample is not completely relaxed and that this fraction rises to 0.5 in the objects at $z > 0.8$.

As consequence of our selection, the sample is not statistically complete and includes targets that were selected differently for their original observations. This implies that some unquantifiable bias could be present and could affect the interpretation of the results. However, we verify that the sample presents a $M_{\text{gas}} - T$ relation that behaves very similarly to the relation estimated locally (see Sect. 6), and that because the selected objects are very luminous in the X-ray band, the selection applied is, in practice, on the total mass and tends to represent the very massive high end of the cluster halo function properly, in particular at high redshift (see Sect. 6.1).

We perform a spatial and a spectral analysis for each cluster, and we extract the radial profiles of the gas temperature and density (obtained from the geometrical deprojection of the surface brightness). We reconstruct the total mass profile by assuming spherical symmetry of the ICM and hydrostatic equilibrium between the ICM and the gravitational potential of the cluster, which is assumed to have a NFW profile described by a scale radius r_s and a concentration c . We obtain constraints on (r_s, c) by minimising a merit function in which the spectral temperature profile is matched with the temperature predicted from the inversion of the hydrostatic equilibrium equation that depends only on these parameters.

We are able to determine temperature profiles up to a median radius of $0.3 R_{200}$ and gas density profiles up to a median radius of $0.5 R_{200}$. Beyond these limits, and at R_{200} in particular, our estimates are the result of an extrapolation. Our hydrostatic mass

estimates are in very good agreement with the result from weak-lensing analysis available in literature. In particular, the $c-M$ relation calculated for the clusters shared with the CLASH sample is fully consistent within the errors.

We estimate a total mass M_{200} in the range (1st and 3rd quartile) $8.1-18.6 \times 10^{14} M_{\odot}$ and a concentration c_{200} between 2.7 and 5. The distribution of concentrations is well approximated by a log-normal function in all the mass and redshift ranges investigated.

Our data confirm the expected trend of lower concentrations for higher mass systems and, at a fixed mass range, lower concentrations for higher redshift systems. The fit to the linear function $\log c_{200} = A + B \times \log M_{200}/(10^{14} M_{\odot}) + C \times \log(1+z) \pm \sigma_{\log c_{200}}$ gives a normalisation $A = 1.15 \pm 0.29$; a slope $B = -0.50 \pm 0.20$, which is slightly steeper than the value predicted by numerical simulations ($B \sim -0.1$); a redshift evolution $C = 0.12 \pm 0.61$, which is consistent with zero; and an intrinsic scatter on the concentration $\sigma_{\log c_{200}} = 0.06 \pm 0.04$.

The predictions from numerical simulations of the estimates of the normalisation A and slope B are in a reasonable agreement with our observational constraints at $z > 0.4$, once the correlation between them is fully considered (see Fig. 9). Values from Dutton & Macciò (2014) are consistent at the 1σ level. Larger deviations, but still close to the $\sim 2\sigma$ level of confidence, are associated with the predictions from Diemer & Kravtsov (2015) and Prada et al. (2012), where the latter is more in tension with our measurements.

In the redshift range $0.8 < z < 1.5$, constraints on the $c-M$ relation were also derived in Sereno & Covone (2013) for a heterogeneous sample of 31 massive galaxy clusters with weak- and strong-lensing signals, obtaining similar results to those discussed here with a slope that is slightly steeper than the theoretical expectation.

With this analysis, which represents one of the most precise determinations of the hydrostatic mass concentrations in high- z galaxy clusters, we characterise the high-mass end of the distribution of galaxy clusters even at $z \sim 1$, which is a regime that is hardly accessible to the present numerical simulations.

A homogeneous sample, and dedicated X-ray follow-up, would improve any statistical evidence presented in our study. In particular, an extension of this analysis to lower redshifts, still using *Chandra* data consistently, and a careful identification of a subsample of the most relaxed systems would constrain, at higher confidence, any evolution in the concentration-mass relation for clusters of galaxies, also as function of their dynamical state.

Acknowledgements. We thank Benedikt Diemer and the anonymous referee for helpful comments that improved the presentation of the work. S.E. and M.S. acknowledge the financial contribution from contracts ASI-INAF I/009/10/0 and PRIN-INAF 2012 “A unique dataset to address the most compelling open questions about X-Ray Galaxy Clusters”. M.S. also acknowledges financial contributions from PRIN INAF 2014 “Glittering Kaleidoscopes in the sky: the multifaceted nature and role of galaxy clusters”. This research has made use of the NASA/IPAC Extragalactic Database (NED), which is operated by the Jet Propulsion Laboratory, California Institute of Technology, under contract with the National Aeronautics and Space Administration.

References

- Arnaud, K. A. 1996, *Astronomical Data Analysis Software and Systems V*, 101, 17
- Arnaud, M., Pointecouteau, E., & Pratt, G. W. 2007, *A&A*, 474, L37
- Bhattacharya, S., Habib, S., Heitmann, K., & Vikhlinin, A. 2013, *ApJ*, 766, 32
- Binney, J., & Tremaine, S. 1987, *Galactic Dynamics* (Princeton University Press)
- Buote, D. A., Gastaldello, F., Humphrey, P. J., et al. 2007, *ApJ*, 664, 123
- Cash, W. 1979, *ApJ*, 228, 939
- Cassano, R., Ettori, S., Giacintucci, S., et al. 2010, *ApJ*, 721, L82
- Correa, C. A., Wyithe, J. S. B., Schaye, J., & Duffy, A. R. 2015, *MNRAS*, 452, 1217
- De Boni, C., Ettori, S., Dolag, K., & Moscardini, L. 2013, *MNRAS*, 428, 2921
- Dickey, J. M., & Lockman, F. J. 1990, *ARA&A*, 28, 215
- Diemer, B., & Kravtsov, A. V. 2015, *ApJ*, 799, 108
- Dolag, K., Bartelmann, M., Perrotta, F., et al. 2004, *A&A*, 416, 853
- Donahue, M., Voit, G. M., Mahdavi, A., et al. 2014, *ApJ*, 794, 136
- Duffy, A. R., Schaye, J., Kay, S. T., & Dalla Vecchia, C. 2008, *MNRAS*, 390, L64
- Dutton, A. A., & Macciò, A. V. 2014, *MNRAS*, 441, 3359
- Ettori, S., & Molendi, S. 2011, *Mem. Soc. Astron. It. Supp.*, 17, 47
- Ettori, S., De Grandi, S., & Molendi, S. 2002, *A&A*, 391, 841
- Ettori, S., Gastaldello, F., Leccardi, A., et al. 2010, *A&A*, 524, A68
- Ettori, S., Donnarumma, A., Pointecouteau, E., et al. 2013, *Space Sci. Rev.*, 177, 119
- Fruscione, A., McDowell, J. C., Allen, G. E., et al., 2006, *Proc. SPIE*, 6270, 62701V
- Hennawi, J. F., Gladders, M. D., Oguri, M., et al. 2008, *AJ*, 135, 664
- Kelly, B. C. 2007, *ApJ*, 665, 1489
- Klypin, A., Yepes, G., Gottlober, S., Prada, F., & Hess, S., 2014, *MNRAS*, submitted [arXiv:1411.4001]
- Ludlow, A. D., Navarro, J. F., Li, M., et al. 2012, *MNRAS*, 427, 1322
- Ludlow, A. D., Navarro, J. F., Angulo, R. E., et al. 2014, *MNRAS*, 441, 378
- Mahdavi, A., Hoekstra, H., Babul, A., et al. 2007, *ApJ*, 664, 162
- Mahdavi, A., Hoekstra, H., Babul, A., et al. 2013, *ApJ*, 767, 116
- Mantz, A., & Allen, S. W., 2011, *MNRAS*, submitted [arXiv:1106.4052]
- Markwardt, C. B. 2009, *Astronomical Data Analysis Software and Systems XVIII*, 411, 251
- Mazzotta, P., Rasia, E., Moscardini, L., & Tormen, G. 2004, *MNRAS*, 354, 10
- Meneghetti, M., & Rasia, E. 2013, *MNRAS*, submitted [arXiv:1303.6158]
- Meneghetti, M., Rasia, E., Vega, J., et al. 2014, *ApJ*, 797, 34
- Merten, J., Meneghetti, M., Postman, M., et al. 2015, *ApJ*, 806, 4
- Muñoz-Cuartas J. C., Macciò A. V., Gottlober S., Dutton A. A. 2011, *MNRAS*, 411, 584
- Navarro, J. F., Frenk, C. S., & White, S. D. M. 1997, *ApJ*, 490, 493
- Nelson, K., Lau, E. T., Nagai, D., Rudd, D. H., & Yu, L. 2014, *ApJ*, 782, 107
- Okabe, N., Takada, M., Umetsu, K., Futamase, T., & Smith, G. P. 2010, *PASJ*, 62, 811
- Poole, G. B., Fardal, M. A., Babul, A., et al. 2006, *MNRAS*, 373, 881
- Postman, M., Coe, D., Benítez, N., et al. 2012, *ApJS*, 199, 25
- Prada, F., Klypin, A. A., Cuesta, A. J., Betancort-Rijo, J. E., & Primack, J. 2012, *MNRAS*, 423, 3018
- Rasia, E., Ettori, S., Moscardini, L. et al. 2006, *MNRAS*, 369, 2013
- Rozo, E., Rykoff, E. S., Bartlett, J. G., & Evrard, A. 2014, *MNRAS*, 438, 49
- Schmidt, R. W., & Allen, S. W. 2007, *MNRAS*, 379, 209
- Sereno, M. 2015, *MNRAS*, 450, 3665
- Sereno, M. 2016, *MNRAS*, 455, 2149
- Sereno, M., & Covone, G. 2013, *MNRAS*, 434, 878
- Sereno, M., & Ettori, S. 2015a, *MNRAS*, 450, 3633
- Sereno, M., & Ettori, S., 2015b, *MNRAS*, 450, 3675
- Sereno, M., Giocoli, C., Ettori, S., & Moscardini, L. 2015, *MNRAS*, 449, 2024
- Umetsu, K., Zitrin, A., Gruen, D., et al., 2016, *ApJ*, 821, 116
- Vikhlinin, A., McNamara, B. R., Forman, W., et al. 1998, *ApJ*, 502, 558
- Vikhlinin, A., Kravtsov, A., Forman, W., et al. 2006, *ApJ*, 640, 691
- Williams, M. J., Bureau, M., & Cappellari, M. 2010, *MNRAS*, 409, 1330

Appendix A: The observed radial profiles of gas density and temperature

We present here the deprojected density and spectral temperature profiles of all of the clusters analysed in this work, as described in Sect. 3.

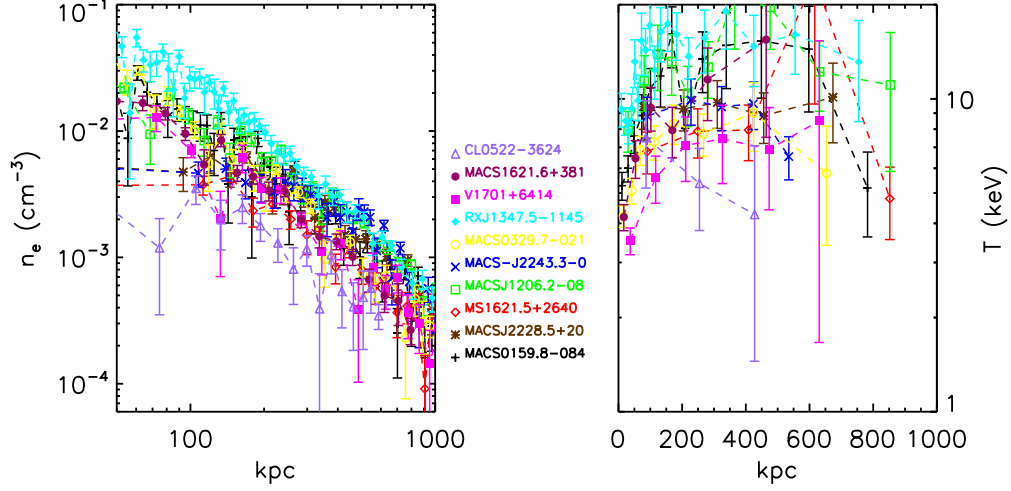


Fig. A.1. Deprojected electron density (*left*) and spectral temperature (*right*) profiles for clusters in the redshift range 0.405–0.472.

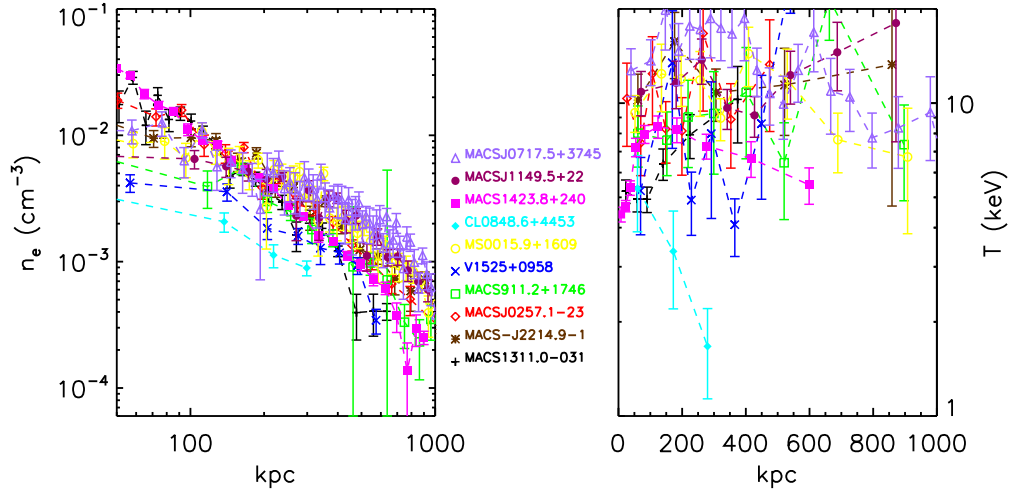


Fig. A.2. Same as in Fig. A.1 for clusters in the redshift range 0.494–0.546.

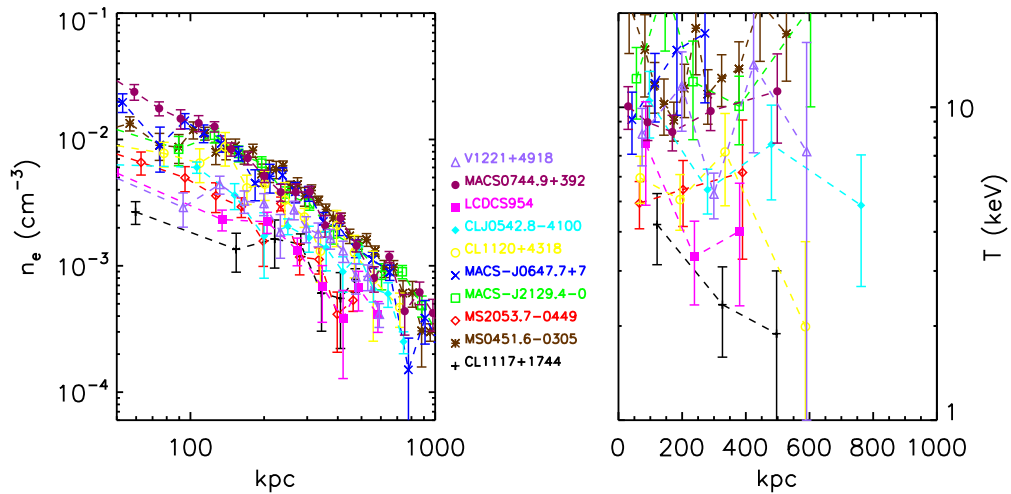


Fig. A.3. Same as in Fig. A.1 for clusters in the redshift range 0.548–0.7.

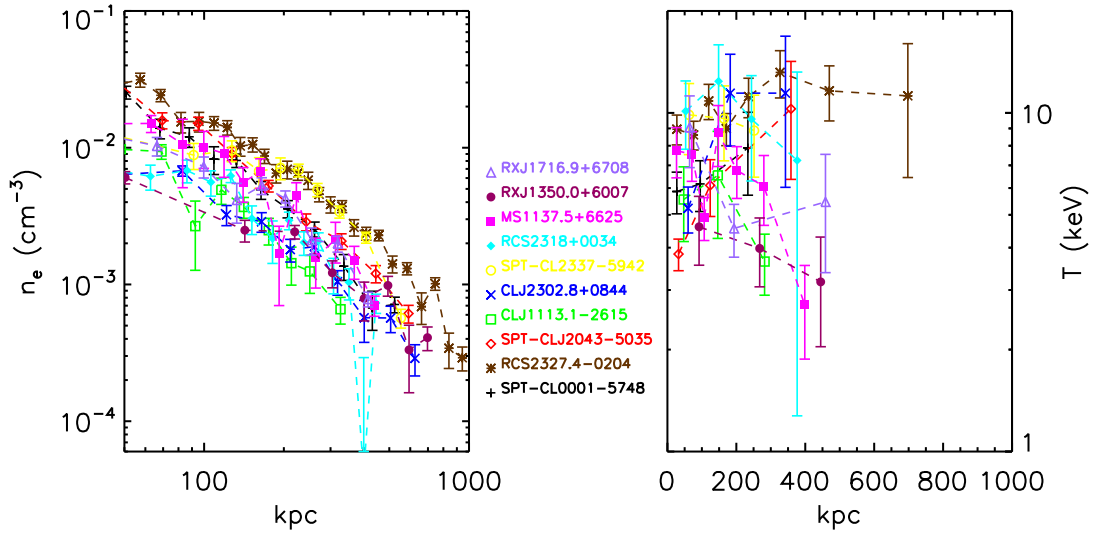


Fig. A.4. Same as in Fig. A.1 for clusters in the redshift range 0.7–0.813.

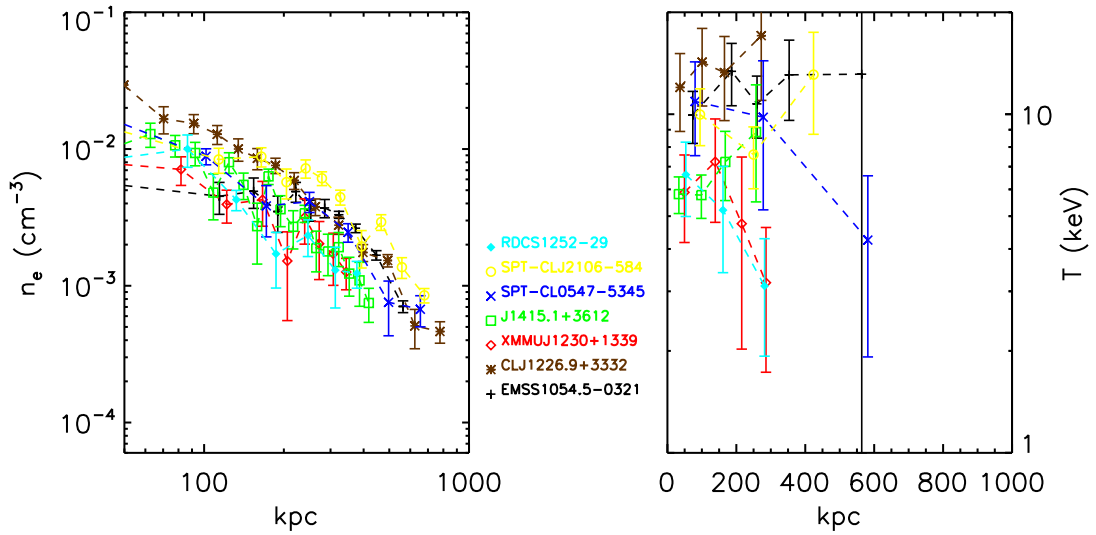


Fig. A.5. Same as in Fig. A.1 for clusters in the redshift range 0.831–1.235.

On the evolution of the entropy and pressure profiles in X-ray luminous galaxy clusters at $z > 0.4$

V. Ghirardini^{1,2}, S. Ettori^{2,3}, S. Amodeo⁴, R. Capasso^{5,6}, and M. Sereno^{1,2}

¹ Dipartimento di Fisica e Astronomia Università di Bologna, via Piero Gobetti, 93/2, 40129 Bologna, Italy
e-mail: vittorio.ghirardini2@unibo.it

² INAF, Osservatorio Astronomico di Bologna, via Piero Gobetti, 93/3, 40129 Bologna, Italy

³ INFN, Sezione di Bologna, viale Berti Pichat 6/2, 40127 Bologna, Italy

⁴ LERMA, Observatoire de Paris, PSL Research University, CNRS, Sorbonne Universités, UPMC Univ. Paris 06, 75014 Paris, France

⁵ Department of Physics, Ludwig-Maximilians-Universität, Scheinerstr. 1, 81679 Muenchen, Germany

⁶ Excellence Cluster Universe, Boltzmannstr. 2, 85748 Garching, Germany

Received 7 December 2016 / Accepted 4 April 2017

ABSTRACT

Context. Galaxy clusters are the most recent products of hierarchical accretion over cosmological scales. The gas accreted from the cosmic field is thermalized inside the cluster halo. Gas entropy and pressure are expected to have a self-similar behaviour with their radial distribution following a power law and a generalized Navarro-Frenk-White profile, respectively. This has also been shown in many different hydrodynamical simulations.

Aims. We derive the spatially resolved thermodynamical properties of 47 X-ray galaxy clusters observed with *Chandra* in the redshift range $0.4 < z < 1.2$, which is one of the largest samples investigated so far with X-ray spectroscopy and masses reconstructed via the hydrostatic equilibrium equation, with particular care taken to reconstruct the gas entropy and pressure radial profiles.

We search for deviation from the self-similar behaviour and look for possible evolution with redshift.

Methods. Under the assumption of a spherically symmetric distribution of the intracluster plasma, we combine the deprojected gas density and deprojected spectral temperature profiles via the hydrostatic equilibrium equation to constrain the concentration and scale radius, which are the parameters that describe a Navarro-Frenk-White profile for each of the clusters in our sample. The temperature profile, which combined with the observed gas density profile reproduces the best-fit mass model, is then used to reconstruct the profiles of entropy and pressure. These profiles cover a median radial interval of $[0.04 R_{500} - 0.76 R_{500}]$. After interpolating on the same radial grid and partially extrapolating up to R_{500} , these profiles are then stacked in three independent redshift bins to increase the precision of the analysis. The gas mass fraction is then used to improve the self-similar behaviour of the profiles by reducing the scatter among the profiles by a factor 3.

Results. The entropy and pressure profiles lie very close to the baseline prediction from gravitational structure formation. We show that these profiles deviate from the baseline prediction as function of redshift, in particular at $z > 0.75$, where, in the central regions, we observe higher values of the entropy (by a factor of ~ 2.2) and systematically lower estimates (by a factor of ~ 2.5) of the pressure. The effective polytropic index, which retains information about the thermal distribution of the gas, shows a slight linear positive evolution with the redshift and concentration of the dark matter distribution. A prevalence of non-cool core, disturbed systems, as we observe at higher redshifts, can explain such behaviours.

Key words. galaxies: clusters: intracluster medium – galaxies: clusters: general – X-rays: galaxies: clusters – intergalactic medium

1. Introduction

Cosmic structures evolve hierarchically from primordial density fluctuations, growing to form larger and larger systems under the action of gravity. Clusters of galaxies are the biggest virialized structures in the Universe and aggregate as bound objects at a relatively late time ($z < 3$). The cosmic baryons fall into the gravitational potential of the cold dark matter (CDM) halo and under the action of the collapse and subsequent shocks, adiabatic compression, and turbulence heat up to the virial temperature of few keV and form a fully ionized X-ray emitting intracluster medium (ICM; Tozzi & Norman 2001; Voit et al. 2005; Zhuravleva et al. 2014).

Modelling the ICM emission by thermal bremsstrahlung allows observations in the X-ray band to provide a direct probe of the gas (electron) density, n_e , and gas temperature, T . Assuming

the perfect gas law and a monoatomic gas, the pressure is recovered as $P = T n_e$ and the specific entropy as $K = T/n_e^{2/3}$.

Entropy is a fundamental quantity to track the thermal history of a cluster, since it always rises when heat is produced (see Voit et al. 2005). In the presence of non-radiative processes only, low-entropy gas would sink to the centre of the cluster while high-entropy gas would expand, producing the typical self-similar radial distribution that follows a power law with a characteristic slope of 1.1 (e.g. Tozzi & Norman 2001). Deviations from this predicted behaviour have been observed in the central region of clusters (see Ponman et al. 1999). Simulations show that non-gravitational cooling and heating processes, such as radiative cooling and subsequent AGN and supernovae feedback, break self-similarity in the inner region of galaxy clusters (e.g. Voit et al. 2005; McCarthy et al. 2017). To justify the observed deviations from self-similarity, Tozzi & Norman (2001)

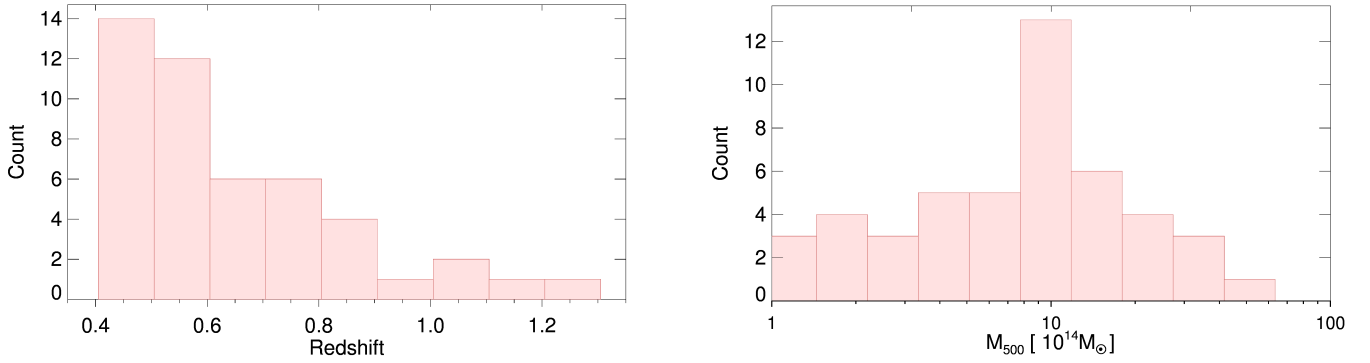


Fig. 1. Redshift (*left*) and total mass (*right*) distribution of the clusters in our sample.

propose a model in which an entropy *floor* is present before the gas is accreted by the dark matter halo.

Some dedicated papers have studied the evolution of the entropy profiles with redshift only in the last few years. McDonald et al. (2013), McDonald et al. (2014), and more recently Bartalucci et al. (2017) have concluded that both cool core clusters (CC) and non-cool core clusters (NCC) in samples selected through their Sunyaev-Zeldovich (Sunyaev & Zeldovich 1980, hereafter SZ) signal have similar entropy profiles with no relevant changes with the cosmic time.

On the other hand, pressure is the quantity the least affected by the dynamical history and non-gravitational physics (Arnaud et al. 2010). Using the model introduced by Nagai et al. (2007), Arnaud et al. (2010) show that pressure has a very regular radial profile with only small deviations about the mean (less than 30 per cent outside the core regions). This is confirmed by recent observations of SZ-selected clusters (e.g. McDonald et al. 2014; Bartalucci et al. 2017) showing no significant deviation from the “universal profile” within R_{500} up to redshift $z = 0.6$.

In this work, we use the analysis of the mass distribution of 47 galaxy clusters in the redshift range 0.405–1.235 presented in Amodeo et al. (2016) to study the radial shape of pressure and entropy at different redshifts, looking for deviations from the self-similar behaviour and for evolution with cosmic time.

In the present study, we assume a flat Λ CDM cosmology with matter density parameter $\Omega_M = 0.3$ and an Hubble constant of $H_0 = 70 \text{ km s}^{-1} \text{ Mpc}^{-1}$.

Therefore the critical density of the Universe is written as

$$\rho_c \equiv \frac{3H^2(z)}{8\pi G} = \frac{3H_0^2}{8\pi G} E^2(z) \approx 136 \frac{M_\odot}{\text{kpc}^3} E^2(z) \quad (1)$$

where $E(z) \equiv H(z)/H_0 = [\Omega_M(1+z)^3 + \Omega_\Lambda]^{1/2}$.

In our study, we also consider a rescaling dependent on the mass of the halo. To apply this, we measure the quantities of interest over the regions of the cluster defined by an overdensity Δ , which is defined as a region for which the mean mass density is Δ times the critical density of the Universe.

In the following analysis, we choose $\Delta = 500$, considering that our profiles have a radial extent of the same order of magnitude as R_{500} (see Fig. C.3). By definition, M_{500} is then equal to $4/3\pi 500\rho_c R_{500}^3$.

All the quoted statistical uncertainties are at 1σ level of confidence.

All the fitting processes are, unless otherwise stated, executed using the IDL routine MPFIT (Markwardt 2009), which performs a Levenberg-Marquardt least-squares fit weighting with both the errors on x - and y -axes.

The paper is organized as follows: in Sect. 2 we present the sample, in Sect. 3 we present the method we apply to reconstruct the entropy and pressure profiles. The data analysis is detailed in Sect. 4 with an exhaustive discussion of our results presented in Sect. 5. We draw our conclusions in Sect. 6.

2. Sample properties

The sample selection and X-ray analysis is thoroughly explained in Amodeo et al. (2016). In this work, however, we recall some of the most important properties. Because they are massive objects, the relatively long *Chandra* exposure time ($t_{\text{exp}} > 20$ ks) considered for each cluster permits us to extract at least three independent spectra over the cluster’s emission; this allows us to carry out a complete X-ray analysis as is usually performed for low redshift clusters. (see Amodeo et al. 2016, for details on the sample selection and X-ray analysis). We point out that clusters that are undergoing a major merger are excluded from the analysis since they would strongly break the hydrostatic equilibrium assumption, which is essential in recovering the mass profile. A completeness analysis of the sample has been made (see Amodeo et al. 2016): the selection criteria have effectively chosen the very massive high end of the cluster halo function in the investigated redshift range.

In Fig. 1, we show the redshift and mass distributions of the objects in our sample, with nine systems at $z > 0.8$ and eight with an estimated M_{500} larger than $2 \times 10^{15} M_\odot$. We use the centroid shift w and the concentration c_{SB} (both resulting from the analysis made in Amodeo et al. 2016) to distinguish clusters with a cool core and clusters without it. We follow the results of Cassano et al. (2010), choosing clusters with $w < 0.012$ and $c_{\text{SB}} > 0.2$ to be the classical relaxed CC. These objects are located in the upper-left quadrant of Fig. 2. The main goal of this paper is to study the evolution of entropy and pressure with cosmic time, therefore the sample is divided into redshift bins. Nevertheless a parallel analysis of the cluster sample has been made, in which clusters are divided in CC and NCC based on their morphological properties, using the criteria found by Cassano et al. (2010) mentioned above.

In our sample, the gas density profiles, obtained from the geometrical deprojection of the observed surface brightness profiles, cover the median radial range of $[0.04 R_{500} - 0.76 R_{500}]$ with a mean relative error of 21%. In Fig. C.3, we show the observed distribution of the minimum and maximum radius in the gas density profiles. We point out that half of the clusters have a radial coverage that extends above $0.77 R_{500}$.

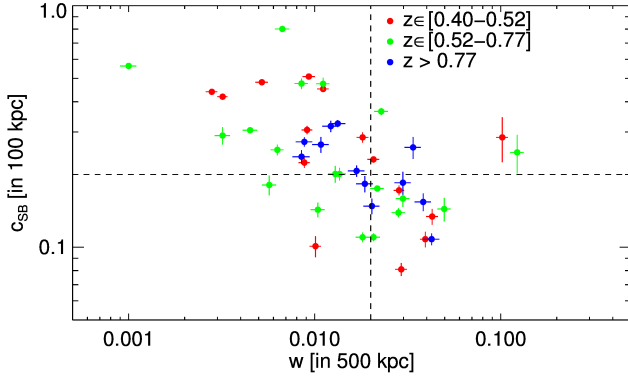


Fig. 2. Morphological parameters distribution in the plane of w vs. concentration c_{SB} .

3. Method to reconstruct $K(r)$ and $P(r)$

Amodeo et al. (2016) presented the method applied to constrain the mass distribution of the galaxy clusters in our sample under the assumption that a spherically symmetric ICM is in hydrostatic equilibrium with the underlying dark matter potential. The backward method adopted (see Ettori et al. 2013) allows us to constrain the parameters of a mass model, i.e. the concentration and scale radius for a NFW model (Navarro et al. 1997), using both the gas density profile, obtained from the geometrical deprojection of the X-ray surface brightness profile, and the spatially resolved spectroscopic measurements of the gas temperature. As a by-product of the best-fit mass model, we obtain the 3D temperature profile associated with the gas density measured in each radial bin. In other words, we obtain an estimate of the ICM temperature in each volume's shell where a gas density is measured from the geometrical deprojection of the X-ray surface brightness profile, in such a way that the best-fit mass model is reproduced by inserting the temperature and density profiles into the hydrostatic equilibrium equation (Binney & Tremaine 1987). From the combination of these profiles, thermodynamical properties such as pressure and entropy are recovered.

Following Voit (2005), temperature, pressure, and entropy associated with this halo's overdensity are, respectively,

$$k_{\text{B}}T_{500} = 10.3 \text{ keV} \left(\frac{M_{500}}{1.43 \times 10^{15} M_{\odot}} \right)^{\frac{2}{3}} E(z)^{2/3} \quad (2)$$

$$P_{500} = 1.65 \times 10^{-3} \text{ keV cm}^{-3} \left(\frac{M_{500}}{3 \times 10^{14} M_{\odot}} \right)^{2/3} E(z)^{8/3} \quad (3)$$

$$K_{500} = 103.4 \text{ keV cm}^2 \left(\frac{M_{500}}{10^{14} M_{\odot}} \right)^{2/3} E(z)^{-2/3} f_{\text{b}}^{-2/3} \quad (4)$$

$$K(R)/K_{500} = 1.42 \left(\frac{R}{R_{500}} \right)^{1.1}, \quad (5)$$

where Eq. (5) is the Voit et al. (2005) prediction for which the radial dependence of K is rescaled from $\Delta = 200$ to 500 with the ratio $\frac{R_{500}}{R_{200}} = 0.66$, as predicted from a NFW mass model with $c_{200} = 4$, which is typical for massive systems.

The importance of using a proper rescaling, which includes the gas mass fraction to reach self-similarity in the entropy profiles, is pointed out in the work of Pratt et al. (2010). The gas fraction, $f_{\text{gas}}(<r) = M_{\text{gas}}(<r)/M_{\text{tot}}(<r)$, is here defined as the ratio between the gas mass obtained from the integration of the gas density over the cluster's volume and hydrostatic mass and is thus reconstructed directly from our data. We show the

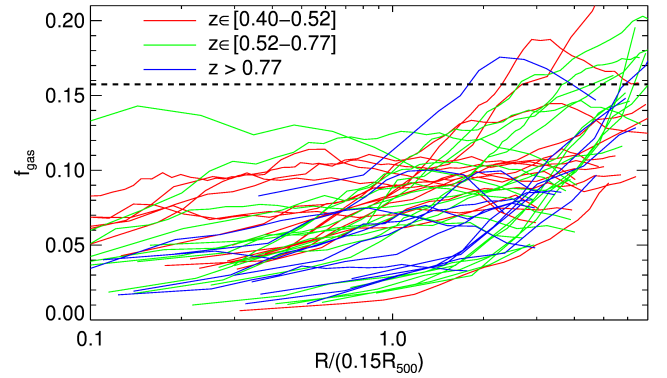


Fig. 3. Gas fraction profile for all our clusters. The black dashed line represents the universal baryon fraction from *Planck* (Planck Collaboration XIII 2016).

radial profiles of the gas fraction in Fig. 3. Throughout this paper we consider the universal baryon fraction to be $f_{\text{b}} = 0.15$ (Planck Collaboration XIII 2016). In Table A.1 we list additional information that is not presented in Amodeo et al. (2016), such as references on the redshifts and gas mass fraction at R_{500} .

4. Data analysis

We combine the profiles because of the poor statistics of each profile. In order to have at least one point in each radial bin, chosen logarithmically with total number of bins equal to 30¹, over the range $[0.015 R_{500}, R_{500}]$, we first extrapolated the data using the best-fit power law plus a constant for the entropy profile and the functional form introduced by Nagai et al. (2007) for the pressure profile,

$$\frac{P(x)}{P_{500}} = \frac{P_0}{(c_{500}x)^{\gamma} [1 + (c_{500}x)^{\alpha}]^{\frac{\beta-\gamma}{\alpha}}}, \quad (6)$$

where $x = R/R_{500}$ and γ , α , and β are the central slope, intermediate slope, and outer slope, respectively, defined by a scale parameter $r_s = R_{500}/c_{500}$ ($R \ll r_s$, $R \sim r_s$ and $R \gg r_s$, respectively). All the parameters of this function are left free except for the outer slope β and the inner slope γ , which is fixed to the ‘‘universal’’ values (5.49 and 0.308; Arnaud et al. 2010).

We calculated the value of the thermodynamical quantities in the extrapolated radial points with the functional forms indicated above. The error associated with the thermodynamic quantities in the extrapolated radial points is the sum in quadrature of the propagated best-fitting parameters and the median uncertainty estimated in the last five radial bins of the raw profiles.

Furthermore, to investigate the average behaviour of these profiles as function of redshift, we divided the dataset into three redshift bins chosen to have approximately the same number of clusters so that the resulting profiles have an approximately constant signal-to-noise ratio: 15 with $z \in [0.4, 0.52]$; 20 with $z \in [0.52, 0.77]$; and 12 with $z > 0.77$. In each redshift bin, the profiles are stacked in logarithmic space using the inverse of the 1σ error as weights, meaning that at each radial point the weighted mean is :

$$\langle x \rangle = \frac{\sum w_i x_i}{\sum w_i} \text{ with } w_i = \sigma_i^{-2},$$

¹ The number of bins equal to 30 is chosen to guarantee a proper radial coverage.

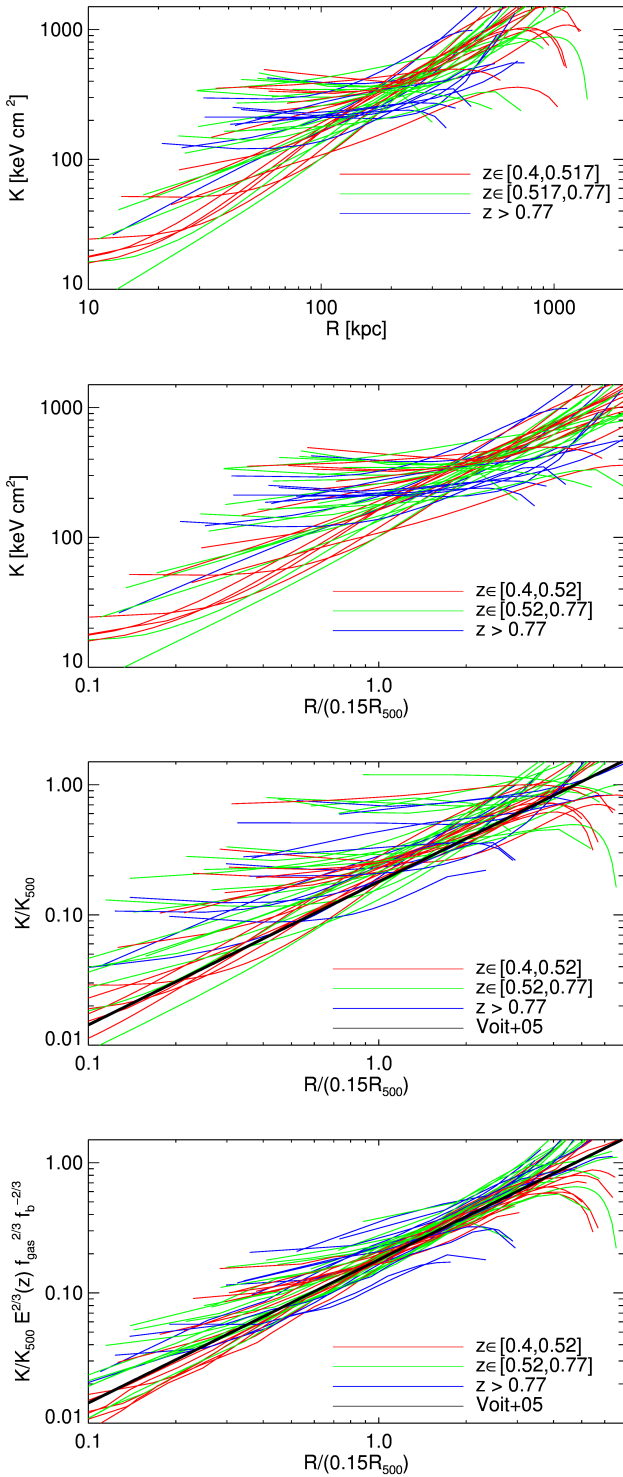


Fig. 4. Complete sample of our data is plotted and colour coded with respect to redshift. We can see the effect of rescaling *from top to bottom*, from largely scattered data to coherent data. No error bars are drawn for sake of clarity.

where x is the logarithm of the considered thermodynamic quantities (pressure or entropy).

This “stacking” procedure ensures a higher statistical significance of the measured “mean” quantities, which propagates into a lower uncertainties in constraining the best-fit parameters of the functional forms adopted.

4.1. Fitting procedure for the entropy profile

In Fig. C.5, we show the reconstructed entropy profiles, rescaled as described below using K_{500} , of the 47 clusters in our sample prior to the application of the extrapolation and stacking procedure.

The radial behaviour of the entropy distribution is commonly described with a power law plus a constant term accounting for the combined action of cooling and heating feedbacks, which affect the central regions (see Cavagnolo et al. 2009),

$$K = K_0 + K_{100} \left(\frac{R}{100 \text{ kpc}} \right)^\alpha. \quad (7)$$

This functional form has an underlying physical sense when we rescale with 100 kpc, since typically deviations from non-radiative simulations are seen below this radius, where cool core clusters and non-cool core clusters actually differ. The parameter K_0 is the central entropy, which has been used in several works (i.e. Cavagnolo et al. 2009; Voit et al. 2005; McDonald et al. 2013) to discriminate between relaxed CC clusters, with $K_0 \sim 30 \text{ keV cm}^2$, and disturbed NCC, with $K_0 > 70 \text{ keV cm}^2$.

We also consider a functional form where the scaling is carried out with respect to $0.15 R_{500}$ to take into account the dimension of the core in systems at different mass and redshift as follows:

$$\frac{K}{K_{500}} = K'_0 + K'_{0.15} \left(\frac{R}{0.15 R_{500}} \right)^{\alpha'}. \quad (8)$$

As shown in Pratt et al. (2010), we expect the scatter among entropy profiles of the clusters to be suppressed even more when the renormalization includes both the global and radial dependence on the gas mass fraction,

$$E(z)^{2/3} \frac{K}{K_{500}} \left(\frac{f_{\text{gas}}}{f_b} \right)^{2/3} = K''_0 + K''_{0.15} \left(\frac{R}{0.15 R_{500}} \right)^{\alpha''}. \quad (9)$$

In Fig. 4 we show how our refinement in the rescaling procedure of the entropy profiles from “no rescaling” at all to the inclusion of the dependence upon the gas fraction (see Eq. (9)), reduces the scatter among the profiles, improving the agreement with the self-similar prediction (Voit et al. 2005).

4.2. No rescaling

In the first panel of Fig. 4 we plot all the entropy profiles without applying any rescaling, i.e. the actual physical size in kpc versus entropy in keV cm^2 . We name these profiles “raw data”, because the physical values are reported without any rescaling. We can deduce that our clusters have very different thermodynamic histories and in fact at each radial point the profiles spans more than one order of magnitude, which excludes self-similarity.

We fit all the entropy profiles via Eq. (7) to look at the occupation of the parameter space in our sample. For each cluster we obtain a value for each one of the parameters K_0 , K_{100} , and α and we plot all those values in Fig. C.1. We fitted each one of the three histograms with a lognormal distribution. We dedicated special attention to the parameter K_0 , since the work of Cavagnolo et al. (2009) showed that central entropy may have a bimodal distribution. We obtained ~ 10 clusters with $K_0 = 0$ and ~ 3 with $\alpha = 0$.

In the central regions of galaxy clusters, no significant emission from gas at very low temperature is observed (e.g. Peterson & Fabian 2006), limiting the central value of the gas

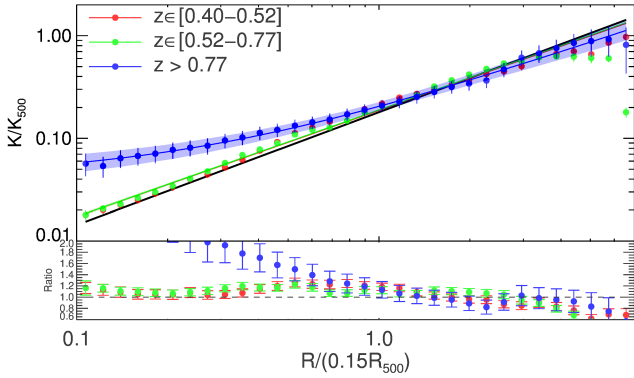


Fig. 5. Stacked entropy profiles and fits in the 3 redshift bins. The shaded areas represents the errors on the fit. The colours of the points are representative of the redshift bin considered. The black line represents the non-radiative prediction (Voit et al. 2005).

entropy to be positive ($K_0 > 0$). For this reason these points are excluded from Fig. C.1.

The parameter K_0 (top panel) does not have a clear bimodal distribution. The data exhibit a peak between 150 and 200 keV cm² and a significative tail for low values of K_0 . The best fit obtained with two lognormal distributions shows one peak at 130 keV cm² and one at 5 keV cm², with $\chi_{\text{red}}^2 = 1.83$, while the unimodal fits yield a peak at 100 keV cm² with $\chi_{\text{red}}^2 = 2.03$. We used the Bayesian information criterion (BIC; Schwarz 1978) to distinguish if there are statistical differences between the two fitted models: a ΔBIC between 2 and 6 indicates positive evidence against the model with higher BIC, while at values greater than 6 the evidence is strong. We obtained $\Delta\text{BIC} = 0.02$ and therefore we cannot discriminate between a unimodal and bimodal distribution. Even though the best-fit centers are close to the values found by Cavagnolo et al. (2009).

The distribution of the parameter K_{100} (middle panel of Fig. C.1) is well fitted by a lognormal distribution with median value corresponding to $104 \pm \frac{1702}{64}$ keV cm² and $\chi_{\text{red}}^2 = 0.17$. The distribution of this parameter is smooth without any significative tail; this indicates that fitting considering 100 kpc as the typical core dimension generates a well-defined distribution for K_{100} resembling a lognormal distribution.

The distribution of the power law index α (bottom panel of Fig. C.1) is, as K_{100} , well fitted by a lognormal distribution with median value $1.40 \pm \frac{0.672}{0.45}$ and $\chi_{\text{red}}^2 = 1.1$. The visible peak has a higher value than the non-radiative prediction (Voit et al. 2005), but nevertheless it is compatible within 1σ .

4.3. Rescaling using K_{500}

The profile of a thermodynamical quantity, including entropy, should have a unique shape for galaxy clusters, after adequate rescaling (Voit 2005). Non-radiative simulations (see Voit et al. 2005) have shown that we should rescale with quantities defined with respect to the critical density in order to achieve this. As it is stated above, we use an overdensity of 500 and rescale the entropy profile using K_{500} , which is defined in Eq. (4). We can observe the effect of the scaling in the third panel of Fig. 4. The profiles we get are less scattered than the raw data, even though the dispersion about the mean is still quite high, about one order of magnitude. Nevertheless we observe that above $0.15 R_{500}$

² This error represents the region that encompasses 68% of the data points from the best fit.

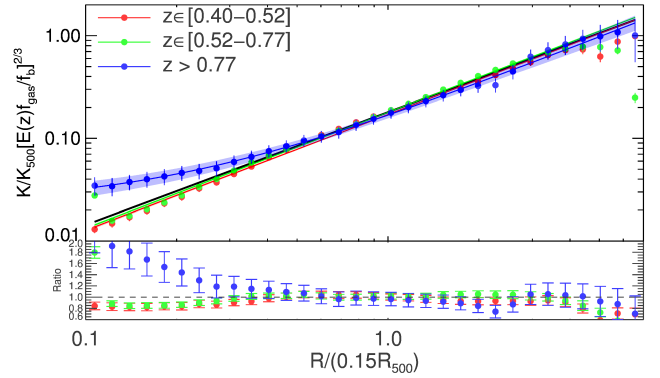


Fig. 6. Fits in different redshift bins showing the errors on the fits using the shaded area. The blue profile ($z > 0.77$) is compatible with the low redshift profiles for intermediate radii ($R > 0.07 R_{500}$) while at low radii there is a difference, where the high redshift entropy profile has a flat profile. The black line represents the non-radiative prediction (Voit et al. 2005).

most of the clusters have a self-similar behaviour. This is because non-gravitational processes are less relevant in the outskirts of galaxy clusters (Voit 2005).

As described in Sect. 4, we radially stack the data and we fit using Eq. (8). We show the regrouped data and the fitting results with their errors bars in Fig. 5 and in top part of Table 1. As we can observe from the ratio between the data and the predicted profile (bottom panel of Fig. 5), self-similarity is present below $0.6 R_{500}$ for the two low redshift bins while it is reached only between $0.15 R_{500}$ and $0.6 R_{500}$ at high redshift ($z > 0.77$). Moreover the high redshift stacked profile is slightly flatter than the others with a slope of 1.0 ± 0.1 and with its best fit requiring a constant term different from 0 to reproduce the data.

In the top part of Table 1 we show the best fit dividing the sample in CC and NCC. These parameters refers to Fig. B.1. As we can see both from the best fit and the plot, CC clusters are compatible with non-radiative prediction (Voit et al. 2005) with both slope and normalization. On the other hand, the NCC subset of clusters have a rather flat entropy profile.

4.4. Rescaling using the gas fraction

The entropy distribution depends on baryon fraction with a mass (or equivalently, temperature) dependence. Consequently entropy has both a radial and global dependence on the gas fraction (Pratt et al. 2010). When corrected by this effect, data become compatible with the non-radiative prediction (Voit et al. 2005) and the dispersion drops dramatically (last panel of Fig. 4).

A practical way to quantify the deviation from the self-similar prediction is shown in Fig. 7, where we show the behaviour of the dimensionless entropy profiles at some specific radii ($0.15 R_{500}$, R_{2500} , and R_{1000})², by interpolating the surrounding data points, with respect to the mass. When the mass decreases the deviation from the self-similar prediction increases. By modelling this dependance with a simple power law, we obtain a slope value which becomes smaller (in modulus) at larger radii. In particular, we point out that at the highest radius considered (R_{1000}), the profile is compatible with a constant, even though the influence of just 2 or 3 points makes the best-fit slope slightly negative.

² Radii as big as R_{500} are extrapolated and would not yield robust results and are therefore not shown.

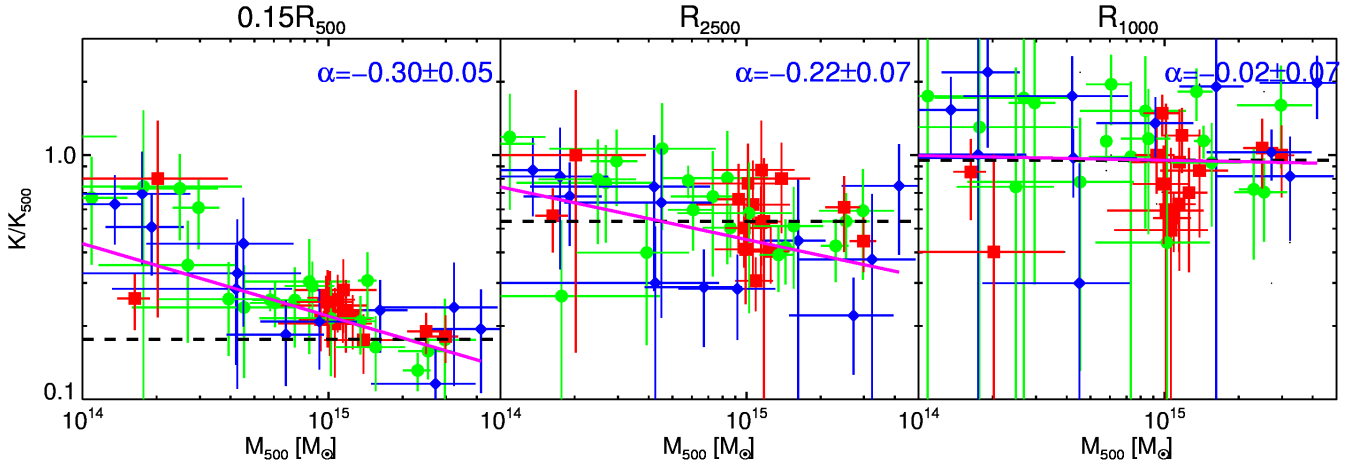


Fig. 7. Dimensionless entropy K/K_{500} as a function of mass M_{500} at different radii. Here the radii of $0.15 R_{500}$, R_{2500} , and R_{1000} are used. The black dashed curve is the expectation from the self-similar model, and the magenta line is the best fit using a power law with index α on all the data points. Red, green, and blue points indicate data points from $z \in [0.4-0.52]$, $z \in [0.52-0.77]$, and $z > 0.77$ respectively.

We renormalized the entropy profiles multiplying them by gas fraction profiles ($K \rightarrow K \times (E(z)f_{\text{gas}}(R)/f_b)^{2/3}$). The resulting profiles are visible in the last panel of Fig. 4. The self-similarity of the entropy profile is now finally clear in our dataset of clusters at different redshift. At $0.15 R_{500}$, for instance, the scatter is reduced by a factor ~ 3 when the rescaling by the gas fraction is applied.

We then stack our profiles and we show the resulting entropy radial distribution in Fig. 6. We notice that the stacked profiles are compatible with the non-radiative prediction (Voit et al. 2005) in the radial range $[0.05 R_{500}-0.7 R_{500}]$, with the two low redshift stacked profile pushing this compatibility down to the lower limit of our analysis. Moreover at large radii, $R > 0.7 R_{500}$, all the stacked profiles are slightly below the prediction.

We fit the stacked entropy profiles with a power law plus a constant and we show the results in Fig. 6 and in the bottom part of Table 1. The goodness of the fit has improved with respect to the rescaling without gas fraction and the parameters we get are closer to the non-radiative prediction.

The slope values we obtain are slightly larger than 1.1, indicating profiles that are steeper than the simulated profile, which agrees with several recent works (Voit et al. 2005; McDonald et al. 2013; Morandi & Ettori 2007; Cavagnolo et al. 2009). The situation is different in the case of $z > 0.77$, where the value of the central entropy is significantly different from zero. This indicates a high average central entropy for clusters at high redshifts.

In the bottom part of Table 1 we show the best fit dividing the sample into CC and NCC. This parameters refers to Fig. B.2, which is the plot analogous to Fig. 6. Similar to what happens to the split in redshift, the entropy profile of CC gets steeper than the prediction. The NCC are still flatter than the prediction and need a central entropy that is different from zero to fit the data.

5. Discussion

In the recent past, the dichotomy between cool core clusters, with a steep density profile and a drop of the temperature in the center, and non-cool core clusters, with a rather flat density profile and a flat temperature profile in the center, has been studied in numerous works. The particular shape of the density profile reflects in the behaviour of the entropy profile, where CC have a

Table 1. Best-fitting values and relative errors of the parameters of the models on entropy rescaled by K_{500} (Top) (Eq. (8)) and on entropy rescaled by both K_{500} and gas fraction (Bottom) (Eq. (9)).

Subset	$K'_{0.15}$	α'	K'_0	χ^2_{red}
$z \in [0.4, 0.52]$	0.188 ± 0.003	1.04 ± 0.01	–	2.34
$z \in [0.52, 0.77]$	0.189 ± 0.002	1.04 ± 0.01	–	2.0
$z > 0.77$	0.16 ± 0.02	1.0 ± 0.1	0.04 ± 0.01	0.14
CC	0.192 ± 0.003	1.12 ± 0.02	–	0.54
NCC	0.217 ± 0.003	0.77 ± 0.01	–	1.86
Subset	$K''_{0.15}$	α''	K''_0	χ^2_{red}
$z \in [0.4, 0.52]$	0.171 ± 0.002	1.13 ± 0.01	–	1.26
$z \in [0.52, 0.77]$	0.179 ± 0.002	1.13 ± 0.01	–	3.68
$z > 0.77$	0.15 ± 0.01	1.16 ± 0.08	0.022 ± 0.005	0.18
CC	0.173 ± 0.002	1.18 ± 0.01	–	0.46
NCC	0.184 ± 0.005	0.97 ± 0.03	0.006 ± 0.003	1.54

Notes. In the bin $z > 0.77$, we have a value for the central entropy that indicates the presence of many more NCC systems at high redshift. The exponent α and the term K_{100} are compatible with the prediction of Voit et al. (2005). We also see that the goodness of the fit improves a lot when we correct by the gas fraction.

low entropy floor in the center while NCC have a higher entropy floor (see Figs. B.1 and B.2).

5.1. Self-similarity

Non-radiative simulations predict that the thermodynamic properties of clusters of galaxies should be self-similar once rescaled to specific physical quantities. In the previous section we have shown that by using a proper rescaling we reach self-similarity (see Fig. 4). Self-similarity is observed for all the redshift ranges. However, only a proper rescaling using the gas fraction makes the agreement with the prediction (Voit et al. 2005) within 20% above $0.05 R_{500}$. This is shown in the bottom panel of Figs. 5 and 6, where the ratios between data rescaled as indicated in Eqs. (8) and (9), respectively, and the non-radiative prediction (Voit et al. 2005) is shown. We observe that rescaling by the gas fraction is only needed in the high redshift bin to recover the self similar behaviour that is reached between 0.05 and $0.7 R_{500}$ within 20% from the theoretical value.

The deviations present in the inner part of the profiles may be interpreted as some form of residual energy (Morandi & Etti 2007), which may be due to some non-gravitational physics processes.

Even though the agreement with simulations is remarkable, we get slightly steeper entropy profiles, i.e. 1.13 ± 0.01 for the low redshift bins, while we get a flatter profile in the high redshift bin, with a power law index that is compatible with the prediction, 1.16 ± 0.08 , but with a non-zero central entropy.

The agreement with the results of Cavagnolo et al. (2009) is excellent in all three redshift bins since we find all slopes between 1.1 and 1.2. For the high redshift bins adding a constant to reproduce the inner part of the profile is required to make our results on the slope compatible with both non-radiative predictions (Voit et al. 2005) and observations (Cavagnolo et al. 2009). Otherwise a simple power law would yield a flat profile with slope 0.90 ± 0.03 .

The excess with respect to the Voit et al. (2005) self-similar prediction is present at low radii where most of our data are above the prediction. This extra entropy is more pronounced in low mass systems, as shown in Fig. 7 and consistent with the results obtained by Pratt et al. (2010).

5.2. Angular resolution effect

In a thermalized system, low entropy gas sinks in the center while high entropy gas floats out in the outskirts, producing an entropy profile that increases monotonously with the radius. The net effect is that the larger the central bin considered for the analysis, the higher the measured value of the entropy. In the top panel of Fig. 8, we plot the value of K_0 for each cluster versus the radius of the innermost data point and measure an evident positive correlation (Pearson's rank correlation of 0.76, corresponding to a significance of 8.6×10^{-8} of its deviation from zero that is associated with the case with no correlation). This correlation becomes even more significant if we consider the same points rescaled by the properties of the halos. This is shown in the bottom panel of Fig. 8, where we measure a very significant Pearson's rank correlation of 0.83. A similar result is shown by Panagoulia et al. (2014): the smaller the innermost radial bin, the smaller the central entropy we measure.

However, as we show in Fig. 8, the correlation between the rescaled central entropy and the innermost radial bin shows a slope value of 1.78 ± 0.04 , which is about 8σ away from the expected value, and therefore does not reproduce the predicted radial dependence from Voit et al. (2005; see Eq. (5)), suggesting that the flattening has a different origin from the lack of spatial resolution.

5.3. Sample completeness

In Amodeo et al. (2016), an extended study on the completeness of the sample analysed here is performed. In their Fig. 13, the completeness functions are compared to the distribution of the objects in the $M_{200} - z$ plane, showing that the applied selection criteria effectively selected the very massive high end of the cluster halo function in the investigated redshift range.

The observed trend to detect lower masses at higher redshifts is intrinsic to the halo mass function predicted for the hierarchical structure formation in the CDM dominated Universe.

Therefore, we conclude that, within the limits of our sample selection and statistics, the observed redshift and mass dependencies are a reasonable representation of the behaviour of the

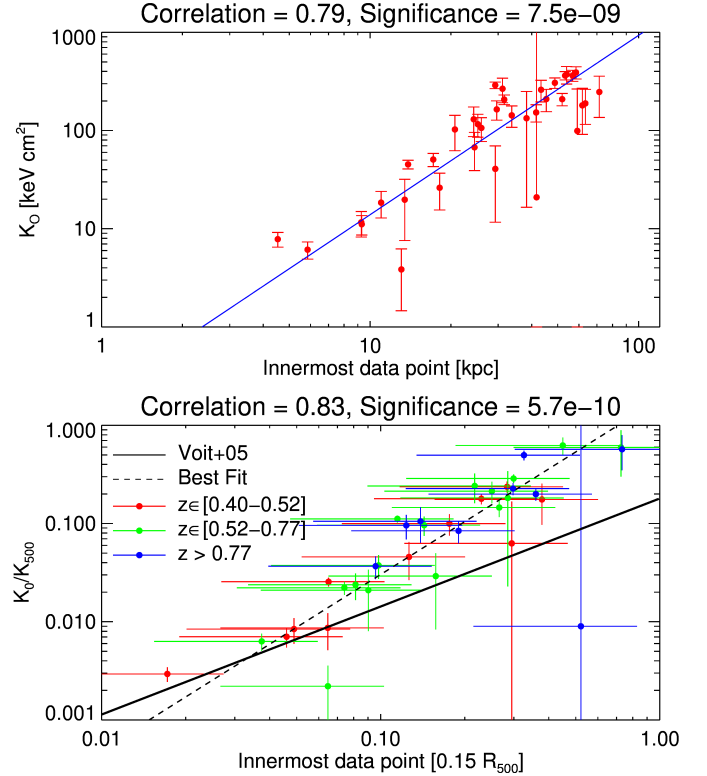


Fig. 8. *Top:* central entropy vs. the innermost data point. A clear positive correlation is measured. *Bottom:* central entropy versus innermost data point rescaled, an even tighter correlation is present.

X-ray luminous cluster population in the high mass end between $z = 0.4$ and $z = 1.2$.

5.4. Bimodality

Cavagnolo et al. (2009) have shown that the distribution of the values of the cluster central entropy reflects the dichotomy between CC and NCC clusters, finding two distinct populations peaking at 15 keV cm^2 and 150 keV cm^2 . This bimodality has not been confirmed in later work (e.g. Santos et al. 2010; Pratt et al. 2010).

In Sect. 3.2 we have shown that using the BIC there are no statistical differences between a unimodal and bimodal distribution. We consider whether this lack of statistical evidence is because of the poor statistics of the cluster sample. We build a bootstrap analysis of our distribution by selecting 10000 samples of our objects (also allowing for repetitions). This approach permits us to determine whether a random sample extracted from our data show an evident bimodal distribution. The results of this analysis are shown in Fig. C.4. We observe a median value of $2.0^{+3.2}_{-5.6}$ and conclude that the distribution of this BIC is compatible with no differences between a unimodal and bimodal distribution.

In Fig. C.2 the effect of redshift on the distribution of the central entropy is shown. As the number of clusters in each redshift bin is too small, we are not able to accurately prove any redshift evolution of the central entropy, however we have indications that an evolution may be present.

At high redshift we have an important peak at entropy higher than 100 keV cm^2 , which represents the NCC systems, and only one cluster with central entropy lower than 10 keV cm^2 .

We observe that from high redshift to low redshift the peak at high entropy becomes less prominent and a larger fraction of clusters get a smaller value of the central entropy, so that in the lower redshift bins the majority of our clusters have a central entropy below 100 keV cm^2 .

Nevertheless there is an indication of evolution from many NCC systems at high redshift towards mostly relaxed CC clusters at low redshift. Owing to the poor statistics of the sample we are not able to prove this scenario using statistical tests.

5.5. Evolution with redshift

We observe, within the central region, an evolution with redshift of the entropy ($r < 0.1 R_{500}$). It suggests that the entropy profiles are flatter at high redshifts in massive objects, or, alternatively, there is a non-zero central entropy at high redshift. This resembles an evolution in the entropy profiles. However, as we show in Fig. C.2, the fraction of NCC clusters is much higher at high redshifts than at low redshifts. This would imply that at $z > 0.77$ the clusters in our dataset are not able to develop a cool core similar to clusters at low redshift, meaning that cool cores are less common in the past, flattening the entropy profiles and creating a non-zero value for the central entropy. Several studies (e.g. Vikhlinin et al. 2007; Santos et al. 2008, 2010; McDonald 2011) that have investigated the evolution of the cool core of clusters, support this scenario, in particular on the lower relative abundance of the strongest CC at high redshift. In other works (e.g. McDonald et al. 2013, 2017), the cuspsiness of the gas density is shown to decrease with increasing redshift, as a consequence of a non-evolving core that is embedded in an ambient ICM, which evolves self-similarly.

If we define the CC clusters as those with central entropy that is lower than 100 keV cm^2 then from Fig. C.2 we derive that in the low redshift bins 67% of clusters are CC, which is a percentage that reduces to 50% and 40% in the intermediate and high redshift bins, respectively.

This result slightly deviates, but not in a significant way, from what has been presented in previous studies (e.g. Vikhlinin et al. 2007; McDonald et al. 2013). For example, McDonald et al. (2013; see their Fig. 12) obtain that CCs represent 40% (10–40%) of the cluster population at low (high) redshift. Their sample is SZ selected and is, therefore, less biased towards CC clusters with respect to an X-ray selected sample.

This result is consistent with the hierarchical scenario of the growth of structure, given that at high redshift ($z \sim 1$) clusters are in the middle of their formation history and cool cores could have easily been destroyed by one of the many merger events, or not even built, if they did not have enough time to relax in the center. Moreover, it is remarkable that even in our sample, which is selected in order to have specific X-ray properties and thus prone to include X-ray bright centrally peaked cool core objects, we observe a relatively larger fraction of NCC at higher redshift.

5.6. Pressure

For the same dataset, we study the behaviour of the electronic pressure profile $P(r) = n_e(r) T(r)$.

A generalized NFW profile, as introduced by Nagai et al. (2007) (see Eq. (6)), has been widely used to study the radial rescaled pressure profile. The best-fitting parameters $[P_0, c_{500}, \gamma, \alpha, \beta] = [8.403, 1.177, 0.3081, 1.0510, 5.49]$ obtained

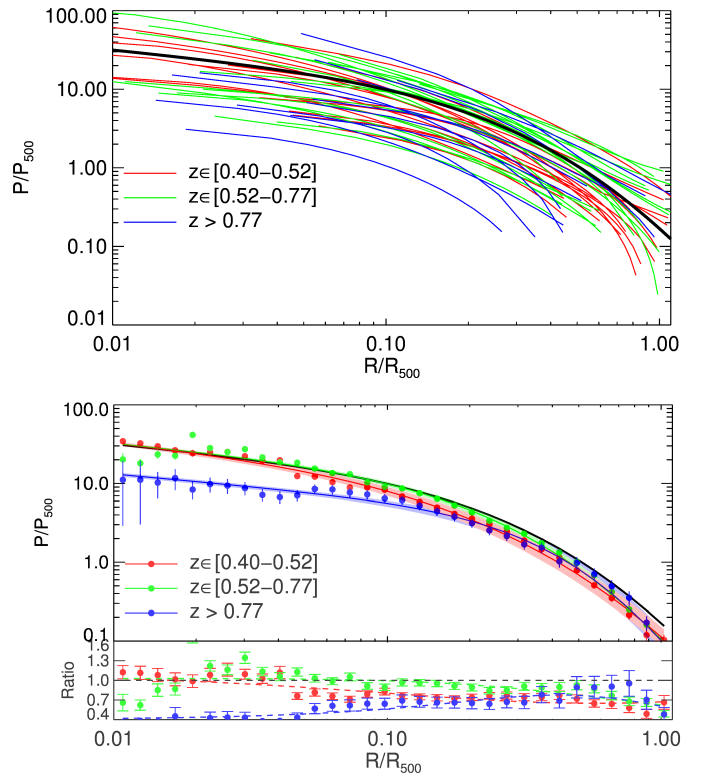


Fig. 9. *Top:* pressure profiles for all our clusters rescaled using an overdensity of 500, colour coded with respect to the redshift bin to which each curve belongs, compared with the best-fit results in Arnaud et al. (2010; black solid line). *Bottom:* stacked pressure profiles (in logarithmic space) compared with the best fit of Arnaud et al. (2010); the *panel at the bottom* shows the ratio with respect to the “universal” pressure profile.

from Arnaud et al. (2010) represent the so-called “universal pressure profile” for galaxy clusters.

Pressure is the quantity less affected by the thermal history of the cluster (Arnaud et al. 2010). Indeed McDonald et al. (2014) found no significant evolution of the pressure profile in the analysis of SPT SZ-selected clusters, just a mild flattening of the profile below $0.1 R_{500}$. Battaglia et al. (2012), however, suggested from the analysis of cosmological hydrodynamical simulations that a significant evolution of the pressure profile should occur beyond $z = 0.7$, and only outside R_{500} , as consequence of the increasing non-thermal support towards the outskirts of galaxy clusters.

In the functional form shown in Eq. (6), we fix the parameters β and γ to the fiducial value found in the work of Arnaud et al. (2010). These parameters are degenerate and therefore fixing at least one of the slopes is advised for tighter parameter distributions and a better comparison (Arnaud et al. 2010).

The pressure profiles are plotted in the top panel of Fig. 9, together with the curve of the universal profile, in order to make a comparison. All the profiles show a very similar shape, surrounding the “universal” one from both sides with an apparent discrepancy only in the normalization of the profiles. At each radius the scatter is of about one order of magnitude.

We applied the same procedure described in Sect. 4 and used in the analysis of the entropy profiles. We interpolated over the same radial grid, extrapolated up to R_{500} using the best-fit model, and stacked these pressure profiles. We obtained that the stacked curves in the two low redshift bins are compatible with

Table 2. Best-fitting values, and relative errors for the pressure profiles modelled with the generalized NFW in Eq. (6).

Subset	P_0	c_{500}	γ	α	β	χ^2_{red}
$z \in [0.4, 0.52]$	9.1 ± 0.3	1.08 ± 0.08	0.308	0.87 ± 0.04	5.49	2.1
$z \in [0.52, 0.77]$	9.2 ± 0.2	1.48 ± 0.05	0.308	1.11 ± 0.04	5.49	4.6
$z > 0.77$	3.6 ± 0.2	1.5 ± 0.1	0.308	1.59 ± 0.14	5.49	0.8
CC	11.3 ± 0.3	1.30 ± 0.07	0.308	0.92 ± 0.03	5.49	2.1
NCC	5.46 ± 0.14	1.57 ± 0.05	0.308	1.43 ± 0.06	5.49	1.9
Universal	8.403	1.177	0.308	1.0510	5.49	–

Notes. The parameters β and γ are frozen to their “universal” values to break some degeneracy and facilitate the comparison between the results. The first column indicates the subset of our sample chosen to fit the data. We observe that the results on c_{500} and α of NCC subsample and the result of high redshift subset are compatible within 1σ . The goodness of the fit is indicated in the last column on the right. In general the value of the parameters are very close to the “universal” results of [Arnaud et al. \(2010\)](#), considering that they are highly degenerate. We point out that the parameter P_0 for the high redshift bin is significantly smaller than its value for the other bins and the “universal” value.

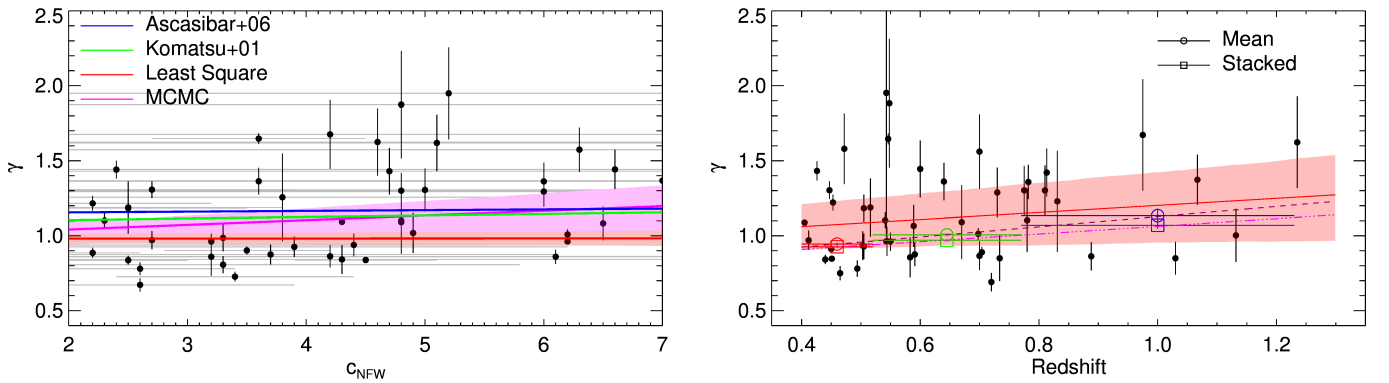


Fig. 10. *Left:* polytropic index for the objects in our sample vs. concentration: γ increases with larger values of c_{NFW} . Black points are the observed data points; the green and blue lines are the results of [Komatsu & Seljak \(2001\)](#) and [Ascasibar et al. \(2006\)](#), respectively; the red line with pink shaded area is the best fit using classical least squares minimization with 1σ confidence region; and the magenta line with lily shaded area is the best fit using an MCMC algorithm. *Right:* polytropic index for all clusters as a function of redshift. The data are better fitted by a linear relation: the effective polytropic index grows with redshift. Black points indicate the observed data points and the red line with pink shaded area indicates the best fit with 1σ dispersion using MCMC algorithm. The empty circles indicate the value of adiabatic index using the mean result for the clusters in each bin; the empty squares indicate the polytropic index of the stacked profiles in each redshift bin; the brown dashed line and dash-dotted magenta line indicate the best linear fit on the “mean” and “stacked” adiabatic index. The parameters describing these lines are listed in Table 3.

the “universal” pressure profile at radii below $0.1 R_{500}$, while above this value the data points are slightly below. Nevertheless the best fit on these stacked data points include the [Arnaud et al. \(2010\)](#) result at all radii within the error bars.

On the other hand, we observe a distinctive flattening below $0.1 R_{500}$ for the high redshift scaled profile for the inner part of these profiles with values that are about 30% of the “universal” pressure profile. Above this radius the data points are very close to the other redshift bins, meaning slightly below the [Arnaud et al. \(2010\)](#) result.

Pressure is indeed a thermodynamic property that is hardly affected by the thermodynamic history of clusters. The observed flattening at high redshift at low radii is also observed in the work of [McDonald et al. \(2014\)](#) and can be easily explained by the minimal presence of CC clusters at high redshift.

In Table 2 we show the best fit of Eq. (6), where we have kept β and γ fixed to the “universal” pressure profile best fit. We obtain a very good fit in all the three redshift bins; only the normalization of this functional in the high redshift bin shows a distinct discrepancy with the results of [Arnaud et al. \(2010\)](#), greater than 5σ . In fact the bottom panel of Fig. 9 shows that the low redshift bins points are almost on top of the “universal” profile, while the high redshift points are compatible only above $0.1 R_{500}$ and below this threshold the discrepancy grows

to be factor 3 at $0.01 R_{500}$. For completeness in the same table we show the fitting performed for the subsets of CC and NCC, referring to the data in Fig. B.3. We observe that NCC clusters best-fit results resembles the high- z subsample, while CC clusters resemble low- z objects.

5.7. Polytropic index

The polytropic index γ , equal to the ratio of specific heats C_P/C_V for an ideal gas, is a common proxy when evaluating the physical state and thermal distribution of the gas. It is defined as

$$P_e = \text{const.} \cdot n_e^\gamma, \quad (10)$$

with values of γ expected to be in the range [1.1, 1.2] ([Komatsu & Seljak 2001](#); [Ascasibar et al. 2006](#); [Shi 2016](#)), i.e. between 1, the value describing an isothermal gas, and 5:3, the value of an isentropic gas, when the gas is well mixed and the gas entropy per atom is constant.

Studying the evolution of the polytropic index with redshift and its relation with the concentration c of the dark matter distribution can provide a more consistent picture of the processes that regulate the hierarchical structure formation. A correlation between γ and c is expected if the radial structure of the ICM and

Table 3. Value of the polytropic index, dependence on concentration, and evolution with redshift.

Subset	Polytropic index γ	
	Mean	Stacked
$z \in [0.4, 0.52]$	0.935 ± 0.008	0.942 ± 0.008
$z \in [0.52, 0.77]$	0.996 ± 0.009	0.906 ± 0.006
$z > 0.77$	1.076 ± 0.031	1.041 ± 0.018
	$\gamma = m \cdot c_{\text{NFW}} + q$	
Method	m	q
Chi-squared	0.0004 ± 0.0057	0.98 ± 0.03
MCMC	0.031 ± 0.020	0.98 ± 0.09
Ascasibar+06	0.005 ± 0.002	1.145 ± 0.007
Komatsu+01	0.01	1.085
	$\gamma = m \cdot z + q$	
Method	m	q
Chi-squared	0.05 ± 0.05	0.94 ± 0.03
MCMC	0.24 ± 0.22	0.97 ± 0.14
Mean	0.29 ± 0.05	0.80 ± 0.030
Stacked	0.11 ± 0.03	0.86 ± 0.02

Notes. Top: values and errors on the polytropic index for the three redshift bins considering the mean and stacked values. We observe evolution with a significance greater than 2σ . Middle: fit of left panel of Fig. 10 using different methods and compared with previous theoretical work. Bottom: fit of right panel of Fig. 10 using different methods.

the host halo depend on the halo mass. Komatsu & Seljak (2001) require a linear relation between concentration and polytropic index by assuming in this theoretical work that the gas traces the dark matter distribution outside the core. Ascasibar et al. (2006) have shown that c and γ conspire to produce the observed scaling relations, matching the self-similar slope at many overdensities.

We estimate an effective polytropic index γ by fitting the pressure with a power law as a function of the gas density. As a first step, γ is calculated for each single cluster. Then, we evaluate the weighted mean in each bin. We also calculate γ for the stacked profiles.

We look for correlations between the polytropic index and dark matter concentration as recovered from the best fit with a NFW model in Amodeo et al. (2016). Ascasibar et al. (2006) and Komatsu & Seljak (2001) have shown that between concentration and polytropic index there is a linear relation with slope of 0.005 and 0.01, respectively. Using the Markov chain Monte Carlo (MCMC) code *emcee* (Foreman-Mackey et al. 2013), we obtain a slope that is much steeper than the theoretical predictions, although with a relative uncertainty of about 70% (see best-fit values in Table 3), which makes it compatible with previous results (Komatsu & Seljak 2001; Ascasibar et al. 2006) within 1σ , and even compatible with 0 at 2σ . Moreover, the intercept we get is much smaller than what has been previously calculated.

In the right panel of Fig. 10, we show the polytropic index as a function of redshift. We measure a positive evolution with redshift, with larger values of γ (by more than 2σ) at higher redshift (see Table 3).

6. Conclusions

From the sample described in Amodeo et al. (2016), which contains one of the largest collections of clusters at $z > 0.8$ that are homogeneously analysed in their X-ray spectral properties, we

have extracted the entropy and pressure profiles of 47 clusters observed with *Chandra* in a redshift range from 0.4 to 1.24.

We observe higher values of the gas entropy in the central region at higher redshift, which cannot be explained as an effect owing to spatial resolution. A plausible explanation of this result is the fact that at high redshift we observe a lack of cool core clusters with respect to the low redshift sample.

Moreover at intermediate radii, between 0.1 R_{500} and 0.7 R_{500} , the self-similarity is recovered when we use entropy dependence on both the redshift and gas fraction and the scatter between the profiles is reduced by a factor ~ 3 . The best fit of the stacked profiles is very similar to the Voit et al. (2005) prediction from non-radiative simulations. We also show that the pressure profiles flatten at high redshift at radii below 0.1 R_{500} with lower values by about 50% than those observed at $z \lesssim 0.5$.

Overall, these results agrees with a scenario in which galaxy clusters are the last gravitationally bound structures to form according to the hierarchical evolution. They start forming at $z \approx 3$, and at $z \sim 1-1.5$ they are still in the middle of their formation. At this epoch, cool cores could either be destroyed by merger events or have not formed yet, thereby reducing their relative number at earlier epoch. Moreover, the merging processes ongoing at high redshift would imply that objects at $z \sim 1$ are mostly unrelaxed, with a flatter entropy profile, which produces a clear excess in the inner parts and a deficit in the outskirts. As we show in Figs. 5 and 6, high redshift clusters indeed have a rather flat stacked entropy profile, supporting the evidence that the floating and sinking of the gas entropy has not been completed yet. The thermodynamical disturbed condition of the high redshift systems is further supported by the observed flattening of thermal pressure in the inner part of the stacked pressure profile (see Fig. 9).

Moreover, we measure a slightly significant evolution of the effective polytropic index of the ICM, we measure it by estimating $d \log P_e / d \log n_e$, using the dark matter concentration and redshift with an 87% significance (1.5σ) for concentration and 73% (1.1σ) for redshift, indicating that the gas possesses a slightly larger polytropic index in systems that have a more concentrated mass distribution at higher redshift. This result supports the observational evidence that at high redshift we recover more isentropic (i.e. more flat) entropy profiles.

References

- Allen, S. W., Schmidt, R. W., Ebeling, H., Fabian, A. C., & van Speybroeck, L. 2004, *MNRAS*, **353**, 457
- Amodeo, S., Ettori, S., Capasso, R., & Sereno, M. 2016, *A&A*, **590**, A126
- Arnaud, M., Pratt, G. W., Piffaretti, R., et al. 2010, *A&A*, **517**, A92, 11
- Ascasibar, Y., Sevilla, R., Yepes, G., Müller, V., & Gottlöber, S. 2006, *MNRAS*, **371**, 193
- Bartalucci, I., Arnaud, M., Pratt, G. W., et al. 2017, *A&A*, **598**, A61
- Battaglia, N., Bond, J. R., Pfrommer, C., & Sievers, J. L. 2012, *ApJ*, **758**, 75
- Binney, J., & Tremaine, S. 1987, *Galactic dynamics* (Princeton, NJ: Princeton University Press)
- Böhringer, H., Voges, W., Huchra, J. P., et al. 2000, *ApJS*, **129**, 435
- Bonamente, M., Joy, M. K., LaRoque, S. J., et al. 2006, *ApJ*, **647**, 25
- Borgani, S., Governato, F., Wadsley, J., et al. 2001, *ApJ*, **559**, L71
- Bryan, G. L. 2000, *ApJ*, **544**, L1
- Cassano, R., Ettori, S., Giacintucci, S., et al. 2010, *ApJ*, **721**, L82
- Cavagnolo, K. W., Donahue, M., Voit, G. M., & Sun, M. 2009, *ApJS*, **182**, 12
- Coble, K., Bonamente, M., Carlstrom, J. E., et al. 2007, *AJ*, **134**, 897
- De Propriis, R., Stanford, S. A., Eisenhardt, P. R., Holden, B. P., & Rosati, P. 2007, *AJ*, **133**, 2209
- Donahue, M., Voit, G. M., O’Dea, C. P., Baum, S. A., & Sparks, W. B. 2005, *ApJ*, **630**, L13
- Ebeling, H., Jones, L. R., Fairley, B. W., et al. 2001, *ApJ*, **548**, L23
- Ebeling, H., Barrett, E., Donovan, D., et al. 2007, *ApJ*, **661**, L33
- Edge, A. C., Ebeling, H., Bremer, M., et al. 2003, *MNRAS*, **339**, 913

- Ellis, S. C., & Jones, L. R. 2004, *MNRAS*, **348**, 165
- Ettori, S., Donnarumma, A., Pointecouteau, E., et al. 2013, *Space Sci. Rev.*, **177**, 119
- Fassbender, R., Böhringer, H., Santos, J. S., et al. 2011, *A&A*, **527**, A78
- Foley, R. J., Andersson, K., Bazin, G., et al. 2011, *ApJ*, **731**, 86
- Foreman-Mackey, D., Hogg, D. W., Lang, D., & Goodman, J. 2013, *PASP*, **125**, 306
- Gioia, I. M., & Luppino, G. A. 1994, *ApJS*, **94**, 583
- Gioia, I. M., Braito, V., Branchesi, M., et al. 2004, *A&A*, **419**, 517
- Gonzalez, A. H., Zaritsky, D., Dalcanton, J. J., & Nelson, A. 2001, *ApJS*, **137**, 117
- Gralla, M. B., Sharon, K., Gladders, M. D., et al. 2011, *ApJ*, **737**, 74
- Henry, J. P., Gioia, I. M., Mullis, C. R., et al. 1997, *AJ*, **114**, 1293
- Hicks, A. K., Ellingson, E., Bautz, M., et al. 2008, *ApJ*, **680**, 1022
- High, F. W., Stalder, B., Song, J., et al. 2010, *ApJ*, **723**, 1736
- Holden, B. P., Stanford, S. A., Squires, G. K., et al. 2002, *AJ*, **124**, 33
- Komatsu, E., & Seljak, U. 2001, *MNRAS*, **327**, 1353
- Kotov, O., & Vikhlinin, A. 2006, *ApJ*, **641**, 752
- Mantz, A. B., Allen, S. W., Morris, R. G., et al. 2014, *MNRAS*, **440**, 2077
- Markwardt, C. B. 2009, *Astronomical Data Analysis Software and Systems XVIII, ASP Conf. Ser.*, **411**, 251
- McCarthy, I. G., Schaye, J., Bird, S., & Le Brun, A. M. C. 2017, *MNRAS*, **465**, 2936
- McDonald, M. 2011, *ApJ*, **742**, L35
- McDonald, M., Benson, B. A., Vikhlinin, A., et al. 2013, *ApJ*, **774**, 23
- McDonald, M., Benson, B. A., Vikhlinin, A., et al. 2014, *ApJ*, **794**, 67
- McDonald, M., Allen, S. W., Bayliss, M., et al. 2017, *ApJ*, **843**, 28
- Morandi, A., & Ettori, S. 2007, *MNRAS*, **380**, 1521
- Morandi, A., & Cui, W. 2014, *MNRAS*, **437**, 1909
- Mullis, C. R., McNamara, B. R., Quintana, H., et al. 2003, *ApJ*, **594**, 154
- Muñoz-Cuartas, J. C., Macciò, A. V., Gottlöber, S., & Dutton, A. A. 2011, *MNRAS*, **411**, 584
- Nagai, D., Kravtsov, A. V., & Vikhlinin, A. 2007, *ApJ*, **668**, 1
- Navarro, J. F., Frenk, C. S., & White, S. D. M. 1997, *ApJ*, **490**, 493
- Panagoulia, E. K., Fabian, A. C., & Sanders, J. S. 2014, *MNRAS*, **438**, 2341
- Perlman, E. S., Horner, D. J., Jones, L. R., et al. 2002, *ApJS*, **140**, 265
- Peterson, J. R., & Fabian, A. C. 2006, *Phys. Rep.*, **427**, 1
- Planck Collaboration XIII. 2016, *A&A*, **594**, A13
- Ponman, T. J., Cannon, D. B., & Navarro, J. F. 1999, *Nature*, **397**, 135
- Pratt, G. W., Croston, J. H., Arnaud, M., Böhringer, H. 2009, *A&A*, **498**, 361
- Pratt, G. W., Arnaud, M., Piffaretti, R., et al. 2010, *A&A*, **511**, A85
- Romer, A. K., Nichol, R. C., Holden, B. P., et al. 2000, *ApJS*, **126**, 209
- Rosati, P., Tozzi, P., Ettori, S., et al. 2004, *AJ*, **127**, 230
- Santos, J. S., Rosati, P., Tozzi, P., et al. 2008, *A&A*, **483**, 35
- Santos, J. S., Tozzi, P., Rosati, P., Böhringer, H. 2010, *A&A*, **521**, A64
- Shi, X. 2016, *MNRAS*, **461**, 1804
- Schindler, S., Guzzo, L., Ebeling, H., et al. 1995, *A&A*, **299**, L9
- Schwarz G. 1978, *Ann. Statist.*, **5**, 461
- Sereno, M., & Ettori, S. 2015, *MNRAS*, **450**, 3675
- Song, J., Zenteno, A., Stalder, B., et al. 2012, *ApJ*, **761**, 22
- Stocke, J. T., Morris, S. L., Gioia, I. M., et al. 1991, *ApJS*, **76**, 813
- Sunyaev, R. A., & Zeldovich, I. B. 1980, *ARA&A*, **18**, 537
- Takey, A., Schwöpe, A., & Lamer, G. 2011, *A&A*, **534**, A120
- Tozzi, P., & Norman, C. 2001, *ApJ*, **546**, 63
- Tozzi, P., Scharf, C., & Norman, C. 2000, *ApJ*, **542**, 106
- Vanderlinde, K., Crawford, T. M., de Haan, T., et al. 2010, *ApJ*, **722**, 1180
- Vikhlinin, A., McNamara, B. R., Forman, W., et al. 1998, *ApJ*, **502**, 558
- Vikhlinin, A., Burenin, R., Forman, W. R., et al. 2007, in *Heating versus Cooling in Galaxies and Clusters of Galaxies* (Berlin Heidelberg: Springer-Verlag), ESO Astrophys. Symp., 48
- Voit, G. M. 2005, *Rev. Mod. Phys.*, **77**, 207
- Voit, G. M., Kay, S. T., Bryan G. L. 2005, *MNRAS*, **364**, 909
- Wang, Q. D., & Walker, S. 2014, *MNRAS*, **439**, 1796
- Wen, Z. L., Han, J. L., & Liu, F. S. 2009, *ApJS*, **183**, 197
- Zhuravleva, I., Churazov, E., Schekochihin, A. A., et al. 2014, *Nature*, **515**, 85

Appendix A: Additional information

Table A.1. Addition to Table 2 in [Amodeo et al. \(2016\)](#): information on the sizes and gas content of these clusters.

Object	z	R_{500} [kpc]	$f_{\text{gas},500}$ [fraction]	Reference for redshift
MACS0159.8-084	0.405	1379 ± 111	0.11 ± 0.02	Kotov & Vikhlinin (2006)
MACSJ2228.5+20	0.412	1418 ± 156	0.13 ± 0.03	Böhringer et al. (2000)
MS1621.5+2640	0.426	1298 ± 127	0.1 ± 0.02	Stocke et al. (1991)
MACSJ1206.2-08	0.44	1874 ± 128	0.08 ± 0.01	Borgani et al. (2001)
MACS-J2243.3-0	0.447	1335 ± 137	0.16 ± 0.03	Coble et al. (2007)
MACS0329.7-021	0.45	1264 ± 113	0.12 ± 0.04	Allen et al. (2004)
RXJ1347.5-1145	0.451	1756 ± 134	0.1 ± 0.02	Schindler et al. (1995)
V1701+6414	0.453	707 ± 48	0.26 ± 0.04	Wang & Walker (2014)
MACS1621.6+381	0.465	1349 ± 242	0.09 ± 0.04	Edge et al. (2003)
CL0522-3624	0.472	754 ± 271	0.11 ± 0.11	Mullis et al. (2003)
MACS1311.0-031	0.494	1420 ± 241	0.06 ± 0.02	Allen et al. (2004)
MACS-J2214.9-1	0.503	1275 ± 253	0.14 ± 0.06	Bonamente et al. (2006)
MACS911.2+1746	0.505	1338 ± 140	0.1 ± 0.07	Ebeling et al. (2007)
MACSJ0257.1-23	0.505	1293 ± 260	0.12 ± 0.05	Ebeling et al. (2007)
V1525+0958	0.516	1259 ± 191	0.05 ± 0.01	Mullis et al. (2003)
MS0015.9+1609	0.541	1381 ± 128	0.13 ± 0.02	Stocke et al. (1991)
CL0848.6+4453	0.543	701 ± 394	0.13 ± 0.2	Takey et al. (2011)
MACS1423.8+240	0.543	1041 ± 16	0.13 ± 0.01	Ebeling et al. (2007)
MACSJ149.5+22	0.544	1187 ± 141	0.19 ± 0.04	Ebeling et al. (2007)
MACSJ0717.5+3745	0.546	1409 ± 59	0.17 ± 0.02	Ebeling et al. (2007)
CL1117+1744	0.548	568 ± 106	0.2 ± 0.09	Wen et al. (2009)
MS0451.6-0305	0.55	1699 ± 229	0.07 ± 0.03	Gioia & Luppino (1994)
MS2053.7-0449	0.583	1239 ± 367	0.04 ± 0.02	Stocke et al. (1991)
MACS-J2129.4-0	0.589	1155 ± 228	0.15 ± 0.07	Ebeling et al. (2007)
MACS-J0647.7+7	0.591	1762 ± 333	0.06 ± 0.02	Ebeling et al. (2007)
CL1120+4318	0.6	894 ± 208	0.16 ± 0.08	Romer et al. (2000)
CLJ0542.8-4100	0.64	801 ± 68	0.13 ± 0.03	De Propriis et al. (2007)
LCDCS954	0.67	567 ± 98	0.16 ± 0.07	Gonzalez et al. (2001)
MACS0744.9+392	0.698	994 ± 93	0.17 ± 0.04	Ebeling et al. (2007)
SPT-CL0001-5748	0.7	902 ± 261	0.12 ± 0.08	Vikhlinin et al. (1998)
V1221+4918	0.7	738 ± 127	0.15 ± 0.07	Mantz et al. (2014)
RCS2327.4-0204	0.704	1547 ± 112	0.08 ± 0.01	Gralla et al. (2011)
SPT-CLJ2043-5035	0.72	1348 ± 255	0.07 ± 0.02	Song et al. (2012)
CJ1113.1-2615	0.73	747 ± 178	0.06 ± 0.04	Perlman et al. (2002)
CLJ2302.8+0844	0.734	1042 ± 207	0.06 ± 0.02	Perlman et al. (2002)
SPT-CL2337-5942	0.775	1590 ± 414	0.04 ± 0.02	Vanderlinde et al. (2010)
RCS2318+0034	0.78	1681 ± 484	0.02 ± 0.01	Hicks et al. (2008)
MS1137.5+6625	0.782	994 ± 203	0.06 ± 0.03	Gioia & Luppino (1994)
RXJ1350.0+6007	0.81	577 ± 71	0.17 ± 0.05	Holden et al. (2002)
RXJ1716.9+6708	0.813	646 ± 89	0.15 ± 0.05	Henry et al. (1997)
EMSS1054.5-0321	0.831	1308 ± 227	0.06 ± 0.02	Gioia et al. (2004)
CLJ1226.9+3332	0.888	1752 ± 409	0.04 ± 0.02	Ebeling et al. (2001)
XMMUJ1230+1339	0.975	792 ± 309	0.08 ± 0.07	Fassbender et al. (2011)
J1415.1+3612	1.03	772 ± 259	0.08 ± 0.05	Ellis & Jones (2004)
SPT-CL0547-5345	1.067	779 ± 188	0.14 ± 0.08	High et al. (2010)
SPT-CLJ2106-584	1.132	963 ± 254	0.13 ± 0.06	Foley et al. (2011)
RDCS1252-29	1.235	533 ± 124	0.13 ± 0.08	Rosati et al. (2004)

Appendix B: CC versus NCC

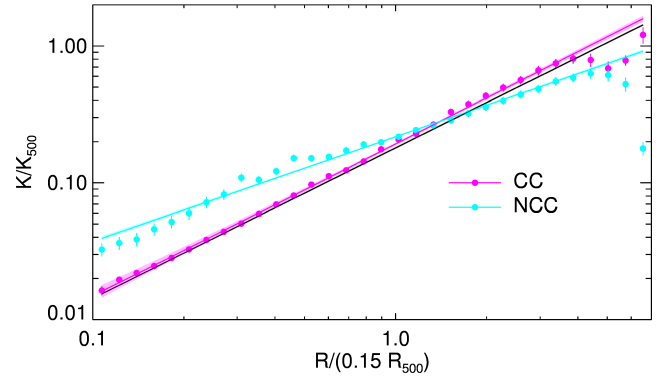


Fig. B.1. Staked entropy profiles for the subsets of CC and NCC based on [Cassano et al. \(2010\)](#) criteria. We observe that CC profile is almost on top of the [Voit et al. \(2005\)](#) prediction.

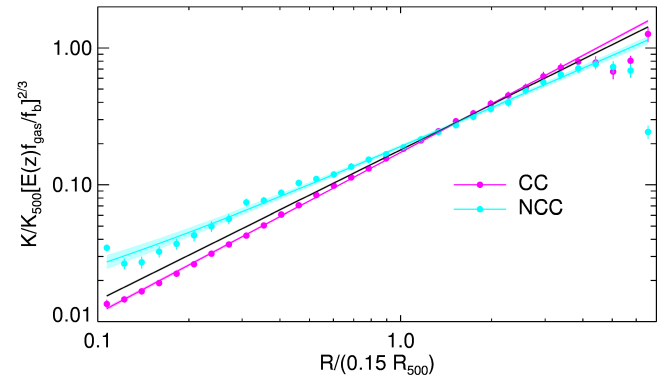


Fig. B.2. Staked entropy profiles corrected using the gas fraction for the subsets of CC and NCC. The CC entropy profile still lies very close to the prediction, while the NCC profile has gotten closer but still flatter than the prediction.

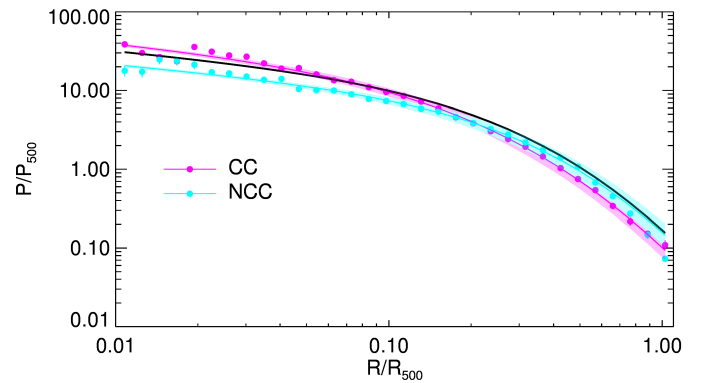


Fig. B.3. Pressure profiles for the subsets of CC and NCC. These profiles are very similar to those in [Fig. 9](#), however the NCC profiles within $0.1 R_{500}$ are about a factor of 2 higher than the high redshift one.

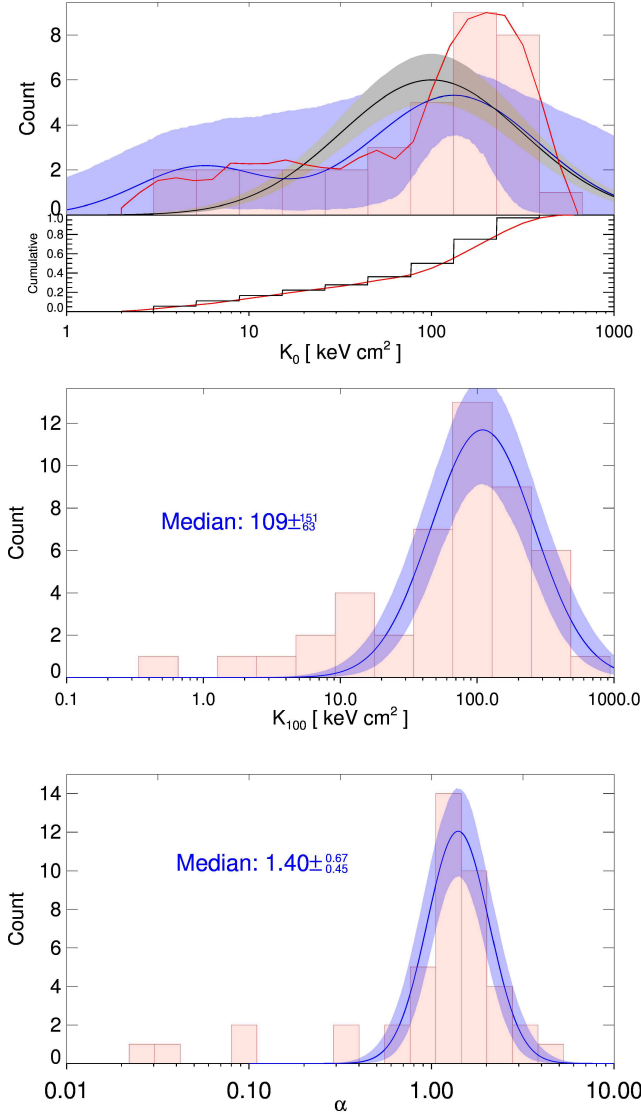
Appendix C: Plots


Fig. C.1. *Top:* distribution of the parameter K_0 . The red line represents the kernel density plot with a smoothing width of 0.1. The black and blue line represents the best fit obtained using one and two lognormal distributions, respectively. The shaded grey and blue regions enclose the 68.3 % probability region around the best fit due to parameter uncertainties. *Middle and bottom:* distribution of the parameters K_{100} and α , respectively. The blue line with shaded area represents the best fit with a single lognormal distribution and the 1σ probability regions around it. The median value of the fit is shown directly on the graph.

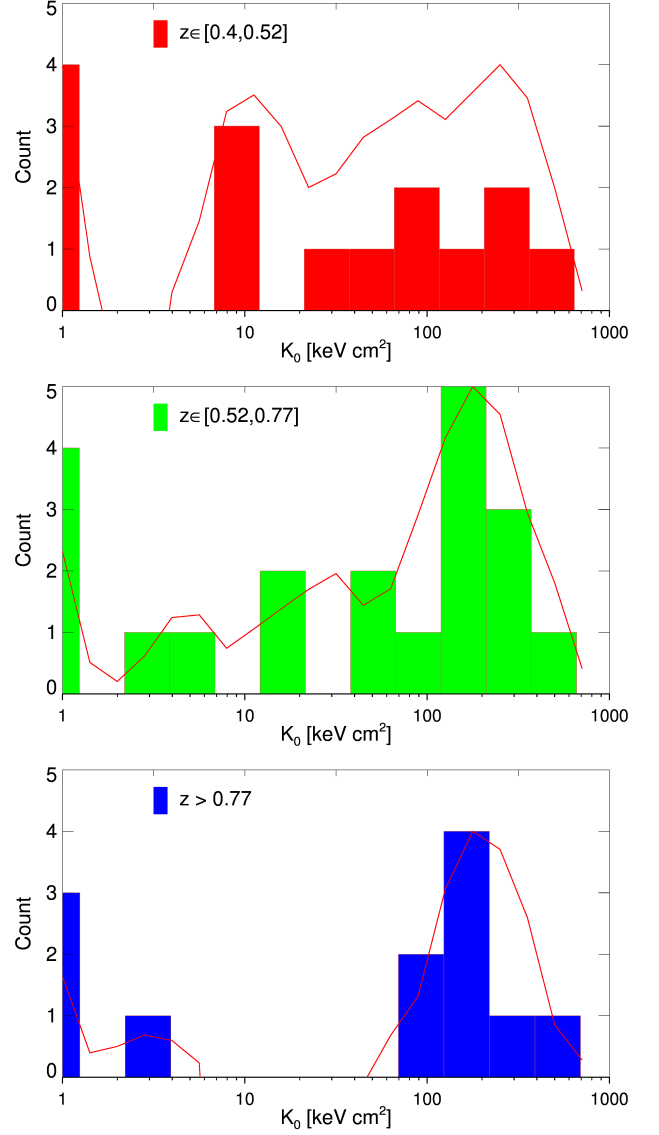


Fig. C.2. Evolution of the central entropy distribution with redshift. We can clearly see an evolution with evidence of bimodality at high redshift. The red lines represents the kernel density estimation of the distributions. The clusters that are best fitted by $K_0 = 0$ are added as if they have the value of 1 keV cm².

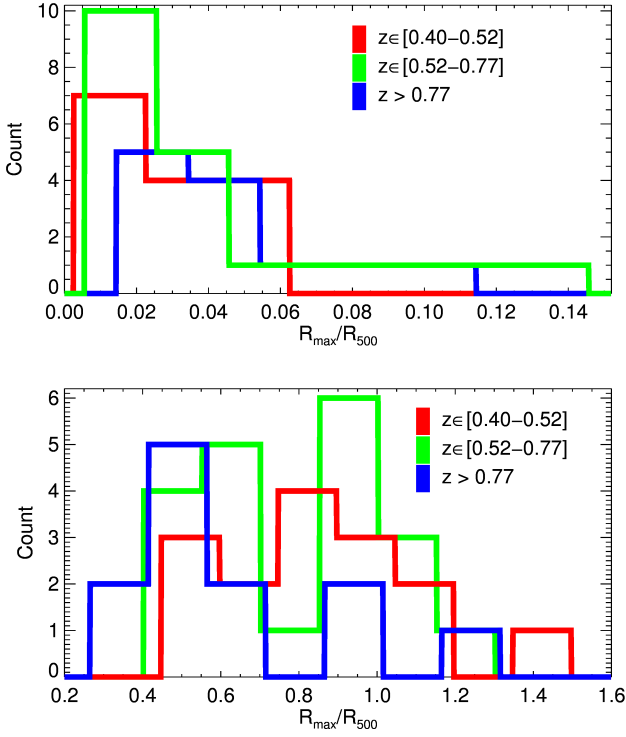


Fig. C.3. Distribution of the rescaled innermost (*top*) and outermost (*bottom*) radial spatial bin colour coded with redshift.

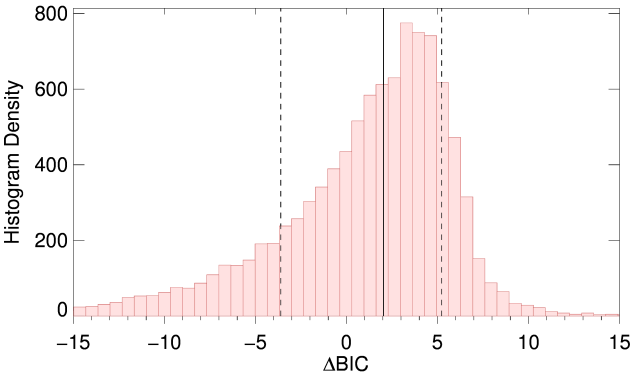


Fig. C.4. Distribution of the bootstraps results. The black solid line represents the position of the median, while the dashed lines represent the region comprising 68% of the distribution. The 1σ region is compatible with $\Delta\text{BIC} = 0$.

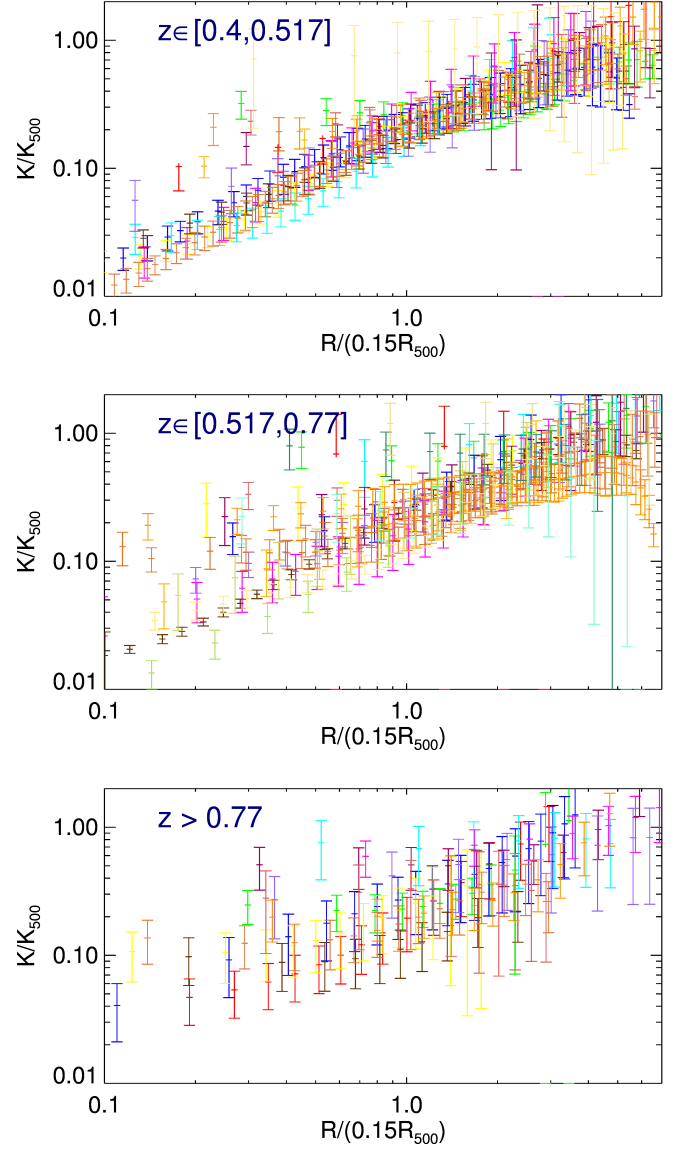


Fig. C.5. Rescaled entropy profiles of clusters in three redshift bins. Each colour represents data from a single cluster.



Probing Cosmology with Dark Matter Halo Sparsity Using X-Ray Cluster Mass Measurements

P. S. Corasaniti¹, S. Ettori^{2,3}, Y. Rasera¹, M. Sereno^{2,4}, S. Amodeo⁵, M.-A. Breton¹, V. Ghirardini^{2,4}, and D. Eckert⁶

¹LUTH, Observatoire de Paris, PSL Research University, CNRS, Université Paris Diderot, Sorbonne Paris Cité, 5 Place Jules Janssen, F-92195 Meudon, France
²INAF, Osservatorio Astronomico di Bologna, via Piero Gobetti 93/3, I-40129 Bologna, Italy
³INFN, Sezione di Bologna, viale Berti Pichat 6/2, I-40127 Bologna, Italy
⁴Dipartimento di Fisica e Astronomia, Università di Bologna, via Piero Gobetti 93/2, I-40129 Bologna, Italy
⁵LERMA, Observatoire de Paris, PSL Research University, CNRS, Sorbonne Université, UPMC Univ. Paris 6, F-75014 Paris, France
⁶Max-Planck-Institute for Extraterrestrial Physics (MPE), Giessenbachstrasse 1, D-85748 Garching, Germany

Received 2017 October 31; revised 2018 June 12; accepted 2018 June 12; published 2018 July 20

Abstract

We present a new cosmological probe for galaxy clusters, the halo sparsity. This characterizes halos in terms of the ratio of halo masses measured at two different radii and carries cosmological information encoded in the halo mass profile. Building on the work of Balmes et al., we test the properties of the sparsity using halo catalogs from a numerical N -body simulation of $(2.6 \text{ Gpc } h^{-1})^3$ volume with 4096^3 particles. We show that at a given redshift the average sparsity can be predicted from prior knowledge of the halo mass function. This provides a quantitative framework to infer cosmological parameter constraints using measurements of the sparsity of galaxy clusters. We show this point by performing a likelihood analysis of synthetic data sets with no systematics, from which we recover the input fiducial cosmology. We also perform a preliminary analysis of potential systematic errors and provide an estimate of the impact of baryonic effects on sparsity measurements. We evaluate the sparsity for a sample of 104 clusters with hydrostatic masses from X-ray observations and derive constraints on the cosmic matter density Ω_m and the normalization amplitude of density fluctuations at the $8 \text{ Mpc } h^{-1}$ scale, σ_8 . Assuming no systematics, we find $\Omega_m = 0.42 \pm 0.17$ and $\sigma_8 = 0.80 \pm 0.31$ at 1σ , corresponding to $S_8 \equiv \sigma_8 \sqrt{\Omega_m} = 0.48 \pm 0.11$. Future cluster surveys may provide opportunities for precise measurements of the sparsity. A sample of a few hundred clusters with mass estimate errors at the few percent level can provide competitive cosmological parameter constraints complementary to those inferred from other cosmic probes.

Key words: cosmological parameters – cosmology: theory – methods: numerical – X-rays: galaxies: clusters

1. Introduction

In the standard bottom-up scenario of cosmic structure formation, initially small dark matter (DM) density fluctuations grow under gravitational instability to eventually form at later times virialized stable objects, the halos. It is inside these gravitationally bounded clumps of DM that baryonic gas falls in to form the visible structures we observe in the universe. Today, the most massive halos host large clusters of galaxies resulting from the hierarchical merging process of lower-mass halos formed at earlier times. Since their assembly depends on the matter content of the universe, the state of cosmic expansion, and the initial distribution of matter density fluctuations, there is a consensus that observations of galaxy clusters can provide a wealth of cosmological information (see, e.g., Allen et al. 2011; Kravtsov & Borgani 2012, for a review of galaxy cluster cosmology).

Galaxy clusters can be observed through a variety of probes, such as the detection of the X-ray emission of the intracluster gas (e.g., Vikhlinin et al. 2005; Ebeling et al. 2010; Piffaretti et al. 2011; Pierre et al. 2016), the Sunyaev–Zel’dovich effect in the microwave (e.g., Staniszewski et al. 2009; Menanteau et al. 2013; Reichardt et al. 2013; Planck Collaboration et al. 2016b), the distribution of the member galaxies in the optical and IR bands (Koester et al. 2007; Rykoff et al. 2014), and the distortion of the background galaxies induced by the halo gravitational potential (e.g., Umetsu et al. 2011; Hoekstra et al. 2012; Postman et al. 2012).

Due to the highly nonlinear nature of the gravitational collapse driving the formation of DM halos, theoretical model

predictions, which are necessary to interpret the data and infer cosmological parameter constraints, have been mainly obtained through cosmological simulations. A remarkable result of these studies is the fact that DM halos exhibit a universal density profile well approximated by the Navarro–Frenk–White formula (Navarro et al. 1997). This entirely characterizes the halo profile in terms of the halo mass M and the concentration parameter c . Numerical simulations have shown that the concentration encodes cosmological information. In particular, it has been found that the median concentration of an ensemble of halos is a power-law function of the halo mass with the overall amplitude of the relation varying with redshift and cosmology (see, e.g., Bullock et al. 2001; Zhao et al. 2003; Dolag et al. 2004; Zhao et al. 2009; Giocoli et al. 2012). This has suggested that estimates of the concentration and halo mass from a sample of galaxy clusters can provide constraints on cosmological models (see, e.g., Ettori et al. 2010, for a cosmological data analysis using cluster concentration–mass measurements).

However, several factors can limit the use of the cluster concentration as cosmological proxy. On the one hand, astrophysical effects may alter the original c – M relation and introduce a systematic bias into the cosmological analysis (see, e.g., Duffy et al. 2010; Mead et al. 2010; King & Mead 2011). On the other hand, theoretical model predictions, despite recent progress (see, e.g., Correa et al. 2015; Diemer & Kravtsov 2015; Klypin et al. 2016; Ludlow et al. 2016; Renneby et al. 2017), have yet to converge into a single model capable of reproducing the ensemble of numerical results currently

available for different cosmological scenarios (Meneghetti & Rasia 2013).

Another limiting factor may result from the large intrinsic dispersion of the halo concentration. N -body simulation studies have found a significant scatter of the concentration at fixed halo mass (Bullock et al. 2001; Wechsler et al. 2002). For example, Maccio et al. (2007) have found $\sigma_{\ln c} \approx 0.25$, while Bhattacharya et al. (2013) quote a scatter $\sigma_{\ln c} \approx 0.33$. A similar result has been found in Diemer & Kravtsov (2015), which quotes $\sigma_{\ln c} \approx 0.37$, while a smaller value was only found for a sample of relaxed halos. Accounting for such a large intrinsic dispersion may strongly relax cosmological parameter constraints from measurements of the concentration–mass relation.

A further point of concern is the case of very massive clusters. These are often easier to detect because they are very luminous and rich. Nonetheless, because of their recent formation, they are also more likely to be perturbed by the presence of other structures that are still in the process of merging with the main DM halo. In such a case, the halo density profile may deviate from the NFW formula, and the concentration parameter no longer encodes information of the halo mass distribution and its cosmological dependence.

Finally, the measurement of the mass–concentration relation is strongly affected by selection effects as shown by Sereno et al. (2015).

In Balmes et al. (2014), two of the authors have introduced the concept of halo *sparsity*, a directly measurable proxy of the DM halo mass profile that overcomes most of the limitations described above. In this work, we present a detailed study of the validity of the halo sparsity as a new cosmological probe. As a proof-of-concept application, we specifically focus on sparsity measurements based on hydrostatic mass estimates from X-ray cluster observations. We show that the redshift evolution of the average halo sparsity carries cosmological information that can be retrieved from prior knowledge of the halo mass function. To this purpose we perform a likelihood analysis over a set of ideal sparsity data with no systematic errors from which we recover the input fiducial cosmology. We discuss various sources of systematic uncertainty. Using results from state-of-the-art simulations of galaxy clusters, we show that mass bias effects due to baryonic feedback processes alter the sparsity of massive systems at the few percent level. When analyzing cluster sparsity, this source of systematic error is therefore subdominant with respect to that affecting mass estimates from currently available cluster data sets. As a first cosmological application, we perform a cosmological parameter inference analysis of sparsity measurements based on hydrostatic mass estimates of a sample of X-ray clusters from *XMM* and *Chandra* observations.

The article is organized as follows. In Section 2, we review the basic properties of the halo sparsity and test its validity as a cosmological proxy. In Section 3, we discuss several sources of systematic errors that can affect the sparsity data analysis. In Section 4, we present the cosmological parameter constraints inferred from sparsity measurements of a sample of X-ray clusters. In Section 5, we perform a cosmological parameter forecast for sparsity data expected from future X-ray cluster surveys. Finally, in Section 6 we present our conclusions.

2. DM Halo Sparsity

2.1. Definition and Properties

The sparsity of a halo is defined as the ratio of the halo mass enclosing two different overdensities Δ_1 and Δ_2 (Balmes et al. 2014):

$$s_{\Delta_1, \Delta_2} \equiv \frac{M_{\Delta_1}}{M_{\Delta_2}}, \quad (1)$$

where $\Delta_1 < \Delta_2$ and M_Δ is the mass enclosed in a sphere of radius r_Δ containing an overdensity Δ with respect to the critical density ρ_c or the mean background density ρ_m . In the following we will consider ρ_c ; however, as shown in Balmes et al. (2014), the general properties of the sparsity are independent of such a choice. Notice that from Equation (1) we can also interpret the sparsity of a halo as a measure of the mass excess between r_{Δ_1} and r_{Δ_2} ($\Delta M = M_{\Delta_1} - M_{\Delta_2}$) relative to the mass enclosed in the inner radius r_{Δ_2} , i.e., $s_{\Delta_1, \Delta_2} = \Delta M / M_{\Delta_2} + 1$.

It is easy to show that there is a one-to-one correspondence between the halo sparsity and the concentration parameter (assuming that the halo follows the NFW profile). For instance, to conform with the standard definition of concentration, let us set $\Delta_1 = 200$ and let Δ_2 be equal to Δ ; then, using the NFW formula, we can write the sparsity as

$$s_\Delta^{-1} \equiv x_\Delta^3 \frac{\Delta}{200} = \frac{\ln(1 + c_{200} x_\Delta) - \frac{c_{200} x_\Delta}{1 + c_{200} x_\Delta}}{\ln(1 + c_{200}) - \frac{c_{200}}{1 + c_{200}}}, \quad (2)$$

where $x_\Delta = r_\Delta / r_{200}$ and $c_{200} = r_{200} / r_s$, with r_s the scale radius of the NFW profile. For a given set of values of the concentration c and overdensity Δ , the above equation can be solved numerically to obtain x_Δ and thus the corresponding value of s_Δ . However, notice that in defining the sparsity as in Equation (1) no explicit assumption has been made concerning the form of the halo density profile. Balmes et al. (2014) have shown that this is sufficient to characterize the mass profiles of halos even when their density profile deviates from NFW.

A key feature of the halo sparsity is the fact that its ensemble average value at a given redshift is nearly independent of the halo mass M_{Δ_1} (even if some of the halos in the ensemble have profiles that deviate from NFW) but depends on the underlying cosmological model with a scatter that is much smaller than that of the halo concentration. Because of this, it can provide a robust cosmological proxy, without requiring any modeling of the halo density profile.

Another important characteristic of the halo sparsity is that its independence on M_{Δ_1} implies that the ensemble average value can be predicted from prior knowledge of the halo mass function at two different mass overdensities. In fact, let us consider the equality

$$\frac{dn}{dM_{\Delta_2}} = \frac{dn}{dM_{\Delta_1}} \frac{dM_{\Delta_1}}{dM_{\Delta_2}} = \frac{dn}{dM_{\Delta_1}} s_{\Delta_1, \Delta_2} \frac{d \ln M_{\Delta_1}}{d \ln M_{\Delta_2}}, \quad (3)$$

where dn/dM_{Δ_1} and dn/dM_{Δ_2} are the mass functions at Δ_1 and Δ_2 , respectively. We can rearrange the above relation and integrate over the halo ensemble mass range to derive the relation between the average inverse halo masses at two different overdensities. Since the sparsity is independent of the halo mass, it can be taken out of the integration on the

right-hand side such that

$$\int_{M_{\Delta_2}^{\min}}^{M_{\Delta_2}^{\max}} \frac{dn}{dM_{\Delta_2}} d \ln M_{\Delta_2} = \langle s_{\Delta_1, \Delta_2} \rangle \int_{(s_{\Delta_1, \Delta_2}) M_{\Delta_2}^{\min}}^{(s_{\Delta_1, \Delta_2}) M_{\Delta_2}^{\max}} \frac{dn}{dM_{\Delta_1}} d \ln M_{\Delta_1}. \quad (4)$$

This equation can be solved numerically for $\langle s_{\Delta_1, \Delta_2} \rangle$ given prior knowledge of dn/dM_{Δ_1} and dn/dM_{Δ_2} , respectively. As shown in Balmes et al. (2014), this reproduces with great accuracy the mean sparsity inferred from N -body halo catalogs. Indeed, this is a direct advantage over predicting the median concentration, since the cosmological and redshift dependences of the mass function are easier to model than the concentration, as they involve a reduced set of assumptions. Moreover, since the sparsity is a mass ratio, it is reasonable to expect that it will be less affected by a constant systematic bias that may affect cluster mass measurements. Also, notice that selection effects can be included in Equation (4) by convolving the integrands with the appropriate selection function. We will discuss both these points in detail in Section 3.

A last remark concerns the choice of Δ_1 and Δ_2 provided that $\Delta_1 < \Delta_2$. As noticed in Balmes et al. (2014), the larger the difference, the greater the amplitude of the cosmological signal. However, the values of Δ_1 and Δ_2 cannot be chosen to be arbitrarily different since the properties of the sparsity discussed above remain valid only in a limited interval that can be determined by physical considerations. A lower bound on Δ_1 can be inferred by the fact that for very small overdensities the identification of a halo as an individual object can be ambiguous, thus suggesting $\Delta_1 \gtrsim 100$. On the other hand, the range of values for Δ_2 can be deduced by the fact that at very large overdensities baryonic processes may alter the DM distribution within the inner core of halos. These are largely subdominant if one conservatively assumes Δ_2 in the range $\Delta_1 < \Delta_2 \lesssim 2000$. Within this interval of values one can set Δ_1 and Δ_2 depending on the availability of optimal mass measurements.

2.2. N-body Simulation Sparsity Tests

In Balmes et al. (2014) the properties of the halo sparsity have been tested using halo catalogs from the Dark Energy Universe Simulations⁷ (DEUS) with masses defined with respect to the background density covering the mass range $10^{12} < M_{200\text{m}} [h^{-1} M_{\odot}] < 10^{15}$.

Here we perform an analysis using halos identified with the Spherical Overdensity (SOD) halo detection algorithm (Lacey & Cole 1994) in one of the simulations of the RayGalGroupSims suite (M.-A. Breton et al. 2018, in preparation) with masses defined with respect to the critical density. Since we are interested in the application to X-ray clusters, we specifically focus on masses at overdensity $\Delta_1 = 500c$ and $\Delta_2 = 1000c$, from which we derive estimates of the halo sparsity $s_{500,1000}$. For completeness, we also consider halo masses measured at $\Delta_1 = 200c$ and show that the properties of the halo sparsity also hold for $s_{200,500}$ and $s_{200,1000}$.

The cosmological model of the RayGalGroupSims simulation considered here is a flat Λ CDM with parameters set consistently with WMAP 7 yr data analysis (Komatsu et al. 2011):

⁷ <http://www.deus-consortium.org/deus-data/>

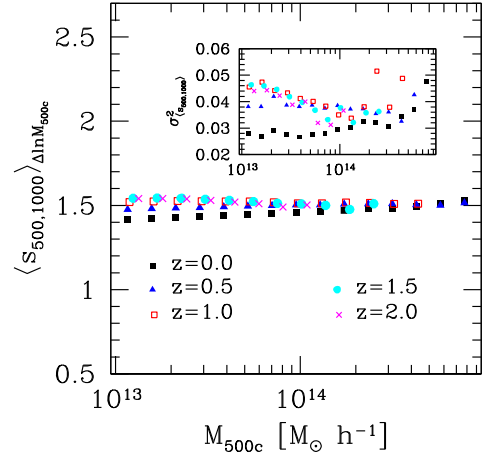


Figure 1. Average halo sparsity as a function of M_{500c} from SOD halo catalogs at $z = 0$ (black filled squares), $z = 0.5$ (blue filled triangles), 1.0 (red open squares), 1.5 (cyan filled circles), and 2.0 (magenta crosses) in mass bins of size $\Delta \ln M_{500c} = 0.3$. The inset plot shows the variance of the halo sparsity in the same mass bins as a function of M_{500c} for the different redshifts.

$\Omega_m = 0.2573$, $\Omega_b = 0.04356$, $h = 0.72$, $n_s = 0.963$, and $\sigma_8 = 0.801$. The simulation consists of a $(2.625 \text{ Gpc } h^{-1})^3$ volume with 4096^3 particles corresponding to particle mass resolution $m_p = 1.88 \cdot 10^{10} M_{\odot} h^{-1}$.

Halos are first detected using the SOD algorithm with overdensity set to $\Delta = 200c$ and centered on the location of maximum density. For each halo we computed SOD masses at $\Delta = 200c$, $500c$, and $1000c$ and estimated the corresponding halo sparsities. In order to avoid mass resolution effects, we have taken a conservative mass cut and considered only halos with more than 10^4 particles.

In Figure 1 we plot the average halo sparsity $\langle s_{500,1000} \rangle_{\Delta \ln M_{500c}}$ in mass bins of size $\Delta \ln M_{500c} = 0.3$ (containing more than 20 halos) as a function of M_{500c} at $z = 0, 0.5, 1.0, 1.5$, and 2.0 , while in the inset plot we show the associated variance. As we can see, $\langle s_{500,1000} \rangle_{\Delta \ln M_{500c}}$ remains constant to very good approximation across the full mass and redshift range. As far as the scatter is concerned, we find the standard deviation to be at the $\lesssim 20\%$ level, consistent with the findings of Balmes et al. (2014).

Let us now test the validity of Equation (4) in predicting the redshift evolution of the ensemble average sparsity. In Figure 2, the black circles are the average sparsity values obtained from the RayGalGroupSims halo catalogs at $z = 0, 0.5, 0.66, 1.0, 1.14, 1.5$, and 2.0 . These have been computed for each halo catalog by averaging the sparsity of halos with $M_{500c} \gtrsim 10^{13} M_{\odot} h^{-1}$. The magenta squares are the average sparsity values at the redshifts of the halo catalogs obtained by solving Equation (4), where we have assumed the Sheth–Tormen (ST) formula (Sheth & Tormen 1999) with coefficients best-fitting the numerical halo mass functions at $\Delta_1 = 500c$ and $\Delta_2 = 1000c$ (see the Appendix for a detailed description of the mass function calibration). As we can see in Figure 2, the predictions from Equation (4) overlap with the average sparsity values directly estimated from the halos in the simulation catalogs with relative differences at the $< 0.1\%$ level.⁸

⁸ In solving Equation (4) we have set $M_{1000c}^{\min} = 2 \cdot 10^{13} M_{\odot} h^{-1}$ consistently with the mass limit of our halo catalogs, while the upper limit of the integration interval can be set to an arbitrarily large number. Nevertheless, as the average sparsity remains approximately constant with mass, we have verified that the solution of Equation (4) is largely independent of the specific choice of M_{1000c}^{\min} .

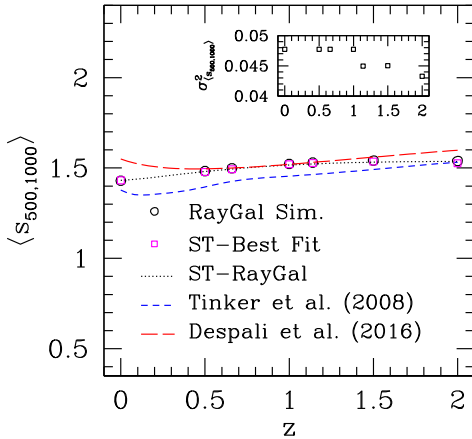


Figure 2. Average sparsity as a function of redshift for halos with $M_{500c} > 10^{13} M_{\odot} h^{-1}$. The black circles correspond to the average sparsity measured from the halo catalogs at the redshift snapshots of the RayGalGroupSims run. The magenta squares correspond to the average sparsity prediction obtained by solving Equation (4) assuming an ST mass function with coefficients best-fitting the halo mass function of the RayGalGroupSims halo catalogs at M_{500c} and M_{1000c} . The black dotted line corresponds to the prediction from Equation (4) using the ST-RayGal mass function, while the blue short-dashed line and the red long-dashed line correspond to the predictions obtained by assuming the mass function from Tinker et al. (2008) and Despali et al. (2016), respectively. The inset plot shows the variance of the halo sparsity from the SOD halo catalogs with $M_{500c} \gtrsim 10^{13} M_{\odot} h^{-1}$ at the different redshift snapshots.

In order to interpolate predictions of the sparsity at redshifts other than those tested by the simulation snapshots, we have performed a quadratic fit of the ST best-fit coefficients as a function of $x \equiv \log_{10}(\Delta_c/\Delta_{\text{vir}}(z))$ for $\Delta_c = 500$ and 1000 ; see Equations (16)–(17) in the Appendix. As suggested by Despali et al. (2016), parameterizing the ST coefficients in terms of x aims to capture the redshift and cosmology dependence of the mass function, though from the work of Courtin et al. (2011) it is clear that this may not be sufficient to model dependencies beyond the Λ CDM scenario. Hereafter, we will refer to the ST formula with coefficients given by Equations (16) and (17) as the ST-RayGal mass function; the corresponding average sparsity prediction from Equation (4) is shown in Figure 2 as a black dotted line. We find differences with respect to the N -body measurements to be at the subpercent level.

In Figure 2 we also plot the average sparsity prediction from Equation (4) obtained by assuming the mass function from Tinker et al. (2008) and Despali et al. (2016). In the former case we can see systematic deviations up to the $\sim 10\%$ level with respect to the N -body estimates that decrease from low to high redshifts. In the latter case differences are within the 1% level in the range $0.5 < z < 1.5$, while they increase up to the $\sim 10\%$ level at lower and higher redshifts. Such discrepancies are due to differences in the parameterizations of the halo mass function, which have been calibrated to halo catalogs from simulations of different cosmological models, volumes, and mass resolutions.

Compared to the simulations used in Tinker et al. (2008) and Despali et al. (2016), the RayGalGroupSims simulation covers a larger volume with greater mass resolution. This provides a better calibration of the ST formulae. As can be seen in Figure 14 in the Appendix, we find logarithmic differences well within the 5% level. On the other hand, it is worth remarking that we have tested the validity of the ST-RayGal mass function to a set of cosmological simulations with parameters that are

not too different from those of the Λ CDM best-fit model to the WMAP 7 yr data (see discussion at the end of the Appendix). Consequently, we are not guaranteed that the ST-RayGal parameterization can fully capture the cosmological parameter dependence of the halo mass function and hence that of the halo sparsity for parameter values that are far from the concordance Λ CDM model. Such uncertainty can indeed introduce systematic errors in the sparsity analysis, a point that we will discuss in detail in Section 3. Here, we are not in a position to solve this issue in a conclusive manner. Hence, we simply opt to quote the results obtained assuming the ST-RayGal parameterization and that from Despali et al. (2016). We will refer to the latter case as ST-Despali.

The properties of the halo sparsity summarized by the trends shown in Figures 1 and 2 also hold for other sparsity definitions. This can be seen in Figure 3, where we plot $\langle s_{200,500} \rangle$ and $\langle s_{200,1000} \rangle$ as a function of M_{200c} and redshift, respectively. These plots suggest that sparsity estimations from mass measurements at $\Delta = 200c$, such as those provided by gravitational lensing observations that probe clusters at larger radii than X-ray measurements, can also provide a viable proxy of the mass distribution in clusters.

2.3. Cosmological Parameter Dependence

The dependence of the halo sparsity on the underlying cosmological model has been studied in Balmes et al. (2014) using N -body halo catalogs from DEUS project simulations (Alimi et al. 2010; Rasera et al. 2010; Courtin et al. 2011). Balmes et al. (2014) have shown that the average value of the sparsity at a given redshift correlates with the linear growth factor of the underlying cosmological model. This can be qualitatively understood in terms of the relation between the growth of structures and the mass assembly of halos. In particular, at any given time, models that form structures earlier will assemble on average more halo mass at large overdensities (inner radii) than those that form structures at later times, thus resulting in smaller values of the average sparsity. In terms of the cosmological model parameters, this implies, for instance, that the larger the cosmic matter density Ω_m or the amplitude of the fluctuations on the 8 Mpc h^{-1} scale σ_8 , the smaller the average sparsity value.

Here, we do not intend to repeat the analysis of Balmes et al. (2014); instead, we use Equation (4) to evaluate the relative change of the average sparsity with respect to a fiducial cosmological model for a positive variation of the cosmological parameters.

We assume as fiducial cosmology a flat Λ CDM model with parameters set to the best-fit values from the Planck cosmological data analysis of cosmic microwave background (CMB) anisotropy spectra (TT, TE, EE + lowP; Planck Collaboration et al. 2016a): $\Omega_m = 0.3156$, $\Omega_b h^2 = 0.02225$, $h = 0.6727$, $\sigma_8 = 0.831$, $n_s = 0.9645$.

We compute $\langle s_{500,1000} \rangle$ from Equation (4) assuming the ST-RayGal and ST-Despali mass functions, respectively.⁹

In Figure 4 we plot $\Delta \langle s_{500,1000} \rangle / \langle s_{500,1000} \rangle_{\text{fid}}$ as a function of redshift in the case of the ST-RayGal mass function (top panel)

⁹ In computing the mass function, we evaluate the linear matter power spectrum of the underlying cosmological model using the approximated formulae from Eisenstein & Hu (1999). We have verified that using power spectra from numerical solutions of linear perturbation equations, such as those given by the CAMB code (Lewis et al. 2000), leads to subpercent difference in the predicted value of the average sparsity.

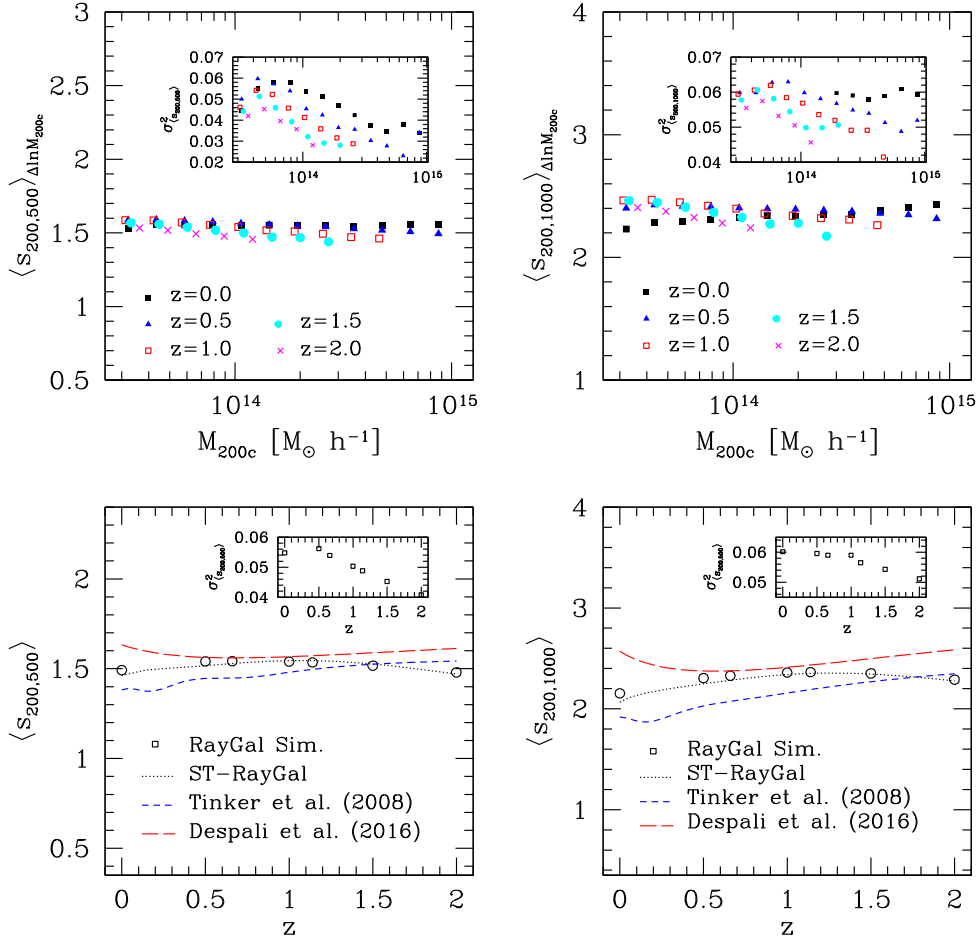


Figure 3. Top panels: average halo sparsity $\langle s_{200,500} \rangle$ (left panel) and $\langle s_{200,1000} \rangle$ as a function of M_{200c} at $z = 0, 0.5, 1, 1.5,$ and 2.0 (legend as in Figure 1) in mass bins of size $\Delta \ln M_{200c} = 0.3$. The inset plot shows the variance of the halo sparsity in the same mass bins as a function of M_{200c} , for the different redshifts. Bottom panels: average halo sparsity $\langle s_{200,500} \rangle$ (left panel) and $\langle s_{200,1000} \rangle$ as a function of redshift for halos (legend as in Figure 2) with $M_{500c} > 10^{13} M_\odot h^{-1}$ consistently with the mass cut adopted for the $s_{500,1000}$ case. The inset plot shows the variance of the halo sparsity at the different redshift snapshots.

and ST-Despali mass function (bottom panel). Independently of the adopted mass function parameterization, we can see that the variation of the average sparsity is negative for a positive variation of the cosmological parameters, except $\Omega_b h^2$. This is essentially because increasing the value of σ_8 , Ω_m , n_s , and h causes structures to form at earlier times and consequently assemble more halo mass at larger overdensities, which results in smaller values of the average sparsity. This is not the case for positive variations of $\Omega_b h^2$. In fact, as we have assumed a flat geometry, increasing the value of $\Omega_b h^2$ corresponds to decreasing the value of Ω_m at constant h . In such a case, structures form later than in models with smaller values of $\Omega_b h^2$, and halos assemble on average less mass at larger overdensities, thus leading to larger values of the average sparsity.

The trends shown in Figure 4 provide an estimate of the sensitivity of the average sparsity to the different cosmological parameters. In the ST-RayGal case we can see that a change in the value of σ_8 produces the largest variation of the average sparsity in the redshift range $0 < z \lesssim 1$. At higher redshifts a change in the value of n_s causes the largest variation, while Ω_m , h , and $\Omega_b h^2$ have smaller effects. A similar trend occurs in the ST-Despali case, though with different amplitudes for the different parameters. Overall, we can see that measurements of the average sparsity are most sensitive to $S_8 = \sigma_8 \sqrt{\Omega_m}$;

consequently, we can expect constraints on Ω_m and σ_8 to be degenerate along curves of constant S_8 values.

It is worth noticing that the variations of the average sparsity predicted by the ST-Despali mass function are slightly larger in amplitude than those from the ST-RayGal. This suggests that cosmological constraints inferred by a sparsity analysis based on the ST-Despali mass function will provide systematically tighter bounds than those inferred assuming the ST-RayGal parameterization. As already mentioned at the end of Section 2.2, the uncertainties in the modeling of the halo mass function may induce a systematic error in the cosmological analysis of sparsity measurements. We will discuss this in detail in Section 3.

2.4. Synthetic Data Analysis

We now check the validity of the average sparsity as cosmological proxy. To this purpose we generate a set of synthetic average sparsity data and perform a cosmological parameter likelihood analysis to test whether we retrieve the input parameter values of the fiducial cosmology. As proof of concept, here we limit ourselves to ideal sparsity measurements and neglect any source of systematic uncertainty. Our goal is to show that the sparsity provides a viable cosmological observable.

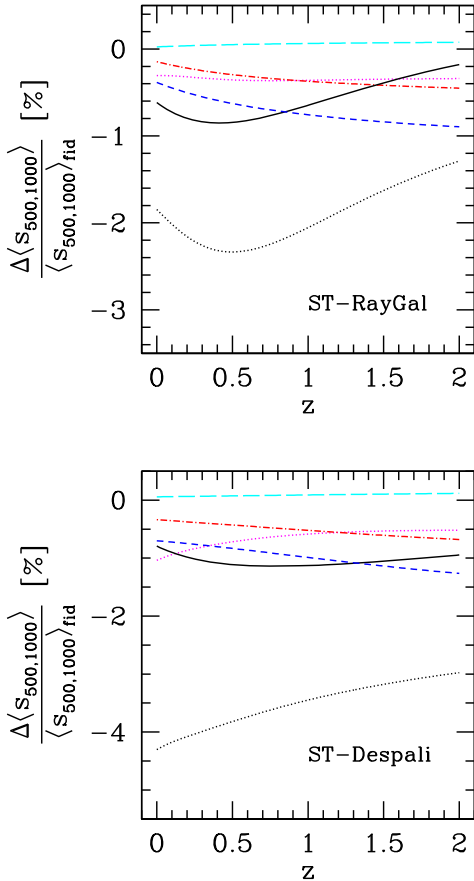


Figure 4. Relative variation of the average halo sparsity as a function of redshift for a 5% variation of the cosmological parameters around the fiducial *Planck* values. The various lines represent variations with respect to σ_8 (black solid line), n_s (blue short-dashed line), Ω_m (magenta dotted line), h (red dot-dashed line), $\Omega_b h^2$ (cyan long-dashed line), and $\sigma_8 \sqrt{\Omega_m}$ (black dotted line). In the top panel we plot the relative variation of the average sparsity obtained assuming the ST-RayGal mass function in Equation (4), while that assuming the ST-Despali mass function is shown in the bottom panel.

We assume as a fiducial model a flat Λ CDM scenario with parameters set to the *Planck* best-fit values quoted in Section 2.3. We generate a sample of $N = 15$ independent sparsity measurements in redshift bins of size $\Delta z = 0.1$ over the range $0 \leq z \leq 1.5$ by solving Equation (4) for a given mass function. We consider two separate configurations, one consisting of sparsity measurements with 1% statistical errors and another with 20% errors. This allows us to test whether degrading the statistical uncertainties has an impact in retrieving the fiducial model. We focus the parameter inference on σ_8 and Ω_m , while assuming hard priors on the remaining cosmological parameters. We realize two independent analyses for the ST-RayGal and the ST-Despali mass functions.

We perform a Markov chain Monte Carlo sampling of the likelihood function and evaluate the χ^2 :

$$\chi^2(\sigma_8, \Omega_m) = \sum_{i=1}^N \left[\frac{\langle s_{500,1000}^i \rangle - \langle s_{500,1000}^{\text{th}}(z_i | \sigma_8, \Omega_m) \rangle}{\sigma_{\langle s_{500,1000} \rangle}} \right]^2, \quad (5)$$

where $\langle s_{500,1000}^i \rangle$ is the i th data point in the synthetic catalog at redshift z_i , $\sigma_{\langle s_{500,1000} \rangle}$ is the associated error, and $\langle s_{500,1000}^{\text{th}} \rangle$ is the theoretical model prediction given by Equation (4) assuming

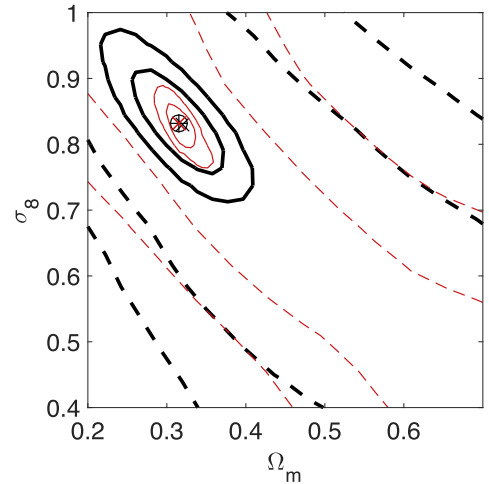


Figure 5. 1σ and 2σ credibility contours in the Ω_m - σ_8 plane obtained in the case of the ST-RayGal mass function (black thick lines) and the ST-Despali mass function (red thin lines). The solid lines correspond to constraints inferred assuming 1% average sparsity errors, while the dashed contours correspond to the case with 20% errors. The black circled plus sign indicates the fiducial model parameters, while the black and red cross markers indicate the best-fit values.

the same mass function parameterization used to generate the data.

The results are summarized in Figure 5, where we plot the 1σ and 2σ credibility contours in the plane Ω_m - σ_8 , which have been inferred assuming the ST-RayGal and ST-Despali mass functions, respectively. In both cases we find the best-fit model parameters to recover the *Planck* fiducial parameters at the subpercent level, independently of the assumed uncertainties on the synthetic data set. On the other hand, we can see that the parameter constraints become much weaker in the case with 20% statistical errors. As expected from the analysis presented in Section 2.3, the analysis of the synthetic data performed using the ST-Despali mass function provides systematically tighter bounds on Ω_m - σ_8 than the ST-RayGal case.

Overall, this suggests that the average sparsity can be used as a cosmic probe. We will discuss extensively in the next section the extent to which systematic errors can contaminate sparsity analyses.

3. Systematic Errors

In this section we present a preliminary evaluation of systematic errors potentially affecting cluster sparsity analyses.

3.1. Mass Function Parameterization

In Section 2.2 we have seen that key to predicting the halo sparsity is the correct modeling of the halo mass function. In particular, we have shown that Equation (4) recovers the average sparsity of the numerical halo catalogs from the RayGalGroupSims simulation provided that the parameterization of the halo mass function for M_{500c} and M_{1000c} also reproduces the numerical halo abundances.

In order to assess the impact of the modeling of the mass function on the cosmological parameter inference from sparsity measurements, we extend the synthetic data analysis presented in Section 2.4. In particular, using the synthetic data set generated by solving Equation (4) with the ST-RayGal mass function, we perform a likelihood analysis assuming the ST-Despali mass function.

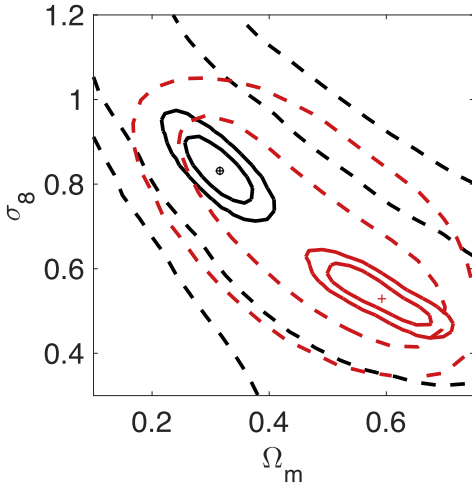


Figure 6. 1σ and 2σ credibility contours in the Ω_m – σ_8 plane from the likelihood analysis of average sparsity data with 1% (solid lines) and 20% (dashed lines) statistical errors generated by solving Equation (4) with the ST-RayGal mass function. The black lines correspond to the constraints shown in Figure 5 inferred assuming the ST-RayGal mass function. The constraints obtained assuming the ST-Despali mass function are shown as red lines. The black circle indicates the fiducial model parameters, while the plus signs indicate the best-fit parameter values for the different parameterizations.

In Figure 6 we plot the 1σ and 2σ credibility contours in the Ω_m – σ_8 plane assuming 1% and 20% statistical errors on the synthetic sparsity data, respectively. For comparison we also plot the contours shown in Figure 5 obtained by assuming the ST-RayGal mass function. We can clearly see that assuming the ST-Despali mass function when the synthetic data have been generated with the ST-RayGal mass function results in a systematic offset of the best-fit parameters. This bias is well above the statistical errors for sparsity measurements with 1% statistical uncertainties. We can also notice that the contours differ according to the assumed mass function. This is not surprising given the fact that the mass function parameterizations have been calibrated to simulations of different volume and mass resolution and encode differently the dependence on the cosmological parameters.

As already mentioned, the RayGalGroupSims simulation with a $(2.625 \text{ Gpc } h^{-1})^3$ volume and a mass resolution of $m_p = 1.88 \cdot 10^{10} M_\odot h^{-1}$ provides a better sampling of the high mass-end of the halo mass function than the simulation ensemble used for the calibration of the ST-Despali mass function. As an example, the largest volume simulation from the SBARBINE suite presented in Despali et al. (2016) consists of a $(2 \text{ Gpc } h^{-1})^3$ box with mass resolution $m_p = 6.35 \cdot 10^{11} M_\odot h^{-1}$. This impacts the accuracy of the mass function calibration, a point that can also be inferred by comparing the amplitude of the logarithmic differences of the calibrated formulae to the numerical estimations. As shown in Figure 14, the ST-RayGal parameterization reproduces the RayGalGroupSims mass function well within 5% across the entire mass range probed by the simulation and in the redshift interval $0 \leq z \leq 2$. In contrast, the ST-Despali parameterization shows differences with respect to the N -body results that at the high mass-end exceed the 5% level in the same redshift interval (see, e.g., Figure 11 in Despali et al. 2016). Conversely, the SBARBINE suite includes simulation runs with cosmological parameter values sufficiently far from the concordance Λ CDM

model to better probe the cosmological dependence of the mass function on Ω_m and σ_8 than the ST-RayGal case. Therefore, this suggests that a simulation suite consisting of runs with volume and mass resolution similar to those of the RayGalGroupSims simulation for very different cosmological parameter values should provide a mass function parameterization sufficiently accurate to guarantee unbiased sparsity analyses in the case of sparsity data with errors at the $\sim 1\%$ statistical level.

3.2. Hydrostatic Mass Estimates

Numerical simulation studies (see, e.g., Nagai et al. 2007; Meneghetti et al. 2010; Rasia et al. 2012; Velliscig et al. 2014; Biffi et al. 2016), as well as the analyses of observed cluster samples (Sereno & Ettori 2015), have shown that X-ray cluster masses obtained by solving the hydrostatic equilibrium (HE) equation are systematically underestimated compared to the true mass of the clusters.

The halo sparsity is unaltered by a constant systematic mass bias, since it is a mass ratio. In contrast, a radial-dependent shift affecting HE masses can alter the sparsity¹⁰ and introduce a systematic error in the cosmological parameter inference. In addition to a bias effect, HE masses suffer from an intrinsic scatter of the order of 10%–20% (Rasia et al. 2012; Sereno & Ettori 2015). However, most of the sources of scatter act similarly over different radial ranges, so that this would induce negligible effects on sparsity.

The overall amplitude of the radial-dependent mass bias has been estimated in several numerical simulation studies. Nevertheless, the results differ as a consequence of the different numerical schemes used in the realization of the simulations, as well as the modeling and the implementation of the astrophysical processes that shape the properties of the gas in clusters. As an example, Rasia et al. (2012) have realized zoom simulations of 20 clusters at $z = 0.2$ with $M_{200c} > 4 \cdot 10^{14} M_\odot h^{-1}$ and found a 33% median mass bias at r_{500c} and 27.5% at r_{1000c} (see Table 2 in Rasia et al. 2012). These induce a relative shift with respect to the true average sparsity of $\sim 8\%$. A smaller amplitude of the mass bias has been found by Nagai et al. (2007); nevertheless, both these studies have neglected the impact of active galactic nuclei (AGNs) on the halo mass.

The Overwhelmingly Large Simulations project (Schaye et al. 2010) has performed a comprehensive study of the impact of baryonic feedback processes such as star formation, metal-line cooling, stellar winds, supernovae, and AGNs on the properties of galaxy clusters. Quite remarkably, these simulations reproduce the optical and X-ray observed features of groups and clusters of galaxies (McCarthy et al. 2010; Le Brun et al. 2014). The effects induced on the halo mass have been studied in detail in Velliscig et al. (2014). In this study, the authors have evaluated the median fractional mass bias y_Δ at $z = 0$ for $\Delta = 200c$, $500c$, and $2500c$ as a function of the halo DM mass. Their results have shown that baryonic effects can alter the total halo mass at the $\sim 15\%$ – 20% level for halos with $M_{200c} \sim 10^{13} M_\odot h^{-1}$ down to a few percent for the most

¹⁰ Let M_Δ^t be the true halo mass and M_Δ^e be the estimated one at overdensity Δ . We define the fraction mass bias as $y_\Delta \equiv (M_\Delta^e - M_\Delta^t)/M_\Delta^t$. Then, the relative variation of the halo sparsity compared to its true value is given by

$$r_{\Delta_1, \Delta_2} \equiv \frac{\Delta s_{\Delta_1, \Delta_2}}{s_{\Delta_1, \Delta_2}} = \frac{1 + y_{\Delta_1}}{1 + y_{\Delta_2}} - 1, \quad (6)$$

from which it is evident that if the mass bias is independent of the cluster radius, $y_{\Delta_1} = y_{\Delta_2}$ and $\Delta s_{\Delta_1, \Delta_2} = 0$.

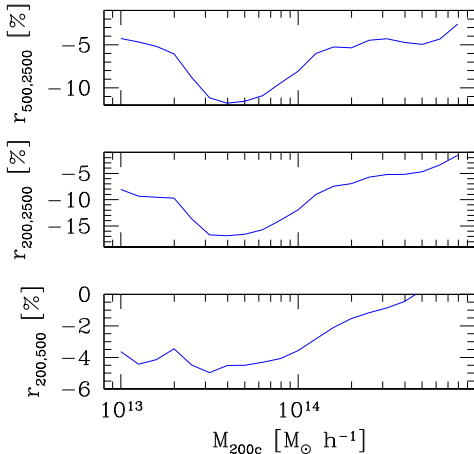


Figure 7. Percentage variation of the median halo sparsity $s_{200,500}$ (bottom panel), $s_{200,2500}$ (middle panel), and $s_{500,2500}$ (top panel) due to the radial mass bias induced by baryonic feedback processes as in the AGN 8.0 model investigated in Velliscig et al. (2014).

massive systems with $M_{200c} \sim 10^{15} M_{\odot} h^{-1}$. We use their results for the feedback model AGN 8.0 (see Figure 2 in Velliscig et al. 2014) reproducing the observed X-ray profile of clusters (Le Brun et al. 2014). In Figure 7 we plot the percentage variation of the median halo sparsity for $s_{200,500}$ (bottom panel), $s_{200,2500}$ (middle panel), and $s_{500,2500}$ (top panel) as given by Equation (6). We can see that at large radii the effect of baryonic feedback causes the sparsity to be underestimated by $\Delta \langle s_{200,500} \rangle / \langle s_{200,500} \rangle \lesssim 4\%$. For inner radii the effect is larger, but limited to $\lesssim 15\%$ for $s_{200,2500}$ and $\lesssim 10\%$ for $s_{500,2500}$. In any case, we notice that for massive systems with $M_{200c} \gtrsim 10^{14} M_{\odot} h^{-1}$ the level of bias on the sparsity is below $\sim 5\%$.

The study presented in Velliscig et al. (2014) has focused on how baryonic processes alter halo masses. On the other hand, in our analysis we are particularly interested in the effects on the HE estimated masses. This has been recently investigated by Biffi et al. (2016), who have performed zoom simulations of 29 clusters at $z = 0$ with masses $M_{200c} \gtrsim 10^{14} M_{\odot} h^{-1}$. These simulations account for metallicity-dependent radiative cooling, time-dependent UV background, star formation, metal enrichment, stellar winds, and AGN feedback. The authors have estimated the fractional median hydrostatic mass bias for cool-core (CC), non-CC, regular, and disturbed systems for overdensity thresholds $\Delta = 200c$, $500c$, and $2500c$ (see Table 1 in Biffi et al. 2016). Using these results, we linearly extrapolate the hydrostatic mass bias at $\Delta = 1000c$ and compute the fraction bias on the sparsity $s_{500,1000}$, which we report in Table 1 for different cluster categories. We can see that the hydrostatic mass bias induces a shift on the true cluster sparsity of 0.1%–0.3% (non-CC and regular) and 2%–4% (CC and disturbed), which is largely in agreement with the estimates we have obtained using the results from Velliscig et al. (2014).

Further numerical analyses are nonetheless necessary since no study has so far investigated in detail how the hydrostatic mass bias evolves with time and therefore how the bias on the sparsity evolves with redshift. Velliscig et al. (2014) have shown that the baryonic effects that alter M_{200c} at $z = 0$ tend to be smaller (by $\sim 5\%$) at $z = 1$. If such a trend holds for larger overdensity thresholds, that would imply that the bias on the halo sparsity is a decreasing function of redshift.

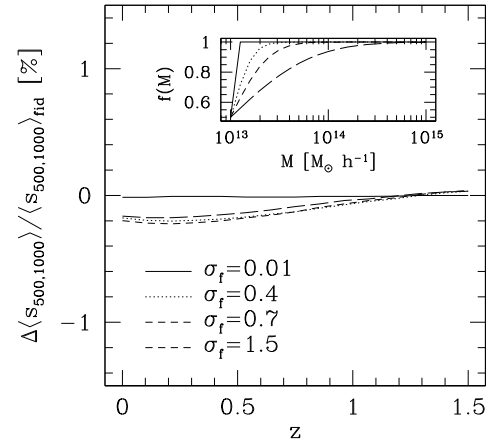


Figure 8. Relative difference of the average sparsity with respect to the case with no selection function for the *Planck* fiducial cosmology and different values of the selection function parameter $\sigma_f = 0.01, 0.4, 0.7$, and 1.5 . The inset plot shows the form of the selection function for the different values of σ_f .

Table 1

Relative Variation of the Sparsity $s_{500,1000}$ due to Hydrostatic Mass Bias for CC, NCC, Regular, and Disturbed Clusters Simulated in Biffi et al. (2016)

Cluster State	$r_{500,1000}$ (%)
CC	−3.7
NCC	0.1
Regular	0.3
Disturbed	−2.0

Overall, all these elements confirm the strength of the cluster sparsity against possible mass bias systematics. The advantage is twofold. In fact, being a mass ratio, any systematic error affecting cluster mass estimates is suppressed. Moreover, one can focus on the sparsity at overdensity thresholds corresponding to external regions of the cluster mass profile where baryonic effects are subdominant. It is also worth noticing that though hydrostatic masses depend on the choice of a fiducial cosmology through the angular diameter distance, the sparsity, being a mass ratio, is independent of such an assumption.

3.3. Selection Effects

A final remark concerns selection effects. In principle, we do not expect a significant contribution since we have seen that average sparsity as predicted by Equation (4) is largely independent of the lower limit of integration. To have a quantitative estimate of potential systematics induced by the shape of the selection function, we multiply the integrands on both sides of Equation (4) by a selection function of the form

$$f(M_{\Delta}) = \frac{1}{2} \left[1 + \operatorname{erf} \left(\frac{\ln M_{\Delta} - \ln M_{\Delta}^{\min}}{\sqrt{2} \sigma_f} \right) \right], \quad (7)$$

where σ_f modulates the shape of the selection function.

In Figure 8 we plot the relative difference of the redshift evolution of the average sparsity with respect to the case $f(M_{\Delta}) = 1$ for the fiducial *Planck* cosmology and for different values of $\sigma_f = 0.01, 0.4, 0.7$, and 1.5 . We can see that the differences are at the subpercent level.

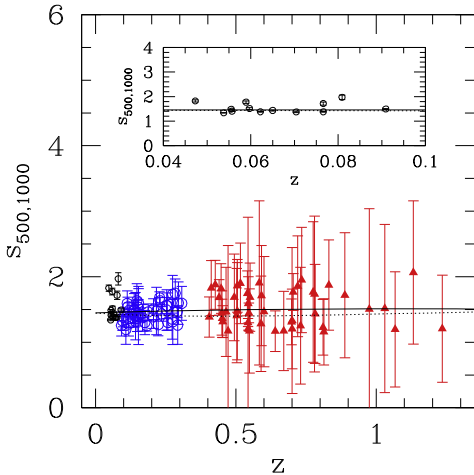


Figure 9. Sparsity of X-ray clusters. The low-redshift sample consists of clusters with mass measurements from Ettori et al. (2017), S. Ettori et al. (2017, in preparation), and V. Ghirardini et al. (2017, in preparation), also shown in the inset plot (black open circles), and Ettori et al. (2010) (blue open circles). The high-redshift sample consists of clusters with mass estimates from Amodeo et al. (2016; red filled triangles). The black solid line and the black dotted line correspond to the best-fit Λ CDM models inferred assuming the ST-RayGal and ST-Despali mass functions, respectively. We may notice four clusters at $z < 0.1$ whose sparsity significantly departs from the best fit. We have checked that excluding these outliers from the analysis does not alter the result of the cosmological parameter inference.

4. Sparsity of X-Ray Clusters and Cosmological Parameter Constraints

We estimate the halo sparsity of a set of X-ray galaxy clusters with hydrostatic mass measurements. The data set consists of a low-redshift sample of 57 clusters ($0.05 < z < 0.3$) from Ettori et al. (2010, 2017), S. Ettori et al. (2017, in preparation), and V. Ghirardini et al. (2017, in preparation) and a high-redshift sample of 47 clusters ($0.4 < z < 1.2$) presented in Amodeo et al. (2016). DM masses M_{500c} and M_{1000c} have been estimated by solving the HE equation (see, e.g., Sarazin 1986; Ettori 2013). We compute the sparsity of each cluster in the catalogs, $\hat{s}_{500,1000} = M_{500c}/M_{1000c}$, and estimate the uncertainty by propagating the mass measurement errors. These are shown in Figure 9.

For simplicity we have neglected mass correlation effects: these may be present as a result of the mass measurement methodology that assumes a functional form of the DM halo profile.¹¹ Systematics affecting the HE mass estimate can be more important. In the case of the high-redshift sample, Amodeo et al. (2016) have tested the consistency of the HE masses for a subset of 32 clusters for which gravitational lensing measurements were available in the literature (LC²-single catalog from Sereno 2015). They have found a good agreement within the large statistical uncertainties with $\ln(M_{\text{HE}}/M_{\text{lens}}) = 0.16 \pm 0.65$. For the low-redshift sample there is no available comparison; however, we noticed that the data set from Ettori et al. (2010) consists of massive clusters for which mass measurement errors are larger than the expected bias from baryonic feedback discussed in Section 3.2. In the case of the very low redshift sample by Ettori et al. (2017),

¹¹ Given that the sparsity is a mass ratio, a positive correlation r between the estimates of M_{500c} and M_{1000c} would imply that we are overestimating the sparsity errors by a factor of $\sim 1/\sqrt{1-r}$. For instance, if $r \sim 0.5$, as is reasonable to expect, this would correspond to a 30% overestimation and thus result in more conservative constraints on the cosmological parameters.

S. Ettori et al. (2017, in preparation), and V. Ghirardini et al. (2017, in preparation), HE mass uncertainties are at the few percent level, and we cannot a priori exclude that some of the sparsity measurements are affected by radial mass bias. After all, we can see in Figure 9 that the sparsity of four of the clusters in the very low redshift sample significantly deviates from the values of the other objects in the data set. We have found that removing these objects from the data analysis leaves the cosmological results unaltered. As seen in Section 2.3, this is a direct consequence of the fact that the cosmological signal is largest at $z \sim 0.5$. Nevertheless, to test the stability of the cosmological analysis against possible contamination from HE mass bias, we perform an additional analysis assuming a systematic redshift-dependent shift of the measured cluster sparsity. More specifically, we assume a 5% shift of the cluster sparsity at $z = 0$ linearly reducing to 2% at $z = 1$. This is an extremely conservative bias model, especially if compared to the level of bias discussed in Section 3.2. In fact, it implies that the HE mass determination of each cluster systematically underestimates M_{500c} by 28% and M_{1000c} by 35% at $z = 0$, and by 23% and 30%, respectively, at $z = 1$ (consistently with the 5% reduction found for M_{200c} estimates in Velliscig et al. 2014).

Since we compare individual cluster sparsity estimates to the predictions of the ensemble average sparsity, we account for the intrinsic dispersion of the halo sparsity discussed in Section 2.2 by adding in quadrature a conservative and absolute 0.2 intrinsic scatter (consistent with N -body simulation results shown in the inset plot of Figure 2) to the statistical error.

We perform a Markov chain Monte Carlo data analysis to derive constraints on the Λ CDM model parameters, $(\Omega_m, \sigma_8, h, n_s, \Omega_b h^2)$. To reduce the effect of parameter degeneracies, we assume a set of Gaussian priors on $n_s \sim \mathcal{N}(0.963, 0.09)$ consistently with *Planck* results (Planck Collaboration et al. 2016a), $h \sim \mathcal{N}(0.688, 0.033)$ from Efstathiou (2014), and $\Omega_b h^2 \sim \mathcal{N}(0.022, 0.002)$ consistent with big bang nucleosynthesis bounds (Cyburt et al. 2016). We assume flat priors for $\Omega_m \sim \mathcal{U}(0.05, 0.95)$ and $\sigma_8 \sim \mathcal{U}(0.2, 1.8)$. In order to evaluate the impact of the prior on h , we have also performed a likelihood analysis of the full cluster sample assuming a Gaussian *HST* prior $h \sim \mathcal{N}(0.732, 0.024)$ from Riess et al. (2016).

We evaluate the following χ^2 :

$$\chi^2 = \sum_i \frac{[\hat{s}_{500,1000}^i - \langle s_{500,1000}^{\text{th}}(z_i) \rangle]^2}{\sigma_{\text{int}}^2 + \sigma_{s_{500,1000}^i}^2}, \quad (8)$$

where $\hat{s}_{500,1000}^i$ is the sparsity of the i th cluster in the catalog, $\langle s_{500,1000}^{\text{th}}(z_i) \rangle$ is the theoretical model prediction given by Equation (4) assuming a given mass function model, $\sigma_{\text{int}} = 0.2$ is the intrinsic scatter of the halo sparsity¹² (conservatively set to a value consistent with the N -body results), and $\sigma_{s_{500,1000}^i}$ is the error on the cluster sparsity measurement.

We use the Metropolis–Hastings algorithm to generate 15 independent random chains of 2×10^5 samples and evaluate the rejection rate every 100 steps and adjust the width of the parameters dynamically. We check the convergence of the chains using the Gelman–Rubin test (Gelman & Rubin 1992).

¹² In principle, one can attempt to infer the intrinsic scatter from the data regression with the other cosmological parameters.

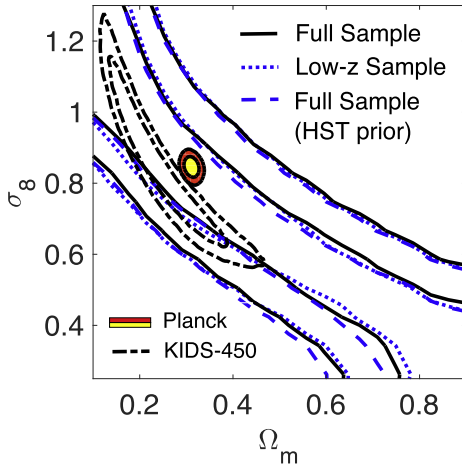


Figure 10. Marginalized 1σ and 2σ contours in the Ω_m - σ_8 plane assuming the ST-RayGal mass function using the full X-ray cluster data set (black solid lines), the low- z redshift sample only (blue dotted lines), and the case of the *HST* prior on h (blue dashed lines). For comparison we also plot the contours from the *Planck* cosmological data analysis (Planck Collaboration et al. 2016a) and KIDS-450 (Hildebrandt et al. 2017).

The results of the likelihood data analysis assuming the ST-RayGal mass function are summarized in Figure 10, where we plot the marginalized 1σ and 2σ credibility contours in the Ω_m - σ_8 plane for the different cases. For comparison we also plot the marginalized credibility contours from the *Planck* cosmological data analysis (Planck Collaboration et al. 2016a) and the weak gravitational lensing from KIDS-450 (Hildebrandt et al. 2017). We can see that the constraints on Ω_m and σ_8 are rather weak. Given the large uncertainties of the sparsity sample at $z \gtrsim 0.4$, this is not surprising since the variation of the sparsity with respect to σ_8 is the largest at $z \sim 0.4$, while that with respect to Ω_m remains quite flat for $z \gtrsim 0.5$ (see top panel in Figure 4). The best-fit model corresponds to $\Omega_m \simeq 0.4$ and $\sigma_8 \simeq 0.6$. We plot the associated average sparsity as a function of redshift as a black solid line in Figure 9. Notice the strong degeneracy between Ω_m and σ_8 . As discussed in Section 2.3, this is expected given the sensitivity of the halo sparsity to $S_8 \equiv \sigma_8 \sqrt{\Omega_m}$, for which we find $S_8 = 0.40 \pm 0.11$ at 1σ .

As we can see in Figure 10, the credibility contours do not significantly differ from those inferred under the *HST* prior. This is also consistent with the analysis presented in Section 2.3, which indicates that the halo sparsity is less sensitive to h than σ_8 , Ω_m , and n_s . Indeed, changing the priors on n_s can have a more significant impact on the inferred constraints. However, n_s is tightly constrained by the *Planck* data, while there are larger uncertainties on the value of h , which is why we have tested the sensitivity of the constraints to the h prior.

In Figure 10 we also plot the credibility contours inferred using the low- z sample ($z \lesssim 0.4$) only. These do not differ from those obtained using the full sample, which is not surprising given the larger uncertainties of the high- z sample. Overall, the inferred credibility contours overlap with those inferred from *Planck* within 1σ , as well as those from the KIDS-450 data set.

In Figure 11 we plot the constraints in the Ω_m - σ_8 plane inferred assuming the ST-Despali mass function. Differently from the ST-RayGal case, we find bounded contours at 1σ , though still spread over a larger portion of the parameter space. The one-dimensional marginalized constraints are

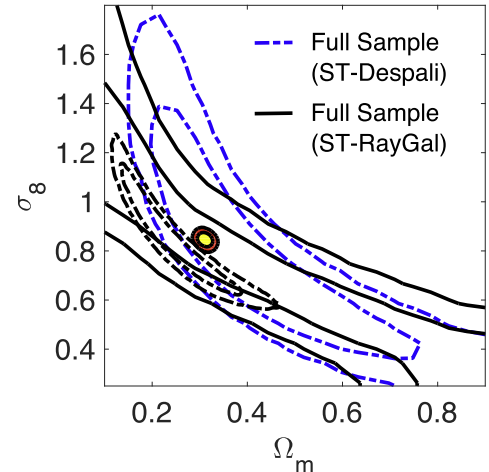


Figure 11. Marginalized 1σ and 2σ contours in the Ω_m - σ_8 plane as in Figure 10. Here, the blue dashed lines are the contours inferred assuming the ST-Despali mass function.

$\Omega_m = 0.42 \pm 0.17$ and $\sigma_8 = 0.80 \pm 0.31$ at 1σ , with the best-fit values being $\Omega_m = 0.36$ and $\sigma_8 = 0.74$. We plot the associated average sparsity as a function of redshift as a black dotted line in Figure 9. From the analysis of the Monte Carlo chains we obtain $S_8 = 0.48 \pm 0.11$ at 1σ , which is consistent with the constraints found using the ST-RayGal mass function. As we can see in Figure 11, the contours are statistically consistent with those inferred from the ST-RayGal analysis, though deviations are noticeable in the tail of the distribution for low values of Ω_m and large values of σ_8 . This is not unexpected since in this range of the parameter space the mass function calibration may deviate from that of the vanilla Λ CDM model of the RayGalGroupSims simulation. The bounds are compatible with the *Planck* results and consistent with those from the KIDS-450 analysis.¹³

We have limited the analysis including the systematic HE mass bias model discussed at the beginning of this section to the case of the ST-Despali mass function. The results of the likelihood data analysis give $S_8 = 0.51 \pm 0.11$, which is consistent with the results obtained assuming no systematic bias model.

5. X-Ray Cluster Sparsity Forecasts

Future observational programs will provide increasingly large samples of clusters. Surveys such as *eROSITA* (Merloni et al. 2012) are expected to detect several hundred thousands of clusters across a large redshift range. Cosmological parameter constraints will be inferred from accurate measurements of cluster number counts and spatial clustering (see, e.g., Pillepich et al. 2012).

Sparsity measurements capable of providing constraints that are competitive with respect to those inferred from other cosmological probes strongly depend on the availability of accurate mass estimations. In the case of large data sets, such as

¹³ Several large-scale structure data analyses have constrained combinations of Ω_m and σ_8 . As an example, SZ cluster abundance data from the South Pole Telescope (SPT) survey give $\sigma_8 (\Omega_m/0.27)^{0.3} = 0.797 \pm 0.031$ (de Haan et al. 2016). The analysis of the cluster sparsity presented here gives consistent bounds, $\sigma_8 (\Omega_m/0.27)^{0.3} = 0.87 \pm 0.26$. Similarly, measurements of the galaxy clustering from the Dark Energy Survey (DES) constrain $\sigma_8 (\Omega_m/0.3)^{0.16} = 0.74 \pm 0.12$ (Kwan et al. 2017), and we find again a result consistent within 1σ , $\sigma_8 (\Omega_m/0.3)^{0.16} = 0.83 \pm 0.29$.

those from *eROSITA*, cluster masses will be measured through the use of observationally calibrated scaling relations (see, e.g., Maughan et al. 2012; Ettori 2013, 2015). More precise estimates, for instance, using HE masses, require observations that are able to resolve the cluster mass profile. However, these may be available only for smaller cluster samples through follow-up observations.

Here we perform a Fisher matrix forecast of the cosmological parameter errors from sparsity measurements to determine the type of galaxy cluster observations needed to derive competitive constraints with respect to those that can be obtained with other standard probes such as the CMB.

To this purpose we evaluate the Fisher matrix:

$$F_{\mu\nu} = \sum_i \frac{1}{\sigma_{z_i}^2} \frac{\partial \langle s_{500,1000}(z_i) \rangle}{\partial \theta_\mu} \frac{\partial \langle s_{500,1000}(z_i) \rangle}{\partial \theta_\nu} \bigg|_{\hat{\theta}_\mu}, \quad (9)$$

where $\theta_\mu = (\Omega_m, \sigma_8, h, n_s, \Omega_b)$ are the cosmological parameters, $\hat{\theta}_\mu$ is the fiducial parameter value, and σ_{z_i} is the statistical error on the mean sparsity. We compute the partial derivatives in Equation (9) using a five-point stencil approximation. We model the error on the average sparsity as

$$\sigma_{z_i} = \langle s_{500,1000}^{\text{fid}}(z_i) \rangle e_M \sqrt{\frac{2}{N(z_i)}}, \quad (10)$$

where $\langle s_{500,1000}^{\text{fid}}(z_i) \rangle$ is the fiducial sparsity value, e_M is the fraction error on mass measurements, and $N(z_i)$ is the number of clusters at redshift z_i , given by

$$N(z_i) \equiv A_{\text{survey}} \Delta z f \frac{dN}{dz dA}(z_i), \quad (11)$$

where A_{survey} is the survey area, Δz is the size of the redshift bins, f is the fraction of clusters with mass measurement error e_M , and $(dN/dz dA)(z)$ is the cluster number count distribution. Again, for simplicity we neglect correlations in the estimation of the masses M_{500c} and M_{1000c} . Notice that, as in the case of the synthetic likelihood test presented in Section 4, we do not add in quadrature the intrinsic scatter of the halo sparsity to the statistical error as in the data analysis described in Section 4. This is because, in the spirit of the Fisher matrix calculation, we compare predictions of the ensemble average sparsity not to the sparsity of an individual cluster at a given redshift, but rather to the estimated average sparsity from an ensemble of $N(z_i)$ clusters.

We assume a *Planck* fiducial Λ CDM cosmology and consider a full-sky survey with cluster number count distribution consistent with an *eROSITA*-like survey. This is expected to detect $\sim 10^5$ clusters with mass $\gtrsim 10^{13} h^{-1} M_\odot$. To this purpose we estimate the cluster number counts as a function of redshift for our fiducial cosmology by integrating the ST-RayGal mass function with M_{500c} and imposing a flux cut $F_{X,\text{cut}} = 4.3 \times 10^{-14} \text{ erg s}^{-1} \text{ cm}^{-2}$, where we have used the luminosity–mass relation from Mantz et al. (2010) with no intrinsic scatter. The predicted number count distribution is shown in Figure 12. We may notice that this is consistent with the redshift distribution estimated by Pillepich et al. (2012; see their Figure 3 for the photon count rate threshold corresponding to $M_{500c}^{\text{cut}} \gtrsim 5 \times 10^{13} h^{-1} M_\odot$), with a total count of $\sim 3 \times 10^7$ clusters. For simplicity, here we only consider redshift bins of size $\Delta z = 0.1$ in the redshift range $0 \lesssim z \lesssim 1.4$.

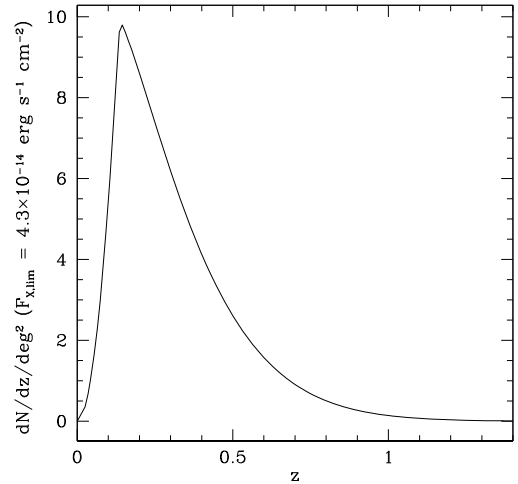


Figure 12. Expected redshift distribution of clusters of an *eROSITA*-like survey with X-ray flux cut $F_{X,\text{cut}} = 4.3 \times 10^{-14} \text{ erg s}^{-1} \text{ cm}^{-2}$ for our fiducial cosmological model.

Table 2
Marginalized Errors on Cosmological Parameters from the Fisher Matrix Analysis of *Small-sample, High-precision* Sparsity Measurements in Combination with *Planck* Constraints

	<i>Planck</i> Only	+ $\langle s_{500,1000}(z) \rangle$ ($e_M = 0.01, f = 0.01$)	+ $\langle s_{500,1000}(z) \rangle$ ($e_M = 0.05, f = 0.1$)
σ_{Ω_m}	0.01082	0.01022/0.00571	0.01035/0.00684
σ_{σ_8}	0.01396	0.00597/0.00780	0.00720/0.00926
σ_{n_s}	0.00428	0.00414/0.00300	0.00418/0.00328
σ_h	0.00763	0.00723/0.00411	0.00732/0.00490
σ_{Ω_b}	0.00095	0.00090/0.00053	0.00091/0.00062

Note. The numbers quoted on the left (right) correspond to the Fisher forecast based on the ST-RayGal (ST-Despali) mass function.

We limit our analysis to two different observational scenarios: *small-sample, high-precision* sparsity measurements with mass errors of $e_M = 0.01$ for ~ 300 clusters ($f = 0.01$) and $e_M = 0.05$ for ~ 3000 clusters ($f = 0.10$), and *large-sample, low-precision* sparsity measurements with mass errors of $e_M = 0.1$ for ~ 6000 clusters ($f = 0.2$) and $e_M = 0.2$ for all clusters ($f = 1$). The latter scenario considers the possibility of measuring masses over a large sample of clusters through well-calibrated scaling relations whose validity should be limited to the $\sim 10\%$ – 30% level.

We combine the Fisher matrix from Equation (9) to the *Planck*–Fisher matrix, which has been computed using the code CosmoFish (Raveri et al. 2016a, 2016b).

The results are summarized in Tables 2 and 3. In all cases we can see that including the information from the halo sparsity improves the CMB constraints from *Planck*. Indeed, the level of improvement depends on the observational configuration considered. Quite remarkably, we find that a 1% mass error estimation for a sample of ~ 300 clusters has the greatest impact in reducing the *Planck* errors on several parameters. For instance, we find an improvement of a factor of ~ 2.3 on the estimation of σ_{σ_8} in the ST-RayGal case, while assuming the ST-Despali mass function we find an improvement of a factor

Table 3As in Table 2, but for *Large-sample, Low-precision* Sparsity Measurements

	<i>Planck</i> Only	$\langle s_{500,1000}(z) \rangle$ ($e_M = 0.10, f = 0.2$)	$\langle s_{500,1000}(z) \rangle$ ($e_M = 0.20, f = 1$)
σ_{Ω_m}	0.01082	0.01044/0.00751	0.01041/0.00731
σ_{σ_8}	0.01396	0.00850/0.01010	0.00805/0.00984
σ_{n_s}	0.00428	0.00420/0.00345	0.00419/0.00340
σ_h	0.00763	0.00738/0.00536	0.00736/0.00522
σ_{Ω_b}	0.00095	0.00092/0.00068	0.00092/0.00066

of ~ 1.9 on σ_{Ω_m} and ~ 1.8 on σ_{σ_8} . Even for the realistic scenario with 20% mass errors, we find up to $\sim 30\%$ improvement of the *Planck* constraints. Again, assuming the ST-Despali mass function systematically predicts smaller parameter errors than those obtained with the ST-RayGal mass function.

Compared to other cosmic probes, such as the combination of CMB constraints with those from cluster number counts and angular clustering studied in Pillepich et al. (2012), we find that the sparsity can provide cosmological parameter constraints of the same order (see, e.g., Table B2 in Pillepich et al. 2012).

6. Conclusions

In this work we have presented a first cosmological analysis of the DM halo sparsity. This characterizes halos in terms of the ratio of halo masses at two different overdensities and carries cosmological information encoded in the mass profile of halos that can be retrieved from mass measurements of galaxy clusters.

Building on the work of Balmes et al. (2014), we have tested the sparsity properties using halo catalogs from a large-volume, high-resolution N -body simulation. In particular, we have shown that the average sparsity of an ensemble of halos can be accurately predicted from prior knowledge of the halo mass function. To this purpose we have introduced the ST-RayGal parameterization, which reproduces to great accuracy the numerical halo mass function for halo masses M_{200c} , M_{500c} , and M_{1000c} and allows us to recover the measured average sparsity values at different redshift snapshots to the subpercent level.

We have tested the accuracy of the theoretical predictions assuming other mass function parameterizations proposed in the literature. Depending on the mass function model, we found deviations with respect to the average sparsity from the N -body halo catalogs up to the 10% level.

The possibility of predicting the average sparsity for a given set of cosmological parameters enables us to perform a cosmological model parameter inference using cluster sparsity measurements. To test this, we have generated a synthetic set of data and performed a likelihood analysis, from which we have retrieved the input fiducial cosmology.

Systematic errors affecting halo sparsity data analyses may arise primarily from uncertainties in the theoretical modeling of the halo mass function and the radial-dependent cluster mass bias from baryonic feedback processes. Here we have performed an analysis of these systematics. Quite importantly, using results from state-of-art numerical simulations, we show that for massive systems baryonic effects alter the halo sparsity at the few percent level. This is subdominant compared to the uncertainties from mass estimation errors of currently available

cluster data sets. We find that cluster selection effects have a negligible impact on sparsity, which is an obvious advantage compared to other cluster cosmological proxies, such as the number counts or the spatial clustering.

We have estimated the sparsity of a sample of X-ray clusters with hydrostatic mass measurements and performed a Markov chain Monte Carlo likelihood data analysis to infer constraints Ω_m and σ_8 . We find weak marginalized bounds on Ω_m and σ_8 . Assuming the mass function from Despali et al. (2016) gives the strongest bound, in particular, we find $\Omega_m = 0.42 \pm 0.17$ and $\sigma_8 = 0.80 \pm 0.31$ at 1σ , corresponding to $S_8 = 0.48 \pm 0.11$. In all cases the inferred constraints are compatible with those inferred from the *Planck* cosmological data analysis within 1σ . We find these results to be stable against a conservative systematic bias model accounting for baryonic effects on cluster mass estimates.

Future cluster surveys can provide larger sparsity data sets. Using a Fisher matrix approach, we have investigated their complementarity with respect to CMB observations from *Planck*. In particular, we have performed a parameter error forecast for different observational scenarios and found that sparsity measurements from a small cluster sample of ~ 300 clusters with mass uncertainties of 1% can improve *Planck* constraints on Ω_m and σ_8 by approximately a factor of 2. However, this requires a control of systematic errors due to hydrostatic mass bias.

Cluster mass measurements from SZ and lensing observations may also provide viable data sets to estimate the halo sparsity, and we leave such studies to future works.

We would like to thank Matteo Martinelli for providing us with the Planck–Fisher matrix. P.S.C. is grateful to Joop Schaye for useful discussions. P.S.C., Y.R., and M.-A.B. are thankful to Fabrice Roy for technical support. S.E. and M.S. acknowledge the financial support from contracts ASI-INAF I/009/10/0, NARO15 ASI-INAF I/037/12/0, and ASI 2015-046-R.0. The research leading to these results has received funding from the European Research Council under the European Union Seventh Framework Programme (FP7/2007-2013 grant agreement no. 279954). We acknowledge support from the DIM ACAV of the Region Île-de-France. This work was granted access to the HPC resources of TGCC under allocation 2016-042287 made by GENCI (Grand Équipement National de Calcul Intensif).

Appendix

Halo Mass Function Parameterization

We use the numerical mass functions estimated from the RayGalGroupSims simulation SOD halo catalogs with mass M_{200c} , M_{500c} , and M_{1000c} , to calibrate at each redshift snapshot the coefficients of the ST mass function formula (Sheth & Tormen 1999):

$$\frac{dn}{dM} = \frac{\rho_m}{M} \left(-\frac{1}{\sigma} \frac{d\sigma}{dM} \right) A \frac{\delta_c}{\sigma} \sqrt{\frac{2a}{\pi}} \left[1 + \left(a \frac{\delta_c^2}{\sigma^2} \right)^{-p} \right] e^{-\frac{a\delta_c^2}{2\sigma^2}}, \quad (12)$$

where ρ_m is the present mean matter density, δ_c is the linearly extrapolated spherical collapse threshold, which we compute using the formula from Kitayama & Suto (1996), and

$$\sigma^2(M, z) = \frac{1}{2\pi^2} \int dk k^2 P(k, z) \tilde{W}^2[k R(M)] \quad (13)$$

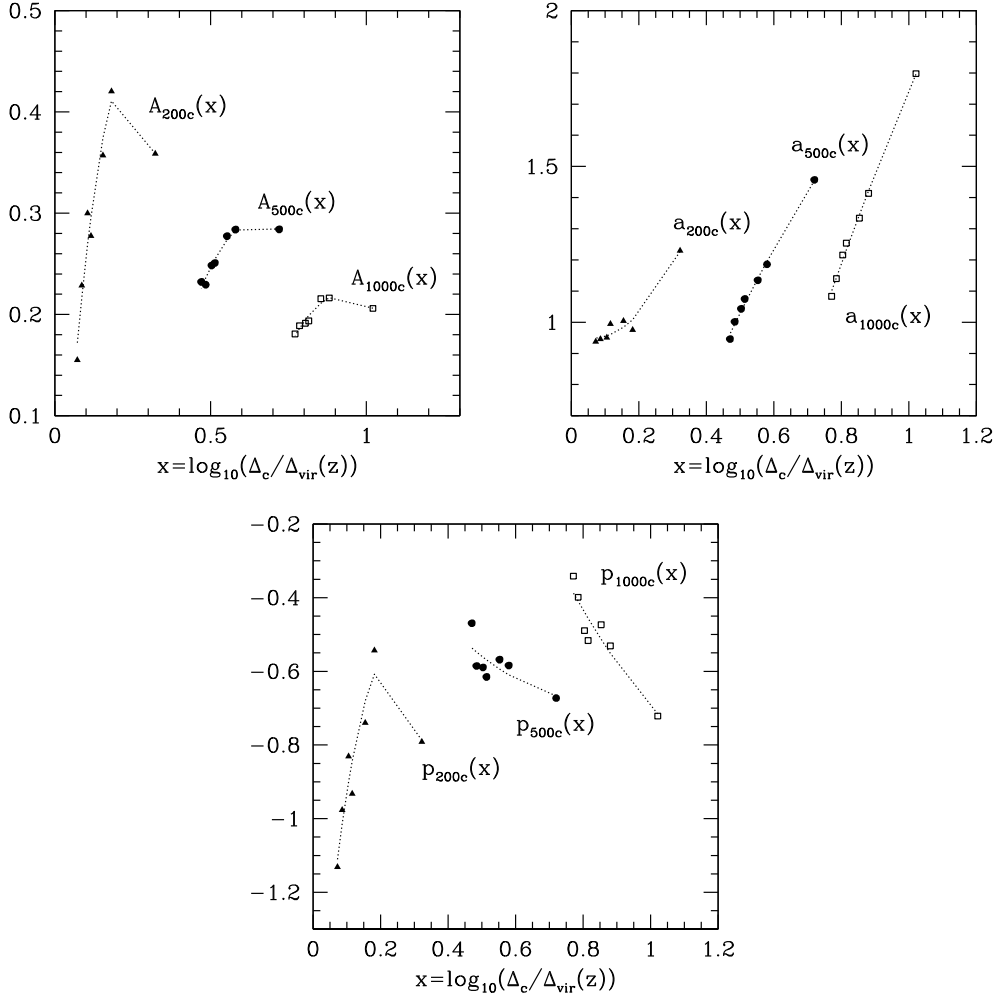


Figure 13. Comparison of the ST best-fit parameters' dependence on $x = \log_{10}(\Delta_c/\Delta_{\text{vir}}(z))$ and the best-fit quadratic functions for A_{Δ_c} (top left panel), a_{Δ_c} (top right panel), and p_{Δ_c} (bottom panel) for $\Delta_c = 200, 500,$ and $1000,$ respectively.

Table 4
Best-fit Coefficients of the ST Mass Function for Halos with Masses M_{200c} , M_{500c} , and M_{1000c} .

z	A_{200c}	a_{200c}	p_{200c}	A_{500c}	a_{500c}	p_{500c}	A_{1000c}	a_{1000c}	p_{1000c}
0.00	0.35884	1.2300	-0.79142	0.28401	1.4568	-0.67260	0.20596	1.7978	-0.72148
0.50	0.42038	0.9752	-0.54330	0.28378	1.1859	-0.58425	0.21628	1.4134	-0.53098
0.66	0.35697	1.0039	-0.74000	0.27724	1.1347	-0.56833	0.21555	1.3339	-0.47343
1.00	0.27751	0.9944	-0.93238	0.25082	1.0470	-0.61536	0.19365	1.2537	-0.51639
1.14	0.29991	0.9505	-0.83109	0.24834	1.0429	-0.58941	0.19134	1.2156	-0.48951
1.50	0.22855	0.9457	-0.97637	0.22936	1.0014	-0.58554	0.18885	1.1400	-0.39898
2.00	0.15502	0.9375	-1.13120	0.23210	0.9459	-0.46949	0.18072	1.0830	-0.34148

is the variance of the linear density field smoothed on a spherical volume of radius R enclosing the mass $M = 4/3\pi\rho_m R^3$, with $P(k, z)$ being the linear matter power spectrum at redshift z and

$$\tilde{W}^2[k R(M)] = \frac{3}{(kR)^3} [\sin(kR) - (kR)\cos(kR)]. \quad (14)$$

We determine the best-fit ST coefficients using a Levenberg–Marquardt minimization scheme. These are quoted in Table 4 for halo masses M_{200c} , M_{500c} , and M_{1000c} . We find the best-fit functions to have logarithmic deviations with respect to the numerical estimates to better than 5%.

In order to extrapolate the mass functions at any given redshift, we follow the approach of Despali et al. (2016) and

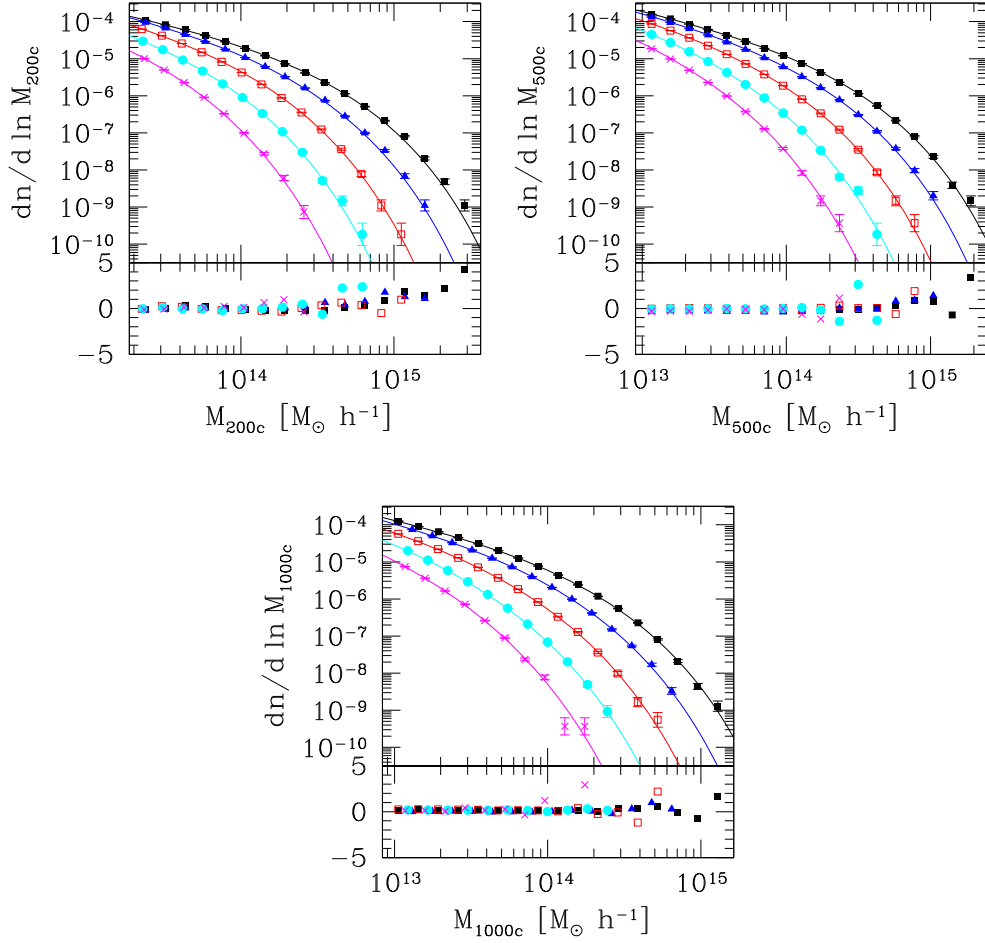


Figure 14. Halo mass function from the RayGalGroupSims simulation for SOD halos with mass M_{200c} (top left panel), M_{500c} (top right panel), and M_{1000c} (bottom panel) at $z = 0, 0.5, 1, 1.5,$ and 2 (top to bottom). The solid lines are the ST-RayGal mass functions with coefficients given by Equations (15), (16), and (17). The logarithmic residual is shown in the bottom panel: as we can see, deviations are within the 5% level across the entire mass range.

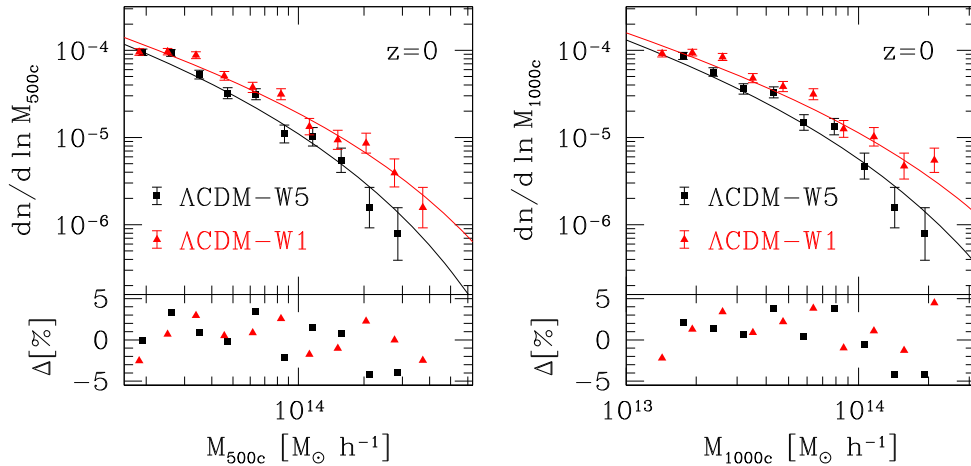


Figure 15. SOD halo mass functions from Λ CDM-W5 (black squares) and Λ CDM-W1 (red triangles) with mass M_{500c} (left panel) and M_{1000c} (right panel), respectively, against the ST-RayGal predictions.

parameterize the redshift dependence of the ST coefficients in terms of the variable $x = \log_{10}(\Delta/\Delta_{\text{vir}}(z))$, where $\Delta_{\text{vir}}(z)$ is the virial overdensity as given by the formula derived in Bryan & Norman (1998). We find that the redshift variation of the best-fit ST coefficients can be described by very good approximation by a quadratic fit as a function of x given by

$$\begin{cases} A_{200c}(x) = -10.2185312 x^2 + 4.78051093 x - 0.1206716 \\ a_{200c}(x) = 4.07275047 x^2 - 0.49618532 x + 0.96372361 \\ p_{200c}(x) = -23.48761585 x^2 + 10.5651697 x - 1.752599071 \end{cases} \quad (15)$$

$$\begin{cases} A_{500c}(x) = -2.08511667 x^2 + 2.71726345 x - 0.59113241 \\ a_{500c}(x) = -1.0788725 x^2 + 3.25302957 x - 0.32810261 \\ p_{500c}(x) = 1.04288295 x^2 - 1.76269479 x + 0.06162189 \end{cases} \quad (16)$$

and

$$\begin{cases} A_{1000c}(x) = -1.65696205 x^2 + 3.07836133 x - 1.20944538 \\ a_{1000c}(x) = -1.18612053 x^2 + 4.91186256 x - 1.98337952, \\ p_{1000c}(x) = 1.33135179 x^2 - 3.7042898 x + 1.67853762 \end{cases} \quad (17)$$

which we plot in Figure 13 against the best-fit values quoted in Table 4.

In Figure 14 we plot the ST mass functions for M_{200c} , M_{500c} , and M_{1000c} with coefficients given by Equations (15)–(17) against the N -body mass function estimates, which we have referred to as the ST-RayGal mass functions. As we can see, logarithmic deviations with respect to the numerical results are still within the 5% level.

We find that the ST-RayGal mass function formulae can also reproduce the SOD mass functions for M_{500c} and M_{1000c} from N -body simulations with different cosmological parameter values. In particular, we have used halo catalogs at $z = 0$ from simulations of $162 h^{-1}$ Mpc box length and 512^3 particles of two flat Λ CDM models: Λ CDM-W1 with $\Omega_m = 0.29$, $\sigma_8 = 0.90$, $\Omega_b = 0.047$, and $n_s = 0.990$, and Λ CDM-W5 with $\Omega_m = 0.26$, $\sigma_8 = 0.79$, $\Omega_b = 0.044$, and $n_s = 0.963$. As shown in Figure 15, the logarithmic differences between the ST-RayGal mass function and the numerical estimates from the Λ CDM-W5 and Λ CDM-W1 catalogs are within the 5% level. Using the same halo catalogs, we estimate the average sparsity at $z = 0$. In the case of the Λ CDM-W5 simulation we find $\langle s_{500,1000} \rangle = 1.41$, while in the Λ CDM-W1 case we find $\langle s_{500,1000} \rangle = 1.36$. These values are consistent to within a few percent with the average sparsity prediction inferred by solving Equation (4) with the ST-RayGal mass functions. In particular, we obtain $\langle s_{500,1000}^{\text{th}} \rangle = 1.43$ for the Λ CDM-W5 model and $\langle s_{500,1000}^{\text{th}} \rangle = 1.39$ for the Λ CDM-W1 cosmology.

ORCID iDs

P. S. Corasaniti  <https://orcid.org/0000-0002-6386-7846>

D. Eckert  <https://orcid.org/0000-0001-7917-3892>

References

- Alimi, J.-M., Füzfa, A., Boucher, V., et al. 2010, *MNRAS*, 401, 775
 Allen, S. W., Evrard, A. E., & Mantz, A. B. 2011, *ARA&A*, 49, 409
 Amodeo, S., Ettori, S., Capasso, R., & Sereno, M. 2016, *A&A*, 590, A126

- Balmes, I., Rasera, Y., Corasaniti, P.-S., & Alimi, J.-M. 2014, *MNRAS*, 437, 2328
 Bhattacharya, S., Habib, S., Heitmann, K., & Vikhlinin, A. 2013, *ApJ*, 766, 16
 Biffi, V., Borgani, S., Murante, G., et al. 2016, *ApJ*, 827, 112
 Bryan, G. L., & Norman, M. L. 1998, *ApJ*, 495, 80
 Bullock, J. S., Kolatt, T. S., & Sigad, Y. 2001, *MNRAS*, 321, 559
 Correa, C. A., Wyithe, J. S. B., Schaye, J., & Duffy, A. R. 2015, *MNRAS*, 452, 1217
 Courtin, J., Rasera, Y., Alimi, J.-M., et al. 2011, *MNRAS*, 410, 1911
 Cyburt, R. H., Fields, B. D., Olive, K. A., & Yeh, T.-H. 2016, *RvMP*, 88, 015004
 de Haan, T., Benson, B. A., Bleem, L. E., et al. 2016, *ApJ*, 832, 95
 Despali, G., Giocoli, C., Angulo, R. E., et al. 2016, *MNRAS*, 456, 2486
 Diemer, B., & Kravtsov, A. V. 2015, *ApJ*, 799, 108
 Dolag, K., Bartelmann, M., Perrotta, F., et al. 2004, *A&A*, 416, 853
 Duffy, A. R., Schaye, J., Kay, S. T., et al. 2010, *MNRAS*, 405, 2161
 Ebeling, H., Edge, A. C., Mantz, A., et al. 2010, *MNRAS*, 407, 83
 Efstathiou, G. 2014, *MNRAS*, 440, 1138
 Eisenstein, D. J., & Hu, W. 1999, *ApJ*, 496, 605
 Ettori, S. 2013, *MNRAS*, 435, 1265
 Ettori, S. 2015, *MNRAS*, 446, 2629
 Ettori, S., Gastaldello, F., Leccardi, A., et al. 2010, *A&A*, 524, 88
 Ettori, S., Ghirardini, V., Eckert, D., Dubath, F., & Pointecouteau, E. 2017, *MNRAS*, 470, L29
 Gelman, A., & Rubin, D. B. 1992, *StatSci*, 7, 457
 Giocoli, C., Tormen, G., & Sheth, R. K. 2012, *MNRAS*, 422, 185
 Hildebrandt, H., Viola, M., Heymans, C., et al. 2017, *MNRAS*, 465, 1454
 Hoekstra, H., Mahdavi, A., Babul, A., & Bildfell, C. 2012, *MNRAS*, 427, 1298
 King, L. J., & Mead, J. M. G. 2011, *MNRAS*, 416, 2539
 Kitayama, T., & Suto, Y. 1996, *MNRAS*, 280, 638
 Klypin, A., Yepes, G., Gottlober, S., Prada, F., & Hess, S. 2016, *MNRAS*, 457, 4340
 Koester, B., McKay, T. A., Annis, J., et al. 2007, *ApJ*, 660, 221
 Komatsu, E., Smith, K. M., Dunkley, J., et al. 2011, *ApJS*, 192, 18
 Kravtsov, A. V., & Borgani, S. 2012, *ARA&A*, 50, 353
 Kwan, J., Sánchez, C., Clampitt, J., et al. 2017, *MNRAS*, 464, 4045
 Lacey, C., & Cole, S. 1994, *MNRAS*, 271, 676
 Le Brun, A. M. C., McCarthy, I. G., Schaye, J., & Ponman, T. J. 2014, *MNRAS*, 441, 1270
 Lewis, A., Challinor, A., & Lasenby, A. 2000, *ApJ*, 538, 473
 Ludlow, A. D., Bose, S., Angulo, R. E., et al. 2016, *MNRAS*, 460, 1214
 Macciò, A. V., Dutton, A. A., Van Den Bosch, F. C., et al. 2007, *MNRAS*, 378, 55
 Mantz, A., Allen, S. W., Ebeling, H., Rapetti, D., & Drlica-Wagner, A. 2010, *MNRAS*, 406, 1773
 Maughan, B. J., Giles, P. A., Randall, S. W., Jones, C., & Forman, W. R. 2012, *MNRAS*, 421, 1583
 McCarthy, I. G., Schaye, J., Ponman, T. J., et al. 2010, *MNRAS*, 406, 822
 Mead, J. M. G., King, L. J., Sijacki, D., et al. 2010, *MNRAS*, 406, 434
 Menanteau, F., Sifon, C., Barrientos, L. F., et al. 2013, *ApJ*, 765, 67
 Meneghetti, M., & Rasia, E. 2013, arXiv:1303.6158
 Meneghetti, M., Rasia, E., Merten, J., et al. 2010, *A&A*, 514, 93
 Merloni, A., Predehl, P., Becker, W., et al. 2011, arXiv:1209.3114
 Nagai, D., Vikhlinin, A., & Kravtsov, A. 2007, *ApJ*, 655, 98
 Navarro, J. F., Frenk, C. S., & White, S. D. M. 1997, *ApJ*, 490, 493
 Pierre, M., Pacaud, F., Adami, C., et al. 2016, *A&A*, 592, 16
 Piffaretti, R., Arnaud, M., Pratt, G. W., Pointecouteau, E., & Melin, J.-B. 2011, *A&A*, 534, 109
 Pillepich, A., Porciani, C., & Reiprich, T. H. 2012, *MNRAS*, 422, 44
 Planck Collaboration, Ade, P. A. R., et al. 2016a, *A&A*, 594, A13
 Planck Collaboration, Ade, P. A. R., et al. 2016b, *A&A*, 594, A19
 Postman, M., Coe, D., Benítez, N., et al. 2012, *Astrophys. J. Suppl.*, 199, 25
 Rasera, Y., Alimi, J.-M., Courtin, J., et al. 2010, in AIP Conf. Proc. 1241, Invisible Universe, ed. J.-M. Alimi & A. Füzfa (Melville, NY: AIP), 1134
 Rasia, E., Meneghetti, M., Martino, R., et al. 2012, *NJPh*, 14, 055018
 Raveri, M., Martinelli, M., Zhao, G., & Wang, Y. 2016a, arXiv:1606.06268
 Raveri, M., Martinelli, M., Zhao, G., & Wang, Y. 2016b, arXiv:1606.06273
 Reichardt, C. L., Stalder, B., Bleem, L. E., et al. 2013, *ApJ*, 763, 127
 Renneby, M., Hilbert, S., & Angulo, R. 2011, arXiv:1710.03251
 Riess, A. G., Macri, L. M., Hoffmann, S. L., et al. 2016, *ApJ*, 826, 56
 Rykoff, E. S., Rozo, E., Busha, M. T., et al. 2014, *ApJ*, 785, 104
 Sarazin, C. L. 1986, *RvMP*, 58, 1
 Schaye, J., Dalla Vecchia, C., Booth, C. M., et al. 2010, *MNRAS*, 402, 1536
 Sereno, M. 2015, *MNRAS*, 450, 3665
 Sereno, M., & Ettori, S. 2015, *MNRAS*, 450, 3633

- Sereno, M., Ettori, S., Giocoli, C., & Moscardini, L. 2015, [MNRAS](#), **449**, 2024
- Sheth, R. K., & Tormen, G. 1999, [MNRAS](#), **308**, 119
- Staniszewski, Z., Ade, P. A. R., Aird, K. A., et al. 2009, [ApJ](#), **701**, 32
- Tinker, J., Kravtsov, A. V., Klypin, A., et al. 2008, [ApJ](#), **688**, 709
- Umetsu, K., Broadhurst, T., Zitrin, A., et al. 2011, [ApJ](#), **738**, 41
- Velliscig, M., van Daalen, M., Schaye, J., et al. 2014, [MNRAS](#), **442**, 2641
- Vikhlinin, A., Markevitch, M., Murray, S. S., Forman, W., & Van Speybroeck, L. 2005, [ApJ](#), **628**, 655
- Wechsler, R. H., Bullock, J. S., Primack, J. R., Kravtsov, A. V., & Dekel, A. 2002, [ApJ](#), **568**, 52
- Zhao, D. H., Jing, Y. P., Mo, H. J., & Börner, G. 2003, [ApJL](#), **597**, L9
- Zhao, D. H., Jing, Y. P., Mo, H. J., & Börner, G. 2009, [ApJ](#), **707**, 354

ACKNOWLEDGEMENTS

This PhD thesis has enormous value for me. It gave me the chance to mature incredibly both professionally and personally. I had the privilege to be part of a fervent astronomical community and learn from great professionals in my field.

For all of this, I am deeply grateful to Simona Mei, for having taken me on board and introduced me with enthusiasm to the research world. She supervised every step of my journey helping me to enhance my qualities while rationally analyze and face my weaknesses. I am grateful for having given me priority at critical moments, especially in the final phases of this thesis, for having invested so much on my education and for her huge help with my job applications. I will treasure her precious advise on how to plan my future career. Being her student was a privilege for me, and I really hope to continue to enjoy her collaboration in the future.

Jim Bartlett constantly guided me in the first part of my thesis, and opened the doors to the *Planck* world for me. I am very grateful to him for having come to my rescue many times, with scientific and linguistic lessons, always with patience and humbleness, and for his support for my job applications.

I also wish to thank in a special way my missed co-advisor, Mauro Giavalisco. Even if our original plans have changed, I really enjoyed our stimulating discussions and I am profoundly grateful for his coaching before my first job interview, and for letting me join his observation run in Las Campanas and living such an amazing experience.

I acknowledge my collaborators that made this thesis possible with their important contribution and feedback. In particular, I thank Jean-Baptiste Melin for having provided the *Planck* maps and mass measurements, for our interesting discussion during meetings and for his constructive feedback on my presentations; Adam Stanford and Daniel Stern for having helped me with the interpretation of the spectroscopic results; Charles Lawrence for having provided the fundings to publish my papers; Gael Noirot for his input for the CARLA photometric analysis; Nina Hatch and Lizzie Cooke for the discussion on the results.

I wish to thank Emiliano Merlin for his help with the installation of T-PHOT and his useful tips on how to use it; the *Spitzer* Science Center for advice on *Spitzer* PSF; Chris Benn for the clarifications on the ACAM photometric calibration; Ivelina Momcheva for the information about the 3D-HST/F140W WCS.

I also acknowledge the stimulating discussions with Stefano Andreon, Raphael Barrena, Andrea Biviano, Joanne Cohn, Gus Evrard, Antonio Ferragamo, Gary Mamon, Ian McCarthy, and Lorenzo Posti about the cluster velocity dispersions and the galaxy velocity bias.

I wish to thank the *Euclid* community that welcomed me in the exciting preparation of the mission. I wish to reserve a special mention to the members of the Galaxy Cluster group with whom I had stimulating discussions on the future of this field: Begonia Ascaso, Jim Bartlett, Fabio Bellagamba, Andrea Biviano,

Gabriella De Lucia, Florence Durret, Stefano Etori, Gary Mamon, Matteo Maturi, Sophie Maurogordato, Lauro Moscardini, Emiliano Munari, Mauro Roncarelli, Alex Saro, Barbara Sartoris, Mauro Sereno, Jochen Weller. Thanks to the *Euclid* France support, I had the privilege to attend the *Euclid* France summer school 2016 and the programming course for *Euclid* members at APC.

I acknowledge the LERMA and GEPI colleagues who allowed me to work in a stimulating environment, Florence Durret and Marta Volonteri for having followed the development of my thesis, and all the support of the École Doctorale 127 and the Paris Observatory, especially of Jacques Le Bourlot and William Thuillot.

It has been a great pleasure sharing everything with my office mates, who also contributed in many ways with practical and psychological support: Begoña Ascaso, Carolina Parroni, Paola di Mauro, Fernando Caro, Edouard Tollet, Gael Noirot, Diego Tuccillo, Vladan Markov.

Besides the great support of by my mentors and colleagues, these results would have not been possible without the love of my big fans: my partner, my sister, my parents, my grandmother. They supported my every choice despite the distance that separates us, and they always believed that I could reach any goal, bringing out the best in me.

BIBLIOGRAPHY

- Abell, G. O. (1958). « The Distribution of Rich Clusters of Galaxies. » In: *ApJS* 3, p. 211. DOI: [10.1086/190036](https://doi.org/10.1086/190036).
- Abell, G. O., H. G. Corwin Jr., and R. P. Olowin (1989). « A catalog of rich clusters of galaxies. » In: *ApJS* 70, pp. 1–138. DOI: [10.1086/191333](https://doi.org/10.1086/191333).
- Albrecht, A. et al. (2006). « Report of the Dark Energy Task Force. » In: *ArXiv Astrophysics e-prints*. eprint: [astro-ph/0609591](https://arxiv.org/abs/astro-ph/0609591).
- Allen, S. W., A. E. Evrard, and A. B. Mantz (2011). « Cosmological Parameters from Observations of Galaxy Clusters. » In: *ARA&A* 49, pp. 409–470. DOI: [10.1146/annurev-astro-081710-102514](https://doi.org/10.1146/annurev-astro-081710-102514). arXiv: [1103.4829](https://arxiv.org/abs/1103.4829) [[astro-ph.CO](https://arxiv.org/abs/astro-ph.CO)].
- Amodeo, S. et al. (2016). « The relation between mass and concentration in X-ray galaxy clusters at high redshift. » In: *A&A* 590, A126, A126. DOI: [10.1051/0004-6361/201527630](https://doi.org/10.1051/0004-6361/201527630). arXiv: [1604.02163](https://arxiv.org/abs/1604.02163).
- Amodeo, S. et al. (2017). « Calibrating the Planck Cluster Mass Scale with Cluster Velocity Dispersions. » In: *ApJ* 844, 101, p. 101. DOI: [10.3847/1538-4357/aa7063](https://doi.org/10.3847/1538-4357/aa7063). arXiv: [1704.07891](https://arxiv.org/abs/1704.07891).
- Amodeo, S. et al. (2018). « Spectroscopic Confirmation and Velocity Dispersions for 20 Planck Galaxy Clusters at $0.16 < z < 0.78$. » In: *ApJ* 853, 36, p. 36. DOI: [10.3847/1538-4357/aa98dd](https://doi.org/10.3847/1538-4357/aa98dd). arXiv: [1711.00021](https://arxiv.org/abs/1711.00021).
- Andreon, S. et al. (2009). « JKCS 041: a colour-detected galaxy cluster at $z_{\text{phot}} \sim 1.9$ with deep potential well as confirmed by X-ray data. » In: *A&A* 507, pp. 147–157. DOI: [10.1051/0004-6361/200912299](https://doi.org/10.1051/0004-6361/200912299). arXiv: [0812.1699](https://arxiv.org/abs/0812.1699).
- Andreon, S. et al. (2014). « JKCS 041: a Coma cluster progenitor at $z = 1.803$. » In: *A&A* 565, A120, A120. DOI: [10.1051/0004-6361/201323077](https://doi.org/10.1051/0004-6361/201323077). arXiv: [1311.4361](https://arxiv.org/abs/1311.4361).
- Arnaud, M., E. Pointecouteau, and G. W. Pratt (2005). « The structural and scaling properties of nearby galaxy clusters. II. The M-T relation. » In: *A&A* 441, pp. 893–903. DOI: [10.1051/0004-6361:20052856](https://doi.org/10.1051/0004-6361:20052856). eprint: [astro-ph/0502210](https://arxiv.org/abs/astro-ph/0502210).
- Arnaud, M. et al. (2010). « The universal galaxy cluster pressure profile from a representative sample of nearby systems (REXCESS) and the $Y_{\text{SZ}} - M_{500}$ relation. » In: *A&A* 517, A92, A92. DOI: [10.1051/0004-6361/200913416](https://doi.org/10.1051/0004-6361/200913416). arXiv: [0910.1234](https://arxiv.org/abs/0910.1234).
- Ascaso, B. et al. (2016). « An accurate cluster selection function for the J-PAS narrow-band wide-field survey. » In: *MNRAS* 456, pp. 4291–4304. DOI: [10.1093/mnras/stv2988](https://doi.org/10.1093/mnras/stv2988). arXiv: [1601.00656](https://arxiv.org/abs/1601.00656).
- Ascaso, B. et al. (2017). « Apples to apples A^2 - II. Cluster selection functions for next-generation surveys. » In: *MNRAS* 464, pp. 2270–2280. DOI: [10.1093/mnras/stw2508](https://doi.org/10.1093/mnras/stw2508). arXiv: [1605.07620](https://arxiv.org/abs/1605.07620).
- Barden, M. et al. (2012). « GALAPAGOS: from pixels to parameters. » In: *MNRAS* 422, pp. 449–468. DOI: [10.1111/j.1365-2966.2012.20619.x](https://doi.org/10.1111/j.1365-2966.2012.20619.x). arXiv: [1203.1831](https://arxiv.org/abs/1203.1831) [[astro-ph.IM](https://arxiv.org/abs/astro-ph.IM)].
- Barrena, R. et al. (2018). « Optical validation and characterization of Planck PSZ1 sources at the Canary Islands observatories. I. First year of ITP13 observations. » In: *ArXiv e-prints*. arXiv: [1803.05764](https://arxiv.org/abs/1803.05764).

- Bartelmann, M. (2010). « TOPICAL REVIEW Gravitational lensing. » In: *Classical and Quantum Gravity* 27.23, 233001, p. 233001. DOI: [10.1088/0264-9381/27/23/233001](https://doi.org/10.1088/0264-9381/27/23/233001). arXiv: [1010.3829](https://arxiv.org/abs/1010.3829).
- Bartelmann, M., L. J. King, and P. Schneider (2001). « Weak-lensing halo numbers and dark-matter profiles. » In: *A&A* 378, pp. 361–369. DOI: [10.1051/0004-6361:20011199](https://doi.org/10.1051/0004-6361:20011199). eprint: [astro-ph/0103465](https://arxiv.org/abs/astro-ph/0103465).
- Battaglia, N. et al. (2015). « Weak-Lensing Mass Calibration of the Atacama Cosmology Telescope Equatorial Sunyaev-Zeldovich Cluster Sample with the Canada-France-Hawaii Telescope Stripe 82 Survey. » In: *ArXiv e-prints*. arXiv: [1509.08930](https://arxiv.org/abs/1509.08930).
- Becker, M. R. and A. V. Kravtsov (2011). « On the Accuracy of Weak-lensing Cluster Mass Reconstructions. » In: *ApJ* 740, 25, p. 25. DOI: [10.1088/0004-637X/740/1/25](https://doi.org/10.1088/0004-637X/740/1/25). arXiv: [1011.1681](https://arxiv.org/abs/1011.1681) [[astro-ph.CO](https://arxiv.org/abs/astro-ph.CO)].
- Beers, T. C., K. Flynn, and K. Gebhardt (1990). « Measures of location and scale for velocities in clusters of galaxies - A robust approach. » In: *AJ* 100, pp. 32–46. DOI: [10.1086/115487](https://doi.org/10.1086/115487).
- Benitez, N. et al. (2014). « J-PAS: The Javalambre-Physics of the Accelerated Universe Astrophysical Survey. » In: *ArXiv e-prints*. arXiv: [1403.5237](https://arxiv.org/abs/1403.5237) [[astro-ph.CO](https://arxiv.org/abs/astro-ph.CO)].
- Benn, C., K. Dee, and T. Agócs (2008). « ACAM: a new imager/spectrograph for the William Herschel Telescope. » In: *Ground-based and Airborne Instrumentation for Astronomy II*. Vol. 7014. Proc. SPIE, p. 70146X. DOI: [10.1117/12.788694](https://doi.org/10.1117/12.788694).
- Bertin, E. (2011). « Automated Morphometry with SExtractor and PSFEx. » In: *Astronomical Data Analysis Software and Systems XX*. Ed. by I. N. Evans et al. Vol. 442. Astronomical Society of the Pacific Conference Series, p. 435.
- Bertin, E. and S. Arnouts (1996). « SExtractor: Software for source extraction. » In: *A&AS* 117, pp. 393–404. DOI: [10.1051/aas:1996164](https://doi.org/10.1051/aas:1996164).
- Bertin, E. et al. (2002). « The TERAPIX Pipeline. » In: *Astronomical Data Analysis Software and Systems XI*. Ed. by D. A. Bohlender, D. Durand, and T. H. Handley. Vol. 281. Astronomical Society of the Pacific Conference Series, p. 228.
- Bhattacharya, S. et al. (2013). « Dark Matter Halo Profiles of Massive Clusters: Theory versus Observations. » In: *ApJ* 766, 32, p. 32. DOI: [10.1088/0004-637X/766/1/32](https://doi.org/10.1088/0004-637X/766/1/32). arXiv: [1112.5479](https://arxiv.org/abs/1112.5479).
- Binney, J. and S. Tremaine (2008). *Galactic Dynamics: Second Edition*. Princeton University Press.
- Birkinshaw, M. (1999). « The Sunyaev-Zel'dovich effect. » In: 310, pp. 97–195. DOI: [10.1016/S0370-1573\(98\)00080-5](https://doi.org/10.1016/S0370-1573(98)00080-5). eprint: [astro-ph/9808050](https://arxiv.org/abs/astro-ph/9808050).
- Blakeslee, J. P. et al. (2006). « Clusters at Half Hubble Time: Galaxy Structure and Colors in RX J0152.7-1357 and MS 1054-03. » In: *ApJ* 644, pp. 30–53. DOI: [10.1086/503539](https://doi.org/10.1086/503539). eprint: [astro-ph/0603058](https://arxiv.org/abs/astro-ph/0603058).
- Bleem, L. E. et al. (2015). « Galaxy Clusters Discovered via the Sunyaev-Zel'dovich Effect in the 2500-Square-Degree SPT-SZ Survey. » In: *ApJS* 216, 27, p. 27. DOI: [10.1088/0067-0049/216/2/27](https://doi.org/10.1088/0067-0049/216/2/27). arXiv: [1409.0850](https://arxiv.org/abs/1409.0850).
- Bocquet, S. et al. (2015). « Mass Calibration and Cosmological Analysis of the SPT-SZ Galaxy Cluster Sample Using Velocity Dispersion σ_v and X-Ray

- Y_X Measurements. » In: *ApJ* 799, 214, p. 214. DOI: [10.1088/0004-637X/799/2/214](https://doi.org/10.1088/0004-637X/799/2/214). arXiv: [1407.2942](https://arxiv.org/abs/1407.2942).
- Böhringer, H. and G. Chon (2016). « Constraints on neutrino masses from the study of the nearby large-scale structure and galaxy cluster counts. » In: *Modern Physics Letters A* 31, 1640008, p. 1640008. DOI: [10.1142/S0217732316400083](https://doi.org/10.1142/S0217732316400083). arXiv: [1610.02855](https://arxiv.org/abs/1610.02855).
- Böhringer, H., G. Chon, and C. A. Collins (2014). « The extended ROSAT-ESO Flux Limited X-ray Galaxy Cluster Survey (REFLEX II). IV. X-ray luminosity function and first constraints on cosmological parameters. » In: *A&A* 570, A31, A31. DOI: [10.1051/0004-6361/201323155](https://doi.org/10.1051/0004-6361/201323155). arXiv: [1403.2927](https://arxiv.org/abs/1403.2927).
- Böhringer, H. et al. (2000). « The Northern ROSAT All-Sky (NORAS) Galaxy Cluster Survey. I. X-Ray Properties of Clusters Detected as Extended X-Ray Sources. » In: *ApJS* 129, pp. 435–474. DOI: [10.1086/313427](https://doi.org/10.1086/313427). eprint: [astro-ph/0003219](https://arxiv.org/abs/astro-ph/0003219).
- Böhringer, H. et al. (2001). « The ROSAT-ESO flux limited X-ray (REFLEX) galaxy cluster survey. I. The construction of the cluster sample. » In: *A&A* 369, pp. 826–850. DOI: [10.1051/0004-6361:20010240](https://doi.org/10.1051/0004-6361:20010240). eprint: [astro-ph/0012266](https://arxiv.org/abs/astro-ph/0012266).
- Borgani, S. (2008). « Cosmology with Clusters of Galaxies. » In: *A Pan-Chromatic View of Clusters of Galaxies and the Large-Scale Structure*. Ed. by M. Plionis, O. López-Cruz, and D. Hughes. Vol. 740. Lecture Notes in Physics, Berlin Springer Verlag, p. 24. DOI: [10.1007/978-1-4020-6941-3_9](https://doi.org/10.1007/978-1-4020-6941-3_9). eprint: [astro-ph/0605575](https://arxiv.org/abs/astro-ph/0605575).
- Borgani, S. et al. (2004). « X-ray properties of galaxy clusters and groups from a cosmological hydrodynamical simulation. » In: *MNRAS* 348, pp. 1078–1096. DOI: [10.1111/j.1365-2966.2004.07431.x](https://doi.org/10.1111/j.1365-2966.2004.07431.x). eprint: [astro-ph/0310794](https://arxiv.org/abs/astro-ph/0310794).
- Bower, R. G., J. R. Lucey, and R. S. Ellis (1992). « Precision photometry of early-type galaxies in the Coma and Virgo clusters: A test of the universality of the colour-magnitude relation. I - The data. II. Analysis. » In: *MNRAS* 254, pp. 589–613. DOI: [10.1093/mnras/254.4.589](https://doi.org/10.1093/mnras/254.4.589).
- Brodwin, M. et al. (2013). « The Era of Star Formation in Galaxy Clusters. » In: *ApJ* 779, 138, p. 138. DOI: [10.1088/0004-637X/779/2/138](https://doi.org/10.1088/0004-637X/779/2/138). arXiv: [1310.6039](https://arxiv.org/abs/1310.6039).
- Bruzual, G. and S. Charlot (2003). « Stellar population synthesis at the resolution of 2003. » In: *MNRAS* 344, pp. 1000–1028. DOI: [10.1046/j.1365-8711.2003.06897.x](https://doi.org/10.1046/j.1365-8711.2003.06897.x). eprint: [astro-ph/0309134](https://arxiv.org/abs/astro-ph/0309134).
- Buote, D. A. et al. (2007). « The X-Ray Concentration-Virial Mass Relation. » In: *ApJ* 664, pp. 123–134. DOI: [10.1086/518684](https://doi.org/10.1086/518684). eprint: [astro-ph/0610135](https://arxiv.org/abs/astro-ph/0610135).
- Caldwell, C. E. et al. (2016). « Cosmology with velocity dispersion counts: an alternative to measuring cluster halo masses. » In: *MNRAS* 462, pp. 4117–4129. DOI: [10.1093/mnras/stw1892](https://doi.org/10.1093/mnras/stw1892). arXiv: [1602.00611](https://arxiv.org/abs/1602.00611).
- Carlstrom, J. E., G. P. Holder, and E. D. Reese (2002). « Cosmology with the Sunyaev-Zel'dovich Effect. » In: *ARA&A* 40, pp. 643–680. DOI: [10.1146/annurev.astro.40.060401.093803](https://doi.org/10.1146/annurev.astro.40.060401.093803). eprint: [astro-ph/0208192](https://arxiv.org/abs/astro-ph/0208192).

- Carlstrom, J. E. et al. (2011). « The 10 Meter South Pole Telescope. » In: *PASP* 123, pp. 568–581. DOI: [10.1086/659879](https://doi.org/10.1086/659879). arXiv: [0907.4445](https://arxiv.org/abs/0907.4445) [astro-ph.IM].
- Carvalho, P. et al. (2012). « PowellSnakes II: a fast Bayesian approach to discrete object detection in multi-frequency astronomical data sets. » In: *MNRAS* 427, pp. 1384–1400. DOI: [10.1111/j.1365-2966.2012.22033.x](https://doi.org/10.1111/j.1365-2966.2012.22033.x). arXiv: [1112.4886](https://arxiv.org/abs/1112.4886).
- Castellano, M. et al. (2007). « A Photometrically Detected Forming Cluster of Galaxies at Redshift 1.6 in the GOODS Field. » In: *ApJ* 671, pp. 1497–1502. DOI: [10.1086/521595](https://doi.org/10.1086/521595). arXiv: [0707.1783](https://arxiv.org/abs/0707.1783).
- Cautun, M. et al. (2014). « Evolution of the cosmic web. » In: *MNRAS* 441, pp. 2923–2973. DOI: [10.1093/mnras/stu768](https://doi.org/10.1093/mnras/stu768). arXiv: [1401.7866](https://arxiv.org/abs/1401.7866).
- Chambers, K. C. et al. (2016). « The Pan-STARRS1 Surveys. » In: *ArXiv e-prints*. arXiv: [1612.05560](https://arxiv.org/abs/1612.05560) [astro-ph.IM].
- Chiang, Y.-K., R. Overzier, and K. Gebhardt (2013). « Ancient Light from Young Cosmic Cities: Physical and Observational Signatures of Galaxy Proto-clusters. » In: *ApJ* 779, 127, p. 127. DOI: [10.1088/0004-637X/779/2/127](https://doi.org/10.1088/0004-637X/779/2/127). arXiv: [1310.2938](https://arxiv.org/abs/1310.2938).
- Clements, D. L. et al. (2014). « Herschel Multitiered Extragalactic Survey: clusters of dusty galaxies uncovered by Herschel and Planck. » In: *MNRAS* 439, pp. 1193–1211. DOI: [10.1093/mnras/stt2253](https://doi.org/10.1093/mnras/stt2253). arXiv: [1311.5758](https://arxiv.org/abs/1311.5758).
- Coles, P. and F. Lucchin (2002). *Cosmology: The Origin and Evolution of Cosmic Structure, Second Edition*, p. 512.
- Cooke, E. A. et al. (2015). « The formation history of massive cluster galaxies as revealed by CARLA. » In: *MNRAS* 452, pp. 2318–2336. DOI: [10.1093/mnras/stv1413](https://doi.org/10.1093/mnras/stv1413). arXiv: [1507.00350](https://arxiv.org/abs/1507.00350).
- Cooke, E. A. et al. (2016). « A Mature Galaxy Cluster at $z=1.58$ around the Radio Galaxy 7C1753+6311. » In: *ApJ* 816, 83, p. 83. DOI: [10.3847/0004-637X/816/2/83](https://doi.org/10.3847/0004-637X/816/2/83). arXiv: [1511.05150](https://arxiv.org/abs/1511.05150).
- Corasaniti, P. S. et al. (2017). « Probing Cosmology with Dark Matter Halo Sparsity Using X-ray Cluster Mass Measurements. » In: *ArXiv e-prints*. arXiv: [1711.00480](https://arxiv.org/abs/1711.00480).
- DES Collaboration et al. (2017). « Dark Energy Survey Year 1 Results: Cosmological Constraints from Galaxy Clustering and Weak Lensing. » In: *ArXiv e-prints*. arXiv: [1708.01530](https://arxiv.org/abs/1708.01530).
- Dahle, H. et al. (2003). « Weak Gravitational Lensing by a Sample of X-Ray-luminous Clusters of Galaxies. III. Serendipitous Weak Lensing Detections of Dark and Luminous Mass Concentrations. » In: *ApJ* 591, pp. 662–676. DOI: [10.1086/375485](https://doi.org/10.1086/375485). eprint: [astro-ph/0208050](https://arxiv.org/abs/astro-ph/0208050).
- Davis, M. and P. J. E. Peebles (1983). « A survey of galaxy redshifts. V - The two-point position and velocity correlations. » In: *ApJ* 267, pp. 465–482. DOI: [10.1086/160884](https://doi.org/10.1086/160884).
- De Boni, C. et al. (2013). « Hydrodynamical simulations of galaxy clusters in dark energy cosmologies - II. c-M relation. » In: *MNRAS* 428, pp. 2921–2938. DOI: [10.1093/mnras/sts235](https://doi.org/10.1093/mnras/sts235). arXiv: [1205.3163](https://arxiv.org/abs/1205.3163).
- De Santis, C. et al. (2007). « ConvPhot: A profile-matching algorithm for precision photometry. » In: 12, pp. 271–288. DOI: [10.1016/j.newast.2006.10.004](https://doi.org/10.1016/j.newast.2006.10.004). eprint: [astro-ph/0701232](https://arxiv.org/abs/astro-ph/0701232).
- Despali, G. et al. (2016). « The universality of the virial halo mass function and models for non-universality of other halo definitions. » In: *MNRAS*

- 456, pp. 2486–2504. DOI: [10.1093/mnras/stv2842](https://doi.org/10.1093/mnras/stv2842). arXiv: [1507.05627](https://arxiv.org/abs/1507.05627).
- Diemer, B. and A. V. Kravtsov (2015a). « A Universal Model for Halo Concentrations. » In: *ApJ* 799, 108, p. 108. DOI: [10.1088/0004-637X/799/1/108](https://doi.org/10.1088/0004-637X/799/1/108). arXiv: [1407.4730](https://arxiv.org/abs/1407.4730).
- Diemer, B. and A. V. Kravtsov (2015b). « A Universal Model for Halo Concentrations. » In: *ApJ* 799, 108, p. 108. DOI: [10.1088/0004-637X/799/1/108](https://doi.org/10.1088/0004-637X/799/1/108). arXiv: [1407.4730](https://arxiv.org/abs/1407.4730).
- Dolag, K. et al. (2004). « Numerical study of halo concentrations in dark-energy cosmologies. » In: *A&A* 416, pp. 853–864. DOI: [10.1051/0004-6361:20031757](https://doi.org/10.1051/0004-6361:20031757). eprint: [astro-ph/0309771](https://arxiv.org/abs/astro-ph/0309771).
- Dressler, A. (1980). « Galaxy morphology in rich clusters - Implications for the formation and evolution of galaxies. » In: *ApJ* 236, pp. 351–365. DOI: [10.1086/157753](https://doi.org/10.1086/157753).
- Dressler, A. and S. A. Shectman (1988). « Evidence for substructure in rich clusters of galaxies from radial-velocity measurements. » In: *AJ* 95, pp. 985–995. DOI: [10.1086/114694](https://doi.org/10.1086/114694).
- Duffy, A. R. et al. (2008). « Dark matter halo concentrations in the Wilkinson Microwave Anisotropy Probe year 5 cosmology. » In: *MNRAS* 390, pp. L64–L68. DOI: [10.1111/j.1745-3933.2008.00537.x](https://doi.org/10.1111/j.1745-3933.2008.00537.x). arXiv: [0804.2486](https://arxiv.org/abs/0804.2486).
- Dutton, A. A. and A. V. Macciò (2014). « Cold dark matter haloes in the Planck era: evolution of structural parameters for Einasto and NFW profiles. » In: *MNRAS* 441, pp. 3359–3374. DOI: [10.1093/mnras/stu742](https://doi.org/10.1093/mnras/stu742). arXiv: [1402.7073](https://arxiv.org/abs/1402.7073).
- Ebeling, H., A. C. Edge, and J. P. Henry (2001). « MACS: A Quest for the Most Massive Galaxy Clusters in the Universe. » In: *ApJ* 553, pp. 668–676. DOI: [10.1086/320958](https://doi.org/10.1086/320958). eprint: [astro-ph/0009101](https://arxiv.org/abs/astro-ph/0009101).
- Ebeling, H. et al. (1998). « The ROSAT Brightest Cluster Sample - I. The compilation of the sample and the cluster log N-log S distribution. » In: *MNRAS* 301, pp. 881–914. DOI: [10.1046/j.1365-8711.1998.01949.x](https://doi.org/10.1046/j.1365-8711.1998.01949.x). eprint: [astro-ph/9812394](https://arxiv.org/abs/astro-ph/9812394).
- Eisenhardt, P. R. M. et al. (2008). « Clusters of Galaxies in the First Half of the Universe from the IRAC Shallow Survey. » In: *ApJ* 684, 905–932, pp. 905–932. DOI: [10.1086/590105](https://doi.org/10.1086/590105). arXiv: [0804.4798](https://arxiv.org/abs/0804.4798).
- Elbaz, D. et al. (2007). « The reversal of the star formation-density relation in the distant universe. » In: *A&A* 468, pp. 33–48. DOI: [10.1051/0004-6361:20077525](https://doi.org/10.1051/0004-6361:20077525). eprint: [astro-ph/0703653](https://arxiv.org/abs/astro-ph/0703653).
- Erben, T. et al. (2005). « GaBoDS: The Garching-Bonn Deep Survey. IV. Methods for the image reduction of multi-chip cameras demonstrated on data from the ESO Wide-Field Imager. » In: *Astronomische Nachrichten* 326, pp. 432–464. DOI: [10.1002/asna.200510396](https://doi.org/10.1002/asna.200510396). eprint: [astro-ph/0501144](https://arxiv.org/abs/astro-ph/0501144).
- Ettori, S. et al. (2010). « Mass profiles and $c-M_{\text{DM}}$ relation in X-ray luminous galaxy clusters. » In: *A&A* 524, A68, A68. DOI: [10.1051/0004-6361/201015271](https://doi.org/10.1051/0004-6361/201015271).
- Ettori, S. et al. (2013). « Mass Profiles of Galaxy Clusters from X-ray Analysis. » In: *Space Sci. Rev.* 177, pp. 119–154. DOI: [10.1007/s11214-013-9976-7](https://doi.org/10.1007/s11214-013-9976-7). arXiv: [1303.3530](https://arxiv.org/abs/1303.3530).

- Ettori, S. et al. (2018). « Hydrostatic mass profiles in X-COP galaxy clusters. » In: *ArXiv e-prints*. arXiv: [1805.00035](https://arxiv.org/abs/1805.00035).
- Evrard, A. E. et al. (2008a). « Virial Scaling of Massive Dark Matter Halos: Why Clusters Prefer a High Normalization Cosmology. » In: *ApJ* 672, 122-137, pp. 122–137. DOI: [10.1086/521616](https://doi.org/10.1086/521616). eprint: [astro-ph/0702241](https://arxiv.org/abs/astro-ph/0702241).
- Evrard, A. E. et al. (2008b). « Virial Scaling of Massive Dark Matter Halos: Why Clusters Prefer a High Normalization Cosmology. » In: *ApJ* 672, 122-137, pp. 122–137. DOI: [10.1086/521616](https://doi.org/10.1086/521616). eprint: [astro-ph/0702241](https://arxiv.org/abs/astro-ph/0702241).
- Evrard, A. E. et al. (2014). « A model for multiproperty galaxy cluster statistics. » In: *MNRAS* 441, pp. 3562–3569. DOI: [10.1093/mnras/stu784](https://doi.org/10.1093/mnras/stu784). arXiv: [1403.1456](https://arxiv.org/abs/1403.1456).
- Farahi, A. et al. (2016). « Galaxy cluster mass estimation from stacked spectroscopic analysis. » In: *MNRAS* 460, pp. 3900–3912. DOI: [10.1093/mnras/stw1143](https://doi.org/10.1093/mnras/stw1143). arXiv: [1601.05773](https://arxiv.org/abs/1601.05773).
- Fasano, G. and A. Franceschini (1987). « A multidimensional version of the Kolmogorov-Smirnov test. » In: *MNRAS* 225, pp. 155–170. DOI: [10.1093/mnras/225.1.155](https://doi.org/10.1093/mnras/225.1.155).
- Fassbender, R. et al. (2011). « The X-ray luminous galaxy cluster XMMU J1007.4+1237 at $z = 1.56$. The dawn of starburst activity in cluster cores. » In: *A&A* 527, L10, p. L10. DOI: [10.1051/0004-6361/201016169](https://doi.org/10.1051/0004-6361/201016169). arXiv: [1101.3313](https://arxiv.org/abs/1101.3313).
- Fazio, G. G. et al. (2004). « The Infrared Array Camera (IRAC) for the Spitzer Space Telescope. » In: *ApJS* 154, pp. 10–17. DOI: [10.1086/422843](https://doi.org/10.1086/422843). eprint: [astro-ph/0405616](https://arxiv.org/abs/astro-ph/0405616).
- Ferrarese, L. et al. (2012). « The Next Generation Virgo Cluster Survey (NGVS). I. Introduction to the Survey. » In: *ApJS* 200, 4, p. 4. DOI: [10.1088/0067-0049/200/1/4](https://doi.org/10.1088/0067-0049/200/1/4).
- Freeman, K. C. (1970). « On the Disks of Spiral and S0 Galaxies. » In: *ApJ* 160, p. 811. DOI: [10.1086/150474](https://doi.org/10.1086/150474).
- Galametz, A. et al. (2012). « The Mid-infrared Environments of High-redshift Radio Galaxies. » In: *ApJ* 749, 169, p. 169. DOI: [10.1088/0004-637X/749/2/169](https://doi.org/10.1088/0004-637X/749/2/169). arXiv: [1202.4489](https://arxiv.org/abs/1202.4489).
- Galametz, A. et al. (2013). « CANDELS Multiwavelength Catalogs: Source Identification and Photometry in the CANDELS UKIDSS Ultra-deep Survey Field. » In: *ApJS* 206, 10, p. 10. DOI: [10.1088/0067-0049/206/2/10](https://doi.org/10.1088/0067-0049/206/2/10). arXiv: [1305.1823](https://arxiv.org/abs/1305.1823) [[astro-ph.CO](https://arxiv.org/abs/astro-ph.CO)].
- Geller, M. J. and T. C. Beers (1982). « Substructure within clusters of galaxies. » In: *PASP* 94, pp. 421–439. DOI: [10.1086/131003](https://doi.org/10.1086/131003).
- Ghirardini, V. et al. (2017). « On the evolution of the entropy and pressure profiles in X-ray luminous galaxy clusters at $z \sim 0.4$. » In: *A&A* 604, A100, A100. DOI: [10.1051/0004-6361/201630209](https://doi.org/10.1051/0004-6361/201630209). arXiv: [1704.01587](https://arxiv.org/abs/1704.01587).
- Giacconi, R. et al. (1972). « The Uhuru catalog of X-ray sources. » In: *ApJ* 178, pp. 281–308. DOI: [10.1086/151790](https://doi.org/10.1086/151790).
- Giavalisco, M. et al. (2004). « The Great Observatories Origins Deep Survey: Initial Results from Optical and Near-Infrared Imaging. » In: *ApJ* 600, pp. L93–L98. DOI: [10.1086/379232](https://doi.org/10.1086/379232). eprint: [astro-ph/0309105](https://arxiv.org/abs/astro-ph/0309105).
- Gioia, I. M. et al. (1990). « The Einstein Observatory Extended Medium-Sensitivity Survey. I - X-ray data and analysis. » In: *ApJS* 72, pp. 567–619. DOI: [10.1086/191426](https://doi.org/10.1086/191426).

- Girardi, M. et al. (1993). « Velocity dispersions in galaxy clusters. » In: *ApJ* 404, pp. 38–50. DOI: [10.1086/172256](https://doi.org/10.1086/172256).
- Girardi, M. et al. (2005). « Internal dynamics of the $z \sim 0.8$ cluster RX J0152.7-1357. » In: *A&A* 442, pp. 29–41. DOI: [10.1051/0004-6361:20053232](https://doi.org/10.1051/0004-6361:20053232). eprint: [astro-ph/0506211](https://arxiv.org/abs/astro-ph/0506211).
- Gladders, M. D. and H. K. C. Yee (2000). « A New Method For Galaxy Cluster Detection. I. The Algorithm. » In: *AJ* 120, pp. 2148–2162. DOI: [10.1086/301557](https://doi.org/10.1086/301557). eprint: [astro-ph/0004092](https://arxiv.org/abs/astro-ph/0004092).
- Gobat, R. et al. (2011). « A mature cluster with X-ray emission at $z = 2.07$. » In: *A&A* 526, A133, A133. DOI: [10.1051/0004-6361/201016084](https://doi.org/10.1051/0004-6361/201016084). arXiv: [1011.1837](https://arxiv.org/abs/1011.1837).
- Gobat, R. et al. (2013). « WFC3 GRISM Confirmation of the Distant Cluster Cl J1449+0856 at $z = 2.00$: Quiescent and Star-forming Galaxy Populations. » In: *ApJ* 776, 9, p. 9. DOI: [10.1088/0004-637X/776/1/9](https://doi.org/10.1088/0004-637X/776/1/9). arXiv: [1305.3576](https://arxiv.org/abs/1305.3576).
- Gott III, J. R. and M. J. Rees (1975). « A theory of galaxy formation and clustering. » In: *A&A* 45, pp. 365–376.
- Grogin, N. A. et al. (2011). « CANDELS: The Cosmic Assembly Near-infrared Deep Extragalactic Legacy Survey. » In: *ApJS* 197, 35, p. 35. DOI: [10.1088/0067-0049/197/2/35](https://doi.org/10.1088/0067-0049/197/2/35). arXiv: [1105.3753](https://arxiv.org/abs/1105.3753).
- Gunn, J. E. and J. R. Gott III (1972). « On the Infall of Matter Into Clusters of Galaxies and Some Effects on Their Evolution. » In: *ApJ* 176, p. 1. DOI: [10.1086/151605](https://doi.org/10.1086/151605).
- Guo, H. et al. (2015). « Redshift-space clustering of SDSS galaxies - luminosity dependence, halo occupation distribution, and velocity bias. » In: *MNRAS* 453, pp. 4368–4383. DOI: [10.1093/mnras/stv1966](https://doi.org/10.1093/mnras/stv1966). arXiv: [1505.07861](https://arxiv.org/abs/1505.07861).
- Guo, Y. et al. (2013). « CANDELS Multi-wavelength Catalogs: Source Detection and Photometry in the GOODS-South Field. » In: *ApJS* 207, 24, p. 24. DOI: [10.1088/0067-0049/207/2/24](https://doi.org/10.1088/0067-0049/207/2/24). arXiv: [1308.4405](https://arxiv.org/abs/1308.4405).
- Gwyn, S. D. J. (2012). « The Canada-France-Hawaii Telescope Legacy Survey: Stacked Images and Catalogs. » In: *AJ* 143, 38, p. 38. DOI: [10.1088/0004-6256/143/2/38](https://doi.org/10.1088/0004-6256/143/2/38). arXiv: [1101.1084](https://arxiv.org/abs/1101.1084).
- Hartley, W. G. et al. (2008). « Nature versus nurture: the curved spine of the galaxy cluster X-ray luminosity-temperature relation. » In: *MNRAS* 386, pp. 2015–2021. DOI: [10.1111/j.1365-2966.2008.13127.x](https://doi.org/10.1111/j.1365-2966.2008.13127.x). arXiv: [0710.3698](https://arxiv.org/abs/0710.3698).
- Hartley, W. G. et al. (2013). « Studying the emergence of the red sequence through galaxy clustering: host halo masses at $z \sim 2$. » In: *MNRAS* 431, pp. 3045–3059. DOI: [10.1093/mnras/stt383](https://doi.org/10.1093/mnras/stt383). arXiv: [1303.0816](https://arxiv.org/abs/1303.0816).
- Hasselfield, M. et al. (2013). « The Atacama Cosmology Telescope: Sunyaev-Zel'dovich selected galaxy clusters at 148 GHz from three seasons of data. » In: 7, 008, p. 008. DOI: [10.1088/1475-7516/2013/07/008](https://doi.org/10.1088/1475-7516/2013/07/008). arXiv: [1301.0816](https://arxiv.org/abs/1301.0816) [[astro-ph.CO](https://arxiv.org/abs/astro-ph)].
- Hayashi, M. et al. (2011). « Properties of star-forming galaxies in a cluster and its surrounding structure at $z=1.46$. » In: *MNRAS* 415, pp. 2670–2687. DOI: [10.1111/j.1365-2966.2011.18892.x](https://doi.org/10.1111/j.1365-2966.2011.18892.x). arXiv: [1104.2121](https://arxiv.org/abs/1104.2121).
- Henry, J. P. et al. (2001). « Overview of the ROSAT North Ecliptic Pole Survey. » In: *ApJ* 553, pp. L109–L113. DOI: [10.1086/320672](https://doi.org/10.1086/320672).

- Herranz, D. et al. (2002). « Filtering techniques for the detection of Sunyaev-Zel'dovich clusters in multifrequency maps. » In: *MNRAS* 336, pp. 1057–1068. DOI: [10.1046/j.1365-8711.2002.05704.x](https://doi.org/10.1046/j.1365-8711.2002.05704.x). eprint: [astro-ph/0203486](https://arxiv.org/abs/astro-ph/0203486).
- Hinshaw, G. et al. (2013). « Nine-year Wilkinson Microwave Anisotropy Probe (WMAP) Observations: Cosmological Parameter Results. » In: *ApJS* 208, 19, p. 19. DOI: [10.1088/0067-0049/208/2/19](https://doi.org/10.1088/0067-0049/208/2/19). arXiv: [1212.5226](https://arxiv.org/abs/1212.5226).
- Hoekstra, H. et al. (2013). « Masses of Galaxy Clusters from Gravitational Lensing. » In: *Space Sci. Rev.* 177, pp. 75–118. DOI: [10.1007/s11214-013-9978-5](https://doi.org/10.1007/s11214-013-9978-5). arXiv: [1303.3274](https://arxiv.org/abs/1303.3274).
- Hoekstra, H. et al. (2015a). « The Canadian Cluster Comparison Project: detailed study of systematics and updated weak lensing masses. » In: *MNRAS* 449, pp. 685–714. DOI: [10.1093/mnras/stv275](https://doi.org/10.1093/mnras/stv275). arXiv: [1502.01883](https://arxiv.org/abs/1502.01883).
- Hoekstra, H. et al. (2015b). « The Canadian Cluster Comparison Project: detailed study of systematics and updated weak lensing masses. » In: *MNRAS* 449, pp. 685–714. DOI: [10.1093/mnras/stv275](https://doi.org/10.1093/mnras/stv275). arXiv: [1502.01883](https://arxiv.org/abs/1502.01883).
- Hook, I. M. et al. (2004). « The Gemini-North Multi-Object Spectrograph: Performance in Imaging, Long-Slit, and Multi-Object Spectroscopic Modes. » In: *PASP* 116, pp. 425–440. DOI: [10.1086/383624](https://doi.org/10.1086/383624).
- Hubble, E. (1929). « A Relation between Distance and Radial Velocity among Extra-Galactic Nebulae. » In: *Proceedings of the National Academy of Science* 15, pp. 168–173. DOI: [10.1073/pnas.15.3.168](https://doi.org/10.1073/pnas.15.3.168).
- Jeans, J. H. (1902). « The Stability of a Spherical Nebula. » In: *Philosophical Transactions of the Royal Society of London Series A* 199, pp. 1–53. DOI: [10.1098/rsta.1902.0012](https://doi.org/10.1098/rsta.1902.0012).
- John, T. L. (1988). « Continuous absorption by the negative hydrogen ion reconsidered. » In: *A&A* 193, pp. 189–192.
- Kaiser, N. (1986). « Evolution and clustering of rich clusters. » In: *MNRAS* 222, pp. 323–345. DOI: [10.1093/mnras/222.2.323](https://doi.org/10.1093/mnras/222.2.323).
- Kaiser, N., G. Squires, and T. Broadhurst (1995). « A Method for Weak Lensing Observations. » In: *ApJ* 449, p. 460. DOI: [10.1086/176071](https://doi.org/10.1086/176071). eprint: [astro-ph/9411005](https://arxiv.org/abs/astro-ph/9411005).
- Kay, S. T. et al. (2012). « Sunyaev-Zel'dovich clusters in Millennium gas simulations. » In: *MNRAS* 422, pp. 1999–2023. DOI: [10.1111/j.1365-2966.2012.20623.x](https://doi.org/10.1111/j.1365-2966.2012.20623.x). arXiv: [1112.3769](https://arxiv.org/abs/1112.3769).
- Kneib, J.-P. and P. Natarajan (2011). « Cluster lenses. » In: *A&A Rev.* 19, 47, p. 47. DOI: [10.1007/s00159-011-0047-3](https://doi.org/10.1007/s00159-011-0047-3). arXiv: [1202.0185](https://arxiv.org/abs/1202.0185) [[astro-ph.CO](https://arxiv.org/abs/astro-ph.CO)].
- Koekemoer, A. M. et al. (2011). « CANDELS: The Cosmic Assembly Near-infrared Deep Extragalactic Legacy Survey The Hubble Space Telescope Observations, Imaging Data Products, and Mosaics. » In: *ApJS* 197, 36, p. 36. DOI: [10.1088/0067-0049/197/2/36](https://doi.org/10.1088/0067-0049/197/2/36). arXiv: [1105.3754](https://arxiv.org/abs/1105.3754).
- Kratochvil, J. M., Z. Haiman, and M. May (2010). « Probing cosmology with weak lensing peak counts. » In: *Phys. Rev. D* 81.4, 043519, p. 043519. DOI: [10.1103/PhysRevD.81.043519](https://doi.org/10.1103/PhysRevD.81.043519). arXiv: [0907.0486](https://arxiv.org/abs/0907.0486) [[astro-ph.CO](https://arxiv.org/abs/astro-ph.CO)].
- Kravtsov, A. V. and S. Borgani (2012). « Formation of Galaxy Clusters. » In: *ARA&A* 50, pp. 353–409. DOI: [10.1146/annurev-astro-081811-125502](https://doi.org/10.1146/annurev-astro-081811-125502). arXiv: [1205.5556](https://arxiv.org/abs/1205.5556).

- Kravtsov, A. V., A. Vikhlinin, and D. Nagai (2006). « A New Robust Low-Scatter X-Ray Mass Indicator for Clusters of Galaxies. » In: *ApJ* 650, pp. 128–136. DOI: [10.1086/506319](https://doi.org/10.1086/506319). eprint: [astro-ph/0603205](https://arxiv.org/abs/astro-ph/0603205).
- Kron, R. G. (1980). « Photometry of a complete sample of faint galaxies. » In: *ApJS* 43, pp. 305–325. DOI: [10.1086/190669](https://doi.org/10.1086/190669).
- Kümmel, M. et al. (2009). « The Slitless Spectroscopy Data Extraction Software aXe. » In: *PASP* 121, p. 59. DOI: [10.1086/596715](https://doi.org/10.1086/596715). arXiv: [0812.1434](https://arxiv.org/abs/0812.1434).
- Kurk, J. et al. (2009). « GMASS ultradeep spectroscopy of galaxies at $z \sim 2$. V. Witnessing the assembly at $z = 1.6$ of a galaxy cluster. » In: *A&A* 504, pp. 331–346. DOI: [10.1051/0004-6361/200809964](https://doi.org/10.1051/0004-6361/200809964). arXiv: [0906.4489](https://arxiv.org/abs/0906.4489).
- LSST Science Collaboration et al. (2009). « LSST Science Book, Version 2.0. » In: *ArXiv e-prints*. arXiv: [0912.0201](https://arxiv.org/abs/0912.0201) [[astro-ph](https://arxiv.org/abs/astro-ph).IM].
- Labbé, I. et al. (2005). « IRAC Mid-Infrared Imaging of the Hubble Deep Field-South: Star Formation Histories and Stellar Masses of Red Galaxies at z_2 . » In: *ApJ* 624, pp. L81–L84. DOI: [10.1086/430700](https://doi.org/10.1086/430700). eprint: [astro-ph/0504219](https://arxiv.org/abs/astro-ph/0504219).
- Laidler, V. G. et al. (2007). « TFIT: A Photometry Package Using Prior Information for Mixed-Resolution Data Sets. » In: *PASP* 119, pp. 1325–1344. DOI: [10.1086/523898](https://doi.org/10.1086/523898).
- Lau, E. T., A. V. Kravtsov, and D. Nagai (2009). « Residual Gas Motions in the Intracluster Medium and Bias in Hydrostatic Measurements of Mass Profiles of Clusters. » In: *ApJ* 705, pp. 1129–1138. DOI: [10.1088/0004-637X/705/2/1129](https://doi.org/10.1088/0004-637X/705/2/1129). arXiv: [0903.4895](https://arxiv.org/abs/0903.4895) [[astro-ph](https://arxiv.org/abs/astro-ph).CO].
- Lau, E. T., D. Nagai, and A. V. Kravtsov (2010). « Effects of Baryon Dissipation on the Dark Matter Virial Scaling Relation. » In: *ApJ* 708, pp. 1419–1425. DOI: [10.1088/0004-637X/708/2/1419](https://doi.org/10.1088/0004-637X/708/2/1419). arXiv: [0908.2133](https://arxiv.org/abs/0908.2133).
- Laureijs, R. et al. (2011). « Euclid Definition Study Report. » In: *ArXiv e-prints*. arXiv: [1110.3193](https://arxiv.org/abs/1110.3193) [[astro-ph](https://arxiv.org/abs/astro-ph).CO].
- Lawrence, A. et al. (2007). « The UKIRT Infrared Deep Sky Survey (UKIDSS). » In: *MNRAS* 379, pp. 1599–1617. DOI: [10.1111/j.1365-2966.2007.12040.x](https://doi.org/10.1111/j.1365-2966.2007.12040.x). eprint: [astro-ph/0604426](https://arxiv.org/abs/astro-ph/0604426).
- Lewis, A. and A. Challinor (2006). « Weak gravitational lensing of the CMB. » In: 429, pp. 1–65. DOI: [10.1016/j.physrep.2006.03.002](https://doi.org/10.1016/j.physrep.2006.03.002). eprint: [astro-ph/0601594](https://arxiv.org/abs/astro-ph/0601594).
- Licitra, R. et al. (2016a). « The Next Generation Virgo Cluster Survey. XX. RedGOLD Background Galaxy Cluster Detections. » In: *ApJ* 829, 44, p. 44. DOI: [10.3847/0004-637X/829/1/44](https://doi.org/10.3847/0004-637X/829/1/44).
- Licitra, R. et al. (2016b). « The RedGOLD cluster detection algorithm and its cluster candidate catalogue for the CFHT-LS W1. » In: *MNRAS* 455, pp. 3020–3041. DOI: [10.1093/mnras/stv2309](https://doi.org/10.1093/mnras/stv2309).
- Lintott, C. J. et al. (2008). « Galaxy Zoo: morphologies derived from visual inspection of galaxies from the Sloan Digital Sky Survey. » In: *MNRAS* 389, pp. 1179–1189. DOI: [10.1111/j.1365-2966.2008.13689.x](https://doi.org/10.1111/j.1365-2966.2008.13689.x). arXiv: [0804.4483](https://arxiv.org/abs/0804.4483).
- Lonsdale, C. J. et al. (2003). « SWIRE: The SIRTf Wide-Area Infrared Extragalactic Survey. » In: *PASP* 115, pp. 897–927. DOI: [10.1086/376850](https://doi.org/10.1086/376850). eprint: [astro-ph/0305375](https://arxiv.org/abs/astro-ph/0305375).
- Macciò, A. V., A. A. Dutton, and F. C. van den Bosch (2008). « Concentration, spin and shape of dark matter haloes as a function of the cosmolog-

- ical model: WMAP1, WMAP3 and WMAP5 results. » In: *MNRAS* 391, pp. 1940–1954. DOI: [10.1111/j.1365-2966.2008.14029.x](https://doi.org/10.1111/j.1365-2966.2008.14029.x). arXiv: [0805.1926](https://arxiv.org/abs/0805.1926).
- Makovoz, D. and I. Khan (2005). « Mosaicking with MOPEX. » In: *Astronomical Data Analysis Software and Systems XIV*. Ed. by P. Shopbell, M. Britton, and R. Ebert. Vol. 347. Astronomical Society of the Pacific Conference Series, p. 81.
- Mantz, A. B. et al. (2015). « Weighing the giants - IV. Cosmology and neutrino mass. » In: *MNRAS* 446, pp. 2205–2225. DOI: [10.1093/mnras/stu2096](https://doi.org/10.1093/mnras/stu2096).
- Markwardt, C. B. (2009). « Non-linear Least-squares Fitting in IDL with MPFIT. » In: *Astronomical Data Analysis Software and Systems XVIII*. Ed. by D. A. Bohlender, D. Durand, and P. Dowler. Vol. 411. Astronomical Society of the Pacific Conference Series, p. 251. arXiv: [0902.2850](https://arxiv.org/abs/0902.2850) [[astro-ph.IM](https://arxiv.org/abs/0902.2850)].
- Marriage, T. A. et al. (2011). « The Atacama Cosmology Telescope: Sunyaev-Zel'dovich-Selected Galaxy Clusters at 148 GHz in the 2008 Survey. » In: *ApJ* 737, 61, p. 61. DOI: [10.1088/0004-637X/737/2/61](https://doi.org/10.1088/0004-637X/737/2/61). arXiv: [1010.1065](https://arxiv.org/abs/1010.1065).
- Martino, R. et al. (2014). « LoCuSS: hydrostatic mass measurements of the high- L_X cluster sample - cross-calibration of Chandra and XMM-Newton. » In: *MNRAS* 443, pp. 2342–2360. DOI: [10.1093/mnras/stu1267](https://doi.org/10.1093/mnras/stu1267). arXiv: [1406.6831](https://arxiv.org/abs/1406.6831).
- Massey, P. and C. Gronwall (1990). « The Kitt Peak spectrophotometric standards - Extension to 1 micron. » In: *ApJ* 358, pp. 344–349. DOI: [10.1086/168991](https://doi.org/10.1086/168991).
- Mather, J. C. et al. (1994). « Measurement of the cosmic microwave background spectrum by the COBE FIRAS instrument. » In: *ApJ* 420, pp. 439–444. DOI: [10.1086/173574](https://doi.org/10.1086/173574).
- Mazzotta, P. et al. (2004). « Comparing the temperatures of galaxy clusters from hydrodynamical N-body simulations to Chandra and XMM-Newton observations. » In: *MNRAS* 354, pp. 10–24. DOI: [10.1111/j.1365-2966.2004.08167.x](https://doi.org/10.1111/j.1365-2966.2004.08167.x). eprint: [astro-ph/0404425](https://arxiv.org/abs/astro-ph/0404425).
- Mei, S. et al. (2009). « Evolution of the Color-Magnitude Relation in Galaxy Clusters at $z \sim 1$ from the ACS Intermediate Redshift Cluster Survey. » In: *ApJ* 690, pp. 42–68. DOI: [10.1088/0004-637X/690/1/42](https://doi.org/10.1088/0004-637X/690/1/42). arXiv: [0810.1917](https://arxiv.org/abs/0810.1917).
- Mei, S. et al. (2015). « Star-forming Blue ETGs in Two Newly Discovered Galaxy Overdensities in the HUDF at $z=1.84$ and 1.9 : Unveiling the Progenitors of Passive ETGs in Cluster Cores. » In: *ApJ* 804, 117, p. 117. DOI: [10.1088/0004-637X/804/2/117](https://doi.org/10.1088/0004-637X/804/2/117). arXiv: [1403.7524](https://arxiv.org/abs/1403.7524).
- Melin, J.-B. and J. G. Bartlett (2015). « Measuring cluster masses with CMB lensing: a statistical approach. » In: *A&A* 578, A21, A21. DOI: [10.1051/0004-6361/201424720](https://doi.org/10.1051/0004-6361/201424720). arXiv: [1408.5633](https://arxiv.org/abs/1408.5633).
- Melin, J.-B., J. G. Bartlett, and J. Delabrouille (2006a). « Catalog extraction in SZ cluster surveys: a matched filter approach. » In: *A&A* 459, pp. 341–352. DOI: [10.1051/0004-6361:20065034](https://doi.org/10.1051/0004-6361:20065034). eprint: [astro-ph/0602424](https://arxiv.org/abs/astro-ph/0602424).
- Melin, J.-B., J. G. Bartlett, and J. Delabrouille (2006b). « Catalog extraction in SZ cluster surveys: a matched filter approach. » In: *A&A* 459, pp. 341–

352. DOI: [10.1051/0004-6361:20065034](https://doi.org/10.1051/0004-6361:20065034). eprint: [astro-ph/0602424](https://arxiv.org/abs/astro-ph/0602424).
- Melin, J.-B., J. G. Bartlett, and J. Delabrouille (2006c). « Catalog extraction in SZ cluster surveys: a matched filter approach. » In: *A&A* 459, pp. 341–352. DOI: [10.1051/0004-6361:20065034](https://doi.org/10.1051/0004-6361:20065034). eprint: [astro-ph/0602424](https://arxiv.org/abs/astro-ph/0602424).
- Meneghetti, M. et al. (2010). « Weighing simulated galaxy clusters using lensing and X-ray. » In: *A&A* 514, A93, A93. DOI: [10.1051/0004-6361/200913222](https://doi.org/10.1051/0004-6361/200913222). arXiv: [0912.1343](https://arxiv.org/abs/0912.1343).
- Merlin, E. et al. (2015). « T-PHOT: A new code for PSF-matched, prior-based, multiwavelength extragalactic deconvolution photometry. » In: *A&A* 582, A15, A15. DOI: [10.1051/0004-6361/201526471](https://doi.org/10.1051/0004-6361/201526471). arXiv: [1505.02516](https://arxiv.org/abs/1505.02516) [[astro-ph](https://arxiv.org/abs/astro-ph).IM].
- Merlin, E. et al. (2016). « T-PHOT version 2.0: Improved algorithms for background subtraction, local convolution, kernel registration, and new options. » In: *A&A* 595, A97, A97. DOI: [10.1051/0004-6361/201628751](https://doi.org/10.1051/0004-6361/201628751). arXiv: [1609.00146](https://arxiv.org/abs/1609.00146) [[astro-ph](https://arxiv.org/abs/astro-ph).IM].
- Merloni, A. et al. (2012). « eROSITA Science Book: Mapping the Structure of the Energetic Universe. » In: *ArXiv e-prints*. arXiv: [1209.3114](https://arxiv.org/abs/1209.3114) [[astro-ph](https://arxiv.org/abs/astro-ph).HE].
- Merten, J. et al. (2015). « CLASH: The Concentration-Mass Relation of Galaxy Clusters. » In: *ApJ* 806, 4, p. 4. DOI: [10.1088/0004-637X/806/1/4](https://doi.org/10.1088/0004-637X/806/1/4). arXiv: [1404.1376](https://arxiv.org/abs/1404.1376).
- Minkowski, R. and G. O. Abell (1963). « The Galactic Distribution of Planetary Nebulae. » In: *PASP* 75, p. 488. DOI: [10.1086/128012](https://doi.org/10.1086/128012).
- Mohr, J. J. et al. (1995). « Cosmological Constraints from Observed Cluster X-Ray Morphologies. » In: *ApJ* 447, p. 8. DOI: [10.1086/175852](https://doi.org/10.1086/175852). eprint: [astro-ph/9501011](https://arxiv.org/abs/astro-ph/9501011).
- Mroczkowski, T. et al. (2015). « Resolving the Merging Planck Cluster PLCK G147.3-16.6 with GISMO. » In: *ApJ* 808, L6, p. L6. DOI: [10.1088/2041-8205/808/1/L6](https://doi.org/10.1088/2041-8205/808/1/L6). arXiv: [1501.05051](https://arxiv.org/abs/1501.05051).
- Mulchaey, J. S., A. Dressler, and A. Oemler (2004). « Clusters of Galaxies: Probes of Cosmological Structure and Galaxy Evolution. » In: *Clusters of Galaxies: Probes of Cosmological Structure and Galaxy Evolution*.
- Munari, E. et al. (2013). « The relation between velocity dispersion and mass in simulated clusters of galaxies: dependence on the tracer and the baryonic physics. » In: *MNRAS* 430, pp. 2638–2649. DOI: [10.1093/mnras/stt049](https://doi.org/10.1093/mnras/stt049). arXiv: [1301.1682](https://arxiv.org/abs/1301.1682) [[astro-ph](https://arxiv.org/abs/astro-ph).CO].
- Murray, S. G., C. Power, and A. S. G. Robotham (2013). « How well do we know the halo mass function? » In: *MNRAS* 434, pp. L61–L65. DOI: [10.1093/mnras/slt079](https://doi.org/10.1093/mnras/slt079). arXiv: [1306.5140](https://arxiv.org/abs/1306.5140).
- Muzzin, A. et al. (2013). « Discovery of a Rich Cluster at $z = 1.63$ Using the Rest-frame $1.6 \mu\text{m}$ “Stellar Bump Sequence” Method. » In: *ApJ* 767, 39, p. 39. DOI: [10.1088/0004-637X/767/1/39](https://doi.org/10.1088/0004-637X/767/1/39). arXiv: [1301.5905](https://arxiv.org/abs/1301.5905).
- Nagai, D., A. Vikhlinin, and A. V. Kravtsov (2007). « Testing X-Ray Measurements of Galaxy Clusters with Cosmological Simulations. » In: *ApJ* 655, pp. 98–108. DOI: [10.1086/509868](https://doi.org/10.1086/509868). eprint: [astro-ph/0609247](https://arxiv.org/abs/astro-ph/0609247).
- Navarro, J. F., C. S. Frenk, and S. D. M. White (1997). « A Universal Density Profile from Hierarchical Clustering. » In: *ApJ* 490, pp. 493–508. eprint: [astro-ph/9611107](https://arxiv.org/abs/astro-ph/9611107).

- Neto, A. F. et al. (2007). « The statistics of Λ CDM halo concentrations. » In: *MNRAS* 381, pp. 1450–1462. DOI: [10.1111/j.1365-2966.2007.12381.x](https://doi.org/10.1111/j.1365-2966.2007.12381.x). arXiv: [0706.2919](https://arxiv.org/abs/0706.2919).
- Newman, A. B. et al. (2014). « Spectroscopic Confirmation of the Rich $z = 1.80$ Galaxy Cluster JKCS 041 using the WFC3 Grism: Environmental Trends in the Ages and Structure of Quiescent Galaxies. » In: *ApJ* 788, 51, p. 51. DOI: [10.1088/0004-637X/788/1/51](https://doi.org/10.1088/0004-637X/788/1/51). arXiv: [1310.6754](https://arxiv.org/abs/1310.6754).
- Noirot, G. et al. (2016). « HST Grism Confirmation of Two $z = 2$ Structures from the Clusters around Radio-loud AGN (CARLA) Survey. » In: *ApJ* 830, 90, p. 90. DOI: [10.3847/0004-637X/830/2/90](https://doi.org/10.3847/0004-637X/830/2/90). arXiv: [1609.04162](https://arxiv.org/abs/1609.04162).
- Noirot, G. et al. (2018). « HST Grism Confirmation of 16 Structures at $1.4 < z < 2.8$ from the Clusters Around Radio-Loud AGN (CARLA) Survey. » In: *ArXiv e-prints*. arXiv: [1804.01500](https://arxiv.org/abs/1804.01500).
- Okabe, N. and G. P. Smith (2016). « LoCuSS: weak-lensing mass calibration of galaxy clusters. » In: *MNRAS* 461, pp. 3794–3821. DOI: [10.1093/mnras/stw1539](https://doi.org/10.1093/mnras/stw1539). arXiv: [1507.04493](https://arxiv.org/abs/1507.04493).
- Oke, J. B. and J. E. Gunn (1983). « Secondary standard stars for absolute spectrophotometry. » In: *ApJ* 266, pp. 713–717. DOI: [10.1086/160817](https://doi.org/10.1086/160817).
- Oke, J. B. et al. (1995). « The Keck Low-Resolution Imaging Spectrometer. » In: *PASP* 107, p. 375. DOI: [10.1086/133562](https://doi.org/10.1086/133562).
- Overzier, R. A. (2016). « The realm of the galaxy protoclusters. A review. » In: *A&A Rev.* 24, 14, p. 14. DOI: [10.1007/s00159-016-0100-3](https://doi.org/10.1007/s00159-016-0100-3). arXiv: [1610.05201](https://arxiv.org/abs/1610.05201).
- Padmanabhan, T. (1993). *Structure Formation in the Universe*, p. 499.
- Papovich, C. (2008). « The Angular Clustering of Distant Galaxy Clusters. » In: *ApJ* 676, 206–217, pp. 206–217. DOI: [10.1086/527665](https://doi.org/10.1086/527665). arXiv: [0712.1819](https://arxiv.org/abs/0712.1819).
- Papovich, C. et al. (2010). « A Spitzer-selected Galaxy Cluster at $z = 1.62$. » In: *ApJ* 716, pp. 1503–1513. DOI: [10.1088/0004-637X/716/2/1503](https://doi.org/10.1088/0004-637X/716/2/1503). arXiv: [1002.3158](https://arxiv.org/abs/1002.3158).
- Peebles, P. J. E. (1993). *Principles of Physical Cosmology*.
- Peng, C. Y. et al. (2002). « Detailed Structural Decomposition of Galaxy Images. » In: *AJ* 124, pp. 266–293. DOI: [10.1086/340952](https://doi.org/10.1086/340952). eprint: [astro-ph/0204182](https://arxiv.org/abs/astro-ph/0204182).
- Penna-Lima, M. et al. (2017). « Calibrating the Planck cluster mass scale with CLASH. » In: *A&A* 604, A89, A89. DOI: [10.1051/0004-6361/201629971](https://doi.org/10.1051/0004-6361/201629971). arXiv: [1608.05356](https://arxiv.org/abs/1608.05356).
- Penzias, A. A. and R. W. Wilson (1965). « A Measurement of Excess Antenna Temperature at 4080 Mc/s. » In: *ApJ* 142, pp. 419–421. DOI: [10.1086/148307](https://doi.org/10.1086/148307).
- Piffaretti, R. and R. Valdarnini (2008). « Total mass biases in X-ray galaxy clusters. » In: *A&A* 491, pp. 71–87. DOI: [10.1051/0004-6361:200809739](https://doi.org/10.1051/0004-6361:200809739). arXiv: [0808.1111](https://arxiv.org/abs/0808.1111).
- Pillepich, A., C. Porciani, and T. H. Reiprich (2012). « The X-ray cluster survey with eRosita: forecasts for cosmology, cluster physics and primordial non-Gaussianity. » In: *MNRAS* 422, pp. 44–69. DOI: [10.1111/j.1365-2966.2012.20443.x](https://doi.org/10.1111/j.1365-2966.2012.20443.x). arXiv: [1111.6587](https://arxiv.org/abs/1111.6587).

- Planck Collaboration et al. (2011a). « Planck early results. IX. XMM-Newton follow-up for validation of Planck cluster candidates. » In: *A&A* 536, A9, A9. DOI: [10.1051/0004-6361/201116460](https://doi.org/10.1051/0004-6361/201116460). arXiv: [1101.2025](https://arxiv.org/abs/1101.2025).
- Planck Collaboration et al. (2011b). « Planck early results. VIII. The all-sky early Sunyaev-Zeldovich cluster sample. » In: *A&A* 536, A8, A8. DOI: [10.1051/0004-6361/201116459](https://doi.org/10.1051/0004-6361/201116459). arXiv: [1101.2024](https://arxiv.org/abs/1101.2024).
- Planck Collaboration et al. (2012). « Planck intermediate results. I. Further validation of new Planck clusters with XMM-Newton. » In: *A&A* 543, A102, A102. DOI: [10.1051/0004-6361/201118731](https://doi.org/10.1051/0004-6361/201118731). arXiv: [1112.5595](https://arxiv.org/abs/1112.5595).
- Planck Collaboration et al. (2013). « Planck intermediate results. IV. The XMM-Newton validation programme for new Planck galaxy clusters. » In: *A&A* 550, A130, A130. DOI: [10.1051/0004-6361/201219519](https://doi.org/10.1051/0004-6361/201219519). arXiv: [1205.3376](https://arxiv.org/abs/1205.3376).
- Planck Collaboration et al. (2014a). « Planck 2013 results. XX. Cosmology from Sunyaev-Zeldovich cluster counts. » In: *A&A* 571, A20, A20. DOI: [10.1051/0004-6361/201321521](https://doi.org/10.1051/0004-6361/201321521). arXiv: [1303.5080](https://arxiv.org/abs/1303.5080).
- Planck Collaboration et al. (2014b). « Planck 2013 results. XXIX. The Planck catalogue of Sunyaev-Zeldovich sources. » In: *A&A* 571, A29, A29. DOI: [10.1051/0004-6361/201321523](https://doi.org/10.1051/0004-6361/201321523). arXiv: [1303.5089](https://arxiv.org/abs/1303.5089).
- Planck Collaboration et al. (2015a). « Planck 2013 results. XXXII. The updated Planck catalogue of Sunyaev-Zeldovich sources. » In: *A&A* 581, A14, A14. DOI: [10.1051/0004-6361/201525787](https://doi.org/10.1051/0004-6361/201525787). arXiv: [1502.00543](https://arxiv.org/abs/1502.00543).
- Planck Collaboration et al. (2015b). « Planck 2015 results. XXVII. The Second Planck Catalogue of Sunyaev-Zeldovich Sources. » In: *ArXiv e-prints*. arXiv: [1502.01598](https://arxiv.org/abs/1502.01598).
- Planck Collaboration et al. (2015c). « Planck intermediate results. XXVI. Optical identification and redshifts of Planck clusters with the RTT150 telescope. » In: *A&A* 582, A29, A29. DOI: [10.1051/0004-6361/201424674](https://doi.org/10.1051/0004-6361/201424674). arXiv: [1407.6663](https://arxiv.org/abs/1407.6663).
- Planck Collaboration et al. (2016a). « Planck 2015 results. XIII. Cosmological parameters. » In: *A&A* 594, A13, A13. DOI: [10.1051/0004-6361/201525830](https://doi.org/10.1051/0004-6361/201525830). arXiv: [1502.01589](https://arxiv.org/abs/1502.01589).
- Planck Collaboration et al. (2016b). « Planck 2015 results. XXIV. Cosmology from Sunyaev-Zeldovich cluster counts. » In: *A&A* 594, A24, A24. DOI: [10.1051/0004-6361/201525833](https://doi.org/10.1051/0004-6361/201525833). arXiv: [1502.01597](https://arxiv.org/abs/1502.01597).
- Planck Collaboration et al. (2016c). « Planck intermediate results. XXXVI. Optical identification and redshifts of Planck SZ sources with telescopes at the Canary Islands observatories. » In: *A&A* 586, A139, A139. DOI: [10.1051/0004-6361/201526345](https://doi.org/10.1051/0004-6361/201526345). arXiv: [1504.04583](https://arxiv.org/abs/1504.04583).
- Postman, M. et al. (2012). « The Cluster Lensing and Supernova Survey with Hubble: An Overview. » In: *ApJS* 199, 25, p. 25. DOI: [10.1088/0067-0049/199/2/25](https://doi.org/10.1088/0067-0049/199/2/25). arXiv: [1106.3328](https://arxiv.org/abs/1106.3328).
- Prada, F. et al. (2012). « Halo concentrations in the standard Λ cold dark matter cosmology. » In: *MNRAS* 423, pp. 3018–3030. DOI: [10.1111/j.1365-2966.2012.21007.x](https://doi.org/10.1111/j.1365-2966.2012.21007.x). arXiv: [1104.5130](https://arxiv.org/abs/1104.5130).
- Press, W. H. and P. Schechter (1974). « Formation of Galaxies and Clusters of Galaxies by Self-Similar Gravitational Condensation. » In: *ApJ* 187, pp. 425–438. DOI: [10.1086/152650](https://doi.org/10.1086/152650).

- Rasia, E. et al. (2006). « Systematics in the X-ray cluster mass estimators. » In: *MNRAS* 369, pp. 2013–2024. DOI: [10.1111/j.1365-2966.2006.10466.x](https://doi.org/10.1111/j.1365-2966.2006.10466.x). eprint: [astro-ph/0602434](https://arxiv.org/abs/astro-ph/0602434).
- Rasia, E. et al. (2012). « Lensing and x-ray mass estimates of clusters (simulations). » In: *New Journal of Physics* 14.5, 055018, p. 055018. DOI: [10.1088/1367-2630/14/5/055018](https://doi.org/10.1088/1367-2630/14/5/055018). arXiv: [1201.1569](https://arxiv.org/abs/1201.1569).
- Rasia, E. et al. (2014). « Temperature Structure of the Intracluster Medium from Smoothed-particle Hydrodynamics and Adaptive-mesh Refinement Simulations. » In: *ApJ* 791, 96, p. 96. DOI: [10.1088/0004-637X/791/2/96](https://doi.org/10.1088/0004-637X/791/2/96).
- Reiprich, T. H. and H. Böhringer (2002). « The Mass Function of an X-Ray Flux-limited Sample of Galaxy Clusters. » In: *ApJ* 567, pp. 716–740. DOI: [10.1086/338753](https://doi.org/10.1086/338753). eprint: [astro-ph/0111285](https://arxiv.org/abs/astro-ph/0111285).
- Rieke, G. H. et al. (2004). « The Multiband Imaging Photometer for Spitzer (MIPS). » In: *ApJS* 154, pp. 25–29. DOI: [10.1086/422717](https://doi.org/10.1086/422717).
- Rines, K. J. et al. (2016). « HeCS-SZ: The Hectospec Survey of Sunyaev-Zeldovich-selected Clusters. » In: *ApJ* 819, 63, p. 63. DOI: [10.3847/0004-637X/819/1/63](https://doi.org/10.3847/0004-637X/819/1/63). arXiv: [1507.08289](https://arxiv.org/abs/1507.08289).
- Rines, K. and A. Diaferio (2006). « CIRS: Cluster Infall Regions in the Sloan Digital Sky Survey. I. Infall Patterns and Mass Profiles. » In: *AJ* 132, pp. 1275–1297. DOI: [10.1086/506017](https://doi.org/10.1086/506017). eprint: [astro-ph/0602032](https://arxiv.org/abs/astro-ph/0602032).
- Rines, K. et al. (2013). « Measuring the Ultimate Halo Mass of Galaxy Clusters: Redshifts and Mass Profiles from the Hectospec Cluster Survey (HeCS). » In: *ApJ* 767, 15, p. 15. DOI: [10.1088/0004-637X/767/1/15](https://doi.org/10.1088/0004-637X/767/1/15). arXiv: [1209.3786](https://arxiv.org/abs/1209.3786).
- Rosati, P., S. Borgani, and C. Norman (2002). « The Evolution of X-ray Clusters of Galaxies. » In: *ARA&A* 40, pp. 539–577. DOI: [10.1146/annurev.astro.40.120401.150547](https://doi.org/10.1146/annurev.astro.40.120401.150547). eprint: [astro-ph/0209035](https://arxiv.org/abs/astro-ph/0209035).
- Rosati, P. et al. (2014). « CLASH-VLT: A VIMOS Large Programme to Map the Dark Matter Mass Distribution in Galaxy Clusters and Probe Distant Lensed Galaxies. » In: *The Messenger* 158, pp. 48–53.
- Rozo, E. et al. (2014a). « A comparative study of local galaxy clusters - I. Derived X-ray observables. » In: *MNRAS* 438, pp. 49–61. DOI: [10.1093/mnras/stt2091](https://doi.org/10.1093/mnras/stt2091). arXiv: [1204.6301](https://arxiv.org/abs/1204.6301).
- Rozo, E. et al. (2014b). « A comparative study of local galaxy clusters - II. X-ray and SZ scaling relations. » In: *MNRAS* 438, pp. 62–77. DOI: [10.1093/mnras/stt2160](https://doi.org/10.1093/mnras/stt2160). arXiv: [1204.6292](https://arxiv.org/abs/1204.6292).
- Rozo, E. et al. (2014c). « Closing the loop: a self-consistent model of optical, X-ray and Sunyaev-Zel'dovich scaling relations for clusters of Galaxies. » In: *MNRAS* 438, pp. 78–96. DOI: [10.1093/mnras/stt2161](https://doi.org/10.1093/mnras/stt2161). arXiv: [1204.6305](https://arxiv.org/abs/1204.6305).
- Ruel, J. et al. (2014). « Optical Spectroscopy and Velocity Dispersions of Galaxy Clusters from the SPT-SZ Survey. » In: *ApJ* 792, 45, p. 45. DOI: [10.1088/0004-637X/792/1/45](https://doi.org/10.1088/0004-637X/792/1/45). arXiv: [1311.4953](https://arxiv.org/abs/1311.4953).
- Rykoff, E. S. et al. (2014). « redMaPPer. I. Algorithm and SDSS DR8 Catalog. » In: *ApJ* 785, 104, p. 104. DOI: [10.1088/0004-637X/785/2/104](https://doi.org/10.1088/0004-637X/785/2/104). arXiv: [1303.3562](https://arxiv.org/abs/1303.3562).
- Santos, J. S. et al. (2011). « Discovery of a massive X-ray luminous galaxy cluster at $z = 1.579$. » In: *A&A* 531, L15, p. L15. DOI: [10.1051/0004-6361/201117190](https://doi.org/10.1051/0004-6361/201117190). arXiv: [1105.5877](https://arxiv.org/abs/1105.5877).

- Santos, J. S. et al. (2015). « The reversal of the SF-density relation in a massive, X-ray-selected galaxy cluster at $z = 1.58$: results from Herschel. » In: *MNRAS* 447, pp. L65–L69. DOI: [10.1093/mnrasl/slu180](https://doi.org/10.1093/mnrasl/slu180). arXiv: [1412.5188](https://arxiv.org/abs/1412.5188).
- Sarazin, C. L. (1988). « Book-Review - X-Ray Emission from Clusters of Galaxies. » In: *Journal of the British Astronomical Association* 98, p. 212.
- Sartoris, B. et al. (2016). « Next generation cosmology: constraints from the Euclid galaxy cluster survey. » In: *MNRAS* 459, pp. 1764–1780. DOI: [10.1093/mnras/stw630](https://doi.org/10.1093/mnras/stw630). arXiv: [1505.02165](https://arxiv.org/abs/1505.02165).
- Schawinski, K. et al. (2014). « The green valley is a red herring: Galaxy Zoo reveals two evolutionary pathways towards quenching of star formation in early- and late-type galaxies. » In: *MNRAS* 440, pp. 889–907. DOI: [10.1093/mnras/stu327](https://doi.org/10.1093/mnras/stu327). arXiv: [1402.4814](https://arxiv.org/abs/1402.4814).
- Schirmer, M. (2013). « THELI: Convenient Reduction of Optical, Near-infrared, and Mid-infrared Imaging Data. » In: *ApJS* 209, 21, p. 21. DOI: [10.1088/0067-0049/209/2/21](https://doi.org/10.1088/0067-0049/209/2/21). arXiv: [1308.4989](https://arxiv.org/abs/1308.4989) [astro-ph.IM].
- Schirmer, M. et al. (2003). « GaBoDS: The Garching-Bonn Deep Survey. I. Anatomy of galaxy clusters in the background of NGC 300. » In: *A&A* 407, pp. 869–888. DOI: [10.1051/0004-6361:20031026](https://doi.org/10.1051/0004-6361:20031026). eprint: [astro-ph/0305172](https://arxiv.org/abs/astro-ph/0305172).
- Schmidt, R. W. and S. W. Allen (2007). « The dark matter haloes of massive, relaxed galaxy clusters observed with Chandra. » In: *MNRAS* 379, pp. 209–221. DOI: [10.1111/j.1365-2966.2007.11928.x](https://doi.org/10.1111/j.1365-2966.2007.11928.x). eprint: [astro-ph/0610038](https://arxiv.org/abs/astro-ph/0610038).
- Seigar, M. S. (2015). *Dark Matter in the Universe*. DOI: [10.1088/978-1-6817-4118-5](https://doi.org/10.1088/978-1-6817-4118-5).
- Sekiguchi, K. and SXDS Team (2004). « Subaru/XMM-Newton Deep Survey (SXDS). » In: *American Astronomical Society Meeting Abstracts*. Vol. 36. Bulletin of the American Astronomical Society, p. 1478.
- Sereno, M. and G. Covone (2013). « The mass-concentration relation in massive galaxy clusters at redshift 1. » In: *MNRAS* 434, pp. 878–887. DOI: [10.1093/mnras/stt1086](https://doi.org/10.1093/mnras/stt1086). arXiv: [1306.6096](https://arxiv.org/abs/1306.6096).
- Sersic, J. L. (1968). *Atlas de Galaxias Australes*.
- Shapiro, S. S. and M. B. Wilk (1965). « An Analysis of Variance Test for Normality (Complete Samples). » In: *Biometrika* 52, pp. 591–611.
- Sifón, C. et al. (2013). « The Atacama Cosmology Telescope: Dynamical Masses and Scaling Relations for a Sample of Massive Sunyaev-Zel'dovich Effect Selected Galaxy Clusters. » In: *ApJ* 772, 25, p. 25. DOI: [10.1088/0004-637x/772/1/25](https://doi.org/10.1088/0004-637x/772/1/25). arXiv: [1201.0991](https://arxiv.org/abs/1201.0991).
- Sifón, C. et al. (2016). « The Atacama Cosmology Telescope: dynamical masses for 44 SZ-selected galaxy clusters over 755 square degrees. » In: *MNRAS* 461, pp. 248–270. DOI: [10.1093/mnras/stw1284](https://doi.org/10.1093/mnras/stw1284). arXiv: [1512.00910](https://arxiv.org/abs/1512.00910).
- Simet, M. et al. (2015). « Weak lensing calibration of mass bias in the REFLEX+BCS X-ray galaxy cluster catalogue. » In: *ArXiv e-prints*. arXiv: [1502.01024](https://arxiv.org/abs/1502.01024).
- Simet, M. et al. (2016). « Weak Lensing Measurement of the Mass–Richness Relation of SDSS redMaPPer Clusters. » In: *ArXiv e-prints*. arXiv: [1603.06953](https://arxiv.org/abs/1603.06953).

- Skelton, R. E. et al. (2014). « 3D-HST WFC3-selected Photometric Catalogs in the Five CANDELS/3D-HST Fields: Photometry, Photometric Redshifts, and Stellar Masses. » In: *ApJS* 214, 24, p. 24. DOI: [10.1088/0067-0049/214/2/24](https://doi.org/10.1088/0067-0049/214/2/24). arXiv: [1403.3689](https://arxiv.org/abs/1403.3689).
- Smith, G. P. et al. (2016). « LoCuSS: Testing hydrostatic equilibrium in galaxy clusters. » In: *MNRAS* 456, pp. L74–L78. DOI: [10.1093/mnrasl/s1v175](https://doi.org/10.1093/mnrasl/s1v175). arXiv: [1511.01919](https://arxiv.org/abs/1511.01919).
- Sorba, R. and M. Sawicki (2010). « Using the 1.6 μm Bump to Study Rest-frame Near-infrared-selected Galaxies at Redshift 2. » In: *ApJ* 721, pp. 1056–1078. DOI: [10.1088/0004-637X/721/2/1056](https://doi.org/10.1088/0004-637X/721/2/1056). arXiv: [1007.4951](https://arxiv.org/abs/1007.4951).
- Stanek, R. et al. (2010). « Massive Halos in Millennium Gas Simulations: Multivariate Scaling Relations. » In: *ApJ* 715, pp. 1508–1523. DOI: [10.1088/0004-637X/715/2/1508](https://doi.org/10.1088/0004-637X/715/2/1508). arXiv: [0910.1599](https://arxiv.org/abs/0910.1599).
- Stanford, S. A. et al. (1997). « An IR-Selected Galaxy Cluster at $\zeta=1.27$. » In: *AJ* 114, p. 2232. DOI: [10.1086/118643](https://doi.org/10.1086/118643). eprint: [astro-ph/9709057](https://arxiv.org/abs/astro-ph/9709057).
- Stanford, S. A. et al. (2006). « The XMM Cluster Survey: A Massive Galaxy Cluster at $z = 1.45$. » In: *ApJ* 646, pp. L13–L16. DOI: [10.1086/506449](https://doi.org/10.1086/506449).
- Stanford, S. A. et al. (2012). « IDCS J1426.5+3508: Discovery of a Massive, Infrared-selected Galaxy Cluster at $z = 1.75$. » In: *ApJ* 753, 164, p. 164. DOI: [10.1088/0004-637X/753/2/164](https://doi.org/10.1088/0004-637X/753/2/164). arXiv: [1205.3786](https://arxiv.org/abs/1205.3786).
- Steigman, G. (2006). « Primordial Nucleosynthesis: Successes and Challenges. » In: *International Journal of Modern Physics E* 15, pp. 1–35. DOI: [10.1142/S0218301306004028](https://doi.org/10.1142/S0218301306004028). eprint: [astro-ph/0511534](https://arxiv.org/abs/astro-ph/0511534).
- Strazzullo, V. et al. (2013). « Galaxy Evolution in Overdense Environments at High Redshift: Passive Early-type Galaxies in a Cluster at $z \sim 2$. » In: *ApJ* 772, 118, p. 118. DOI: [10.1088/0004-637X/772/2/118](https://doi.org/10.1088/0004-637X/772/2/118). arXiv: [1305.3577](https://arxiv.org/abs/1305.3577).
- Streblyanska, A. et al. (2018). « Characterization of a subsample of the Planck SZ source cluster catalogues using optical SDSS DR12 data. » In: *ArXiv e-prints*. arXiv: [1804.01356](https://arxiv.org/abs/1804.01356).
- Sunyaev, R. A. and Y. B. Zeldovich (1970). « Small-Scale Fluctuations of Relic Radiation. » In: *Ap&SS* 7, pp. 3–19. DOI: [10.1007/BF00653471](https://doi.org/10.1007/BF00653471).
- Sunyaev, R. A. and Y. B. Zeldovich (1972). « Formation of Clusters of Galaxies; Protocluster Fragmentation and Intergalactic Gas Heating. » In: *A&A* 20, p. 189.
- Tadaki, K.-i. et al. (2012). « A large-scale structure traced by [O II] emitters hosting a distant cluster at $z=1.62$. » In: *MNRAS* 423, pp. 2617–2626. DOI: [10.1111/j.1365-2966.2012.21063.x](https://doi.org/10.1111/j.1365-2966.2012.21063.x). arXiv: [1204.1165](https://arxiv.org/abs/1204.1165).
- Tanaka, M., A. Finoguenov, and Y. Ueda (2010). « A Spectroscopically Confirmed X-ray Cluster at $z = 1.62$ with a Possible Companion in the Subaru/XMM-Newton Deep Field. » In: *ApJ* 716, pp. L152–L156. DOI: [10.1088/2041-8205/716/2/L152](https://doi.org/10.1088/2041-8205/716/2/L152). arXiv: [1004.3606](https://arxiv.org/abs/1004.3606).
- Thanjavur, K., J. Willis, and D. Crampton (2009). « K2: A New Method for the Detection of Galaxy Clusters Based on Canada-France-Hawaii Telescope Legacy Survey Multicolor Images. » In: *ApJ* 706, pp. 571–591. DOI: [10.1088/0004-637X/706/1/571](https://doi.org/10.1088/0004-637X/706/1/571). arXiv: [0910.4358](https://arxiv.org/abs/0910.4358).
- Tinker, J. et al. (2008). « Toward a Halo Mass Function for Precision Cosmology: The Limits of Universality. » In: *ApJ* 688, pp. 709–728. DOI: [10.1086/591439](https://doi.org/10.1086/591439).

- Tran, K.-V. H. et al. (2010). « Reversal of Fortune: Confirmation of an Increasing Star Formation-Density Relation in a Cluster at $z = 1.62$. » In: *ApJ* 719, pp. L126–L129. DOI: [10.1088/2041-8205/719/2/L126](https://doi.org/10.1088/2041-8205/719/2/L126). arXiv: [1005.5126](https://arxiv.org/abs/1005.5126).
- Truemper, J. (1993). « ROSAT - A new look at the X-ray sky. » In: *Science* 260, pp. 1769–1771. DOI: [10.1126/science.260.5115.1769](https://doi.org/10.1126/science.260.5115.1769).
- Umetsu, K. et al. (2016). « CLASH: Joint Analysis of Strong-lensing, Weak-lensing Shear, and Magnification Data for 20 Galaxy Clusters. » In: *ApJ* 821, 116, p. 116. DOI: [10.3847/0004-637X/821/2/116](https://doi.org/10.3847/0004-637X/821/2/116). arXiv: [1507.04385](https://arxiv.org/abs/1507.04385).
- Urry, C. M. and P. Padovani (1995). « Unified Schemes for Radio-Loud Active Galactic Nuclei. » In: *PASP* 107, p. 803. DOI: [10.1086/133630](https://doi.org/10.1086/133630). eprint: [astro-ph/9506063](https://arxiv.org/abs/astro-ph/9506063).
- Valentino, F. et al. (2015). « Metal Deficiency in Cluster Star-Forming Galaxies At $Z = 2$. » In: *ApJ* 801, 132, p. 132. DOI: [10.1088/0004-637X/801/2/132](https://doi.org/10.1088/0004-637X/801/2/132). arXiv: [1410.1437](https://arxiv.org/abs/1410.1437).
- Vikhlinin, A. et al. (2009). « Chandra Cluster Cosmology Project III: Cosmological Parameter Constraints. » In: *ApJ* 692, pp. 1060–1074. DOI: [10.1088/0004-637X/692/2/1060](https://doi.org/10.1088/0004-637X/692/2/1060). arXiv: [0812.2720](https://arxiv.org/abs/0812.2720).
- Voit, G. M. (2005). « Tracing cosmic evolution with clusters of galaxies. » In: *Reviews of Modern Physics* 77, pp. 207–258. DOI: [10.1103/RevModPhys.77.207](https://doi.org/10.1103/RevModPhys.77.207). eprint: [astro-ph/0410173](https://arxiv.org/abs/astro-ph/0410173).
- Wang, T. et al. (2016). « Discovery of a Galaxy Cluster with a Violently Starbursting Core at $z = 2.506$. » In: *ApJ* 828, 56, p. 56. DOI: [10.3847/0004-637X/828/1/56](https://doi.org/10.3847/0004-637X/828/1/56). arXiv: [1604.07404](https://arxiv.org/abs/1604.07404).
- Webb, T. M. A. et al. (2015). « The Star Formation History of BCGs to $z = 1.8$ from the SpARCS/SWIRE Survey: Evidence for Significant In Situ Star Formation at High Redshift. » In: *ApJ* 814, 96, p. 96. DOI: [10.1088/0004-637X/814/2/96](https://doi.org/10.1088/0004-637X/814/2/96). arXiv: [1508.07302](https://arxiv.org/abs/1508.07302).
- Weinberg, D. H. et al. (2013). « Observational probes of cosmic acceleration. » In: 530, pp. 87–255. DOI: [10.1016/j.physrep.2013.05.001](https://doi.org/10.1016/j.physrep.2013.05.001). arXiv: [1201.2434](https://arxiv.org/abs/1201.2434).
- Wen, Z. L., J. L. Han, and F. S. Liu (2012). « A Catalog of 132,684 Clusters of Galaxies Identified from Sloan Digital Sky Survey III. » In: *ApJS* 199, 34, p. 34. DOI: [10.1088/0067-0049/199/2/34](https://doi.org/10.1088/0067-0049/199/2/34). arXiv: [1202.6424](https://arxiv.org/abs/1202.6424) [[astro-ph.CO](https://arxiv.org/abs/astro-ph)].
- Whitaker, K. E. et al. (2014). « Constraining the Low-mass Slope of the Star Formation Sequence at $0.5 < z < 2.5$. » In: *ApJ* 795, 104, p. 104. DOI: [10.1088/0004-637X/795/2/104](https://doi.org/10.1088/0004-637X/795/2/104). arXiv: [1407.1843](https://arxiv.org/abs/1407.1843).
- White, M., J. D. Cohn, and R. Smit (2010). « Cluster galaxy dynamics and the effects of large-scale environment. » In: *MNRAS* 408, pp. 1818–1834. DOI: [10.1111/j.1365-2966.2010.17248.x](https://doi.org/10.1111/j.1365-2966.2010.17248.x). arXiv: [1005.3022](https://arxiv.org/abs/1005.3022).
- White, S. D. M. and M. J. Rees (1978). « Core condensation in heavy halos - A two-stage theory for galaxy formation and clustering. » In: *MNRAS* 183, pp. 341–358. DOI: [10.1093/mnras/183.3.341](https://doi.org/10.1093/mnras/183.3.341).
- Williams, M. J., M. Bureau, and M. Cappellari (2010). « The Tully-Fisher relations of early-type spiral and S0 galaxies. » In: *MNRAS* 409, pp. 1330–1346. DOI: [10.1111/j.1365-2966.2010.17406.x](https://doi.org/10.1111/j.1365-2966.2010.17406.x). arXiv: [1007.4072](https://arxiv.org/abs/1007.4072).

- Williams, R. J. et al. (2009). « Detection of Quiescent Galaxies in a Bicolor Sequence from $Z = 0-2$. » In: *ApJ* 691, pp. 1879–1895. DOI: [10.1088/0004-637X/691/2/1879](https://doi.org/10.1088/0004-637X/691/2/1879). arXiv: 0806.0625.
- Wittman, D. et al. (2001). « Discovery of a Galaxy Cluster via Weak Lensing. » In: *ApJ* 557, pp. L89–L92. DOI: [10.1086/323173](https://doi.org/10.1086/323173). eprint: [astro-ph/0104094](https://arxiv.org/abs/astro-ph/0104094).
- Wittman, D. et al. (2003). « Weak-Lensing Discovery and Tomography of a Cluster at $z = 0.68$. » In: *ApJ* 597, pp. 218–224. DOI: [10.1086/378344](https://doi.org/10.1086/378344). eprint: [astro-ph/0210120](https://arxiv.org/abs/astro-ph/0210120).
- Woody, D. et al. (2012). « The CCAT 25m diameter submillimeter-wave telescope. » In: *Ground-based and Airborne Telescopes IV*. Vol. 8444. Proc. SPIE, p. 84442M. DOI: [10.1117/12.925229](https://doi.org/10.1117/12.925229).
- Wu, H.-Y. et al. (2013). « Virial scaling of galaxies in clusters: bright to faint is cool to hot. » In: *MNRAS* 436, pp. 460–469. DOI: [10.1093/mnras/stt1582](https://doi.org/10.1093/mnras/stt1582). arXiv: 1307.0011 [[astro-ph.CO](https://arxiv.org/abs/astro-ph)].
- Wuyts, S. et al. (2007). « What Do We Learn from IRAC Observations of Galaxies at $2 < z < 3.5$? » In: *ApJ* 655, pp. 51–65. DOI: [10.1086/509708](https://doi.org/10.1086/509708). eprint: [astro-ph/0609548](https://arxiv.org/abs/astro-ph/0609548).
- Wylezalek, D. et al. (2013). « Galaxy Clusters around Radio-loud Active Galactic Nuclei at $1.3 < z < 3.2$ as Seen by Spitzer. » In: *ApJ* 769, 79, p. 79. DOI: [10.1088/0004-637X/769/1/79](https://doi.org/10.1088/0004-637X/769/1/79). arXiv: 1304.0770.
- Wylezalek, D. et al. (2014). « The Galaxy Cluster Mid-infrared Luminosity Function at $1.3 < z < 3.2$. » In: *ApJ* 786, 17, p. 17. DOI: [10.1088/0004-637X/786/1/17](https://doi.org/10.1088/0004-637X/786/1/17). arXiv: 1403.2390.
- Yahil, A. and N. V. Vidal (1977). « The Velocity Distribution of Galaxies in Clusters. » In: *ApJ* 214, pp. 347–350. DOI: [10.1086/155257](https://doi.org/10.1086/155257).
- Yamada, T. et al. (2005). « The Number Density of Old Passively Evolving Galaxies at $z=1$ in the Subaru/XMM-Newton Deep Survey Field. » In: *ApJ* 634, pp. 861–878. DOI: [10.1086/496954](https://doi.org/10.1086/496954). eprint: [astro-ph/0508594](https://arxiv.org/abs/astro-ph/0508594).
- Yang, X. et al. (2011). « Cosmological information in weak lensing peaks. » In: *Phys. Rev. D* 84.4, 043529, p. 043529. DOI: [10.1103/PhysRevD.84.043529](https://doi.org/10.1103/PhysRevD.84.043529). arXiv: 1109.6333.
- York, D. G. et al. (2000). « The Sloan Digital Sky Survey: Technical Summary. » In: *AJ* 120, pp. 1579–1587. DOI: [10.1086/301513](https://doi.org/10.1086/301513). eprint: [astro-ph/0006396](https://arxiv.org/abs/astro-ph/0006396).
- Zaldarriaga, M. and U. Seljak (1999). « Reconstructing projected matter density power spectrum from cosmic microwave background. » In: *Phys. Rev. D* 59.12, 123507, p. 123507. DOI: [10.1103/PhysRevD.59.123507](https://doi.org/10.1103/PhysRevD.59.123507). eprint: [astro-ph/9810257](https://arxiv.org/abs/astro-ph/9810257).
- Zeimann, G. R. et al. (2012). « IDCS J1433.2+3306: An Infrared-selected Galaxy Cluster at $z = 1.89$. » In: *ApJ* 756, 115, p. 115. DOI: [10.1088/0004-637X/756/2/115](https://doi.org/10.1088/0004-637X/756/2/115). arXiv: 1207.4793.
- Zhao, G.-B. et al. (2016). « The extended Baryon Oscillation Spectroscopic Survey: a cosmological forecast. » In: *MNRAS* 457, pp. 2377–2390. DOI: [10.1093/mnras/stw135](https://doi.org/10.1093/mnras/stw135). arXiv: 1510.08216.
- Ziparo, F. et al. (2015). « LoCuSS: Exploring the selection of faint blue background galaxies for cluster weak-lensing. » In: *ArXiv e-prints*. arXiv: 1507.04376.

- Zwicky, F. (1937). « On the Masses of Nebulae and of Clusters of Nebulae. » In: *ApJ* 86, p. 217. DOI: [10.1086/143864](https://doi.org/10.1086/143864).
- de Haan, T. et al. (2016). « Cosmological Constraints from Galaxy Clusters in the 2500 square-degree SPT-SZ Survey. » In: *ArXiv e-prints*. arXiv: [1603.06522](https://arxiv.org/abs/1603.06522).
- de Jong, J. T. A. et al. (2013). « The Kilo-Degree Survey. » In: *The Messenger* 154, pp. 44–46.
- de Vaucouleurs, G. (1948). « Recherches sur les Nebuleuses Extragalactiques. » In: *Annales d'Astrophysique* 11, p. 247.
- van Weeren, R. J. et al. (2014). « The Discovery of a Radio Halo in PLCK G147.3-16.6 at $z = 0.65$. » In: *ApJ* 781, L32, p. L32. DOI: [10.1088/2041-8205/781/2/L32](https://doi.org/10.1088/2041-8205/781/2/L32). arXiv: [1401.6175](https://arxiv.org/abs/1401.6175) [[astro-ph.CO](https://arxiv.org/abs/1401.6175)].
- von der Linden, A. et al. (2014a). « Robust weak-lensing mass calibration of Planck galaxy clusters. » In: *MNRAS* 443, pp. 1973–1978. DOI: [10.1093/mnras/stu1423](https://doi.org/10.1093/mnras/stu1423). arXiv: [1402.2670](https://arxiv.org/abs/1402.2670).
- von der Linden, A. et al. (2014b). « Robust weak-lensing mass calibration of Planck galaxy clusters. » In: *MNRAS* 443, pp. 1973–1978. DOI: [10.1093/mnras/stu1423](https://doi.org/10.1093/mnras/stu1423). arXiv: [1402.2670](https://arxiv.org/abs/1402.2670).

RÉSUMÉ

Cette thèse porte sur le rôle des amas de galaxies dans la cosmologie et l'évolution des galaxies. J'utilise des observations photométriques et spectroscopiques multi-longueur d'onde (optiques, mm, proche/moyen-IR) que j'analyse avec des méthodes statistiques. Pour un échantillon d'amas détectés par le satellite Planck et ré-observés avec le télescope optique Gemini, j'étudie la dynamique des galaxies dans les amas afin de déterminer leur masse et de comprendre les erreurs systématiques sur ces estimations, d'une importance cruciale dans la cosmologie à l'heure actuelle.

Dans le cadre de la collaboration CARLA (Clusters Around Radio Loud AGN), j'étudie les populations stellaires des galaxies dans les amas et les proto-amas dans leurs premières phases d'assemblage ($z > 1.4$), afin d'étudier la suppression de la formation des étoiles et le rôle de l'environnement sur l'évolution des galaxies.

MOTS CLÉS

Galaxies, amas de galaxies, observations, evolution de galaxies, cosmologie.

ABSTRACT

This thesis focuses on the role of galaxy clusters in cosmology and galaxy evolution. I use multi-wavelength photometric and spectroscopic observations (optical, mm, near/mid-IR) which I analyse with statistical methods.

For a sample of clusters detected by the Planck satellite and re-observed with the Gemini optical telescope, I have studied the dynamics of member galaxies to probe their mass and understand possible systematics affecting such estimates, of crucial importance in cluster cosmology at present.

Within the CARLA (Clusters Around Radio Loud AGN) collaboration, I examine morphology and stellar populations of galaxies in clusters and proto-clusters in their first assembly phases ($z > 1.4$), with the aim of shedding light on the quenching of star formation and the role of the environment on galaxy evolution.

KEYWORDS

Galaxies, galaxy clusters, observations, galaxy evolution, cosmology.

